

UNIVERSITY OF
BIRMINGHAM

ULTRASONIC-ASSISTED MILLING OF ADVANCED TITANIUM ALLOYS

By

YIMING ZHANG

A thesis submitted to the University of Birmingham for the degree of

DOCTOR OF PHILOSOPHY

Department of Mechanical Engineering

School of Engineering

College of Engineering and Physical Sciences

The University of Birmingham

August 2024

UNIVERSITY OF
BIRMINGHAM

University of Birmingham Research Archive

e-theses repository

This unpublished thesis/dissertation is copyright of the author and/or third parties. The intellectual property rights of the author or third parties in respect of this work are as defined by The Copyright Designs and Patents Act 1988 or as modified by any successor legislation.

Any use made of information contained in this thesis/dissertation must be in accordance with that legislation and must be properly acknowledged. Further distribution or reproduction in any format is prohibited without the permission of the copyright holder.

SYNOPSIS

Titanium alloys, known for their outstanding mechanical properties, are highly utilised in cross-generation aeroengine applications. Amongst these alloys, γ-TiAl has been developed as a potential substitute for nickel-based superalloys, specifically components used in the hot section of gas turbine engines due to its superior lightweight characteristics. However, the extremely poor ductility of γ-TiAl at room temperature presents a major bottleneck, restricting its broader engineering applications. Researchers have extensively explored the machinability of γ-TiAl, with most investigations concentrating on conventional processing methods. The primary challenges in cutting γ-TiAl include severe tool wear/low tool life, high cutting forces, and poor machined surface integrity. Therefore, further research is essential to develop innovative methods for the efficient and high-quality processing of γ-TiAl. One promising approach is ultrasonic-assisted cutting, a hybrid manufacturing process well-suited for hard and brittle materials. However, research on ultrasonic-assisted cutting of γ-TiAl remains scarce, while theoretical investigations into ball-end ultrasonic-assisted milling, particularly in developing models for cutting force and tool wear, require more in-depth study.

Following a comprehensive literature review covering the properties of aerospace metallic materials, machinability, tool wear and failure, workpiece surface integrity, ultrasonic-assisted cutting technology and theoretical modelling, particularly for milling titanium alloys, two principal phases of experimental work (Phase 1 and 2) were conducted. These were aimed to investigate the performance of the ultrasonic system, influence of cutting parameters on machinability of γ-TiAl, associated tool wear mechanisms/failure and the effect of ultrasonic vibration on cutting γ-TiAl. Phase 1 involved preliminary trials to evaluate the stability of the integrated ultrasonic system and identify significant cutting parameters. Initially, the influence of tool parameters on the ultrasonic system was systematically studied to determine the ideal tool size and clamping method for achieving the maximum vibration amplitude. The results indicated that lightweight tools with small size or low-weight materials consistently achieved the largest amplitude when the overhang was about 70% of the overall tool length. For example, an amplitude of 7.6 μm was recorded for high-speed steel (HSS) tools while tungsten carbide (WC) cutters of the same size and geometry only reached 3.5 μm. Similarly, amplitudes of up to 8.0 μm were produced using Ø4 mm (12.13 g) tools compared to 2.4 μm with Ø6 mm (25.96 g) tools. The existence of an operating threshold for the ultrasonic system was also discovered,

as when cutting forces exceeded a critical value of approximately 90 N, the ultrasonic actuation of the tool was effectively suppressed. Subsequently, the influence of cutting parameters on machinability of γ-TiAl following conventional/ball-end ultrasonic-assisted milling was investigated in terms of cutting force, tool wear and machined workpiece surface integrity using a fractional factorial Taguchi experimental design. In general, higher cutting speeds, smaller depths of cut, lower feed rates and dry cutting environment resulted in longer tool life and better machining quality.

Based on the conclusions from Phase 1 trials, Phase 2 tests involved a more in-depth investigation of tool wear mechanisms/failure and machinability of γ-TiAl via a full factorial comparative experiment. Four primary wear mechanisms were identified during the milling of γ-TiAl including abrasion, adhesion, oxidation and diffusion wear. Under wet cutting conditions, the TiAlN coating was prevented from fully interacting oxygen in the air, with the large temperature gradient in the cutting zone leading to coating failure. As a result, abrasive wear dominated when machining with cutting fluid, while adhesive wear was the primary wear mechanism in dry cutting when using TiAlN coated tools. Additionally, the high aluminium and titanium content in γ-TiAl induced a protective film on the tool surface during dry machining. The comparative experimental results showed that ultrasonic-assisted milling significantly improved tool life by 15.9% and reduced cutting forces by up to 47.2% compared to conventional operation in the first 100 m distance machined. Surface defects were noticeably reduced while the edge burr at the tool exit position was alleviated. The high-frequency energy from ultrasonic vibration resulted in strain hardening, increased surface microhardness, and high surface compressive residual stress. These effects suppressed subsurface cracks and likely improved fatigue life.

Phase 3 work focused on the theoretical/analytical evaluation of ball-end ultrasonic-assisted milling. A modified surface morphology model was initially developed based on the kinematics of ball-end ultrasonic-assisted milling using the Z-map method. This was followed by formulation of a static cutting force model that accounted for tool bending deflection, while a tool flank wear prediction model was proposed by extending the pin-on-disc approximation. Validation tests demonstrated that the improved models were capable of predicting workpiece surface morphology, cutting forces and tool flank wear after ball-end ultrasonic-assisted milling with high accuracy and significantly reduced calculation time. For instance, compared with

similar methods, the calculation of modified surface morphology simulation was improved by 68%. The maximum error in predicted cutting force was 18.42% while the minimum coefficient of determination for tool flank wear trend was 0.7773. Axial runout was identified as the root cause of multiple/overlapping feed marks on the machined surface, while the effect of increasing tool vibrational amplitude in reducing cutting forces was theoretically verified. Results from the models can be used to provide a basis for selecting optimal/preferred operating parameters in practical applications.

ACKNOWLEDGEMENTS

Completing a PhD is a tremendous task, and it would not have been possible without the support and guidance of many individuals and institutions. I would like to take this opportunity to express my sincere gratitude to those who have supported me throughout this journey.

First and foremost, I would like to express my deepest appreciation to my supervisor, Dr. Sein Leung Soo (Reader in Manufacturing Science and Technology). Your continuous support, insightful feedback and encouragement have been invaluable. Your dedication to your students is truly inspiring and I am immensely grateful for the many hours you spent guiding me through the intricacies of my research.

I am also indebted to my co-supervisor, Dr. Richard Hood (Associate Professor) for his expert advice and unwavering support. Your critical insights and constructive feedback have significantly contributed to the refinement of the work in this thesis. I am grateful for the opportunities you provided me to grow as a researcher and scholar.

I would like to extend my gratitude to the members of technical staff in the Schools of Engineering as well as Metallurgy and Materials, in particular Mr. Andrew Loat (Technical Engineer in the Machining Research Group), Ms. Amy Newell (Professional Services staff in the Metallurgy and Materials Labs) and Mr. Thomas Collins (Electron Microscope Applications Technician), for their time, effort and valuable suggestions with experimental work. Your diverse perspectives and expertise have greatly enriched my research.

Special thanks go to my colleagues and friends in the Machining Research Group. The camaraderie, intellectual discussions and shared experiences have made my time here truly memorable. I am especially grateful to Dr. Luis Soriano Gonzalez, Dr. Fernanda Medina Aguirre, Dr. Guojie Deng, Mr. Wenjian Huang and Mr. Mohammed Monshi, for their support and friendship. I would also like to thank Dr. Cetengfei Zhang, Dr. Yu-Chung Chuang and Mr. Tianxiao Si and many other friends for their time, effort and valuable suggestions. Your unfailing encouragement, help, and diverse perspectives have greatly enriched my research and life.

I would like to acknowledge the financial support provided by School of Engineering. Without this funding, this research would not have been possible. I am also grateful to the Machining Research Group for providing a stimulating and supportive environment that fostered my academic growth.

My heartfelt and deepest thanks also go to my family. Your unwavering belief in me and endless support have been the bedrock of my journey. Your sacrifices, encouragement and constant love have given me the strength to persevere. I am forever grateful for the values you instilled in me and the confidence you placed in my abilities.

Lastly, I would like to express my deepest gratitude to my girlfriend, Ms. Tia Guo. Your love, patience and unwavering support have been my greatest strength. Thank you for standing by me through the highs and lows, for believing in me, and for making countless sacrifices to help me achieve my dreams. This thesis is as much yours as it is mine.

In conclusion, I am profoundly grateful to everyone who has contributed to this journey in one way or another. Completing this PhD has been a challenging but rewarding experience, and I am thankful to have had the support of such wonderful individuals.

TABLE OF CONTENTS

SYNOPSIS I
ACKNOWLEDGEMENTS IV
TABLE OF CONTENTS VI
LIST OF FIGURES XI
LIST OF TABLES XXIII
NOMENCLATURE XXV
1 INTRODUCTION 1
1.1 Background to the project 1
1.2 Project collaborators and funding 2
1.3 Aims and objectives 2
1.4 Thesis overview 3
2 LITERATURE REVIEW 5
2.1 Metallic aerospace materials 5
2.1.1 Introduction 5
2.1.2 Properties and characteristics of key metallic aerospace materials 9
2.1.2.1 Titanium alloys 10
2.1.2.2 Titanium aluminide 17
2.1.2.3 Aluminium alloys 21
2.1.2.4 Steels 25
2.2 Machinability of γ-TiAl intermetallic alloys 27
2.2.1 Overview 27
2.2.2 Cutting force, temperature and chip formation 30
2.2.3 Tool wear and failure 35
2.2.3.1 Introduction 35
2.2.3.2 Tool wear mechanisms and failure 36
2.2.4 Workpiece surface integrity 42
2.2.4.1 Introduction 42
2.2.4.2 Surface morphology and edge quality 43
2.2.4.3 Surface roughness 45
2.2.4.4 Microhardness 49

2.2.4.5 Residual stress 51
2.2.4.6 Metallographic/microstructural alterations 53
2.3 Ultrasonic-assisted cutting techniques 58
2.3.1 Introduction 58
2.3.2 Characteristics and classification of ultrasonic-assisted cutting 63
2.3.3 Application of ultrasonic-assisted milling in advanced aerospace alloys 66
2.3.3.1 Cutting force 68
2.3.3.2 Tool wear and failure 69
2.3.3.3 Surface morphology and roughness 71
2.3.3.4 Microhardness, residual stress and metallographic/microstructural alterations 72
2.4 Modelling of cutting processes 76
2.5 Summary and research gaps 79
3 EXPERIMENTAL WORK 82
3.1 Introduction 82
3.2 Workpiece materials 83
3.3 Tooling 85
3.3.1 Cutting tools for mainstream Phase 1 and 2 experiments 85
3.3.2 Cutting tools for Phase 3 model validation trials 86
3.4 Equipment 86
3.4.1 Machine tool, fixturing and experimental setup 86
3.4.2 Integrated ultrasonic tool holder system 89
3.4.3 Cutting force measurement 89
3.4.4 Tool wear measurement 90
3.4.5 Workpiece height position measurement 91
3.4.6 Surface roughness, burr and morphology assessment 91
3.4.7 Residual stress evaluation 93
3.4.8 Workpiece specimen preparation and subsurface microhardness measurement 94
3.4.9 Subsurface metallographic/microstructural analysis 98
3.5 Experimental design, variable parameters and test procedures 99
3.5.1 Phase 1A: Stability assessment of integrated ultrasonic system 99
3.5.1.1 Influence of tool characteristics on ultrasonic vibration characteristics 99

3.5.1.2 Comparative study of effective ultrasonic vibration amplitude measurement 100
3.5.1.3 Operating limits assessment of ultrasonic-assisted milling 101
3.5.2 Phase 1B: Influence of operating parameters on machinability when milling γ-TiAl 102
3.5.3 Phase 2A: Tool wear mechanisms and failure of γ-TiAl in B-UAM 102
3.5.4 Phase 2B: Comparative evaluation between the effects of CM and B-UAM on machinability of γ-TiAl 105
3.5.5 Phase 3A: Experimental validation of analytical model for predicting machined surface morphology in B-UAM 106
3.5.6 Phase 3B: Experimental validation of analytical model for predicting cutting forces in B-UAM 107
3.5.7 Phase 3C: Experimental validation of analytical model for predicting tool flank wear in B-UAM 109
4 ANALYTICAL MODELLING OF BALL-END ULTRASONIC-ASSISTED MILLING 110
4.1 Kinematics modelling and geometrical simulation in B-UAM (Phase 3A) 110
4.1.1 Establishment of the tool motion reference coordinate systems 110
4.1.2 Kinematic modelling of B-UAM 112
4.1.3 Geometrical simulation of workpiece surface morphology in B-UAM 117
4.2 Modelling of instantaneous cutting force in B-UAM (Phase 3B) 123
4.2.1 Theoretical foundation for modelling instantaneous cutting forces 124
4.2.2 Establishment of tool static deflection model 125
4.2.3 Identification of CWE status 129
4.2.4 Instantaneous uncut chip thickness, length of cutting element and chip width 132
4.2.5 Identification of cutting force coefficients 134
4.3 Tool flank wear prediction model in B-UAM (Phase 3C) 135
5 RESULTS AND DISCUSSION 139
5.1 Phase 1A: Stability assessment of integrated ultrasonic system 139
5.1.1 Characteristics and influencing factors of ultrasonic actuation system 139
5.1.2 Effectiveness and operating limits of ultrasonic actuation system 141
5.1.3 Typical machining characteristics of B-UAM 144

5.2 Phase 1B: Influence of operating parameters on machinability when milling γ-TiAl ..148
5.2.1 Influence of cutting parameters on tool wear ..148
5.2.2 Effects of cutting parameters on cutting force ..153
5.2.3 Assessment of cutting parameters on workpiece surface integrity ..158
5.2.3.1 Surface morphology and edge quality ..158
5.2.3.2 Surface roughness and dimensional accuracy ..165
5.2.3.3 Microhardness ..171
5.2.3.4 Metallographic/microstructural alteration ..174
5.3 Phase 2A: Tool wear mechanisms and failure of γ-TiAl in B-UAM ..177
5.3.1 Abrasive wear ..177
5.3.2 Adhesive wear ..178
5.3.3 Oxidation and diffusion wear ..181
5.3.4 Gross fracture and edge chipping ..187
5.4 Phase 2B: Comparative evaluation between the effects of CM and B-UAM on machinability of γ-TiAl ..188
5.4.1 Influence of cutting parameters on tool wear ..188
5.4.2 Effects of cutting parameters on cutting force ..189
5.4.3 Assessment of cutting parameters on workpiece surface integrity ..191
5.4.3.1 Surface morphology and edge quality ..191
5.4.3.2 Surface roughness and dimensional accuracy ..194
5.4.3.3 Microhardness and residual stress ..197
5.4.3.4 Metallographic/microstructural alteration ..201
5.5 Phase 3A: Experimental validation of analytical model for predicting machined surface morphology in B-UAM ..204
5.5.1 Influence of axial runout on surface morphology ..204
5.5.2 Geometrical simulation and analysis of B-UAM surface morphology ..206
5.6 Phase 3B: Experimental validation of analytical model for predicting cutting forces in B-UAM ..212
5.6.1 Prediction of tool bending deflection in B-UAM operation ..212
5.6.2 Calibration of cutting force coefficients ..212
5.6.3 Improved cutting force prediction model considering true trajectory of cutting edge in B-UAM ..213

5.7 Phase 3C: Experimental validation of analytical model for predicting tool flank wear in B-UAM 219
5.7.1 Calibration of coefficients in tool flank wear model 219
5.7.2 Validation of tool flank wear model in B-UAM 219
5.8 Discussion 221
6 CONCLUSIONS AND RECOMMENDATIONS FOR FUTURE WORK 228
6.1 Literature review 228
6.2 Experimental work 229
6.2.1 Phase 1A: Stability assessment of integrated ultrasonic system 229
6.2.2 Phase 1B: Influence of operating parameters on machinability when milling γ-TiAl 229
6.2.3 Phase 2A: Tool wear mechanisms and failure of γ-TiAl in B-UAM 231
6.2.4 Phase 2B: Comparative evaluation between the effects of CM and B-UAM on machinability of γ-TiAl 232
6.3 Modelling of ball-end ultrasonic-assisted milling 233
6.3.1 Phase 3A: Experimental validation of analytical model for predicting machined surface morphology in B-UAM 233
6.3.2 Phase 3B: Experimental validation of analytical model for predicting cutting forces in B-UAM 233
6.3.3 Phase 3C: Experimental validation of analytical model for predicting tool flank wear in B-UAM 234
6.4 Overall conclusions and recommended operating conditions 234
6.5 Recommendations for future work 236
7 REFERENCES 238
APPENDIX A SUPPLEMENTAL INFORMATION 264
APPENDIX B ADDITIONAL RESULTS 265
APPENDIX C PUBLICATIONS UNDER PREPARATION 271

LIST OF FIGURES

Figure 1.1 Schematic diagram of Rolls-Royce XWB turbofan engine [2]. 1
Figure 1.2 Flow chart of phases in the PhD research work. 4
Figure 2.1 Structural materials and their weight percentage used in the airframes of civilian and military aircraft [1]. (a) Boeing 737, (b) Airbus 340-330, (c) Airbus A380, (d) Boeing 787, (e) F-18 Hornet (C/D) and (f) F-22 Raptor. 9
Figure 2.2 Specific strength of various materials [9]. 10
Figure 2.3 Application of titanium alloys in various civilian and military aircraft [14]. 12
Figure 2.4 Components manufactured with titanium alloys in a F-22 fighter [18]. 12
Figure 2.5 Crystal structure of (a) HCP α phase and (b) BCC β phase in titanium alloys. 13
Figure 2.6 Influence of alloying elements on phase diagrams of titanium alloys [8]. 13
Figure 2.7 Qualitative comparison of different titanium alloy family groups [8]. 14
Figure 2.8 Three typical microstructures of titanium alloys [8,19]. 15
Figure 2.9 Ti-6Al-4V blisk manufactured for the Joint Strike Fighter project [1]. 16
Figure 2.10 Crystal structures of (a) $L1_0$ and (b) DO_{19} types [20]. 17
Figure 2.11 Binary Ti-Al phase diagram [23]. 18
Figure 2.12 Mid-section of the binary Ti-Al phase diagram and representative microstructures showing (a) Lamellar/Fully Lamellar, (b) Pseudo duplex/Near Lamellar γ, (c)Duplex and (d) Equiaxed/Near Gamma (γ-TiAl appears dark, whereas α_2 shows a light contrast) [28]. 19
Figure 2.13 GEnx-1B aircraft engine with high/low pressure turbine section featuring γ-TiAl blades [31]. 21
Figure 2.14 New aluminium alloys and tempers used in the Boeing 777 [33]. 22
Figure 2.15 Typical issues in cutting aluminium alloys; (a) Material adhesion to the cutting edge [38] and (b) burr formation in milling [37]. 25
Figure 2.16 Steels used in manufacturing landing gear components [41]. 26
Figure 2.17 Main areas and focus of research relating to machinability of γ-TiAl since the 1990s. 29
Figure 2.18 Experimental results of temperature in milling γ-TiAl; (a) Measured cutting temperatures at varying cutting speeds with new and worn tools [64] and (b) measured cutting temperature in milling TNB with a new tool [65]. 31

Figure 2.19 Chip formation and morphology following cutting of γ-TiAl; (a) Discontinuous serrated chips in milling (v_c = 20 m/min, f_z = 0.1 mm/tooth) [56], (b) sawtooth with crack in turning (v_c = 50 m/min, a_p = 5 μm) [86] and (c) sawtooth in milling (v_c = 50 m/min, f_z = 0.1 mm/tooth) [63]. 32
Figure 2.20 Effect of different lubrication conditions when milling γ-TiAl [61]. 33
Figure 2.21 Measured cutting forces in turning 45XD referring to dry and cryogenic (LN2) conditions [66]. 34
Figure 2.22 Variation of B/L with time for a lightly loaded conical pin in pin-on-disc test [98]. 36
Figure 2.23 SEM images of flank wear on uncoated carbide tools when machining under; (a) and (d) MQL, (b) and (e) cryogenic and (c) and (f) MWF environment [87]. 39
Figure 2.24 Tool wear condition and EDS results of PVD-TiAlN coated WC insert following turning of γ-TiAl [76]. 40
Figure 2.25 Influence of tool materials and geometry on flank wear; (a) and (b) The maximum flank wear with different geometry and coating tool under dry cutting conditions (v_c = 50 m/min, f_z = 0.1 mm/tooth) [63] and (c) the maximum flank wear with different coating tool under wet cutting conditions (v_c = 80 m/min, f_z = 0.1 mm/tooth) [73]. 41
Figure 2.26 Schematic diagram of potential surface integrity effect/parameters due to machining. 43
Figure 2.27 Machined surface morphology of γ-TiAl; (a) Rough surface obtained under 25°C [91], (b) fine surface machined under 650°C [91], (c) material pull-out on machined surface (v_c = 140 m/min) [65], (d), (e) and (f) edge break, pit, crack and adhesion (v_c = 80 m/min) [81]. 44
Figure 2.28 Chips and cutting surfaces depend on the uncut chip thickness h, (a) h = 0.006 mm and (b) h = 0.053 mm [60]. 45
Figure 2.29 Arithmetical mean height (for a roughness profile) [106]. 46
Figure 2.30 Surface roughness following IAM; (a) Impact of preheating temperature and (b) impact of feed rate and comparison against CM [91]. 46

Figure 2.31 Morphologies and surface roughness following turning of 4822 γ-TiAl; (a) Surface contours machined by different tools and (b) effects of cutting parameters on surface roughness [76]. 48
Figure 2.32 Measurement of microhardness in previous research; (a) Impact of preheating temperature on surface microhardness in ball-end milling [91], (b) effect of lubrication conditions on microhardness in turning [67], (c) effect of cutting speed on microhardness in milling [81] and (d) influence of tool wear on microhardness in milling [58]. 50
Figure 2.33 Measurement of residual stress in previous research; (a) Effects of preheating temperature on residual stress [91], (b) effects of depth of cut on residual stress in different directions [69], (c) impact of machining processes on residual stress [76] and (d) impact of cutting parameters on residual stress [76]. 53
Figure 2.34 TEM images of the partially formed chips in fully lamellar microstructure; (a) Bright-field image with overall view of FIB sample, (b) magnified images of region 1 showing the $\alpha_2 + \gamma$ lamellar structure and high-density dislocations, (c) magnified images of region 2 showing the bended lamella, (d) magnified image of region 3 showing the formation of twins within γ lamella and (e) SADP patterns of regions A and B denotes the α_2 and γ phases, respectively [86]. 54
Figure 2.35 Subsurface defects following machining; (a) Trans-lamellar crack of turned 45XD subsurface at v_c = 25 m/min, f = 0.1 mm/rev and a_p = 0.7 mm [50] and (b) interface delamination and trans-lamellar crack of turned 45XD subsurface at v_c = 80 m/min, f = 0.1 mm/rev, and a_p = 0.25 mm [67]. 55
Figure 2.36 Metallographic alterations of machined subsurface; (a) Cross-section of the turned surface at v_c = 80 m/min, f = 0.1 mm/rev, and a_p = 0.4 mm, MQL [66], (b) and (c) comparison between as-cast and turned specimens [67] and (e) metallographic alteration of ground surface at v_s = 30 m/s, v_w = 1000 mm/min and a_p = 0.5 mm [90]. 56
Figure 2.37 EBSD microscopic characterisation of the partially formed chip of fully lamellar microstructure; (a) Inverse pole figure presenting that PSZ maintains better lamellar microstructure integrity without sever plastic

deformation, (b) phase contrast map indicating that phase transformation was not observed in PSZ and (c) KAM map depicting low strain distribution in PSZ [86]. 57
Figure 2.38 EBSD microscopic characterisation of the partially formed chip of near gamma microstructure; (a) Inverse pole figure presenting that region 1 and 2 have same orientation, (b) phase contrast map indicating that phase transformation was not observed in PSZ and (c) KAM map depicting high strain distribution in PSZ [86]. 57
Figure 2.39 Basic elements of USM system [132]. 59
Figure 2.40 Material removal mechanisms in USM [136] 59
Figure 2.41 Comparison of material removal modes; (a) Free abrasive grits in USM and (b) fixed abrasive grits in RUM [157]. 62
Figure 2.42 Schematic of ultrasonic machining technologies; (a) Free abrasive ultrasonic machining (USM), (b) rotary ultrasonic machining (RUM) and (c) ultrasonic-assisted drilling (UAD) [182]. 63
Figure 2.43 Classification of UAC depends on ultrasonic vibration source; (a) Workpiece vibration and (b) cutting tool vibration. 64
Figure 2.44 Summary of the principal UAC modes reviewed. 65
Figure 2.45 Measurement cutting force following UAC: (a) Effect of cutting speed on average cutting force (f_z = 0.03 mm/tooth, a_p = 4 mm, a_e = 0.8 mm, A_U = 5 μm) [211], (b) axial component force and decrease percentage (f_z = 0.015 mm/tooth, a_p = 0.2 mm, a_e = 6 mm, A_U = 2 μm) [212], (c) effect of feed rate on average cutting force (N = 5000 rpm, a_p = 0.02 mm, A_U = 5.6 μm) [213] and (d) effect of depth of cut on average cutting force (N = 5000 rpm, f = 100 mm/min, A_U = 5.6 μm) [213]. 69
Figure 2.46 Tool wear following UAC: (a) Flank wear versus machined area (N = 2000 rpm, f_z = 0.05 mm/tooth, a_p = 0.4 mm, A_U = 5 μm) [215], (b) flank wear versus machined hole number (N = 2500 rpm, f_z = 0.03 mm/tooth, a_p = 0.15 mm/rev, A_U = 4–6 μm) [216], (c) and (d) comparison of worn morphology of tool in CM and UAM processes [217]. 70
Figure 2.47 Comparison of surface monography and roughness between conventional cutting and ultrasonic-assisted cutting; (a) The variation of surface roughness

with cutting speed in both CM and EUAM (f_z = 0.015 mm/tooth, a_p = 0.2 mm, a_e = 12 mm, A_U = 5 μm) [221], (b) effect of UAM on surface morphology (v_c = 2400 rpm, f_z = 0.015 mm/tooth, a_p = 0.2 mm, a_e = 6 mm, A_U = 2 μm) [212], (c) the variation of surface roughness with cutting speed [221] and (d) effects of cutting speed on Sq [212]. 72

Figure 2.48 Comparison results of surface microhardness and residual stress. (a) Comparison of microhardness at helical CM and UAM (N = 2500 rpm, f_z = 0.03 mm/tooth, a_p = 0.15 mm, A_U = 4–6 μm) [216], (b) surface residual stress for CM and UAM at different spindle speeds (f_z = 0.015 mm/tooth, a_p = 0.2 mm, a_e = 6 mm, A_U = 2 μm) [212], (c) comparison of residual stress with different cutting processes [216] and (d) surface residual stress for CM and LUAM at different spindle speeds (f_z = 0.03 mm/tooth, a_p = 4 mm, a_e = 0.8 mm, A_U = 5 μm) [211]..... 73

Figure 2.49 The EBSD analysis of microstructure between CM and UAM; (a) and (b) Orientation image microscopy (OIM) maps, (c) and (d) Kernel average misorientation (KAM) maps, (e) and (f) grain size distribution of specimens [223]..... 75

Figure 3.1 Micrograph of Ti-45Al-8Nb-0.2C intermetallic with lamellar microstructure; (a) ×80 magnification and (b) ×1000 magnification..... 84

Figure 3.2 Schematic and image of a ball nose end mill..... 85

Figure 3.3 DMG Mori Ultrasonic 20 linear machining centre..... 87

Figure 3.4 Fixtures for holding workpieces with (a) a clamping vice and (b) direct fixation..... 88

Figure 3.5 Illustration of (a) machine axes motion and (b) setup for measuring runout..... 88

Figure 3.6 (a) Schematic of key internal components in the integrated ultrasonic tool holder [251]; and (b) image of HSK-E32 ultrasonic tool holder..... 89

Figure 3.7 Cutting force measurement system including: (a) Kistler 9257A platform dynamometer and (b) Kislter 5011A charge amplifiers..... 90

Figure 3.8 Setup for tool wear measurement system..... 91

Figure 3.9 Renishaw PowerProbe 400 optical machine probe system..... 91

Figure 3.10 Mitutoyo Formtracer Avant S-3000 contour/surface roughness measuring system..... 92

Figure 3.11 Alicona G5 InfiniteFocus optical microscope.....92
Figure 3.12 Keyence VHX-7000 digital microscope. 93
Figure 3.13 AgieCharmilles Robofil FI240cc wire EDM machine.....93
Figure 3.14 Residual stress measurement setup: (a) Arrangement for incremental drilling and (b) detail of gauge installation on sample. 94
Figure 3.15 Mounted sample preparation: (a) Buehler Simplimet-2 mounting press; and (b) example of mounted specimens showing workpiece placement position. 94
Figure 3.16 Buehler Alpha 2 speed grinder-polisher machine. 95
Figure 3.17 Microhardness testers: (a) Mitutoyo HM-100 with Knoop indenter and (b) Struers DuraScan with Vickers indenter. 96
Figure 3.18 Schematic diagram of the microhardness depth profile indent positions. 97
Figure 3.19 Schematic diagram of Knoop and Vickers indentations. 97
Figure 3.20 Etching of γ-TiAl specimens with Kroll's reagent. 98
Figure 3.21 Scanning electron microscope Zeiss EVO10 with Oxford Instruments X-act detector. 99
Figure 3.22 Diagram illustrating the cutting orientations in ball-end milling. 103
Figure 3.23 Flow chart showing the experimental procedure for Phase 1B tests. 104
Figure 4.1 Reference coordinate systems of ball-end milling process. 110
Figure 4.2 Illustration of spherical helical cutting edge with (a) axonometric view and (b) top view. 112
Figure 4.3 Diagram of tool orientation adjustment. 115
Figure 4.4 Flow chart detailing the modelling procedure for surface morphology in B-UAM. 118
Figure 4.5 Diagram illustrating the Z-map model in B-UAM. 119
Figure 4.6 Diagram illustrating the working state of the ball nose end mills in B-UAM. ...120
Figure 4.7 Schematic diagram of ISP on the workpiece. 121
Figure 4.8 Schematic diagram of angle accumulation method. 122
Figure 4.9 Schematic diagram of bending deflection load in ball-end milling. 126
Figure 4.10 Simplified ball nose end mill model: (a) Tool deflection model; and (b) simplified two-step cylindrical beam model. 127
Figure 4.11 Illustration of end mill cross-sectional shapes. 128
Figure 4.12 Flow chart showing the calculation procedure of tool static deflection.....129

Figure 4.13 Extracting mesh point swept by the cutting edge segment. 130
Figure 4.14 Schematic diagram of the falling point $Q\kappa$ calculation. 131
Figure 4.15 Schematic diagram of uncut chip thickness definition: (a) First cut; and (b) full immersion cut. 132
Figure 4.16 Schematic diagram of the Ray-triangle intersection. 133
Figure 4.17 Schematic diagram of stress distribution on tool. 136
Figure 5.1 Variation of ultrasonic power and amplitude against vibrational frequency. 139
Figure 5.2 Influence of tool specification on ultrasonic amplitude; (a) Materials and geometries and (b) diameter and weight. 140
Figure 5.3 Effect of tool length and overhang on ultrasonic amplitude. 141
Figure 5.4 Assessment of maximum tool vibration amplitude using SDC method at different axial depths of cut. 142
Figure 5.5 Effect of depth of cut on axial cutting force in conventional milling and ultrasonic-assisted milling of Ti-6Al-4V. 143
Figure 5.6 Differences in chip material adhesion level under; (a) conventional milling and (b) ultrasonic-assisted milling operations. 145
Figure 5.7 Comparison of machined surface morphology generated following UAM and CM. 146
Figure 5.8 Machined surface texture features by Keyence VHX-7000 Opt-SEM mode; (a) UAM and (b) CM. 146
Figure 5.9 Comparison of chip morphology generated following CM and UAM under (a) and (c) low magnification and (b) and (d) high magnification optical microscopy. 147
Figure 5.10 Maximum flank wear against distance machined for Phase 1B experiments. 148
Figure 5.11 Maximum flank wear against material removal volume for Phase 1B experiments. 149
Figure 5.12 Morphology of cutting tool surface in test T11 with dry cut condition; (a), (b) and (c) flank face and (d), (e) and (f) rake face. 150
Figure 5.13 Morphology of cutting tool surface in test T16 with wet cut condition; (a), (b) and (c) flank face and (d), (e) and (f) rake face. 150
Figure 5.14 Main effects plot for average tool wear rate. 152
Figure 5.15 Main effects plot for average tool wear rate S/N ratios. 152

Figure 5.16 Characteristics of instantaneous cutting force changes in B-UAM. 154
Figure 5.17 Average cutting force against distanced machined for Phase 1B experiments... 155
Figure 5.18 Average cutting force against material removal volume for Phase 1B experiments. 155
Figure 5.19 Main effects plot for initial average cutting force F_z. 157
Figure 5.20 Main effects plot for initial average cutting force F_z S/N ratios. 157
Figure 5.21 Typical defect forms on γ-TiAl machined surface. 159
Figure 5.22 Machined surface morphology under different cutting conditions; (a) and (b) are from T13 (v_c = 100 m/min, a_p = 0.05 mm, a_e = 0.30 mm, f_z = 0.03 mm/tooth, HD, CM, wet cut) and (c) and (d) are from T14 (v_c = 100 m/min, a_p = 0.10 mm, a_e = 0.25 mm, f_z = 0.02 mm/tooth, HD, UAM, dry cut)..... 160
Figure 5.23 Different manifestations of edge defects machined by (a) T8 worn tool, (b) T7 new tool, (c) T5 new tool and (d) T16 worn tool. 161
Figure 5.24 The size of entrance and exit burrs under different tool wear stages. 162
Figure 5.25 The formation process of burr; (a) Positive burr and (b) negative burr. 163
Figure 5.26 Main effects plot for initial exit burr size along the stepover direction. 164
Figure 5.27 Main effects plot for initial exit burr size S/N ratios. 164
Figure 5.28 Surface roughness change rate against distance machined for Phase 1B trials. . 165
Figure 5.29 Main effects plot for initial surface roughness Ra. 167
Figure 5.30 Main effects plot for initial surface roughness Ra S/N ratios. 167
Figure 5.31 Depth of cut achievement rate against distance machined for Phase 1B trials... 168
Figure 5.32 Changes in F_z, R_{Cd}, and Ra with tool wear in the T3 test. 169
Figure 5.33 Main effects plot for initial depth of cut achievement rate R_{Cd} 170
Figure 5.34 Main effects plot for initial depth of cut achievement rate R_{Cd} S/N ratios. 170
Figure 5.35 Variation of microhardness with new tools in Phase 1B trials. 171
Figure 5.36 Variation of microhardness with worn tools in Phase 1B trials. 172
Figure 5.37 Main effects plot for initial work hardening degree N_{wh}. 173
Figure 5.38 Main effects plot for initial work hardening degree N_{wh} S/N ratios. 174
Figure 5.39 Typical micrographs of machined subsurface microstructures in T4 with the (a) new tool and (b) worn tool. 175
Figure 5.40 Main effects plot for initial deformed layer thickness. 176
Figure 5.41 Main effects plot for initial deformed layer thickness S/N ratios. 176

Figure 5.42 Abrasive wear in wet cutting with TiAlN coated tungsten carbide tool; (a), (b) and (c) UAM and (d), (e) and (f) CM. 177
Figure 5.43 Adhesive wear in dry cutting with TiAlN coated tungsten carbide tool; (a), (b) and (c) UAM and (d), (e) and (f) CM. 179
Figure 5.44 EDS analysis of the worn tool surface produced in ultrasonic-assisted milling TNB under wet cut conditions. 179
Figure 5.45 EDS analysis of the worn tool surface produced in ultrasonic-assisted milling TNB under dry cut conditions. 180
Figure 5.46 Chemical element distributions imaged by EDS mapping mode. 180
Figure 5.47 Too wear formations in cutting different materials after 55 m distance machined: (a), (b) and (c) Wet cut and (d), (e) and (f) dry cut. 181
Figure 5.48 EDS analysis of the worn tool (TiAlN coating) surface produced in milling TNB under dry cut conditions with 205.6 m distance machined. 183
Figure 5.49 EDS analysis of the worn tool (uncoated) surface produced in milling TNB under dry cut conditions with 100.5 m distance machined. 183
Figure 5.50 Flank face element distributions of worn cutting tool under dry cut conditions. 184
Figure 5.51 EDS analysis of milling surfaces of different materials and cutting conditions; (a), (d) and (g) Low-alloy steel + wet cut, (b), (e) and (h) γ-TiAl + dry cut and (c), (f) and (i) γ-TiAl + wet cut. 184
Figure 5.52 EDS element distributions of the adhered chip on workpiece machined surface. 185
Figure 5.53 Changes in tool surface and machined surface elements distribution. 186
Figure 5.54 Variations in element content along cross-section depth. 186
Figure 5.55 Edge chipping on the rake face for Phase 2A experiments: (a) CM + wet cut, (b) CM + dry cut, (c) UAM + wet cut and (d) UAM + dry cut. 187
Figure 5.56 Maximum flank wear against distance machined for Phase 2B trials. 188
Figure 5.57 Average cutting force against distance machined for Phase 2B trials. 190
Figure 5.58 The influence of cutting conditions on the cutting force for Phase 2B trials. 191
Figure 5.59 Surface morphology under wet cut imaged by Keyence VHX-7000 Opt-SEM. 192

Figure 5.60 Surface morphology under dry cut imaged by Keyence VHX-7000 Opt-SEM. 192
Figure 5.61 Changes in exit edge profile in stepover direction under different conditions: (a) UAM + wet cut, (b) CM + wet cut, (c) UAM + dry cut and (d) CM + dry cut. 193
Figure 5.62 Influence of cutting conditions on the average areal surface roughness Sa for Phase 2B experiments. 195
Figure 5.63 Influence of cutting conditions on the root mean square gradient Sdq for Phase 2B experiments. 195
Figure 5.64 Depth of cut achievement rate against distance machined for Phase 2B experiments. 196
Figure 5.65 The cutting-edge motion trajectory in (a) CM and (b) UAM. 197
Figure 5.66 Microhardness profiles under different cutting conditions for Phase 2B experiments: (a) new tool and (b) worn tool. 198
Figure 5.67 Degree of work hardening against distance machined for Phase 2B experiments. 199
Figure 5.68 Effects of cutting conditions on residual stress in the feed direction for Phase 2B experiments: (a) new tool and (b) worn tool. 200
Figure 5.69 Effects of cutting conditions on residual stress in the stepover direction for Phase 2B experiments: (a) new tool and (b) worn tool. 201
Figure 5.70 Subsurface microstructures along the feed direction in wet cutting for Phase 2B trials. 202
Figure 5.71 Subsurface microstructures along the feed direction in dry cutting for Phase 2B trials. 203
Figure 5.72 Deformed layer thickness under different cutting conditions for Phase 2B trials. 203
Figure 5.73 Schematic diagram of influence of axial runout on surface morphology; (a), (b) and (c) Axial runout = 0 and (d), (e) and (f) axial runout = 1 μm. 204
Figure 5.74 Experimental results of influence of axial runout on surface morphology. 206
Figure 5.75 Schematic diagram of comparison between modelling prediction and experimental results of machined surface morphology (N = 3000 rpm, f_z = 0.10 mm/tooth, a_p = 0.4 mm, a_e = 0.4 mm, α = 0°, A_U = 0 μm). 207

Figure 5.76 Schematic diagram of comparison between modelling prediction and experimental results of machined surface morphology (N = 3000 rpm, f_z = 0.10 mm/tooth, a_p = 0.4 mm, a_e = 0.4 mm, α = 45°, A_U = 0 μm).....208
Figure 5.77 Schematic diagram of comparison between modelling prediction and experimental results of machined surface morphology (N = 6000 rpm, f_z = 0.04 mm/tooth, a_p = 0.2 mm, a_e = 0.2 mm, α = 45°, A_U = 6 μm).....209
Figure 5.78 Schematic diagram of comparison between modelling prediction and experimental results of machined surface morphology (N = 3000 rpm, f_z = 0.10 mm/tooth, a_p = 0.4 mm, a_e = 0.4 mm, α = 45°, A_U = 6 μm).....211
Figure 5.79 The prediction results of tool bending deflection model using Phase 1B data...212
Figure 5.80 Diagram of cutting force (a) before and after (b) down-sampling operation.....214
Figure 5.81 Comparison of the predicted cutting forces with experimental data in T10; (a) Total cutting forces, (b) F_x component, (c) F_y component and (d) F_z component.....215
Figure 5.82 Comparison of the predicted cutting forces with experimental data in T11; (a) Total cutting forces, (b) Fx component, (c) Fy component and (d) Fz component.....216
Figure 5.83 Comparison of the predicted cutting forces with experimental data in T12; (a) Total cutting forces, (b) Fx component, (c) Fy component and (d) Fz component.....216
Figure 5.84 Comparison of the predicted cutting forces with experimental data in T13; (a) Total cutting forces, (b) Fx component, (c) Fy component and (d) Fz component.....217
Figure 5.85 Comparison of the predicted cutting forces with experimental data in T14; (a) Total cutting forces, (b) Fx component, (c) Fy component and (d) Fz component.....217
Figure 5.86 The influence of ultrasonic amplitude on the cutting forces for Phase 3B.....218
Figure 5.87 Comparison of the predicted flank wear with experimental data: (a) T7 with axial position angle θ = 28.268°, (b) T8 with axial position angle θ = 23.645°, (c) T9 with axial position angle θ = 23.958° and (d) T10 with axial position angle θ = 24.958°. 220
Figure B.1 EDS analysis of the TiAlN coated tool under new condition. 265

Figure B.2 EDS analysis of the worn tool (no coating) surface produced in milling low-alloy steel in dry cut conditions. 265
Figure B.3 EDS analysis of the worn tool (no coating) surface produced in milling low-alloy steel in wet cut conditions. 266
Figure B.4 Schematic diagram of comparison between modelling prediction and experimental results of machined surface morphology (N = 3000 rpm, f_z = 0.10 mm/tooth, a_p = 0.4 mm, a_e = 0.33 mm, α = 30°, A_U = 0 μm). 267
Figure B.5 Schematic diagram of comparison between modelling prediction and experimental results of machined surface morphology (N = 6000 rpm, f_z = 0.04 mm/tooth, a_p = 0.2 mm, a_e = 0.2 mm, α = 30°, A_U = 0 μm). 268
Figure B.6 Tool flank wear evolution for T7 (N = 3000 rpm, f_z = 0.06 mm/tooth, a_p = 0.15 mm, a_e = 0.20 mm, α = 45°, A_U = 6 μm). 269
Figure B.7 Tool flank wear evolution for T8 (N = 3000 rpm, f_z = 0.06 mm/tooth, a_p = 0.25 mm, a_e = 0.20 mm, α = 45°, A_U = 6 μm). 269
Figure B.8 Tool flank wear evolution for T9 (N = 3000 rpm, f_z = 0.05 mm/tooth, a_p = 0.20 mm, a_e = 0.20 mm, α = 45°, A_U = 6 μm). 270
Figure B.9 Tool flank wear evolution for T10 (N = 3000 rpm, f_z = 0.07 mm/tooth, a_p = 0.20 mm, a_e = 0.20 mm, α = 45°, A_U = 6 μm). 270

LIST OF TABLES

Table 2.1 Selection factors for aerospace structural materials [1]. 6
Table 2.2 Aerospace applications/idealisations [8]. 7
Table 2.3 Grading of various aerospace materials relative to key design factors/properties [1]. 8
Table 2.4 Comparison of mechanical properties of titanium alloys with other aerospace structural materials [1]. 11
Table 2.5 Important commercial titanium alloys [1,8]. 15
Table 2.6 Influence of microstructure characteristics on mechanical properties [8]. 16
Table 2.7 Comparison of mechanical/physical properties between titanium aluminides and nickel-based superalloys [4]. 19
Table 2.8 Room temperature mechanical properties of γ-TiAl [29]. 20
Table 2.9 Aluminium alloy designation system for wrought/cast alloys [1,8]. 23
Table 2.10 Temper designations for aluminium alloys [1]. 23
Table 2.11 Advantages and disadvantages of aluminium alloys. 24
Table 2.12 Composition and properties of selected steels used in aircraft [1]. 26
Table 2.13 Summary of cutting and processes evaluated in published research involving the machining of γ-TiAl. 30
Table 2.14 Classification of materials and fields of application of USM [153]. 61
Table 2.15 Main classification of UAC based on the direction of ultrasonic vibration. 66
Table 2.16 Summary of UAC applications in published research involving the machining of aerospace alloys. 67
Table 3.1 Key specifications for tools used in Phase 1A. 85
Table 3.2 Specifications of ball nose end mill used in Phase 3 [248]. 86
Table 3.3 Main specifications of the DMG Mori Ultrasonic 20 linear machining centre [249]. 87
Table 3.4 Technical specifications of the Kistler 9257A dynamometer [252]. 90
Table 3.5 Grinding and polishing route and parameters for mounted γ-TiAl samples. 95
Table 3.6 Test array for assessing the effect of tool characteristics on ultrasonic vibration amplitude. 100
Table 3.7 Variable factors and levels for effective ultrasonic vibration amplitude trials. 101

Table 3.8 Test parameters and variable levels for operating limits evaluation of ultrasonic system. 101
Table 3.9 Variable factors and levels for Phase 1B experiments. 102
Table 3.10 Taguchi L_{16} ($4^4 \times 2^3$) orthogonal array for Phase 1B experiments. 103
Table 3.11 Test array for Phase 2A experiments. 105
Table 3.12 Test array for Phase 2B experiments. 106
Table 3.13 Validation trials for workpiece surface morphology prediction model. 106
Table 3.14 Test array to determine force coefficients for cutting force prediction model. 108
Table 3.15 Test array for experimental validation of cutting force prediction model. 108
Table 3.16 Test array to determine abrasive wear coefficient for tool wear prediction model. 109
Table 3.17 Test array for experimental validation of tool wear prediction model. 109
Table 5.1 Modified ANOVA analysis of average tool wear rate. 151
Table 5.2 Modified ANOVA analysis of initial average cutting force F_z. 156
Table 5.3 Modified ANOVA analysis of initial exit burr size along the stepover direction. 163
Table 5.4 Modified ANOVA analysis of initial surface roughness Ra. 166
Table 5.5 Modified ANOVA analysis of initial depth of cut achievement rate R_{Cd}. 169
Table 5.6 Modified ANOVA analysis of initial work hardening degree N_{wh} 173
Table 5.7 Modified ANOVA analysis of initial deformed layer thickness. 175
Table 5.8 Comparison of average cutting force F_x between the experiment and prediction. 218
Table 6.1 List of recommended cutting parameters for milling γ-TiAl. 235
Table A.1 Key information of materials used in Phase 2 and Phase 3 experiments [324,325]. 264
Table A.2 F-table of critical values for significance level = 0.10 [290]. 264

NOMENCLATURE

%	Percentage
<	Less than
>	Larger than
°C	Degree Celsius
α	Tilt angle
β	Lead angle
γ_d	Tool rake angle
γ_c	Tool clearance angle
Ø	Diameter
θ	Axial position angle
ψ	Lag angle
γ_0	Nominal helical angle
δ	Tool defection
δ_s	Shank deflection
δ_f	Flute deflection
ϕ_s	Shank deflection angle
λ_θ	Axial position angle interval
λ_t	Time interval
at%	Atomic percentage
a_p	Depth of cut
a_e	Radial depth of cut / stepover
A_U	Ultrasonic vibration amplitude
B-UAM	Ball-end ultrasonic-assisted milling
BUE	Built-up edge
BCC	Body-centred cubic
CM	Conventional milling
CBN	Cubic boron nitride
CWE	Cutter-workpiece engagement
db	Width of cutting chip element
dS	Length of cutting chip element
d_{fm}	Distance of feed mark

DO_{19}	Hexagonal structure
F	Feed rate
f_z	Feed per tooth
f_U	Ultrasonic frequency
F_x	Cutting force in feed direction
F_y	Cutting force in stepover direction
F_z	Cutting force in axial direction
F_t	Tangential cutting force
F_r	Radial cutting force
F_a	Axial cutting force
F_{def}	Normal force for bending deflection
F_h	Applied load for microhardness
FP	Falling points
FCC	Face-centred cubic
h	Uncut chip thickness
H_t	Hardness of cutting tool
HD	Horizontal downward
HU	Horizontal upward
HV	Vicker microhardness
HK	Knoop microhardness
HSM	High-speed machining
HSS	High-speed steel
HCP	Hexagonal close-packed
K_w	Abrasive wear constant
L_{SC}	Length of single feed
$L1_0$	Tetragonal structure
LTUAM	Longitudinal-torsional ultrasonic-assisted milling
MQL	Minimum quantity lubrication
N	Spindle speed
N_{wh}	Work hardening degree
N_t	Total teeth number
PCD	Polycrystalline diamond
PVD	Physical vapour deposition
PSZ	Primary shear zone

q	Tool feeding sequence number
R	Radius of the tool
Ra	Arithmetical mean height of surface roughness profile
R_{Cd}	Depth of cut achievement rate
Sa	Areal surface roughness
Sdq	Root means square gradient
UCT	Uncut chip thickness
UAC	Ultrasonic-assisted cutting
UAD	Ultrasonic-assisted drilling
UAM	Ultrasonic-assisted milling
UAT	Ultrasonic-assisted turning
v_c	Cutting speed
VB	Flank wear
WC	Tungsten carbide
w_h	Height of workpiece
wt%	Weight percentage

1 INTRODUCTION

1.1 Background to the project

Metallics are the most commonly used materials in constructing aerospace systems, with titanium alloys amongst the most widely used due to their excellent mechanical and lightweight properties. Typical titanium alloys such as the α-β Ti-6Al-4V, are known for their high tensile strength (~1100 MPa), good corrosion resistance and low density (~4.6 g/cm^3), is currently constituting up to ~25%–30% of the weight in most modern aircraft engines [1]. Figure 1.1 illustrates some of the major components in a Rolls-Royce XWB turbofan aeroengine, particularly highlighting where conventional titanium alloys are used in the fan system, while nickel-based superalloys are commonly adopted for high-temperature sections like the combustor and turbine [2].

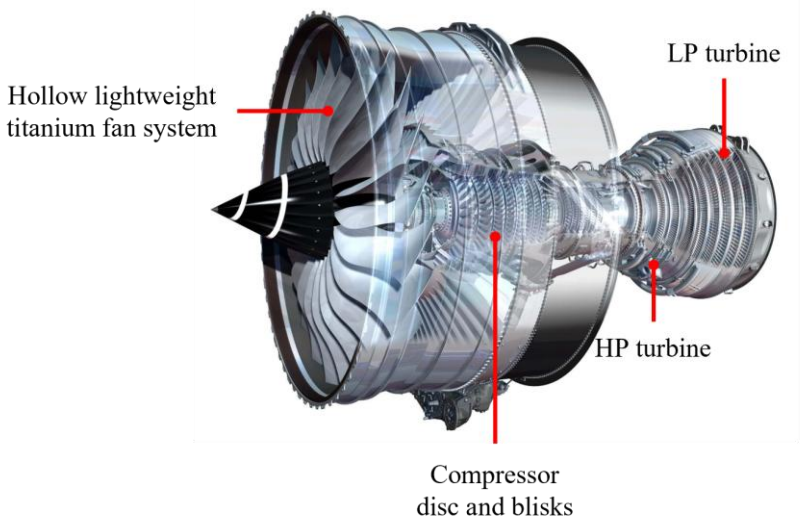


Figure 1.1 Schematic diagram of Rolls-Royce XWB turbofan engine [2].

The working temperature in the high-pressure (HP) turbine can typically reach up to 1500°C, exceeding the operating limits of conventional titanium alloys, hence requiring the use of nickel-based superalloys for components in this area of the engine [3]. Nevertheless, the high density of superalloys significantly increases the engine mass, thus lowering thrust-to-weight ratios. In this context, gamma titanium aluminide (γ-TiAl) alloys have been identified as a potential alternative to superalloys for manufacturing low-pressure turbines (LPT) with ~700°C working temperature due to their considerably lower density coupled with high strength and elevated temperature resistance (up to 1000°C) [4], [5]. In addition to high specific strength,

the material also possesses strong oxidation and creep resistance, and is expected to reduce aeroengine weight by 20%–30% compared to traditional nickel-based superalloys [6].

Despite its favourable mechanical/physical properties, the extremely poor ductility of γ-TiAl, with only 2%–4% elongation at room temperature, has however become an obstacle that limits its engineering applications, especially from a manufacturing standpoint. Although processes such as casting, forming and additive manufacturing can alleviate this issue to a certain extent, conventional cutting operations currently remain the most efficient method for finish manufacturing of blisk and blade components. The main challenges in machining γ-TiAl include high cutting forces and temperatures, severe tool wear and poor workpiece surface integrity. Consequently, research into improving the machinability of γ-TiAl has been a key area of study over the last ~30 years, especially for the aerospace industry.

One particular technology that has shown promise is ultrasonic-assisted cutting, which has developed rapidly in recent years. Classed as a hybrid manufacturing process, it has been shown to generally reduce cutting forces and temperature while improving tool life and workpiece surface quality for some difficult-to-cut materials [7]. However, there are relatively few studies to date exploring the ultrasonic-assisted cutting of γ-TiAl, with existing investigations primarily focusing on ultrasonic-assisted grinding operations. Given the characteristics of the material and associated challenges in machining, there is considerable scope for research into ultrasonic-assisted cutting as a route to improve the machinability of γ-TiAl, which was the principal motivation for the work presented in this thesis.

1.2 Project collaborators and funding

The research was carried out as a part of a Doctor of Philosophy (PhD) degree program based within the Machine Research Group in the Department of Mechanical Engineering, School of Engineering at the University of Birmingham. Finance for the project was provided through a PhD research scholarship from the Department of Mechanical Engineering at the University of Birmingham.

1.3 Aims and objectives

The overall aim of the project was to investigate the influence of cutting parameters on machinability of γ-TiAl and comprehensively evaluate the effectiveness of ultrasonic-assisted

milling through experimental testing supported by the development of analytical predictive models. Machinability and process performance were primarily assessed based on tool wear mechanisms/life, cutting forces and workpiece surface integrity. The specific objectives were to:

I. Undertake a comprehensive literature review relating to the machinability of γ-TiAl, with a focus on the effects of cutting parameters, tool wear conditions, and cutting forces on workpiece surface integrity.

II. Investigate the performance/stability of the integrated ultrasonic actuation system on the 5-axis DMG Mori Ultrasonic 20 linear high speed machining centre and understand the effects of cutting tool size/materials and machining loads on vibration amplitude.

III. Benchmark the influence of varying cutting parameters when milling γ-TiAl on key response criteria including machined surface morphology, edge quality, surface roughness, microhardness, residual stress and subsurface metallographic/microstructural alterations.

IV. Identify the dominant tool wear mechanisms and failure when milling γ-TiAl under different cutting conditions.

V. Evaluate the influence of ultrasonic-assisted milling operation and corresponding cutting environment on the material removal mechanism, tool life, cutting forces and workpiece surface integrity when machining γ-TiAl.

VI. Establish analytical models for the ball-end ultrasonic-assisted milling process to predict machined surface geometry, instantaneous cutting forces and tool flank wear.

1.4 Thesis overview

The PhD work involved multiple serial and parallel phases with each phase divided into further sub-phases. A flow chart of work phases is detailed in Figure 1.2.

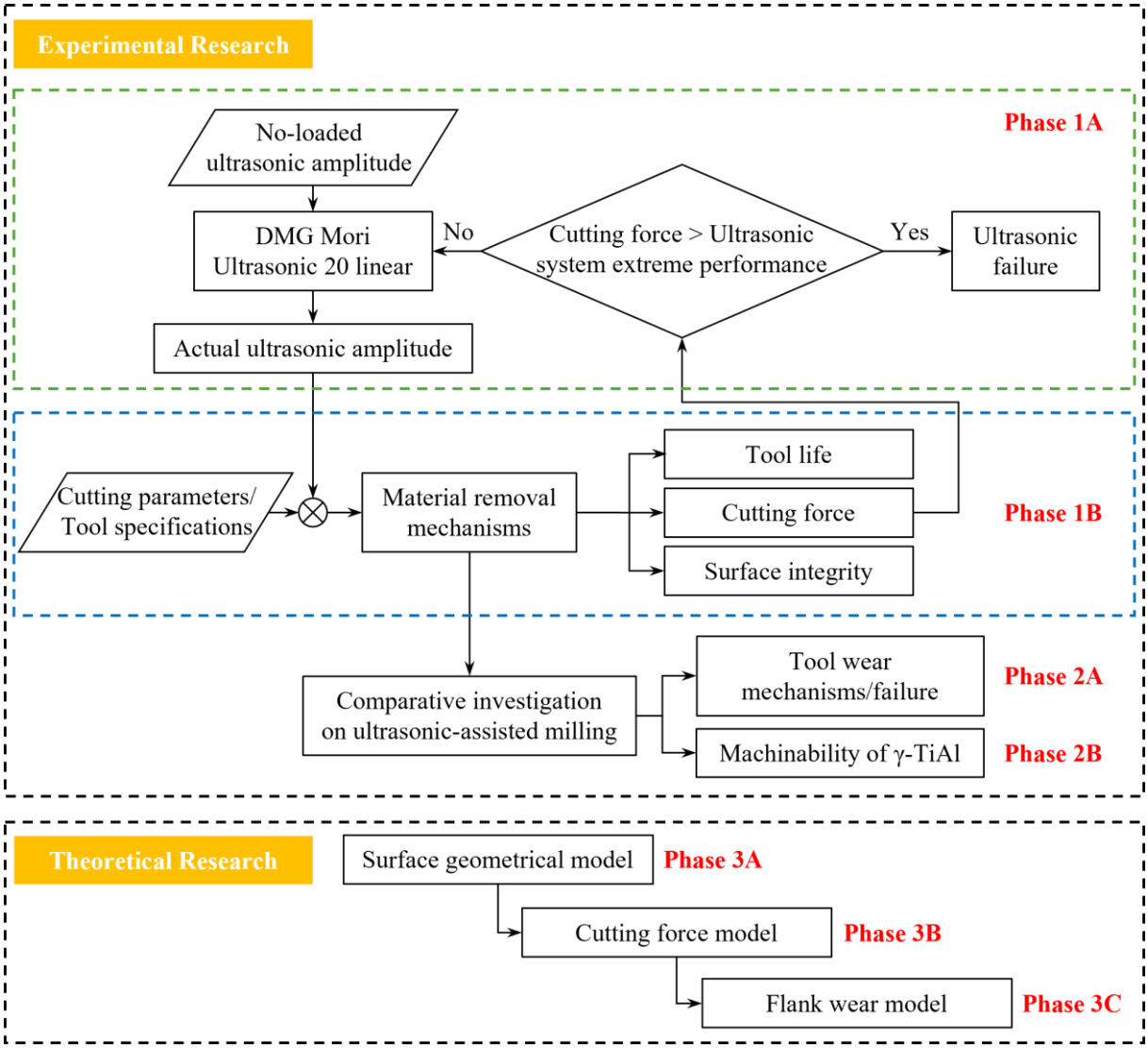


Figure 1.2 Flow chart of phases in the PhD research work.

2 LITERATURE REVIEW

2.1 Metallic aerospace materials

2.1.1 Introduction

The rapid development of the aerospace industry hinges crucially on advancements in materials and processing technologies. Structural optimisation of aircraft and advancements in material technology occur in tandem, each driving the other towards greater performance such as lightweight and high strength at a reduced cost. Concurrently, the evolution of propulsion systems is perpetually geared towards the principal objective of enhancing fuel efficiency.

Amidst a growing need to increase the load capacity of civil airplanes as well as to expand the scope and complexity of space exploration, the demands on material properties have expanded. These requirements include, but are not limited to, low mass density, high strength, high stiffness, damage tolerance, durability, high power density, high corrosion resistance, high-temperature resistance and high-pressure resistance. In some studies, aerospace materials are specifically categorised as structural materials, focusing primarily on their mechanical properties. Table 2.1 summarises the essential requirements and selection criteria for aerospace structural materials. Furthermore, the design function of various components, such as load bearing, heat transfer, and energy storage, dictates the choice of materials to ensure optimal performance in manufacturing. Table 2.2 lists several aerospace components along with a simplified idealisation of their loading formations.

The selection of materials in aerospace manufacturing plays a pivotal role in the successful design, construction, certification, operation, and maintenance of aircraft and spacecraft. It is estimated that the aerospace industry has access to over 120,000 possible materials for constructing airframes and jet engines [1]. However, less than 0.05% of these materials meet the stringent criteria for aerospace use while also being cost-effective and easy to manufacture, which significantly narrows the options for application in this sector.

Table 2.1 Selection factors for aerospace structural materials [1].

Costs	Purchase cost. Processing costs. In-service maintenance cost. Recycling and disposal costs.
Resources availability	Plentiful, consistent and long-term supply.
Manufacturing	Ease of manufacturing. Low-cost and rapid manufacturing processes.
Physical property	Low specific gravity for lightweight structures.
Static mechanical properties	Stiffness (elastic modulus). Strength (yield and ultimate strength).
Fatigue durability	Resistance against initiation and growth of cracks from various sources of fatigue (e.g. stress, stress-corrosion, thermal, acoustic).
Damage tolerance	Fracture toughness and ductility to resist crack growth and failure under load. Notch sensitivity owing to cut-outs (e.g. windows), holes (e.g. fasteners) and changes in structural shape. Damage resistance against bird strike, maintenance accidents (e.g. dropped tools on aircraft), impact from runway debris, hail impact.
Environmental durability	Corrosion resistance. Oxidation resistance. Moisture absorption resistance. Wear and erosion resistance. Space environment (e.g. micrometeoroid impact, ionising radiation).
Thermal properties	Thermally stable at high temperatures. High softening temperatures. Cryogenic properties. Low thermal expansion properties. Non/low flammability. Low-toxicity smoke
Electrical/magnetic properties	High electrical conductivity for lightning strikes. High radar (electromagnetic) transparency for radar domes. Radar absorbing properties for stealth military aircraft.

Table 2.2 Aerospace applications/idealisations [8].

Application	Idealisation	Loading	Constraints
Truss framework	Tie	Tension	Strength
Fuselages	Cylinder	Compression/tension/bending	Buckling/strength/ deflection
Shafts	Thin-walled tube/beam	Torque/rotation/bending	Bending/shear/ vibration
Combustion chambers	Thin-walled cylinder/internal pressure	Pressure/noise	Thermal/oxidation
Blades (fan, compressor, turbine)	Tie/beam	Bending/tension/fatigue/ thermal/creep	Deflection/strength/vibration/ erosion/temperature
Disks (compressor, turbine)	Disk	Rotation/thermomechanical fatigue	Strength/ductility/toughness/ oxidation
Space truss framework	Tie rod	Axial loading	Strength/buckling
Nozzles	Thin-walled cylinder	Pressure/noise/thermal	Strength/vibration
Wing	Plate	Bending/tension/twist/ vibration/fatigue	Buckling vibration/strength/ deflection
Cryogenic tanks	Spherical shell	Internal pressure/thermal	Strength/low temperature yield before break/leak before break

Aerospace materials are broadly categorised into four groups comprising metallics, polymer, composites and ceramic materials. The primary materials utilised in aerospace structures include aluminium alloys, titanium alloys, steels and composites. Additionally, nickel-based superalloys serve as crucial structural materials particularly in the high-temperature section of jet engines. While other materials are employed for specific types of aircraft, they are not commonly used in substantial quantities. These include for instance, magnesium alloys, fibre-metal laminates, metal matrix composites, wood, ceramics (heat insulation tiles in rockets and spacecraft) and radar-absorbing materials like transition metal carbides MXene (stealth military aircraft). Table 2.3 outlines several widely used material types in aerospace manufacturing, highlighting key factors and properties pertinent to airframes and engines.

Table 2.3 Grading of various aerospace materials relative to key design factors/properties [1].

Property	Aluminium alloy	Titanium alloy	Magnesium alloy	High-strength steel	Nickel-based superalloy	Carbon fibre composite
Cost	Cheap	Expensive	Medium	Medium	Expensive	Expensive
Weight (density)	Light	Medium	Very light	Heavy	Heavy	Very light
Stiffness (elastic modulus)	Low/medium	Medium	Low	Very high	Medium	High
Strength (yield stress)	Medium	Medium/high	Low	Very high	Medium	High
Fracture toughness	Medium	High	Low/medium	Low/medium	Medium	Low
Fatigue	Low/medium	High	Low	Medium/high	Medium	High
Corrosion resistance	Medium	High	Low	Low/medium	High	Very high
High-temperature creep strength	Low	Medium	Low	High	Very high	Low
Ease of recycling	High	Medium	Medium	High	Medium	Very low

Despite the rapid development and increasing use of composites over the last ~15 years, metallics still form the bulk of materials employed in the construction of many aerospace systems. Figure 2.1 illustrates a breakdown of structural materials used in the airframes of various civil and military aircraft currently in production/service. A notable characteristic across different types of aircraft is the consistent utilisation of aluminium and titanium-based alloys as well as steels and composites. Although their weight percentages vary between the different types of aircraft, metallic materials constitute between 40% to 90% of the total structural mass. Given this prevalence, studies concerning the machinability of metallic materials assumes a critical role within the manufacturing sector.

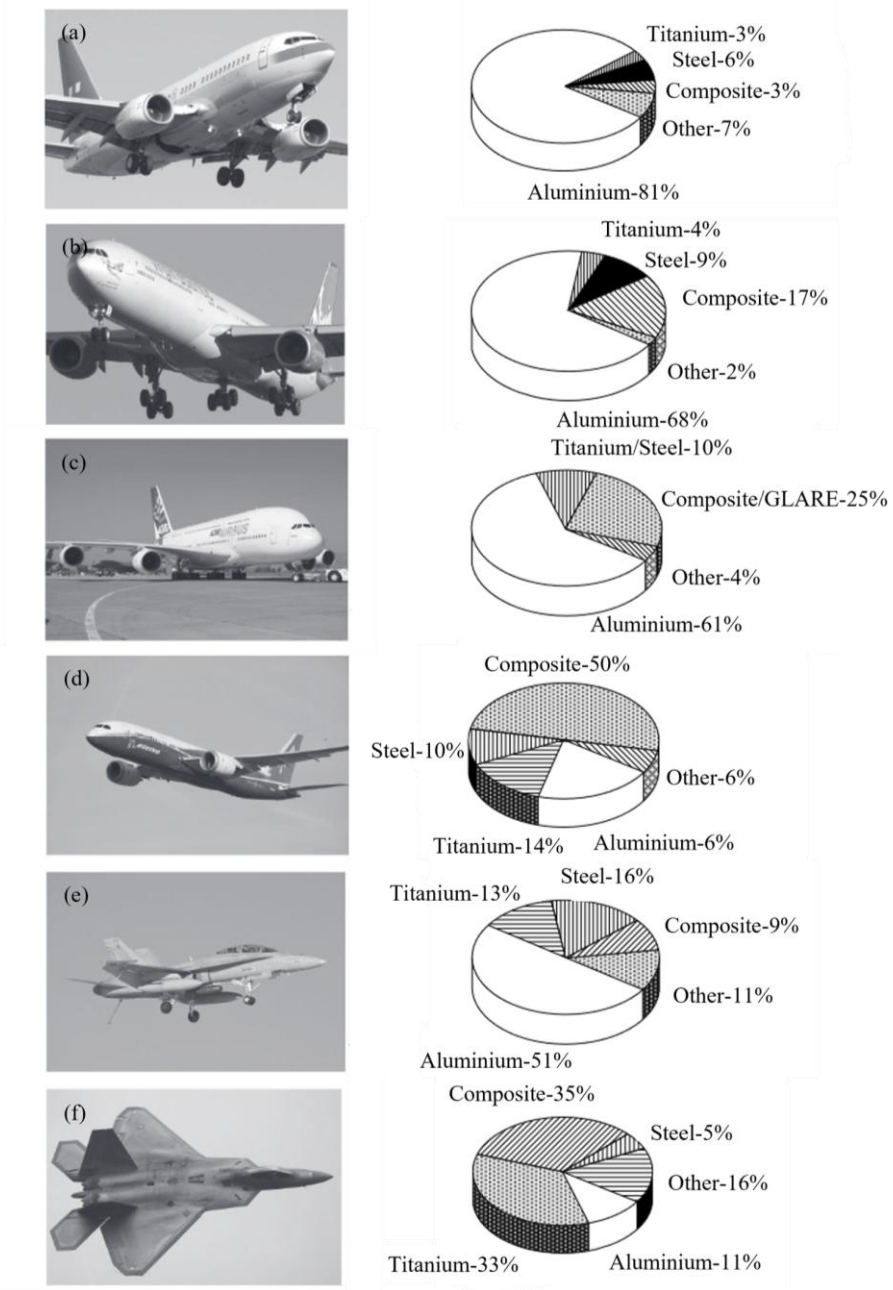


Figure 2.1 Structural materials and their weight percentage used in the airframes of civilian and military aircraft [1]. (a) Boeing 737, (b) Airbus 340-330, (c) Airbus A380, (d) Boeing 787, (e) F-18 Hornet (C/D) and (f) F-22 Raptor.

2.1.2 Properties and characteristics of key metallic aerospace materials

Titanium alloys, aluminium alloys and high-strength steel are regarded as quintessential metallic aerospace materials due to their indispensable qualities in specific application domains. The subsequent sections provide a detailed examination of these materials' properties, principal classifications, key applications and challenges associated with their machinability.

2.1.2.1 Titanium alloys

Titanium (Ti) is the ninth most abundant element in the Earth's crust and ranks as the fourth most abundant structural metal, after aluminium, iron and magnesium. Titanium alloys are distinguished by their exceptional physical and mechanical properties, such as high corrosion resistance and specific strength, as illustrated in Figure 2.2 [9]. Additionally, certain near-α titanium alloys such as Timetal 834, Ti-SF60 and Ti-SF61 display robust mechanical performance even at high temperatures (up to 500℃–600℃) [10], [11]. This exceeds the operating temperature limits of other lightweight aerospace materials such as aluminium alloys (up to 150℃), magnesium alloys (~200℃), and fibre reinforced polymer composites (up to 150℃) [8], [12], [13]. These attributes have positioned titanium alloys as a key driver in the industrial advancements of the 21st century, particularly within the aerospace sector [14], [15]. Table 2.4 compares and contrasts the mechanical properties of various titanium alloys against other aerospace structural materials. The specific stiffness of titanium alloys is typically somewhat lower compared to aluminium, magnesium and ferrous based materials, thereby negating its use in applications requiring high stiffness. In contrast, the strength properties of titanium alloys are generally superior, thus making them more suitable for manufacturing components that are subjected to high in-service loads.

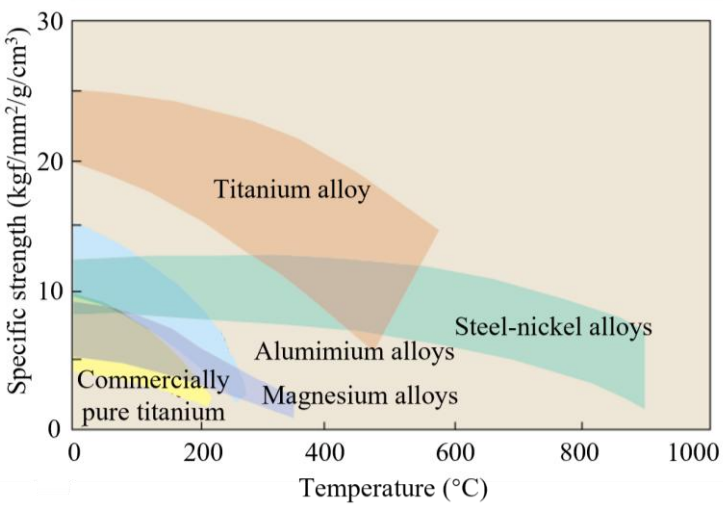


Figure 2.2 Specific strength of various materials [9].

Table 2.4 Comparison of mechanical properties of titanium alloys with other aerospace structural materials [1].

Materials	Average density (g/cm^3)	Young's modulus (GPa)	Specific modulus ($MPam^3/kg$)	Yield strength (MPa)	Specific strength ($kPam^3/kg$)
Pure titanium	4.6	103	22.4	170–480	37–104
α-Ti alloys	4.6	100–115	21.7–25.1	800–1000	174–217
β–Ti alloys	4.6	100–115	21.7–25.1	1150–1300	180–282
α + β-Ti alloys	4.6	100–115	21.7–25.1	830–1300	180–282
Al-2024-T6	2.7	70	25.9	385	142
Al-7075-T76	2.7	70	25.9	470	174
Magnesium	1.7	45	26.5	200	115
High-strength low-alloy steel	7.8	210	26.9	1000	128
Carbon-epoxy composite	1.7	50	29.4	760	450

Lightweight properties rank among the most crucial attributes of titanium alloys. For over fifty years, titanium has been a pivotal engineering material in gas turbine engines, currently comprising 25%–30% of the weight in most modern systems. Key engine components fabricated using titanium-based alloys include fan blades, shafts and casings in the inlet region, low-pressure compressors, as well as plug and nozzle assemblies in the exhaust section. Additionally, titanium also finds applications in engine frames, casings, manifolds, ducts and tubes.

Nonetheless, titanium is not suitable for all engine parts, particularly within the combustion chamber and other areas where operating temperatures exceed 600°C. Beyond this threshold, conventional titanium alloys tend to soften, creep and oxidise rapidly, necessitating the use of more heat-resistant materials such as nickel-based superalloys. The utilisation of titanium in both civilian and military aircraft has progressively increased over the years since the 1960's, as depicted in Figure 2.3 [14], [16], [17]. Initially prominent in military aircraft, titanium usage constitutes as much as 27% of the structural components in U.S. fifth-generation F-35 fighter jets, while this level increases to almost 39% for the advanced F-22 Raptor air superiority fighter. The range of components manufactured using titanium alloys in the F-22 aircraft is detailed in Figure 2.4 [18].

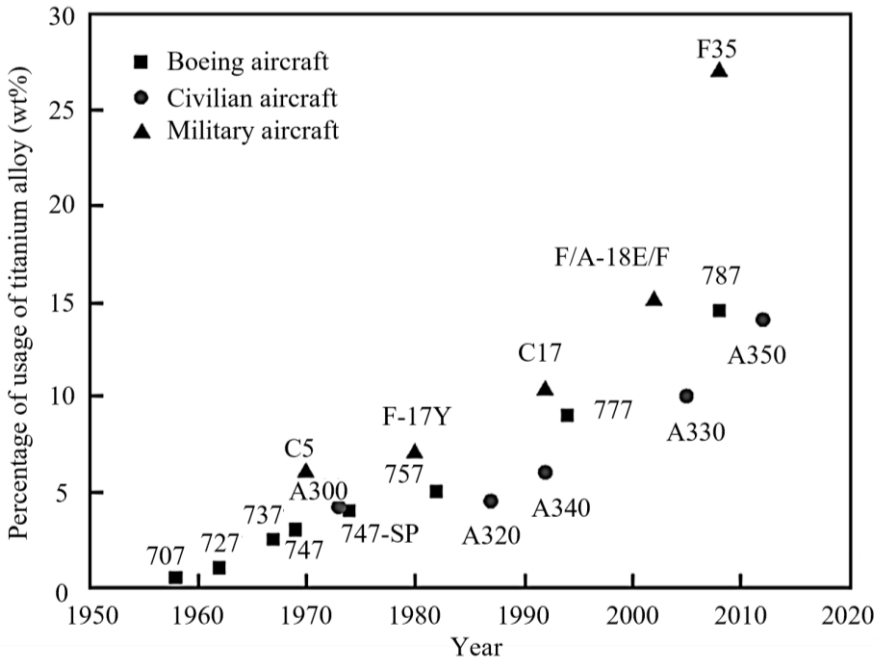


Figure 2.3 Application of titanium alloys in various civilian and military aircraft [14].

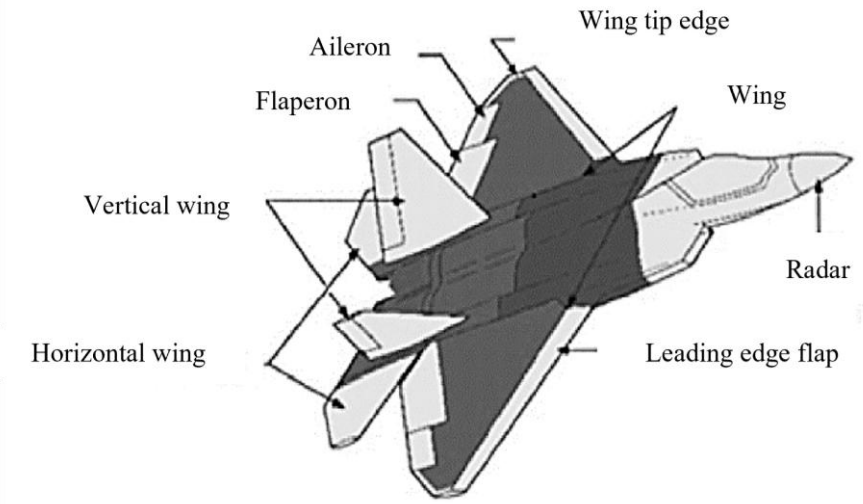


Figure 2.4 Components manufactured with titanium alloys in a F-22 fighter [18].

Titanium is identified as a transition metal due to its unfilled 3d electron shell. It exhibits allotropy, existing in two distinct forms involving a hexagonal close-packed (HCP) crystal structure in the α phase, which is stable up to 880°C, and a body-centred cubic (BCC) β phase, that remains stable up to the melting point of 1670°C. Figure 2.5 displays the basic crystal structure diagrams for both the α and β. The HCP crystal structure typically offers low to medium strength, exceptional high-temperature creep resistance, weldability, ductility and good toughness. In contrast, the BCC structure provides high strength, high fatigue resistance

and full heat treatability, albeit with reduced ductility. Alloying elements added to Ti are classified based on their impact on the β-transition temperature (α→β phase transition temperature), as illustrated in Figure 2.6. Aluminium (Al) is the most prevalent α stabiliser, forming a substitutional solid solution, while interstitial solid solutions are produced by oxygen (O), nitrogen (N), and carbon (C). The β phase is stabilised through two types of elemental additions classified as either isomorphous or eutectoid. Neutral additions contribute to the development of an enhanced base alloy, optimised for high-temperature applications.

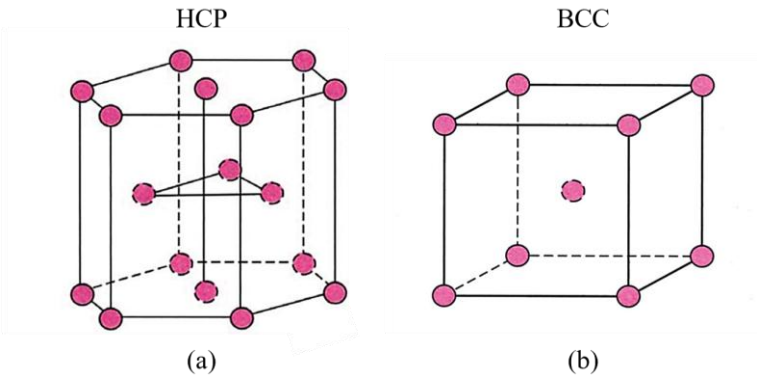


Figure 2.5 Crystal structure of (a) HCP α phase and (b) BCC β phase in titanium alloys.

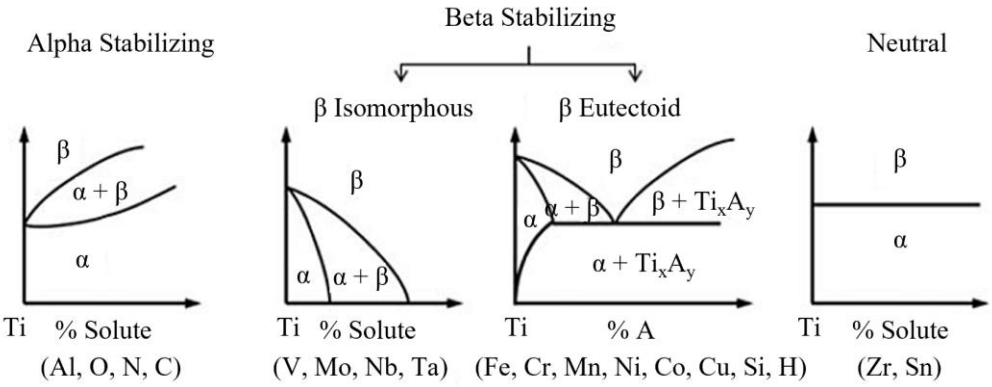


Figure 2.6 Influence of alloying elements on phase diagrams of titanium alloys [8].

Commercial titanium alloys are organised into five primary categories: α, near-α, α + β, near-β, and β. Each category possesses unique properties, which are qualitatively compared in Figure 2.7, especially against the backdrop of the typical α + β alloy, Ti-6Al-4V. This particular alloy represents approximately 60% of the titanium-based materials utilised in jet engines and 80%–90% in airframes. The figure highlights several critical trends:

- Alloys with a higher beta content can be heat treated to achieve greater strengths, but they typically exhibit reduced weldability.

- Alloys with a leaner beta content generally display enhanced high-temperature creep resistance.
- Near-β alloys, when compared at equivalent strength levels, offer superior cold formability.

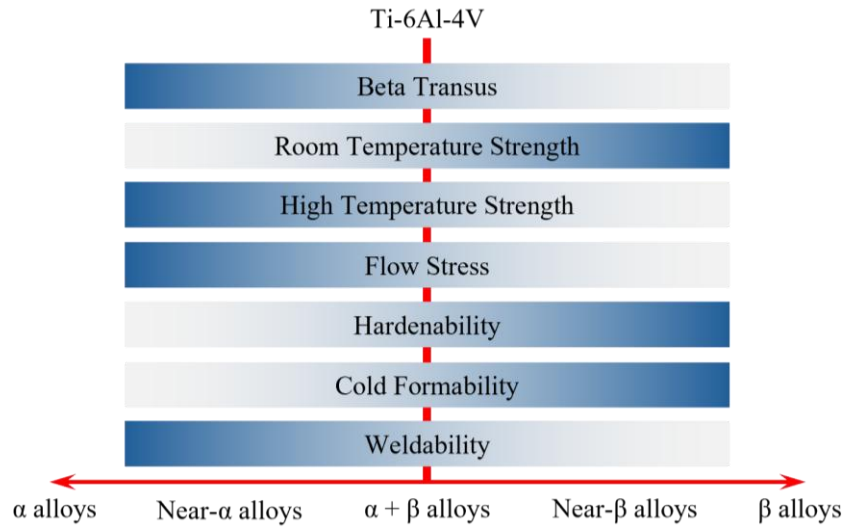


Figure 2.7 Qualitative comparison of different titanium alloy family groups [8].

These distinctions underscore the trade-offs and specific applications of each titanium alloy grade within the aerospace industry. Some titanium alloys commonly used in the aerospace industry are listed in Table 2.5.

In addition to substitutional alloying elements, the mechanical properties of titanium alloys can be significantly influenced by interstitial elements such as O, C, N, and H. These elements may be present as impurities in the raw materials or can be intentionally added within controlled specification limits to enhance strength, while maintaining acceptable levels of ductility and damage tolerance. For instance, incorporating approximately 0.1 wt% N can more than double the strength of a titanium alloy, albeit at the cost of halving its ductility.

The microstructure of conventional titanium alloys is predominantly characterised by the size and arrangement of the two principal phases, α and β. Two common types of phase configurations in titanium alloys are illustrated in Figure 2.8, where a lamellar microstructure forms upon cooling from the β phase field while an equiaxed microstructure typically results from a recrystallisation process. Both forms of microstructure can involve either a fine or coarse arrangement of these phases. A combination of lamellar and equiaxed structures, known as

bimodal or duplex microstructure, is often employed to achieve a balanced set of properties for specific applications. Table 2.6 details the impact of various microstructural characteristics on key material mechanical properties.

Table 2.5 Important commercial titanium alloys [1], [8].

Alloy type	Composition	Application
α/Near-α	Ti-5Al-2.5Sn Ti-6Al-2Sn-4Zr-6Mo Ti-5.5Al-3.5Sn-3Zr-1Nb Ti-5.8Al-4Sn-3.5Zr-0.7Nb Ti-2.25Al-11Sn-5Zr-1Mo	Gas turbine engines
α + β	Ti-6Al-4V Ti-6Al-2Sn-4Zr-6Mo Ti-5Al-2Sn-2Zr-4Mo-4Cr Ti-6Al-6V-2Sn Ti-2Al-2Sn-4Mo-0.5Si	Engine compressor fan
β/Near-β	Ti-6Al-2Sn-4Zr-6Mo Ti-5Al-2Sn-2Zr-4Mo-4Cr Ti-4.5Al-3V-2Mo-2Fe Ti-10V-2Fe-3Al Ti-3Al-8V-6Cr-4Mo-4Zr	Heavily loaded parts

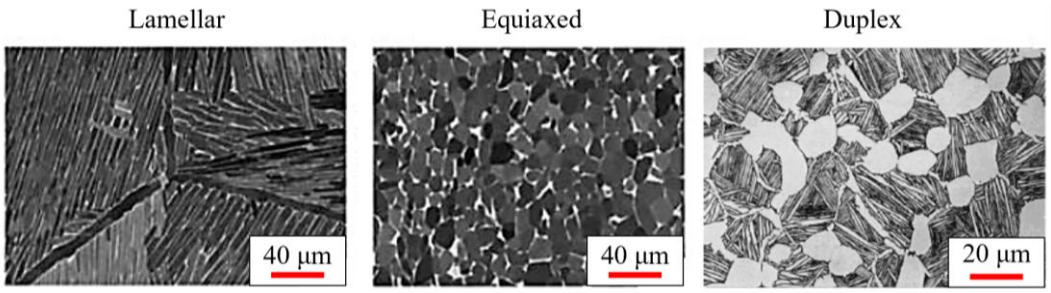


Figure 2.8 Three typical microstructures of titanium alloys [8], [19].

The chemical composition of the α and β phases in titanium alloys are virtually identical, yet they exhibit distinct properties due to their differing crystal structures. The α-Ti alloys with their superior creep resistance and ductility at high temperatures (500°C–600°C), are more suited for aeroengine components. Additionally, α-Ti is favoured for its excellent corrosion resistance and fabricability, which includes formability and weldability, making it also ideal for use in chemical processing equipment, heat exchangers, pumps, piping and similar applications. Conversely, β-Ti is characterised by higher tensile strength and fatigue resistance compared to α-Ti, which stem from fewer slip systems in its BCC crystal structure, rendering it more

appropriate for use in highly loaded aircraft structures. For example, the Boeing 777 utilises β-Ti alloys in various components such as landing gear, exhaust plugs, nozzles and sections of the nacelle [1].

Table 2.6 Influence of microstructure characteristics on mechanical properties [8].

Fine	Coarse	Property	Lamellar	Equiaxed
↑	↓	Strength	↓	↑
↑	↓	Ductility	↓	↑
↓	↑	Fracture toughness	↑	↓
↑	↓	Fatigue crack initiation	↓	↑
↓	↑	Fatigue crack growth rate	↑	↓
↓	↑	Creep strength	↑	↓
↑	↓	Superplasticity	↓	↑
↑	↓	Oxidation behaviour	↑	↓

It is also common for titanium alloys to contain a mix of both α and β phases. This occurs in α + β-Ti, where the material structure includes grains of both α-Ti and β-Ti, with corresponding properties typically a balance between those of pure α-Ti and β-Ti alloys. Generally, α + β-Ti alloys offer greater strength than pure α-Ti alloys as well as superior creep strength and ductility compared to β-Ti alloys. This makes α + β-Ti alloys extensively utilised and particularly valuable in applications demanding higher strength, enhanced fracture resistance, greater fatigue strength or elevated temperature performance (300°C–450°C) with robust corrosion resistance, such as in aircraft structures, gas turbine jet engines, steam turbine blades and spacecraft components. An example application is illustrated in Figure 2.9, which is a Ti-6Al-4V engine blisk designed for the F-35 fighter.



Figure 2.9 Ti-6Al-4V blisk manufactured for the Joint Strike Fighter project [1].

2.1.2.2 Titanium aluminide

Titanium aluminide (TiAl) represents a distinct class of titanium-based alloys that falls within the category of intermetallic materials, known for their unique mechanical properties such as lower density and higher Young's modulus derived from their crystal structures. As a high-temperature material (up to 800°C), titanium aluminide is increasingly critical for the development of next-generation aeroengines [1], [4]. In this compound, titanium (BCC) and aluminium (FCC) are combined in a fixed ratio to form crystalline structures distinct from those of the individual metals. This results in the formation of hexagonal (DO_{19}) Ti_3Al and face-centred cubic transitioning to tetragonal ($L1_0$) TiAl compounds, as depicted in Figure 2.10. Within this context, the Ti_3Al structure is also referred to as the α_2 phase, while the TiAl structure is known as the γ phase.

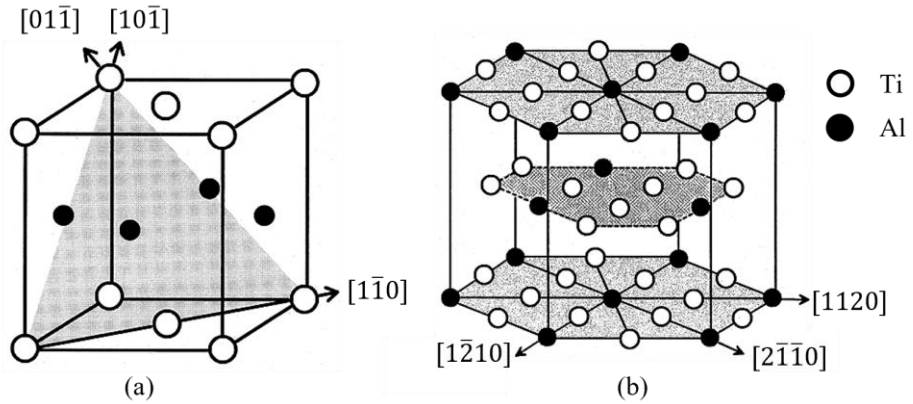


Figure 2.10 Crystal structures of (a) $L1_0$ and (b) DO_{19} types [20].

According to the phase diagram shown in Figure 2.11, TiAl alloys undergo a solidification process that initially transitions through the single-phase region of the α solid solution. Upon further cooling, the material decomposes via reactions such as $\alpha \rightarrow \alpha + \gamma \rightarrow \alpha_2 + \gamma$ or $\alpha \rightarrow \alpha_2 \rightarrow \alpha_2 + \gamma$. The cooling rate significantly influences these phase transformations, allowing for the formation of diverse microstructures. This variability provides the opportunity to control microstructures to enhance specific properties tailored for applications. Both the α_2 and γ phases demonstrate high-temperature strength, although they are characterised by low ductility. Notably, γ-TiAl exhibits extremely low ductility (1%–3%) at room temperature due to the limited number of available slip systems [6], [21]. Compared to the α_2 phase, which has a density of 4.1–4.7 g/cm^3 and a creep limit of 1000°C, the γ phase is lighter (density of 3.7–3.9 g/cm^3) and is capable of withstanding higher temperatures (up to 1000°C) [22]. Duplex phase

structures, particularly $\alpha_2 + \gamma$, are favoured for structural engineering applications due to the flexibility they offer in controlling phase distribution.

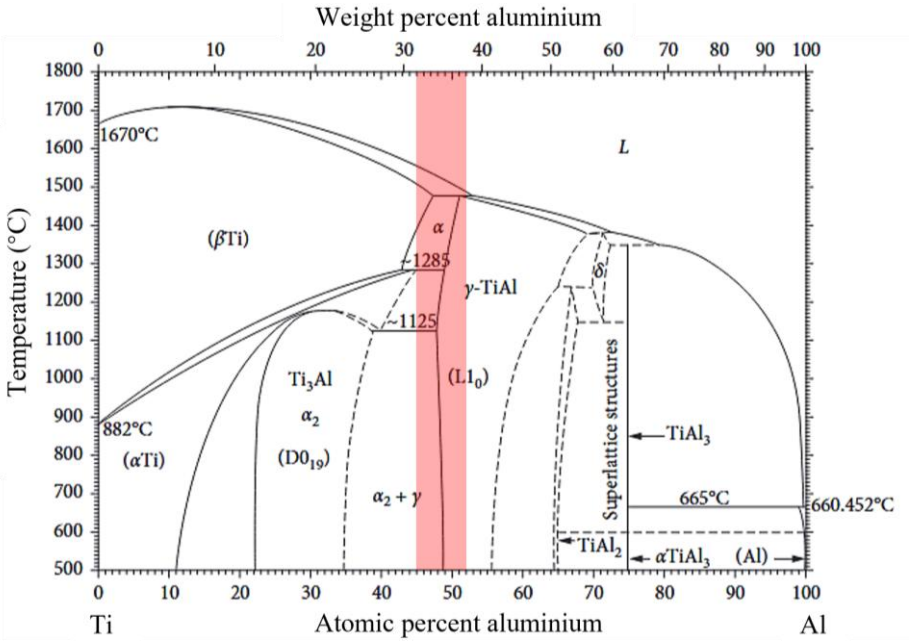


Figure 2.11 Binary Ti-Al phase diagram [23].

Among titanium aluminides and their various alloys, two-phase structures composed of predominantly γ and minor α/α_2 phases (γ-TiAl) are the most extensively studied. The scope of engineering application for γ-TiAl is specifically highlighted in Figure 2.11. TiAl boasts a high melting point of 1460°C, low density, high thermal stability, high specific strength and modulus, low diffusivity, excellent structural stability, and strong resistance to oxidation, corrosion, and ignition [24]. These characteristics render TiAl an attractive alternative to nickel-based superalloys in aerospace applications, especially in sections of aircraft jet engines that operate at high temperatures [25], [26]. Table 2.7 details a comparison between the properties of γ-TiAl and nickel-based superalloys at both room and elevated temperatures. The high-temperature properties of γ-TiAl alloys, which include good thermal stability and high strength, are comparable to those of nickel-based superalloys, but having only half the density. Therefore, γ-TiAl is potentially a viable alternative to nickel-based superalloys for components operating at temperatures of approximately 800°C and above, offering exceptional high-temperature oxidation resistance, creep resistance and stiffness [6], [23], [27].

In the engineering of γ-TiAl alloys, four main classifications of microstructures are prevalent, which are equiaxed, lamellar, duplex and pseudo duplex [15], as illustrated in Figure 2.12. A

single-phase γ-TiAl, containing equal proportions of Ti and Al, undergoes heat treatment slightly above the eutectoid temperature around 1125°C. This treatment results in a microstructure composed of equiaxed γ grains with α_2 precipitates at the grain boundaries, as depicted in Figure 2.12(d). This microstructure, also referred to as near-γ, is noted for a high elastic modulus (160–176 GPa) and enhanced high-temperature properties, though it exhibits low fracture toughness and ductility [4].

Table 2.7 Comparison of mechanical/physical properties between titanium aluminides and nickel-based superalloys [4].

Property	γ-TiAl alloys	Superalloys
Density (g/cm^3)	3.7–3.9	8.3
Room temperature modulus (GPa)	160–176	206
Yield strength (MPa)	400–630	1000
Tensile strength (MPa)	450–700	1200
Room temperature ductility (%)	1–3	15
Creep limit (°C)	1000	1090
Oxidation (°C)	900–1000	1090

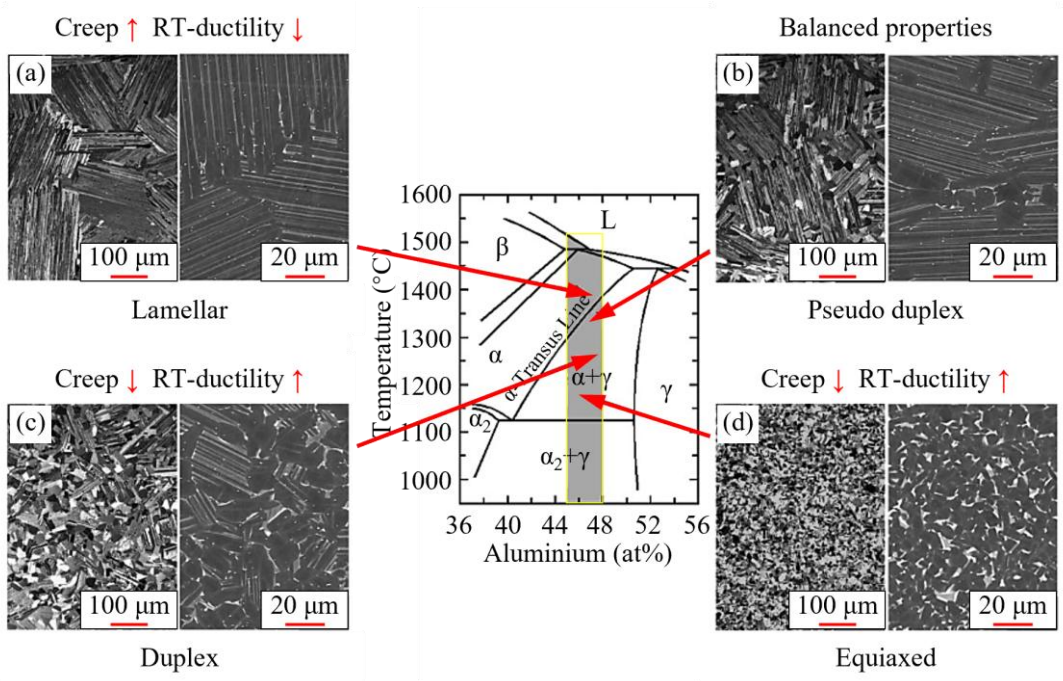


Figure 2.12 Mid-section of the binary Ti-Al phase diagram and representative microstructures showing (a) Lamellar/Fully Lamellar, (b) Pseudo duplex/Near Lamellar γ, (c)Duplex and (d) Equiaxed/Near Gamma (γ-TiAl appears dark, whereas α_2 shows a light contrast) [28].

Fully lamellar microstructures are produced when heat treatment occurs above the α-Transus line. During cooling, α-Ti precipitates form into alternating layers of α (which orders into α_2) and γ, resulting in a lamellar morphology. This lamellar structure exhibits greater ductility compared to the equiaxed structure due to the presence of gaps between the lamellar plates, although it still demonstrates poor ductility at room temperature. The grains within a lamellar structure are coarse, typically ranging in size from 200 μm to 1000 μm [6].

The duplex microstructure develops when the heat treatment temperature is set between the eutectoid temperature and the α-Transus temperature, as depicted in Figure 2.12(c). This microstructure comprises an equiaxed γ phase interspersed with a small number of lamellar colonies. Such a configuration enhances ductility while also improving high-temperature strength, creep resistance, and fracture toughness, benefits attributed to the lamellar microstructure [15], [20]. Kothari et al. [29] presented same results by comparing the mechanical properties of γ-TiAl with different microstructures, as shown in Table 2.8.

Table 2.8 Room temperature mechanical properties of γ-TiAl [29].

Microstructure type	Elongation (%)	Elastic modulus (GPa)	Flexural strength (MPa)
Near gamma	0.4	217.53	815.98
Pseudo duplex	0.3	203.90	746.54
Duplex	2.3	154.48	1238.62
Lamellar	1.5	134.59	578.51

The pseudo duplex microstructure, also referred to as near lamellar γ, is illustrated in Figure 2.12(b). This structure forms with heat treatment temperatures below the α-Transus temperature and features a larger amount of lamellar α_2 + γ phase compared to standard duplex microstructures, typically measuring approximately 150 μm to 200 μm. The γ phase in the lamellar colonies and the equiaxed γ grains in the pseudo-duplex structure are crystallographically identical [30].

General Electric (GE) currently employs γ-TiAl, specifically the second-generation Ti-48Al-2Cr-2Nb (at%), for low-pressure turbine (LPT) blades in the GEnx™ engines used by Boeing's 787s and 747-8s airplanes, as illustrated in Figure 2.13. The turbine configuration includes two high-pressure stages and seven low-pressure stages, with the 6th and 7th stages comprising TiAl LPT blades. The adoption of TiAl in the GEnx™ engines resulted in a 20% reduction in fuel consumption, a 50% decrease in noise and an 80% reduction in NOx emissions compared to

previous engines in its class. Additionally, the new LEAP^{TM} engines, which are also equipped with TiAl LPT blades, are set to be featured in Boeing 737, Airbus A320neo, and Comac C919 aircraft [31].

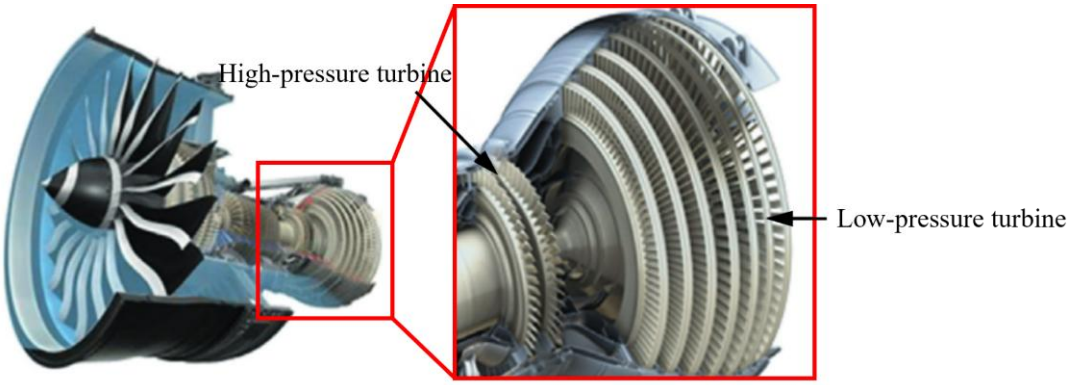


Figure 2.13 GEnx-1B aircraft engine with high/low pressure turbine section featuring γ-TiAl blades [31].

2.1.2.3 Aluminium alloys

Aluminium alloys exhibit highly favourable mechanical properties at moderate temperatures (up to 150°C), including high specific strength (~150 kPam^3/kg), durability, and damage tolerance. Since the 1930s, aluminium--based alloys have played a crucial role in the development of weight-efficient airframes. In comparison to other materials, aluminium is utilised in considerably larger quantities in critical airframe components such as the fuselage and wings, comprising 60%–80% of the airframe weight [8].

Despite increasing competition from composite materials, aluminium continues to hold a significant presence in the construction of both military and civilian aircraft due to its cost-effectiveness and performance. While composites are becoming more popular, they have several drawbacks such as low impact resistance, complex mechanical behaviours under varying environmental conditions including moisture absorption as well as challenges related to repair and recycling [32]. A notable example of aluminium usage is the Boeing 777, where the majority of the airframe is constructed using high-strength aluminium alloys, with the exception of the landing gear and turbine engines. Figure 2.14 highlights the components manufactured with different aluminium alloys in the Boeing 777.

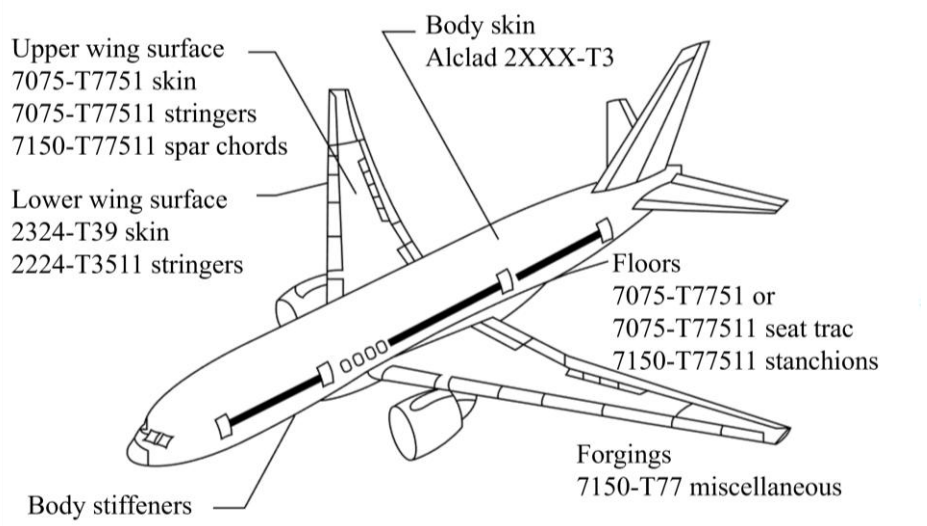


Figure 2.14 New aluminium alloys and tempers used in the Boeing 777 [33].

Two major types of aluminium alloys are available based on the processing method, which are cast and wrought. Cast alloys are generated by casting without further mechanical or heat treatment. The designation system for cast aluminium alloys has a three-digit number and the first digit refers to the major alloying elements. Notably, the zero after the decimal point represents casting. Wrought alloys, which are produced through an initial casting process followed by deformation processing, are typically designated by a four-digit number according to the international alloy designation system. These alloys fall into eight categories (1xxx–8xxx series) based on the primary alloying element. This system helps differentiate them from cast alloys, which generally exhibit limited strength and ductility. The designation system for wrought and cast aluminium alloys is detailed in Table 2.9.

The temper designation system, a series of letters and numbers, is utilised to specify the type of tempering applied to an aluminium alloy. "Temper" refers to the combination of mechanical (e.g., cold working and hot working) and thermal treatments (e.g., annealing and age-hardening) administered to an aluminium product to achieve desired metallurgical properties. This system has been endorsed by the American Standards Association and is widely used in the USA and many other countries. It is applicable to all wrought and cast forms of aluminium (excluding ingots), involving processes such as solution treatment followed by artificial ageing, as detailed in Table 2.10.

Table 2.9 Aluminium alloy designation system for wrought/cast alloys [1], [8].

Category	Digit Series	Major alloying elements
Wrought alloys	1xxx	Commercially pure Al (>99% Al)
	2xxx	Copper (most also contain magnesium)
	3xxx	Manganese
	4xxx	Silicon
	5xxx	Magnesium
	6xxx	Magnesium and silicon
	7xxx	Zine (most also contain magnesium and copper)
	8xxx	Others
Cast alloys	1xx.0	Commercially pure Al (>99% Al)
	2xx.0	Copper
	3xx.0	Silicon with added copper or magnesium
	4xx.0	Silicon
	5xx.0	Magnesium
	6xx.0	Unused
	7xx.0	Zinc
	8xx.0	Tin
	9xx.0	Others

Table 2.10 Temper designations for aluminium alloys [1].

Symbol	Description
F	As fabricated (e.g. Hot-worked, forged, etc.)
O	Annealed (wrought products only)
H	Cold-worked (strain hardened) H1x – cold-worked only (x refers to amount of cold working and strengthening) H2x – cold-worked and partially annealed H3x – cold-worked and stabilised at a low temperature to prevent age hardening
W	Solution-treated
T	Age-hardened T1 – cooled from fabrication temperature and naturally aged T2 – cooled from fabrication temperature, cold-worked and naturally aged T3 – solution treated, cold-worked and naturally aged T4 – solution treated and naturally aged T5 – cooled from fabrication temperature and artificially aged T6 – solution-treated and artificially aged T7 – solution-treated and stabilised by over-ageing T8 – solution-treated, cold-worked and artificially aged T9 – solution-treated, artificially aged and cold-worked T10 – cooled from fabrication temperature, cold-worked and artificially aged

The most common classes of aluminium alloys used in aerospace applications are from the 2xxx and 7xxx series [34], [35]. The 2000 series alloys, known for their excellent resistance to fatigue crack growth and superior damage tolerance, are frequently employed in aircraft

fuselage skins and lower wings, where fracture toughness (resistance to crack growth) is a critical design consideration. The Al2024-T3 is the most widely used 2000 series alloy for fuselage construction. Conversely, the 7000 series is typically employed in the upper wing skins, where high strength is the primary design requirement with Al7075-T6 the most notable 7000 series alloy utilised in aircraft applications.

The advantages and disadvantages of aluminium alloys are concisely outlined in Table 2.11. Compared to titanium alloys, aluminium alloys are generally easier to machine due to their lower hardness. However, this advantage can sometimes be negated by their low melting point and high ductility, which can cause aluminium chips to adhere more severely to cutting tools and form built-up edge [36]. This can significantly impede the cutting process and lead to premature tool failure.

Table 2.11 Advantages and disadvantages of aluminium alloys.

Property	Characteristics
Advantage	Moderate cost. Ease of fabrication, including casting, forging and heat-treatment. Light weight (density of only 2.7 g/cm3). High specific stiffness and specific strength. Ductility, fracture toughness and fatigue resistance. Good control of properties by mechanical and thermal treatments.
Disadvantage	Low mechanical properties at elevated temperature (softening occurs above ~150). Corrosion when in contact with carbon-fibre composites. Age-hardenable alloys cannot be easily welded.

The high ductility of the material also results in pronounced burr formation at the edges or entrance/exit locations of workpieces, particularly during drilling and milling operations. The typical response to mitigate these issues involves the use of wet cutting with coolant to reduce heat generation and alleviate the problem of chip adhesion. However, this approach is environmentally unfriendly. Figure 2.15 illustrates common problems encountered in machining of aluminium alloys [37].

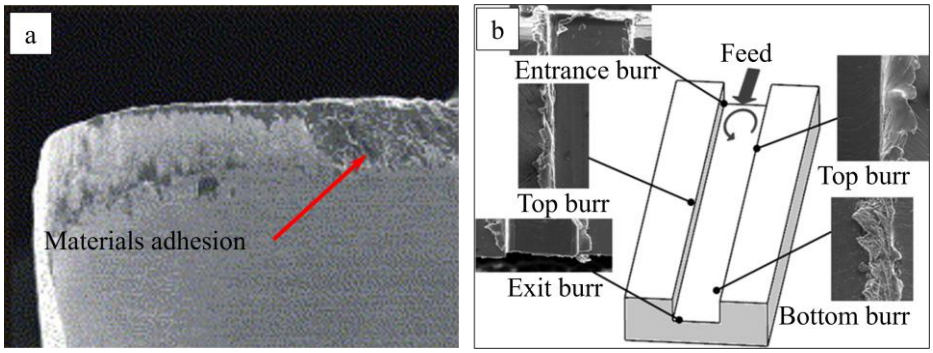


Figure 2.15 Typical issues in cutting aluminium alloys; (a) Material adhesion to the cutting edge [38] and (b) burr formation in milling [37].

2.1.2.4 Steels

Steel, an iron/ferrous based alloy, incorporates carbon with one or more additional alloying elements and is the most commonly used metallic material in structural applications worldwide due to its high strength and ductility combined with its relatively low cost. Globally, steel consumption is approximately 100 times greater than that of aluminium alloys. The grades of steel used in the aircraft construction generally boast yield strengths ranging from 1500 MPa to 2000 MPa, surpassing that of high-strength aluminium alloys (500–650 MPa), α + β titanium alloys (830–1300 MPa) and quasi-isotropic carbon-epoxy composites (750–1000 MPa). In addition to high strength, steels employed in aerospace applications also exhibit high elastic modulus (~210 GPa), excellent fatigue resistance and superior fracture toughness, which are largely retained even at elevated temperatures of approximately 300℃ to 450℃ [1].

Whilst there are hundreds of steel grades available, only a select few meet the high strength and toughness requirements essential for aircraft structures. Among the most significant are mild steels, high-strength low-alloy steels, medium-carbon low-alloy steels, maraging steels and stainless steels. Specifically, medium-carbon low-alloy steels, maraging steels and precipitation-hardened (PH) stainless steels are the most widely utilised in the manufacture of aircraft parts. The alloy compositions and mechanical properties of several key steel grades are detailed in Table 2.12. One notable application of stainless steels is for landing gear components, as illustrated in Figure 2.16, which demands high strength and corrosion resistance [39]. However, the outstanding physical/mechanical properties of such steels also make them challenging to machine, with typical issues including high temperature strength, tendency for work hardening and strong adhesion of chips. These factors necessitate stringent control of

operating parameters and the use of appropriate cutting tool materials, such as ceramics tools, CBN tools, coated carbide tools, etc [40].

Table 2.12 Composition and properties of selected steels used in aircraft [1].

Steel	Average composition	Yield strength (MPa)	Ultimate strength (MPa)	Elongation (%)
Maraging steels				
18Ni (200)	0.03 max C, 18Ni, 8.5 Co, 3.3 Mo, 0.2 Ti, 0.1 Al	660	970	17
18Ni (250)	0.03 max C, 18Ni, 8.5 Co, 5 Mo, 0.4 Ti, 0.1 Al	1700	1790	11
18Ni (300)	0.03 max C, 18Ni, 9 Co, 5 Mo, 0.7 Ti, 0.1 Al	1950	2000	9
18Ni (350)	0.03 max C, 18Ni, 12.5 Co, 4.2 Mo, 1.6 Ti, 0.1 Al	2300	2370	6
Medium-carbon low-alloy steels				
4130	0.3 C, 1.0 Cr, 0.5 Mn, 0.25 Si, 0.2 Mo	540	700	25
4340	0.4 C, 1.8 Ni, 0.8 Cr, 0.7 Mn, 0.25 Si, 0.25 Mo	410	750	22
300M	0.38 C, 1.8 Ni, 1.6 Si, 0.8 Cr, 0.8 Mn, 0.4 Mo, 0.05 min V	1590	1930	7
Aermet 100	0.25 C, 13.5 Co, 11 Ni, 3 Cr, 1.2 Mo	1720	1960	14
H11	0.35 C, 5.0 Cr, 1.5 Mo, 1.0 Si, 0.45 V, 0.4 Mn,0. 0.3 Ni	1650	2000	9
Precipitation-hardening stainless steels				
15-5 PH	0.07 C, 15 Cr, 4.5 Ni, 3.5 Cu, 1 Mn, 1 Si, 0.3 Nb	1400	1470	10
17-4 PH	0.07 C, 16 Cr, 4 Ni, 4 Cu, 1 Mn, 1 Si, 0.3 Nb	1150	1330	10

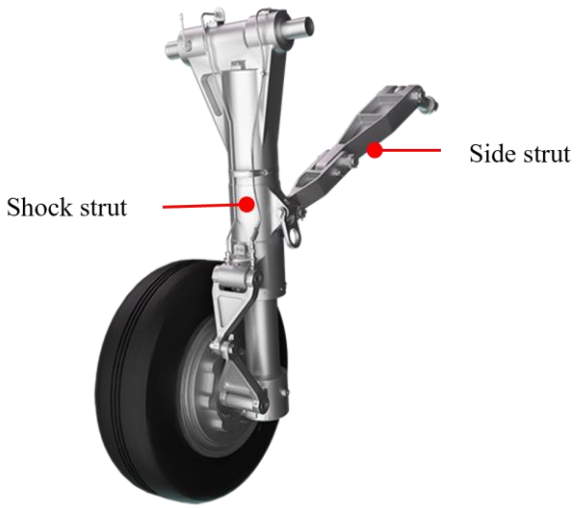


Figure 2.16 Steels used in manufacturing landing gear components [41].

2.2 Machinability of γ -TiAl intermetallic alloys

2.2.1 Overview

Titanium alloys, especially those used for aerospace applications are generally considered as difficult to machine, due in part to the following characteristics [42], [43], [44]:

- Work hardening: During conventional machining of titanium alloys, plastic deformation of the surface material leads to a work hardened zone. In addition, a dense, high-hardness oxide layer can also form on the workpiece surface at high cutting temperatures, further enhancing the material hardness.

- Small chip-tool contact area: The contact length between the chip and the tool is extremely short, which is less than one third of steel under same cutting conditions, leading to high cutting temperature and high stress close to the cutting edge.

- High cutting temperature: Compared to steels (~30–60 W/m·k) and aluminium alloys (~170–200 W/m·k), the poor thermal conductivity of titanium alloys (~8 W/m·k) results in elevated temperatures within the cutting zone, which contributes to increased tool wear and softening of the workpiece material.

- Large cutting forces: Due to the low material deformation coefficient, the contact area between the chip and rake face is small during processing, resulting in substantial cutting forces. Additionally, significant work hardening of the surface can further increase the cutting forces.

- Low modulus of elasticity: Titanium alloys following machining are susceptible to material spring-back, severely impacting the dimensional/geometrical accuracy of parts.

These aspects typically result in low production efficiency and increased risk of compromised surface quality. Compared to other metallic aerospace materials such as stainless steels and aluminium alloys, titanium alloys are more likely to exhibit surface defects and subsurface damage following machining, which can significantly affect the service performance and lifespan of the parts.

Unlike conventional titanium alloys, a critical mechanical property of γ-TiAl is its pronounced room temperature brittleness (up to 4% elongation), a characteristic common to intermetallic

materials due to their low dislocation density and inadequate mobile dislocations [22], [45]. This intrinsic brittleness of γ-TiAl limits its ability to accommodate the strain rates typically encountered during use. The adverse outcomes of machining γ-TiAl include high cutting forces, severe tool wear, elevated cutting temperatures and compromised workpiece surface/subsurface integrity. The underlying factors leading to these issues can be summarised as follows:

- Workpiece cracking: The low ductility of γ-TiAl at room temperature impedes material sliding during cutting, resulting in frequent initiation and propagation of subsurface cracking.
- Work hardening: Significant work hardening not only intensifies tool wear but also facilitates the propagation of cracks.
- Thermal conductivity: The low thermal conductivity of γ-TiAl causes heat to accumulate at the tool nose instead of being carried away by the chips. This steep temperature gradient can lead to rapid tool damage.
- Chemical reactivity: The high titanium content in γ-TiAl can react with elements such as oxygen and carbon at high temperatures, potentially accelerating the formation of adhesion. This reaction negatively impacts both tool life and workpiece surface integrity.

Over the past two decades, significant progress has been made in the fabrication of components using γ-TiAl, with notable advancements in casting, extrusion and forging [46], [47], [48]. However, there is a relatively scarcity of publications on the cutting of γ-TiAl. Figure 2.17 summarises the main research results and trends concerning the machinability of γ-TiAl over the past approximately 30 years [22], [49], [50], [51], [52], [53], [54], [55], [56], [57], [58], [59], [60], [61], [62], [63], [64], [65], [66], [67], [68], [69], [70], [71], [72], [73], [74], [75], [76], [77], [78], [79], [80], [81], [82], [83], [84], [85], [86], [87], [88], [89], [90], [91], [92], [93], [94]. Recent studies have shifted their focus from evaluating the influence of machining on workpiece surface integrity to investigating tool wear mechanisms, which are now considered a critical aspect of research. Much of the research has predominantly focused on turning and milling operations, with relatively fewer studies addressing drilling and grinding. The majority of relevant studies on γ-TiAl cutting were published between 2011 and 2015. Furthermore, a significant proportion of the published research has largely concentrated on a

limited number of γ-TiAl material compositions, specifically Ti-48Al-2Cr-2Nb (Ti-4822), Ti-45Al-8Nb-0.2C (TNB) and Ti-45Al-2Mn-2Nb + 0.8% TiB_2 (45XD), due in part to their relatively broader industrial applications.

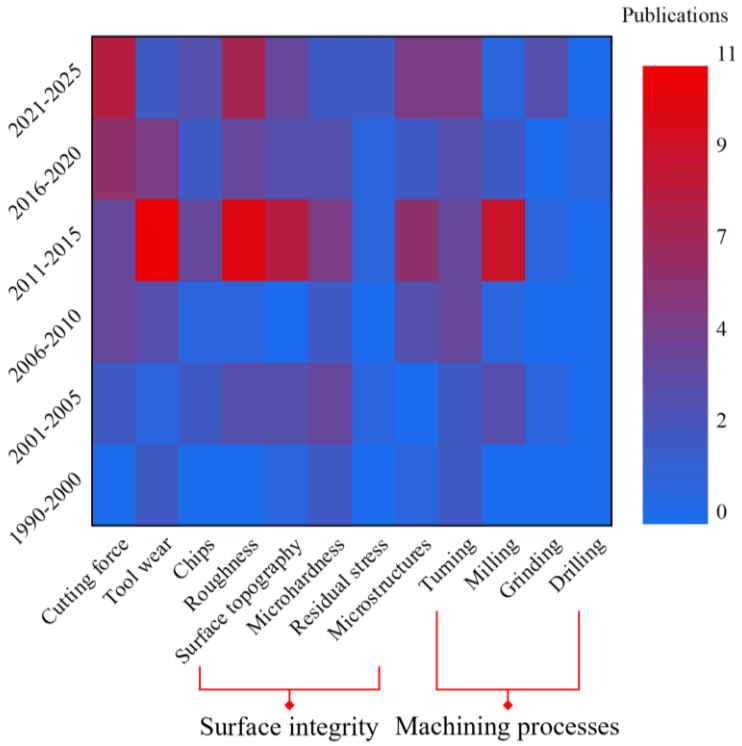


Figure 2.17 Main areas and focus of research relating to machinability of γ-TiAl since the 1990s.

Documented initial research into the machining of γ-TiAl dates back to the early 1990s. A summary of the operating parameters tested and the corresponding cutting processes in key publications is provided in Table 2.13.

Table 2.13 Summary of cutting and processes evaluated in published research involving the machining of γ-TiAl.

Material	Process	Cutting parameters
Ti-4822	Turning	v_c: 20–40 m/min, a_p: 1.0 mm, f: 0.13–0.25 mm/rev [49].
Ti-4822	Turning	v_c: 10–25 m/min, a_p: 0.3 mm, f: 0.05–0.10 mm/rev[50].
Ti-4822	Turning	v_c: 25–40 m/min, a_p: 0.05–0.1 mm, f: 0.05 mm/rev [53].
Ti-4822	Turning	v_c: 135–198 m/min, a_p: 0.005 mm f: 0.03 mm/rev [54].
Ti-4822	Grinding	v_c: 1760 m/min, a_p: 0.010 mm, f: 6 m/min [54].
Ti-4822	Milling	v_c: 40 m/min, a_p: 3 mm, f_z: 0.04–0.08 mm/tooth [80].
Ti-4822	Milling	v_c: 60–240 m/min, a_p: 5 mm, a_e: 0.5 mm, f_z: 0.08 mm/tooth [58].
Ti-4822	Turning	v_c: 0.01 m/min, a_p: 0.003–0.075 mm, a_e: 1.3 mm [60].
Ti-4822	Milling	v_c: 35–71 m/min, a_p/a_e: 0.3 mm, f_z: 0.06–0.10 mm/tooth [61].
Ti-4822	Turning	v_c: 60–100 m/min, a_p: 0.1–0.4 mm, f: 0.05–0.20 mm/rev [66].
Ti-4822	Milling	v_c: 50–345 m/min, a_p/a_e: 0.2–0.5 mm, f_z: 0.06–0.12 mm/tooth [64], [65].
Ti-4822	Milling	v_c: 50 m/min, a_p/a_e: 0.3 mm, f_z: 0.10 mm/tooth, rake angle: 4°/12° [63].
Ti-4822	Milling	v_c: 300–600 m/min, a_p: 5 mm, a_e: 0.1–0.2 mm, f_z: 0.05 mm/tooth [72].
Ti-4822	Milling	v_c: 100 m/min, a_p: 0.3 mm, a_e: 0.5 mm, f: 0.06 mm/rev [75].
Ti-4822	Turning	v_c: 35–50 m/min, a_p: 0.2–1.0 mm, f: 0.06–0.10 mm/rev [76].
TNB	Milling	v_c: 50–345 m/min, a_p/a_e: 0.2–0.5 mm, f_z: 0.06–0.12 mm/tooth [64], [65].
45XD	Milling	v_c: 70–120 m/min, a_p/a_e: 0.2–0.5 mm, f_z: 0.06–0.12 mm/tooth [51].
45XD	Turning	v_c: 80 m/min, a_p: 0.25 mm, f: 0.1 mm/rev, cooling: MQL/Cryo/Con [67].
45XD	Milling	v_c: 55–160 m/min, a_p/a_e: 0.05–0.2 mm, f_z: 0.05–0.10 mm/tooth [69].
45XD	Grinding	v_c: 30 m/s, v_w: 1000 mm/min, a_p: 0.5–1.0 mm [90].
45XD	Grinding	v_c: 140 m/s, v_w: 3 m/min, a_p: 0.5 mm, A_u: 6 μm [94].
45XD	Grinding	v_c: 80–140 m/s, v_w: 1.5–6 m/min, a_p: 0.15–0.6 mm, A_u: 8 μm [89].
Ti-46.8Al-1Mo-0.2Si	Turning	v_c: 60–300 m/min, a_p: 0.3 mm, f_z:0.02–0.05 mm/tooth [57].
MoCuSi	Turning	v_c: 100–500 m/min, a_p: 0.1 mm, f: 0.05 mm/rev [59].
MoCuSi	Milling	v_c: 50–70 m/min, a_p/a_e: 1 mm, f_z: 0.04–0.06 mm/tooth [62].
TNM	Turning	v_c: 80 m/min, a_p: 0.25 mm, f: 0.1 mm/rev, coating: AlCrN/TiAlN/TiN [73].
TNM	Turning	N: 500–800 rpm, a_p: 0.03 mm, f: 0.14–0.28 mm/rev, uncoated/PVD [87].
Ti-47.5Al-2.5V-1Cr	Turning	v_c: 25–100 m/min, a_p: 0.15–0.35 mm, f: 0.05–0.20 mm/rev [77].
Ti-47.5Al-2.5V-1Cr	Milling	v_c: 40–120 m/min, a_p: 0.05–0.25 mm, f_z: 0.005–0.025 mm/tooth [81].
Ti-47.5Al-2.5V-1Cr	Turning	v_c: 60–210 m/min, a_p: 0.2 mm, f: 0.1 mm/rev, cooling: dry/LN_2/cryo [88].
4822/45XD/TNB	Milling	v_c: 90 m/min, a_p/a_e: 0.3 mm, f_z: 0.1 mm/tooth, tile: 45° [71].
Ti-44Al-4Nb-2Cr	Milling	N: 5000 rpm, a_p/a_e: 0.15 mm, f: 100–300 mm/min, temp:25°C–650°C [91].

2.2.2 Cutting force, temperature and chip formation

Aspinwall et al. [64] reported that higher temperatures were observed with the workpiece (45XD) at 45° in ball-end milling process. Maximum constantan-workpiece thermocouple temperatures were recorded at 375°C for new tools and 413°C for worn tools at a cutting speed of 345 m/min. The measured temperatures demonstrated a 43%–47% increase as cutting speed varied from 50 m/min to 135 m/min. Notably, cutting temperatures were significantly higher when utilising worn tools compared to new cutters across all test conditions, as depicted in Figure 2.18(a). Hood et al. [65] reported the highest cutting temperature, approximately 250°C, occurred at the interface when a cutting speed of 160 m/min was utilised in ball-end milling TNB, as shown in Figure 2.18(b).

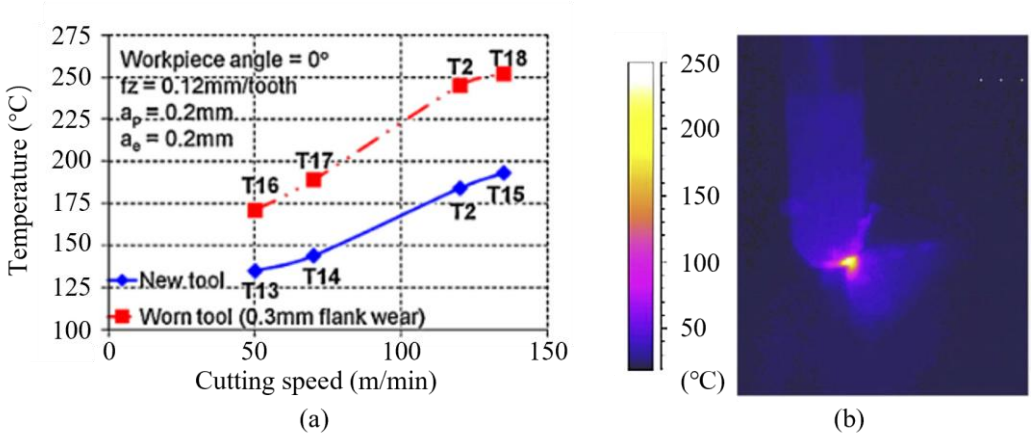


Figure 2.18 Experimental results of temperature in milling γ-TiAl; (a) Measured cutting temperatures at varying cutting speeds with new and worn tools [64] and (b) measured cutting temperature in milling TNB with a new tool [65].

A study by Uhlmann and Herter [57] indicated that locally heating up intermetallic alloys above the quasi-brittle-ductile transition temperature (~650°C) through interaction between the tool and workpiece material helped to facilitate more effective machining of γ-TiAl when using conventional cutting processes. Further research showed that higher cutting speeds, leading to elevated temperatures in the shear zone, enhanced chip formation as the material's brittleness decreased, resulting in a crack-free surface. By employing minimum quantity lubrication (MQL) in longitudinal external turning tests using uncoated round and chamfered RCMX 120400 carbide inserts, it was possible to achieve low roughness (Ra <0.4 μm) surfaces with no signs of cracking. Although transverse cross-sections of the machined samples showed deformation of the lamellar structure, the free-crack surface obtained at a cutting speed of 100 m/min indicated that the increased temperature also improved the material's ductility [66]. In contrast, Priarone et al. [63] noted that the lower deformability of γ-TiAl during the milling process with AlSiTiN coated carbide tools (v_c = 50 m/min, f_z = 0.1 mm/tooth, a_p/a_e = 0.3 mm) at high temperatures resulted in the formation of very small, powder-like, segmented chips with sharp edges, as shown in Figure 2.19(c). This differing view highlights the complexities involved in understanding the behaviour of γ-TiAl under varying thermal and mechanical conditions during machining.

Ge et al. [58] evaluated the high-speed milling of 45XD using TiAlN coated tools under dry conditions, in which revealed significant reduced tool life and higher cutting forces. Compared to the TA15, the milling forces of γ-TiAl were 190%, 180% and 200% greater for F_x, F_y and

F_z, respectively. Pérez [56] conducted a comprehensive examination of machinability and tool wear during face milling of Ti-4822 using a carbide insert tool, with cutting speeds varied from 20 m/min to 400 m/min and feed rates from 0.1 mm/tooth to 0.5 mm/tooth. The results showed that cutting forces increased more noticeably with an increase in cutting speed, indicating the strain rate sensitivity of γ-TiAl. Additionally, the chips produced were characterised by a fragmented and serrated morphology, as depicted in Figure 2.19(a), due to the material's high strength and low plasticity together with strain hardening that occurred during cutting. The brief immobility of crack initiation in the shear plane, followed by segments sliding, leads to a temperature increase at the tool tip, causing softening and subsequent wear as the segment slides over this area.

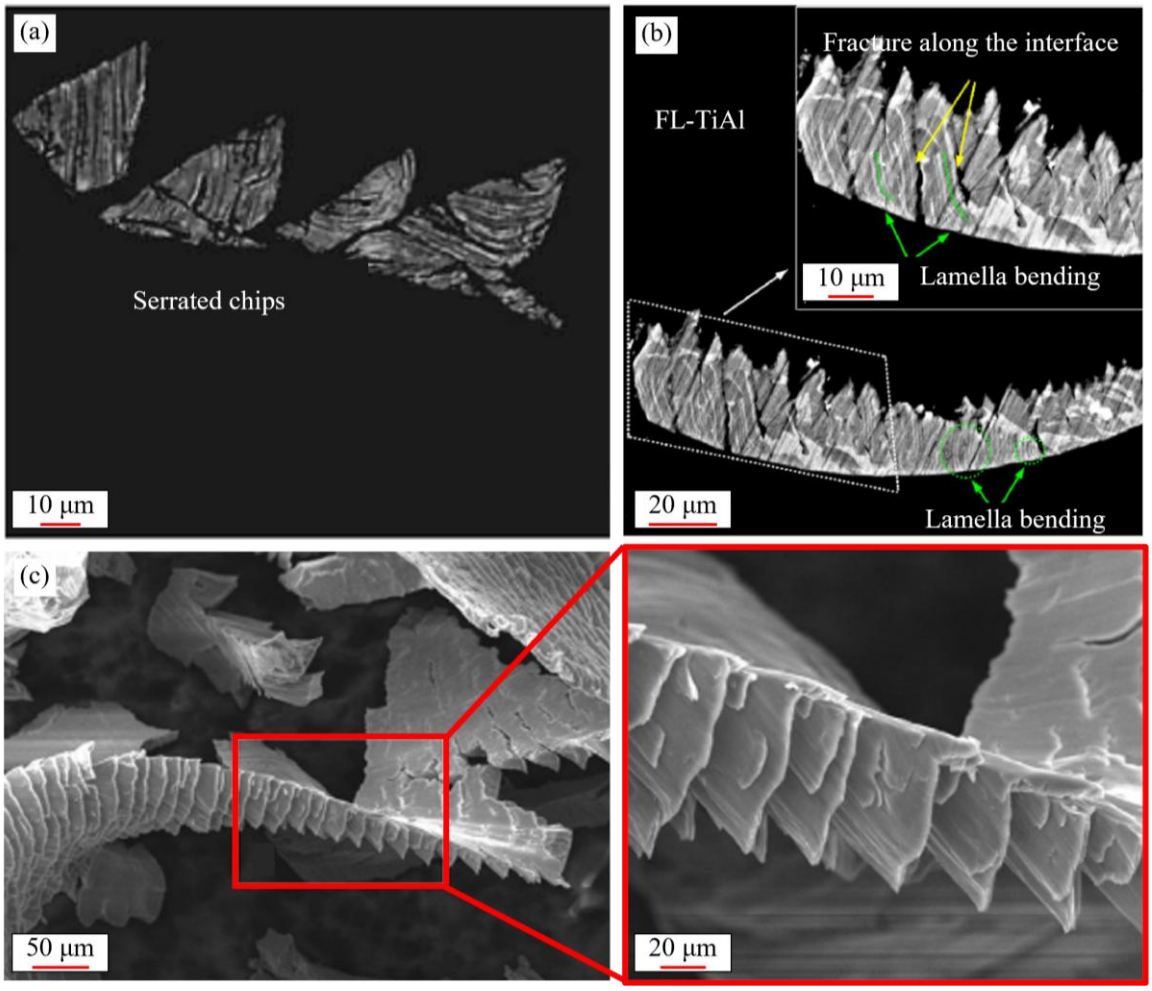


Figure 2.19 Chip formation and morphology following cutting of γ -TiAl; (a) Discontinuous serrated chips in milling (v_c = 20 m/min, f_z = 0.1 mm/tooth) [56], (b) sawtooth with crack in turning (v_c = 50 m/min, a_p = 5 μm) [86] and (c) sawtooth in milling (v_c = 50 m/min, f_z = 0.1 mm/tooth) [63].

Considering that γ-TiAl alloys exhibit more ductility at high temperatures, Fan et al. [91] developed a hybrid induction-assisted milling (IAM) process that heats the workpiece material in the cutting area using an induction coil. Compared to conventional milling at room temperature (25°C), cutting forces were reduced by up to 30.5% at a preheat temperature 450°C, likely due to a decrease in hardness and strength. Furthermore, at a preheat temperature of 450°C, cutting forces at different feed rates (100, 200, and 300 mm/min) decreased by more than 35%, proving that the machinability of γ-TiAl at high temperatures had improved.

Lubrication strategies are crucial for mitigating adverse high-temperature conditions within the cutting zone. In a preliminary study, Priarone et al. [61] assessed the performance of different lubrication conditions (flood, dry and MQL) when milling γ-TiAl and identified MQL as the most effective for extending tool life, outperforming both dry and wet conditions. However, there was no significant improvement in cutting forces, as shown in Figure 2.20. MQL promoted lubrication of the tool and workpiece without significantly reducing the temperature, thereby ensuring better ductility of γ-TiAl at high temperatures.

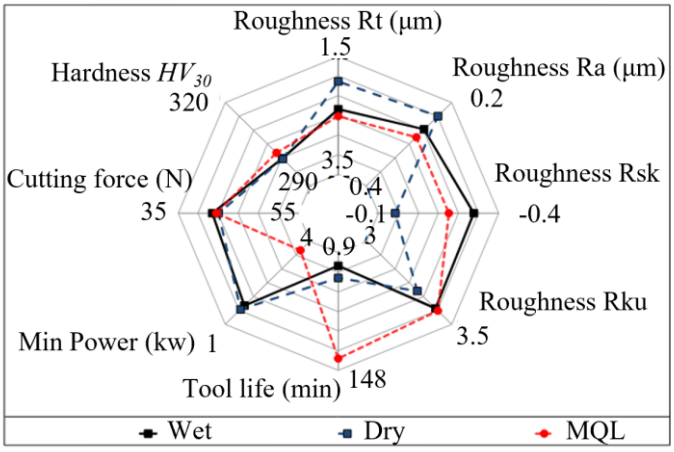


Figure 2.20 Effect of different lubrication conditions when milling γ-TiAl [61].

Klocke et al. [66] also evaluated the effects of various lubrication methods (dry, MQL and LN_2) and tool geometries (sharp, $b_{\gamma n}$ = 0.25 mm and $b_{\gamma n}$ = 0.50 mm) on cutting forces when turning TNB alloy. The results demonstrated a substantial reduction in cutting forces under cryogenic cooling conditions, with a threefold decrease compared to dry cutting, as illustrated in Figure 2.21(a) and (b). Meanwhile, a reduction of cutting forces was observed when sharp tools were used, as shown in Figure 2.21(b) and (c). Building on previous research, further experiments were conducted on the turning of 45XD using various pressure lubrication levels (6–300 bar).

The study found that the passive force measured under 300 bar flood cooling was reduced by 17% compared to that observed under conventional flood cooling conditions (6 bar) [67].

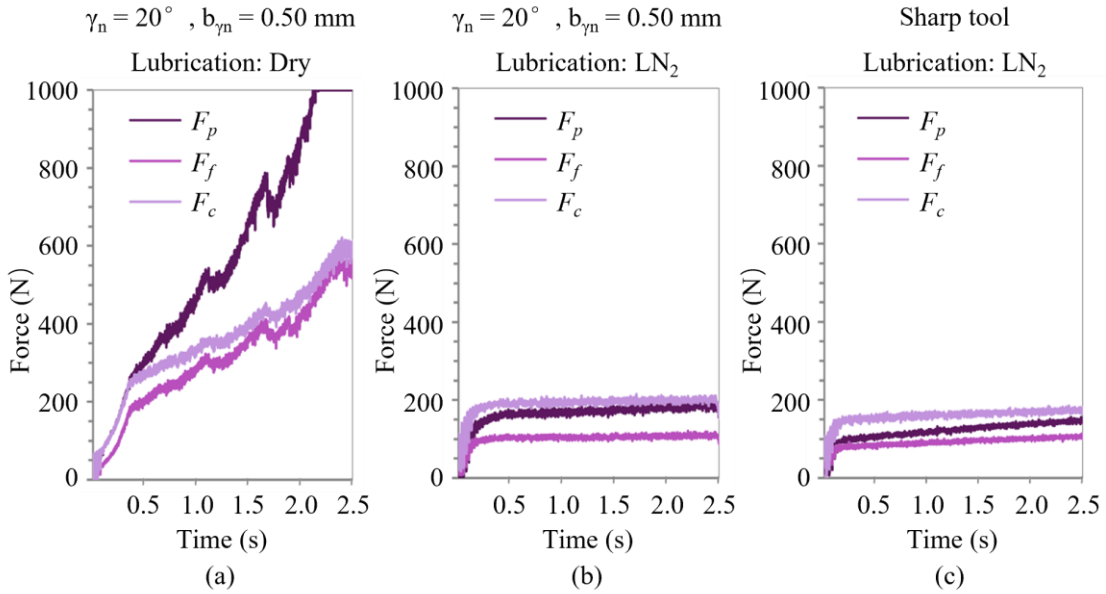


Figure 2.21 Measured cutting forces in turning 45XD referring to dry and cryogenic (LN_2) conditions [66].

In a comprehensive review of previous research, cutting speed was highlighted as a critical variable with Mantle and Aspinwall [55] noting that for certain γ-TiAl materials, employing high-speed operating regimes (>125 m/min) to soften the workpiece in the shear zone has been counterproductive, leading to cracking, hardened layers and tensile residual stresses in the machined surface/subsurface. However, Kolahdouz et al. [72] suggested that in HSM (v_c = 600 m/min), the heat generated softens the γ-TiAl, facilitating easier cutting with better surface roughness and reduced work hardening. This contradiction may stem from the significant difference in cutting speeds, despite both being classified as HSM.

Lower cutting speed can relieve the strain strengthening effect. At this stage, the work hardening effect becomes more dominant compared to the softening effect. However, high cutting speed leads to rapid increase in cutting temperature, causing material softening effect to surpass the work hardening effect. Consequently, the cutting force decreases, and a better machined surface would be obtained [81]. These findings collectively underscore the importance of temperature in machining γ-TiAl, highlighting the complex interplay between temperature, cutting speed and material behaviour.

2.2.3 Tool wear and failure

2.2.3.1 Introduction

Tool wear can be defined as "the alteration in the shape of the cutting edge or section of a tool from its original configuration, resulting from gradual loss of tool material during the cutting process." [95]. This type of wear occurs due to contact and relative sliding between the cutting tool, the workpiece and the chips, under the extreme conditions prevalent in the cutting zone. Several factors influence tool wear in complex machining environments, including the material properties of the tool and workpiece, together with the cutting forces and temperatures generated during machining processes [96]. The rate of tool wear is commonly quantified empirically and can be expressed through Equation 2-1 [97].

$$\frac{B}{L} = K\frac{P}{H} \tag{2-1}$$

where

B = volume of tool worn away

L = sliding length

P = applied load

H = hardness of material

K = probability that a real contact will result in wear

The ratio K/H is typically constant for a given loaded surface, with K, representing the wear coefficient, remaining constant as long as there are no changes in the chemistry of the system. This principle is central to the pin-on-disc model, which is used to measure wear volume across various sliding lengths and under different load conditions. Burwell illustrated this concept by showing how the ratio B/L varies over time for a lightly loaded conical pin, as depicted in Figure 2.22 [98]. This model helps in understanding how wear behaviours develop under specific conditions, providing valuable insights for predicting wear dynamics in practical applications.

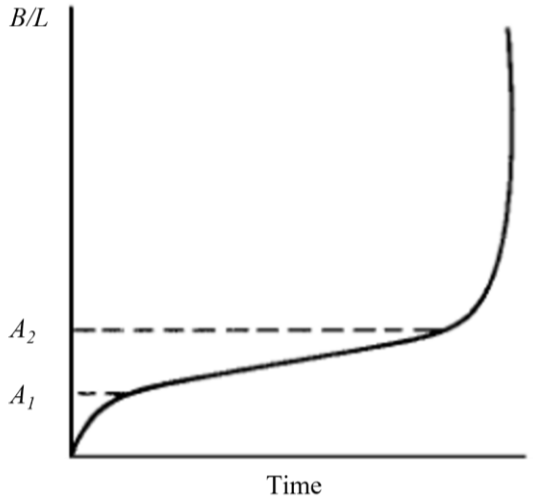


Figure 2.22 Variation of *B/L* with time for a lightly loaded conical pin in pin-on-disc test [98].

2.2.3.2 Tool wear mechanisms and failure

Tool wear and failure can be categorised into several types, including adhesive wear, abrasive wear, diffusion wear, fatigue, delamination wear, microchipping, gross fracture, and plastic deformation. It is important to recognise that tool wear does not result from a single process but from a combination of these mechanisms. Key mechanisms of tool wear and failure are explained below [96], [97]:

- Abrasive wear

  Abrasive wear arises when hard particles or asperities in the workpiece contact with the tool surface, resulting in material removal through mechanical actions such as micro-cutting, ploughing and fracture. This type of wear is prevalent in machining operations that involve hard-to-cut materials or workpieces containing hard inclusions, scale, or embedded particles.

- Adhesive wear

  Adhesive wear occurs when workpiece material adheres to tool surface due to greater inter bonding strength at the tool-chip interface compared to the internal strength of the material. This wear mechanism often leads to the formation of a built-up edge (BUE), a common indication of adhesive wear.

- Diffusion wear

  Diffusion wear happens when atoms from the tool material migrate to the workpiece (or vice versa) due to concentration variances, altering the microstructure and consequently strength of the material. This type of wear accelerates with rising temperatures, driven by concentration gradients at the tool-workpiece interface. Elements such as carbon, tungsten and titanium are commonly involved in this transfer.

- Oxidation wear

  Oxidation wear in cutting tools is a degradation process resulting from the chemical reaction between the tool material and atmospheric oxygen at elevated temperatures generated during machining. Such wear is characterised by oxide formation on the tool surface, which diminishes the tool's mechanical strength and thermal conductivity.

- Fatigue wear

  Fatigue wear results from cyclic loading and unloading of the cutting tool during machining, leading to crack initiation and propagation within the tool material. This wear is intensified under conditions of high mechanical stress and strain, typical in interrupted cutting operations like milling. Over time, these repetitive stress cycles can cause the tool material to crack and eventually flake off from the surface, a process often referred to as spalling.

- Gross fracture and edge chipping

  Gross fracture and edge chipping represent the predominant failure mechanisms in cutting tools, particularly in those made from inherently brittle materials. Fracture issues intensify during interrupted cutting or when machining exceptionally hard and strong such as polycrystalline boron nitride (PCBN) and tungsten carbide. The primary sources of tool fracture include excessive steady loading, shock loading due to interrupted cuts, the rapid unloading of a system that retains significant elastic energy, thermal stresses, cyclical stress repetition, and compromised surface integrity of the tools.

The extent of tool wear and corresponding life can be quantified based on the measurement of various wear patterns including flank wear (*VB*), face wear (*KT*), chipping (*CH*), cracks (*CR*),

flaking (*FL*) and catastrophic failure (*CF*) according to ISO 8688: 1989 [99]. Flank wear is the most commonly utilised measure in tool wear evaluation, as it provides an indication of the cutting tool's condition and operational efficacy.

Research has consistently shown that the poor machinability of γ-TiAl typically results in low tool life, with edge fatigue, abrasion and adhesion being the primary mechanisms of wear observed. Zhang et al. [49] investigated the turning of Ti-48Al-2Nb-2Mn under dry conditions and found that the high-temperature strength of γ-TiAl led to severe wear issues with most cutting tool materials (H1P, H6F, H10F, H13A), primarily due to the heat generated during the cutting process. The tool wear increased with higher cutting speeds, although the maximum cutting speed was only 40 m/min. The maximum flank wear after 30 seconds of cutting achieve ~0.9 mm. In all of grades of tools, H6F presented best performance in turning γ-TiAl.

Lubrication strategies are important for controlling the tool wear. Priarone et al. [61] investigated that MQL was believed to be the most effective method for extending tool life compared to dry and wet conditions when milling γ-TiAl. Further work reported that compared with conventional flood cooling (6 bar) there was a notable 41% reduction in tool flank wear when a high pressure flood cooling strategy was utilised [67]. By the same token, Benedicto et al. [87] explored the tool wear mechanisms of Ti-43.5Al-4Nb-1Mo-0.1B by comparing different lubrication conditions (dry, CCA, MQL, cryogenic, MWF, and Eco MWF) and tool categories (uncoated carbide and PVD coated carbide) in turning process (N = 500 or 800 rpm). This study revealed severe tool wear, leading to catastrophic failure under all cooling conditions, as illustrated in Figure 2.23. Dry cut was not considered suitable for turning γ-TiAl while MQL was the best way to minish tool wear due to the lubricating film generated by ester. Meanwhile, adhered materials and hard particles were observed in both uncoated and PVD coated tools, but less edge crack occurred when using PVD tools. In contrast, Klocke et al. [66] observed that after 10 seconds of turning, the maximum flank wear with MQL (~110 μm) was even higher than that with conventional flood cooling (~95 μm) and far exceeded high-pressure cooling (~70 μm) and cryogenic cooling (~50 μm). The reason was attributed to the larger corner radius of the main cutting edge, which led to high cutting forces. As a result, the lubrication film of MQL was ineffective and the temperature in the cutting area remained too high.

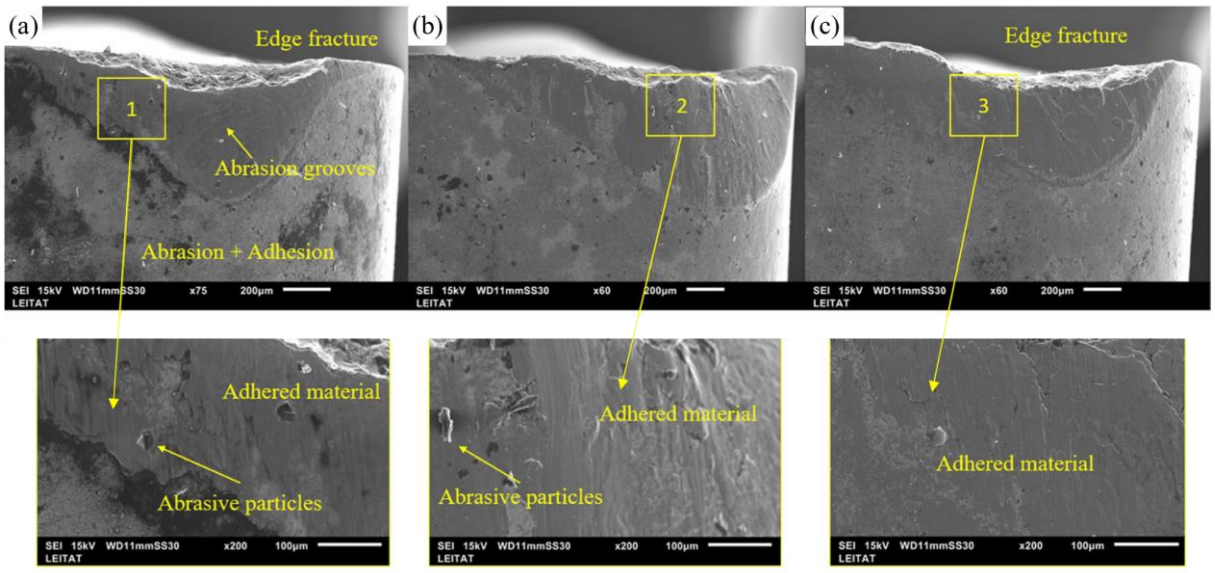


Figure 2.23 SEM images of flank wear on uncoated carbide tools when machining under; (a) and (d) MQL, (b) and (e) cryogenic and (c) and (f) MWF environment [87].

Yao et al. [76] examined the impact of different coating materials (PVD-TiCN and PVD-TiAlN) on tool wear when dry turning γ-TiAl. As indicated in Figure 2.24, results from energy dispersive spectrometry (EDS) measurements of the worn inserts not only identified elements from the workpiece material, such as Ti, Al, and Nb, but also showed a higher proportion of oxygen (zone 2#). This increase was attributed to oxidation reactions occurring at elevated cutting temperatures [76], [88], highlighting the complex interactions at the tool-chip interface in γ-TiAl machining.

Pérez [56] conducted detailed face milling experiments at cutting speeds ranging from 20 m/min to 300 m/min with feeds between 0.05 mm/tooth and 0.3 mm/tooth by using coarse/fine grain size carbide tools. Tool life improved significantly when face milling at a cutting speed of 20 m/min, a feed of 0.1 mm/tooth and 1 mm depth of cut with micro-grain carbide inserts. Beranoagirre et al. [62] conducted milling experiments on three different γ-TiAl alloys under various cutting conditions (v_c = 50, 60, or 70 m/min; f_z = 0.04, 0.05, or 0.06 mm/tooth) and concluded that cutting speed was the principal factor affecting tool life. The recommended cutting speed ranged from 50 m/min to 70 m/min, while the feed rate was maintained between 0.05 mm/tooth and 0.06 mm/tooth, using AlTiN coated tungsten carbide tools to achieve optimal tool life. Wang and Liu [81] observed that tool life (distance machined) decreased dramatically from 60 m to 1 m as cutting speeds increased from 60 m/min to 120 m/min,

although the level of surface defects were found to reduce when cutting speed rose from 80 m/min to 120 m/min, most likely due to the higher cutting temperatures involved.

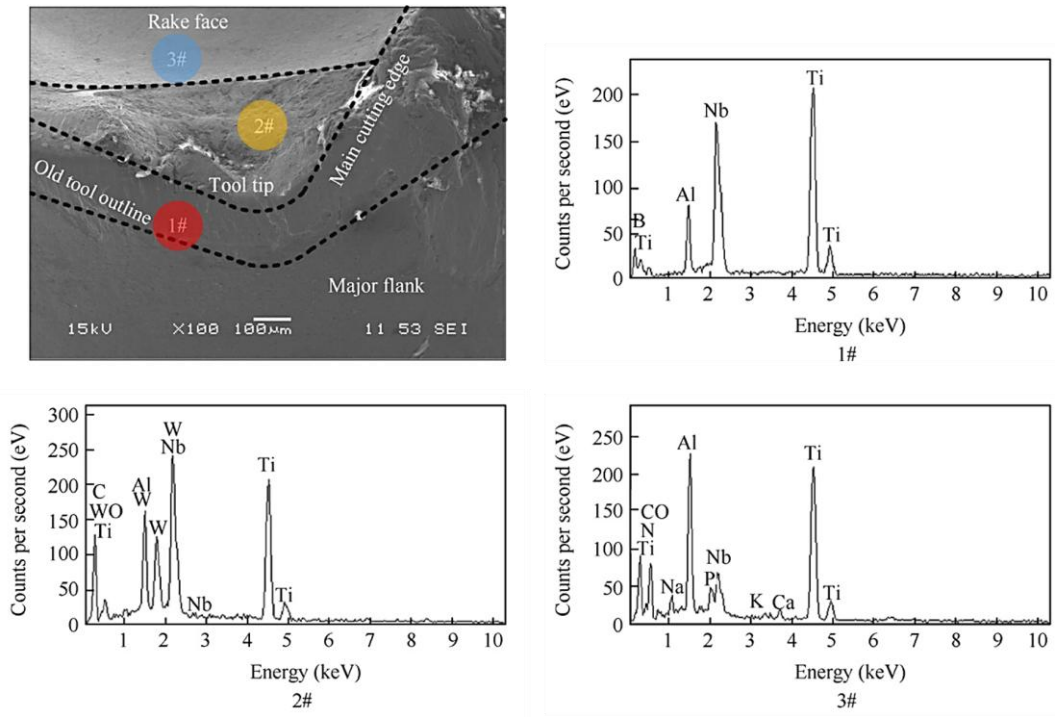


Figure 2.24 Tool wear condition and EDS results of PVD-TiAlN coated WC insert following turning of γ-TiAl [76].

To enhance tool life when milling γ-TiAl, Priarone et al. [63] recommended using a small radial rake angle ($\gamma = 4°$) and employing a drag finishing process. This approach could extend the tool life from 8 minutes to 20 minutes, as shown in Figure 2.25(a). Additionally, AlSiTiN coated tools could significantly increase tool life by nearly 50% compared to CrAlSiN coated tools. On this basis, applying polishing treatment could further improve the working time by approximately 50%, as illustrated in Figure 2.25(b). Priarone et al. [73] further assessed the performance of ultra hard cubic boron nitride (CBN) and polycrystalline diamond (PCD) tool materials against carbide tool when turning γ-TiAl with wet condition. Meanwhile, different CBN contents (50%–90%), PCD grain size (7–10 μm, 2 μm) and coating of carbide (uncoated, TiAlN coated) were considered. Figure 2.25(c) indicated that the life of uncoated carbide tools was approximately 2 minutes, while CBN tools (92%) retained effectiveness for about 8 minutes. PCD tools showed the best performance in turning γ-TiAl. The tool with a smaller grain size (2 μm) achieved at least 16 minutes of turning before reaching tool wear criterion of 1000 μm. This is largely attributed to the highest hardness of PCD tool (~6597 *HV*) to maintain

a sharp cutting edge over extended periods. However, it was noted that tool failure occurred abruptly when using coated carbide and low-content CBN inserts.

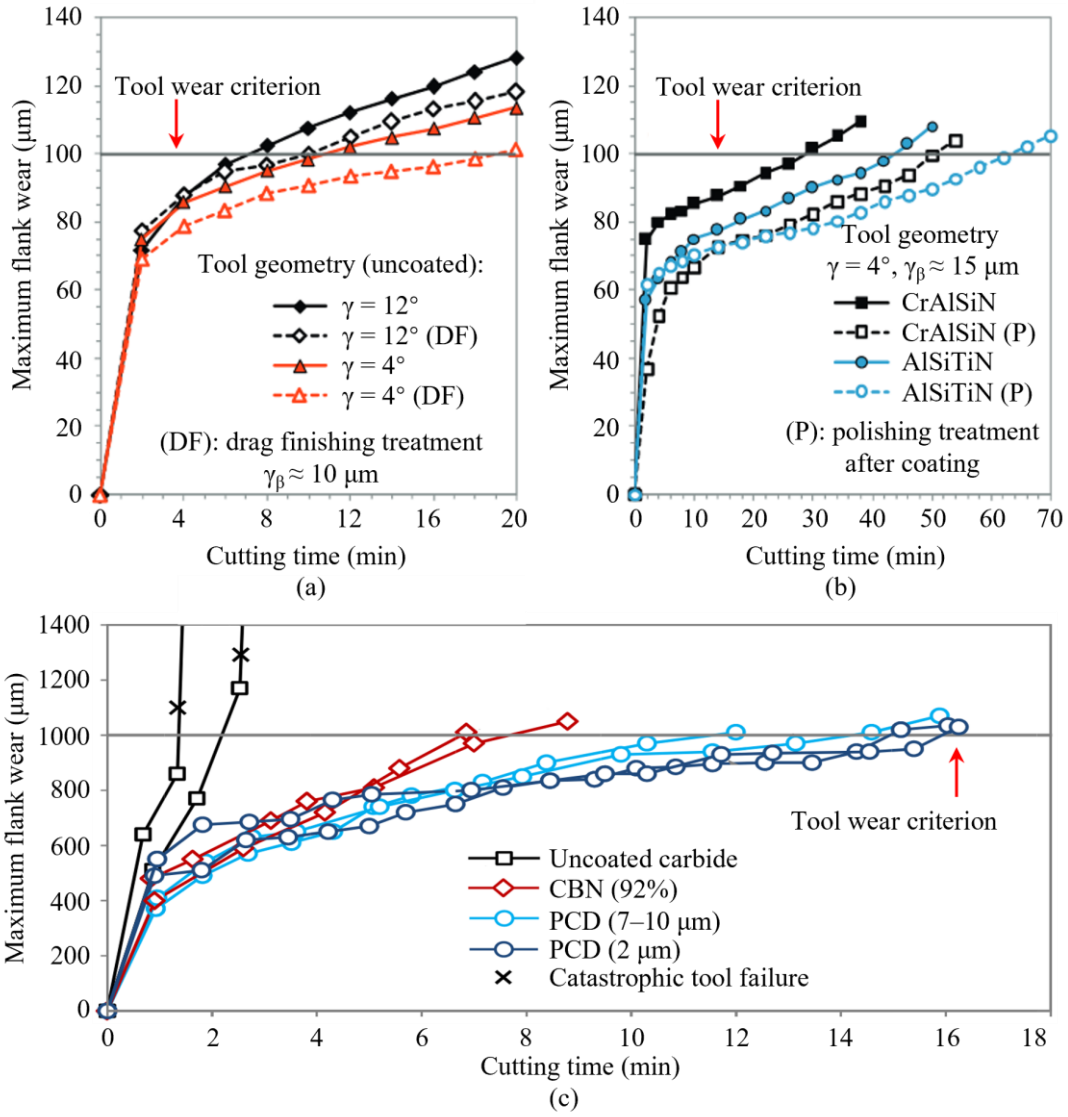


Figure 2.25 Influence of tool materials and geometry on flank wear; (a) and (b) The maximum flank wear with different geometry and coating tool under dry cutting conditions (v_c = 50 m/min, f_z = 0.1 mm/tooth) [63] and (c) the maximum flank wear with different coating tool under wet cutting conditions (v_c = 80 m/min, f_z = 0.1 mm/tooth) [73].

However, Ren et al. [75] revealed differing results. Their findings indicated that compared with AlCrN coated carbide tools, uncoated tools were more advantageous for high-speed milling at a spindle speed of 8000 rpm, leading to less etching and peeling. Besides, the impact of tool geometries (rake angle: 2°–14°; primary relief angle: 8°–14°; helix angle: 30°–60°) was

discussed and it was found that the primary relief angle was the dominant factor. Tool wear was approximately 65 μm with an 8° relief angle and about 190 μm with a 14° relief angle.

From the perspective of material structure, alloys with larger grains tend to demonstrate lower microstructural anisotropy, resulting in a longer effective distance for dislocation movement along the slip system. This typically makes deformation and cracks more likely to form on machined surfaces. According to Figure 2.12, the lamellar microstructure in γ-TiAl exhibits the largest grain size (>100 μm), which consequently impacts its machinability. Settineri et al. [71] carried out a comparative study on machinability of TiAl-4822, 45XD and TNB compositions through benchmark turning and milling tests. Significant differences in machinability were observed between the various alloys, with TiAl-4822 identified as the easiest to machine due to its lower tensile strength and hardness. Conversely, 45XD was found to be the most challenging to machine, which was similarly reported by Hood et al. [65] when milling TNB and 45XD due to the increased abrasive wear caused by the presence of TiB_2 ceramic particles in the latter. Further comparative experimental trials undertaken by Ge et al. [58] between γ-TiAl and near-α titanium alloy TA15 using TiAlN coated carbide tools showed that tool life for γ-TiAl was only 35 minutes, which was approximately half that of TA15. These studies underline the significant influence of material composition and microstructural characteristics on machining performance and tool wear for different titanium alloys.

2.2.4 Workpiece surface integrity

2.2.4.1 Introduction

General machining studies revealed that structural damage to components in service often occurs within several tens of microns from the working surface [100], [101]. This suggests that machining influences not only the surface topography but also has a profound impact on the microstructure as well as mechanical and physical/chemical properties of the workpiece material. Consequently, traditional precision control for detecting geometrical/dimensional inaccuracies is insufficient for assessing the quality of processing nor to ensure the fatigue life of components. Instead, evaluating machining quality from a more particular perspective requires examining the variations in geometrical structure, mechanical and material properties of both the surface and subsurface layers. This comprehensive approach can provide a better indication of component integrity and performance.

Surface integrity is typically assessed based on three main aspects comprising the surface, subsurface layer and edge quality of a machined part. Surface quality encompasses the measurement of surface morphology and roughness while subsurface layer evaluation generally includes the assessment of residual stress, metallographic alterations, microcracks and microhardness variation. Assessment of edge quality largely focuses on the size and shape of burrs formed following machining. The standards for evaluating surface integrity vary depending on the specific machining operation and requirements of the components involved. In this thesis, the assessment of machined workpiece surface integrity will involve parameters such as surface morphology, surface roughness, subsurface metallographic/microstructural alterations, microhardness, residual stress and edge quality (see Figure 2.26). This comprehensive evaluation aims to provide a thorough understanding of the influence of machining on the properties and performance of the workpiece material.

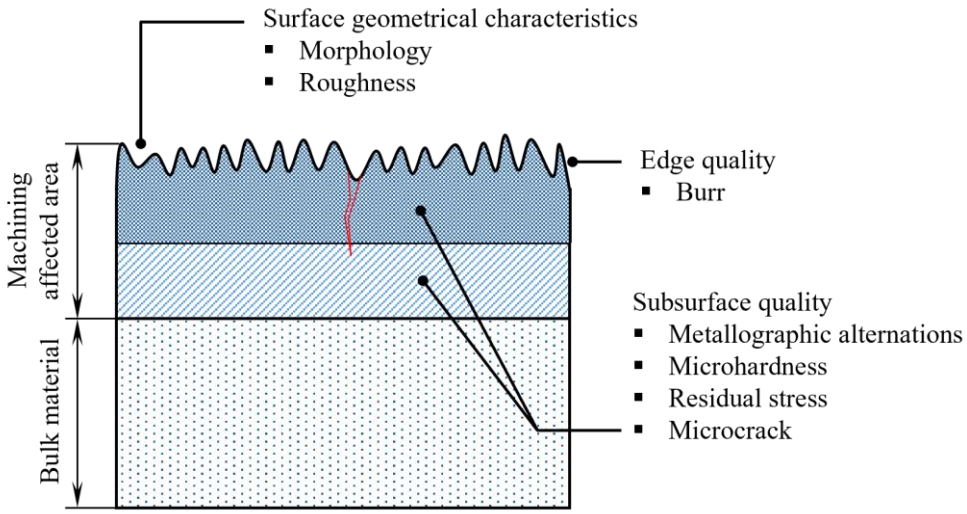


Figure 2.26 Schematic diagram of potential surface integrity effect/parameters due to machining.

2.2.4.2 Surface morphology and edge quality

Tool geometry and trajectory of the cutting edge play crucial roles in shaping the morphology of the machined surface, serving as the most direct indicators of the machining effects. Various factors influence surface morphology and different machining methods can produce distinct surface characteristics while variations in cutting parameters can further affect the results. Consequently, surface morphology represents the microscopic geometric structure created by tool movement, heat transfer and plastic deformation during the machining process.

Surface morphology comprises waviness, defects and geometric profile of the surface. Notably, surface defects offer the most direct insight into surface morphology, with typical forms of damage including scratches, material peeling, burns, material adhesion and macro/micro-cracks. Therefore, evaluating surface morphology is an effective approach to assess the efficacy of machining methods and the appropriateness of parameter settings.

The surface defects typically observed following machining of γ-TiAl alloys include work-hardening, material pull-out, lamella deformation, edge breakage and micro-cracks [53], [55], [102], examples of which are illustrated in Figure 2.27. Furusawa et al. [54] investigated the surface defects arising from ultra-precision turning (v_c = 135–198 m/min, a_p = 5 μm) and grinding processes (v_c = 1760 m/min, a_p = 10 μm). Significant defects were observed on the machined surface in both operations with cracks typically forming due to the weak bonding strength of lamellar structure of the γ and α_2 phase. Opening cracks were easier generated when the cutting direction was close to perpendicular to the layer orientation. Moreover, Uhlmann et al. [60] presented the surface quality greatly benefited in quasi-static cutting experiment from a reduction in undeformed chip thickness, as illustrated in Figure 2.28. Similar studies have reported that selecting smaller depths of cut and feed rates substantially improves both surface integrity and tool life [50], [53].

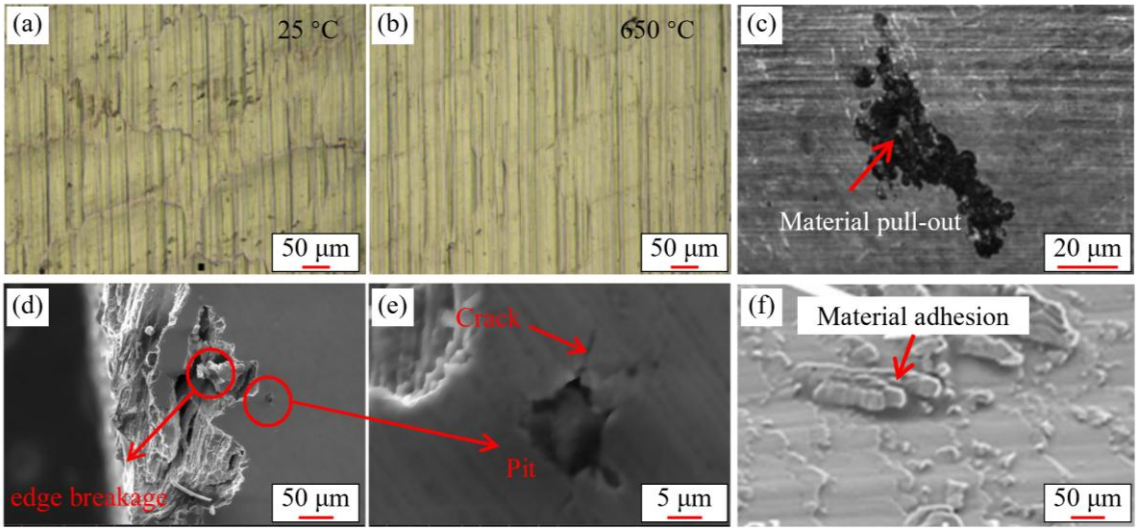


Figure 2.27 Machined surface morphology of γ-TiAl; (a) Rough surface obtained under 25°C [91], (b) fine surface machined under 650°C [91], (c) material pull-out on machined surface (v_c = 140 m/min) [65], (d), (e) and (f) edge break, pit, crack and adhesion (v_c = 80 m/min) [81].

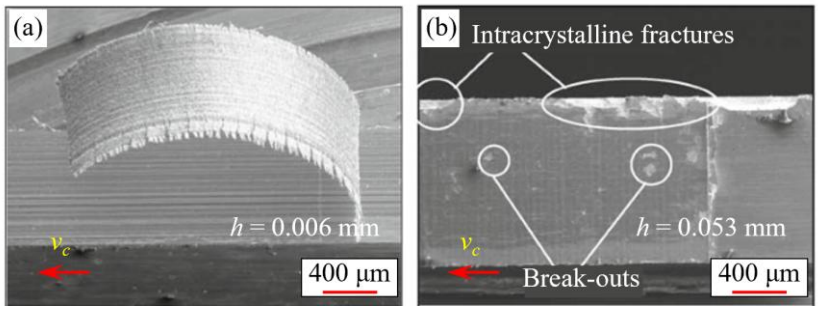


Figure 2.28 Chips and cutting surfaces depend on the uncut chip thickness h, (a) h = 0.006 mm and (b) h = 0.053 mm [60].

Mantle and Aspinwall [51] investigated the workpiece surface integrity of 45XD following high-speed ball-end milling and found that surface roughness Ra values were maintained below 1.5 µm when using a 6 mm diameter ball-end mill (v_c = 70–120 m/min; a_p/a_e = 0.2–0.5 mm; f_z = 0.06–0.12 mm/tooth; tile angle: 0°, 45°). However, damage such as material pullout and fractures was evident on the machined surface. In a related study, Hood et al. [69] explored the machinability of 45XD using a 2 mm diameter AlTiN coated WC ball-end mill for slotting. The findings indicated that maximum flank wear reached approximately 65 µm after 25 minutes of machining, with microcracks, smeared material and edge fractures observed on the machined surface. These studies highlight the challenges in maintaining damage free surfaces when machining γ-TiAl.

2.2.4.3 Surface roughness

Surface roughness serves as a key measure that effectively reflects the microscopic geometric shape errors of a workpiece surface, which has been shown to have considerable influence on fatigue life [51], [100], [103], [104]. It is closely related to various physical factors including deformation, elastic recovery and tool path interference. The arithmetic mean deviation of the profile, known as Ra and depicted in Figure 2.29, is the most commonly used parameter for describing and quantifying surface roughness. Additionally, Sa, which is the arithmetical mean height of an area, extends Ra's principles to provide a more comprehensive evaluation of surface roughness over larger areas. Equation 2-2 and Equation 2-3 give the mathematical definition of linear surface roughness Ra and areal surface roughness Sa [105].

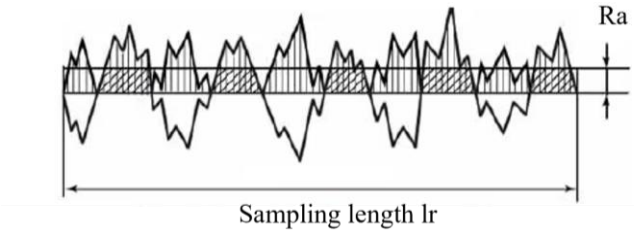


Figure 2.29 Arithmetical mean height (for a roughness profile) [106].

$$Ra = \frac{1}{lr}\int_{0}^{lr}|z(x)|dx \tag{2-2}$$

$$Sa = \frac{1}{A}\iint|z(x,y)|dxdy \tag{2-3}$$

The high brittleness of γ-TiAl at room temperature complicates its processing and leads to poor surface quality. The use of induction-assisted milling (IAM), developed by Fan et al. [91], resulted in a reduction in surface roughness by pre-heating the workpiece, achieving a maximum reduction of 42.9% at 450℃ compared to room temperature at 25℃, as illustrated in Figure 2.30(a). This improvement in surface roughness can be attributed to the decrease in hardness and yield strength, which increases ductility at higher temperatures. Furthermore, as depicted in Figure 2.30 (b), surface roughness was consistently lower when employing IAM compared to conventional machining (CM), although the scale of reduction diminished with increasing feed rate.

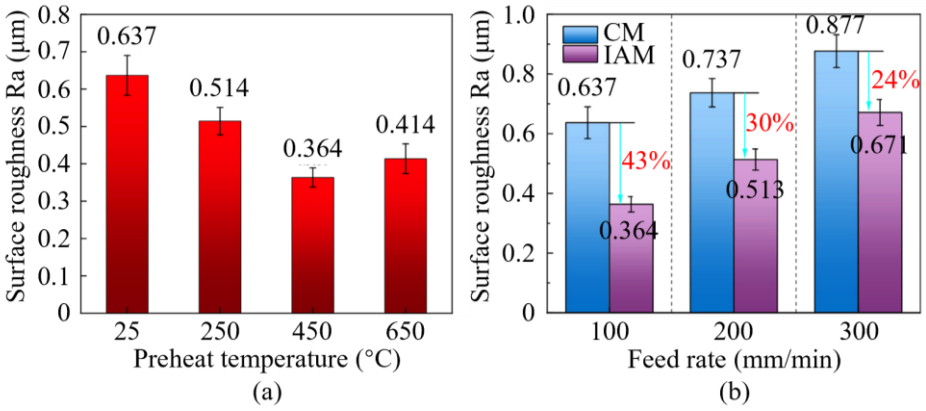


Figure 2.30 Surface roughness following IAM; (a) Impact of preheating temperature and (b) impact of feed rate and comparison against CM [91].

The microstructure of γ-TiAl also plays a significant role in influencing the resulting machined surface roughness. In the study by Zhang et al. [86], it was observed that fully lamellar

microstructures (grain size ~100 μm) were more difficult to machine by turning compared to near gamma (grain size ~30 μm) and duplex (grain size ~15–60 μm) microstructures. This was attributed to the larger grain size in fully lamellar microstructures, as finer grain sizes tend to enhance the anisotropy of the microstructure, resulting in shorter effective distances for dislocation movement along specific slip systems. Consequently, lower levels of deformation and smaller cracks were generated on the machined surface. Comparably, Fan et al. [91] presented that the orientation of lamellar structures of γ-TiAl decided the surface roughness in milling process. Lamellar fractures, lamellar bending and minimal deformation were observed when the cutting direction formed an obtuse angle, a near right angle and an acute angle with the lamellar orientation reprehensively. Lower surface roughness would be obtained with the acute angle due to less microcracks developed during this condition.

Numerous studies have examined the influence of tool characteristics and cutting parameters on workpiece surface roughness. Priarone et al. [63] assessed the impact of tool geometry and coatings on surface roughness when milling γ-TiAl. Machining dry at cutting parameters of v_c = 50 m/min, f_z = 0.10 mm/tooth, axial depth of cut a_p = 0.3 mm and radial depth of cut a_e = 0.3 mm, surface roughness was maintained at Ra = 0.21 μm using uncoated tools with a 4° radial rake angle, which was slightly better than the surface machined with 12° radial rake angle tools (Ra = 0.24 μm). In addition, compared to CrAlSiN coated tool (Ra = 0.21 μm), AlSiTiN coating tools yielded better surface roughness with 0.18 μm, due to the long-term maintenance of tool sharpness.

Yao et al. [76] investigated the effects of different chip breaker grooves (SM and MF4) and varying operating parameters when turning γ-TiAl on surface roughness. As shown in Figure 2.31, compared to MF4 tools with a 1.2 mm corner radius, SM tools with a 0.8 mm corner radius produced significant lower Ra values while varying the cutting parameters at each level. Noticeable rises in surface roughness were observed when depth of cut changed from 0.2 mm to 1.0 mm and feed increased from 0.06 mm/rev to 0.10 mm/rev. Rapidly increased cutting forces, which resulted in severe tool wear, were believed to be the root cause. In contrast, no clear trend in surface roughness was observed with changes in cutting speed. The increase in cutting speed raised the cutting temperature, reducing built-up edge formation, which ultimately led to fluctuations in surface roughness. The effect of cutting speed on surface roughness was also validated by the study of Priarone et al. [61], which indicated that as cutting speed in

milling γ-TiAl increased from 35 m/min to 71 m/min, surface roughness decreased from 0.265 μm to 0.205 μm Ra.

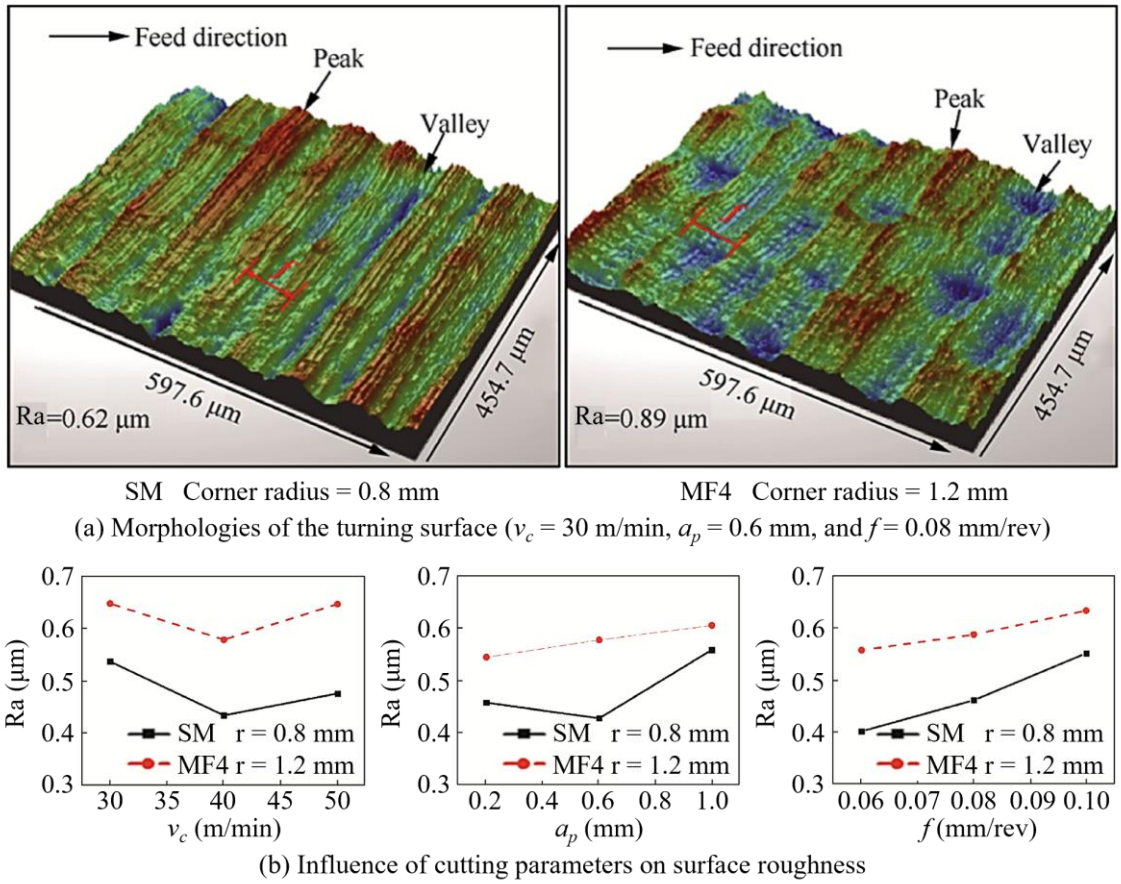


Figure 2.31 Morphologies and surface roughness following turning of 4822 γ-TiAl; (a) Surface contours machined by different tools and (b) effects of cutting parameters on surface roughness [76].

Similarly, Wang and Liu [81] reported that surface roughness increased with depth of cut and feed rate when milling γ-TiAl. A rise in surface roughness was apparent as cutting speed increased from 40 m/min to 80 m/min but subsequently decreased when operating above 80 m/min, which was consistent with the variation of cutting force. This response suggests that higher cutting speeds reduced the uncut chip thickness, thereby lowering surface roughness. Simultaneously, the increased cutting speed led to severe tool wear, resulting in more rubbing and consequently lower surface roughness. This might explain the result observed by Pérez [56] in milling γ-TiAl, where surface roughness presented a reduction trend when flank wear exceeded 100 μm. Additionally, higher temperature induced by the increased temperature also caused workpiece softening, which reduced cutting forces with better surface quality.

Correspondingly, the IAM method was proposed by Fan et al. [91] to increase the workpiece temperature instead of using higher cutting speeds to soften the material, thereby reducing cutting forces and achieving a milled surface with lower surface roughness. From these studies, it can be concluded that temperature has a significant effect on the machining of γ-TiAl. Balancing the material's machinability and tool life through the adjustment of cutting parameters remains an area requiring further exploration.

2.2.4.4 Microhardness

During the machining process, the workpiece material undergoes plastic deformation due to the mechanical action of the tool, leading to increased internal dislocation slip within the grains [107], [108]. This process causes the grains to fracture and refine, resulting in the formation of smaller sub-grains and an increase in overall surface hardness [109]. The primary factors contributing to the change in hardness of the surface layer are cutting forces and temperatures. Cutting forces induce grain distortion and deformation leading to strain hardening, while elevated cutting temperatures can thermally soften the sub-surface layer of the material. The degree of work hardening (N_{wh}) is quantified by the ratio of the increase in surface microhardness following machining over the initial bulk hardness of the base material, as defined in Equation 2-4 [90]:

$$N_{wh} = \frac{HV - HV_0}{HV_0} \times 100\% \tag{2-4}$$

where HV is the machined surface microhardness and HV_0 is the initial bulk microhardness of the workpiece material.

Figure 2.32(a) illustrates a clear correlation between preheating temperature in IAM and resulting workpiece microhardness depth profiles, where the degree of strain hardening diminishes with increasing temperature. The comparative experiment showed that conventional milling (25°C) yielded the highest cutting force with 66.1 N led to significant degree of work hardening (53.3%) while the cutting force measured in preheating condition (650°C) was 50.2 N and hardening degree was only 31.3% [91]. Microhardness is affected by continuous mechanical load and thermal load. Mechanical load applied to the cutting process leads to plastic deformation with increased density of dislocation and the intensified dislocations resist further deformation, resulting in the raise of microhardness. However, when the elevated

temperature induced in material will make dislocations move more easily within the crystal and promote grain deformation. The high sensitivity of γ-TiAl to thermal load reveals that increasing the temperature in the cutting zone can effectively improve its machinability.

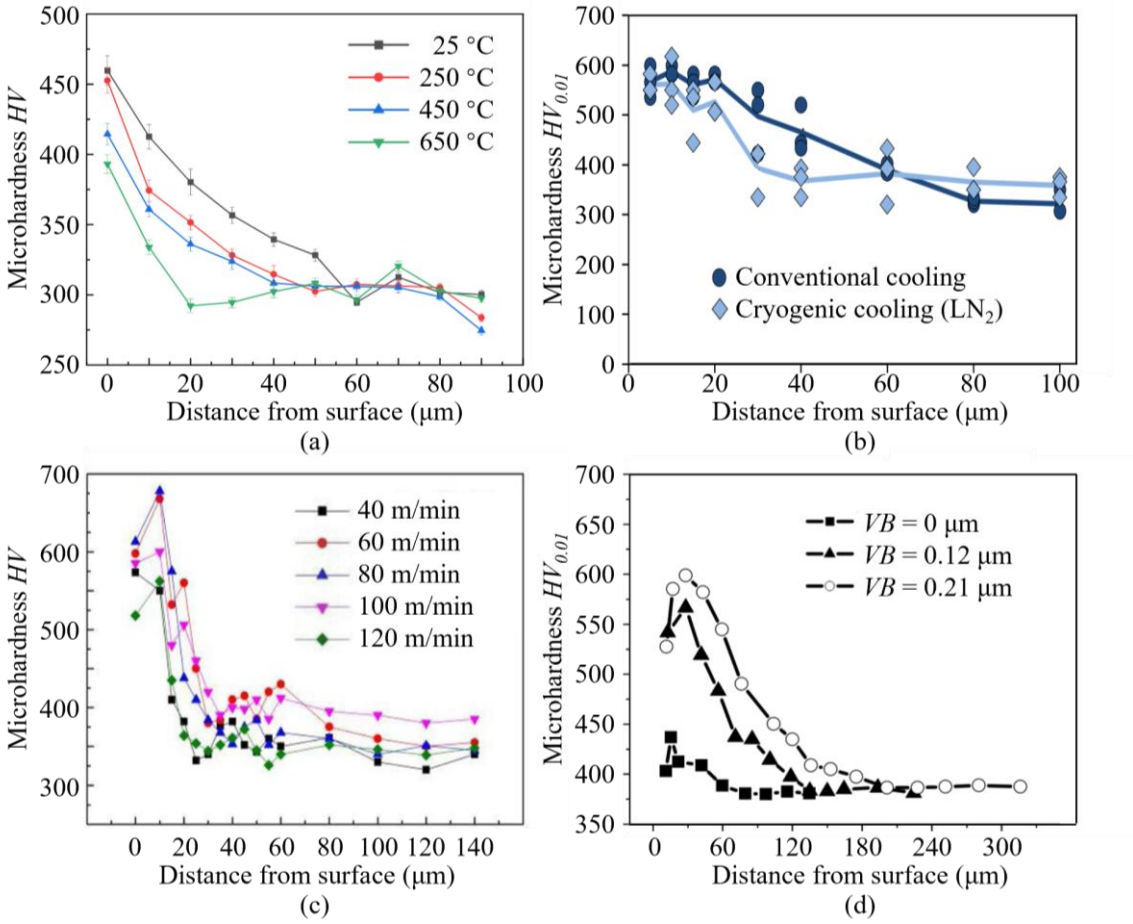


Figure 2.32 Measurement of microhardness in previous research; (a) Impact of preheating temperature on surface microhardness in ball-end milling [91], (b) effect of lubrication conditions on microhardness in turning [67], (c) effect of cutting speed on microhardness in milling [81] and (d) influence of tool wear on microhardness in milling [58].

Klocke et al. [67] compared the changes in microhardness under different cooling conditions (flood cooling, cryogenic cooling) during the turning of 45XD, as shown in Figure 2.32(b). Although the maximum microhardness of these two methods were closed (~550 $HV_{0.01}$), under the cryogenic cooling, the thickness of work hardening was about 30 μm while conventional cooling generated an 80 μm hardening layer. A reduction of strain hardening was expected due to the lower tool wear and cutting forces were observed in cryogenic cooling condition.

Wang and Liu [81] conducted detailed experiments on the surface integrity of milled γ-TiAl and studied the influence of cutting parameters on microhardness. The maximum microhardness was observed at a cutting speed of 80 m/min, with a hardened layer depth of approximately 60 μm, as shown in Figure 2.32(c). When the cutting speed was below 80 m/min, the increase in cutting speed led to larger tool wear and higher cutting forces, resulting in heavy strain hardening. Further increased the cutting speed beyond 80 m/min, thermal effect was dominant and presented the reduction of microhardness. Similar, when the feed rate varied from 0.005 mm/tooth to 0.025 mm/tooth and the depth of cut changed from 0.005 mm to 0.025 mm, the maximum microhardness increased up to f_z = 0.020 mm/tooth and a_p = 0.020 mm, respectively, and then decreased.

Ge et al. [58] evaluated the high-speed milling of 45XD using TiAlN coated tools under dry conditions, which revealed significantly reduced tool life and higher cutting forces compared to TA15. As the cutting speed increased from 60 m/min to 240 m/min, the minimum depth of handed layer was approximately 75 μm, with a maximum microhardness of ~440 $HV_{0.1}$ at 60 m/min. When the cutting speed reached to 240 m/min, the depth of the hardened layer increased to about 100 μm. However, the maximum microhardness (~560 $HV_{0.1}$) measured was still much lower than that presented by Mantle and Aspinwall [51] in a similar experiment (~680 $HV_{0.025}$), due to the higher cutting speeds used (up to 240 m/min). Meanwhile, as flank wear increased, the work hardening phenomenon became more pronounced due to the generation of larger cutting forces, as shown in Figure 2.32(d).

2.2.4.5 Residual stress

During machining, the combination of thermo-mechanical loads cause intragranular distortion within the crystal grains, resulting in internal stress. After machining, the altered surface stress state of the workpiece begins to recover and the material stress condition following this recovery is referred to as surface residual stress [97]. Mechanical stress, phase change stress and thermal stress are the primary factors that influence the residual stress state of the workpiece surface. In general, mechanical and thermal stresses have a more pronounced impact than phase change stress. However, the dominant stress will be dependent on the machining process and the associated levels of cutting parameter, manifesting either as macroscopic tensile or compressive residual stress. Research has indicated that milled surfaces typically exhibit substantially higher fatigue strength compared to ground or polished surfaces, attributable to

increased subsurface hardness and material deformation, which induce higher levels of compressive residual stress at the workpiece surface [51], [110]. Compressive residual stresses are advantageous for extending fatigue life in tension-tension working conditions, as they reduce the peak tensile load at the workpiece surface. Additionally, compressive residual stresses are more likely to inhibit the growth and propagation of surface cracks, thereby further enhancing the structural integrity of the component.

Research on assessing workpiece residual stress following machining of γ-TiAl is relatively limited. Figure 2.33(a) details the residual stress depth profiles of induction assisted milled γ-TiAl workpieces at different preheating temperatures. All of the samples exhibited compressive residual stresses on the machined surface, but with the magnitude decreasing from −600.2 MPa when machining at room temperature to −168.6 MPa under a preheating temperature of 650°C, while the depth of penetration also exhibited a reduction of ~20 μm [91]. Mantle and Aspinwall [51] utilised the hole drilling method to measure workpiece residual stress depth profiles following milling of γ-TiAl. The data consistently showed surface/subsurface compressive residual stress and reduced to zero to tensile at approximately 0.3 mm, which aligns with changes in corresponding microhardness levels. The use of worn tools was found to increase the contact area between the flank face and the workpiece, thereby causing greater plastic deformation, which in turn enhanced compressive residual stresses. Experimental results presented by Hood et al. [69] and Yao et al. [76] further highlighted the significant influence of machining operations and cutting parameters on resulting residual stress distribution. For instance, larger depths of cut led to increased cutting forces, thereby intensifying surface compressive residual stress due to more severe plastic deformation, as depicted in Figure 2.33(b) and (d). Post-processing techniques such as shot peening, ultrasonic rolling, grinding and polishing can be employed to induce desired surface/subsurface residual stress regimes. As shown in Figure 2.33(c), post-process polishing can effectively alleviate the compressive residual stress on the turned surface by removing a thin layer of material from the machined surface.

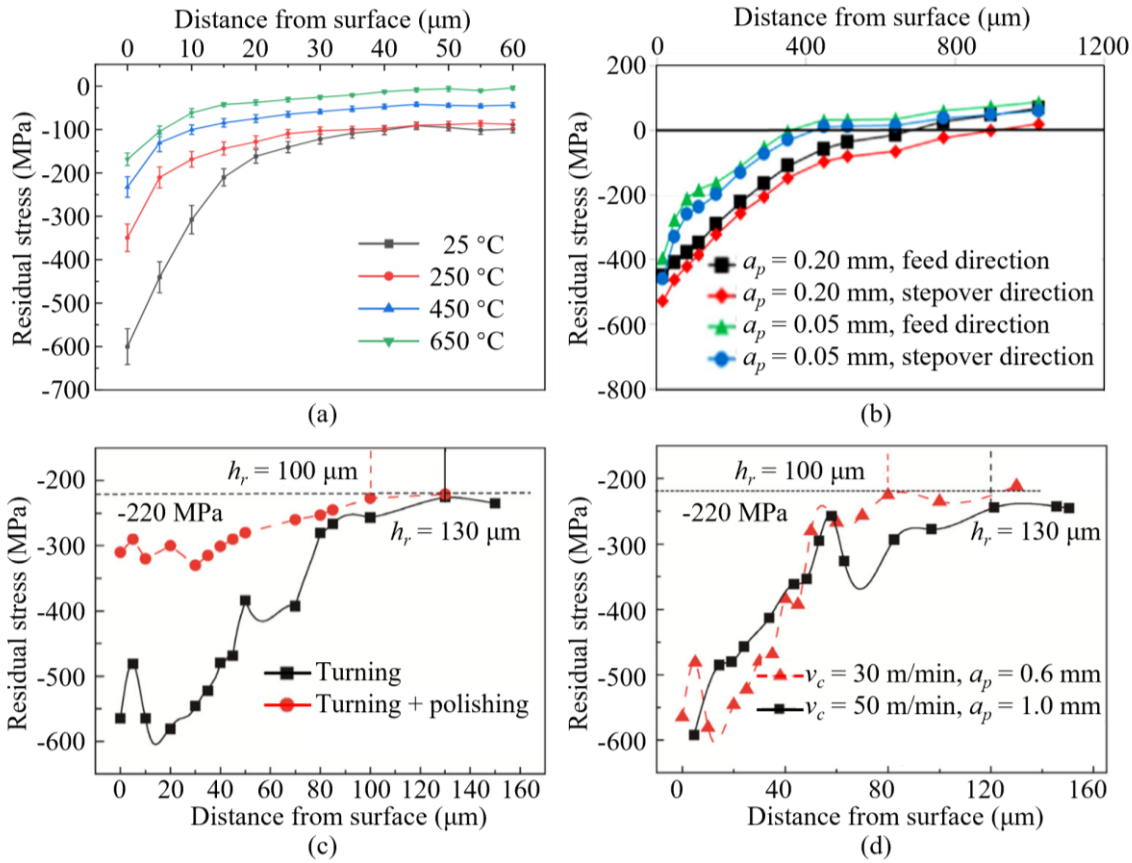


Figure 2.33 Measurement of residual stress in previous research; (a) Effects of preheating temperature on residual stress [91], (b) effects of depth of cut on residual stress in different directions [69], (c) impact of machining processes on residual stress [76] and (d) impact of cutting parameters on residual stress [76].

2.2.4.6 Metallographic/microstructural alterations

Materials are subjected to combined mechanical and thermal loads during machining, leading to complex surface metallographic alterations. This can result in microstructural deformation, grain boundary distortion and grain refinement. The surface material typically undergoes plastic deformation along the direction of force, visibly elongating the crystal grains. Guo et al. [111] noted that the microstructural evolution during machining was closely dependent on the strain, strain rate and temperature in the shear zone. Subsurface grain deformation due to machining is particularly noted in γ-TiAl with lamellar structures, which have been the focus of numerous studies [60], [65], [66], [67], [81], [86], [88], [90], [94]. Zhang et al. [86] observed that damage and bending of the grain structures ($\alpha_2 + \gamma$) were prominent when cutting fully lamellar γ-TiAl due to substantial cutting forces, which led to dislocations crossing the lamellar interfaces, see Figure 2.34(a) and 2.33(b). Lamella bending was mainly influenced by the dislocation

movement and twinning. High-density dislocations were observed to be confined within the lamella, as shown in Figure 2.34(b) and (c), indicating a significant resistance to dislocation movement across lamellar boundaries. Additionally, the cutting process activated refined mechanical twins within the γ lamella, further illustrating the dynamic changes occurring during machining, see Figure 2.34(d).

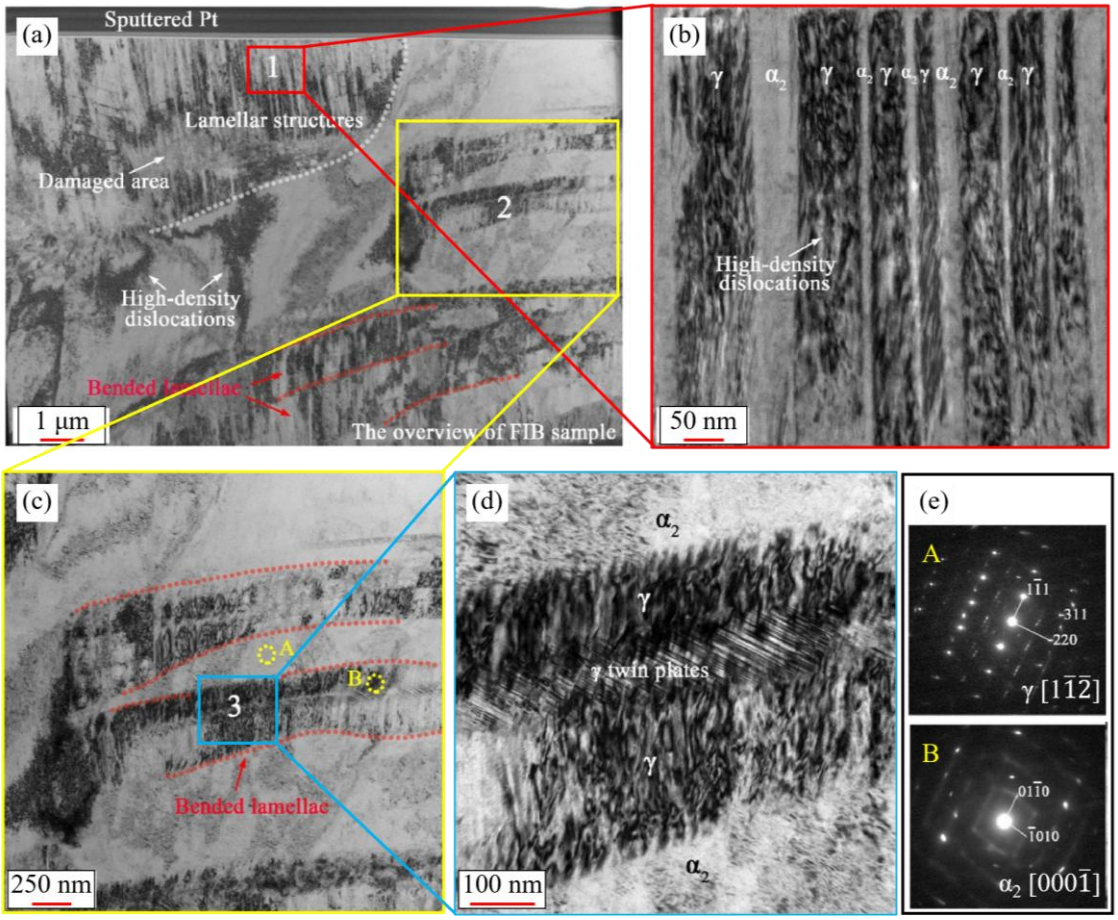


Figure 2.34 TEM images of the partially formed chips in fully lamellar microstructure; (a) Bright-field image with overall view of FIB sample, (b) magnified images of region 1 showing the $\alpha_2 + \gamma$ lamellar structure and high-density dislocations, (c) magnified images of region 2 showing the bended lamella, (d) magnified image of region 3 showing the formation of twins within γ lamella and (e) SADP patterns of regions A and B denotes the α_2 and γ phases, respectively [86].

Crystal structures and orientations significantly influence the mechanical deformation mechanisms in materials. For γ-TiAl with fully lamellar microstructures, the lamellar spacing and angle between the lamellar planes together with the loading axis greatly affect its plastic

behaviour [112], [113]. Key sources of fracture include trans-lamellar fracture, $\alpha_2 + \gamma$ interface delamination and de-cohesion of $\alpha_2 + \gamma$ colony boundaries [114]. When stress is applied either parallel or perpendicular to the lamellar planes, a condition known as hard orientation, shear deformation across the lamellae can lead to fractures or boundary de-cohesion in the $\alpha_2 + \gamma$ colonies. Initiating slip on the pyramidal planes of the α_2 phase in these orientations requires higher stresses, due to the limited number of independent sliding systems available in the hexagonal α_2 phase. Conversely, when loading stress is applied at a 45° angle to the lamellar interface, referred to as soft orientation, the slip deformation tends not to cross the lamellar interface. In this scenario, microcracks are more likely to form and propagate parallel to the lamellar direction, facilitating easier proliferation along these planes.

Subsurface microcracking is a common occurrence when machining γ-TiAl due to its room temperature brittleness and high strength [50], [65], [67]. Figure 2.35 displays various crack formations in 45XD alloy after turning, which are strongly influenced by the lamellar orientation angle. Klocke et al. [66] observed significant bending deformation during the turning of TNB under MQL condition (see Figure 2.36(a)), which was attributed to strain at high temperatures. Plastic deformation was evident after turning as demonstrated by bending of the lamella along the feed direction, which was not present in the initial as-cast workpiece, see Figure 2.36(b) and (c) [67]. Chen et al. [90] also observed plastic deformation during creep feed grinding of γ-TiAl, with a deformed layer thickness of 16.5 µm at a_p = 0.5 mm, as shown in Figure 2.36(d). The thickness of deformed layer achieved to 31.3 µm when the depth of cut was 1 mm, due to the larger cutting force.

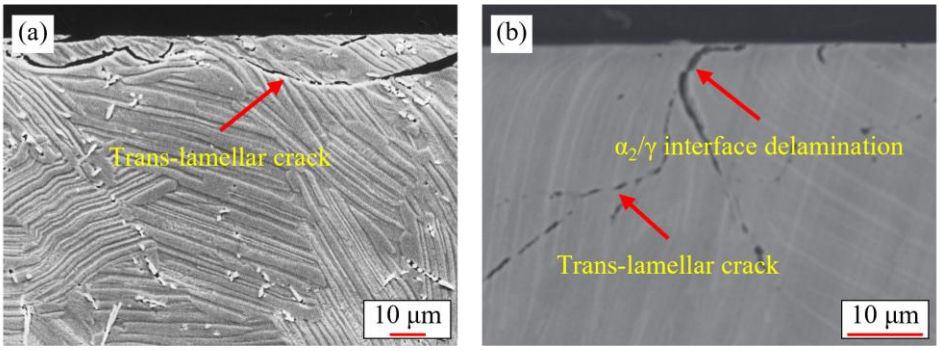


Figure 2.35 Subsurface defects following machining; (a) Trans-lamellar crack of turned 45XD subsurface at v_c = 25 m/min, f = 0.1 mm/rev and a_p = 0.7 mm [50] and (b) interface delamination and trans-lamellar crack of turned 45XD subsurface at v_c = 80 m/min, f = 0.1 mm/rev, and a_p = 0.25 mm [67].

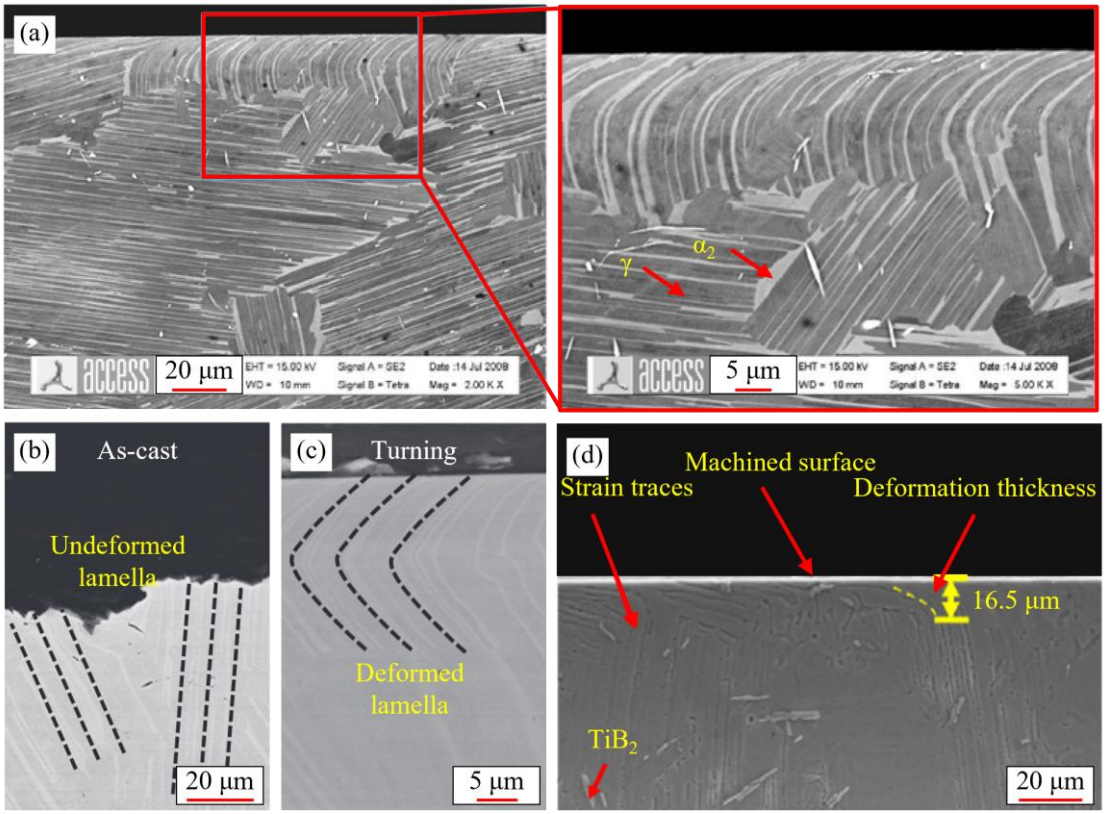


Figure 2.36 Metallographic alterations of machined subsurface; (a) Cross-section of the turned surface at v_c = 80 m/min, f = 0.1 mm/rev, and a_p = 0.4 mm, MQL [66], (b) and (c) comparison between as-cast and turned specimens [67] and (e) metallographic alteration of ground surface at v_s = 30 m/s, v_w = 1000 mm/min and a_p = 0.5 mm [90].

Zhang et al. [86] conducted a systematic study on machinability of Ti-43Al-9V-0.2Y featuring three different microstructures (Near gamma, Fully lamellar and Pseudo duplex). Under micro-cutting conditions at v_c = 50 mm/min and a_p = 5 µm, the fully lamellar microstructure demonstrated brittle fracture during chip formation. This was attributed to the weak bonding force between the hexagonal α_2 and tetragonal γ phases, which led to preferential micro-cracking along each interface. Figure 2.37(a) shows that the lamellar colonies maintained their structural integrity with no severe plastic deformation in the primary shear zone (PSZ). The strain concentration region was not observed in the PSZ from the kernel average misorientation (KAM) image, which was used to evaluate the strain distribution of microstructures, see Figure 2.37(c). Furthermore, no signs of phase transformation were observed since the temperature in the PSZ remained much lower than the transus temperature, as shown in Figure 2.37(b). When turning near gamma structured γ-TiAl, Figure 2.38(a) and (b) demonstrate that plastic deformation occurred in several grain regions, with a large concentration of strain measured

(see Figure 2.38(c)). Compared to the lamellar microstructure, pseudo duplex structure can sustain severe plastic deformation without interface delamination.

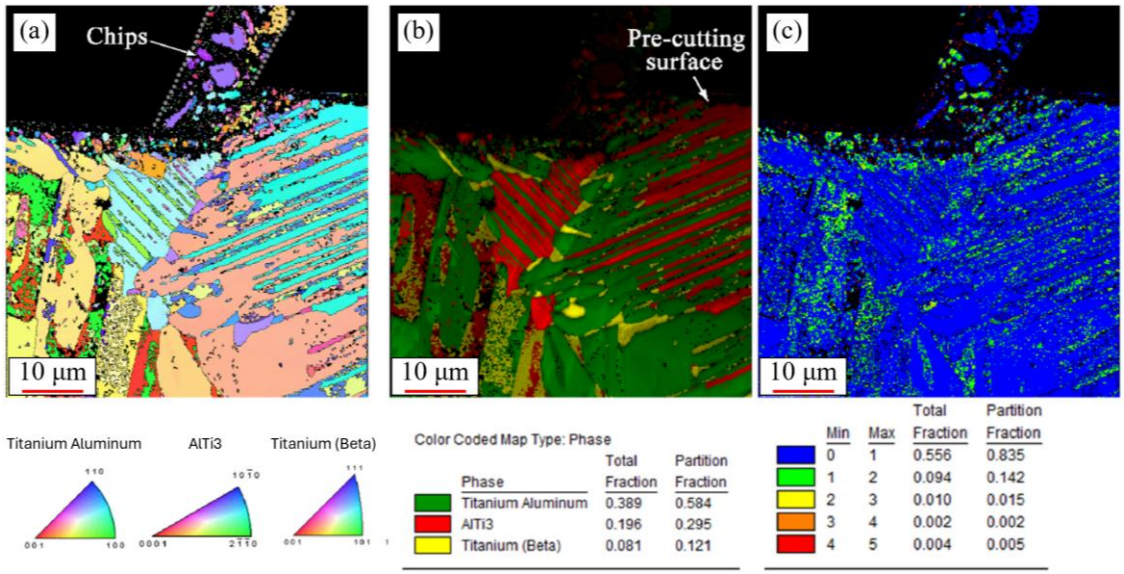


Figure 2.37 EBSD microscopic characterisation of the partially formed chip of fully lamellar microstructure; (a) Inverse pole figure presenting that PSZ maintains better lamellar microstructure integrity without sever plastic deformation, (b) phase contrast map indicating that phase transformation was not observed in PSZ and (c) KAM map depicting low strain distribution in PSZ [86].

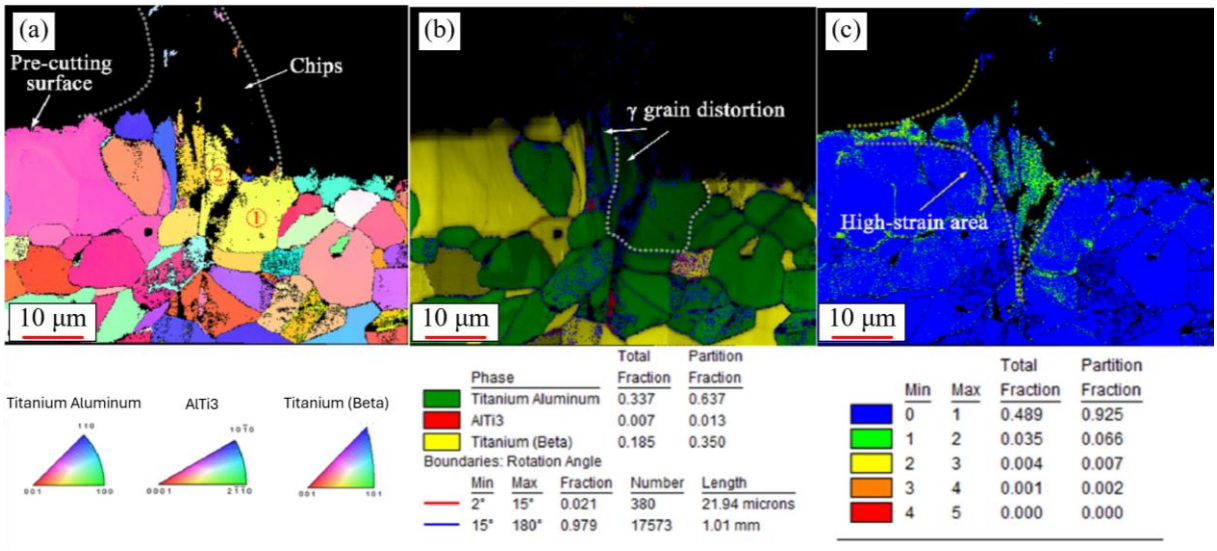


Figure 2.38 EBSD microscopic characterisation of the partially formed chip of near gamma microstructure; (a) Inverse pole figure presenting that region 1 and 2 have same orientation, (b) phase contrast map indicating that phase transformation was not observed in PSZ and (c) KAM map depicting high strain distribution in PSZ [86].

2.3 Ultrasonic-assisted cutting techniques

2.3.1 Introduction

Ultrasound, defined by the American National Standards Institute as "sound at frequencies greater than 20 kHz", is a type of mechanical energy that propagates through medium as an oscillating wave of alternating pressure [115]. In terms of basic propagation laws such as reflection, refraction, diffraction, and scattering, ultrasound shares similarities with other forms of sound. However, its characteristics of short wavelength and high frequency confer specific properties such as better directional propagation, higher energy density, and enhanced waveform conversions at interfaces. These unique properties make ultrasound widely used in both industrial and medical applications, including ultrasonic testing (UT), ultrasound identification (USID), and acoustic microscopy. Moreover, the alternating low and high-pressure waves generated by ultrasound can induce cavitation, creating high-speed liquid jets and strong hydrodynamic shear-forces [116]. This characteristic underpins technologies used in de-agglomeration and milling of micro/nano materials, cells disintegration or mixing of reactants [117], [118]. In manufacturing, the mechanical effects of ultrasound are particularly significant. Tissue or materials vibrated at ultrasonic frequencies and large amplitudes can enhance the generation or removal of material [119], demonstrating the critical role of this technology in advanced manufacturing processes.

Ultrasonic machining (USM) was first developed in 1927 by R.W. Wood and A.L. Loomis [119], [120], [121], utilising a tapered glass tube combined with the action of a piezo-electric crystal vibrator to achieve material removal. Initially used for drilling of stone, USM has since been expanded to process a variety of hard and brittle materials [122]. In USM, mechanical vibrations are generated by converting high-frequency electrical energy through a transducer/booster, which are subsequently amplified by an energy-focusing device [123], [124], [125]. This is channelled to vibrate a tool at amplitudes of 5–50 μm along the longitudinal axis at frequencies of 15 kHz or higher [126], [127], [128], which primarily serves as an energy transfer medium. Concurrently, an abrasive slurry comprising abrasive grits (25–60 μm) such as SiC, B_4C or Al_2O_3 suspended in water or another suitable liquid, is fed into the cutting area. This slurry performs micro-edge cutting, facilitating the material removal process [129], [130], [131]. Figure 2.39 illustrates the basic simplified components of a USM system.

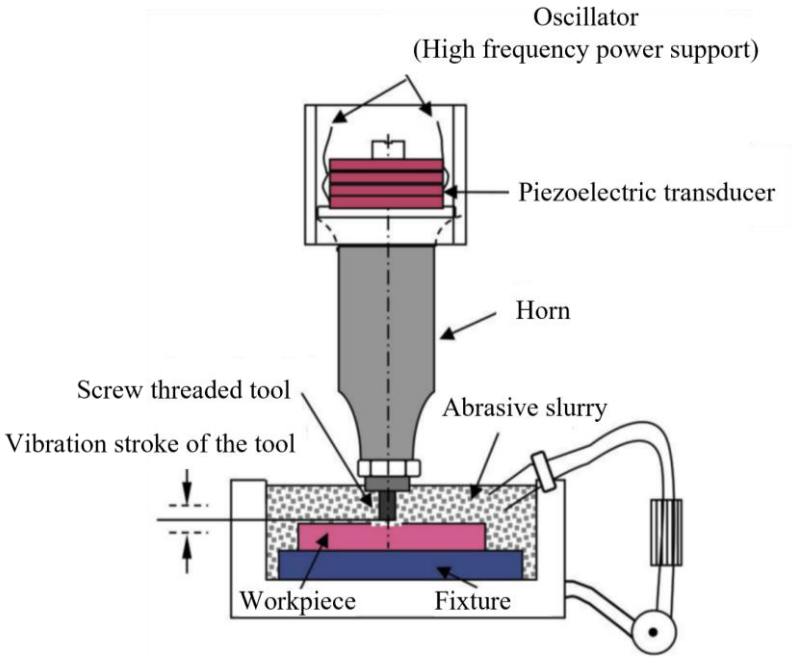


Figure 2.39 Basic elements of USM system [132].

There are four primary material removal mechanisms in USM involving mechanical abrasion, micro chipping, cavitation erosion and chemical reactions, as demonstrated in Figure 2.40 [130], [133], [134], [135].

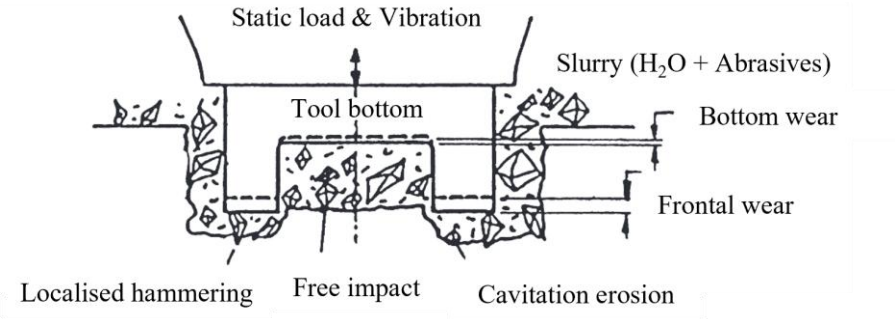


Figure 2.40 Material removal mechanisms in USM [136]

- Mechanical abrasion: The abrasive particles in the gap between the tool and workpiece erode the material due to the hammering effect of high-frequency ultrasonic vibrations applied to the tool. According to fracture mechanics, this hammering action induces surface cracks, which subsequently expand to create brittle fractures [137], [138].

- Micro chipping: Under ultrasonic vibration, free abrasive particles scratch the surface of the workpiece. The tiny fragments of these abrasive grains function as micro-cutting edges, removing material through plastic deformation [131], [139], [140].

- Cavitation erosion: Cavitation modifies the surface due to the generation and collapse of vapour bubbles that form on the workpiece surface [141]. The high-frequency vibrations in USM create a pressure differential that leads to bubble collapse, resulting in material removal through the action of shock waves and high-pressure microjets [142], [143], [144].

- Chemical action: Brittle materials typically have a limited capacity to convert elastic energy into plastic deformation [145], [146]. To enhance the material removal process, a specific level of acid solution, such as hydrofluoric acid (HF), can be added to the slurry. This addition chemically alters the surface material into a structure with weaker molecular bonds, significantly improving the material removal rate of USM when combined with mechanical effects [147], [148].

Although the material removal process in USM results from the interaction of several mechanisms, many studies have identified the mechanical hammering effect as the dominant factor [144], [149]. For specific materials, careful control of processing parameters can enhance cavitation and chemical effects, thereby improving the material removal rate. USM is particularly suited for machining materials with low ductility and hardness above 40 HRC [123], [150], [151], as detailed in Table 2.14. Compared to conventional machining processes, USM is capable of achieving smaller dimensions, less than 100 μm [152]. Nonetheless, several challenges limit the broader application of USM, including poor surface quality, low material removal rates and reduced effectiveness when machining ductile materials. These issues underscore the need for further research and optimisation of USM parameters to expand its applicability and efficiency across various industrial contexts.

Table 2.14 Classification of materials and fields of application of USM [153].

Material	Brittleness criterion	Predominant deformation	Type of failure	Application of USM
glass mica quartz ceramic diamond germanium silicon ferrite	>2	elastic	brittle	Making parts of semiconducting materials Cutting industry diamonds Cutting special ceramics Making parts of glass, quartz, and minerals in optical and jewellery industries Machining ferrite and other materials of high connectivity
alloys tempered to high hardness carburised and nitride steels titanium alloys	1–2	elastic-plastic	brittle after work hardening by plastic deformation	Making and repairing alloy dies, press tools, and purchases Shaping and sharpening hard alloy tool
lead copper soft steel	<1	plastic	practically no failure	Unsuitable for USM

A major adaptation developed to address some of the limitations in traditional USM was the rotary ultrasonic machining (RUM) process introduced in 1964 [154], [155]. The RUM configuration typically involves the rotary motion of a cylindrical tool bonded/electroplated with diamond abrasives along with ultrasonic vibration in the axial direction. This simultaneous rotary action and ultrasonic actuation of the tool combine the mechanisms of conventional superabrasive grinding with ultrasonic machining, which qualifies it to be classified as a hybrid manufacturing process as per the definition proposed by Lauwers et al. [156]. Compared to USM, RUM offers significantly enhanced machining precision, reduced tool wear and increased material removal rates, due to the integration of high-speed tool rotation [157]. The advancements in RUM are partly attributable to the development of diamond abrasive tools [158] and also the miniaturisation and structural optimisation of the ultrasonic vibration system [150]. A key distinction in the material removal mechanisms between RUM and USM is that the micro chipping action by free abrasive particles in USM is replaced by the high-speed cutting action of the bonded diamond abrasives in RUM [159], [160], [161]. Figure 2.41 demonstrates the contrasting material removal modes of USM and RUM, highlighting the effectiveness of hybrid approaches in enhancing machining capabilities [157].

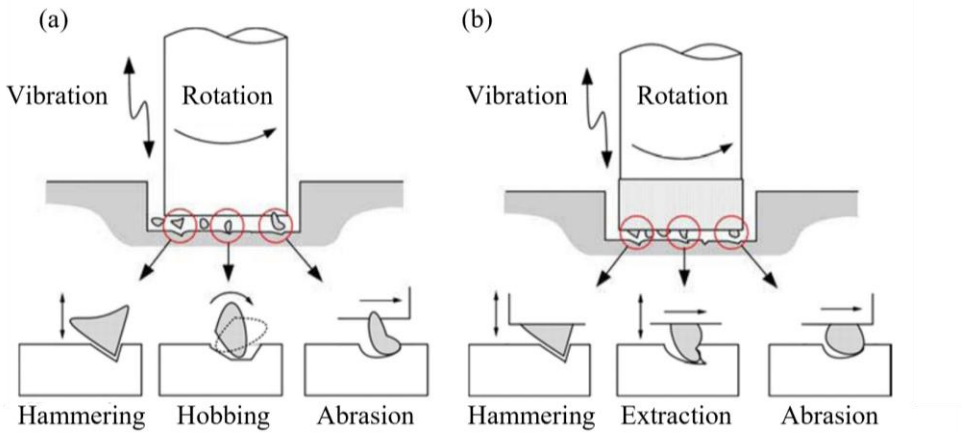


Figure 2.41 Comparison of material removal modes; (a) Free abrasive grits in USM and (b) fixed abrasive grits in RUM [157].

More recent developments in tooling and process configurations have extended the capabilities of RUM beyond producing simple cavities, with operations such as milling and drilling having been adapted to leverage the characteristics of RUM [159], [162], [163], [164], [165], [166], [167]. The principal material removal mechanism of RUM however remains the combined action of ultrasonic hammering and abrasive machining. Consequently, RUM is still primarily employed in the machining of hard and brittle materials such as glass and ceramics, where its benefits are most pronounced. Although RUM offers significantly improved material removal rates compared to both USM and conventional grinding, it is not without its drawbacks. Notably, issues such as severe entry/exit edge chipping and relatively low processing efficiency for ductile materials persist. To overcome these challenges, ongoing research into tool design and parameter optimisation is crucial. These efforts focus on enhancing both the quality and efficiency of machining processes, with the aim of broadening the applicability and effectiveness of RUM in various industrial applications.

Despite their effectiveness in machining hard and brittle workpiece materials, both USM and RUM (including other derivative configurations) are characterised by comparatively low material removal rates in contrast to traditional cutting processes that involve larger cutting edges and greater chip volumes. The idea of incorporating mechanical oscillations of the tool in conventional turning was first investigated in the late 1950s, where low frequency vibration (up to ~125 Hz) was applied in the feed direction [168], [169]. Lower cutting forces and tool wear were observed to enhance the stability of the cutting operation. The influence of actuating the cutting tool at frequencies in the ultrasonic domain while machining has also been assessed

and is commonly denoted as ultrasonic-assisted cutting (UAC). Here, a range of machining process configurations have been investigated, including ultrasonic-assisted turning (UAT) [170], [171], [172], [173], ultrasonic-assisted milling (UAM) [174], [175], [176], [177] and ultrasonic-assisted drilling (UAD) [178], [179], [180], [181]. Figure 2.42 takes hole making as an example to compare the difference between USM, RUM and UAC.

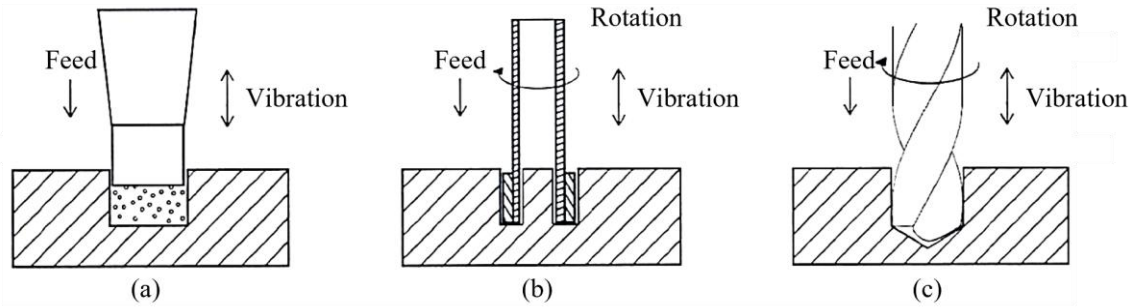


Figure 2.42 Schematic of ultrasonic machining technologies; (a) Free abrasive ultrasonic machining (USM), (b) rotary ultrasonic machining (RUM) and (c) ultrasonic-assisted drilling (UAD) [182].

2.3.2 Characteristics and classification of ultrasonic-assisted cutting

The characteristics of UAC include unique actions in USM generated by ultrasonic vibration such as hammering and cavitation. Additionally, UAC exhibits several new features compared to conventional cutting, as outlined below [7], [18], [183], [184]:

- Chip breaking action: During the material cutting process, the tool vibrates at the ultrasonic frequency, transforming the continuous chips typical of conventional cutting into interrupted chips.

- Lower cutting force: The application of one-dimensional or multi-dimensional ultrasonic vibration alters the cutting motion trajectory of the tool. From the moment the cutting edge enters the workpiece until it exits, ultrasonic vibration changes the contact between the tool and the workpiece from continuous to intermittent. This transformation at the micro-scale results in a macroscopic decrease in average cutting forces, which generally leads to lower tool wear and improved tool life.

- Reduced cutting temperature: The primary sources of heat during the cutting process are the severe plastic deformation of the material and the friction between the chip and

the rake face. Ultrasonic actuation vibration facilitates the formation of interrupted chips, reducing frictional heat and consequently lowering the overall cutting temperature.

UAC offers greater machining flexibility compared to USM and is particularly effective for cutting alloy materials commonly used in aerospace, enabling the efficient machining of workpieces with complex structures. This is especially beneficial for machining hard-to-cut aerospace ductile materials, such as titanium alloys, aluminium alloys and nickel-based alloys [185], [186], [187]. Additionally, UAC features fewer size restrictions on workpieces, lower tool and equipment costs, and facilitates easier system integration. UAC can be categorised based on various classification methods.

- Source of vibration: There are two primary categories (refer to Figure 2.43):

  (a) Applying ultrasonic vibration to the worktable or workpiece, which requires minimal hardware modifications to the machine tool.

  (b) Vibrating the tool itself, achieved by integrating the ultrasonic system within the machine tool's spindle. This method is generally preferred for operational efficiency.

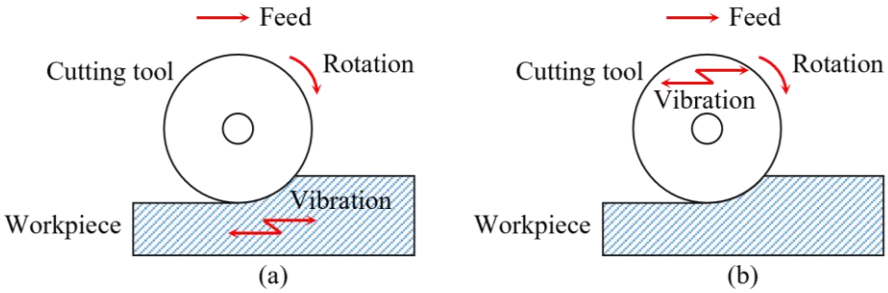


Figure 2.43 Classification of UAC depends on ultrasonic vibration source; (a) Workpiece vibration and (b) cutting tool vibration.

- Direction of ultrasonic vibration: UAC features three modes based on the direction of ultrasonic vibration (see Figure 2.44) [7]:

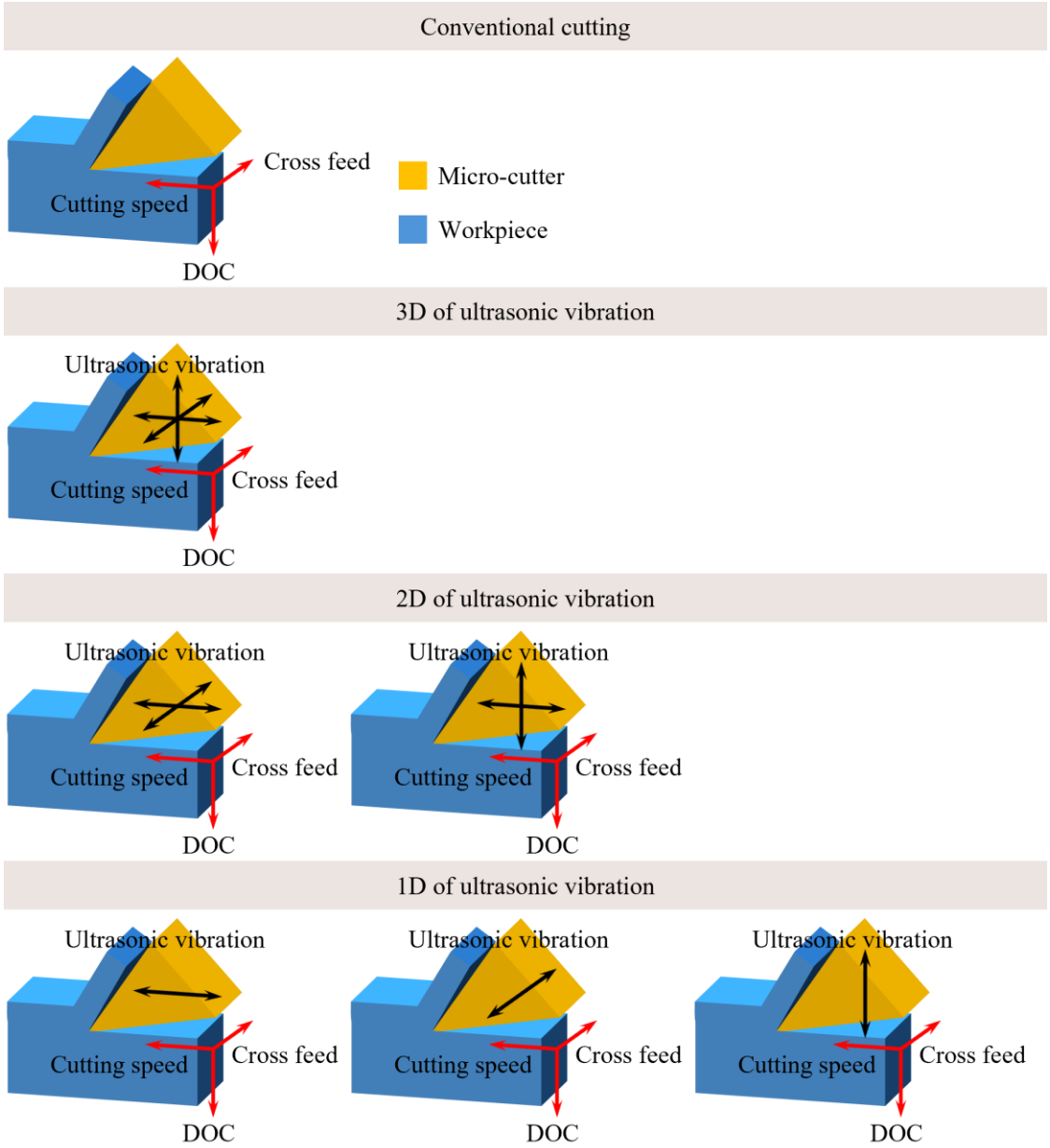


Figure 2.44 Summary of the principal UAC modes reviewed.

(a) 1D-UAC mode. Widely utilised in ultrasonic-assisted turning, the 1D-UAC mode primarily operates in the vertical direction, also referred to as the longitudinal or axis direction in end milling and drilling. Commonly known as ultrasonic-assisted milling or drilling, this mode vibrates along the tool axis by default. The theoretical tool trajectory relative to the workpiece resembles a sine curve with periodic reciprocating characteristics.

(b) 2D-UAC mode. This mode encompasses two main processes: Elliptical ultrasonic-assisted turning (EUAT) and longitudinal-torsional ultrasonic-assisted cutting

(LTUAC). The tool's theoretical trajectory forms a planar elliptic curve, integrating movements in two orthogonal directions.

(c) 3D-UAC mode. Currently a focus of theoretical research, 3D-UAC mode involves a trajectory that traces a spatial elliptic curve [188], [189]. This mode is explored less in practical applications and remains primarily within the research domain.

These modes can either operate independently or in combination, affecting the cutting, cross-feed and vertical directions. This division allows the transformation of any tool into a micro-cutter through the application of ultrasonic vibrations in these specific orientations. Table 2.15 outlines main tool-tip trajectories and displacements commonly observed in each mode [7], [125], [126], [136].

Table 2.15 Main classification of UAC based on the direction of ultrasonic vibration.

UAC mode	Specific process	Trajectory diagram	Trajectory equation
Conventional cutting			$\begin{cases} x(t) = v_c t \\ z(t) = 0 \end{cases}$
1D	UAT		$\begin{cases} x(t) = v_c t + a\cos(2\pi f_U t) \\ z(t) = 0 \end{cases}$
	UAT		$\begin{cases} x(t) = v_c t \\ z(t) = a\sin(2\pi f_U t) \end{cases}$
1D	UAM/UAD/RUM		$\begin{cases} x(t) = f_z t + r\sin(\frac{2\pi N}{60} t) \\ y(t) = r\cos(\frac{2\pi N}{60} t) \\ z(t) = a\sin(2\pi f_U t) \end{cases}$
2D	EUAT		$\begin{cases} x(t) = v_c t + a\cos(2\pi f_{U1} t) \\ z(t) = b\sin(2\pi f_{U2} t) \end{cases}$

2.3.3 Application of ultrasonic-assisted milling in advanced aerospace alloys

Aerospace alloys discussed in Section 2.1 demonstrate various levels of difficulty during machining with conventional cutting processes. Research on ultrasonic-assisted cutting indicates that the incorporation of ultrasonic vibrations alters the actual motion trajectory of the cutting tool, which leads to the development of a new material removal mechanism. Consequently, ultrasonic-assisted cutting shows significant improvements in cutting forces, cutting temperatures, tool wear and the integrity of the machined surface compared to

conventional machining methods. Applications of ultrasonic-assisted cutting across different aerospace alloys, categorised by processing methods and material categories, are detailed in Table 2.16 [177], [179], [190], [191], [192], [193], [194], [195], [196], [196], [197], [198], [199], [200], [200], [201], [202], [203], [204], [205], [206], [207]. In recent years, 6xxx/7xxx series aluminium alloys, Ti-6Al-4V titanium alloy, AISI 304 stainless steel and Inconel 718 superalloy have emerged as focal points of research. Some typical conclusions about ultrasonic-assisted milling titanium alloys are summarised in following.

Table 2.16 Summary of UAC applications in published research involving the machining of aerospace alloys.

Processing method	Material category	Material designation
UAT	Aluminium alloys	2A12/2017/2024/5056/6061/6061-T6/6063/7050/7075/7075-T6/7075-T651/7050-T7451/Al7Si0.3Mg/AlSiMg0.75
	Titanium alloys	Ti-6Al-4V/Ti 15-3-3-3/Ti 5553/Titanium Grade 2/Ti-25Nb-10Ta-1Zr-0.2Fe/Ti-6Al-7Zr-3Nb-4Mo-0.9Nd
	Steel	235/304/420/1045/4140/4340/DF2/GCr15
	Superalloys	Inconel 625/Inconel 718/Nimonic-90
UAM	Aluminium alloys	2A12/2195/6061-T6/6063/7050/7075
	Titanium alloys	Ti-6Al-4V/TC18/Ti-2Al-Nb
	Steel	316L/420/1020/1045/4140/H11/H13/Duplex stainless Steel 2205
	Superalloys	Inconel 718
UAD	Aluminium alloys	2024-T351/2024-T6/6061/6061-T6/7075-T6/AlMgSi0.5
	Titanium alloys	Ti-6Al-4V
	Steel	304/316/1045/4340
	Superalloys	Inconel 718LC/Inconel 738-LC/DD6/0Cr17Ni4Cu4Nb

2.3.3.1 Cutting force

The decrease of cutting forces during ultrasonic-assisted cutting primarily stems from two factors. First, there is a significant reduction in friction between the tool and the workpiece within the cutting region. Second, the process benefits from separation and pulse cutting characteristics, resulting in change of uncut chip thickness [208], [209]. The study by Jamshidi and Nageth [210] found notable differences when comparing the normal and friction forces between conventional turning and UAT. As the amplitude increased from 4 μm to 10 μm, the normal cutting force in UAT was reduced by approximately 19%–82%, and the friction force at the tool-chip interface decreased by about 24%–76%.

Xie et al. [211] conducted an experiment on LTUAM for TC18 titanium alloy using side milling. The results showed a significant reduction (up to ~16%) in the average cutting force in the cross-feed direction compared to the feed and axial directions, as illustrated in Figure 2.45(a). As the spindle speed increased from 600 rpm to 1400 rpm, this reduction tended to decrease. In a subsequent UAM experiment, Xie et al. [212] demonstrated that variations in the depth of cut and the pulling action of the cutting edge led to oscillating friction at the tool-workpiece interface. This oscillation effectively reduced the cutting force by up to 35%. However, it was noted that as the spindle speed increased, the effectiveness of this reduction diminished, as shown in Figure 2.45(b).

Similar outcomes were observed by Ren et al. [213] in LTUAM experiments with ball-end milling of Ti-6Al-4V, as depicted in Figure 2.45(c) and (d). LTUAM presented lower cutting forces in all directions under different cutting parameters (f = 100–400 mm/min and a_p = 100–400 μm). During the high-frequency separation phase of the LTUAM process, the interaction time between the tool and workpiece was extremely short, leading to a pulse-like curve of the cutting force due to periodic separations between the tool and micro-chip. This mechanism not only lowered the cutting temperature in the active area by ventilating the stagnant zones but also minimised thermal stresses, further reducing the overall cutting forces. Additionally, Xiang et al [214] believed that the reduction in cutting forces was associated with the torsional vibrations temporarily decreasing the tool's blade wedge angle.

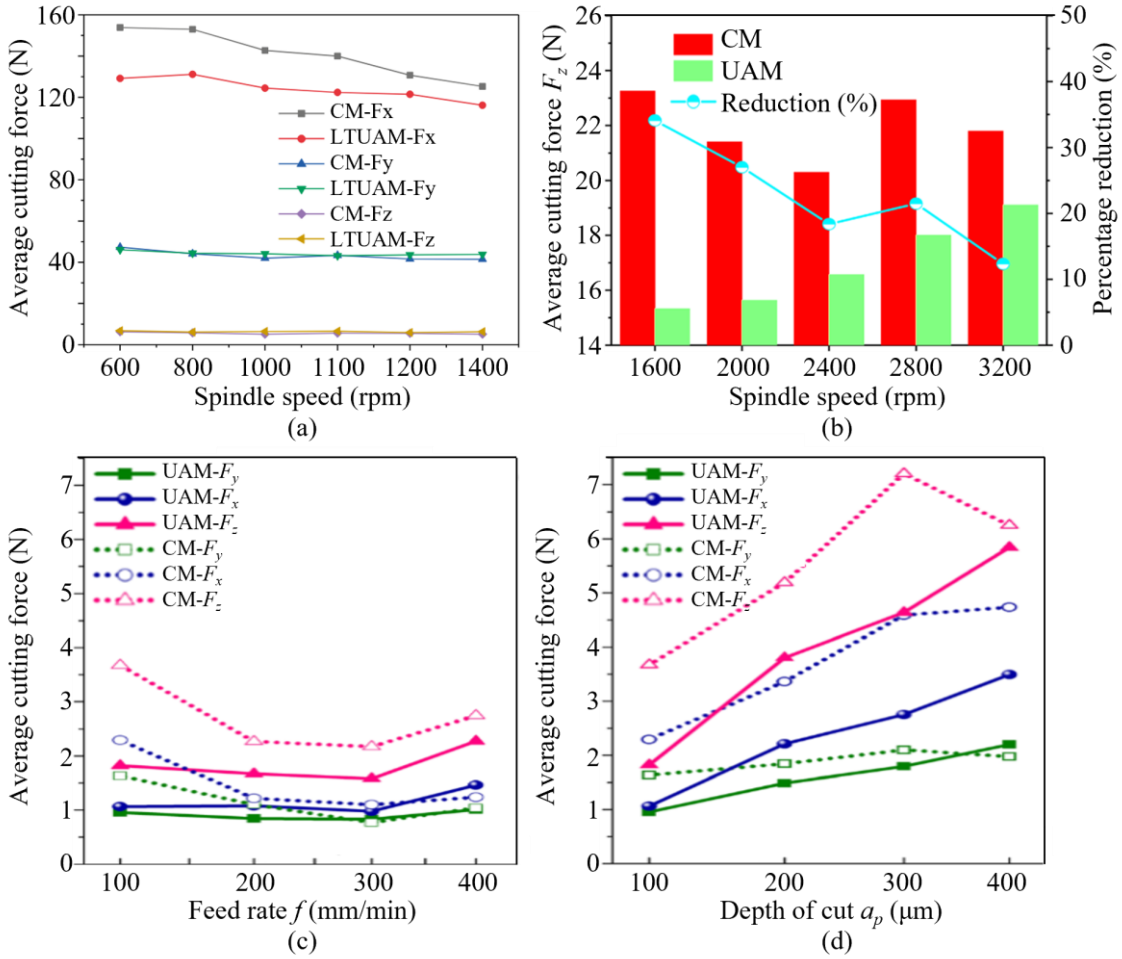


Figure 2.45 Measurement cutting force following UAC: (a) Effect of cutting speed on average cutting force (f_z = 0.03 mm/tooth, a_p = 4 mm, a_e = 0.8 mm, A_U = 5 μm) [211], (b) axial component force and decrease percentage (f_z = 0.015 mm/tooth, a_p = 0.2 mm, a_e = 6 mm, A_U = 2 μm) [212], (c) effect of feed rate on average cutting force (N = 5000 rpm, a_p = 0.02 mm, A_U = 5.6 μm) [213] and (d) effect of depth of cut on average cutting force (N = 5000 rpm, f = 100 mm/min, A_U = 5.6 μm) [213].

2.3.3.2 Tool wear and failure

The improvement of tool life is frequently highlighted as a significant advantage of UAC in scholarly literature. In studies by Chen et al. [215], LTUAM of Ti-6Al-4V demonstrated up to a 30% decrease in flank wear compared to conventional milling, as detailed in Figure 2.46(a). Similar findings were reported in helical UAM of Ti-6Al-4V, as presented in Figure 2.46(b) [216]. The average flank wear measured in helical UAM was only half of that in CM. The observed decrease in tool wear is primarily attributed to the reduction in the cutting force and heat during the UAC process. Unlike conventional cutting, which is a continuous process in the

same cut-in and cut-out phase where cutting heat tends to accumulate at the tool-workpiece interface, leading to adhesive wear on the cutting edge, UAC modifies the tool-workpiece contact into a periodic intermittent mode. This periodic separation and contact significantly reduce the generation of cutting heat and the forces required for cutting [7].

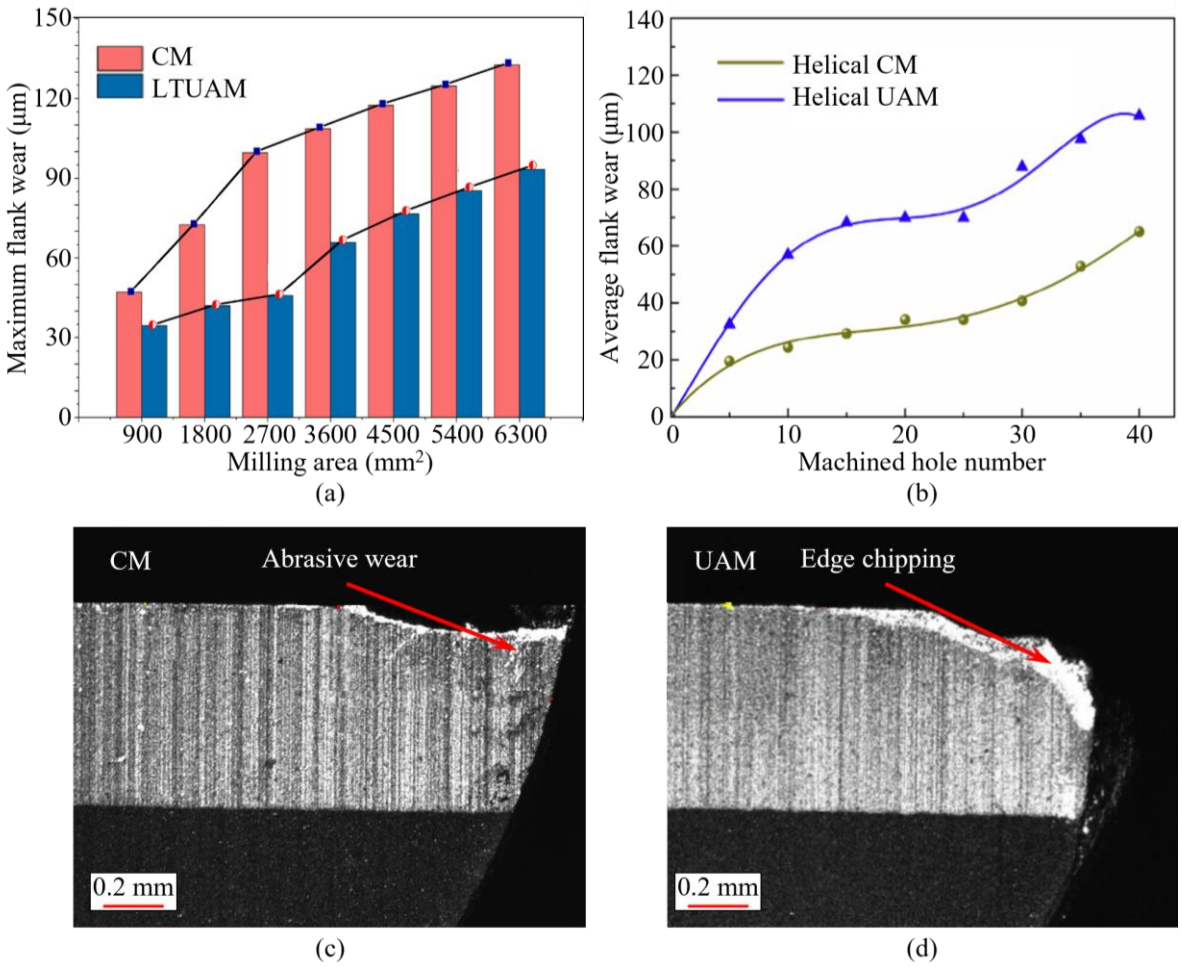


Figure 2.46 Tool wear following UAC: (a) Flank wear versus machined area (N = 2000 rpm, f_z = 0.05 mm/tooth, a_p = 0.4 mm, A_U = 5 μm) [215], (b) flank wear versus machined hole number (N = 2500 rpm, f_z = 0.03 mm/tooth, a_p = 0.15 mm/rev, A_U = 4–6 μm) [216], (c) and (d) comparison of worn morphology of tool in CM and UAM processes [217].

Contrary to other findings, research reported by Ni et al. [217] highlighted fatigue wear and abrasive wear as the predominant mechanisms during UAM of Ti-6Al-4V, under cutting parameters of N = 600 rpm, f_z = 0.008 mm/tooth, a_p = 0.2 mm, MQL, tool size Ø = 6 mm and A_U = 8 μm. In UAM, the workpiece is driven by ultrasonic vibrations to achieve high linear velocities and intense accelerations, thereby imparting significant impact kinetic energy to the

cutting edge. As cutting operations initiate from a state of separation, the inherently sharp but fragile tool edge becomes prone to microfractures and microcracks due to dynamic impacts at ultrasonic frequency. Additionally, the cutting tool endure pulsed cutting forces at ultrasonic-frequency/doubled-ultrasonic-frequency alternating friction forces. These forces induce pulsating compressive and tensile stresses, predisposing the tool to impact microcracks and abrasive wear. Over time, the synergistic effect of dynamic cutting forces, alternating friction and high impact energy causes existing fractures and microcracks to expand, leading to flaking and crack failures at the cutting edge, as depicted in Figure 2.46(c) and (d).

2.3.3.3 Surface morphology and roughness

Surface integrity is crucial for assessing the quality of machined surfaces. In UAC, the tool's ultrasonic frequency vibrations combined with standard cutting movements produce a distinct topographic scale texture, as shown in Figure 2.47(a) and (b). Research consistently demonstrated that UAC can reduce surface roughness with the change of uncut chip thickness [211], [218], [219], [220], [221]. End milling experiments were conducted by Ni et al. [220] and results showed that the surface roughness reduction ranged from 25.9% to 48.3% at cutting speeds of 5 m/min and 17 m/min in UAM, respectively. This enhancement was attributed to the ultrasonic vibrations altering the tool's motion trajectory and affecting the uncut chip thickness, thereby improving the surface quality. Meanwhile, the reduced cutting forces also improved the tool life with better cutting ability, resulting in lower surface roughness. In contrast, Xie et al. [212] reported a deterioration in surface roughness due to ultrasonic impacts, as depicted in Figure 2.47(b) and (d). Zhang et al. [221] compared surface roughness outcomes between CM and EUAM when cutting Ti-6Al-4V, finding that EUAM resulted in significantly greater surface roughness at cutting speed ranging from 40 m/min to 160 m/min (see Figure 2.47(c)). It is suggested that surface roughness outcomes depend on the cutting process, cutting parameters and ultrasonic amplitudes, which collectively determine the cutting conditions. Ultrasonic vibrations applied along the direction of the machined surface generally enhance surface quality. In contrast, vibrations perpendicular to the surface can potentially degrade it and increase the surface roughness. Moreover, a low ultrasonic amplitude combined with a large depth of cut can alter the tool-workpiece contact from periodic intermittent to continuous contact with changed uncut chip thickness, reducing the effectiveness of ultrasonic vibrations [222].

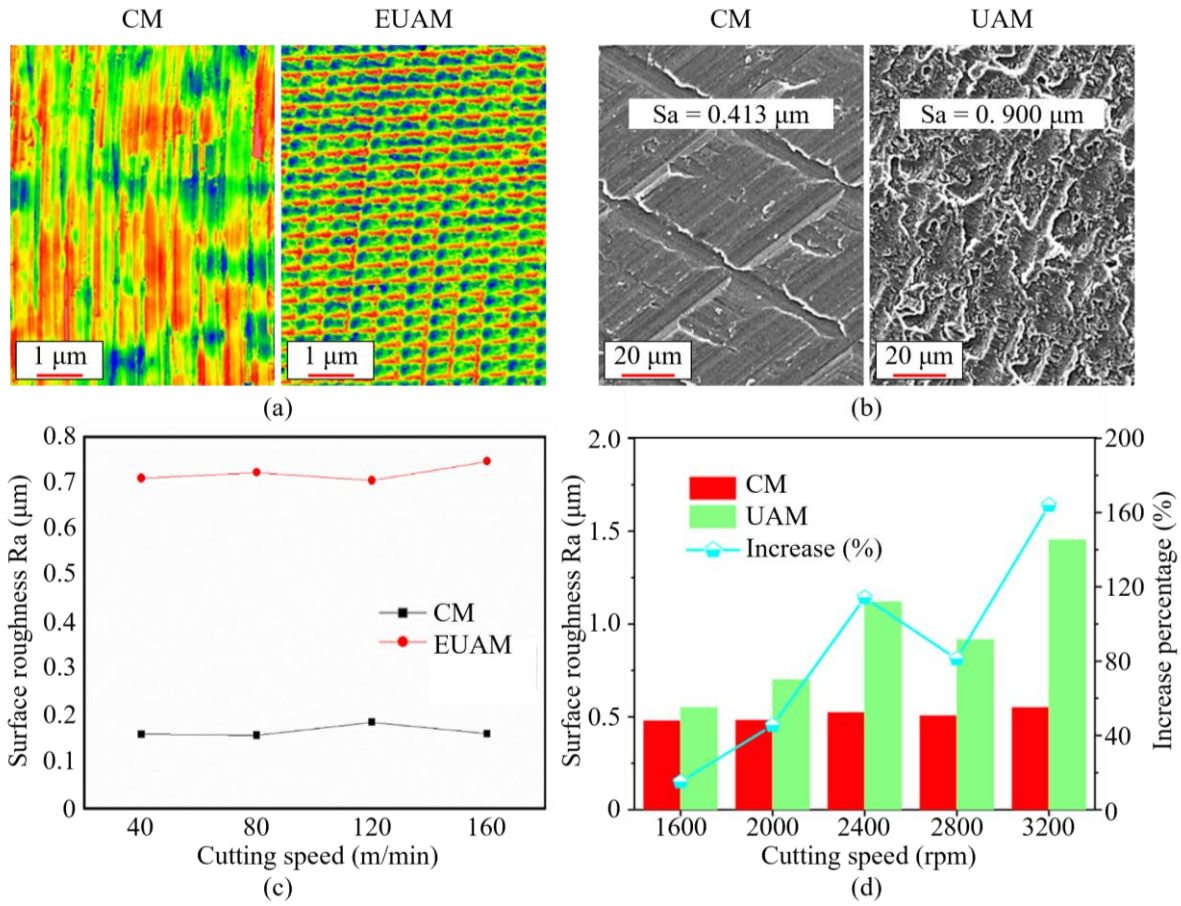


Figure 2.47 Comparison of surface monography and roughness between conventional cutting and ultrasonic-assisted cutting; (a) The variation of surface roughness with cutting speed in both CM and EUAM (f_z = 0.015 mm/tooth, a_p = 0.2 mm, a_e = 12 mm, A_U = 5 μm) [221], (b) effect of UAM on surface morphology (v_c = 2400 rpm, f_z = 0.015 mm/tooth, a_p = 0.2 mm, a_e = 6 mm, A_U = 2 μm) [212], (c) the variation of surface roughness with cutting speed [221] and (d) effects of cutting speed on Sq [212].

2.3.3.4 Microhardness, residual stress and metallographic/microstructural alterations

According to Section 2.2.4, subsurface characteristics are influenced by mechanical and thermal loads. Chen et al. [216] conducted experiments on helical UAM of Ti-6Al-4V, comparing surface microhardness and residual stress between helical CM and helical UAM. Figure 2.48(a) shows that the maximum average microhardness of UAM is higher than that of CM and same results were confirmed at various spindle speeds (N = 2000–4000 rpm). The higher microhardness in UAM was attributed to more work hardening effect due to the severe plastic deformation. Chen et al. [219] also pointed that the vibration generated rubbing and friction effects, intensifying work hardening in UAM. Similar conclusions were reported in

UAC as well [211], [212], [219], [221]. Moreover, the peripheral edge in UAM achieved significantly higher instantaneous cutting speeds than those in conventional milling, resulting in enhanced strain hardening.

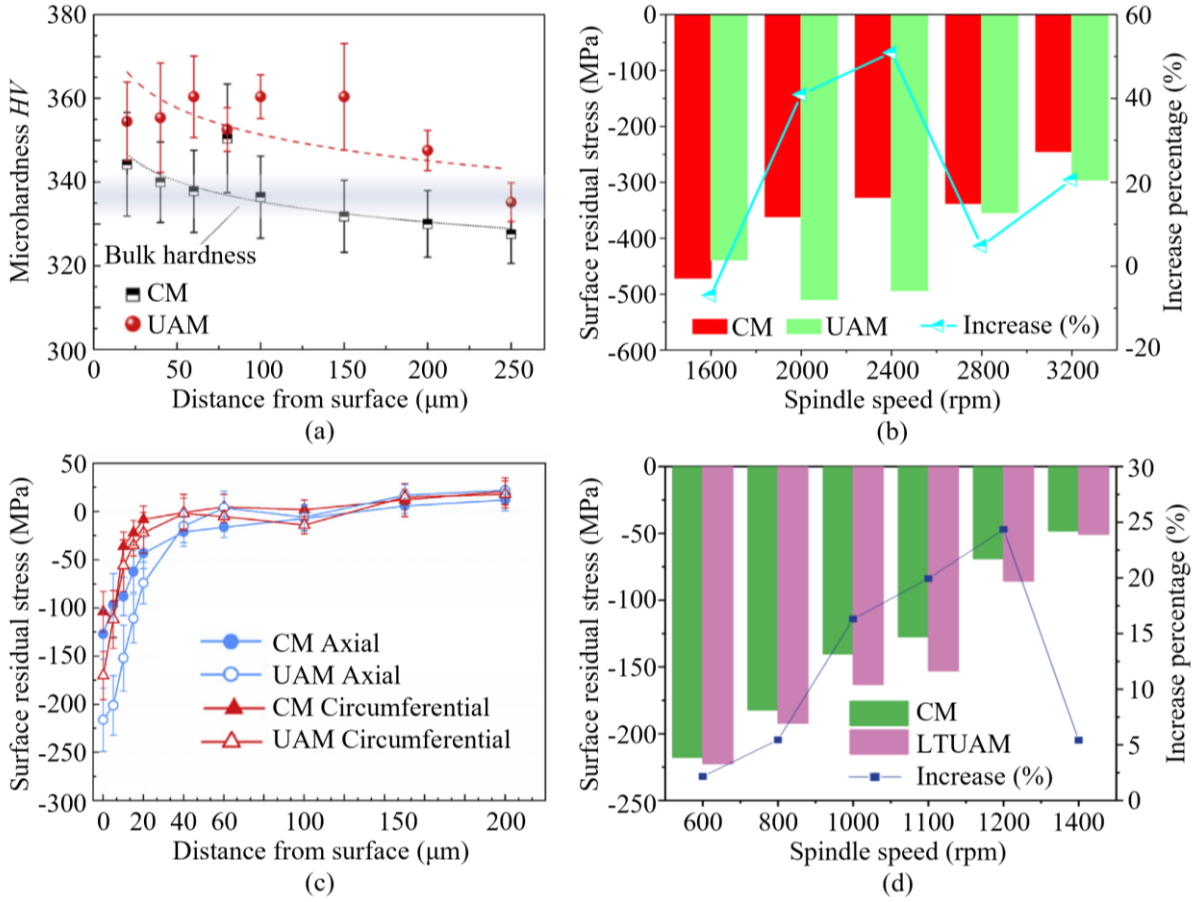


Figure 2.48 Comparison results of surface microhardness and residual stress. (a) Comparison of microhardness at helical CM and UAM (N = 2500 rpm, f_z = 0.03 mm/tooth, a_p = 0.15 mm, A_U = 4–6 μm) [216], (b) surface residual stress for CM and UAM at different spindle speeds (f_z = 0.015 mm/tooth, a_p = 0.2 mm, a_e = 6 mm, A_U = 2 μm) [212], (c) comparison of residual stress with different cutting processes [216] and (d) surface residual stress for CM and LUAM at different spindle speeds (f_z = 0.03 mm/tooth, a_p = 4 mm, a_e = 0.8 mm, A_U = 5 μm) [211].

Chen et al. [216] also stated higher compressive residual stress in UAM (−216 MPa), which only was −127 MPa in CM, as shown in Figure 2.48(c). In UAM, intensified plastic deformation introduced by ultrasonic vibration led to higher compressive residual stress. Findings echoed by similar studies are shown in Figure 2.48(b) and (d). UAM presented higher compressive residual stress at every level of spindle speeds. Although the average cutting force in UAC was lower than that in CM, instantaneous cutting forces were higher and led to heavier strain

hardening. The lower cutting temperature in UAC also restricted the effect of thermal load and presented higher compressive residual stress. Furthermore, as spindle speed increased, the thermal effect intensified, and the compressive residual stress decreased, although UAM still maintained a higher residual stress state.

The ultrasonic vibration also has a considerable impact on the microstructure of materials. Chang et al. [223] observed significant grain refinement in UAM of GH4169, as demonstrated in Figure 2.49(a) and (b). The microstructure in UAM exhibited a pronounced grain refinement compared to CM. The strain distribution, as shown in Figure 2.49(c) and (d), indicated higher dislocation density and more extensive plastic deformation, which contributed to work hardening. Research indicated that implementing gradient nanostructures or refining grain structures through plastic deformation of surfaces can greatly enhance material resistance to wear, corrosion and fatigue. These modifications substantially improve the material's durability and longevity under various environmental conditions and mechanical stresses [224], [225], [226]. Therefore, surfaces machined by UAC may have better fatigue properties.

From a system energy perspective, UAC involves additional effects beyond those of conventional cutting, such as high-frequency rubbing, burnishing, hammering and cutting-extrusion. These actions induce a high-frequency energy impact on the workpiece surface, leading to more significant grain deformation and refinement compared to the conventional cutting process [223]. Figure 2.49(e) and (f) illustrate that the reduction in average grain diameter near the machined surface in UAM reached 10.4%. This change was attributed to the dynamic impacts of high-frequency ultrasonic energy, which continuously stretches and compresses the grains, leading to increased friction and boundary fracturing among grains. Such activity refined the grain structure. The continuous application of ultrasonic energy drives grain fragmentation and increases dislocation density, thereby promoting the formation of smaller grains and significantly reducing the average grain diameter.

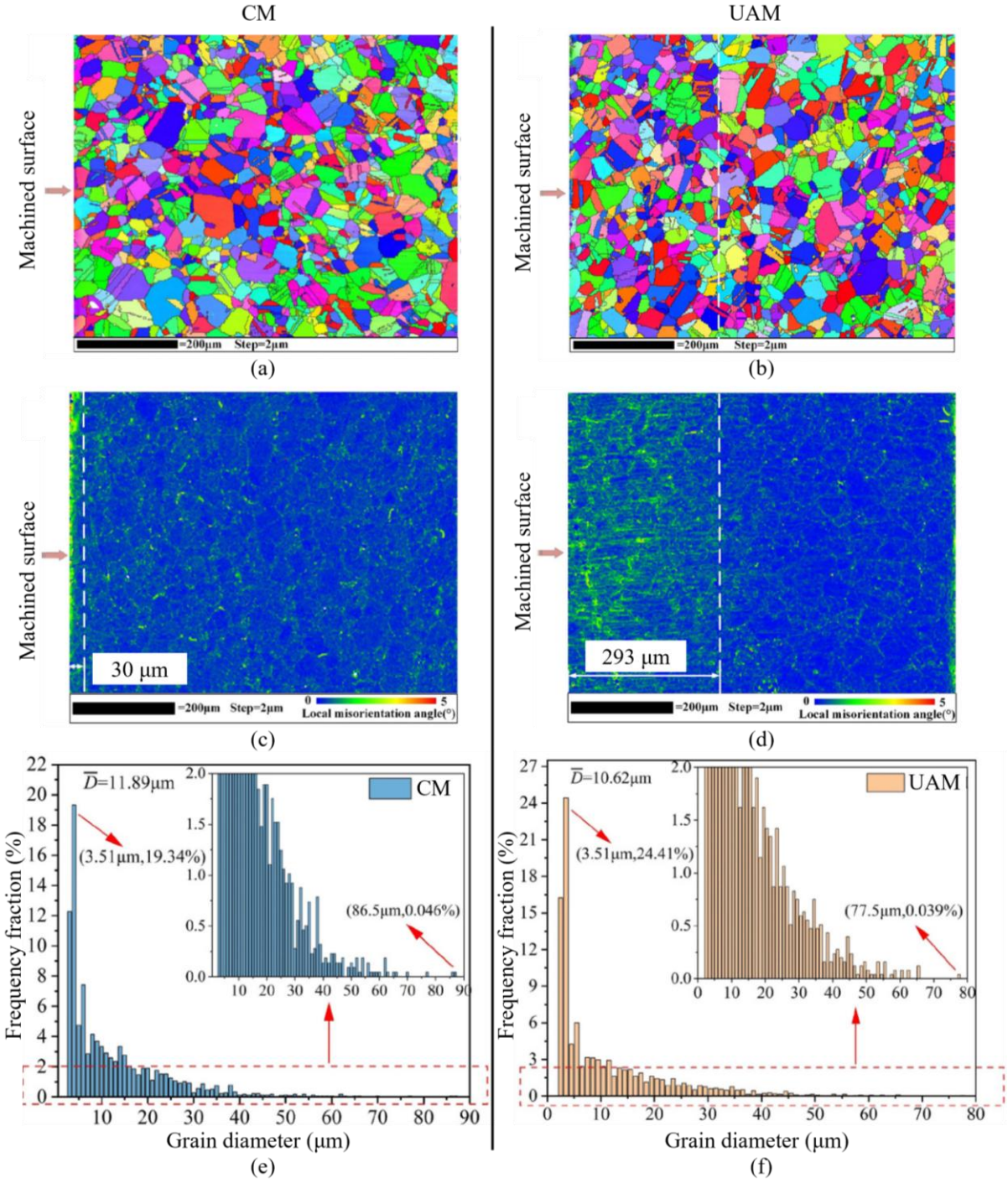


Figure 2.49 The EBSD analysis of microstructure between CM and UAM; (a) and (b) Orientation image microscopy (OIM) maps, (c) and (d) Kernel average misorientation (KAM) maps, (e) and (f) grain size distribution of specimens [223].

Much of the current research is centred around common titanium alloys such as Ti-6Al-4V. However, there is a notable scarcity of studies on the application of UAC in machining γ-TiAl. Only a handful of publications have explored the integration of ultrasonic vibration in high-

efficiency deep grinding processes. Investigations conducted by Wang et al. [89], [94] into the effects of grinding parameters on surface integrity revealed that the use of ultrasonic vibration improved surface quality, reduced cutting force, and lower cutting temperatures. Additionally, Li et al. [227] developed an analytical model to predict grinding forces in ultrasonic-assisted grinding of γ-TiAl, which yielded relatively accurate predictions.

2.4 Modelling of cutting processes

The creation of surface topography using ball-end milling cutters is a complex task. Accurately predicting surface topography requires modelling and simulating the milling force, dynamic stability, and dynamic displacement throughout the machining process. These components are crucial as they lay the groundwork for advanced research and help elucidate the mechanisms of ball-end milling. Comprehensive studies in these domains are essential for making informed choices about machining parameters and improving manufacturing quality. Currently, three primary methodologies are utilised to model milling forces [228], [229], [230], [231], [232], [233]:

- Experimental methods: These involve direct measurement and observation during the milling process to gather empirical data.

  The experimental method, a traditional approach to modelling milling forces, typically begins by identifying key machining parameters that influence milling forces through single-factor experimental analysis. Milling experiments are then systematically conducted using techniques such as orthogonal arrays, and the forces exerted under various cutting parameters are measured with dynamometers. The collected data is subsequently analysed using linear regression, nonlinear regression and response surface methodology to derive empirical formulas related to the principal machining parameters.

  While this method effectively predicts maximum or average milling forces, it has limitations in modelling instantaneous milling forces, thus providing restricted insights into milling dynamics. However, the integration of intelligent algorithms, including BP neural networks, genetic algorithms, ant colony algorithms and fuzzy systems, has greatly enhanced experimental methods. These advancements offer new avenues for the

accurate prediction of milling forces, enriching the traditional experimental approach with greater analytical depth and predictive power.

- Finite element methods (FEM): This approach uses numerical simulations to predict and analyse the forces and deformations in the milling process.

  The Finite element method (FEM) is a numerical approach used to calculate cutting forces by interpolating a finite number of mesh elements based on the known constitutive relations of the material and the actual conditions of machining contact. This method can leverage widely used finite element analysis software such as LS-DYNA, Abaqus, and ANSYS, or specialised cutting simulation software like AdvantEdge for accurate predictions.

  The effectiveness of FEM hinges on precise configurations of the constitutive models for both tool and workpiece materials, as well as the friction at the tool-workpiece interface and the criteria for chip separation. When these settings are optimally configured, FEM not only accurately predicts cutting forces but also provides detailed simulations of other critical machining data, including temperature, stress, strain, and tool wear. However, a significant drawback of this method is its complexity and the substantial computational time required, which may make it less suitable for real-time dynamic analysis and on-the-fly adjustments during machining processes.

- Analytical modelling methods: These involve creating mathematical models that approximate the physical behaviours of the milling process.

  The analytical modelling method conceptualises that the total cutting force is the vector sum of infinitesimal cutting forces. These forces are calculated as the product of the cutting force coefficient and the instantaneous uncut chip area. The cutting force coefficient itself depends on the shear angle and the friction angle, which are pivotal to this approach.

  A critical aspect of this method is the determination of the shear angle, guided by the theory of metal deformation zone during the cutting process. This method primarily accounts for shear slippage in the primary deformation zone, friction between the chip

and tool in the secondary deformation zone, and the energy consumed by the ploughing of the cutting edge against the machined surface in the tertiary deformation zone.

The shear angle is typically derived using the principle of maximum shear stress or the principle of minimum energy. Following this, a micro-element stress model is constructed. The overall cutting force is then ascertained by transforming coordinates and summing the vectors of infinitesimal cutting forces [234]. Foundational contributions to this field, such as Merchant's orthogonal cutting model [235], Stabler's chip flow law [236], Armarego's oblique cutting model [237], and Oxley's cutting prediction theory [238], have significantly advanced the understanding and modelling of machining processes.

Given the challenges and uncertainties in obtaining accurate parameters such as the shear angle, in traditional analytical modelling, an improved approach combines calibration experiments with mathematical analysis to enhance precision [239], [240]. This method typically involves discretising the cutting edge into multiple elements along the axial direction, with each cutting edge element is treated as performing oblique cutting on the workpiece. This approach views the cutting process as the collaborative action of these elemental components.

The force exerted by each micro-element is calculated as the product of the uncut micro-element chip area and the cutting force coefficients. These elemental cutting forces are categorised into axial, radial and tangential components. These components are then transformed into X, Y and Z directional forces through coordinate transformation. By summing all these elemental forces, the method calculates the triaxial cutting forces that the tool experienced at any given moment. This hybrid experimental and theoretical approach significantly enhances the prediction of varying milling forces throughout the machining process, offering greater adaptability and improved predictive accuracy [241]. The elemental tangential, radial and axial forces exerted during the milling process are quantified using Equation 2-5 [240].

$$\begin{cases} dF_t(\theta,z) = K_{te}dS + K_{tc}h(\theta,\psi,\kappa)db \\ dF_r(\theta,z) = K_{re}dS + K_{rc}h(\theta,\psi,\kappa)db \\ dF_a(\theta,z) = K_{ae}dS + K_{ac}h(\theta,\psi,\kappa)db \end{cases} \tag{2-5}$$

where $h(\theta, \psi, \kappa)$ is the uncut chip thickness normal to the cutting edge, while *dS* and *db* denote the differential length and width of the curved cutting edge element, respectively. K_{tc}, K_{rc}, K_{ac}, K_{te}, K_{re} and K_{ae} are the cutting force coefficients.

To achieve more precise calculations of the uncut elemental chip dimensions, methods such as the solid model approach, analytical methods and the Z-map method have been employed. Among these, the Z-map method is widely utilised due to its high computational efficiency and simplicity in modelling. Originally, Z-map referred to a method of representing the geometric model of a workpiece based on a discretisation concept. Typically, it involves dividing the bottom surface of the workpiece into a two-dimensional grid, where the height of the top surface at each grid point is represented by a two-dimensional matrix corresponding to the grid point index. This identification method for the tool-work contact area involves using the Z-map model to represent the workpiece [239], [240], [242]. By assessing the contact relationship between the tool teeth and the material above the mesh grid points of the workpiece within a unit time period, it determines whether the tool teeth have engaged with the workpiece. Based on the Z-map model, Kim et al. [243] developed a method for identifying the tool-work contact area when milling complex surfaces with a ball nose end mill and established a corresponding milling forces model.

2.5 Summary and research gaps

This chapter provides a comprehensive literature review, covering various aspects including the characteristics and challenges of advanced aerospace materials, tool wear mechanisms and failure, workpiece surface integrity and the principles and applications of ultrasonic-assisted cutting technology. Additionally, the commonly used modelling ideas in cutting operations are briefly explained.

- **Advanced titanium alloys: Challenges and opportunities**

Advanced titanium alloys are noted for their excellent mechanical properties with lightweight characteristic. In particular, γ-TiAl alloys present good hight-temperature properties, making them ideal substitutes for nickel-based superalloys in aerospace engine blade manufacturing. However, low ductility and high brittleness at room temperature pose significant challenges to machinability, often resulting in poor surface quality and severe tool wear. Current research

focuses on enhancing the surface integrity of machined workpieces and extending tool life by optimising machining methods and cutting parameters.

- **Ultrasonic-assisted cutting: Hybrid processing method**

Ultrasonic-assisted cutting, a hybrid processing method, is extensively studied across various materials, including hard and brittle materials like glass and crystal, as well as metals with better ductility. The consensus in current research highlights the benefits of this technique, such as reduction of cutting force, decrease in cutting temperature, extension of tool life, and enhancement of the machined surface. However, studies specifically on ultrasonic-assisted milling of γ-TiAl are scarce, primarily focusing on grinding due to this alloy's high brittleness at room temperature. Investigating the cutting mechanisms and effects of milling γ-TiAl through the introduction of ultrasonic vibration presents a significant research opportunity. Further comprehensive studies on tool wear mechanisms, including the impact of coating materials, are crucial to improve the machinability of γ-TiAl.

- **Theoretical and modelling studies**

In addition to the experimental work, this thesis introduces typical methods used in previous modelling research. Selecting an appropriate modelling method based on the actual processing technique can significantly enhance the accuracy of model predictions and deepen the theoretical understanding of the cutting process. By integrating experimental research with theoretical study, a more comprehensive exploration of the machining mechanisms can be achieved, leading to better applications of advanced titanium alloys.

Based on the preceding literature review, this thesis identifies several key research gaps:

I. **Limited research on ultrasonic-assisted milling of γ-TiAl:** Previous studies on ultrasonic-assisted milling of γ-TiAl have been sparse, restricting opportunities to enhance its machinability at room temperature. This research aims to systematically examine the machinability of γ-TiAl, focusing on aspects such as cutting force, workpiece surface integrity and tool wear, to address this underexplored area.

II. **Challenges with tool wear during cutting γ-TiAl:** Severe tool wear remains a significant challenge in machining γ-TiAl. Existing research has largely discussed tool wear from

limited perspectives, lacking a thorough analysis of how cutting conditions and tool materials influence tool wear mechanisms when machining γ-TiAl. This study seeks to fill this gap by providing a more comprehensive examination.

III. **Lack of models for ball-end ultrasonic-assisted milling:** Current models primarily address conventional milling and rarely cover tool wear for ultrasonic-assisted processes. The absence of models that consider geometry, cutting force, and tool flank wear for ball-end ultrasonic-assisted milling limits understanding of its cutting mechanisms. This thesis will work to develop such models to support further exploration in this area.

3 EXPERIMENTAL WORK

3.1 Introduction

Two major phases of the experimental work and one phase of the theoretical work were carried out over the course of this research.

Phase 1 trials were designed to assess the stability of the integrated ultrasonic system and verify the operating limits of ultrasonic-assisted milling on a 5-axis DMG Mori Ultrasonic 20 linear machine tool. Additionally, work was also carried out to explore the influence of operating parameters on cutting forces, tool wear and workpiece surface integrity, providing a preliminary assessment of significant variable factors in ball-end milling of γ-TiAl.

Phase 2 focused on identifying the main tool wear mechanisms in ultrasonic-assisted milling of γ-TiAl, together with a comparative study of conventional milling (CM) and ball-end ultrasonic-assisted milling (B-UAM) was conducted to investigate the effects of ultrasonic vibration on aspects including cutting forces, tool wear and workpiece surface integrity.

Phase 3 involved experimental trials performed to validate kinematic based analytical models for the ball-end ultrasonic-assisted milling process developed to predict topography of machined surface, tool bending deflection, cutting forces and tool flank wear. Detailes of the analytical model formulations are outlined in Chapter 4.

Each phase was further divided into several sub-phases as outlined below:

Phase 1A: Stability assessment of integrated ultrasonic system.

Phase 1B: Influence of operating parameters on machinability when milling γ-TiAl.

Phase 2A: Tool wear mechanisms and failure of γ-TiAl in B-UAM.

Phase 2B: Comparative evaluation between the effects of CM and B-UAM on machinability of γ-TiAl.

Phase 3A: Experimental validation of analytical model for predicting machined surface morphology in B-UAM.

Phase 3B: Experimental validation of analytical model for predicting cutting forces in B-UAM.

Phase 3C: Experimental validation of analytical model for predicting tool flank wear in B-UAM.

Further details regarding the workpiece materials, cutting tools and equipment used for the experimental trials, as well as the experimental design and test procedures, are provided in the following sections.

3.2 Workpiece materials

Four different workpiece materials were employed for the experimental programme comprising a γ-TiAl intermetallic, an α + β titanium alloy, an aluminium alloy and a low-alloy steel grade. The γ-TiAl intermetallic served as the primary material for the majority of experimental work, with low-alloy steel used for a limited comparative study of tool wear mechanisms when milling γ-TiAl. Validation trials of the kinematic analytical model for predicting surface morphology were undertaken using an aluminium alloy, while a conventional α + β titanium alloy was utilised to experimentally verify the cutting force and tool wear models in ball-end ultrasonic-assisted milling. This facilitated a clearer assessment of the various analytical models by minimising the effects of tool bending deflection and adhesion wear encountered when cutting γ-TiAl.

The γ-TiAl intermetallic employed had a nominal composition of Ti-45Al-8Nb-0.2C (at%), which was produced as a cylindrical billet measuring 225 mm in diameter and 275 mm in height. The billet underwent hot isostatic pressing (HIP) at 1260°C and 150 MPa for 4 hours, achieving a bulk hardness of approximately 365 HV_{30}, density of ~4.2 g/cm^3 and room temperature elongation rate about 1%–2% [244], [245], [246]. This material is capable of operating at temperatures of up to 800°C and has a tensile strength of approximately 900 MPa but with an average grain size of ~2 mm with limited treatment [24]. The lamellar microstructure, consisting of α_2 and γ phases, is depicted in Figure 3.1, with the γ phase appearing dark and the α_2 phase showing a lighter contrast. For the cutting tool wear tests included in Phase 1B and Phase 2, γ-TiAl blocks measuring 27.5 × 38.5 × 100 mm were prepared, while smaller blocks (Phase 1B) of 19.5 × 7 × 100 mm were employed for cutting force measurement trials and workpiece surface integrity assessment. Specimens with dimensions of 29 × 13 × 100 mm were used for workpiece surface integrity evaluation in all Phase 2 experiments.

A polyurethane tooling board BM 5460 (40 × 30 × 50 mm) was employed to calibrate ultrasonic vibration before all experimental trials. The AISI 4000 series low-alloy steel was machined to provide limited comparative benchmarking data against γ-TiAl relating to the investigation of tool wear mechanisms in Phase 2A. All low-alloy steel blocks were uniformly sized at 19.5 × 7 × 100 mm. Experimental validation tests of the kinematic model for predicting machined surface topography after B-UAM in Phase 3A involved AA6082-T6 aluminium alloy (30 × 10 × 80 mm), which was selected to simplify model complexity generated by tool bending deflection. In contrast, conventional solution treated and annealed α + β titanium alloy, Ti-6Al-4V, was utilised in trials to assess operating limits of ultrasonic-assisted milling in Phase 1A and verify the accuracy of cutting force (100 × 100 × 10 mm) and tool wear (55.8 × 19.2 × 80 mm) model predictions in Phase 3B and 3C, respectively. The key mechanical and physical properties of the workpiece materials mentioned in experimental work are listed in Table A.1.

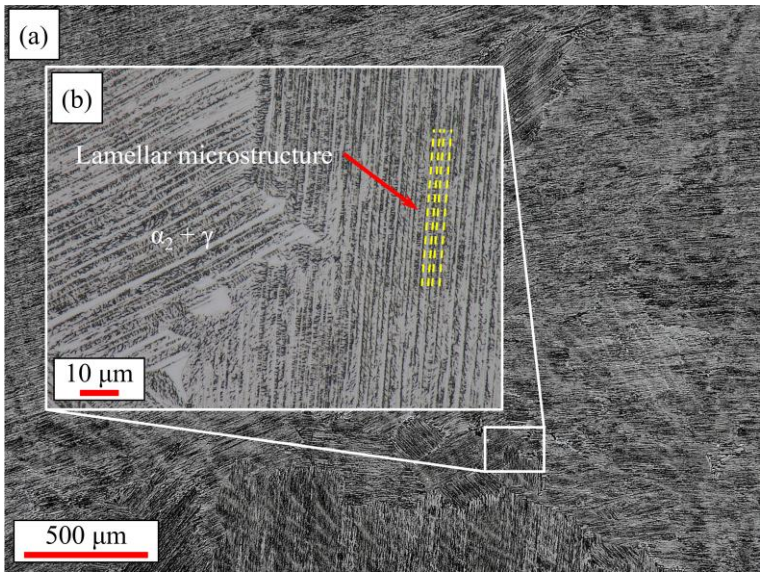


Figure 3.1 Micrograph of Ti-45Al-8Nb-0.2C intermetallic with lamellar microstructure; (a) ×80 magnification and (b) ×1000 magnification.

All blocks were pre-machined to ensure flatness prior to commencement of tests, using 6 mm diameter end mills (SECO-JS754060E2C.0Z4A-HXT) at relatively low operating parameters: v_c = 131.8 m/min (N = 7000 rpm), f = 400 mm/min, a_p = 0.02 mm and a_e = 0.20 mm, under flood coolant conditions. The total depth of cut was designed as 0.5 mm. The parameters were selected to minimise surface/subsurface damage on the workpieces as much as possible to reduce any adverse impact in subsequent formal experiments.

3.3 Tooling

3.3.1 Cutting tools for mainstream Phase 1 and 2 experiments

A range of rotary cutting tools comprising twist drills and end/ball end mills made from either high-speed steel (HSS) or tungsten carbide (WC), with varying tool diameters and lengths were selected for Phase 1A work to investigate the stability of the integrated ultrasonic system on the DMG Mori Ultrasonic 20 linear machining centre. Key specifications of the cutting tools are detailed in Table 3.1. A critical variable in the investigation was the tool overhang length, which was varied to understand its influence on the resulting tool vibration amplitude. Based on Phase 1A results, the overhang length of the tool was kept constant at 32 mm for all subsequent machining experiments.

In Phase 1B experiments, 4-fluted, 4 mm diameter PVD coated TiAlN WC ball nose end mills (WIDIA-HANITA-40100400T025) with a helix angle of 30° were chosen (see Figure 3.2) [247]. The overall length of the tools was reduced from 75 mm to 55 mm using EDM in order to control/minimise deflection, although this did not compromise the 25 mm maximum cutting depth.

Table 3.1 Key specifications for tools used in Phase 1A.

Tool type	Tool material	Diameter (mm)	Total length (mm)	Mass (g)
Twist drill	HSS	4	75	5.41
Twist drill	HSS	6	50	8.19
Twist drill	HSS	6	58	9.90
Twist drill	HSS	6	65	11.68
4-flute end mill	HSS	6	58	11.21
4-flute end mill	WC	6	58	20.49
4-flute ball end mill	WC	6	58	20.41
4-flute ball end mill	WC	4	50	8.17
4-flute ball end mill	WC	4	75	12.13
4-flute ball end mill	WC	5	75	18.27
4-flute ball end mill	WC	6	75	25.96

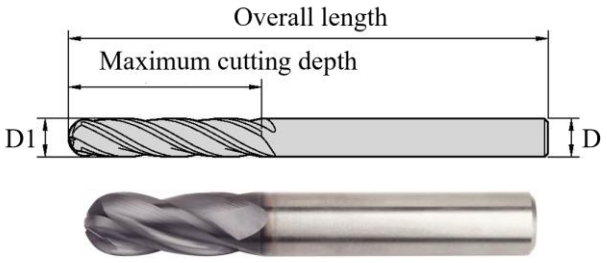


Figure 3.2 Schematic and image of a ball nose end mill.

For Phase 2 trials, similar 4-fluted, 4 mm diameter TiAlN coated WC ball nose end mills (WIDIA-HANITA-40000400T014) were employed but with shorter overall length and maximum cutting depth of 50 mm and 14 mm respectively. The overhang length was constant 32 mm. For the purposes of a comparative study, uncoated ball nose end mills (ITC-BC044BN) with identical tool geometry were also employed. All coated tools were supplied by Widia Hanita, whereas the uncoated tools were produced by Industrial Tooling Corporation (ITC) Ltd.

3.3.2 Cutting tools for Phase 3 model validation trials

To streamline calculations and reduce the complexity of the analytical models developed in Phase 3, 2-fluted, 4 mm diameter uncoated WC ball nose end mills (ITC-BC042BN) were selected for the model verification trials. Detailed specifications of the tool are provided in Table 3.2.

Table 3.2 Specifications of ball nose end mill used in Phase 3 [248].

Tool parameters	Specification
Overall length	55 mm
Maximum cutting length	14 mm
Overhang length	32 mm
Rake angle	9°
Clearance angle	15°
Nominal helical angle	30°
Hardness *HV*	2,600
Young's modulus	550,000 N/mm^2
Core ratio	0.632

3.4 Equipment

3.4.1 Machine tool, fixturing and experimental setup

All of the experimental trials were carried out on a DMG Mori Ultrasonic 20 linear 5-axis CNC machining centre as shown in Figure 3.3, which has a maximum spindle rotational speed of 42,000 rpm and capable of simultaneous ultrasonic axial vibration of tools at a frequency of up to 60,000 Hz via an integrated ultrasonic tool holder (detailed in next section). It can accommodate a maximum workpiece height of 180 mm with a working table diameter of 250 mm and linear drives in each axis with >2 g acceleration [249]. Table 3.3 shows the specifications of machine tool.



Figure 3.3 DMG Mori Ultrasonic 20 linear machining centre.

Table 3.3 Main specifications of the DMG Mori Ultrasonic 20 linear machining centre [249].

Parameter	Level	Unit
Max. X axis travel	200	mm
Max. Y axis travel	220	mm
Max. Z axis travel	280	mm
Max. table load	15	kg
Table diameter	250	mm
Max. workpiece height	180	mm
A-axis range	−15/+130	°
C-axis range	360	°
Max. speed	42,000	rpm
Rated power	15	kW
Torque (100% DC)	6	Nm
Vibration frequency range	15–55	kHz
Max. vibration amplitude	10	μm

For the mainstream machining experiments in Phase 1B and 2, the workpieces were held in a clamping vice that was mounted on a platform dynamometer, as shown in Figure 3.4(a). Phase 3A and 3C were undertaken with the same way for machined surface topography and tool flank wear model validation trials. To increase rigidity and minimise deflection, workpieces with a height of 10 mm were attached directly onto the platform dynamometer using four corner bolts, as illustrated in Figure 3.4(b), for all of the cutting force model validation trials in Phase 3B.

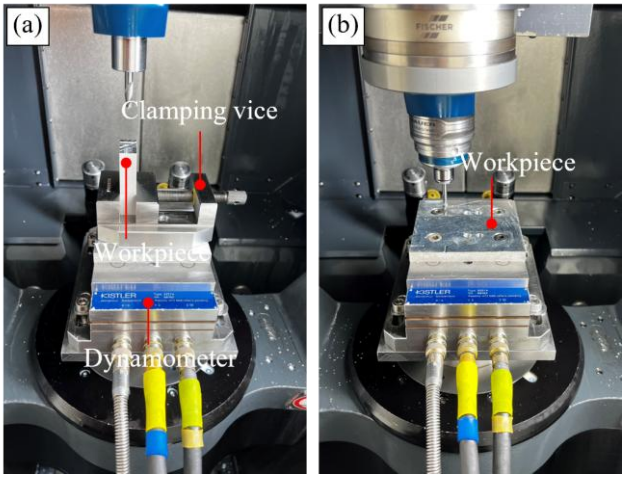


Figure 3.4 Fixtures for holding workpieces with (a) a clamping vice and (b) direct fixation.

The three linear axis motions of the spindle (X, Y, and Z) and two rotational axis movements of the worktable (C and A) are illustrated in Figure 3.5(a). The resolutions of linear movement and rotation were 1 μm and 0.01°, respectively. Tool size, including length and diameter, was measured using a Renishaw NC4+ high-accuracy laser tool setting system with a repeatability (2σ) of ±0.5 μm (see Figure 3.5 (b)) [250]. After each tool loading, a dial indicator with 1 μm resolution was employed to detect the radial runout of the cutter, to ensure it does not exceed 5 μm in all of the tests performed. The spindle features four coolant nozzles for either cutting fluid or air cooling, as shown in Figure 3.5(b). The cutting fluid used in all experiments was an emulsion containing water-soluble Houghton Hocut 795 B-EU mineral oil at a concentration of approximately 10%, as recommended by DMG Mori guidelines, and regularly monitored using a refractometer. The pressure of the cutting fluid was set to the default value of ~5.5 bar.

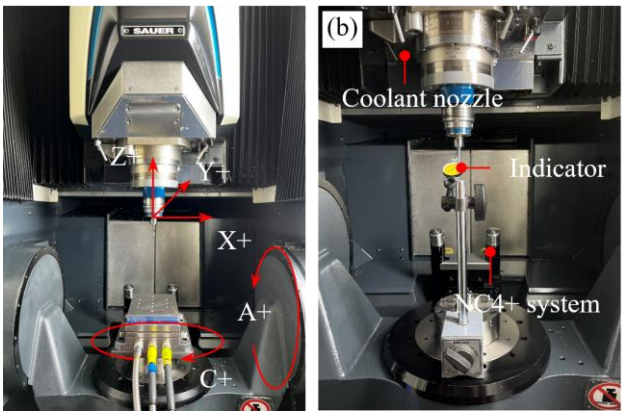


Figure 3.5 Illustration of (a) machine axes motion and (b) setup for measuring runout.

3.4.2 Integrated ultrasonic tool holder system

The superimposition of ultrasonic vibration along the vertical axis of cutting tools was achieved via an integrated HSK-E32 ultrasonic tool holder interface. Figure 3.6(a) details a cross-sectional schematic illustrating the key internal components of the HSK-E32 and operating principle. Energy generated by the ultrasonic power supply integrated into the ultrasonic spindle is transmitted to a piezoelectric transducer through an inductive transmission system, which then converts the electrical signal into mechanical vibrations.

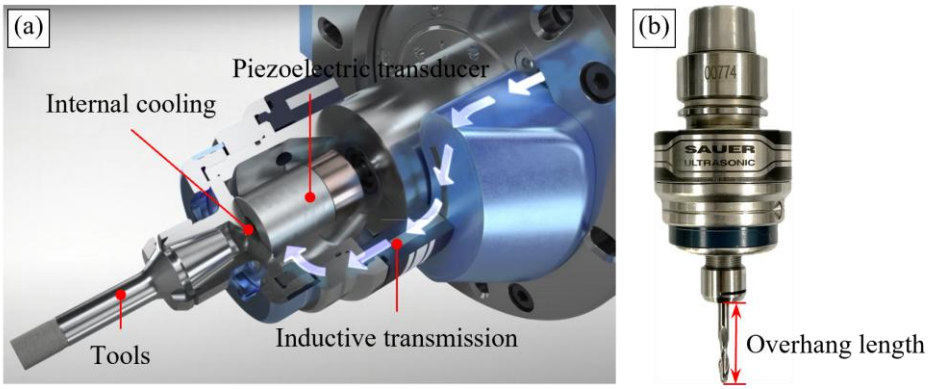


Figure 3.6 (a) Schematic of key internal components in the integrated ultrasonic tool holder [251]; and (b) image of HSK-E32 ultrasonic tool holder.

The HSK-E32 ultrasonic tool holder (see Figure 3.6(b)) was designed by Sauer (part of the DMG Mori Group) and utilised for all of the machining tests. The cutting tools were secured to the tool holder using an ER 11-UP ultra precision collet supplied by Rego-Fix. Conversely, a conventional tool holder, HSK-E32-MEGA6S-60 manufactured by Big Daishowa was used for workpiece surface preparation operations.

3.4.3 Cutting force measurement

Cutting forces (F_x, F_y and F_z) were measured with a Kistler 9257A piezoelectric multicomponent platform dynamometer, as shown in Figure 3.7. Force data were collected and transmitted to the data acquisition card on the computer as digital signals through a series of charge amplifiers (Kistler 5011A), and subsequently analysed using Kistler Dynoware software. Due to limitations of the PC's performance, the ideal theoretical sampling frequency (twice the ultrasonic frequency) could not be achieved. Instead, a sampling frequency of 9,000 Hz was applied for the cutting force measurement. Technical specifications of the Kistler 9257A are listed in Table 3.4.

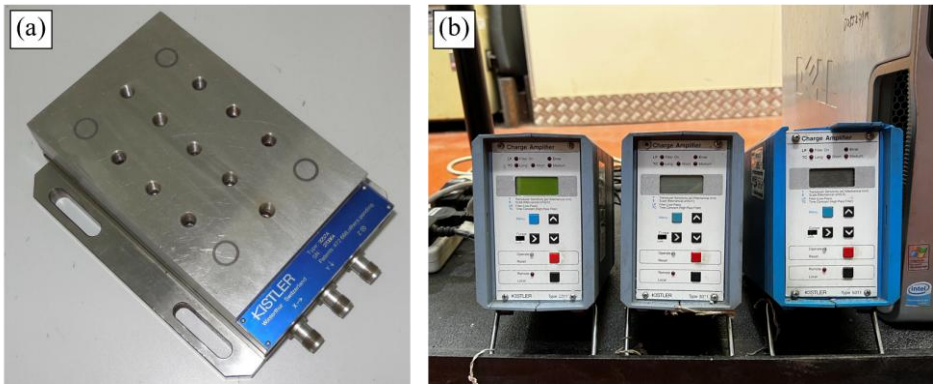


Figure 3.7 Cutting force measurement system including: (a) Kistler 9257A platform dynamometer and (b) Kislter 5011A charge amplifiers.

Table 3.4 Technical specifications of the Kistler 9257A dynamometer [252].

Specifications	F_x	F_y	F_z
Measuring range (N)	0–5,000	0–5,000	0–10,000
Sensitivity (pC/N)	−7.94	−8.03	−3.76
Linearity ≤ ±%FSO	0.3	0.3	0.3
Temperature ℃	0–70		

3.4.4 Tool wear measurement

A Wild M3Z optical light microscope connected to a digital camera and equipped with a X-Y digital micrometre platform, was used to measure wear on both the flank and rake faces of the cutting tools, as depicted in Figure 3.8. As the milling tests were performed at a 45° tilt angle, corresponding tool wear measurements were undertaken at the same orientation using an adjustable fixture for angle control. Additionally, the wear on the rake face was imaged by placing the tool on a V-block in a horizontal orientation. The image of each cutting tool in the new condition was used as a fixed initial reference, which was superimposed on subsequent images of worn tools (using EOS Utility software), to ensure the accuracy of the wear measurements.

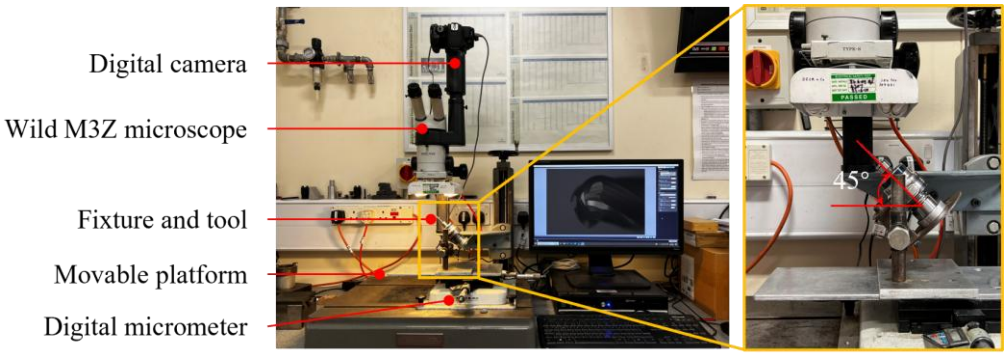


Figure 3.8 Setup for tool wear measurement system.

3.4.5 Workpiece height position measurement

The actual depth of material removed was measured after each complete pass of the workpiece surface to calculate the depth of cut achievement rate (R_{Cd}). As repeated mounting and removal of the workpiece from the machine can affect cutting accuracy, a Renishaw PowerProbe 400 optical machine probe system (OMP), see Figure 3.9, was utilised for rapid real-time measurement of the initial workpiece surface position and actual cutting depth. The repeatability (2σ) of the OMP400 was 0.25 µm, and the measurement deviation was ±0.25 µm [253]. The diameter of the ruby ball was 6 mm.



Figure 3.9 Renishaw PowerProbe 400 optical machine probe system.

3.4.6 Surface roughness, burr and morphology assessment

Machined surfaces were assessed using both linear (2D) and areal (3D) surface roughness parameters. A Mitutoyo Formtracer Avant S-3000 contour and surface roughness measuring system was employed to determine 2D surface roughness in Phase 1B, as shown in Figure 3.10. The detector had a stylus radius of 1 µm while a Gaussian profile filter with a sampling length of 0.8 mm and an evaluation length of 4 mm was used in accordance with ISO 21920-3 standards [254]. Measurements of mean surface roughness parameter (Ra) were conducted three times along the stepover direction with the average value calculated.

Surface characteristics including roughness (linear and areal parameters), contour and exit edge quality of the machined workpieces in Phase 2B trials, were assessed using an Alicona G5

InfiniteFocus optical microscope, see Figure 3.11. Measurements were undertaken at ×50 magnification with optical resolutions of 10 nm and 1.5 μm in the vertical and lateral directions, respectively. Areal surface roughness was evaluated over an area of 1 mm × 1 mm, and a Gaussian profile filter with a 0.8 mm sampling length was employed.

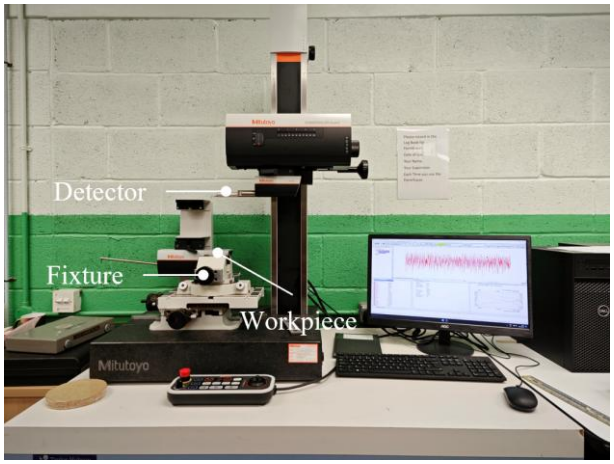


Figure 3.10 Mitutoyo Formtracer Avant S-3000 contour/surface roughness measuring system.

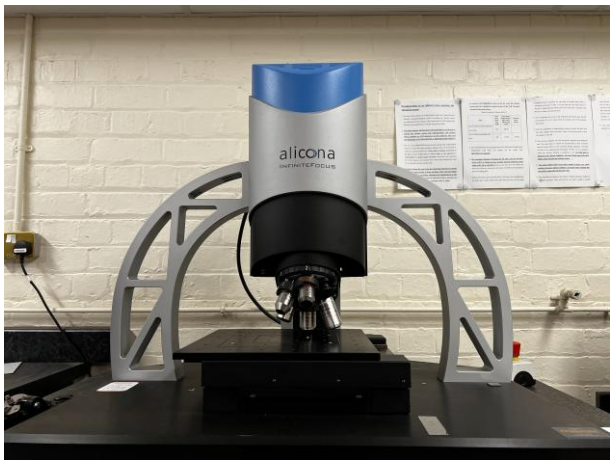


Figure 3.11 Alicona G5 InfiniteFocus optical microscope.

In addition to the Alicona G5, a Keyence VHX-7000 digital microscope was also utilised to evaluate machined workpiece surface topography features in all phases, as shown in Figure 3.12. The Keyence VHX-7000 has a maximum magnification of ×6,000, while its Optical Shadow Effect Mode (Opt-SEM) function is capable of producing images similar to that of a scanning electron microscope (SEM), providing more detailed views of the machined surface. Burr size was also measured using the Keyence microscope.

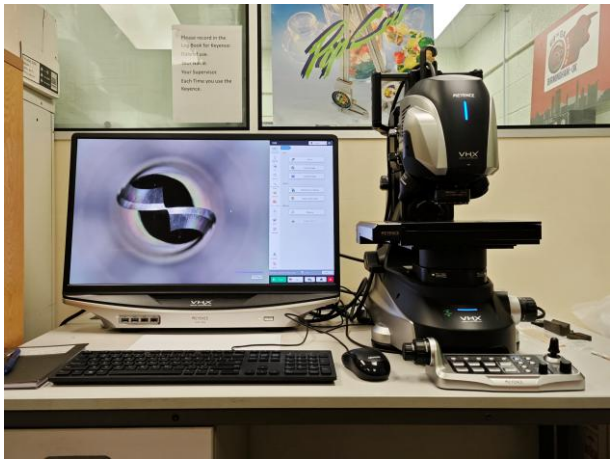


Figure 3.12 Keyence VHX-7000 digital microscope.

3.4.7 Residual stress evaluation

Residual stress depth profile evaluation of machined surfaces was conducted by Stresscraft Ltd., using the hole drilling technique. Samples for measurement with dimensions of 29 × 13 × 8.5 mm were appropriately sectioned from the machined workpiece using an AgieCharmilles Robofil FI240cc wire electrical discharge machining (WEDM) system with a Ø0.25 mm brass core Broncocut type X wire electrode, as shown in Figure 3.13. A target strain gauge rosette was attached at the centre of the machined surface for each specimen. Target site surfaces were prepared for gauge installation by two passes of fine (400 grade) SiC paper under light hand pressure, followed by thorough degreasing.



Figure 3.13 AgieCharmilles Robofil FI240cc wire EDM machine.

The strain gauge rosettes were Type EA-06-031RE-120 from Vishay Measurements Group. Figure 3.14(a) shows the arrangements for incremental drilling. Each gauge was subjected to orbital drilling using an inverted cone T/C cutter with depth increments set at 4 × 16 μm + 4 ×

32 μm + 8 × 64 μm to give a final hole depth of 704 μm. In each case, gauge element 3 was aligned with the machining stepover direction, while element 1 was aligned with the feed direction, see Figure 3.14(b). Therefore, the calculated residual stresses of σ1 and σ3 corresponded to those in the feed and stepover directions, respectively. Relevant material properties used for strain-to-stress data reduction (γ-TiAl) were Young's modulus of 170 GPa and Poisson's ratio of 0.270.

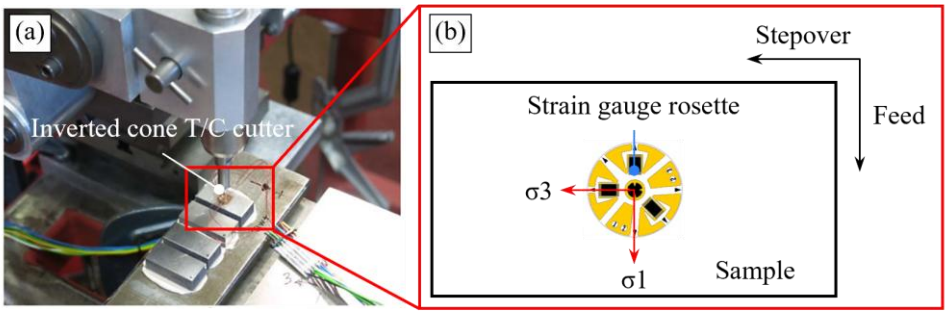


Figure 3.14 Residual stress measurement setup: (a) Arrangement for incremental drilling and (b) detail of gauge installation on sample.

3.4.8 Workpiece specimen preparation and subsurface microhardness measurement

Machined workpieces for surface integrity assessment were initially cross-sectioned in both the feed and stepover direction using WEDM. The specimens were soaked in an acetone solution and cleaned in an ultrasonic bath for more than 10 minutes in order to remove any impurities and grease. The sectioned samples were then mounted in edge-retentive bakelite using the Buehler Simplimet-2 metallurgical mounting press, as illustrated in Figure 3.15.

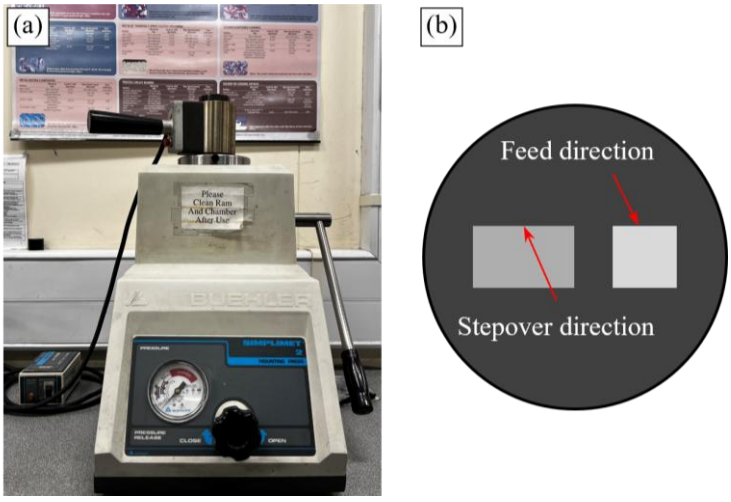


Figure 3.15 Mounted sample preparation: (a) Buehler Simplimet-2 mounting press; and (b) example of mounted specimens showing workpiece placement position.

The mounted samples were subsequently ground and polished using a Buehler Alpha 2 speed grinder-polisher machine, as shown in Figure 3.16. Table 3.5 details the grinding and polishing route for the γ-TiAl specimens. The rotational directions of the grinder polisher head and grinding/polishing disc were kept contra for all steps. Following each grinding or polishing step, the machine was thoroughly cleaned while the samples were also placed in the ultrasonic bath for at least 10 minutes to remove any residual abrasive particles on the workpiece surfaces.



Figure 3.16 Buehler Alpha 2 speed grinder-polisher machine.

Table 3.5 Grinding and polishing route and parameters for mounted γ-TiAl samples.

No.	Surface	Abrasive/Size	Load (N/specimen)	Time (min)
1	CarbiMet Discs	120 (P120) grit	27	Until plane
2	CarbiMet Discs	220 (P240) grit	27	3 min
3	CarbiMet Discs	320 (P400) grit	27	3 min
4	CarbiMet Discs	360 (P600) grit	27	3 min
5	CarbiMet Discs	400 (P800) grit	27	3 min
6	CarbiMet Discs	600 (P1200) grit	22	5 min
7	TriDent Cloth	9 μm MetaDi Diamond suspension	27	Until last traces disappear
8	TriDent Cloth	6 μm MetaDi Diamond suspension	27	Until last traces disappear
9	TriDent Cloth	3 μm MetaDi Diamond suspension	27	Until last traces disappear
10	Micro Cloth	0.05 μm MasterMet Colloidal Silica	27	Until last traces disappear

Microhardness depth profile assessment of the ground and polished specimens from Phase 1B tests was carried out using a Mitutoyo HM-100 microhardness tester equipped with a Knoop indenter, see Figure 3.17(a). Measurements were carried out at an applied load of 0.05 kg over a 15-second dwell period. In Phase 2B experiments, Vickers microhardness test was selected to evaluate the machined surfaces quality using a Struers DuraScan system, as shown in Figure 3.17(b). Here, the indent load was set to 0.025 kg and applied for a 15-second period

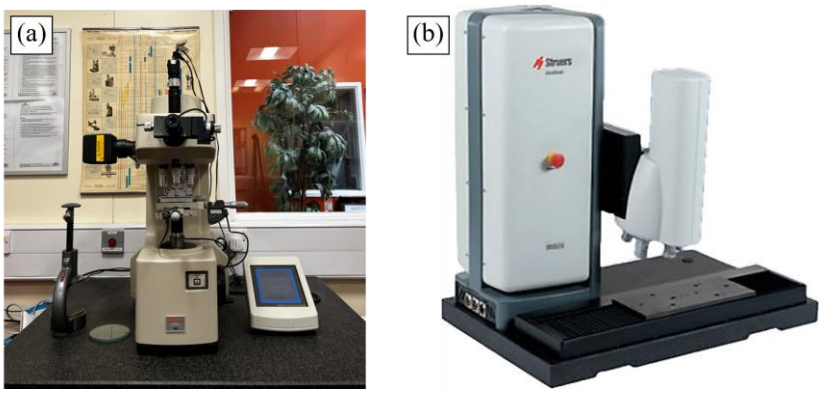


Figure 3.17 Microhardness testers: (a) Mitutoyo HM-100 with Knoop indenter and (b) Struers DuraScan with Vickers indenter.

Fourteen points at various depths (10, 20, 30, 40, 50, 75, 100, 125, 150, 200, 250, 300, 400 and 500 µm) below the machined surface were measured for every sample, with each set repeated three times and the results averaged to minimise measurement errors. Preliminary assessment showed that the spacing between initial indentation points was too small (10 µm) when aligned in the vertical depth direction, which caused the material around the points to bulge, affecting the accuracy of subsequent measurements. Instead, a Z-shaped distribution was employed for indentations close to the machined surface, as exhibited in Figure 3.18, where the lateral spacing between adjacent measuring points was 100 µm.

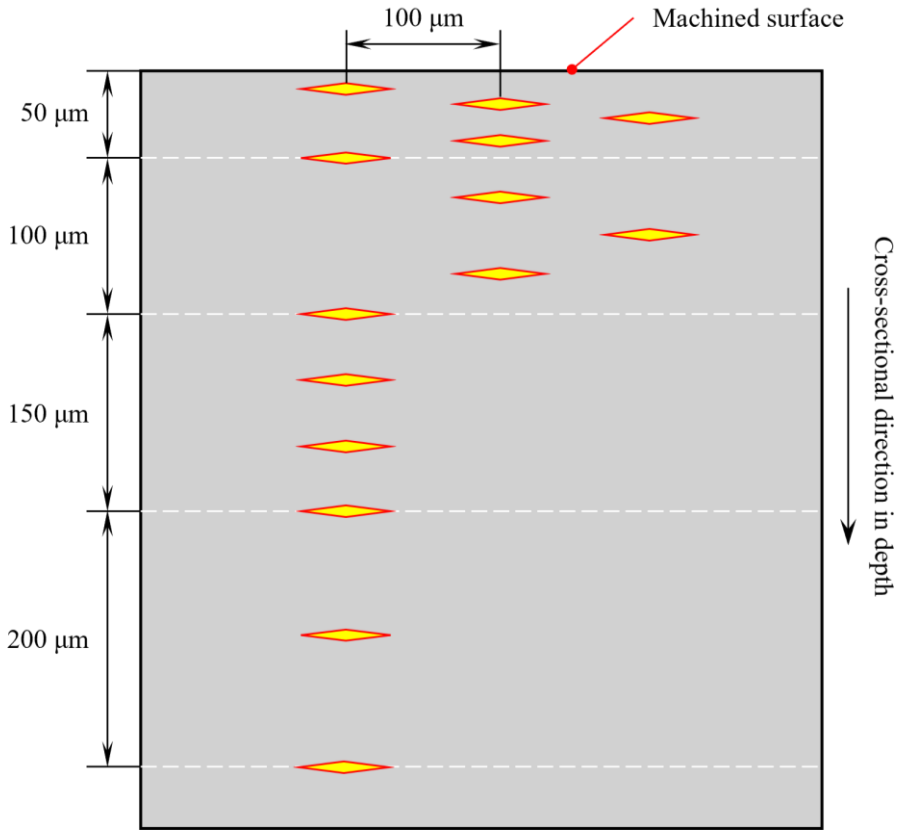


Figure 3.18 Schematic diagram of the microhardness depth profile indent positions.

The Knoop microhardness (*HK*) was determined by measuring the length of the rhombohedral shaped indent (d_l), while the d_l parameter for Vickers microhardness (*HV*) was the average of the diagonal lengths of the square base pyramid shaped indent (d_1 and d_2), as depicted in Figure 3.19. The Keyence VHX-7000 was employed to measure the diagonal distances/lengths of the respective indentations, with the *HK* and *HV* microhardness values calculated according to Equation 3-1 [255].

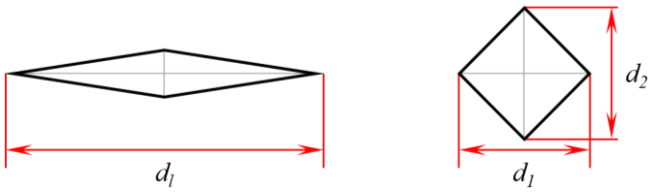


Figure 3.19 Schematic diagram of Knoop and Vickers indentations.

$$\begin{cases} HK = \dfrac{1.451F_h}{d_l^2} \\ HV = \dfrac{0.1891F_h}{d_l^2} \end{cases} \tag{3-1}$$

where F_h was the applied load (N) and gravitational acceleration was 9.81 m/s^2.

3.4.9 Subsurface metallographic/microstructural analysis

The ground and polished γ-TiAl specimens were etched for metallographic analysis using standard Kroll's reagent, consisting of 92 ml water, 6 ml nitric acid, and 2 ml hydrofluoric acid [256]. The setup for the etching procedure is shown in Figure 3.20. A cotton ball soaked in Kroll's reagent was used to wipe the polished surface for ~40 seconds, followed by rinsing of the etched specimen three times with clean water.

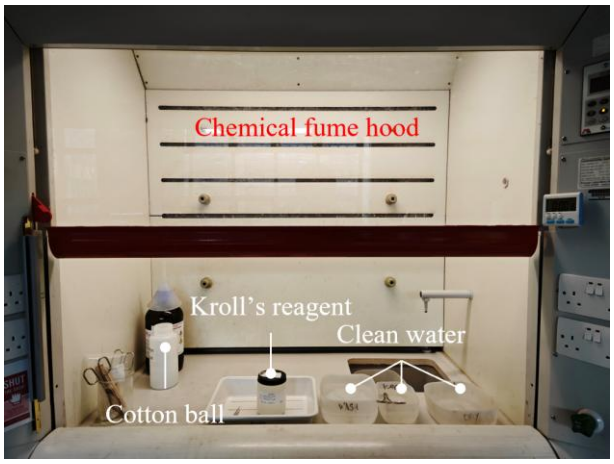


Figure 3.20 Etching of γ-TiAl specimens with Kroll's reagent.

Workpiece subsurface microstructural analysis was primarily conducted using the Keyence VHX-7000 digital microscope with full coaxial light. Additionally, a Zeiss EVO10 scanning electron microscope integrated with an Oxford Instruments X-act detector, was employed for energy dispersive spectroscopy (EDS) analysis and surface/subsurface evaluation, see Figure 3.21.



Figure 3.21 Scanning electron microscope Zeiss EVO10 with Oxford Instruments X-act detector.

3.5 Experimental design, variable parameters and test procedures

3.5.1 Phase 1A: Stability assessment of integrated ultrasonic system

The principal objective of Phase 1A was to assess the stability of the integrated tool holder ultrasonic system, as tool specifications such as size, material and mass can influence the resulting vibrational amplitude. A stable amplitude is crucial to ensure the effectiveness of ultrasonic-assisted machining. Hence, three experiments were designed and performed to evaluate measurement of the effective ultrasonic vibration amplitude, impact of cutting tool characteristics as well as operating limits of the system, which are described in the following sub-sections.

3.5.1.1 Influence of tool characteristics on ultrasonic vibration characteristics

The effect of tool geometry, mass and overhang length on ultrasonic vibration amplitude were evaluated according to the test array outlined in Table 3.6. As ultrasonic excitation can cause a rise in temperature that potentially affects the resonant frequency of the system [222], the machine tool was left to stand idle for 5 minutes after each test. This cooling period ensured that the ultrasonic tool holder system returned to a stable temperature before proceeding with further measurements. Renishaw NC4+ high-accuracy laser tool setting system to detect no-load ultrasonic vibration amplitude by using default measuring programme provided by DMG CELOS system. In this section, all trials were conducted under no-load and tool rotated (3000 rpm) conditions for 2 minutes. In addition, the resonant frequency of the current tool was found

by manually adjusting the excitation frequency (minimum step of 50 Hz) and measuring the no-load ultrasonic vibration amplitude at this frequency.

Table 3.6 Test array for assessing the effect of tool characteristics on ultrasonic vibration amplitude.

Tool type	Material	Diameter (mm)	Total length (mm)	Overhang length (mm)	Mass (g)
Twist drill	HSS	6	50	30, 35, 40	8.19
Twist drill	HSS	6	58	40, 50, 55	9.90
Twist drill	HSS	6	65	44.5	11.68
Ball nose end mill	WC	6	58	40	20.41
Twist drill	HSS	6	58	40	9.90
End mill	WC	6	58	40	20.49
End mill	HSS	6	58	40	11.21
Ball nose end mill	WC	4	75	55	12.13
Ball nose end mill	WC	5	75	55	18.27
Ball nose end mill	WC	6	75	55	25.96

3.5.1.2 Comparative study of effective ultrasonic vibration amplitude measurement

Real-time assessment of ultrasonic vibration amplitude during machining remains a significant research challenge, as current measurements are typically conducted under no-load/non-cutting conditions. To more accurately verify the magnitude of tool vibration amplitude, a small-depth-cut (SDC) method was introduced. This experiment involved two different workpiece materials, which was a polyurethane BM 5460 board with extremely low hardness (~60–65 Shore D) to simulate no-load conditions and AA6082-T6 aluminium alloy, a metallic material with relatively low hardness (~100 $HV_{0.01}$), to evaluate changes in ultrasonic vibration amplitude under low load conditions whilst cutting. The difference in height between the pre- and post-machined surfaces were measured using a Renishaw PowerProbe 400 optical system, enabling determination of the vibration amplitude during cutting. The DMG Mori machine was equipped with a Renishaw NC4+ high-accuracy laser tool setting system to detect no-load ultrasonic vibration amplitude, which served as the benchmark in this study. The tests were carried out at fixed parameters of v_c = 53.31 m/min (N = 6000 rpm), f_z = 0.02 mm/tooth, a_e = 0.1 mm and 45° tile angle, under dry cut conditions with BM 5460 and wet cut conditions with AA6082-T6, while axial depth of cut was varied between 0 mm and 0.4 mm for both workpiece materials. The cutting area was 10 × 10 mm with 0.5 m distance machined. Details of the variable factors and corresponding levels are provided in Table 3.7.

Table 3.7 Variable factors and levels for effective ultrasonic vibration amplitude trials.

Workpiece material	Depth of cut (mm)
Polyurethane BM 5460, AA6082-T6	0, 0.01, 0.05, 0.10, 0.20, 0.40

3.5.1.3 Operating limits assessment of ultrasonic-assisted milling

Numerous studies have demonstrated that processing parameters significantly influence the amplitude stability of ultrasonic actuation systems during machining [222], [257], [258]. Changes in cutting forces can alter the resonant frequency of the ultrasonic transducer, subsequently affecting the vibration conditions. As cutting force increases, the resonant frequency also rises, potentially exceeding the adjustment capabilities of the excitation frequency. This escalation often results in amplitude attenuation, a condition that is also referred to as ultrasonic suppression.

It has been widely documented that the key benefit of ultrasonic-assisted cutting is the reduction in cutting forces. To evaluate the effectiveness of ultrasonic assistance and overall machine tool/system performance, slotting with ball nose end mills trials on Ti-6Al-4V workpieces were carried out at varying depths of cut (0.1–1.0 mm) for both conventional (no ultrasonic actuation) and ultrasonic-assisted cutting conditions. All tests were performed dry using 2-fluted, 4 mm diameter uncoated carbide ball nose end mills at a fixed spindle rotational speed and feed rate of 3000 rpm and 300 mm/min, respectively. New tools were utilised for each slot cutting with 5 mm distance machined. Test parameters and variable levels are detailed in Table 3.8. Axial cutting forces were recorded for each depth of cut level, with the results compared between conventional (marked as ‘0’) and ultrasonic-assisted milling operations (marked as ‘1’).

Table 3.8 Test parameters and variable levels for operating limits evaluation of ultrasonic system.

Spindle speed (rpm)	Depth of cut (mm)	Feed rate (mm/min)	Ultrasonic actuation
3000	0.10, 0.20, 0.40, 0.60, 0.80, 0.90, 1.00	300	0, 1

3.5.2 Phase 1B: Influence of operating parameters on machinability when milling γ-TiAl

The main objective of Phase 1B trials was an initial assessment of the significant cutting parameters in conventional milling (CM) and ball-end ultrasonic-assisted milling (B-UAM) of Ti-45Al-8Nb-0.2C γ-TiAl alloy. Table 3.9 details the test variables comprising seven factors with four at four levels and a further three at two levels, which were selected based on published literature to cover a relatively broad scope. All tests were conducted in down milling mode with 4-fluted, 4 mm diameter TiAlN coated WC ball nose end mills supplied by Widia Hanita. For trials involving ultrasonic actuation, the transducer frequency was maintained at 33.5 ± 0.2 kHz with manual confirmation, as this was found to provide the largest tool vibration amplitude of approximately 6 μm, as measured using the SDC method on the polyurethane workpiece. The tool life criterion was a maximum flank wear of 180 μm and the end of test criterion was a machining distance of 230 m.

Table 3.9 Variable factors and levels for Phase 1B experiments.

Symbol	Factor	Level 1	Level 2	Level 3	Level 4
A	Cutting speed (m/min)	40	60	80	100
B	Depth of cut (mm)	0.05	0.10	0.15	0.20
C	Width of cut (mm)	0.15	0.20	0.25	0.30
D	Feed rate (mm/tooth)	0.02	0.03	0.04	0.05
E	Cutting orientation	HU	HD		
F	Ultrasonic assistance	0	1		
G	Cutting environment	Dry	Wet		

Figure 3.22 illustrates the cutting orientations including vertical upward (VU), vertical downward (VD), horizontal upward (HU) and horizontal downward (HD). Due to the large number of variable factors and levels considered, a Taguchi L_{16} fractional factorial orthogonal array was employed to minimise the number of tests, however this prohibited the assessment of interactions between factors. Table 3.10 details the orthogonal array employed.

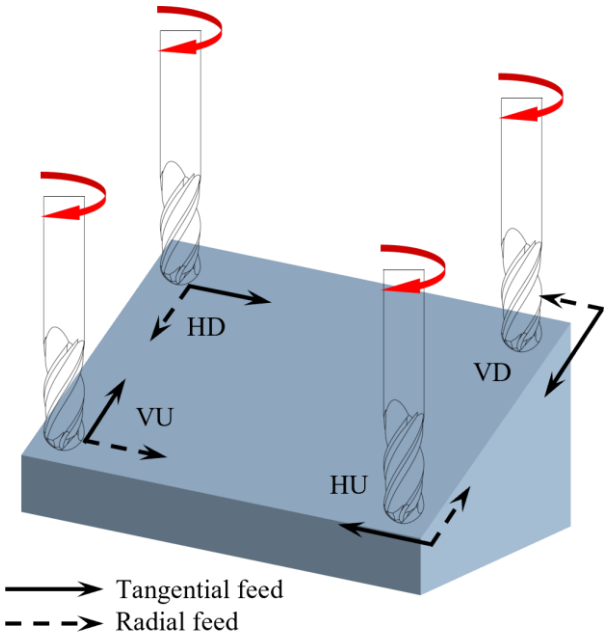


Figure 3.22 Diagram illustrating the cutting orientations in ball-end milling.

Table 3.10 Taguchi L_{16} ($4^4 \times 2^3$) orthogonal array for Phase 1B experiments.

No.	A	B	C	D	E	F	G
1	1	1	1	1	1	1	1
2	1	2	2	2	1	2	2
3	1	3	3	3	2	1	2
4	1	4	4	4	2	2	1
5	2	1	2	3	2	2	1
6	2	2	1	4	2	1	2
7	2	3	4	1	1	2	2
8	2	4	3	2	1	1	1
9	3	1	3	4	1	2	2
10	3	2	4	3	1	1	1
11	3	3	1	2	2	2	1
12	3	4	2	1	2	1	2
13	4	1	4	2	2	1	2
14	4	2	3	1	2	2	1
15	4	3	2	4	1	1	1
16	4	4	1	3	1	2	2

Statistical analysis involving main effects plots and analysis of variance (ANOVA) were carried out to identify the significant factors with respect to the various response measures evaluated, which included cutting forces (F), depth of cut achievement rate (R_{Cd}), tool wear and workpiece surface integrity parameters. The R_{Cd} value was quantified using Equation 3-2.

$$R_{Cd} = \frac{Actual\ depth\ of\ cut}{Nominal\ depth\ of\ cut} \times 100\% \quad (3\text{-}2)$$

All of the response measures were assessed or recorded at regular intervals over the duration of each test. The specific experimental procedure is detailed in the flow chart presented in Figure 3.23.

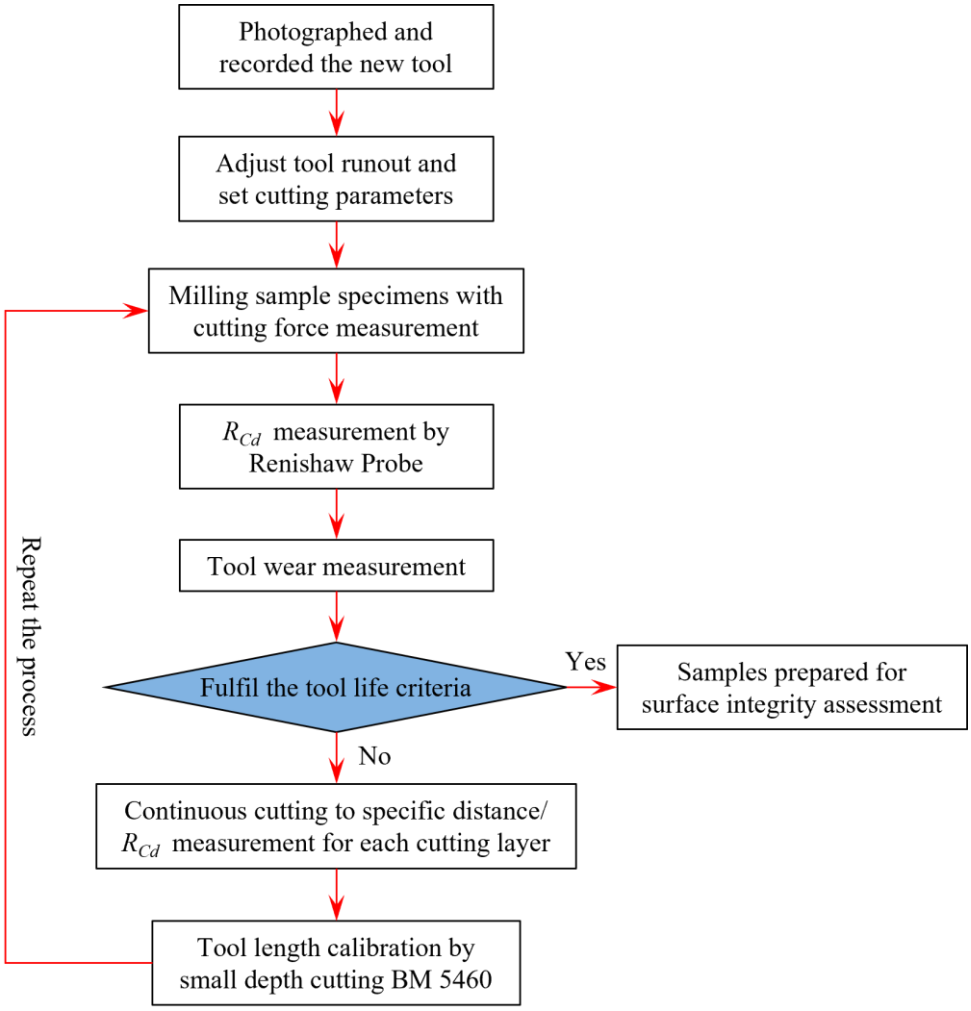


Figure 3.23 Flow chart showing the experimental procedure for Phase 1B tests.

3.5.3 Phase 2A: Tool wear mechanisms and failure of γ-TiAl in B-UAM

Results from Phase 1B experiments revealed that tool wear was particularly severe under wet cutting conditions, despite the use of TiAlN coated ball nose end mills. The experiment in Phase 2A was designed to further investigate the influence of ultrasonic actuation, tool coating, cutting environment and workpiece material on tool wear mechanisms when milling γ-TiAl. The corresponding test array is depicted in Table 3.11. Tests 1–4 were conducted to study the effects of ultrasonic assistance and cutting environment on tool wear, whereas Tests 5 and 6 served as benchmark trials to verify the influence of tool coatings. The comparative performance when ball nose end milling an alternative workpiece material (AISI 4000 series low-alloy steel) was

evaluated in Tests 7 and 8 to validate conjectures about the influence of workpiece composition on tool wear mechanisms.

Table 3.11 Test array for Phase 2A experiments.

No.	Material	Ultrasonic assistance	Cutting environment	Tool coating
1	γ-TiAl	1	Wet	TiAlN
2	γ-TiAl	1	Dry	TiAlN
3	γ-TiAl	0	Wet	TiAlN
4	γ-TiAl	0	Dry	TiAlN
5	γ-TiAl	0	Dry	Uncoated
6	γ-TiAl	0	Wet	Uncoated
7	Low-alloy steel	0	Dry	Uncoated
8	Low-alloy steel	0	Wet	Uncoated

All tests were performed at fixed parameters of v_c = 60 m/min, f_z = 0.03 mm/tooth, a_p = 0.15 mm, a_e = 0.15 mm and 45° workpiece tilt angle with HD cutting orientation. The end-of-test criteria were a machining distance of 205.6 m for Tests 1–4, 100 m for Test 5 and 6 and 55 m for Test 7 and 8. The tool vibration frequency was maintained at 33.3 ± 0.1 kHz with manual confirmation, corresponding to an amplitude of ~6 μm (determined by SDC method on an epoxy workpiece). The topography of tool flank and rake faces were imaged after machining 2.5 m, 55.1 m, 100.5 m, 153.1 m and 205.6 m. After cutting experiments, ball nose end mills were separated using WEDM as samples. Energy dispersive spectroscopy (EDS) integrated in Zeiss EVO 10 SEM was employed to quantitatively analyse the distribution of different elements on the surface of tools and machined workpieces.

3.5.4 Phase 2B: Comparative evaluation between the effects of CM and B-UAM on machinability of γ-TiAl

Statistically significant parameters that substantially impact the milling of γ-TiAl were identified from Phase 1B trials. Based on the findings, a further detailed investigation was undertaken focusing on the effects of ultrasonic vibration and cutting environment when ball-end milling γ-TiAl. Performance measures included cutting forces, tool wear and workpiece surface integrity in addition to an analysis of the material removal mechanisms in UABM. The test array is outlined in Table 3.12.

The experimental procedure for this phase was consistent with that used in Phase 1B, as detailed previously in Figure 3.23. In addition to standard workpiece surface integrity evaluation (roughness, microhardness, microstructure deformation), depth profile residual stress

measurements were carried out. The constant cutting parameters were v_c = 60 m/min, f_z = 0.03 mm/tooth, a_p = 0.15 mm, a_e = 0.15 mm and 45° workpiece tilt angle with HD cutting orientation. Similarly, the applied ultrasonic vibration frequency and resulting amplitude were 33.3 ± 0.1 kHz (manual confirmation) and 6 μm, respectively. The end of test criterion was a machining distance of 205.6 m and topography of tool flank and rake faces were imaged after machining 2.5 m, 55.1 m, 100.5 m, 153.1 m and 205.6 m.

Table 3.12 Test array for Phase 2B experiments.

No.	Material	Ultrasonic assistance	Cutting environment	Tool coating
1	γ-TiAl	1	Wet	TiAlN
2	γ-TiAl	1	Dry	TiAlN
3	γ-TiAl	0	Wet	TiAlN
4	γ-TiAl	0	Dry	TiAlN

3.5.5 Phase 3A: Experimental validation of analytical model for predicting machined surface morphology in B-UAM

A set of tests were performed according to Table 3.13 to validate the predicted results from the analytical surface morphology model. Tests were performed on AA6082-T6 workpieces to minimise the impact of tool deflection on machined surface morphology, while flood cooling was also employed to reduce the effects of cutting temperature. Ultrasonic frequency and vibration amplitude parameters were constant at 35.2 ± 0.1 kHz and ~6 μm, respectively. The cutting distance was approximately 140 mm and formed a 7 × 8 mm machined surface. The machined surface morphology generated after each test was analysed using an Alicona G5 microscope, with a focus on the overall topographical structure and contours both in the feed and stepover directions.

Table 3.13 Validation trials for workpiece surface morphology prediction model.

Spindle speed (rpm)	Depth of cut (mm)	Width of cut (mm)	Feed rate (mm/tooth)	Ultrasonic assistance	Workpiece tilt angle (°)
3000	0.40	0.40	0.10	0	0
3000	0.40	0.33	0.10	0	30
3000	0.40	0.40	0.10	0	45
3000	0.40	0.40	0.10	1	45
6000	0.20	0.20	0.04	0	30
6000	0.20	0.20	0.04	1	45

3.5.6 Phase 3B: Experimental validation of analytical model for predicting cutting forces in B-UAM

Model coefficients required for the analytical prediction of cutting forces were determined based on average forces from experimental slotting tests using B-UAM (using ball nose end mills). Use of the average forces in slotting to identify cutting coefficients has the following advantages:

- Tool eccentricity does not significantly affect the calculation of average milling forces in machining slot using ball nose end mills. Although tool eccentricity can disrupt the symmetry of chip thickness distribution relative to the feed direction, the average chip thickness remains equivalent to the theoretical value. Consequently, the average milling force can be accurately computed using analytical methods, effectively eliminating the influence of tool eccentricity.

- Systematic errors in cutting force measurement systems, typically manifesting as random errors, can influence data accuracy. These errors usually follow a standard normal distribution. By utilising the average milling force as the input variable for cutting coefficients identification, the impact of these random system errors on the coefficients identification results can be significantly reduced. This approach enhances the reliability of the experimental data and the precision of the analysis.

The test array to determine cutting force coefficients of machining Ti-6Al-4V is shown in Table 3.14, with the coefficient values obtained by least squares approximation of the recorded average milling forces. A total of 10 tests (twice the minimum requirement) under dry cut conditions were performed to ensure sufficient data for solving the unknown model variables, while the levels of cutting parameters were also carefully selected to avoid numerical errors during the calculations. The machining distance was constant 5 mm and the new tool was employed for each cutting.

Table 3.14 Test array to determine force coefficients for cutting force prediction model.

Spindle speed (rpm)	Depth of cut (mm)	Feed rate (mm/tooth)
3000	0.10	0.040
3000	0.10	0.080
3000	0.20	0.040
3000	0.20	0.080
3000	0.30	0.030
3000	0.30	0.060
3000	0.40	0.030
3000	0.40	0.060
3000	0.50	0.025
3000	0.50	0.050

A series of ball-end ultrasonic-assisted milling experiments under dry cut conditions were conducted as listed in Table 3.15 to verify the prediction accuracy of the cutting force model. The ultrasonic parameters including excitation frequency and amplitude were 35.2 ± 0.1 kHz and 6 μm, respectively, while the workpiece material employed was Ti-6Al-4V. The machining mode was adopted with a single cutting distance of 5 mm and 5 consecutive cuttings.

Table 3.15 Test array for experimental validation of cutting force prediction model.

Spindle speed (rpm)	Depth of cut (mm)	Width of cut (mm)	Feed rate (mm/tooth)
3000	0.25	0.25	0.035
3000	0.25	0.15	0.035
3000	0.35	0.25	0.035
3000	0.35	0.25	0.065

Notably, tool radial deflection was ignored when the workpiece tile angle was 0. However, in the actual machining process, ball nose end mills were employed at a certain angle to avoid the tool centre velocity of 0. Consequently, tool bending deflection was considered in the cutting force model when establishing tool flank wear prediction model, as the workpiece tile angle was not 0. Cutting forces and deflection data used to validate deflection model were collected from Phase 1B results.

3.5.7 Phase 3C: Experimental validation of analytical model for predicting tool flank wear in B-UAM

For the tool flank wear prediction model, the abrasive wear coefficient was determined based on experimental B-UAM tests performed according to parameters detailed in Table 3.16. As with Phase 3B, Ti-6Al-4V was selected as the workpiece material due the tendency for severe adhesive wear during the milling of γ-TiAl. The vibration frequency was maintained at 35.2 ± 0.1 kHz while the corresponding amplitude was approximately 6 μm. All tests were conducted using uncoated tools under dry conditions. The end of test criterion was a machining distance of 53.85 m and topography of tool flank face was imaged at regular intervals over the duration of each test. The position with the maximum flank wear after each test was selected as the target cutting point and its axial position angle could be calculated based on the geometric relationship of the tool image. Relevant cutting forces in tool flank wear model were generated by cutting forces model established in Section 4.2. The abrasive wear coefficient was then calculated by using 1stopt software.

Table 3.16 Test array to determine abrasive wear coefficient for tool wear prediction model.

Spindle speed (rpm)	Depth of cut (mm)	Width of cut (mm)	Feed rate (mm/tooth)
3000	0.10	0.20	0.040
3000	0.10	0.20	0.080
3000	0.20	0.20	0.040
3000	0.20	0.20	0.080
3000	0.30	0.20	0.040
3000	0.30	0.20	0.080

A further four B-UAM tests were subsequently performed to validate the accuracy of the predicted flank wear results, as shown in Table 3.17. The rest of experimental conditions and measurement process were consistent with the previous content.

Table 3.17 Test array for experimental validation of tool wear prediction model.

Spindle speed (rpm)	Depth of cut (mm)	Width of cut (mm)	Feed rate (mm/tooth)
3000	0.15	0.20	0.06
3000	0.25	0.20	0.06
3000	0.20	0.20	0.05
3000	0.20	0.20	0.07

4 ANALYTICAL MODELLING OF BALL-END ULTRASONIC-ASSISTED MILLING

Three analytical models were formulated to predict workpiece surface morphology, cutting force and tool flank wear in ball-end ultrasonic-assisted milling. Initially, a tool kinematic model was established and integrated with the Z-map method to accurately capture the cutting topography. This allowed for the derivation of chip element size data, which was crucial for developing the cutting force model. The cutting force model was subsequently used to determine cutting force element at any specified position along the cutting edge element, which then informed the tool wear modelling research.

4.1 Kinematics modelling and geometrical simulation in B-UAM (Phase 3A)

The kinematic model considered a comprehensive array of factors to ensure accuracy and relevance in machining simulations. These factors included geometrical characteristics of the tool, cutting parameters and ultrasonic parameters. Additionally, the model incorporated the influence tool path, tool runout and any required adjustments to the tool orientation.

4.1.1 Establishment of the tool motion reference coordinate systems

The principle of homogeneous coordinate transformation was utilised to develop a kinematic model for ball-end ultrasonic-assisted milling. Then, the mathematical expression of the cutting point *P* presented in the workpiece coordinate system could be established later. The reference coordinate systems are used to describe the trajectory shown in Figure 4.1.

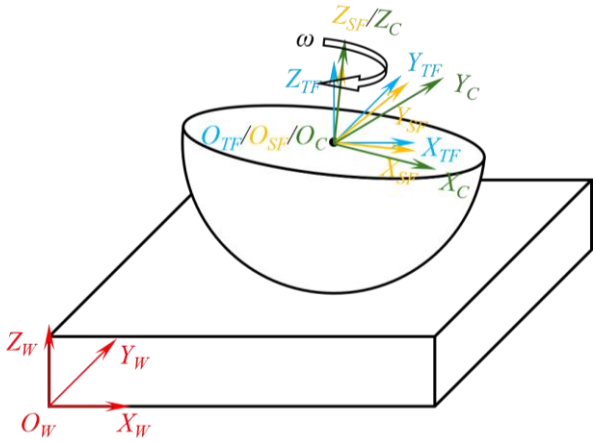


Figure 4.1 Reference coordinate systems of ball-end milling process.

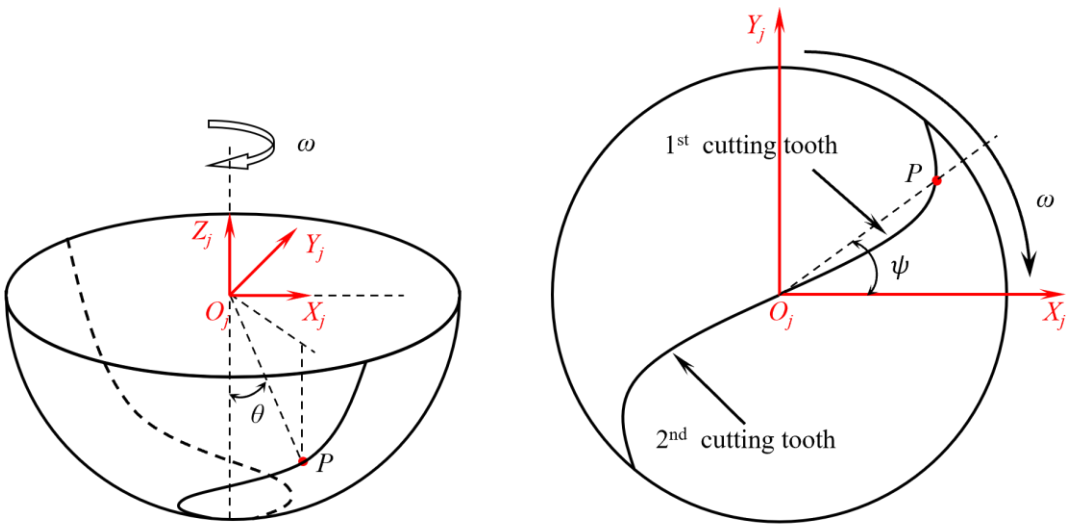
- Workpiece coordinate system $\{W\}$, denoted as $O_W - X_W Y_W Z_W$, is a reference system used to determine the position and orientation of the workpiece in relation to the ball-end mill. This coordinate system is always fixed to the workpiece.

- Transient feed coordinate system $\{TF\}$, denoted as $O_{TF} - X_{TF} Y_{TF} Z_{TF}$, is defined such that its coordinate axis $\overrightarrow{O_{TF}X_{TF}}$ coincided with the tangent direction of the feed speed $\vec{f}$. The coordinate axis $\overrightarrow{O_{TF}Z_{TF}}$ corresponds to the main normal direction $\vec{n}$ of the cutting trajectory, pointing outward from the workpiece as positive. The coordinate axis $\overrightarrow{O_{TF}Y_{TF}}$ is the cross-product vector $\vec{t}$ of $\vec{n}$ and $\vec{f}$. The coordinate origin O_{TF} is selected as the tool position point on the ball-end mill at the intersection of the transition plane between the cylindrical and the ball-end sections of the tool and the axis of the spindle. During the milling operation, tool movement is described by the positional change of $\{TF\}$ relative to $\{W\}$.

- Spindle follow-up coordinate system $\{SF\}$, denoted as $O_{SF} - X_{SF} Y_{SF} Z_{SF}$, has its Z_{SF}-axis coinciding with the rotational axis of the machine tool spindle, with the positive direction pointing away from the workpiece. The coordinate system moves together with the spindle relative to the workpiece under the control of the motion trajectory. When there is no adjustment of the tool orientation during the machining process, this coordinate system aligns completely with $\{TF\}$. However, in practical machining operations, it is often necessary to adjust the tool orientation to fulfil processing requirements. This adjustment is achieved by the spatial transformation of $\{SF\}$ relative to $\{TF\}$.

- Cutting tool local coordinate system $\{C\}$, denoted as $O_C - X_C Y_C Z_C$, is fixed on the tool, with its origin O_C located at the centre of the ball-end portion. The coordinate X_C-axis is tangent to the starting point of the projection line of the reference tooth (first cutting tooth) curve on the tool cross-section of the tool. The coordinate axis $\overrightarrow{O_C Z_C}$ coincides with the central axis of the tool. It is aligned with the positive direction of $\overrightarrow{O_{SF}Z_{SF}}$, but these two coordinate axes do not coincide when there is an offset of the tool generated by the installation error of machine or system vibration action.

- Tooth local coordinate system $\{j\}$, denoted as $O_j - X_j Y_j Z_j$, has its coordinate axis $\overrightarrow{O_j Z_j}$ coinciding with the Z_C-axis in $\{C\}$, which also coincides with the central axis of the tool. The coordinate axis $\overrightarrow{O_j X_j}$ is tangent to the starting point of the projection line of the cutting edge curve of tooth N_j on the tool cross-section, as shown in Figure 4.2.



(a) Axonometric view (b) Top view

Figure 4.2 Illustration of spherical helical cutting edge: (a) axonometric view and (b) top view.

With the above coordinate systems and homogeneous coordinate matrix transformations, the motion trajectory equation of any cutting point P on any tooth of the tool relative to the workpiece coordinate system can be established.

4.1.2 Kinematic modelling of B-UAM

(a) Mathematical modelling of the cutting tooth in the tooth local coordinate system {*j*}

The main cutting area of the ball nose end mill is the hemispherical section and hence the focus of this model focused. The cutting edge lies on the tool envelop surface, which consisted of a cylindrical surface with a radius R and a hemispherical surface with the same radius. Coordinates of the current cutting point P on the tooth N_j in the $\{j\}$ coordinate system are defined by Equation 4-1:

$$\begin{cases} x_P^j = \sin\theta\cos\psi \\ y_P^j = R\sin\theta\sin\psi \\ z_P^j = -R\cos\theta \end{cases} \tag{4-1}$$

where R (mm) is the radius of the cutting tool, θ (°) is the axial position angle, which is the angle between the line connecting current point P on the tooth to the centre O_j of the ball nose end mill and the axis of the tool ($\theta \in [0°, 90°]$) and ψ (°) is the lag angle between the tooltip and point P on the helical flute at the current height, as illustrated in Figure 4.2. The ball nose end mill with constant lead helical curve was selected as the research subject, and the lag angle ψ can be calculated by Equation 4-2 [259]:

$$\psi = 180\tan\gamma_0(1-\cos\theta)/\pi \tag{4-2}$$

where γ_0 (°) is the nominal helical angle. The teeth of the ball nose end mill are usually uniformly distributed in the circumferential direction. Hence, the angle between the axis $\overrightarrow{O_jX_j}$ of $\{j\}$ and axis $\overrightarrow{O_CZ_C}$ of $\{C\}$ is obtained from Equation 4-3:

$$\varphi_j^C = 360\big(N_j - 1\big)/N_t \tag{4-3}$$

where N_t is the total number of teeth, the script N_j in symbols represented the tooth number ($N_j = 1, 2, \dots, N_t$). The homogeneous coordinate transformation matrix of $\{j\}$ coordinate system relative to the coordinate system $\{C\}$ during the cutting motion is calculated by Equation 4-4:

$$\boldsymbol{M_{Cj}} = \begin{bmatrix} \cos\varphi_j^C & -\sin\varphi_j^C & 0 & 0 \\ \sin\varphi_j^C & \cos\varphi_j^C & 0 & 0 \\ 0 & 0 & 1 & 0 \\ 0 & 0 & 0 & 1 \end{bmatrix} \tag{4-4}$$

The homogeneous coordinate of any point P on the tooth N_j in the cutting tool local coordinate system $\{C\}$ can be expressed by the relationship in Equation 4-5:

$$[x_P^C \quad y_P^C \quad z_P^C \quad 1]^T = \boldsymbol{M_{Cj}}\big[x_P^j \quad y_P^j \quad z_P^j \quad 1\big]^T \tag{4-5}$$

(b) Mathematical modelling of the cutting tool local coordinate system {C} in the spindle follow-up coordinate system {SF}

Due to factors such as manufacturing and clamping errors, there might be deviations between the axis of the tool and the spindle during the machining process. Assuming the deviation between the centre of tool O_C and center of spindle O_{SF} was ρ (mm), the angle μ (°) that vector $\overrightarrow{O_{SF}O_C}$ rotates around $\overrightarrow{O_{SF}Z_{SF}}$ in $\{SF\}$ is denoted as the radial position angle of eccentric vector $\overrightarrow{O_{SF}O_C}$. The clockwise rotation direction is specified to be positive. Moreover, it is assumed that the axial runout of the tool is a sinusoidal motion with an amplitude r_a (mm), and the angular frequency is the same as that of the spindle rotation. In machining, the spindle rotates clockwise to achieve cutting and the angular velocity is $\omega = \pi N/30$ (rad/s), where N is the spindle rotational speed in revolutions per minute (rpm). Hence, the angle that the tool has rotated at the current moment t (s) is $\phi_C = 180\omega t/\pi$ (°). The transformation matrix of $\{C\}$ relative to $\{SF\}$ is defined by Equation 4-6:

$$\boldsymbol{M_{SFC}} = \begin{bmatrix} \cos\phi_C & \sin\phi_C & 0 & \rho\sin\mu \\ -\sin\phi_C & \cos\phi_C & 0 & \rho\cos\mu \\ 0 & 0 & 1 & r_a\sin v \\ 0 & 0 & 0 & 1 \end{bmatrix} \tag{4-6}$$

where v is the phase angle of spindle axial runout, and $\mu = \mu_0 + \phi_C$, $v = v_0 - \phi_C$. To simplify the model, the initial values of μ_0 and v_0 are 0°.

(c) Mathematical modelling of the spindle follow-up coordinate system {SF} in the transient feed coordinate system {TF}

To avoid interference between the tool and workpiece or to prevent the vertex of the ball nose end mill from participating in the cutting (v_c = 0), the milling trajectory of the ball-end mill included both the movement of the tool position and the adjustment of angular orientation. Tool orientation adjustment refers to positioning the tool so that its central axis forms a certain angle with the normal of the machined surface, which is reflected as a tilt or/and lead of the tool relative to the machined surface.

As shown in Figure 4.3, the direction of the vector $\overrightarrow{O_{TF}X_{TF}}$ is the tool feed direction, while $\overrightarrow{O_{TF}Y_{TF}}$ is the tool stepover direction. The spindle follow-up coordinate system $\{SF\}$ is rotated

around these two coordinate axis vectors to adjust the spindle orientation. After adjusting the spindle orientation, the angle between the projection ($Proj_Y_{TF}O_{TF}Z_{TF}$) of the coordinate axis vector $\overrightarrow{O_{SF}Z_{SF}}$ of the $\{SF\}$ onto the coordinate plane $Y_{TF}O_{TF}Z_{TF}$ and the vector $\overrightarrow{O_{TF}Z_{TF}}$ is called the tilt angle, denoted as α. Conversely, the angle between the projection $Proj_X_{TF}O_{TF}Z_{TF}$ of the coordinate axis vector $\overrightarrow{O_{SF}Z_{SF}}$ onto the coordinate plane $X_{TF}O_{TF}Z_{TF}$ and the vector $\overrightarrow{O_{TF}Z_{TF}}$ is called the lead angle, denoted as β.

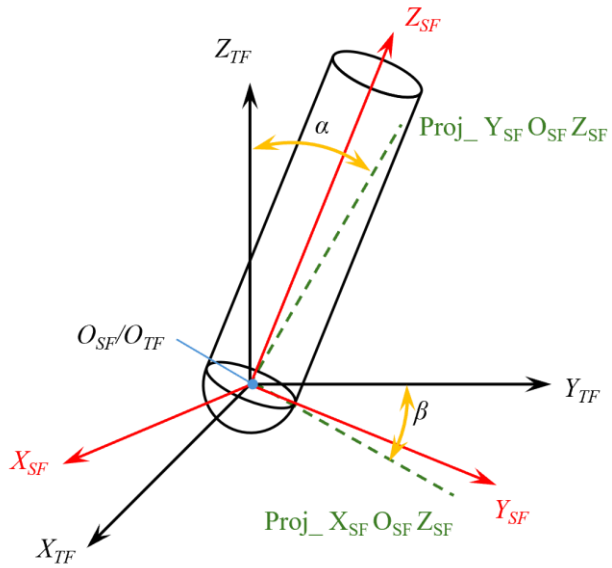


Figure 4.3 Diagram of tool orientation adjustment.

When rotating $\{SF\}$ around $\overrightarrow{O_{TF}Y_{TF}}$ by an angle of β' and then rotating $\{SF\}$ around $\overrightarrow{O_{TF}X_{TF}}$ by an angle of α, the relationship between the angles is described by $\beta' = \arctan(\tan\beta\cos\alpha)$. Rotating counterclockwise around the respective reference axes is denoted as positive while clockwise rotation is termed as negative. The homogeneous coordinate transformation matrices for tool tilt and lead angles are defined by Equations 4-7 and 4-8 respectively.

$$\boldsymbol{R_\alpha} = \begin{bmatrix} 1 & 0 & 0 & 0 \\ 0 & \cos\alpha & -\sin\alpha & 0 \\ 0 & \sin\alpha & \cos\alpha & 0 \\ 0 & 0 & 0 & 1 \end{bmatrix} \tag{4-7}$$

$$\boldsymbol{R_\beta} = \begin{bmatrix} \cos\beta' & 0 & \sin\beta' & 0 \\ 0 & 1 & 0 & 0 \\ -\sin\beta' & 0 & \cos\beta' & 0 \\ 0 & 0 & 0 & 1 \end{bmatrix} \tag{4-8}$$

(d) Mathematical modelling of the transient feed coordinate system {TF} in the workpiece coordinate system {W}

The analytical model developed primarily focuses on machining planar surfaces. Through different tool orientations in unidirectional linear feed, different milling path strategies can be obtained. A 5-axis DMG Mori Ultrasonic 20 linear CNC machining centre used in this study can generate one-dimensional ultrasonic vibration, and the vibration direction is coincident with the spindle axis $\overrightarrow{O_{SF}Z_{SF}}$ and the tool axis $\overrightarrow{O_CZ_C}$. The overall vibration of the tool can be regarded as a change in the position of the tool in the Z-axis direction. In this case, assuming the cutting direction is along the positive X-axis and ignoring the auxiliary time between adjacent stepover feeds, the homogeneous coordinate transformation matrix of $\{SF\}$ relative to $\{W\}$ in the horizontal plane of unidirectional linear feed milling is given by Equation 4-9:

$$\boldsymbol{M_{WTF}} = \begin{bmatrix} 1 & 0 & 0 & x_0 + \dfrac{Nf_zN_tt}{60} - (q-1)L_{sc} + \sin(\beta')\,A_U\sin(2\pi f_U t) \\ 0 & 1 & 0 & y_0 - (q-1)a_e - y_{def} - \sin(\alpha)\cos(\beta')\,A_U\sin(2\pi f_U t) \\ 0 & 0 & 1 & w_h + R - a_p + z_{def} + \cos(\alpha)\cos(\beta')\,A_U\sin(2\pi f_U t) \\ 0 & 0 & 0 & 1 \end{bmatrix} \quad (4\text{-}9)$$

where (x_0, y_0) (mm) is the start position of O_{SF} in $\{W\}$, q is the tool feeding sequence number ($q = 1, 2, 3, \ldots, n_q$), f_z (mm/tooth) is the feed per tooth, L_{sc} (mm) is the length of single feed, w_h (mm) is the height of bulk workpiece, a_e (mm) is the width of cut, a_p (mm) is the depth of cut, z_{def} and y_{def} are tool deflections introduced by cutting forces along the normal direction of the workpiece and stepover feed direction, which can be measured directly in cutting tests, A_U (mm) is the amplitude of ultrasonic vibration and f_U (Hz) is the ultrasonic excitation frequency. For the surface morphology simulation, z_{def} is ignored in order to simplify the model.

The trajectory equations of any cutting point P on the tooth N_j in the $\{W\}$ coordinate can be defined according to the homogeneous coordinate matrix transformation as shown in Equation 4-10:

$$[x_P^W(t,\theta) \quad y_P^W(t,\theta) \quad z_P^W(t,\theta) \quad 1]^T = \boldsymbol{M_{WTF}R_\alpha R_\beta M_{SFC}M_{Cj}}\left[x_P^j \quad y_P^j \quad z_P^j \quad 1\right]^T \quad (4\text{-}10)$$

4.1.3 Geometrical simulation of workpiece surface morphology in B-UAM

The influence of cutting forces or system vibration on workpiece surface morphology is generally not significant in finish processing with small depths of cut and high cutting/spindle speeds [242], [260]. The cutting system can be simplified as a rigid contact system between the tool and workpiece, with the corresponding geometrical interactions generating the machined surface.

The introduction of tool ultrasonic vibration makes the motion trajectory of the cutting edge more complex, with the resulting machined surface exhibiting surface textures and morphology that are markedly different than those generated from conventional milling. Surface morphology formation is a relatively complex process, which is dependent on various factors including tool shape/edge geometry, process parameters, system geometric errors, material properties and system dynamic characteristics. However, compared with tool shape, cutting parameters and system geometric errors, the influence of material properties and system dynamic characteristics on surface morphology is relatively small. Therefore, the current model only considers the geometric motion of the tool with static topography simulation based on kinematic analysis.

Through numerical simulation based on the Z-map method, the surface morphology of the ball-end ultrasonic-assisted milling was predicted and simulated to explore the surface formation mechanism, and to study the influence of process parameters, ultrasonic vibration parameters and system geometric errors. The detailed steps for using the Z-map method to predict workpiece surface morphology are outlined below and Figure 4.4 shows the flow chart of the modelling procedure.

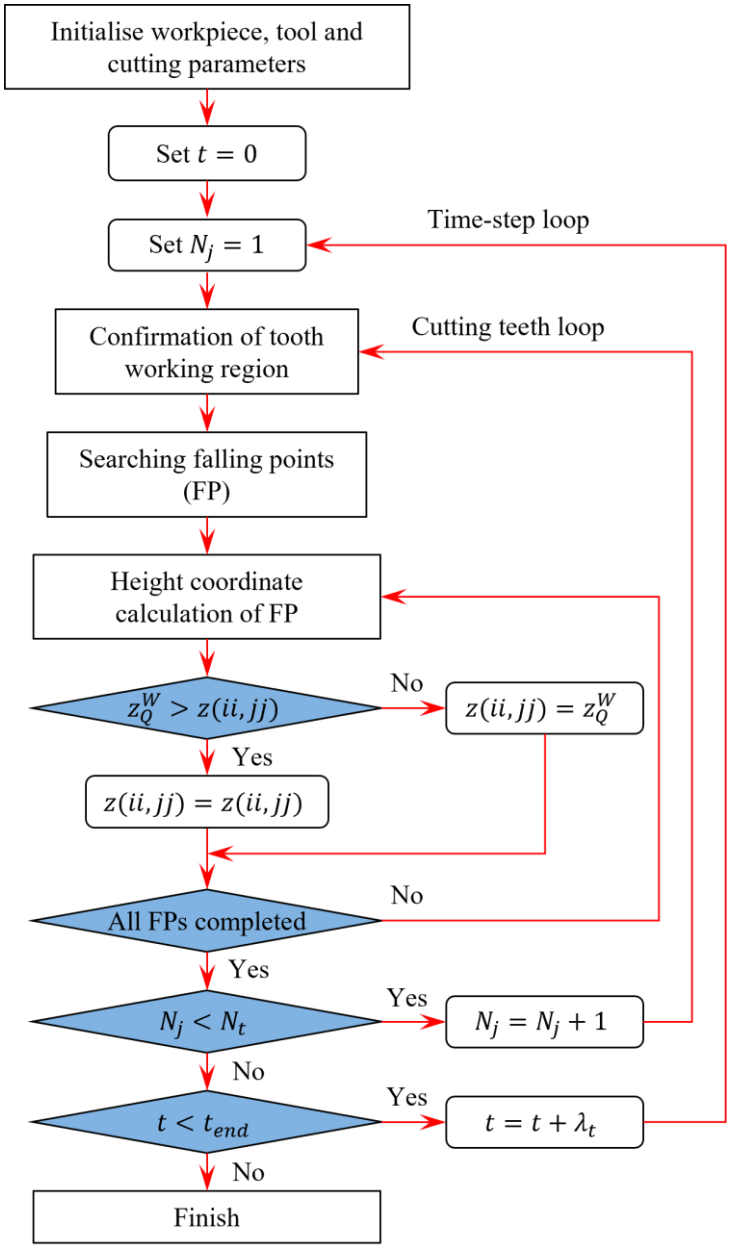


Figure 4.4 Flow chart detailing the modelling procedure for surface morphology in B-UAM.

(a) Initialisation of workpiece and tool

- Set ball nose end mill geometrical parameters: the tool radius R and the total number of teeth N_t.
- Define the size of workpiece as $l_x \times l_y \times w_h$ and discretise surface into mesh $(m \times n)$ according to Equation 4-11, where dx and dy (mm) are the mesh size in X and Y directions respectively. Figure 4.5 presents the diagram of mesh design in Z-map configuration. The height information of the workpiece is recorded in the matrix $z[ii,jj]$

($ii = 1, 2, \dots, m+1; jj = 1, 2, \dots, n+1$), and all elements of the initial matrix z are set to the initial height of the workpiece w_h.

$$max(dx, dy) \leq \frac{1}{5} min(f_z, a_e) \tag{4-11}$$

- Set cutting parameters including spindle speed N, feed rate f_z, depth of cut a_p, width of cut a_e, single cutting length L_{sc}, ultrasonic amplitude A_U and ultrasonic frequency f_U. Tool orientation including tile angle α, lead angle β and start position point (x_0, y_0) are similarly confirmed.

- Discretise machining period according to the time taken for the tool to rotate by 10–20° as the time step λt. The iterative algorithm used in this model can solve the cutting point position corresponding to the swept point of the workpiece surface mesh grid. This method can avoid discretisation of the cutting edge, ensuring accuracy while improving computational efficiency.

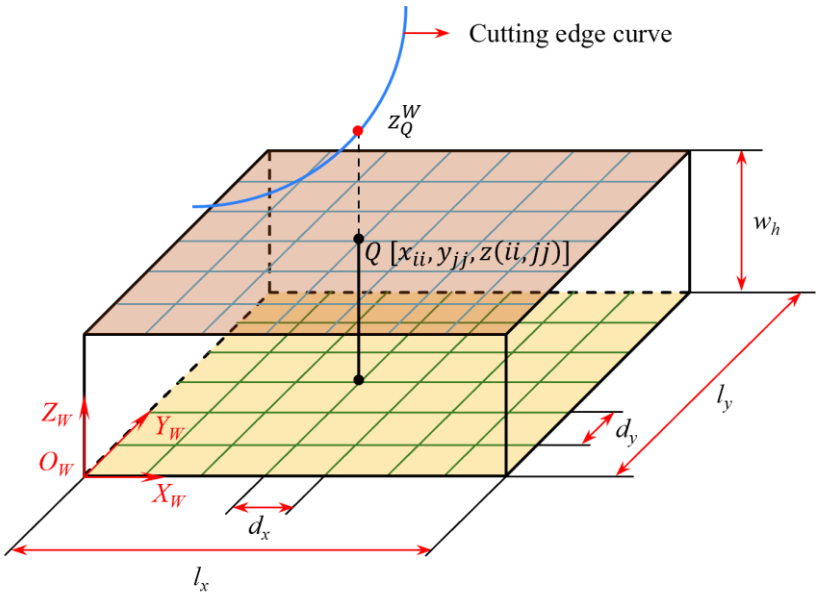


Figure 4.5 Diagram illustrating the Z-map model in B-UAM.

(b) Confirmation of tooth working region

For any cutting tooth, the region of milling is determined by cutting parameters, tool size and tool orientation. Figure 4.6 shows the tool orientation in ball-end ultrasonic-assisted milling and the relative angle can be calculated by Equation 4-12.

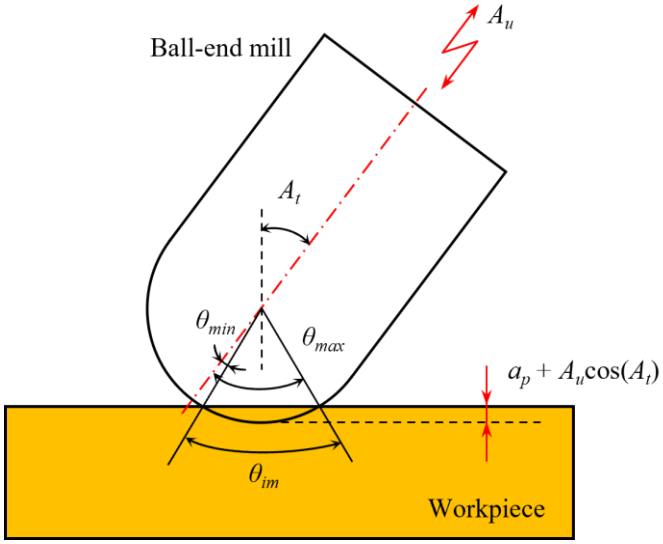


Figure 4.6 Diagram illustrating the working state of the ball nose end mills in B-UAM.

$$\begin{cases} A_t = \cos^{-1}(\cos\alpha\cos\beta') \\ \theta_{im} = 2\cos^{-1}\left(\dfrac{R - a_p - A_U\cos A_t}{R}\right) \\ \theta_{min} = A_t - 0.5\theta_{im} \\ \theta_{max} = A_t + 0.5\theta_{im} \end{cases} \tag{4-12}$$

where θ_{im} is the cutting region angle, θ_{min} is the minimum axial position angle and θ_{max} is maximum axial position angle. The symmetrical structure of the ball nose end mill defines the range of axial position angle. If $\theta_{min} < 0°$, $\theta_{min} = 0°$, else if $\theta_{max} > 90°$, $\theta_{max} = 90°$, where $\theta_{min}, \theta_{max} \in [0°, 90°]$. Projection of the cutting point on workpiece surface (PCP) including P_0 with θ_{min} at $t = T_t$, P_1 with θ_{max} at $t = T_t$, the coordinates for P_0 at the next time step P_0' and P_1', which is the position of P_1 at the next time step, can be defined by Equation 4-13. The maximum cutting region is defined as an instantaneous swept quadrilateral (ISQ) in terms of the four points P_0, P_1, P_1' and P_0', as shown in Figure 4.7.

$$\begin{cases} \begin{bmatrix} x_{P_0} & y_{P_0} & z_{P_0} \end{bmatrix}^T = \begin{bmatrix} x_P^w(t,\theta) & y_P^w(t,\theta) & z_P^w(t,\theta) \end{bmatrix}^T|_{t=T_t,\theta=\theta_{min}} \\ \begin{bmatrix} x_{P_1} & y_{P_1} & z_{P_1} \end{bmatrix}^T = \begin{bmatrix} x_P^w(t,\theta) & y_P^w(t,\theta) & z_P^w(t,\theta) \end{bmatrix}^T|_{t=T_t,\theta=\theta_{max}} \\ \begin{bmatrix} x_{P_0'} & y_{P_0'} & z_{P_0'} \end{bmatrix}^T = \begin{bmatrix} x_P^w(t,\theta) & y_P^w(t,\theta) & z_P^w(t,\theta) \end{bmatrix}^T|_{t=T_t+\lambda_t,\theta=\theta_{min}} \\ \begin{bmatrix} x_{P_1'} & y_{P_1'} & z_{P_1'} \end{bmatrix}^T = \begin{bmatrix} x_P^w(t,\theta) & y_P^w(t,\theta) & z_P^w(t,\theta) \end{bmatrix}^T|_{t=T_t+\lambda_t,\theta=\theta_{max}} \end{cases} \tag{4-13}$$

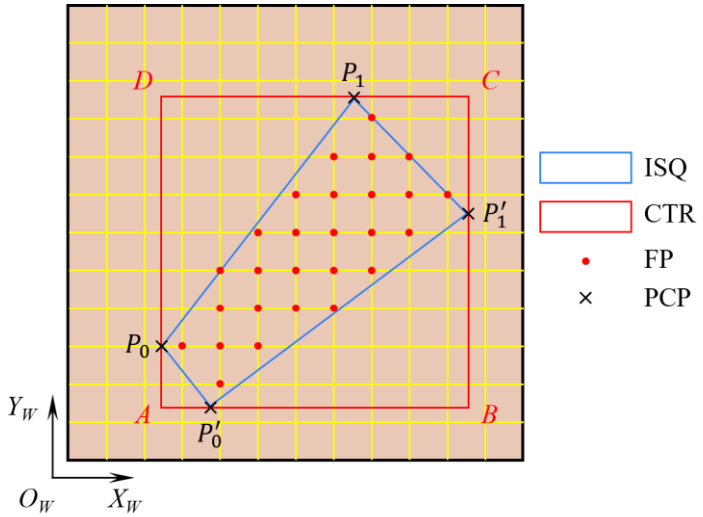


Figure 4.7 Schematic diagram of ISP on the workpiece.

To correspond the cutting region with workpiece mesh grids, the tracking rectangle of cutting region (CTR) $ABCD$ is determined based on Equation 4-14. The vertex coordinates are calculated using Equation 4-15.

$$\begin{cases} x_{min} = min(x_{P_0}, x_{P_0'}, x_{P_1}, x_{P_1'}) \\ x_{max} = max(x_{P_0}, x_{P_0'}, x_{P_1}, x_{P_1'}) \\ y_{min} = min(y_{P_0}, y_{P_0'}, y_{P_1}, y_{P_1'}) \\ y_{max} = max(y_{P_0}, y_{P_0'}, y_{P_1}, y_{P_1'}) \end{cases} \tag{4-14}$$

$$\begin{cases} A[min(x_{P_0}, x_{P_0'}, x_{P_1}, x_{P_1'}), min(y_{P_0}, y_{P_0'}, y_{P_1}, y_{P_1'})] \\ B[max(x_{P_0}, x_{P_0'}, x_{P_1}, x_{P_1'}), min(y_{P_0}, y_{P_0'}, y_{P_1}, y_{P_1'})] \\ C[max(x_{P_0}, x_{P_0'}, x_{P_1}, x_{P_1'}), max(y_{P_0}, y_{P_0'}, y_{P_1}, y_{P_1'})] \\ D[min(x_{P_0}, x_{P_0'}, x_{P_1}, x_{P_1'}), max(y_{P_0}, y_{P_0'}, y_{P_1}, y_{P_1'})] \end{cases} \tag{4-15}$$

(c) Search for falling points (FP) from CTR

The angle accumulation method was conducted to determine whether the workpiece mesh point $[x_{ii}, y_{jj}]$ in the CTR boundary fell into ISQ of the tooth in terms of Equations 4-16–4-19. Figure 4.8 shows a schematic diagram of the angle accumulation method. When $A_1 + A_2 + A_3 + A_4 = 360$, the point Q falls into the instantaneous swept quadrilateral.

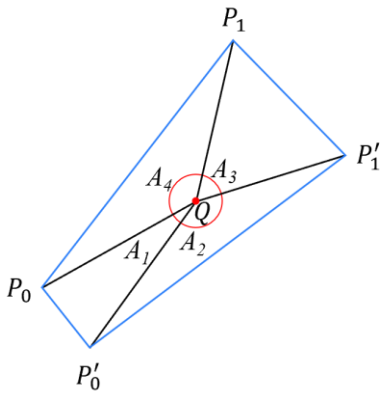


Figure 4.8 Schematic diagram of angle accumulation method.

$$A_1 = \cos^{-1}\left(\frac{(x_p - x_{P_0})(x_p - x_{P_0'}) + (y_p - y_{P_0})(y_p - y_{P_0'})}{\sqrt{(x_p - x_{P_0})^2 + (y_p - y_{P_0})^2} \cdot \sqrt{(x_p - x_{P_0'})^2 + (y_p - y_{P_0'})^2}}\right) \tag{4-16}$$

$$A_2 = \cos^{-1}\left(\frac{(x_p - x_{P_0'})(x_p - x_{P_1'}) + (y_p - y_{P_0'})(y_p - y_{P_1'})}{\sqrt{(x_p - x_{P_0'})^2 + (y_p - y_{P_0'})^2} \cdot \sqrt{(x_p - x_{P_1'})^2 + (y_p - y_{P_1'})^2}}\right) \tag{4-17}$$

$$A_3 = \cos^{-1}\left(\frac{(x_p - x_{P_1'})(x_p - x_{P_1}) + (y_p - y_{P_1'})(y_p - y_{P_1})}{\sqrt{(x_p - x_{P_1'})^2 + (y_p - y_{P_1'})^2} \cdot \sqrt{(x_p - x_{P_1})^2 + (y_p - y_{P_1})^2}}\right) \tag{4-18}$$

$$A_4 = \cos^{-1}\left(\frac{(x_p - x_{P_0})(x_p - x_{P_1}) + (y_p - y_{P_0})(y_p - y_{P_1})}{\sqrt{(x_p - x_{P_0})^2 + (y_p - y_{P_0})^2} \cdot \sqrt{(x_p - x_{P_1})^2 + (y_p - y_{P_1})^2}}\right) \tag{4-19}$$

(d) Height coordinate calculation of FP

The FP $Q\,[x_{ii}, y_{jj}]$ is confirmed by step (c). Combined with Equation 4-10, a system of nonlinear constraint equations as a function of cutting time t and the axial position angle θ is obtained as shown in Equation 4-20:

$$\begin{cases} f_x(t,\theta) = x_P^W(t,\theta) - x_{ii} = 0 \\ f_y(t,\theta) = y_P^W(t,\theta) - y_{jj} = 0 \end{cases} \tag{4-20}$$

Initial values are selected $\begin{bmatrix} t^* \\ \theta^* \end{bmatrix} = \begin{bmatrix} T_t - 0.5\lambda_t \\ 0.5(\theta_{min} + \theta_{max}) \end{bmatrix}$ and the Newton-Raphson method is applied to solve the system of Equation 4-20. Convergence accuracy was defined as 0.000001 and the maximum number of iterations was 1000. The characteristic value of the point on the ball nose end mill tooth corresponding to FP can be obtained by Equation 4-21:

$$\begin{bmatrix} t_0 \\ \theta_0 \end{bmatrix} = \begin{bmatrix} t^* \\ \theta^* \end{bmatrix} - \begin{bmatrix} \frac{\partial f_x}{\partial t} & \frac{\partial f_x}{\partial \theta} \\ \frac{\partial f_y}{\partial t} & \frac{\partial f_y}{\partial \theta} \end{bmatrix}^{-1} \begin{bmatrix} f_x(t^*, \theta^*) \\ f_y(t^*, \theta^*) \end{bmatrix} \tag{4-21}$$

The solution is substituted into Equation 4-10 to obtain the height coordinate value of FP, as shown in Equation 4-22.

$$z_Q^W = z_P^W(t, \theta)|_{t=t_0, \theta=\theta_0} \tag{4-22}$$

Comparing the z_Q^W with current $z(ii, jj)$, if $z_Q^W < z(ii, jj)$, means that the ball nose end mill has cut the workpiece. In this case, $z(ii, jj)$ is replaced by z_Q^W as the current workpiece height, otherwise keep the original $z(ii, jj)$.

(e) Steps (c)–(d) repeated until all falling points in the ISQ are confirmed and updated height information of corresponding mesh grids.

(f) Steps (b)–(d) repeated and calculated $z(ii, jj)$ generated by the next tooth motion.

(g) Steps (b)–(f) repeated and updated $z(ii, jj)$ generated by the next time step until cutting process completed.

(h) Finally, the three-dimensional surface topography of ball-end ultrasonic-assisted milling surface can be plotted based on the value of $z(ii, jj)$.

4.2 Modelling of instantaneous cutting force in B-UAM (Phase 3B)

Cutting force prediction is critical for optimising machining processes and for an in-depth understanding of cutting mechanisms. Compared to experimental or finite element method (FEM) approaches, the semi-analytical method offers a good balance between precision and

efficiency. In this method, small elemental cutting forces are predicted and subsequently aggregated into the total cutting force.

Accurately modelling the interaction between the tool and workpiece in milling is challenging due to the trochoidal motion trajectory of the cutting edge and the dynamically changing geometry of the workpiece. Determining the cutter-workpiece engagement (CWE) and uncut chip thickness (UCT) is particularly difficult. Moreover, the impact of tool deflection, which is critical for tools with large aspect ratios, must be considered. Tool deflection will change the UCT directly and impact calculation of elemental cutting forces.

To address these complexities, a modified cutting force prediction model was developed. This model incorporated considerations for tool deflection and in-process geometry of the workpiece during ball-end ultrasonic-assisted milling, aiming with the aim of enhancing the precision and reliability of the prediction.

4.2.1 Theoretical foundation for modelling instantaneous cutting forces

By discretising the axial position angle of cutting tooth at equal intervals and dividing the tooth into cutting edge elements, the total cutting force exerted on the tool is the sum of forces from all the individual tooth elements involved in cutting. The cutting force of the cutting edge element with axial position angle θ on the tooth j at time t can be decomposed into tangential cutting force $dF_t(\theta,j,t)$, radial cutting force $dF_r(\theta,j,t)$ and axial cutting force $dF_a(\theta,j,t)$ components, which can be calculated by the mechanistic approach as follows [240]:

$$\begin{cases} dF_r(\theta,j,t) = c(\theta,j,t)\cdot[K_{rc}\cdot h(\theta,j,t)\cdot db(\theta,j,t) + K_{re}\cdot dS(\theta,j,t)] \\ dF_t(\theta,j,t) = c(\theta,j,t)\cdot[K_{tc}\cdot h(\theta,j,t)\cdot db(\theta,j,t) + K_{te}\cdot dS(\theta,j,t)] \\ dF_a(\theta,j,t) = c(\theta,j,t)\cdot[K_{ac}\cdot h(\theta,j,t)\cdot db(\theta,j,t) + K_{ae}\cdot dS(\theta,j,t)] \end{cases} \quad (4\text{-}23)$$

where $c(\theta,j,t)$ represents the CWE status, $c(i,j,t) = 1$ means that the tool contacted with the workpiece otherwise $c(\theta,j,t) = 0$; K_{rc}, K_{tc} and K_{ac} (N/mm^2) are the shearing coefficients relating to the shearing action introduced by chip formation in the radial, tangential and axial directions respectively; K_{re}, K_{te} and K_{ae} (N/mm^2) are the ploughing coefficients from the ploughing and rubbing action introduced by flank contact in the radial, tangential and axial directions; $h(\theta,j,t)$ (mm) is the uncut chip thickness, $db(\theta,j,t)$ (mm) is the width of chip element and $dS(\theta,j,t)$ (mm) is the length of the cutting edge element.

Tangential, radial and axial forces acting on the cutting edge element at a particular instant can be transformed into forces in the transient feed coordinate system $\{SF\}$ in accordance with Equations 4-24 and 4-25.

$$\boldsymbol{R_{Trans}} = \begin{bmatrix} -\cos[\varphi(\theta,j,t)] & -\sin[\varphi(\theta,j,t)]\sin\theta & -\sin[\varphi(\theta,j,t)]\cos\theta \\ \sin[\varphi(\theta,j,t)] & -\cos[\varphi(\theta,j,t)]\sin\theta & -\cos[\varphi(\theta,j,t)]\cos\theta \\ 0 & \cos\theta & -\sin[\varphi(\theta,j,t)] \end{bmatrix} \tag{4-24}$$

$$\begin{bmatrix} dF_x^{SF}(\theta,j,t) \\ dF_y^{SF}(\theta,j,t) \\ dF_z^{SF}(\theta,j,t) \end{bmatrix} = \boldsymbol{R_{Trans}} \begin{bmatrix} dF_r(\theta,j,t) \\ dF_t(\theta,j,t) \\ dF_a(\theta,j,t) \end{bmatrix} \tag{4-25}$$

where $\varphi(\theta,j,t)$ is the radial position angle of the cutting edge element with axial position angle θ on the tooth j at time t. Combined with Equations 4-7, 4-8 and 4-25, elemental cutting forces in the workpiece coordinate system $\{W\}$ can be determined from Equation 4-26:

$$\begin{bmatrix} dF_x^W(\theta,j,t) \\ dF_y^W(\theta,j,t) \\ dF_z^W(\theta,j,t) \end{bmatrix} = \begin{bmatrix} \cos\alpha & -\sin\alpha & 0 \\ \sin\alpha & \cos\alpha & 0 \\ 0 & 0 & 1 \end{bmatrix} \begin{bmatrix} \cos\beta' & 0 & \sin\beta' \\ 0 & 1 & 0 \\ -\sin\beta' & 0 & \cos\beta' \end{bmatrix} \begin{bmatrix} dF_x^{SF}(\theta,j,t) \\ dF_y^{SF}(\theta,j,t) \\ dF_z^{SF}(\theta,j,t) \end{bmatrix} \tag{4-26}$$

The instantaneous cutting forces on the tool at time t can be expressed according to Equation 4-27:

$$\begin{cases} F_x^W(t) = \sum_{j=1}^{N_t} \sum_{\theta_{min}}^{\theta_{max}} dF_x^W(\theta,j,t) \\ F_y^W(t) = \sum_{j=1}^{N_t} \sum_{\theta_{min}}^{\theta_{max}} dF_y^W(\theta,j,t) \\ F_z^W(t) = \sum_{j=1}^{N_t} \sum_{\theta_{min}}^{\theta_{max}} dF_z^W(\theta,j,t) \end{cases} \tag{4-27}$$

4.2.2 Establishment of tool static deflection model

Cutting tools can undergo deformation during milling because of high cutting forces, which can induce geometrical errors, especially in the machining of non-thin-walled parts or when using high aspect ratio tools. Ball-end mills are widely used for finishing operations, which typically demands high machining precision. When studying the deformation of static or quasi-static milling, the tool is usually approximated as a cantilever beam with a fixed end and tool

deformation is analogous to deflection of the cantilever beam under load at the free end. In the present work, an analytical bending deflection model was established with results from Phase 1B trials used to validate the model.

Tool bending deflection is considered for the case where tool orientation (with respect to workpiece surface) is at 45° in line with the experimental trials. Although milling is an interrupted cutting operation, it was assumed that when the bending load F_{def} is fixed, the associated deflection is constant as well in order to simplify the model. Bending load F_{def} can be expressed as the resultant force of cutting forces F_y and F_z (see Equation 4-28). The direction of F_{def} is parallel to the plane $Y_W O_W Z_W$ and perpendicular to the tool axis, as shown in Figure 4.9. The components of the total bending deflection b_{def} along the F_y and F_z directions are represented by y_{def} and z_{def}, of which z_{def} is equal to the depth of cut error measured using the Renishaw PowerProbe 400.

$$F_{def} = F_y \cos\alpha + F_z \sin\alpha \tag{4-28}$$

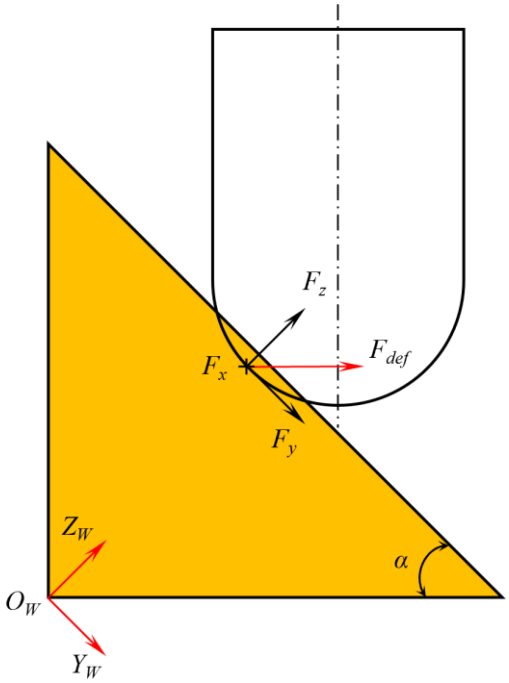


Figure 4.9 Schematic diagram of bending deflection load in ball-end milling.

The static deflection model was established by considering three main aspects comprising the cantilever beam, load distribution and bending stiffness. The ball nose end mill consists of two distinct sections, the shank and the cutting region. The shape of the shank is usually a regular

cylinder while the cutting region comprises the flute with cutting edges. The main reason for distinguishing between the different regions is the variation in inertia. The principal error would increase significantly if the inertia of the cutting region was calculated based on a circular cross-section approximation.

The horizontal cutting force component is known as the principal reason for cutter and clamping apparatus deflection. While the vertical force acts along the neutral axis of the tool, the axial deflection is usually ignored due to the relatively high stiffness in this. To reduce calculations, a stepped cantilever beam model was used in this thesis and the deflection can be expressed according to Equation 4-29 [261]:

$$\delta = \delta_t + \delta_c \tag{4-29}$$

where δ_t is the cutter bending deflection and δ_c is the clamping apparatus deflection. Figure 4.10 exhibits a two-step cylindrical beam model. Clamping unit deflection (δ_c) was ignored to simplify the model due to high stiffness of the tool holder. Considering different shapes of ball nose end mills in the two-step model, the total bending deflection was calculated by Equation 4-30.

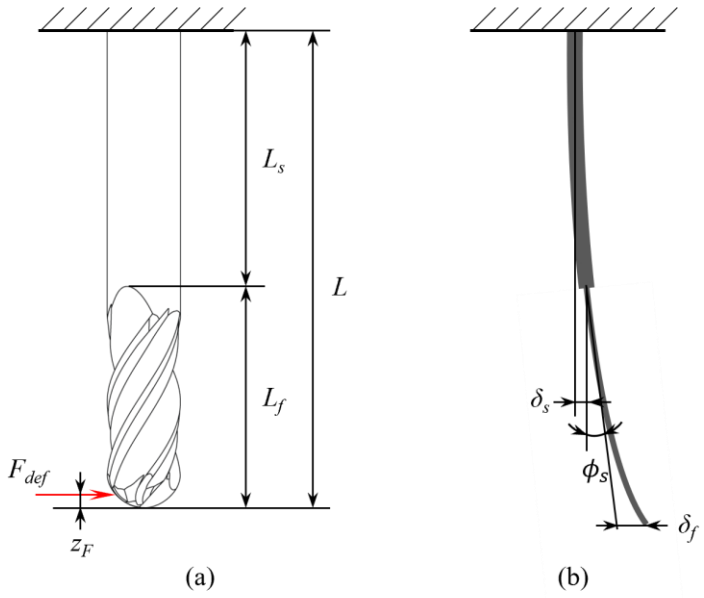
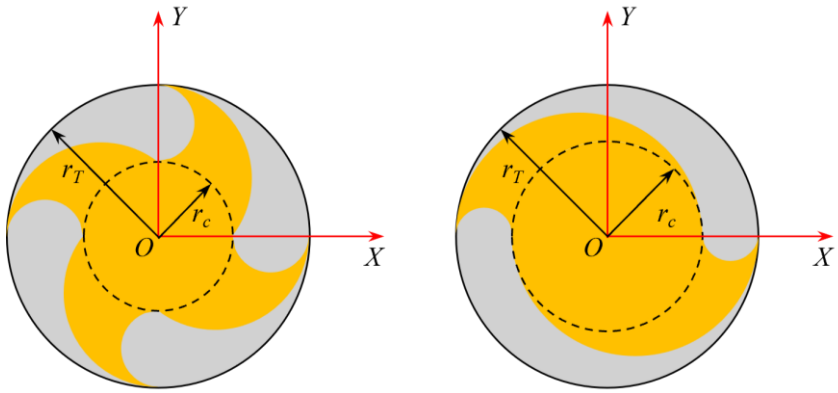


Figure 4.10 Simplified ball nose end mill model: (a) Tool deflection model; and (b) simplified two-step cylindrical beam model.

$$\begin{cases} \delta = \delta_s + \delta_f + \phi_s(L_f - z) \\ \delta_s = \dfrac{F_{def}}{6EI_s}\left[-(L - L_f)^3 + 3(L - L_f)^2(L - z_F)\right] \\ \delta_f = \dfrac{F_{def}}{6EI_f}\left[< z_F - z >^3 - (L_f - z)^3 + 3(L_f - z)^2(L_f - z_F)\right] \\ \phi_s = \dfrac{F_{def}}{2EI_s}\left[-(L - L_f)^2 + 2(L - L_f)(L - z_F)\right] \end{cases} \tag{4-30}$$

where δ_s is the shank deflection, δ_f is the deflection of the flute, ϕ_s is the deflection angle of the shank, L_f is the length of the cutting area, I_s is the inertia of the shank and I_f is the inertia of the flute.

The calculation of the flute moment of inertia was primary consideration in this model. Due to the limitation of experimental conditions, this study used the discretised method to calculate flute inertia based on the work of Wang et al. [262]. The inertia of a 4-fluted cutter can be expressed as a function of the tool radius r_T and core ratio r_c (see Figure 4.11) in a product of power law and linear relationship as shown in Equation 4-31 [262].



4-fluted mill 2-fluted mill

Figure 4.11 Illustration of end mill cross-sectional shapes.

$$I_{4x} = I_{4y} = (0.914\xi - 0.195) \cdot r_T^4 \tag{4-31}$$

Similarly, the inertia of a 2-fluted tool can be expressed according to Equation 4-32 [262]:

$$\begin{cases} I_{2x} = (0.517\xi + 0.0863) \cdot r_T^4 \\ I_{2x} = (0.707\xi - 0.139) \cdot r_T^4 \end{cases} \tag{4-32}$$

where I_{2x}, I_{2y}, I_{4x} and I_{4y} are moments of inertia (for 2 and 4 fluted tools) in the x and y directions respectively; ξ is the core radius ratio, $\xi = r_c/r_T$, with $\xi \in [0.5, 0.75]$ and $r_T \in [2, 10]$.

Tool deflection is considered in the tool flank wear model to improve the accuracy of the predicted chip size when milling at a 45° tilt angle in Phase 3B. Initial bending deflection is calculated by an iterative method, as illustrated in Figure 4.12. The z^*_{def} parameter is the deflection calculated by using the static deflection model while F_{def} is determined from the cutting force model, with λ_{def} as the deflection increments and ε is the tolerance.

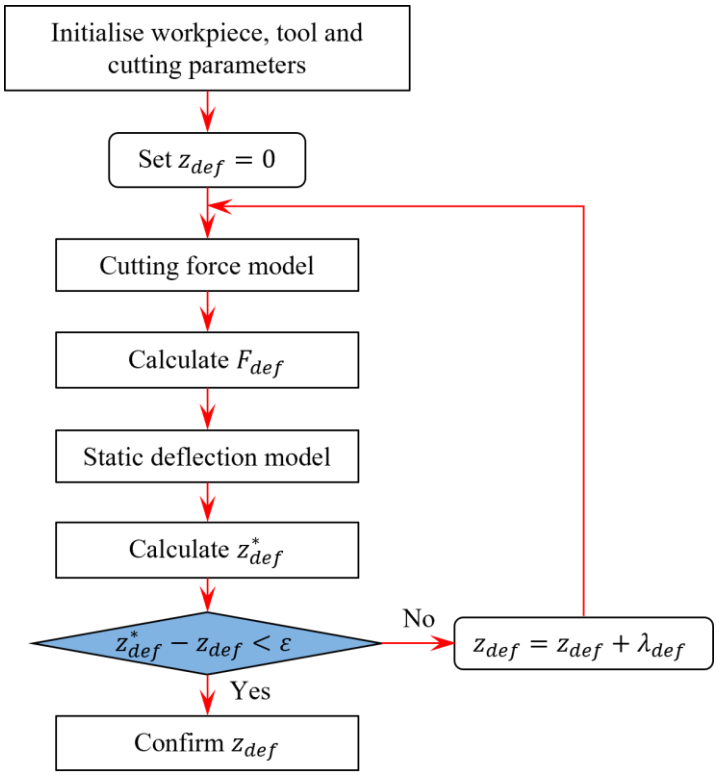


Figure 4.12 Flow chart showing the calculation procedure of tool static deflection.

4.2.3 Identification of CWE status

Based on the improved Z-map method discussed in Section 4.1, the tracking rectangle and the instantaneous swept quadrilateral of cutting edge elements within a certain time period have been established. The angle accumulation method is used to determine if workpiece mesh points fall within the swept quadrilateral. Simultaneously, the Taylor expansion formula is directly applied to calculate the height coordinates of the workpiece mesh points, which allows for the accurate determination of whether a mesh point is instantaneously swept. If the mesh point is

swept, it indicates that the corresponding cutting point of the tooth is in contact with the workpiece. Notably, a triangular mesh is used in this part for calculating uncut chip thickness.

In contrast to the previous section where only the workpiece and cutting time are discretised, the cutting force also requires discrete operations on the cutting edge. For any cutting point with the axial position angle θ on the tooth j at the time t, its ISQ consists of projection points (a, b, c and d) of four vertices of the cutting edge element on the plane $Y_W O_W X_W$ (see Figure 4.13), where coordinates of these points are expressed by Equation 4-33:

$$\begin{cases} a = [x_P^W(t,\theta), y_P^W(t,\theta)] \\ b = [x_P^W(t+\lambda_t,\theta), y_P^W(t+\lambda_t,\theta)] \\ c = [x_P^W(t+\lambda_t,\theta+\lambda_\theta), y_P^W(t+\lambda_t,\theta+\lambda_\theta)] \\ d = [x_P^W(t,\theta+\lambda_\theta), y_P^W(t,\theta+\lambda_\theta)] \end{cases} \tag{4-33}$$

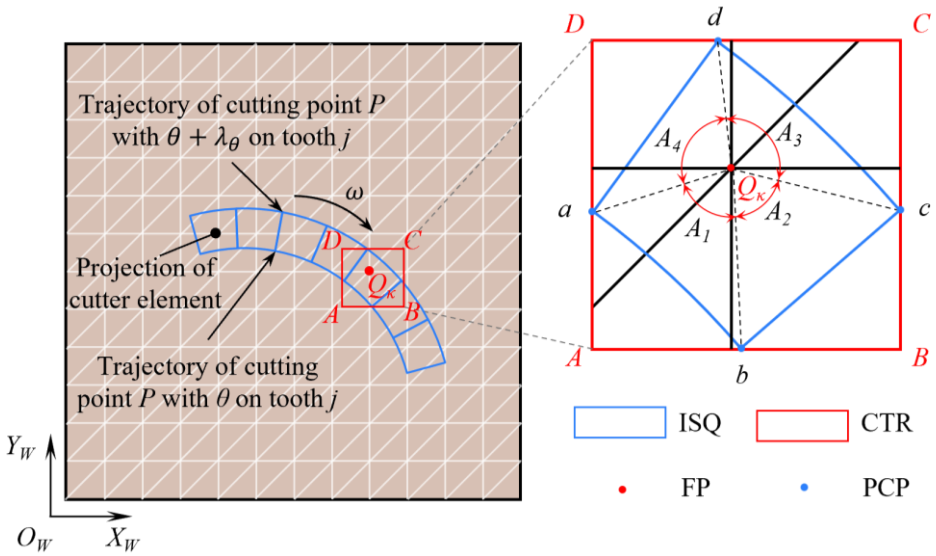


Figure 4.13 Extracting mesh point swept by the cutting edge segment.

To improve the calculation precision, λ_θ is determined by Equation 4-34 to ensure that only one mesh grid point can fall within the ISQ. In addition, considering the effect of high frequency vibration on tool trajectory, the time increment λ_t is set according to the sampling theorem, see Equation 4-35. The value of λ_t must be small enough to satisfy the principle that there is at most one falling point.

$$\lambda_\theta = \frac{180 \min(dx, dy)}{\pi R \sqrt{2}} \tag{4-34}$$

$$\lambda_t < \frac{1}{2f_U} \tag{4-35}$$

The angle accumulation method detailed in Section 4.1.3 is employed to search for falling point Q_κ. The length between $Q_\kappa a$, $Q_\kappa b$, $Q_\kappa c$ and $Q_\kappa d$ is compared to confirm the point closest to Q_κ as the calculation point P^*. The coordinate of point P^* in $\{W\}$ system is denoted as $[x_P^W(t_\kappa, \theta_\kappa), y_P^W(t_\kappa, \theta_\kappa)]$. The coordinates of the falling point $Q_\kappa(\theta, j, t)$ can be established using the Taylor formula as illustrated in Equation 4-36:

$$\begin{cases} x_{Q_\kappa} = x_P^W(t_\kappa, \theta_\kappa) + \Delta x = x_P^W(t_\kappa, \theta_\kappa) + \left(\Delta t_\kappa \dfrac{\partial}{\partial t} + \Delta\theta_\kappa \dfrac{\partial}{\partial \theta}\right) x_P^W(t_\kappa, \theta_\kappa) \\ y_{Q_\kappa} = y_P^W(t_\kappa, \theta_\kappa) + \Delta y = y_P^W(t_\kappa, \theta_\kappa) + \left(\Delta t_\kappa \dfrac{\partial}{\partial t} + \Delta\theta_\kappa \dfrac{\partial}{\partial \theta}\right) y_P^W(t_\kappa, \theta_\kappa) \end{cases} \tag{4-36}$$

where t_κ is the cutting time corresponding to the calculation point P^*, θ_κ is the matched axial position angle, Δx and Δy were increments of the falling point Q_κ in $\overrightarrow{O_W X_W}$ and $\overrightarrow{O_W Y_W}$ directions respectively, Δt_κ and $\Delta\theta_\kappa$ are time and axial position angle increments of Q_κ relative to P^*. The coordinate of Q_κ in $\{W\}$ system is expressed as $(x_{Q_\kappa}, y_{Q_\kappa})$. By solving the system of Equation 4-36, Δt_κ and $\Delta\theta_\kappa$ can be obtained. The height coordinate of the point $Q_\kappa^*(\theta, j, t)$ on the swept surface of the cutting edge element within the current time step, as shown in Figure 4.14, can be calculated using Equation 4-37.

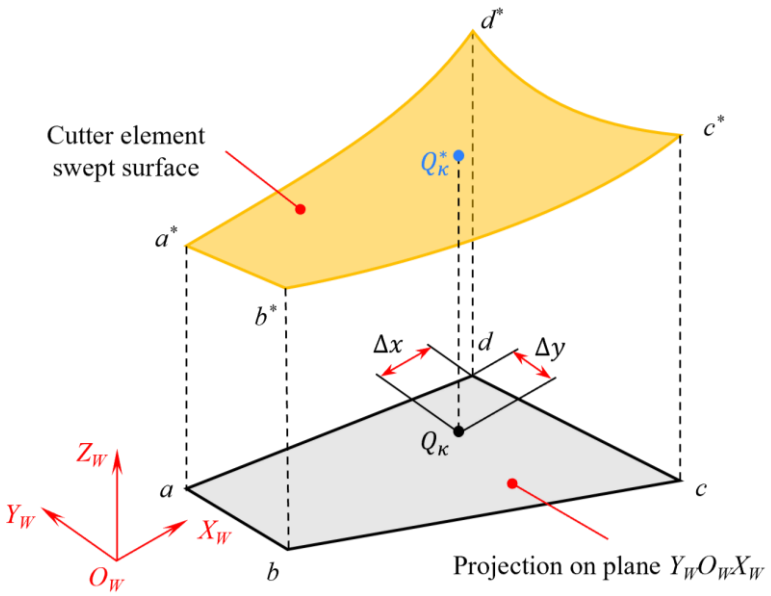


Figure 4.14 Schematic diagram of the falling point Q_κ calculation.

$$z_{Q_\kappa}(\theta, j, t) = z_P^W(t_\kappa + \Delta t_\kappa, \theta_\kappa + \Delta\theta_\kappa) \tag{4-37}$$

Comparing $z_{Q_\kappa}(\theta, j, t)$ with the current $z(x_{Q_\kappa}, y_{Q_\kappa})$, if $z_{Q_\kappa}(\theta, j, t) < z(x_{Q_\kappa}, y_{Q_\kappa})$, it indicates that the ball nose end mill has cut the workpiece. In this case, $z(x_{Q_\kappa}, y_{Q_\kappa})$ is replaced by $z_{Q_\kappa}(\theta, j, t)$ as the current workpiece height, otherwise, keep original $z(x_{Q_\kappa}, y_{Q_\kappa})$.

4.2.4 Instantaneous uncut chip thickness, length of cutting element and chip width

The challenge of modelling ball-end milling is that due to the complexity of CWE, the traditional method of calculating uncut chip thickness h needs to be discussed case by case. Figure 4.15 demonstrates several possible situations that may occur during the ball-end milling.

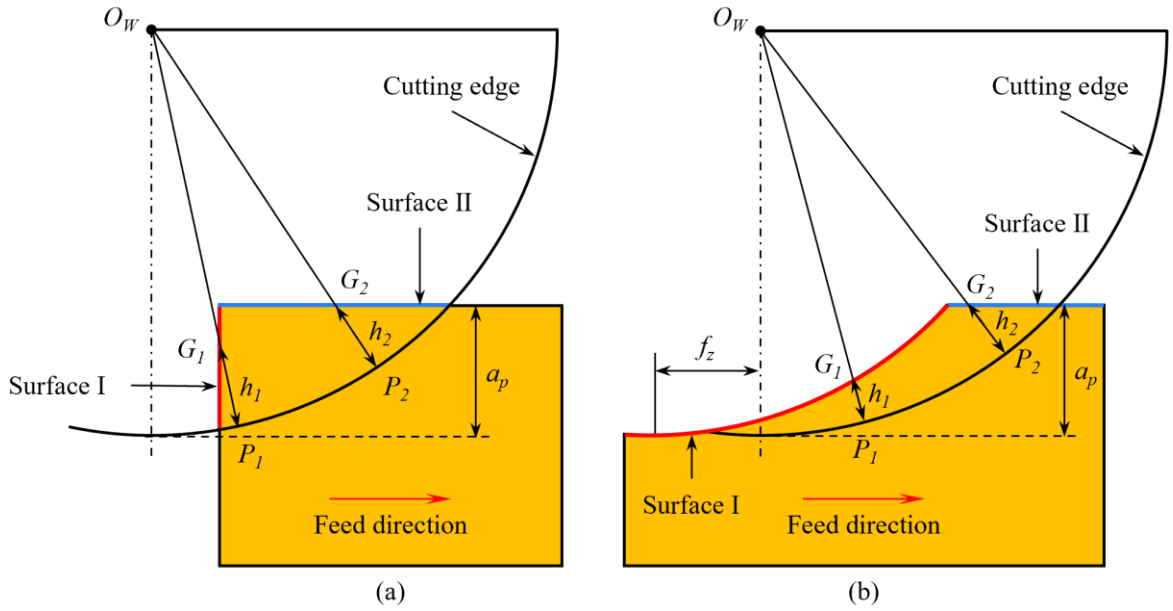


Figure 4.15 Schematic diagram of uncut chip thickness definition: (a) First cut; and (b) full immersion cut.

The uncut chip thickness (UCT) is the dimension of the cut layer measured from the selected cutting point P along the reference line $\overrightarrow{PO_W}$, as shown in Figure 4.15. The reference is a ray starting from the selected cutting point P and pointing to the tool origin O_W. The uncut chip thickness h is defined by calculating the distance between P and G according to Equation 4-38:

$$h(\theta, j, t) = \sqrt{(x_P - x_G)^2 + (y_P - y_G)^2 + (z_P - z_G)^2} \tag{4-38}$$

where G is the intersection between the real-time workpiece surface and the reference ray of the cutting point P.

To calculate the uncut chip thickness, a triangular mesh is used to alter the conventional mesh grids. A Ray-triangle intersection is employed to achieve uncut chip thickness h without the need to classify and discuss specific cutting situations, as depicted in Figure 4.15 [263]. A tracking bounding box is established to improve computational efficiency. The box range for current the cutting point P is determined using Equation 4-39:

$$\begin{cases} x_P^W - 2f_z \le x \le x_P^W + 2f_z \\ y_P^W - 2f_z \le y \le y_P^W + 2f_z \end{cases} \tag{4-39}$$

A ray $R(d)$ with the origin P and the destination O_W is defined according to Equation 4-40, and a triangle bounded by three vertices V_0, V_1 and V_2, as shown in Figure 4.16. The parameter K is normalised direction of $\overrightarrow{PO_W}$, which is equivalent to $\overrightarrow{PO_W}/\left|\overrightarrow{PO_W}\right|$.

$$R(d) = P + dK \tag{4-40}$$

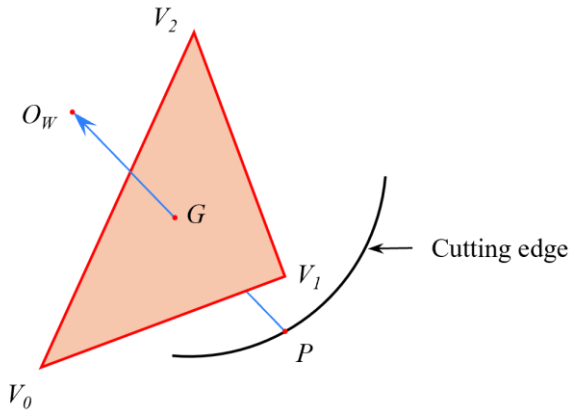


Figure 4.16 Schematic diagram of the Ray-triangle intersection.

The point $G(u, v)$, on the triangle is given by Equation 4-41:

$$G(u, v) = (1 - u - v)V_0 + uV_1 + vV_2 \tag{4-41}$$

where (u, v) are the barycentric coordinate, which must fulfil $u \ge 0$, $v \ge 0$ and $u + v \ge 1$. To confirm the intersection between the ray and triangle, $R(d)$ is equivalent to $G(u, v)$, which yields the relationship in Equation 4-42:

$$P + dK = (1 - u - v)V_0 + uV_1 + vV_2 \tag{4-42}$$

Denoting $E_1 = V_1 - V_0$, $E_2 = V_2 - V_0$ and $U = P - V_0$, the solution to Equation 4-42 is obtained by using Cramer's rule as shown in Equation 4-43:

$$\begin{bmatrix} d \\ u \\ v \end{bmatrix} = \frac{1}{(K \times E_2) \cdot E_1} \begin{bmatrix} (U \times E_1) \cdot E_2 \\ (K \times E_2) \cdot U \\ (U \times E_1) \cdot K \end{bmatrix} \tag{4-43}$$

When the uncut chip thickness is nonzero and the cutter is in contact with workpiece, the CWE parameter $c(\theta, j, t)$ can be described as follows in Equation 4-44:

$$c(\theta, j, t) = \begin{cases} 1 & h(\theta, j, t) \neq 0 \\ 0 & else \end{cases} \tag{4-44}$$

The length of cutting edge element P is be calculated by the linear distance between the current cutting point $P(\theta, j, t)$ and the next time step cutting point $P(\theta, j, t + \lambda_t)$, as expressed in Equation 4-45 [264].

$$dS(\theta, j, t) = R\sqrt{(1 + \sin^4\theta \tan^2\gamma_0}\ \lambda_\theta \tag{4-45}$$

The width of chip element is given a constant value based on Equation 4-46:

$$db(\theta, j, t) = R\lambda_\theta \tag{4-46}$$

4.2.5 Identification of cutting force coefficients

Determination of cutting coefficients is an important aspect in cutting force modelling. The reliability of this semi-analytical model depends to a large extent on the quality of cutting coefficients. Considering that the characteristics of the effective cutting radius and helix angle of each point on the cutting edge of the ball nose end mill changes along the axial position of the cutting edge element, a method to identify variable cutting coefficients through use of average milling forces in slotting was previously proposed [265], [266]. Slotting with ball nose end mill has the advantage of eliminating the influence of tool eccentricity. During cutting process, the uncut chip thickness is theoretically symmetrically distributed with respect to the feed direction. However, while symmetry is lost when the tool is eccentric, the average uncut chip thickness will remain equal to the theoretical value.

The shearing coefficients of the ball-end milling are usually expressed as a polynomial function of the axial position angle θ, while the ploughing coefficients were set as constants. The cutting force coefficients can therefore be expressed as in Equation 4-47:

$$\begin{cases} K_{rc} = K_{rc0} + K_{rc1}\theta + K_{rc2}\theta^2 + K_{rc3}\theta^3 \\ K_{tc} = K_{tc0} + K_{tc1}\theta + K_{tc2}\theta^2 + K_{tc3}\theta^3 \\ K_{ac} = K_{ac0} + K_{ac1}\theta + K_{ac2}\theta^2 + K_{ac3}\theta^3 \\ K_{re} = K_{re0} \\ K_{te} = K_{te0} \\ K_{ae} = K_{ae0} \end{cases} \tag{4-47}$$

where K_{rc0}, K_{rc1}, K_{rc2}, K_{rc3}, K_{tc0}, K_{tc1}, K_{tc2}, K_{tc3}, K_{ac0}, K_{ac1}, K_{ac2}, K_{ac3}, K_{re0}, K_{te0} and K_{ae0} are cutting force coefficients need to be calibrated using experimental data.

The average component cutting forces are given in Equation 4-48:

$$\begin{cases} \overline{F_x} = \dfrac{t_E - t_S + 1}{\lambda_t} \displaystyle\sum_{t=t_S}^{t=t_E} F_x^W(t) \\ \overline{F_y} = \dfrac{t_E - t_S + 1}{\lambda_t} \displaystyle\sum_{t=t_S}^{t=t_E} F_y^W(t) \\ \overline{F_z} = \dfrac{t_E - t_S + 1}{\lambda_t} \displaystyle\sum_{t=t_S}^{t=t_E} F_z^W(t) \end{cases} \tag{4-48}$$

where t_S and t_E are start and end cutting time, respectively. Cutting force coefficients can be identified by using measured average cutting forces in milling slot using B-UAM with the least squares method.

4.3 Tool flank wear prediction model in B-UAM (Phase 3C)

As demonstrated later in Section 5.2, cooling and coating conditions significantly impact the milling of γ-TiAl. Under dry cutting conditions with uncoated tools, severe adhesive wear was observed. In these conditions, a protective film was formed from the workpiece material and oxides, extending the tool's life. Coated tools provided additional protection, performing as expected under dry conditions. However, when fluid cooling was applied, rapid abrasive wear became predominant, diminishing the effectiveness of the coating material. This complexity in wear mechanisms presents challenges in establishing a predictive model for tool flank wear in

ball-end ultrasonic-assisted milling. Consequently, Ti-6Al-4V was selected to validate the tool wear model due to its hard-to-cut nature and lower adhesive wear under the cutting parameters used in this study. Some studies have also indicated that abrasive wear is the dominant mechanism of tool flank wear in dry cutting of Ti-6Al-4V using uncoated tools [267], [268]. The wear rate is primarily determined by the sliding velocity and the load applied on the flank face. Assuming that flank wear develops according to the typical wear progression as described in the pin-on-disc test mentioned in Section 2.2, the wear rate can be calculated according to Equation 4-49 [269]:

$$\frac{dVB}{dt} = \frac{K_w}{H_t}\sigma_{nt} v_c \tag{4-49}$$

where VB is the flank wear (mm), H_t is the hardness (HV) of the cutting tool, σ_{nt} is the normal stress (N/mm^2) on the flank face, v_c is the cutting velocity (mm/min) and K_w is the abrasive wear constant. The variation of the normal stress distribution on the flank face is assumed to be linear, as illustrated in Figure 4.17 [270]. The average stress on the flank (σ_n) is given by Equation 4-50:

$$\sigma_n = \frac{F_n}{w l_c} \tag{4-50}$$

where F_n is the normal force on the flank face, w is the width of the cutting edge element and l_c is the contact length on the flank edge.

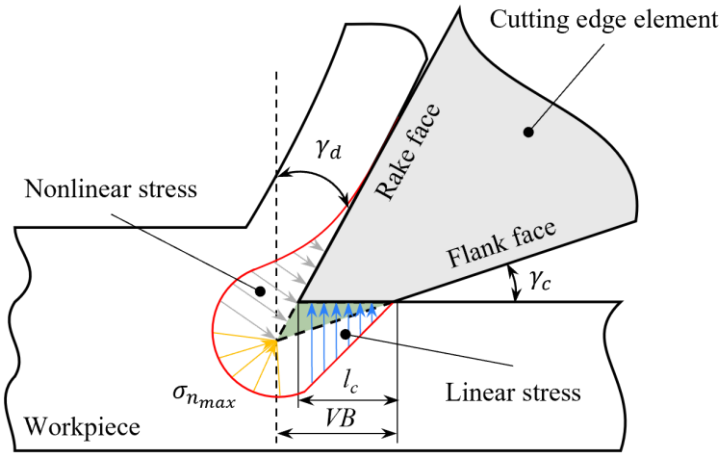


Figure 4.17 Schematic diagram of stress distribution on tool.

Depending on the tool geometry, the cutting velocity of the cutting point along the cutting edge direction will vary. The same discretisation operation is performed on the cutting edge as described previously in Section 4.2, and the wear rates of each cutting edge element are different. For any cutter element corresponding to cutting point $P(\theta, j, t)$, the width of cutter element w is equivalent to $dS(\theta, j, t)$. Moreover, the initial normal force F_{n0} is expressed by the average radial cutting force on the point P during one rotation of the tool, as shown in Equation 4-51:

$$F_{n0} = \overline{F_r} = \frac{t_E - t_S + 1}{\lambda_t} \sum_{t=t_S}^{t=t_E} dF_r(\theta, j, t) \tag{4-51}$$

The contact length of the flank l_c at any instant could be given from trigonometric relationship by Equation 4-52:

$$l_c = VB - VB \frac{\tan \gamma_d}{\cot \gamma_c} \tag{4-52}$$

where γ_d is the rake angle (°) and γ_c is the clearance angle (°).

However, the normal force exhibits significant rise as tool wear increases. Previous research found that when cutting time increased, there was a corresponding increase in the cutting force [271], [272], [273]. Moreover, the growth rate was affected by the initial cutting parameters. Equation 4-53 expresses the change in normal force F_n over cutting time (min) as a polynomial with respect to constant cutting parameters including cutting speed (mm/min), feed rate (mm/tooth) and depth of cut (mm):

$$F_n = F_{n0} + k_1 {v_c}^{k_2} {f_z}^{k_3} {a_p}^{k_4} t^{k_5} \tag{4-53}$$

The v_c in the equation is the cutting velocity at a selected cutting point P, and is calculated using Equation 4-54:

$$v_c = 2\pi NR \sin \theta \tag{4-54}$$

where N is the spindle speed (rpm), R is the radius (mm) of the ball nose end mill and θ is the axial position angle (°) of the cutting point P while k_1, k_2, k_3, k_4 and k_5 are correction

coefficients obtained from experimental data using the 1stopt software with Levenberg-Marquardt method. It should be noted that the radial cutting force of the selected cutting point cannot be measured directly using dynamometer directly. In this model, it was assumed that the ratio of the average radial force at cutting point P during cutting to the average cutting force at this point in the workpiece coordinate system, which can be measured, remained constant, as shown in Equation 4-55.

$$\frac{\bar{F}_r^{\,*}}{\bar{F}^*(\bar{F}_x^{\,*}, \bar{F}_y^{\,*}, \bar{F}_z^{\,*})} = \frac{\bar{F}_r}{\bar{F}(\bar{F}_x, \bar{F}_y, \bar{F}_z)} \tag{4-55}$$

where $\bar{F}_r^{\,*}$ and $\bar{F}^*$ are obtained from the cutting force model and $\bar{F}$ is obtained from experimental data. When flank wear increases from 0 to VB, combining Equations 4-49–4-54, given that $VB(0) = 0$, the flank wear VB can be obtained by Equation 4-56:

$$VB(t) = \sqrt{\frac{2K_w v_c}{H_t w\left(1 - \frac{\tan\gamma_d}{\cot\gamma_c}\right)}\left(F_{n0} + \frac{k_1 {v_c}^{k_2} {f_z}^{k_3} {a_p}^{k_4} t^{k_5+1}}{k_5 + 1}\right)} \tag{4-56}$$

5 RESULTS AND DISCUSSION

5.1 Phase 1A: Stability assessment of integrated ultrasonic system

5.1.1 Characteristics and influencing factors of ultrasonic actuation system

Characteristics of amplitude-frequency were key to the ultrasonic actuation system, with actuation amplitude typically the most important parameter in the ultrasonic-assisted cutting process. Figure 5.1 shows that ultrasonic power and amplitude reached peak values at the same time when the excitation frequency was 26.09 kHz (HSS twist drill with Ø4 mm, overall length 75 mm and overhang length 52 mm), which was defined as the current resonant frequency of the ultrasonic actuation system. The real-time measurement of ultrasonic amplitude was challenging in practical cutting operations while ultrasonic power can be monitored relatively easily. Wang et al. [274] reported the same result using a DMG Ultrasonic 50 machine tool and fitted the relationship between ultrasonic power and amplitude.

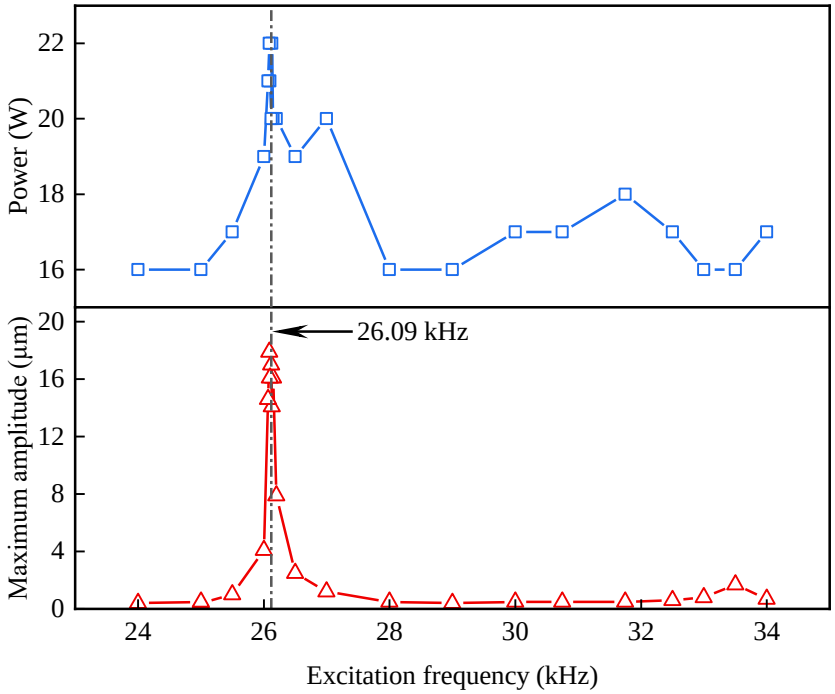


Figure 5.1 Variation of ultrasonic power and amplitude against vibrational frequency.

Notably, parameters including overall length, overhang length, tool diameter and mass directly influences the resonant frequency of the ultrasonic actuation system. The maximum amplitude variances between different tools of the same diameter are performed in Figure 5.2(a). The variation in amplitude level was mainly attributed to the cutting tool material but also partly

due to tool geometry/type. Further research proved that the ultrasonic resonant frequency and amplitude were strongly material mass sensitive, as shown in Figure 5.2(b). When using tools of the same geometry, the ultrasonic amplitude of the HSS tool with lower density (T1) was more than double that of the carbide tool (T3). Similarly, using the Ø4 mm tool (12.13 g) generated the largest amplitude of up to 8 µm while a maximum value of 2.4 µm was observed when utilising the Ø6 mm tool (25.96 g). The density of carbide was significantly higher than high speed steel leading to heavier mass. Since $f \propto \sqrt{\frac{k}{m}}$, where k represents stiffness and m represents mass, the natural frequency decreases with the mass, resulting in a low amplitude [182], [275].

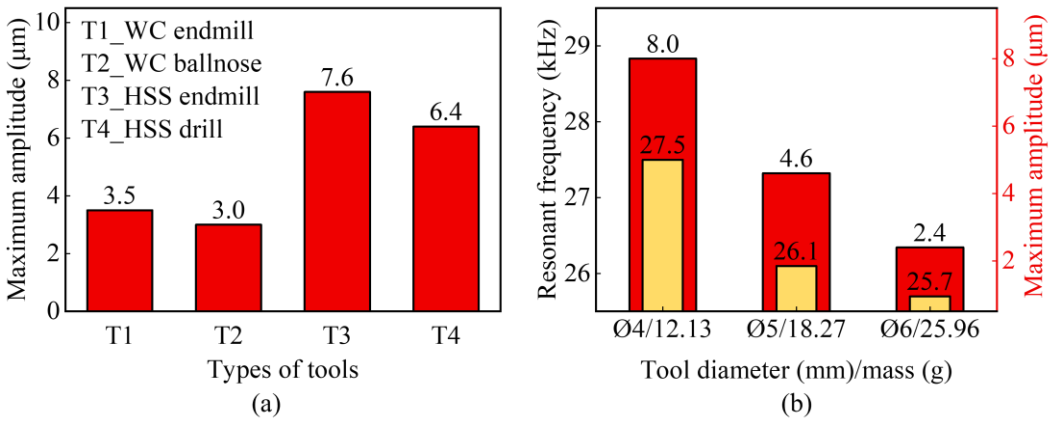


Figure 5.2 Influence of tool specification on ultrasonic amplitude; (a) Materials and geometries and (b) diameter and weight.

The importance of tool specification was further highlighted by the observation that cutter overhang length had a considerable effect on ultrasonic amplitude. Figure 5.3 compares the variation in ultrasonic amplitude for tools having different total lengths and overhangs. The results indicated that the maximum vibration amplitude was attained when the ratio of tool overhang to overall length was about 70%. Consequently, selecting appropriate tool specification and maintaining consistent tool overhang to total length ratios were prerequisites for ensuring stable vibration of the ultrasonic system. Li [182] suggested that there were multi-order vibration frequencies in the design of the horn and the cutting tool reduced the system frequency, where larger cross-sectional areas led to greater offset. For a given cutter, shorter overhang lengths resulted in an increase in resonant frequency with a corresponding reduction in ultrasonic amplitude.

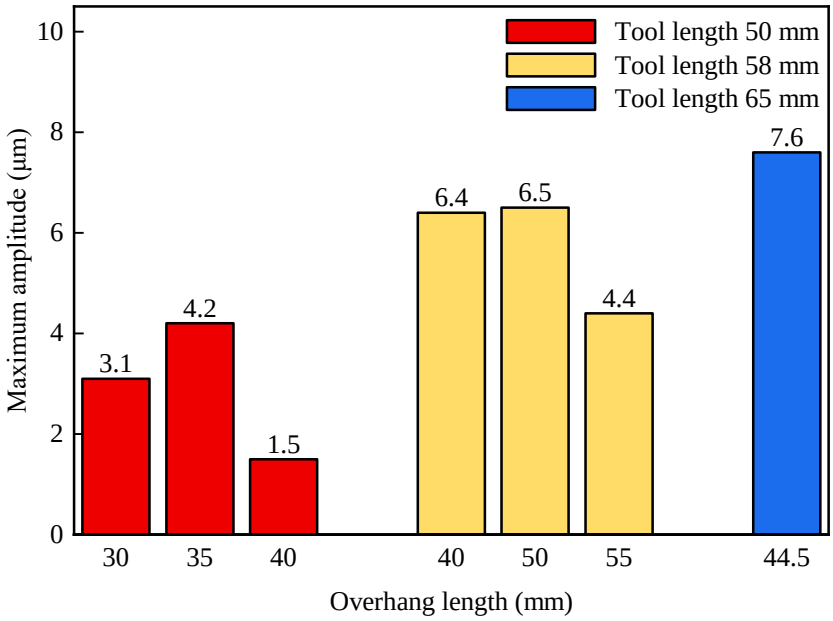


Figure 5.3 Effect of tool length and overhang on ultrasonic amplitude.

5.1.2 Effectiveness and operating limits of ultrasonic actuation system

Ultrasonic amplitude was measured by a Renishaw NC4+ high-accuracy laser tool setting system under no-load conditions. However, it was difficult to determine the in-process amplitude of the tool during machining. A method involving small-depth-cutting (SDC) was employed to assess the effective ultrasonic tool vibration amplitude during machining, with a similar strategy adopted and validated previously by Zhang et al. [276]. The effective ultrasonic amplitude was defined as the difference between the actual depth of cut measured with a Renishaw PowerProbe 400 and the nominal depth of cut. Figure 5.4 shows the maximum tool vibration amplitude measured when machining polyurethane and AA6082-T6 under different axial depth of cut. The value determined by the Renishaw NC4+ was set as the benchmark.

Polyurethane tooling board BM 5460 which has extremely low hardness (~60–65 Shore D) was utilised to simulate no-load/low-load cutting conditions, while the AA6082-T6 aluminium alloy workpiece was adopted as representative of machining typical metallic materials. Compared with the amplitude measured by the Renishaw NC4+ laser tool setter (5.8 μm) under non-machining conditions, the in-process vibration amplitudes obtained from the SDC tests showed considerably different results and variation with depth of cut. The change in maximum tool amplitude when milling AA6082-T6 aluminium alloy revealed an initial rise from 5.7 μm to 8.5 μm followed by a subsequent decrease to 4.7 μm, as the depth of cut increased from 0.01

mm to 0.40 mm, suggesting that the cutting forces generated likely led to damping of the vibration amplitude.

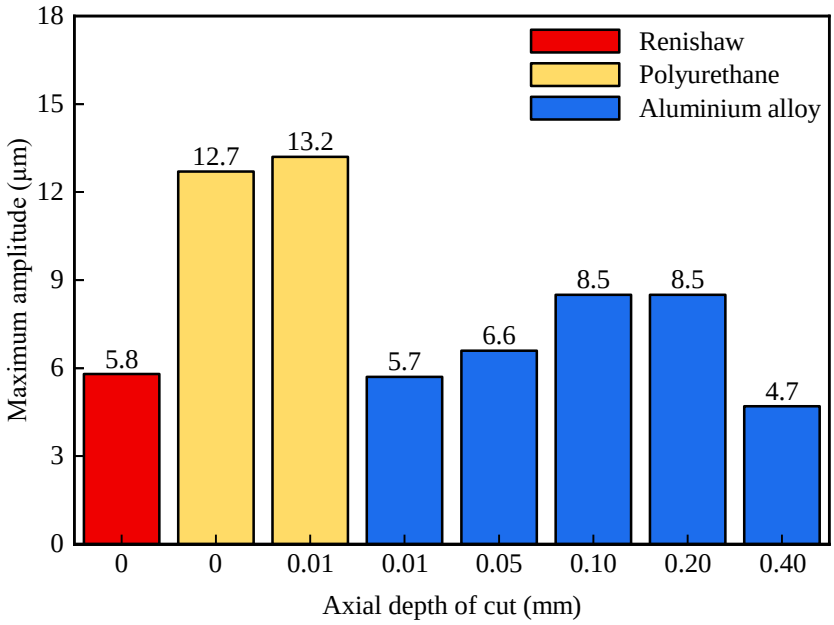


Figure 5.4 Assessment of maximum tool vibration amplitude using SDC method at different axial depths of cut.

A typical characteristic of ultrasonic-assisted machining is the reduction of cutting forces, with a maximum decrease of 24.1% recorded compared to conventional milling over the range of depths of cut evaluated, as illustrated in Figure 5.5. The level of force reduction however showed an obvious decreasing trend with the increase in depth of cut (above 0.2 mm) and corresponding cutting forces. Wang [222], and Wang et al. [274] reported that the stability of ultrasonic vibration amplitude was affected by the change in resonant frequency of the system due to the cutting forces.

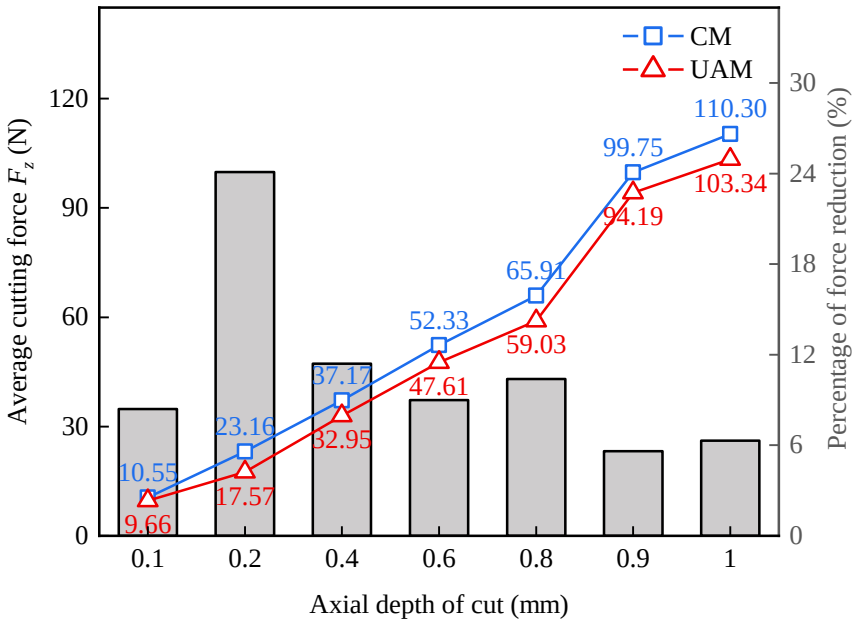


Figure 5.5 Effect of depth of cut on axial cutting force in conventional milling and ultrasonic-assisted milling of Ti-6Al-4V.

Large variations in cutting forces due to a change in cutting parameters or severe tool wear can lead to a mismatch between the resonant and excitation frequencies, eventually resulting in rapid attenuation of the ultrasonic amplitude. Li [182] also reported that while spindle speed was found to have little influence on the resonant frequency, it increased with a rise in feed rate and conversely decreased at larger ultrasonic amplitudes in the ultrasonic-assisted drilling operations. In addition, thermal loads also had a considerable influence on ultrasonic amplitude. Wang et al. [277] investigated the thermal effects on the stability of ultrasonic amplitude and presented the following conclusions:

- When the excitation frequency was lower than the resonant frequency at room temperature, heat generation from the ultrasonic vibration caused a rise in temperature of the ultrasonic system, leading to a decrease in the machine resonant frequency. The deviation between the excitation frequency and resonant frequency was reduced, resulting in the gradual increase of ultrasonic power until a new balance was reached gradually.

- When the excitation frequency was greater than the resonant frequency, the temperature of the ultrasonic system increased due to heat generation from the ultrasonic actuation. This caused the deviation between the excitation frequency and resonant frequency to

widen due to the drop in resonant frequency, leading to reduction in ultrasonic power until a new equilibrium was achieved.

- Lower deviations between the excitation frequency and resonant frequency at room temperature translates to greater initial ultrasonic power, resulting in elevated thermal effects, which in turn lead to increased fluctuations in the system's resonant frequency. Consequently, greater variation in ultrasonic power was observed.

The increase in horn surface temperature during machining experiments indicated the likelihood of thermal effects influencing the ultrasonic actuation characteristics of the tool. Although the DMG Mori Ultrasonic 20 linear CNC machining centre incorporated real-time resonant frequency finding/tracking and simultaneous power control to maintain optimal process stability, there were limitations in the tuning capability of the tracking system. When the variance in thermomechanical loads exceeded the adjustment range/threshold, the ultrasonic amplitude and power were found to decay rapidly. Therefore, a comprehensive understanding of the ultrasonic actuation system on the DMG Mori Ultrasonic 20 linear together with appropriate selection of cutting tools and parameters is necessary to maximise performance of ultrasonic-assisted machining operations.

5.1.3 Typical machining characteristics of B-UAM

Chip breaking is a common feature in ultrasonic-assisted cutting operations, with the resulting chip shape reflective of the contact conditions between the workpiece and the tools. The combined effects of ultrasonic actuation and rotational motion of the tools causes more frequent breakage and shorter chip segments. The occurrence of chip breaking in ultrasonic-assisted cutting has been widely reported in the literature [174], [278], [279], [280]. This periodic engagement and disengagement between the tool and workpiece was also considered the main reason for the decrease in cutting forces and temperature during ultrasonic-assisted cutting [281], [282], [283]. Compared to conventional cutting, the introduction of axial ultrasonic vibration was conducive to material shear slip and hence led to lower requisite forces [282]. Chip material adhesion was the primary form of tool wear when dry conventional milling aluminium alloy (v_c = 16.43 m/min (N = 3000 rpm), f_z = 0.08 mm/tooth, a_p = 0.2 mm and a_e = 0.2 mm), as shown in Figure 5.6(a). This was significantly reduced when operating in UAM mode as evident from Figure 5.6(b) due to lower cutting force and temperature.

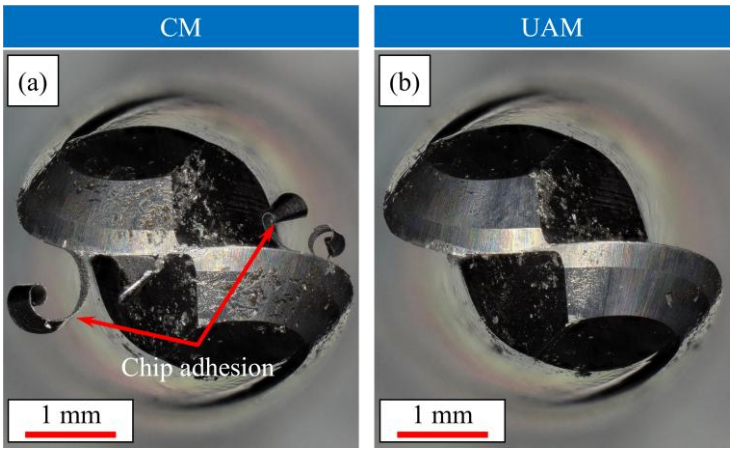


Figure 5.6 Differences in chip material adhesion level under; (a) conventional milling and (b) ultrasonic-assisted milling operations.

Figure 5.7 exhibits the typical workpiece surface texture produced following ultrasonic-assisted milling compared to conventional milling. A matte appearance was observed following UAM instead of the relatively shinier surface generated with conventional milling. Under the same depth of cut, UAM could achieve a larger actual cutting depth according to the contour plot. Clear parallel feed marks were observed on the machined surface after CM, as shown in Figure 5.8(a). In contrast, Figure 5.8(b) exhibits the regular and scale-like texture obtained when employing UAM operation, similar to results outlined in previously published research relating to ultrasonic-assisted machining [174], [221], [284], [285]. The texture of machined surfaces are largely influenced by the tool tip trajectory and Chen et al. [285] reported that when the ultrasonic frequency was an odd multiple of the spindle rotation frequency, scale features were generated by the overlapping adjacent cutting tool teeth. Zhang et al. [221] also investigated surface morphology in elliptical ultrasonic-assisted milling and revealed that increased cutting speed resulted in more obvious ultrasonic textures.

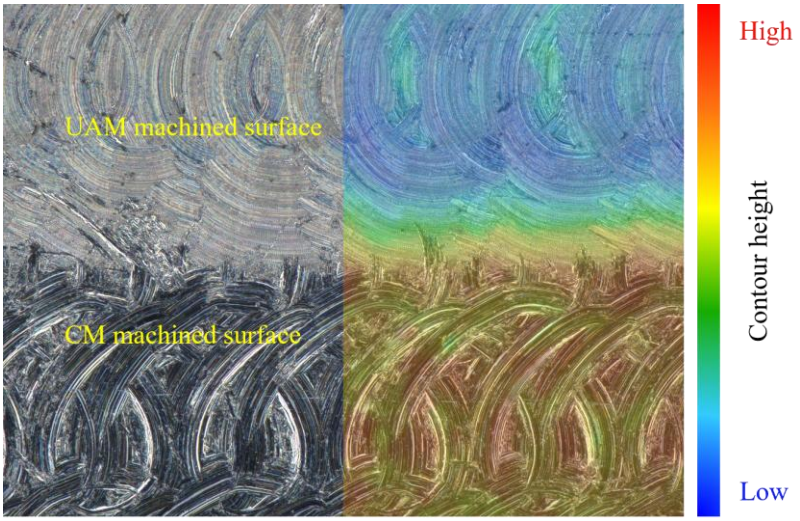


Figure 5.7 Comparison of machined surface morphology generated following UAM and CM.

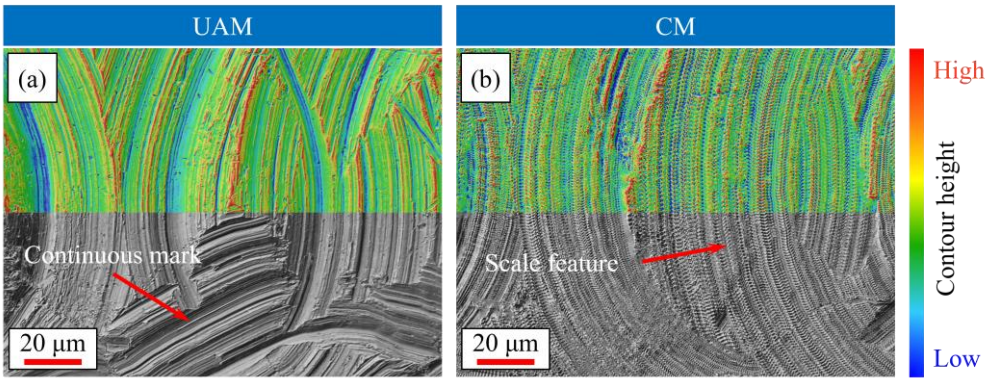


Figure 5.8 Machined surface texture following; (a) UAM and (b) CM.

Figure 5.9(a) depicts the chip surface morphology obtained under the CM with continuous marks. The ultrasonic vibration of the cutting edge in UAM conversely induced intermittent cutting in micro-localities, resulting in more uniform and regular scaly contours in accordance with Figure 5.9(b). The chips shown in Figure 5.9 were obtained from machining aluminium alloys, which have relatively high ductility, causing the continuous ribbon shaped chip formation. However, the sawtooth or wavy chip were often observed when machining materials like titanium alloys and steel. Ahmed et al. [174], [213] believed that the large cutting forces in CM led to a significant ploughing effect, which, combined with unstable plastic deformation and adiabatic plastic slip, ultimately resulted in sawtooth or wavy chip formation. UAM process presented stability of the shearing process and lower cutting force, which indicated the generation of a smooth chip surface. However, Nakayama et al. [286] reported that periodic crack formation was the root cause of sawtooth chip morphology rather than the periodic

formation of adiabatic concentrated shear bands. Furthermore, the main driver responsible for wavy chip formation was identified as a negative stress-strain characteristic on the shear plane due to the presence of microcracks [287]. Gao and Jin [288] investigated the influence of ultrasonic-assisted cutting on the chip formation mechanism in Ti-6Al-4V and found that the introduction of ultrasonic vibration promoted lower temperature and cutting forces in the primary zone due to the periodic tool-workpiece contact condition.

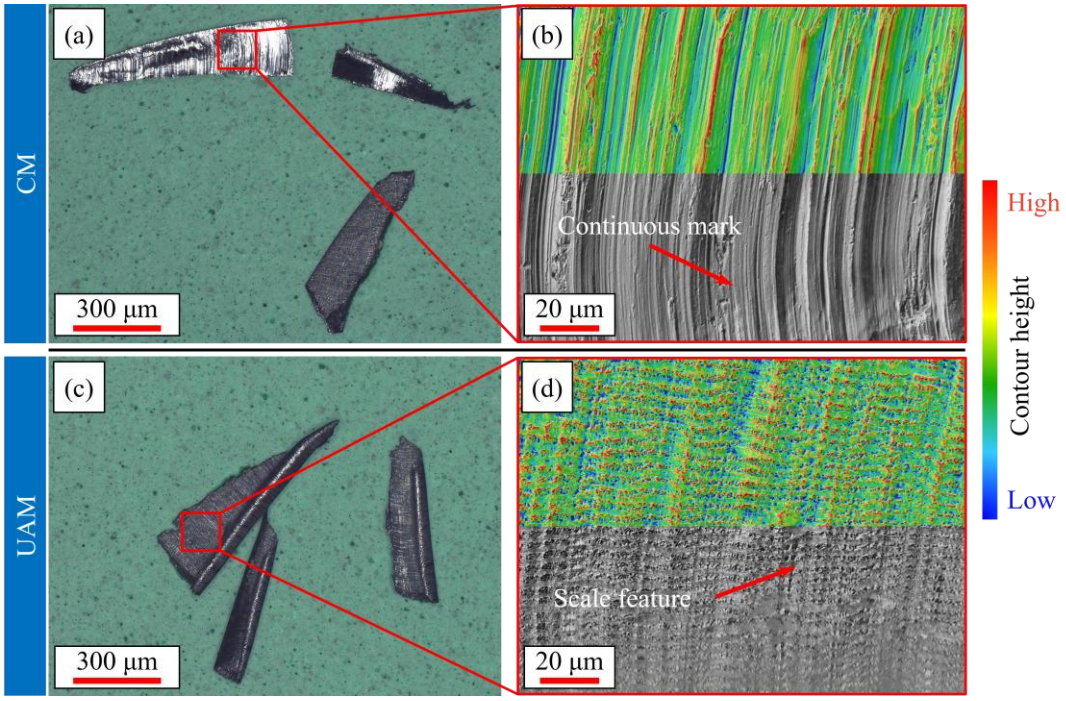


Figure 5.9 Comparison of chip morphology generated following CM and UAM under (a) and (c) low magnification and (b) and (d) high magnification optical microscopy.

5.2 Phase 1B: Influence of operating parameters on machinability when milling γ-TiAl

5.2.1 Influence of cutting parameters on tool wear

Figure 5.10 exhibits the maximum tool flank wear as a function of cutting distance for all tests in the Taguchi L_{16} orthogonal array experiment. A significant proportion of tests achieved the end of the test criterion (CL_{max}) of 230 m distance machined without reaching the tool life criterion (VB_{max}) of 180 µm flank wear. In general , tool wear rate was typically faster in tests involving ultrasonic assistance, while trials undertaken dry attained longer cutting distances.

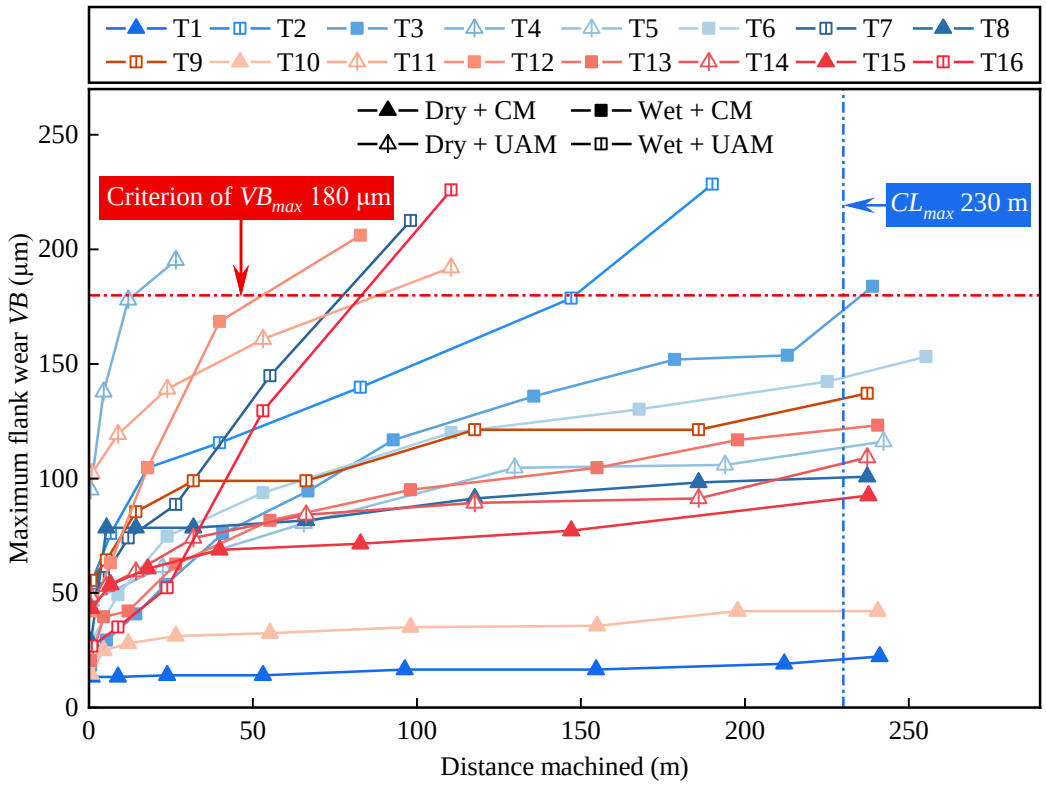


Figure 5.10 Maximum flank wear against distance machined for Phase 1B experiments.

However, the machined distance could not accurately reflect the machinability. Hence, the change in flank wear with machined distance was converted into flank tool wear with material removal volume, as shown in Figure 5.11. Intuitively, the impact of ultrasonic vibration could not be clearly defined, although dry cut conditions still appear to result in longer tool life. Statistical analysis was employed to investigate the effect of each cutting parameter on tool life, as the Taguchi approach involved factors changing their levels for each test.

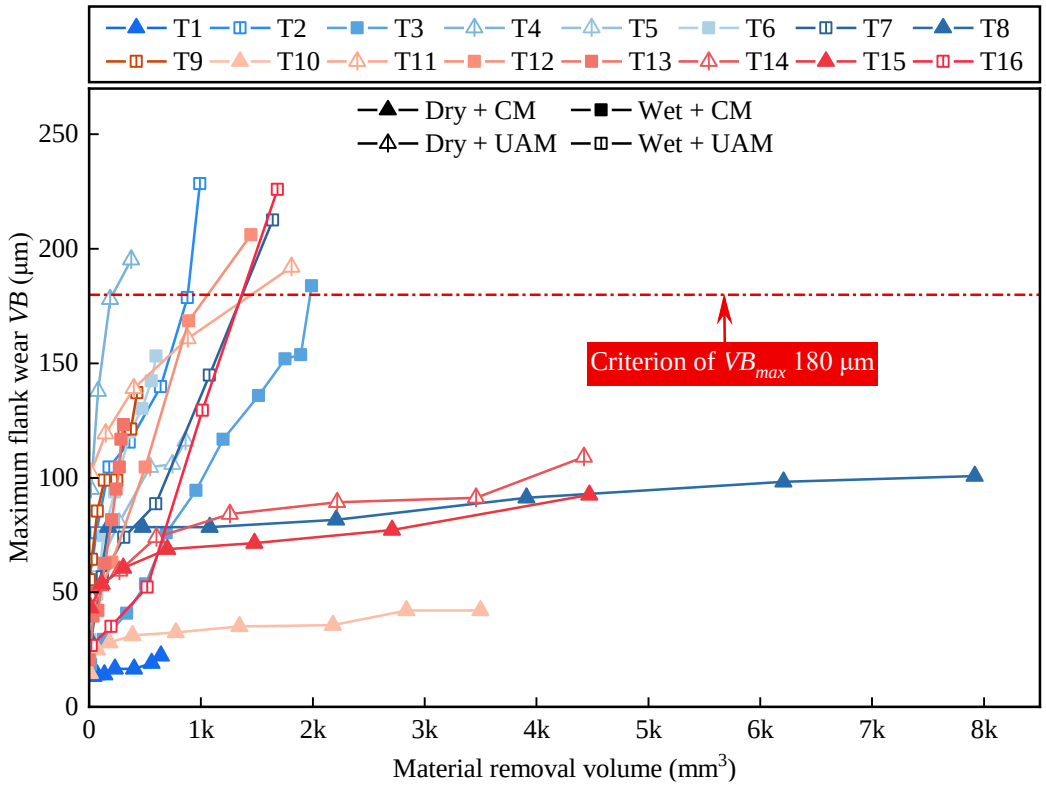


Figure 5.11 Maximum flank wear against material removal volume for Phase 1B experiments.

Figure 5.12 and Figure 5.13 displays the typical tool wear observed from the tool flank face and rake face in the representative tests T11 and T16 while the early, middle, and last stages of the tool life trial. The dry cut condition was employed in T11, while T16 was conducted under the wet cut. The morphology of cutting edge under wet conditions had advantages in the early wear stage. However, the subsequent wear process was stable for dry cut and showed rapid deterioration for wet cut, as illustrated in Figure 5.13(b) and (c). All the ball nose end mills used in Phase 1B were tungsten carbide with PVD TiAlN coating. The fast disappearance of the coating in the cutting region was also one of the characteristics discovered in wet cutting.

Meanwhile, tool failure formation edge chipping was widely observed in the last stages of wet cut, see Figure 5.13(f). The low thermal conductivity property of γ-TiAl was believed to be the main cause of tool failure. Heat accumulation and low heat dissipation in cutting edge regions introducing steep temperature gradients would lead to tool damage. Additionally, severe tool failure was reported in cutting γ-TiAl [63], [65], [81]. They explained that the edge chipping was because as the tool wear augmented, the cutting force increased. The cutting edge was subjected to cyclic impact loads during the intermittent milling process, eventually leading to edge chipping.

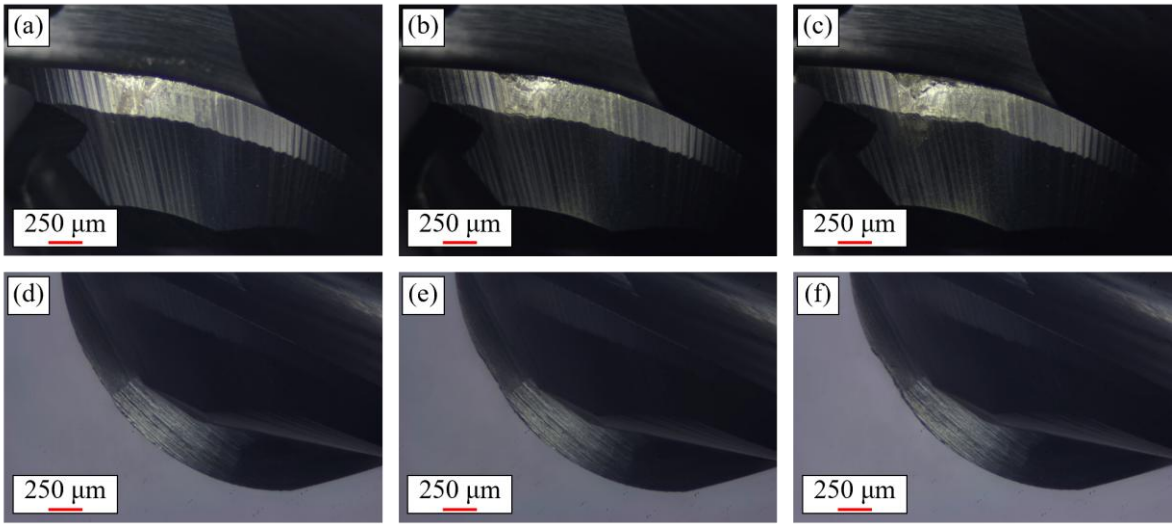


Figure 5.12 Morphology of cutting tool surface in test T11 with dry cut condition; (a), (b) and (c) flank face and (d), (e) and (f) rake face.

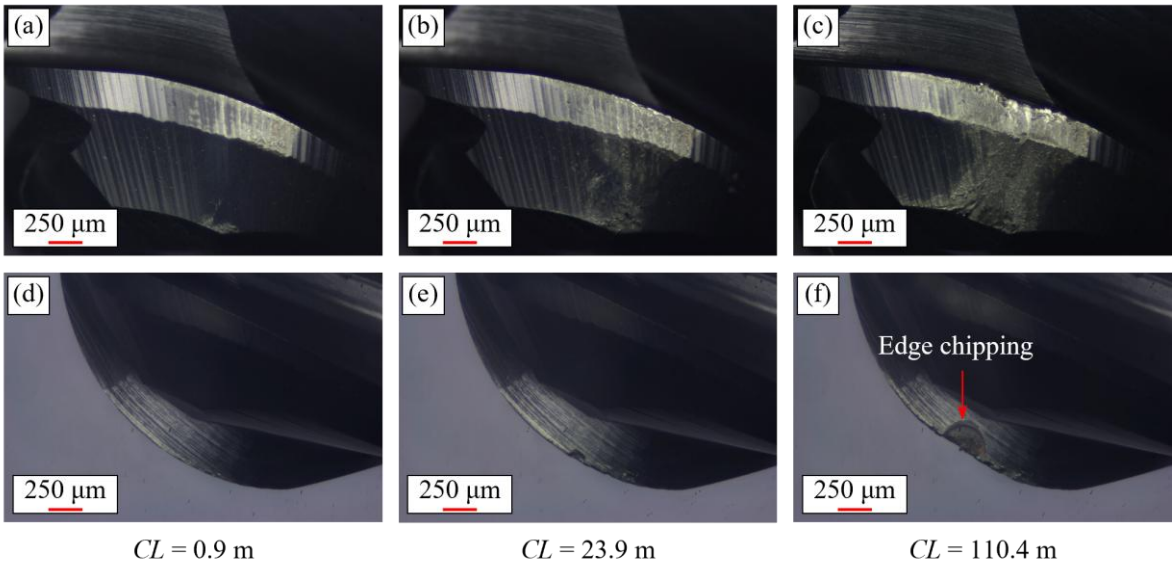


Figure 5.13 Morphology of cutting tool surface in test T16 with wet cut condition; (a), (b) and (c) flank face and (d), (e) and (f) rake face.

Tool wear on the secondary relief face was found, especially when the tool was at a high wear level, as presented in Figure 5.13(c). Sharman et al. [289] analysed that large tool bending deflection occurred due to cutting tools with longer overhang lengths. Tool deflection would reduce the actual depth of cut as the tool rotated and triggered contact between the secondary relief face and machined surface. The wear on the relief face was only induced by rubbing against the workpiece. However, tool wear and failure mechanisms were a complicated topic.

It was a composite problem affected by thermomechanical load, including diffusion wear and oxidation wear caused by element transfer or reaction. The tool wear and failure mechanisms will be discussed in-depth in Section 5.3.

The average tool wear rate was defined as the incremental amount of flank wear per unit volume (cm^3) of removed material at each stage. The full-form design used in the Taguchi L16 fractional factorial orthogonal array did not have enough total degrees of freedom (DF), making it impossible to perform an Analysis of Variance (ANOVA). The residual error was the factor with the lowest sum of squares (SS) and the modified ANOVA was conducted. Factor ultrasonic assistance had the minimum SS and was set as the residual error. The ANOVA results for the average tool wear rate are shown in Table 5.1. According to the F-table (see Table A.2) of critical values for significance level = 0.1, $F_{0.10}(3,1) = 53.59$ and $F_{0.10}(1,1) = 39.86$ [290]. The analysis revealed no factors significantly influenced the average tool wear rate at the 10% significance level.

Table 5.1 Modified ANOVA analysis of average tool wear rate.

Source	DF	Seq SS	Adj MS	F-Value	P-Value	Contribution
A	3	11056	3685	0.79	0.656	4.98%
B	3	27817	9272	2.00	0.470	12.52%
C	3	40332	13444	2.90	0.402	18.16%
D	3	71676	23892	5.15	0.311	32.27%
E	1	24898	24898	5.37	0.259	11.21%
G	1	41682	41682	8.99	0.205	18.77%
Error	1	4638	4638	-	-	2.09%
Total	15	222099	-	-	-	100.00%

* None of the factors significantly influence the average tool wear rate at the 10% level.

Figure 5.14 is the main effects plot for the average tool wear rate. Considering the main effects of signal-to-noise (S/N) ratio results, as shown in Figure 5.15, optimal cutting parameters were confirmed. Notably, a smaller-is-better S/N ratio was employed to calculate the average tool wear rate characteristic. To maximise the material removal volume at the test parameters factor level while maintaining a low average wear rate, 80 m/min cutting speed, 0.15 mm depth of cut, 0.15 mm width of cut, 0.02 mm/tooth feed rate, HU cutting orientation, conventional milling, and dry cut should be used. Besides, since the average S/N ratio of the feed rate had the largest delta value at 10.87, the feed rate was the factor that had the greatest impact on the average tool wear rate in milling γ-TiAl among the above seven factors, where the delta value in Minitab

Statistical Software was the difference between the highest average response characteristic and lowest average response characteristic.

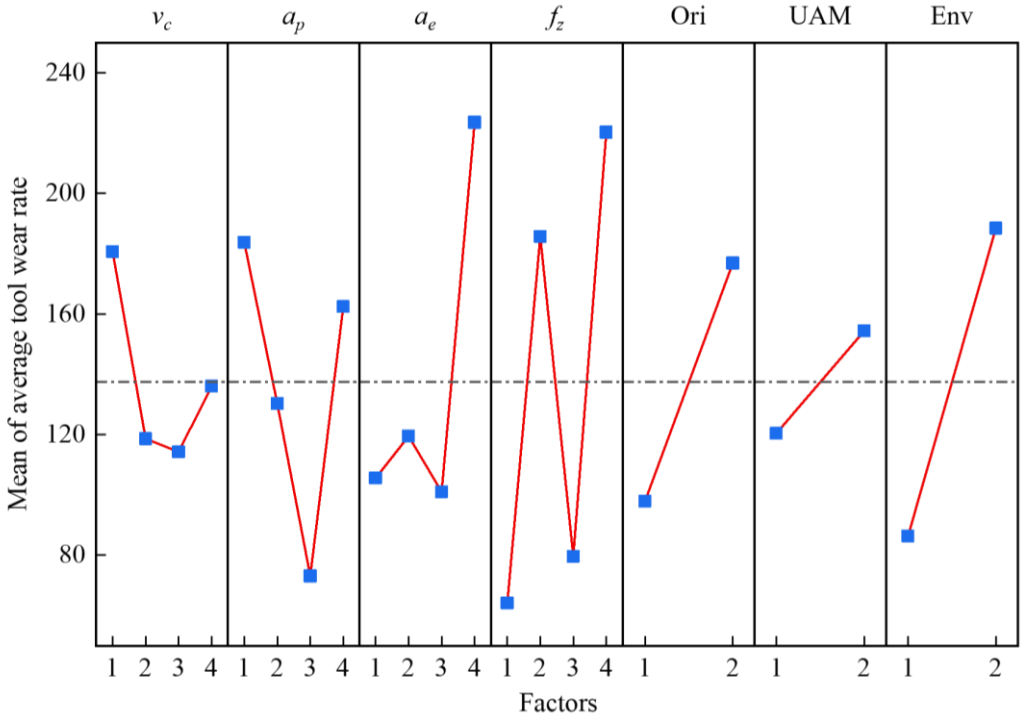


Figure 5.14 Main effects plot for average tool wear rate.

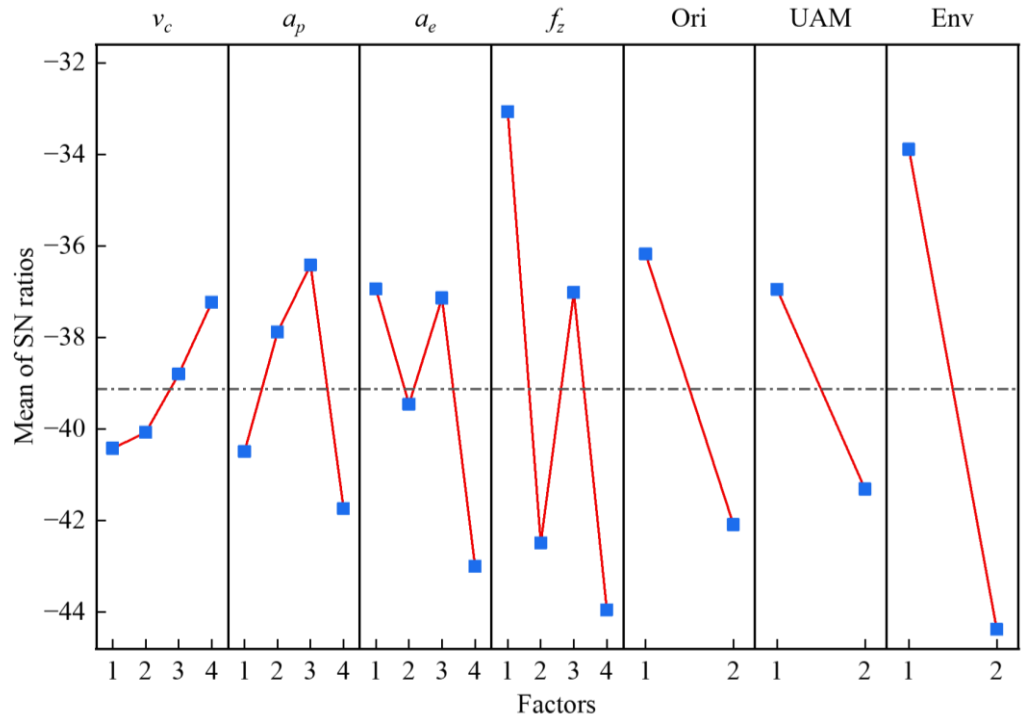


Figure 5.15 Main effects plot for average tool wear rate S/N ratios.

Cutting speed was generally considered to have the most sensitive effect on tool life, which increment would result in rising temperature [97], [291]. In Hood's research [292], when cutting speed in high-speed milling γ-TiAl exceeded 100 m/min, the machined distanced, representing tool life, decreased rapidly. However, in the Phase 1B test, the cutting speed was increased from 40 m/min to 80 m/min, and the average tool wear rate was significantly reduced. Further up to cutting speed, the average wear rate began to show an upward trend. Low ductility and extreme brittleness of γ-TiAl at room temperature were the root causes of it being difficult to cut in terms of the conclusion reported by Fan et al. [91], higher workpiece temperature could significantly enhance the machinability of γ-TiAl. The tool life was improved by appropriately increasing the cutting speed with an induced higher temperature, resulting in lower cutting force. Furthermore, higher cutting speed would aggravate abrasive wear and the impact of thermal load on the tool-workpiece contact region, triggering the drop in tool life.

5.2.2 Effects of cutting parameters on cutting force

Different from the smooth curve of cutting force in conventional milling, high-frequency vibration in ultrasonic-assisted milling caused the instantaneous cutting force to show intensive fluctuations based on changes in conventional curves, as depicted in Figure 5.16. The forces in the feed direction, stepover direction, and normal direction of the workpiece were defined as Fx, Fy and F_z. In accordance with all data from the Phase 1B experiment, the force change trends in three directions were consistent. Hence, F_z was selected as the representative parameter to analyse the influence of cutting parameters on cutting forces because the mean change of F_z was more obvious than the other two forces.

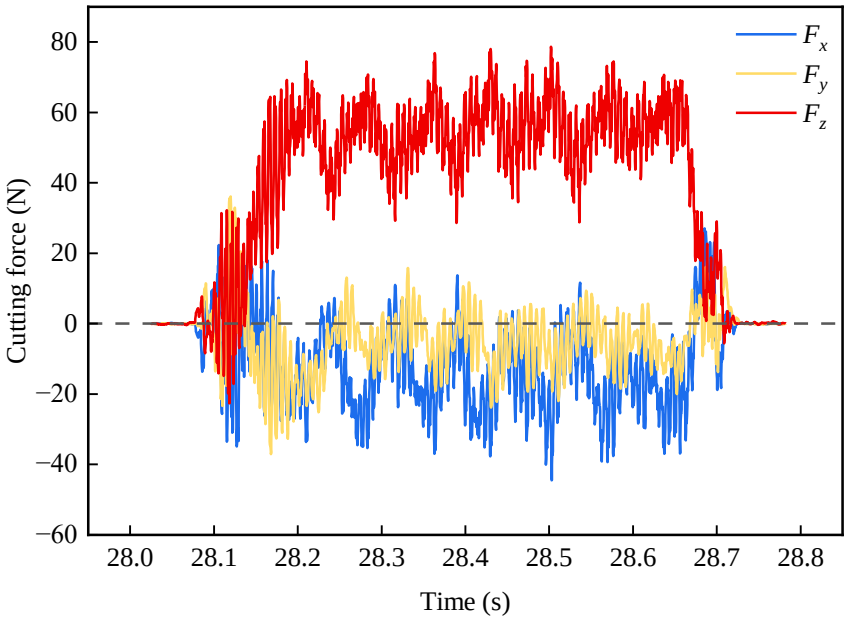


Figure 5.16 Characteristics of instantaneous cutting force changes in B-UAM.

Figure 5.17 details the cutting force F_z as a function of the distance machined for all Taguchi experiments. In addition, the changing plot of cutting force and material removal volume is shown in Figure 5.18. From an overall perspective, the cutting force variation increased sharply under most wet cut conditions. In contrast, dry cutting could complete machining with a lower growth rate of cutting force before reaching the tool life criteria. Meanwhile, the cutting force growth rate seems to be lower under ultrasonic-assisted milling. The deterioration of the cutting tool, including tool wear and failure, was the root reason for the increase in cutting force.

Regarding the point view summarised before, dry cut conditions exhibited more beneficial cutting results for γ-TiAl. Ge et al. [58] conducted high-speed milling using a TiAlN coated tool under dry conditions, significantly improving both cutting force and tool. Benedicto et al. [87] reported similar conclusions in turning 43.5Al-4Nb-1Mo-0.1B under different cooling strategies, including MQL, cryogenic, and dry. Dry cutting provided longer tool life than cryogenic cooling, whereas MQL was preferred. Hood et al. [65] also validated that average cutting forces along the stepover, feed, and thrust directions significantly reduced in dry cutting.

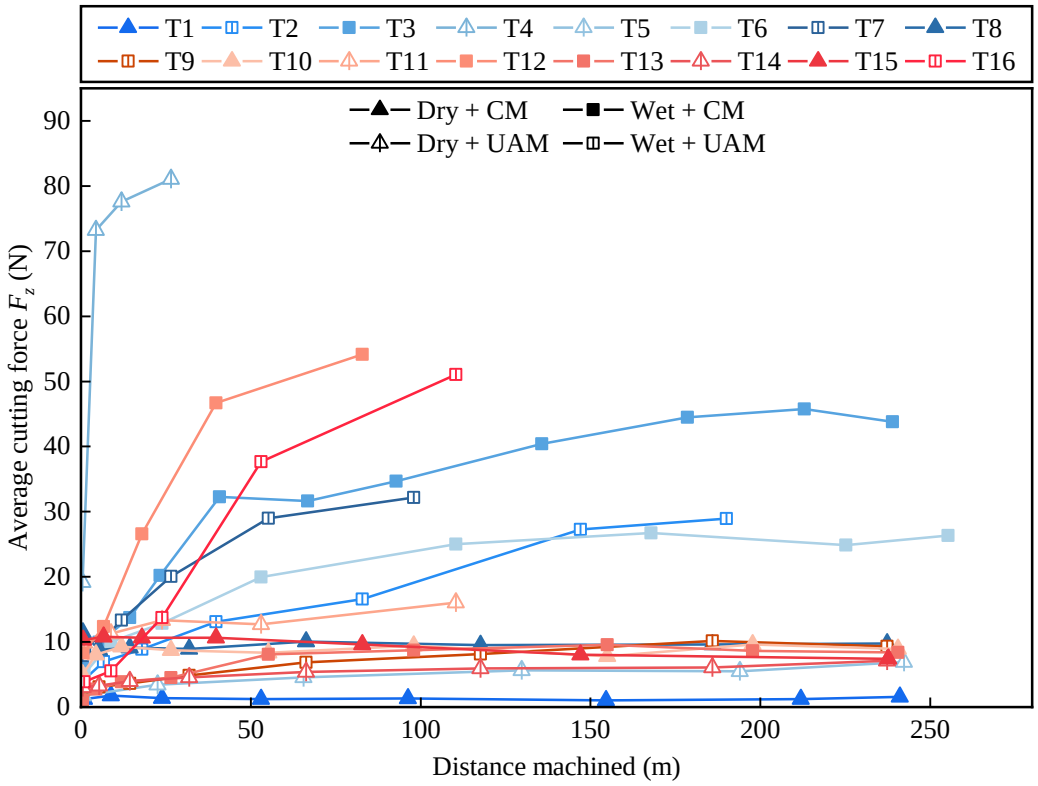


Figure 5.17 Average cutting force against distanced machined for Phase 1B experiments.

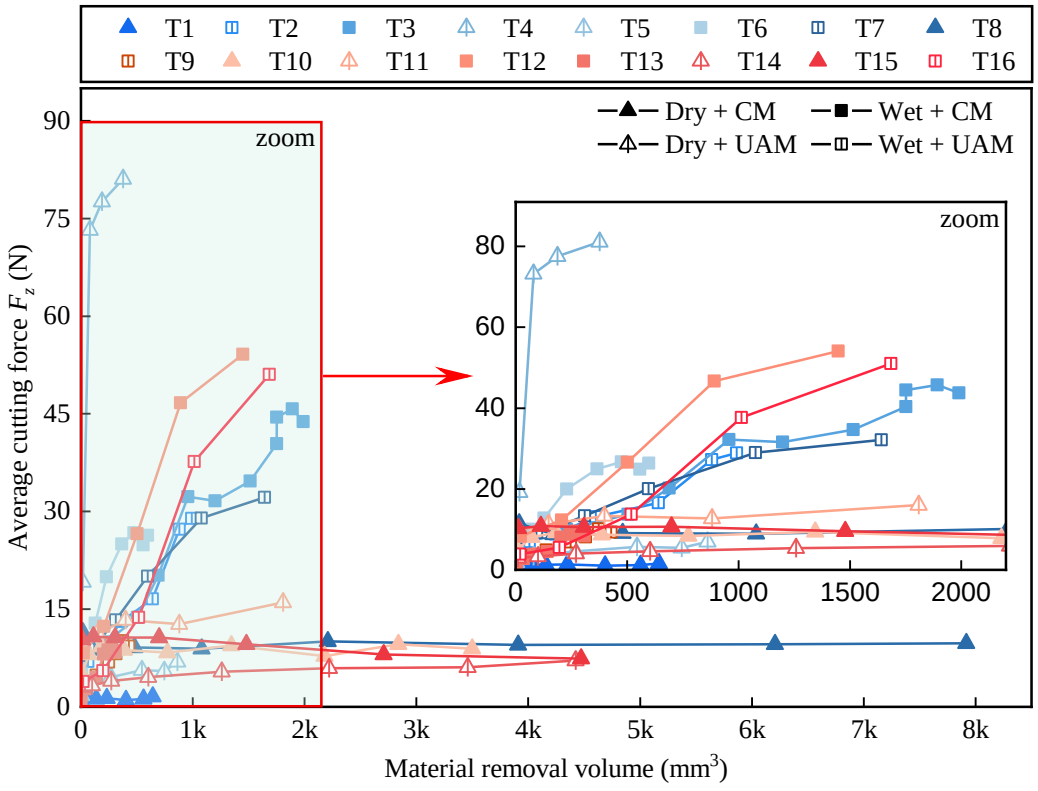


Figure 5.18 Average cutting force against material removal volume for Phase 1B experiments.

Table 5.2 is the ANOVA analysis results for the initial average cutting force F_z. Factor ultrasonic assistance had the minimum SS and was set as a residual error. The depth of cut and the cutting environment were determined as statistically significant at the 10% significance level.

Table 5.2 Modified ANOVA analysis of initial average cutting force F_z.

Source	DF	Seq SS	Adj MS	F-Value	P-Value	Contribution
A	3	22.491	7.4969	10.40	0.233	6.69%
B	3	199.053	66.3511	92.06*	0.076	59.19%
C	3	22.621	7.5403	10.46	0.223	6.73%
D	3	58.044	19.3480	26.85	0.141	17.26%
E	1	4.389	4.3886	6.09	0.245	1.31%
G	1	28.954	28.9544	40.17*	0.100	8.61%
Error	1	0.721	0.7207	-	-	0.21%
Total	15	336.273	-	-	-	100.00%

* Depth of cut and cutting environment significantly influence the initial average cutting force F_z at the 10% level.

Figure 5.19 is the main effects plot for the initial average cutting force F_z and the main effects for the S/N ratio are shown in Figure 5.20. The cutting force was influenced by tool wear, and analysis was conducted under the condition that all tools were new, which meant the tool wear status was uniformly zero. The smaller-is-better S/N ratio was utilised in the calculation. To maintain lower cutting force at the test parameters factor level, 100 m/min cutting speed, 0.05 mm depth of cut, 0.15 mm width of cut, 0.04 mm/tooth feed rate, and dry cut should be arranged. Changes in cutting orientation and ultrasonic assistance did not differ significantly over the range of test levels.

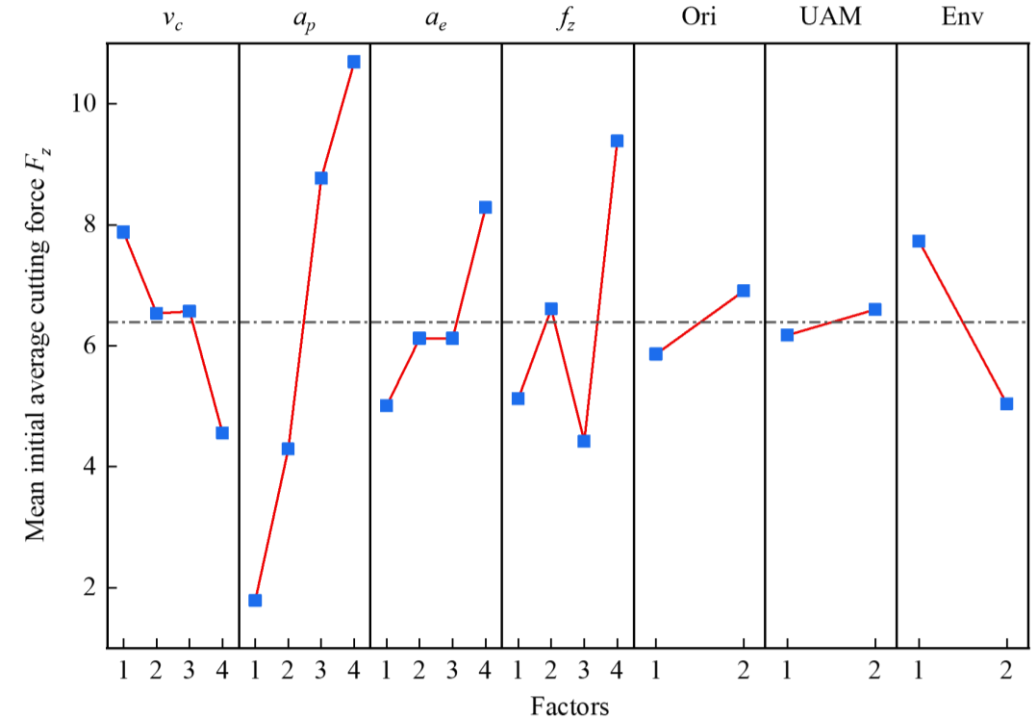


Figure 5.19 Main effects plot for initial average cutting force F_z.

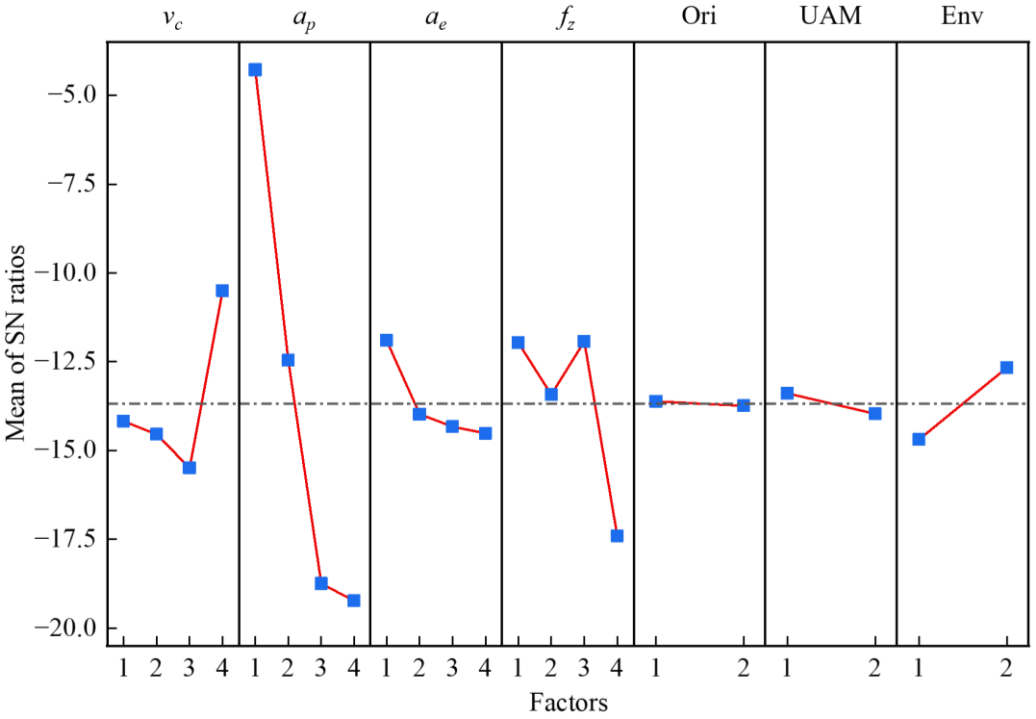


Figure 5.20 Main effects plot for initial average cutting force F_z S/N ratios.

The depth of cut was the factor that had the greatest effect on the initial average cutting force F_z in milling γ-TiAl among the above seven factors since the average S/N ratio of the depth of cut had the largest delta value at 14.955. Hood [292] also emphasised the axial depth of cut had

the biggest impact on cutting force, which led each force component to increase by up to 400% in some cases.

5.2.3 Assessment of cutting parameters on workpiece surface integrity

5.2.3.1 Surface morphology and edge quality

Figure 5.21 shows typical defect forms in milling γ-TiAl, including material pullout, breakage, negative burrs and positive burrs. γ-TiAl exhibits extremely low ductility at room temperature due to a limited number of slip systems [21], resulting in poor surface quality. Similar damage formations have been reported in most investigations on cutting γ-TiAl [53], [55], [102]. Furusawa et al. [54] presented that large-scale chipping often occurs when cracks develop near the edges of the workpiece. In accordance with experimental results presented by Hood et al. [65], extensive material fracture or pullout appeared with high frequency, especially when selecting high level cutting parameters. Increasing the temperature in the shear zone to exceed the brittle-plastic transition temperature of the γ-TiAl could improve the ductility of the γ-TiAl. Increasing cutting speed was one of the most common methods. Uhlmann and Herter [57] obtained free defects surface by controlling the cutting speed at 300 m/min. Mantle and Aspinwall [51] also presented an improved surface in milling γ-TiAl with spindle speed reaching 20,000 rpm. On the other hand, Fan et al. [91] designed an induction-assisted milling process to preheat the workpiece and also observed a better machined surface. Certainly, choosing a smaller depth of cut and feed rate could also control the cutting process in ductile mode removal to realise low damage cutting.

Figure 5.22 displays the typical machined surface morphology under various cutting parameters at the initial and final stages of tool wear. As shown in Figure 5.22(a), a near defect-free CM surface was achieved with a new tool, where a distinct texture created by the trajectory of the cutter edge was evident. However, this initial surface quality deteriorated, giving way to a coarse surface characterised by material pullout and chip adhesion. A similar degradation in surface quality was observed in ultrasonic-assisted milling, where the distinct scale features attributable to ultrasonic vibration were diminished after significant tool wear, as depicted in Figure 5.22(c) and (d).

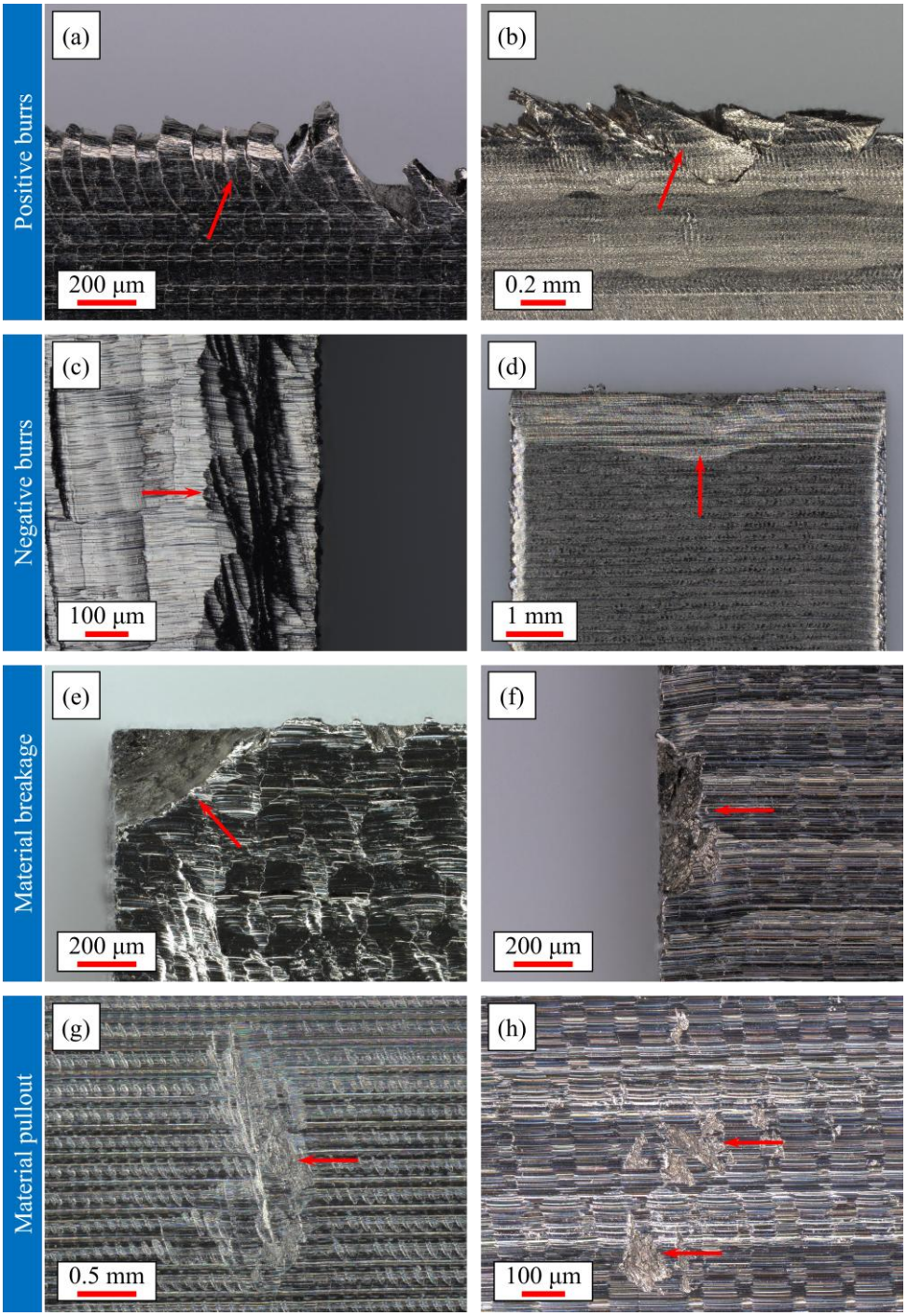


Figure 5.21 Typical defect forms on γ-TiAl machined surface.

The cutting ability of the tool decreased due to the geometry changes, which in turn led to greater cutting forces, resulting in the increment of microcracks. Microcracks were more likely to expand and eventually break after being subjected to higher stress [54], [114]. Meanwhile, the cutting tool with a long overhang length induced bending deflection during the cutting process, which triggered contact between the secondary relief face and the machined surface.

Intense rubbing between the cutter and the machined surface caused secondary extrusion of the machined surface [289]. The chips remaining on the cutter surface would adhere to the workpiece, and it would also induce the machined surface material to stick to the cutting tool and be pulled out to form pits.

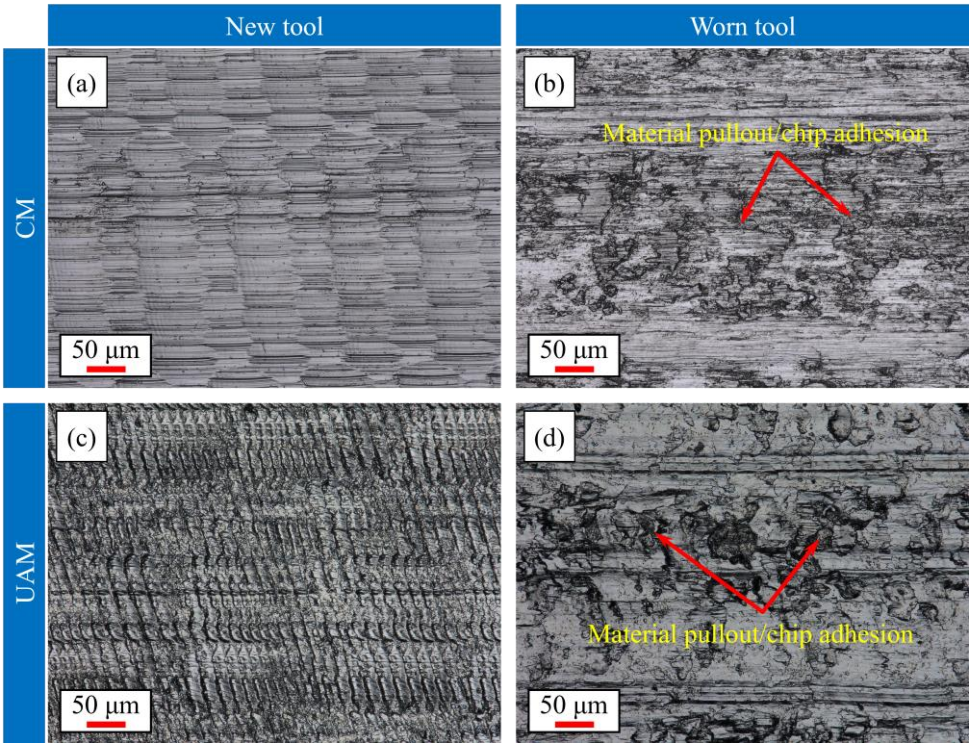


Figure 5.22 Machined surface morphology under different cutting conditions; (a) and (b) are from T13 (v_c = 100 m/min, a_p = 0.05 mm, a_e = 0.30 mm, f_z = 0.03 mm/tooth, HD, CM, wet cut) and (c) and (d) are from T14 (v_c = 100 m/min, a_p = 0.10 mm, a_e = 0.25 mm, f_z = 0.02 mm/tooth, HD, UAM, dry cut).

There are three main defect manifestations on the edge, as shown in Figure 5.23. Burr-free or short burr occurred in the entry of cutting, while long burr was observed in the exit. As tool wear intensified, the long burr decreased and was switched by more serious edge chipping or negative burr. Long burr was normally observed in cutting metals with good ductility, like aluminium [293]. Burr formation was defined as four stages, namely initiation, development, pivoting point and final formation stages, and further developed into 8 detailed stages considering the difference between ductile and brittle materials [294]. The initial five stages of the cutting process, including continuous cutting, pre-initiation, initiation, pivoting and burr development, are depicted as facilitating burr formation without inducing crack generation in both ductile and brittle material cutting. In ductile materials, cracks begin and propagate around

the tool tip within the primary shear zone, closely following the cutting line. Conversely, in brittle materials, cracks are initiated in the negative shear zone around the tool tip and extended along this zone. Subsequently, as the chips are sheared away along the cutting line, positive burrs form in ductile material cutting. In contrast, in brittle materials, the shearing-induced cracks could transform into openings, leading to a fractured surface with a negative burr on the edge.

γ-TiAl exhibits significant brittleness at room temperature and becomes more ductile as the temperature increases. Positive burr and negative burr occurred at the same time during the γ-TiAl milling experiment in Phase 1B, as depicted in Figure 5.23(c) and (d). That means γ-TiAl performed both ductile and brittle characteristics with certainty cutting conditions.

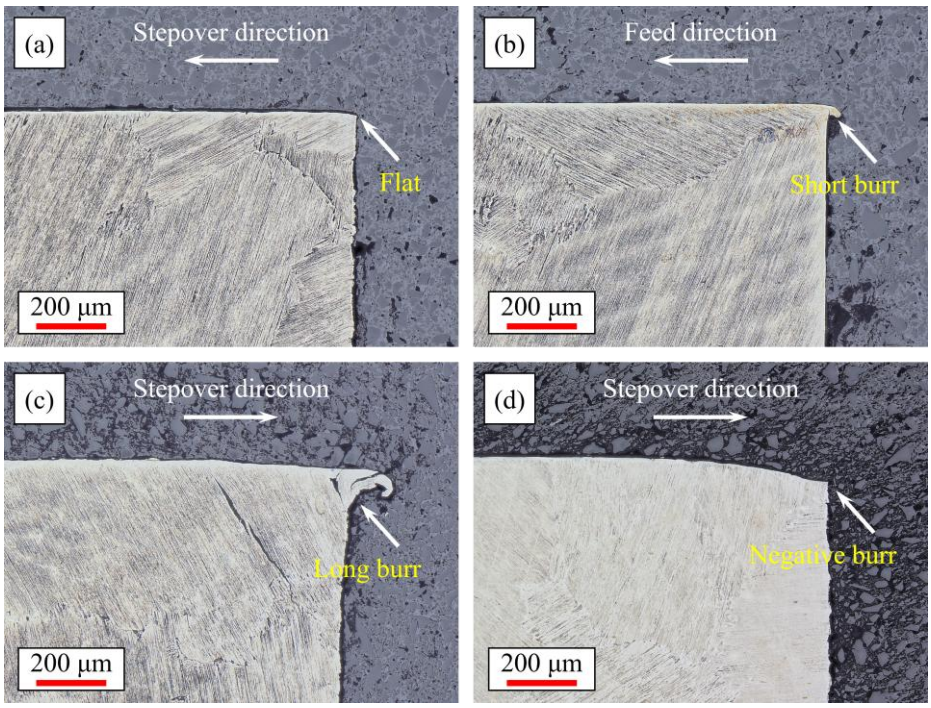


Figure 5.23 Different manifestations of edge defects machined by (a) T8 worn tool, (b) T7 new tool, (c) T5 new tool and (d) T16 worn tool.

For brittle materials, according to the strength criteria of plastic materials, traditional research believed that when the maximum principal stress σ_{max} inside the material exceeded the yield limit stress σ_b of the material, the material will fracture and fail, resulting in edge chipping [295]. However, Wang et al. [296] proposed a modified edge chipping formation mechanism for drilling brittle materials based on brittle fracture mechanics. When the thickness of the remaining material supporting the axial cutting force continued to decrease to a certain critical

value, the microcracks generated during the material removal process expanded under the action of the axial cutting force, forming exit chipping. A similar viewpoint was mentioned in drilling ductile material. Costa et al. [297] believed that the thin layer with high flexibility material at the end hindered the drilling process but was pushed out by the drill, and burrs were formed. Analogous to the milling process, this explains why the exit had more significant burrs than the entrance, as summarised in Figure 5.24.

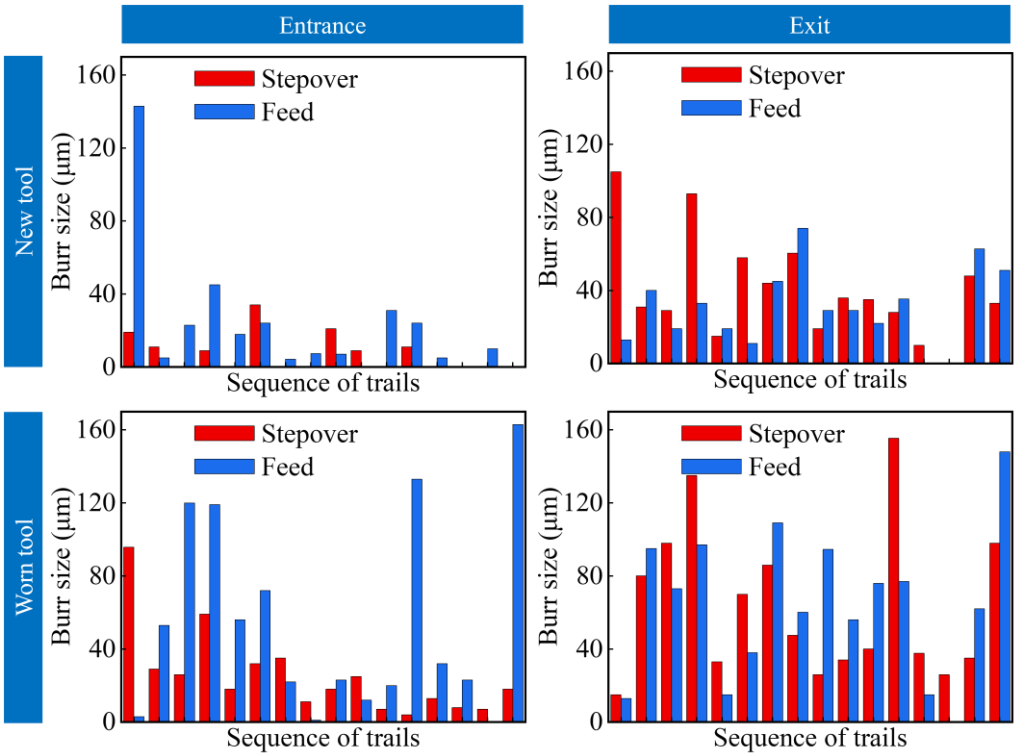


Figure 5.24 The size of entrance and exit burrs under different tool wear stages.

From the perspective of material structure, the lamellar microstructure of γ-TiAl intensified this phenomenon. Three main fracture sources of interface delamination were summarised by Chan and Kim [114] including trans-lamellar fracture, α_2/γ interface delamination, and de-cohesion of the α_2/γ colony boundaries. Creaks led by de-cohesion of α_2/γ colony boundaries were observed in T5 under dry cutting conditions, as shown in Figure 5.25(a). The crack propagated along the lamellar microstructures and promoted the rapid increase through high shear stress [86]. On the contrary, γ-TiAl presented more brittleness under the cooling conditions, chip separated along the negative shear zone, resulting in negative burrs occurred, as displayed in Figure 5.25(b).

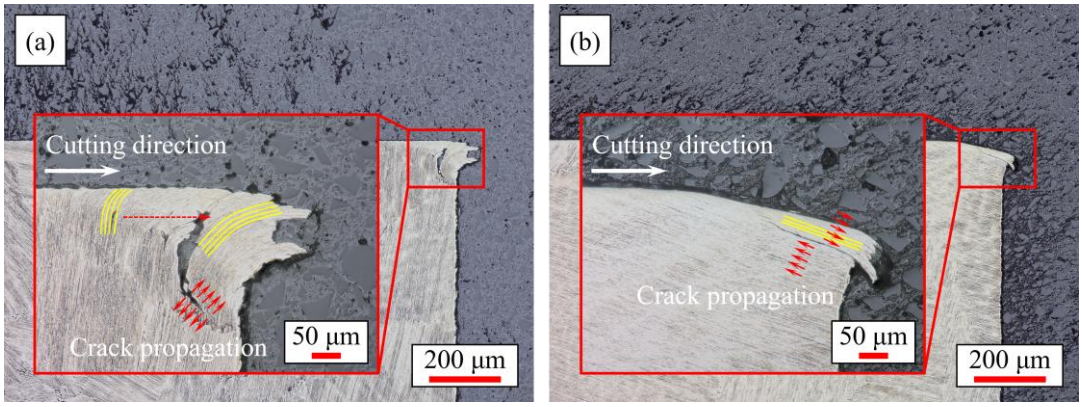


Figure 5.25 The formation process of burr; (a) Positive burr and (b) negative burr.

Excluding the influence of tool wear, the main effect of cutting parameters on exit burrs in the stepover direction was investigated. Table 5.3 is the ANOVA analysis results for the initial exit burr size along the stepover direction. Factor ultrasonic assistance had the minimum SS and was set as a residual error. The analysis revealed that none of the factors significantly influenced the exit burr size along the stepover direction at the 10% significance level.

Table 5.3 Modified ANOVA analysis of initial exit burr size along the stepover direction.

Source	DF	Seq SS	Adj MS	F-Value	P-Value	Contribution
A	3	4090.1	1363.4	2.02	0.468	34.61%
B	3	1072.8	357.6	0.53	0.737	9.08%
C	3	2402.2	800.7	1.18	0.574	20.32%
D	3	1606.3	535.4	0.79	0.657	13.59%
E	1	729.0	729.0	1.08	0.488	6.17%
G	1	1242.6	1242.6	1.84	0.405	10.51%
Error	1	676	676	-	-	5.72%
Total	15	11818.9	-	-	-	100.00%

* None of the factors significantly influence the initial exit burr size along the stepover direction at the 10% level.

Figure 5.26 is the main effects plot for initial exit burr size along the stepover direction. The main effects plot for S/N ratio is shown in Figure 5.27. S/N ratio analysis adopted smaller-is-better criteria. To improve the edge quality with lower burr size at the test parameters factor lever, 100 m/min cutting speed, 0.10 mm depth of cut, 0.25 mm width of cut, 0.04 mm/tooth feed rate, HD cutting orientation, ultrasonic assistance, and wet cut should be used. The cutting speed was the factor that had the greatest effect on initial exit burr size along the stepover direction in milling γ-TiAl among the above seven factors since the average S/N ratio of the cutting speed had the largest delta value at 15.22.

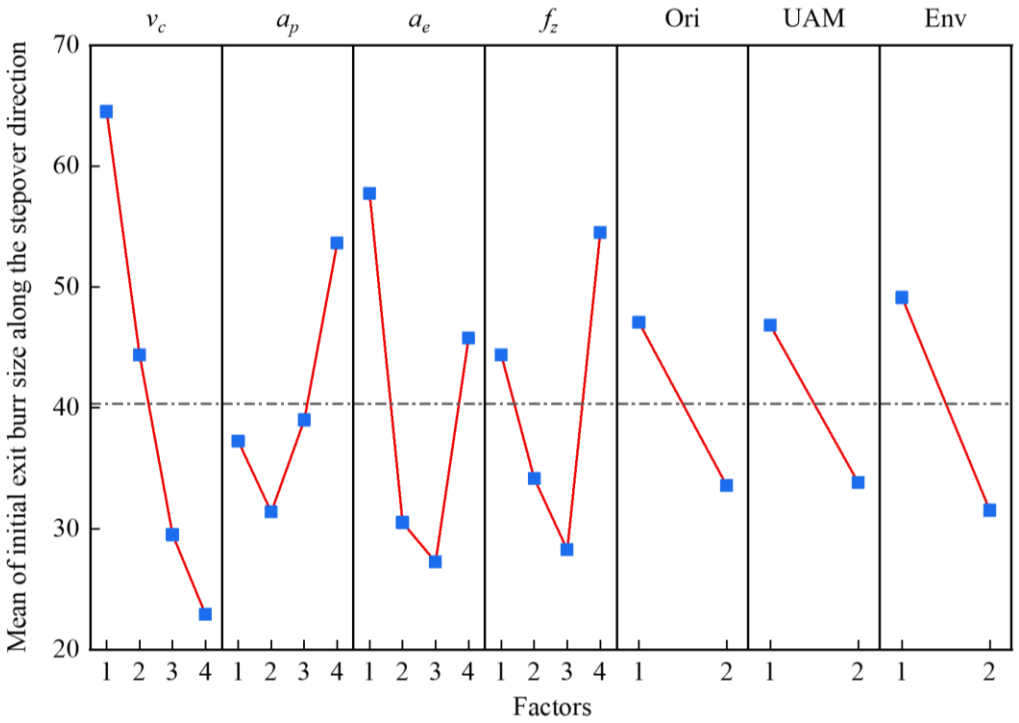


Figure 5.26 Main effects plot for initial exit burr size along the stepover direction.

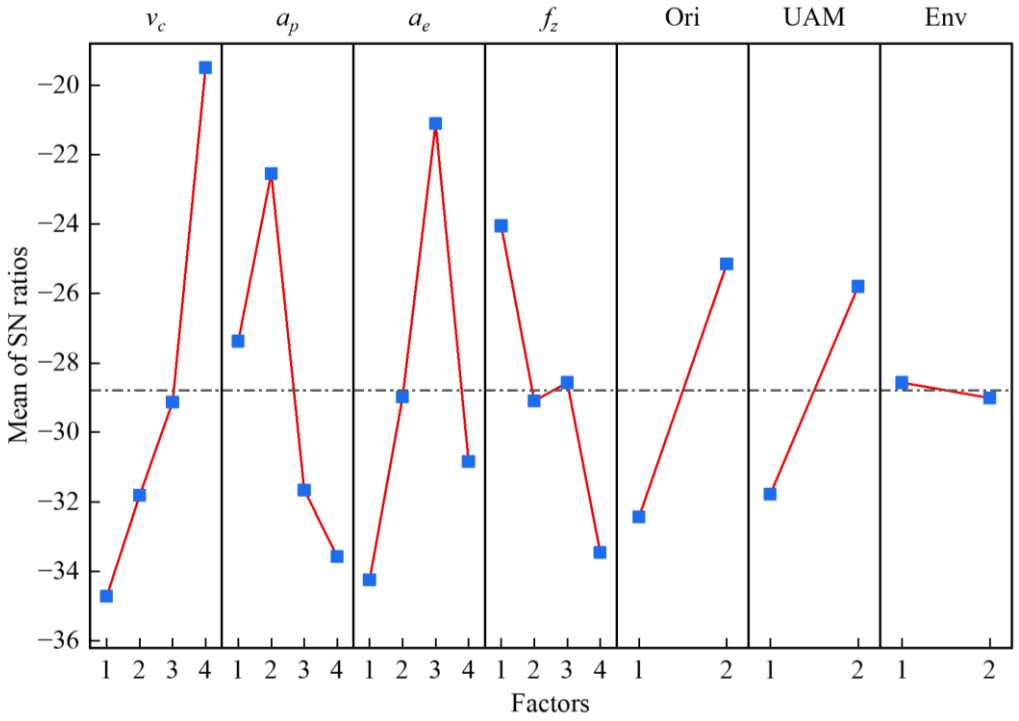


Figure 5.27 Main effects plot for initial exit burr size S/N ratios.

In accordance with the previous analysis, the variance of cutting speed would significantly impact the temperature in the primary shear zone. Aspinwall et al. [64] reported that the cutting region temperature showed a 115% increase as the cutting speed varied from 50 m/min to 345

m/min. Combined with conclusions presented by Fan et al. [293], [298] that higher workpiece temperature led to the improvement of cutting γ-TiAl, fewer burrs could be realised. Burrs could not be avoided completely in actual cutting. However, optimising the tool's geometry, arranging tool path planning, and designing a reasonable combination of cutting parameters may achieve burr minimisation.

5.2.3.2 Surface roughness and dimensional accuracy

The change rate for surface roughness was defined as the ratio of current surface roughness Ra measured along the stepover direction to the initial value, representing new tool conditions. The Taguchi approach involved factors changing their levels for each test, which means it could not directly observe the influence of cutting parameters on surface roughness. The influence of the processing parameters was eliminated through normalisation processing and only reflects the total change rate of surface roughness Ra with tool wear at the corresponding factor level, as depicted in Figure 5.28. The surface roughness of any group shows a trend of first increasing and then decreasing as the machined distance increases.

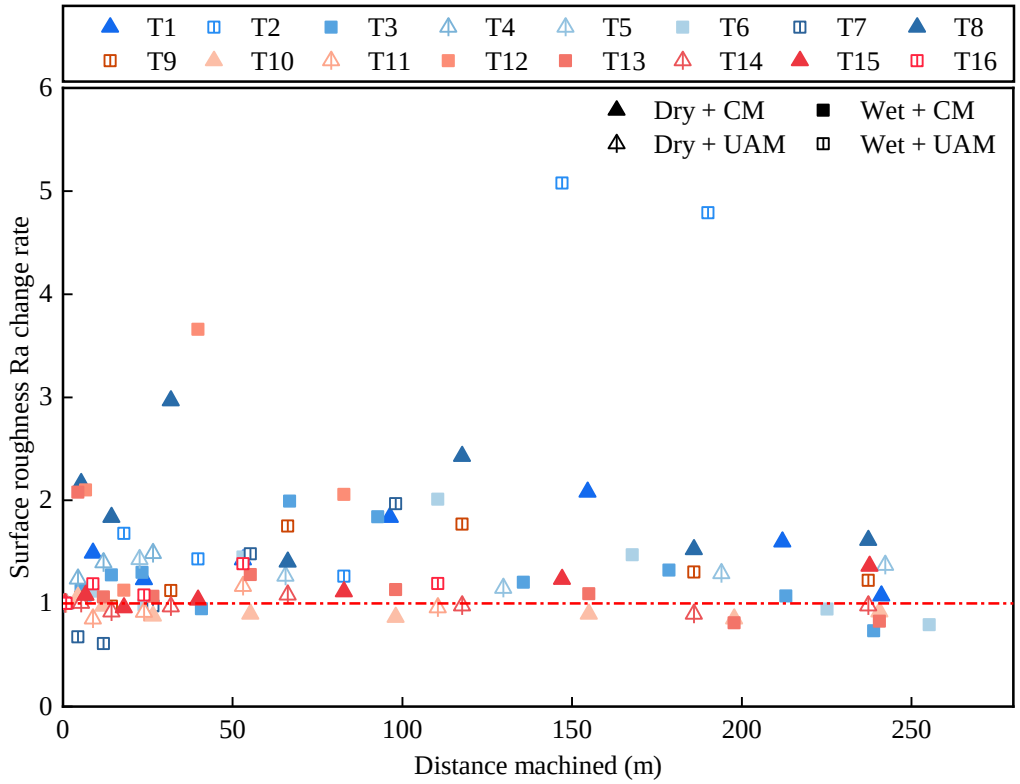


Figure 5.28 Surface roughness change rate against distance machined for Phase 1B trials.

Pérez [56] conducted the face milling test of γ-TiAl and the same phenomenon was observed. On the one hand, the worn tool with a larger radius of the tool nose led to an increase in surface roughness [63]. At the same time, significant work hardening introduced by the rising cutting force also highlighted the surface roughness. However, the worn tool also enhanced cutting heat generation and improved the machinability of γ-TiAl, resulting in smaller surface roughness. The impact of tool bending deflection was more obvious for the ball-end mill. The bending deflection intensified with the greater cutting force induced by severe tool wear and strengthened the contact between the secondary relief face and the machined surface. The surface became smooth under the rubbing action, exhibiting the reduction of surface roughness [289].

The main effect of cutting parameters on the initial surface roughness Ra was analysed under the new tool conditions. Table 5.4 is the ANOVA analysis results for initial surface roughness Ra along the stepover direction. The factor cutting environment had the minimum SS and was set as a residual error. The analysis revealed that none of the factors significantly influenced the initial surface roughness Ra along the stepover direction at the 10% significance level.

Table 5.4 Modified ANOVA analysis of initial surface roughness Ra.

Source	DF	Seq SS	Adj MS	F-Value	P-Value	Contribution
A	3	0.88090	0.29363	10.62	0.221	31.17%
B	3	0.04024	0.01341	0.49	0.753	1.42%
C	3	0.76102	0.25367	9.18	0.237	26.93%
D	3	0.38481	0.12827	4.64	0.326	13.62%
E	1	0.24472	0.24472	8.85	0.206	8.66%
F	1	0.48652	0.48652	17.6	0.149	17.22%
Error	1	0.02764	0.02764	-	-	0.98%
Total	15	2.82584	-	-	-	100.00%

* None of the factors significantly influence the initial surface roughness Ra at the 10% level.

Figure 5.29 is the main effects plot for initial surface roughness Ra and the main effects plot for S/N ratio is shown in Figure 5.30. S/N ratio analysis adopted smaller-is-better criteria. To improve the surface roughness Ra at the test parameters factor lever, 40 m/min cutting speed, 0.05 mm depth of cut, 0.15 mm width of cut, 0.03 mm/tooth feed rate, HU cutting orientation, conventional cutting, and wet cut should be selected. The width of cut was the factor that had the greatest effect on initial surface roughness in milling γ-TiAl among the above seven factors since the average S/N ratio of the width of cut had the largest delta value at 5.2892. Hood [292]

highlighted that the depth of cut was also a significant factor in high-speed ball nose end milling Ti-4522.

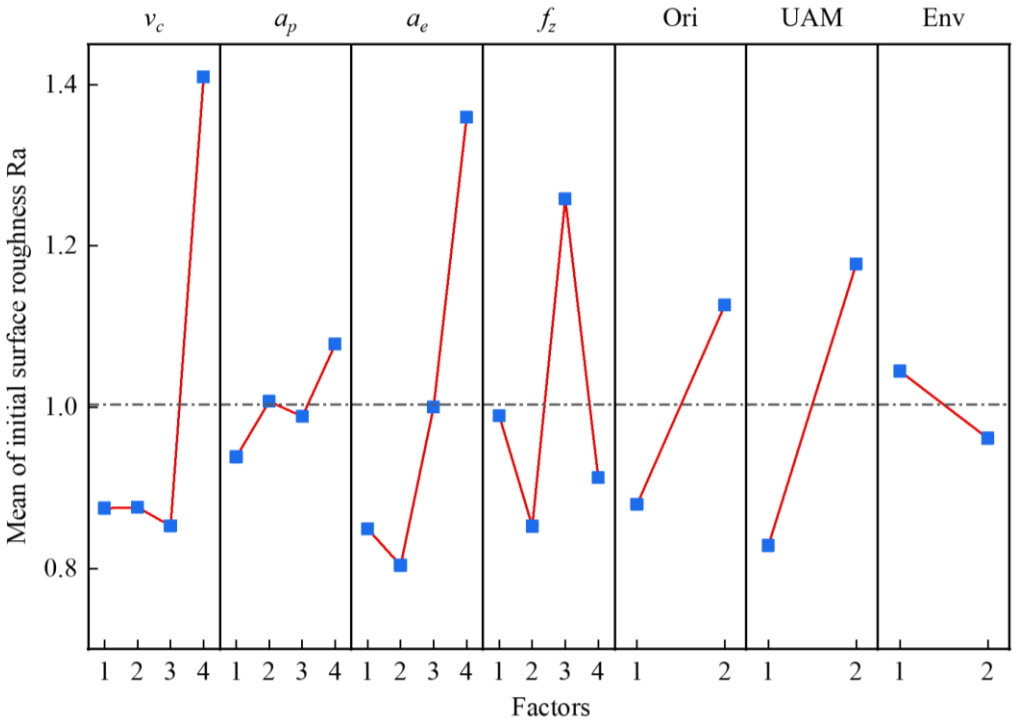


Figure 5.29 Main effects plot for initial surface roughness Ra.

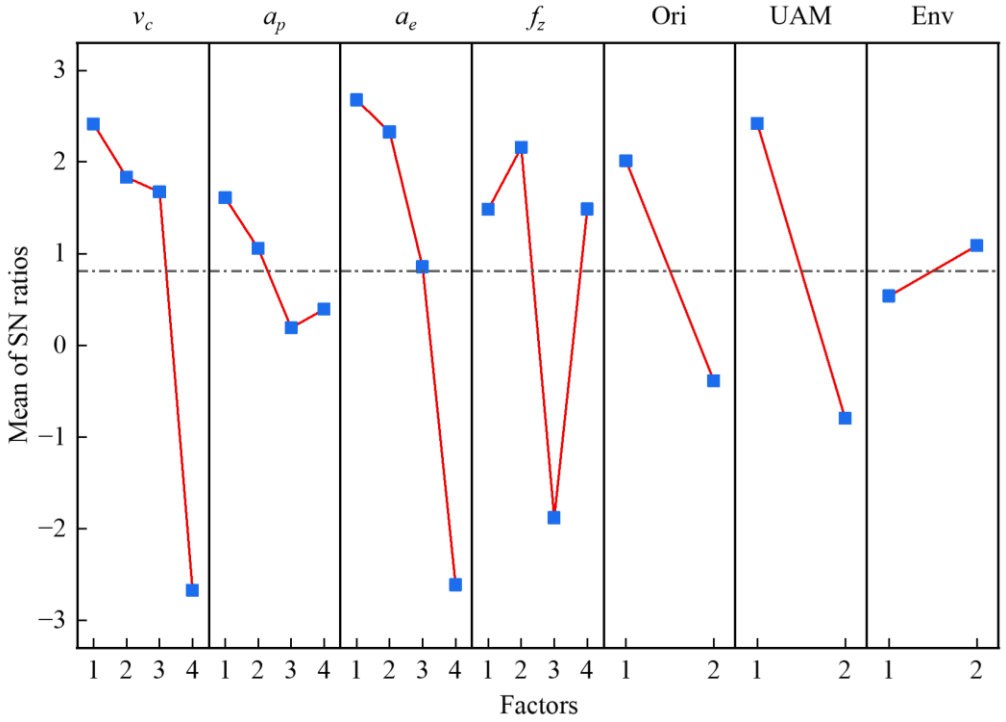


Figure 5.30 Main effects plot for initial surface roughness Ra S/N ratios.

Figure 5.31 presents the depth of cut achievement rate R_{Cd} as a function of distance machined. R_{Cd} could intuitively reflect the current machinability of cutting tools without disassembling the cutter to measure the tool wear. From the trends of a total of 16 tests, most dry cutting group experiments could maintain a relatively stable R_{Cd} value, but wet cutting did lead to an obvious rapid decline. Notably, due to the influence of tool bending defection, the actual depth of cut could never approximate 1, and the maximum value in this test was only around 0.8. Meanwhile, when the cutting force increased significantly, the bending degree of the tool intensified and the actual cutting depth decreased accordingly, ultimately reducing the depth of cut achievement rate.

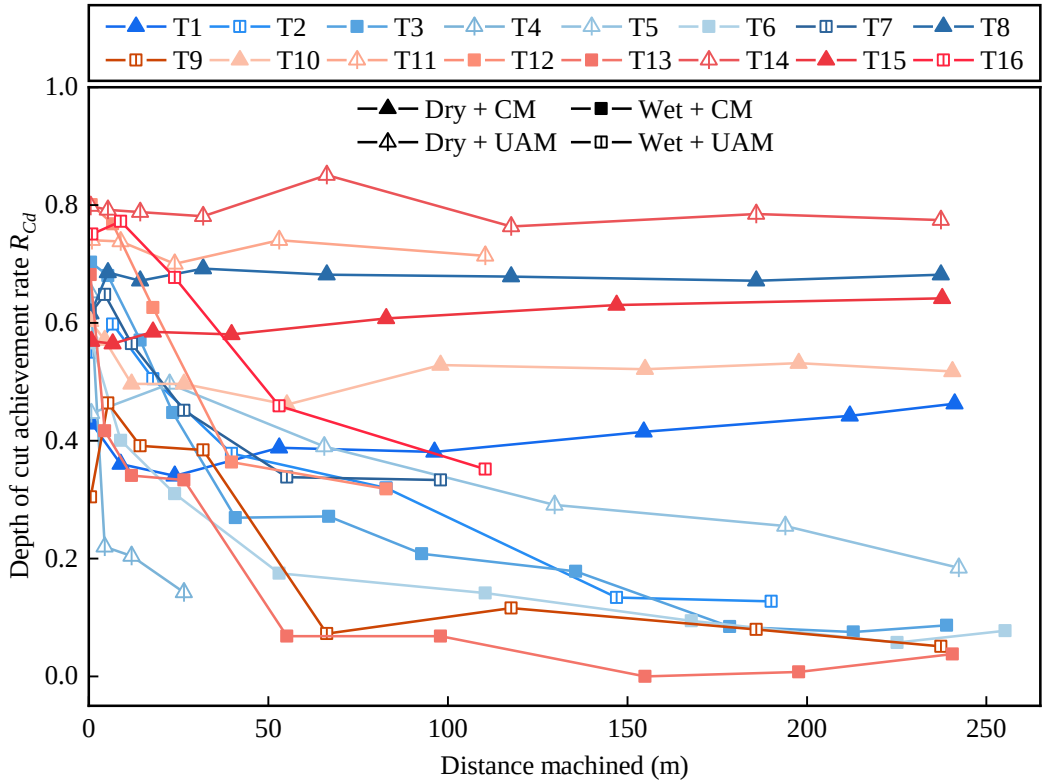


Figure 5.31 Depth of cut achievement rate against distance machined for Phase 1B trials.

Figure 5.32 depicts the data of the complete cutting process of one set of tests T3. As tool wear intensified, the average cutting force gradually increased while the depth of cut achievement rate decreased rapidly. The surface roughness first increased and then decreased as tool wear augmented. The higher cutting force induced by tool wear was the root cause of surface quality deterioration. Table 5.5 is the ANOVA analysis results for the initial depth of cut achievement rate R_{Cd}. The influence of tool wear was excluded and the main effect of cutting parameters on depth of cut achievement rate was analysed. Factor ultrasonic assistance had the minimum SS

and was set as a residual error. The depth of cut and the cutting direction were determined as statistically significant at the 10% significance level.

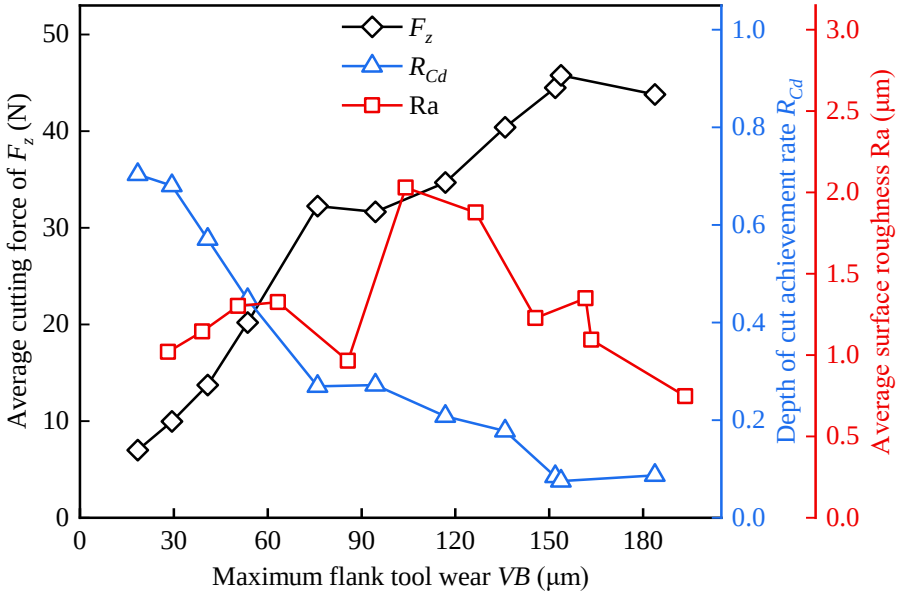


Figure 5.32 Changes in F_z, R_{Cd}, and Ra with tool wear in the T3 test.

Table 5.5 Modified ANOVA analysis of initial depth of cut achievement rate R_{Cd}.

Source	DF	Seq SS	Adj MS	F-Value	P-Value	Contribution
A	3	0.044648	0.014883	19.76	0.164	15.71%
B	3	0.129409	0.043136	57.27*	0.097	45.54%
C	3	0.004808	0.001603	2.13	0.458	1.69%
D	3	0.047089	0.015696	20.84	0.159	16.57%
E	1	0.056593	0.056593	75.14*	0.073	19.92%
G	1	0.000870	0.000870	1.16	0.477	0.31%
Error	1	0.000753	0.000753	-	-	0.27%
Total	15	0.284170	-	-	-	100.00%

* Depth of cut and cutting orientation significantly influence the initial R_{Cd} at the 10% level.

Figure 5.33 is the main effects plot for the initial depth of cut achievement rate R_{Cd}. The main effects plot for S/N ratio is shown in Figure 5.34. S/N ratio analysis adopted larger-is-better criteria. To improve the material removal depth at the test parameters factor lever, 100 m/min cutting speed, 0.20 mm depth of cut, 0.30 mm width of cut, 0.02 mm/tooth feed rate, and HD cutting orientation should be used. Changes in ultrasonic assistance and cutting environment did not differ significantly over the range of test levels. The depth of cut was the factor that had the greatest effect on initial R_{Cd} in milling γ-TiAl among the above seven factors since the average S/N ratio of the depth of cut had the largest delta value at 3.912.

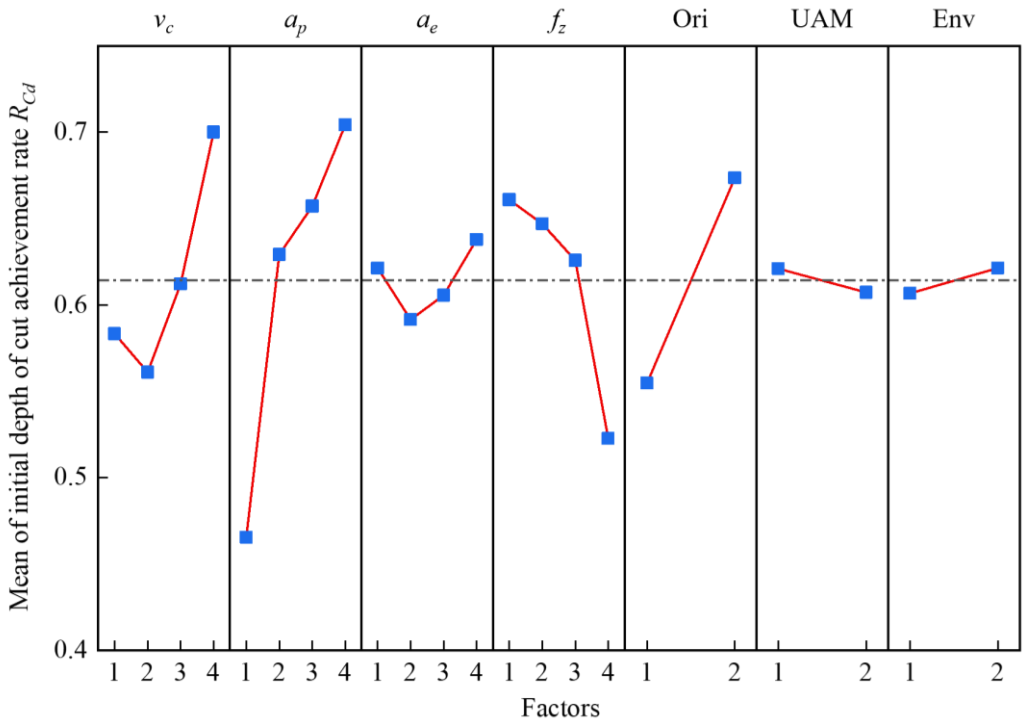


Figure 5.33 Main effects plot for initial depth of cut achievement rate R_{Cd}.

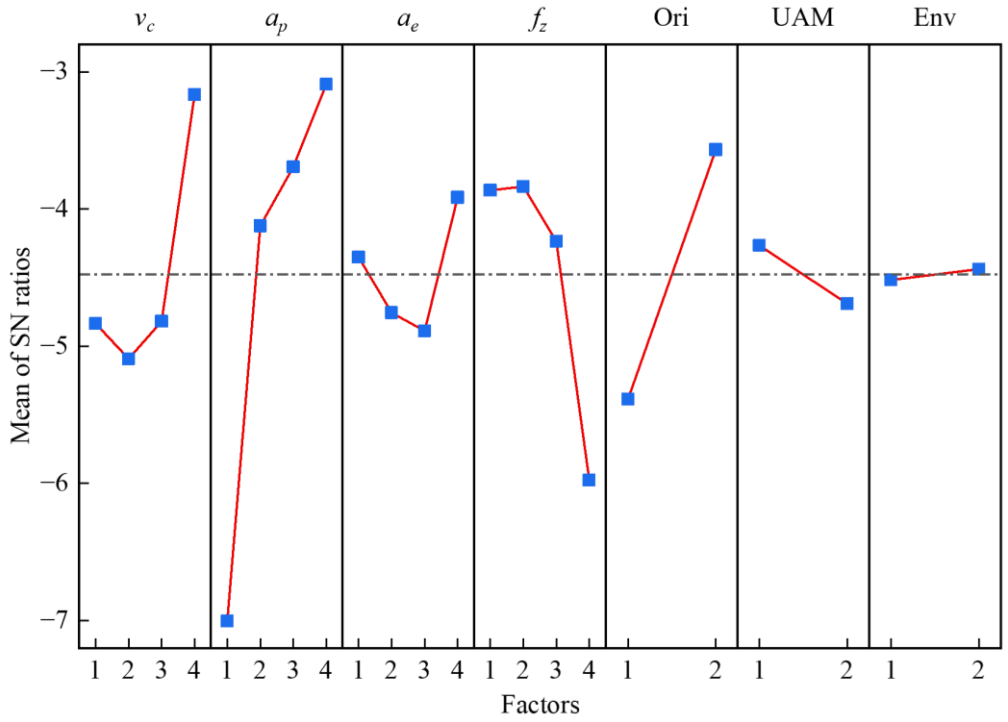


Figure 5.34 Main effects plot for initial depth of cut achievement rate R_{Cd} S/N ratios.

Except for bending deflection, the minimum uncut chip thickness is a critical parameter closely associated with the tool's nose radius. When the chip thickness closes to the radius size, it typically leads to a reduced shear-plane angle, larger negative rake angles, and the elastic-

plastic deformation of the workpiece materials [299], [300]. When the cutting process occurs below this minimum uncut chip thickness, it is predominantly characterised by ploughing, which represents a form of plastic deformation that does not form chips [301], [302]. This also explains why, as the tool wear intensified in the test, the depth of cut achievement rate decreased rapidly, and even some groups (T6, T9, T12) had a phenomenon of approximately 0 of R_{Cd}.

5.2.3.3 Microhardness

Microhardness profiles presenting hardness against distance from the machined surface for all 16 tests with the new tool condition are shown in Figure 5.35. Generally, the surface microhardness for dry cutting exhibited a slightly lower value than that of the bulk materials, while wet cutting resulted in higher microhardness than bulk value. In terms of the previous viewpoint that the rising temperature of the cutting zone was beneficial to improve the machinability of γ-TiAl [91]. In addition, introducing ultrasonic actuation vibration commonly increases surface microhardness. The higher dislocation density and plastic deformation induced by ultrasonic vibration enhanced strain and strain rate hardening, resulting in larger hardness [216].

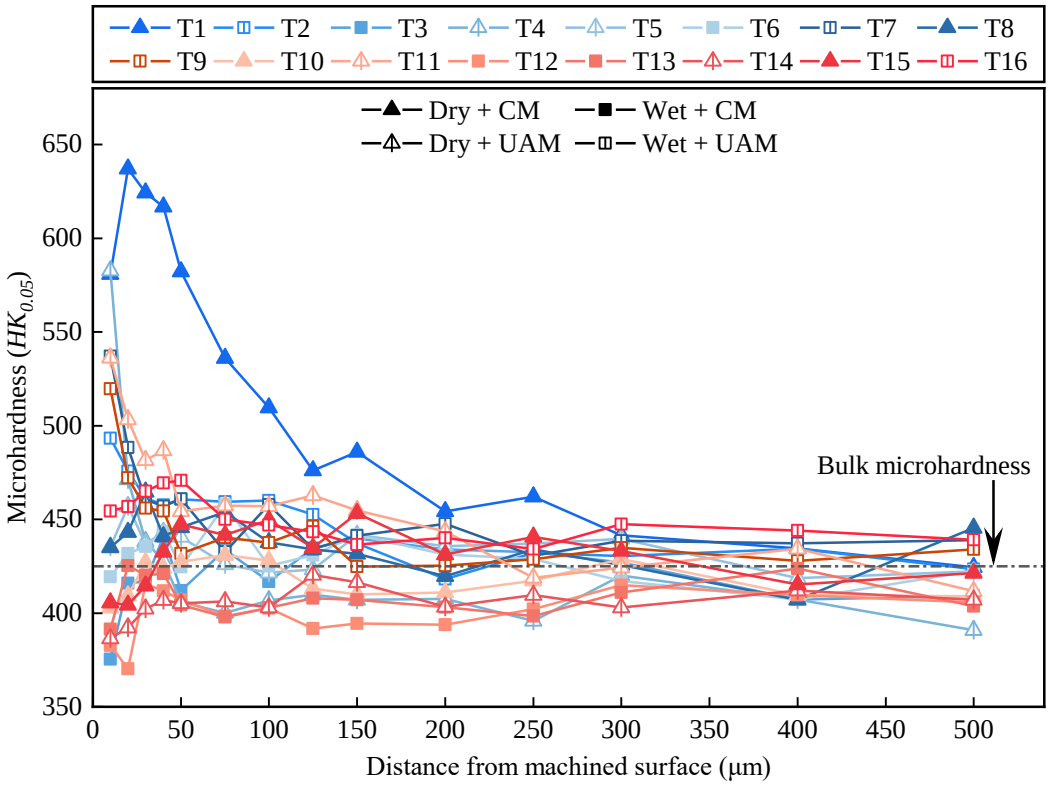


Figure 5.35 Variation of microhardness with new tools in Phase 1B trials.

However, when the cutting tool was in worn condition, the surface microhardness presented significantly higher than the bulk microhardness, as shown in Figure 5.36. Both mechanical and thermal loads significantly influenced subsurface characteristics during the cutting process. Unlike using a new tool, where mechanical load predominated, worn tools exhibited different dynamics. As the tool wore, the parameters that had once increased the temperature of the cutting zone, thereby softening the material and reducing its hardness, became less influential. Conversely, the cutting forces escalated markedly due to tool wear, enhancing plastic deformation of the material and increasing strain, strain rate, and dislocation density. This sequence of events led to a pronounced increase in work hardening of the material [303]. Comparable findings were validated by Hood and Mantle [51], [292] after milling Ti-4522.

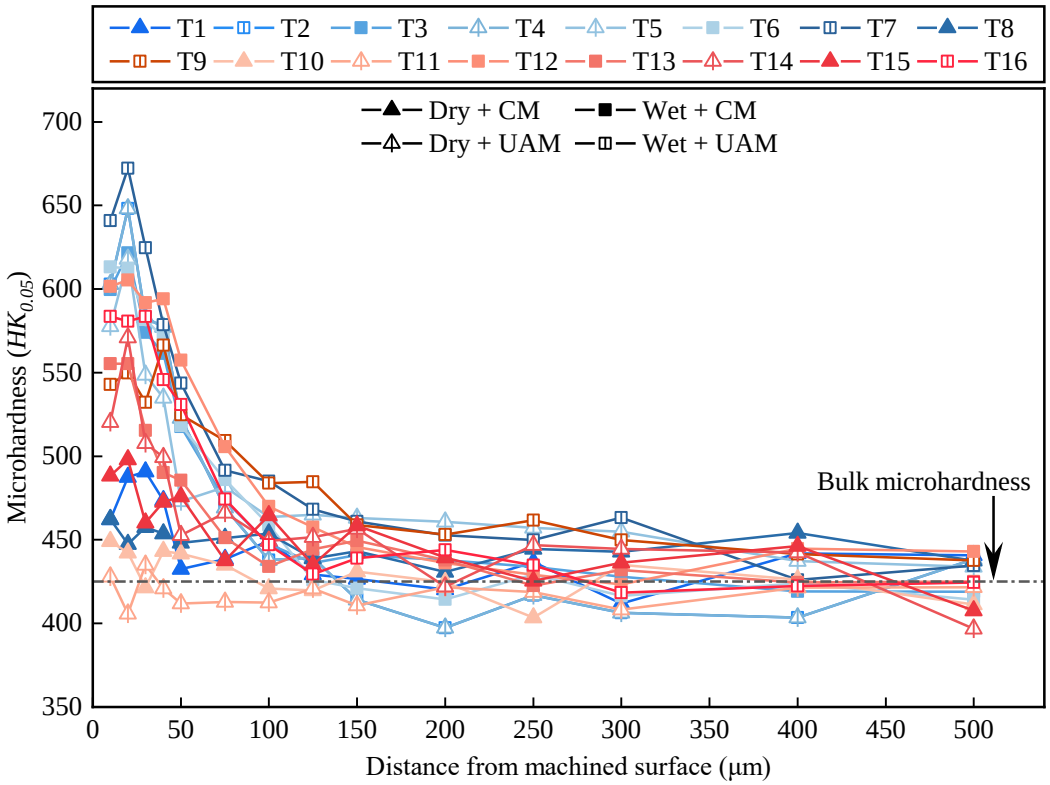


Figure 5.36 Variation of microhardness with worn tools in Phase 1B trials.

Excluding the influence of tool wear, the main effect of cutting parameters on the work hardening degree was analysed. Table 5.6 is the ANOVA analysis results for initial work hardening degree N_{wh}. The factor cutting environment had the minimum SS and was set as a residual error. The analysis revealed no factors significantly influenced the initial work hardening degree at the 10% significance level.

Table 5.6 Modified ANOVA analysis of initial work hardening degree N_{wh}.

Source	DF	Seq SS	Adj MS	F-Value	P-Value	Contribution
A	3	0.10771	0.03590	2.82	0.406	24.81%
B	3	0.03733	0.01244	0.98	0.614	8.06%
C	3	0.05475	0.02696	2.12	0.459	18.63%
D	3	0.03518	0.01825	1.43	0.535	12.61%
E	1	0.10558	0.03518	2.76	0.345	8.10%
F	1	0.01272	0.10558	8.30	0.213	24.32%
Error	1	0.43415	0.01272	-	-	2.93%
Total	15	11818.9	-	-	-	100.00%

* None of the factors significantly influence the initial work hardening degree N_{wh} at the 10% level.

Figure 5.37 is the main effects plot for initial work hardening degree N_{wh} and the main effects plot for S/N ratios is shown in Figure 5.38. S/N ratio analysis adopted smaller-is-better criteria. To diminish the work hardening degree at the test parameters factor lever, 100 m/min cutting speed, 0.10 mm depth of cut, 0.25 mm width of cut, 0.04 mm/tooth feed rate, HD cutting orientation, conventional cutting, and wet cut should be utilised. The width of cut was the factor that had the greatest effect on the initial work hardening degree in milling γ-TiAl among the above seven factors since the average S/N ratio of the width of cut had the largest delta value at 14.47.

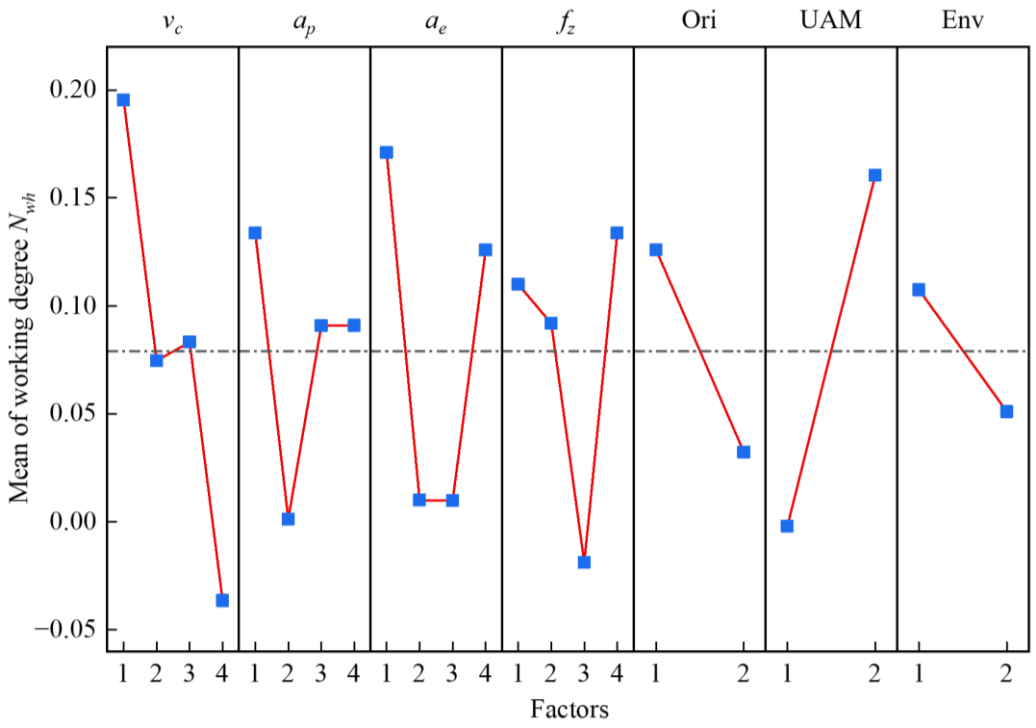


Figure 5.37 Main effects plot for initial work hardening degree N_{wh}.

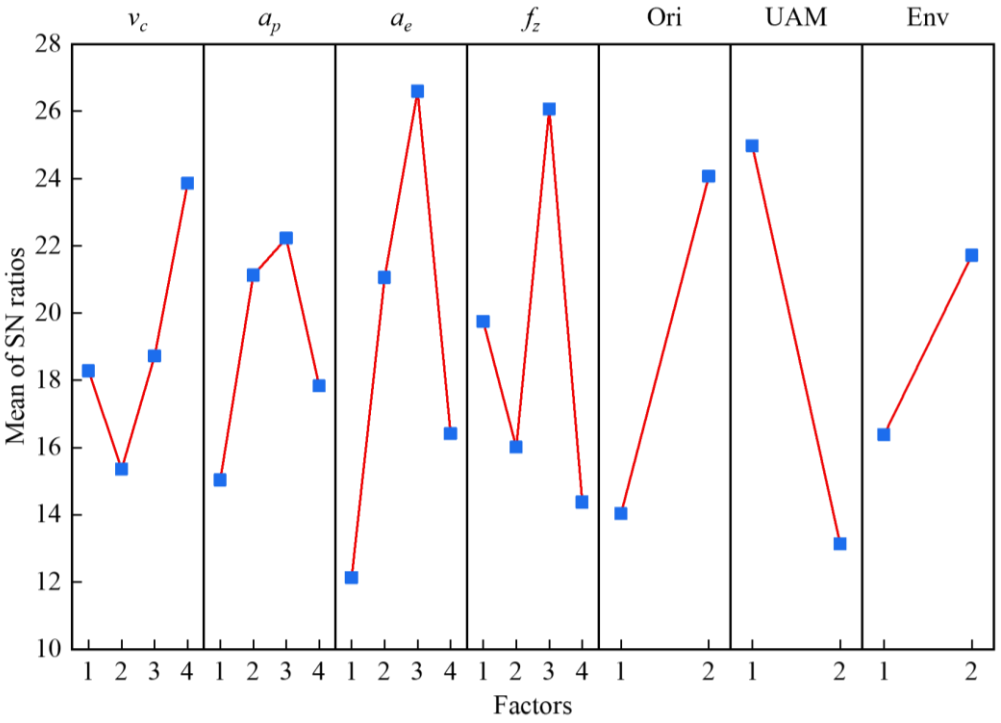


Figure 5.38 Main effects plot for initial work hardening degree N_{wh} S/N ratios.

5.2.3.4 Metallographic/microstructural alteration

The alteration of typical microstructures obtained under the new and worn tool conditions is shown in Figure 5.39. The bend of the lamella structure along the cutting direction could be observed, and the thickness of the deformed layer in T4 expanded from 11.64 μm to 44.93 μm, where the current tool wear was 195 μm. Zhang et al. [86] also confirmed that damage and bending of lamellar structures ($\alpha_2 + \gamma$) were prominent features when cutting fully lamellar γ-TiAl. Guo et al. [111] believed that the microstructural evolution during machining depended on the strain, strain rate, and temperature. Increased cutting force introduced by severe tool wear was the root cause of augmenting the deformed layer. In some published investigations, subsurface microcracking was considered a wide phenomenon when cutting γ-TiAl due to its brittleness and high strength at room temperature [50], [65], [67]. In addition, the weak bonding force between the hexagonal α_2 and tetragonal γ phases led to preferential micro-cracking along each interface [86]. However, no obvious microcracks were found except at the exit position in Phase 1B. This is probably because the tool size and cutting parameters used in the experiment were generally at a smaller level, resulting in relatively low cutting forces.

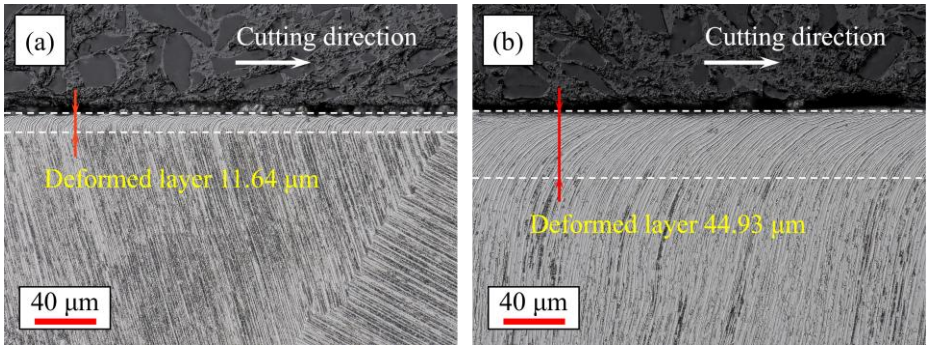


Figure 5.39 Typical micrographs of machined subsurface microstructures in T4 with the (a) new tool and (b) worn tool.

Table 5.7 is the ANOVA analysis results for the initial deformed layer thickness. The influence of tool wear was excluded and the main effect of cutting parameters on deformed layer thickness was analysed. Factor cutting environment had the minimum SS and was set as a residual error. The ultrasonic assistance was determined to be statistically significant at the 10% significance level.

Table 5.7 Modified ANOVA analysis of initial deformed layer thickness.

Source	DF	Seq SS	Adj MS	F-Value	P-Value	Contribution
A	3	54.970	18.323	16.38	0.179	23.02%
B	3	54.943	18.314	16.38	0.179	23.01%
C	3	25.291	8.430	7.54	0.260	10.59%
D	3	33.268	11.089	9.92	0.228	13.93%
E	1	55.913	55.913	50.00*	0.089	23.42%
F	1	13.268	13.268	11.86	0.180	5.56%
Error	1	1.118	1.118	-	-	0.47%
Total	15	238.771	-	-	-	100.00%

* Cutting orientation significantly influences the initial deformed layer thickness at the 10% level.

Figure 5.40 is the main effects plot for the initial deformed layer thickness. The main effects plot for S/N ratios is shown in Figure 5.41. S/N ratio analysis adopted larger-is-better criteria. To diminish the deformed layer thickness at the test parameters factor lever, 100 m/min cutting speed, 0.10 mm depth of cut, 0.20 mm width of cut, 0.04 mm/tooth feed rate, HD cutting orientation, and ultrasonic assistance should be employed. Changes in the cutting environment did not differ significantly over the range of test levels. The depth of cut was the factor that had the greatest effect on initial deformed layer thickness in milling γ-TiAl among the above seven factors since the average S/N ratio of the depth of cut had the largest delta value at 5.17. Combined with the investigation of the influence of cutting parameters on cutting force in

Section 5.2.2, it can be found that those parameters with lower cutting force also have lower deformed layer thickness. The idea that cutting force is the dominant factor causing surface damage was again confirmed.

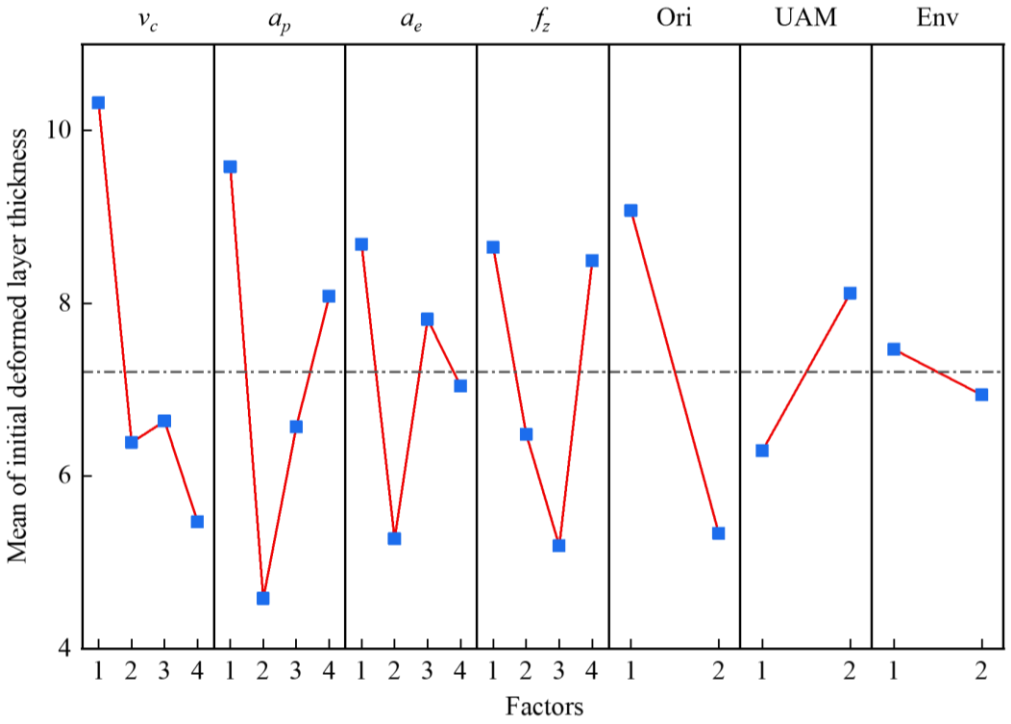


Figure 5.40 Main effects plot for initial deformed layer thickness.

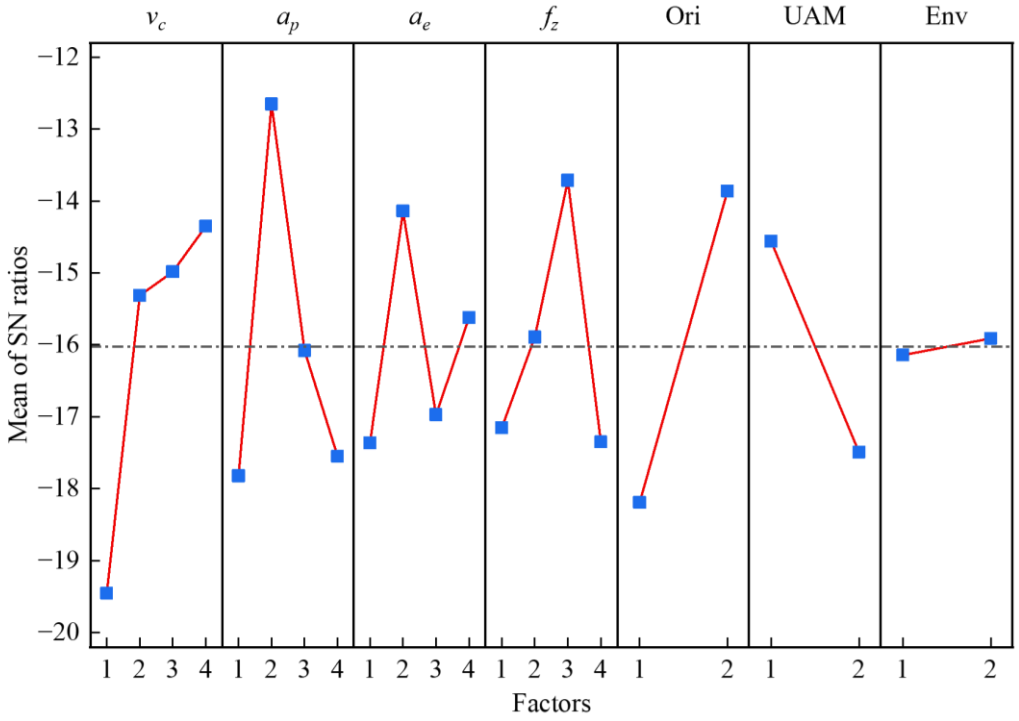


Figure 5.41 Main effects plot for initial deformed layer thickness S/N ratios.

5.3 Phase 2A: Tool wear mechanisms and failure of γ-TiAl in B-UAM

5.3.1 Abrasive wear

Abrasive wear was the most common formation in cutting γ-TiAl under wet cutting conditions by using coated cutting tools. Figure 5.42 displays micrographs of the wear station in the early, mid and late stages of tool life under the different cutting methods. The coating peeled off in the early machining stages and deteriorated rapidly during the cutting processes. Under ultrasonic-assisted milling, the wear amount of the flank face was always at the same level as that of conventional milling, but the wear area of the secondary relief face due to the bending deflection was much smaller than that of conventional milling, as shown in Figure 5.42(b) and (e). The advantage of ultrasonic vibration in decreasing cutting forces alleviated the bending deflection phenomenon.

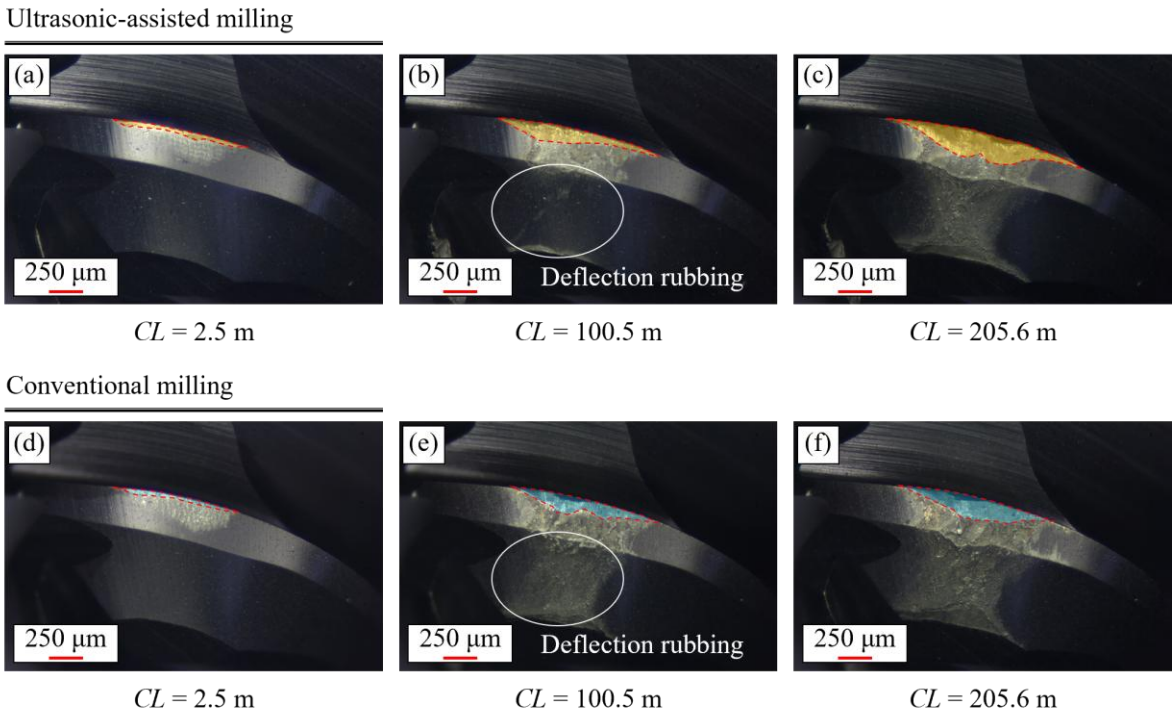


Figure 5.42 Abrasive wear in wet cutting with TiAlN coated tungsten carbide tool; (a), (b) and (c) UAM and (d), (e) and (f) CM.

The aluminium-rich (up to 65–67 at%) PVD TiAlN coating shows improved tool life in machining aerospace alloys with the following benefits:

- The outstanding combination of hardness and oxidation stability at elevated temperatures, improved plasticity and excellent fatigue fracture resistance [304], [305].
- Low thermal conductivity protects the tool surface from heat transfer [306].
- Form protective alumina-like tribo-films during cutting due to high aluminium content and the nano-crystalline structure [304]. High thermal and chemical stability of the alumina tribo-layers prevents intensive sticking of the workpiece to the cutting tool [307].

Nevertheless, it should be noted that the application of copious amounts of fluid during intermittent cutting could increase a large fluctuation in cutting temperature. This in turn leads to thermal shock and could initiate thermal cracks of the cutting edge and, eventually tool failure due to edge fracture [97], [308], [309]. Liao et al. [310], [311] adopted the MQL cooling method, which could lubricate the cutting region without promoting thermal cracks when the TiAlN/TiN coated tool was utilised. The TiAlN coating did not perform as well as it should under wet cutting conditions. Hood et al. [65] presented the comparable result from high-speed milling Ti-4522 and TNB by using AlTiN coated tool. The same phenomenon was reported by Ren et al. [75] when conducting an end milling test with the AlCrN coating tool.

5.3.2 Adhesive wear

Adhesive wear was observed in all cutting tests. Figure 5.43 shows tool wear status in different cutting stages and there is no obvious increment of abrasive wear. Close contact between the cutting tool and workpiece led to workpiece material adhering to the tool surface, sometimes resulting in a built-up edge. Figure B.1 displays the element distributions of TiAlN coating used in the test with content of 27.52 at% Ti, 16.42 at% Al, and 56.02 at% N. Scattered workpiece material was detected to adhere to the tool surface and appears dark contrast in Figure 5.44. High concentrations of Al, Ti, and especially Nb (spectrum 1), which were unique to the workpiece material, could verify the content of adhesion. Meanwhile, the base was exposed to high concentrations of W and Co in spectrum 2, which were the main compositions of tungsten carbide. However, under dry cutting conditions, adhesions were evenly distributed along the cutting edge, as presented in Figure 5.45. The workpiece feature element Nb was detected by EDS as well. Spectrum 1 maintained the initial contents of the coating material, which represented that the coating did not disappear as fast as in the case of wet cutting. Three zones

with different compositions were named coating zone (spectrum 1), base zone (spectrum 2), and adhesion zone (spectrum 3).

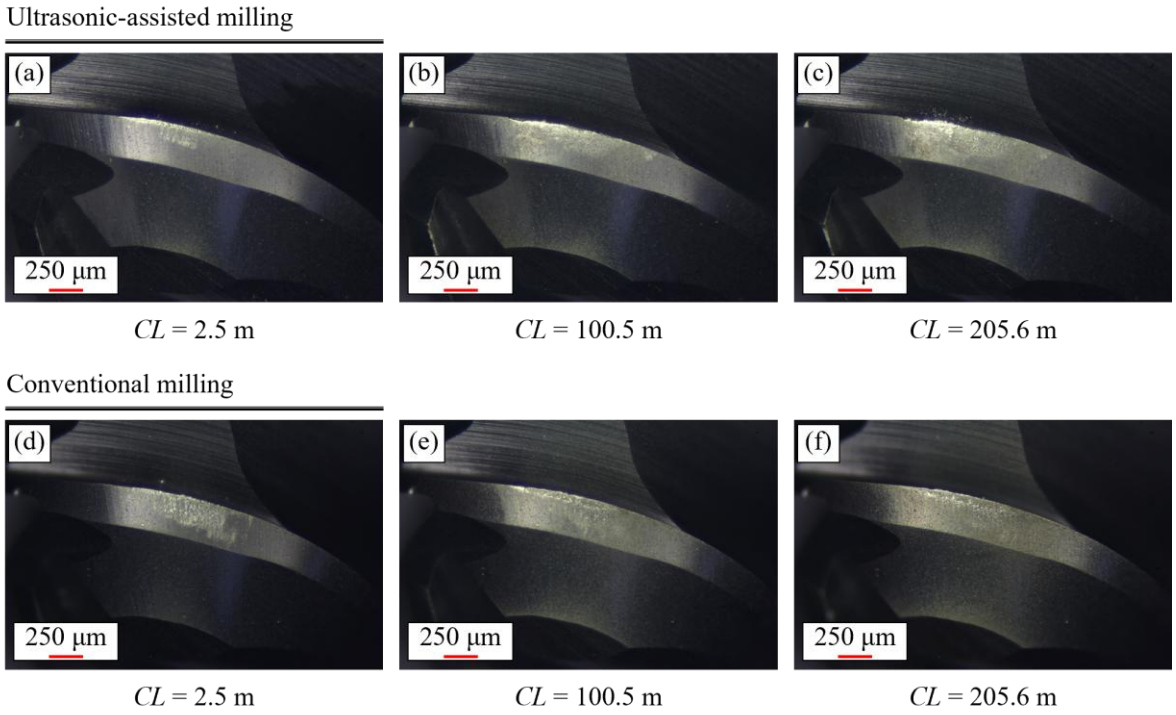


Figure 5.43 Adhesive wear in dry cutting with TiAlN coated tungsten carbide tool; (a), (b) and (c) UAM and (d), (e) and (f) CM.

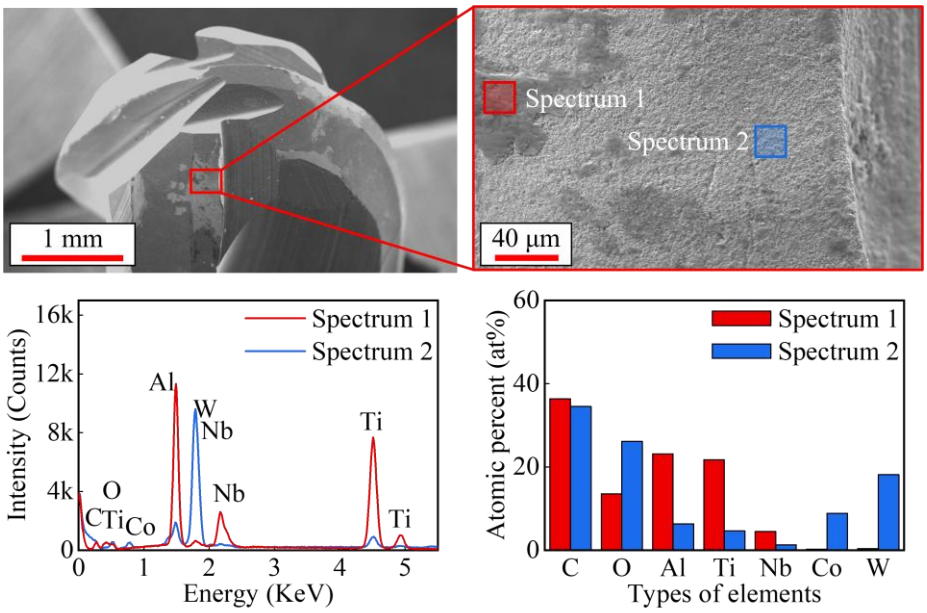


Figure 5.44 EDS analysis of the worn tool surface produced in ultrasonic-assisted milling TNB under wet cut conditions.

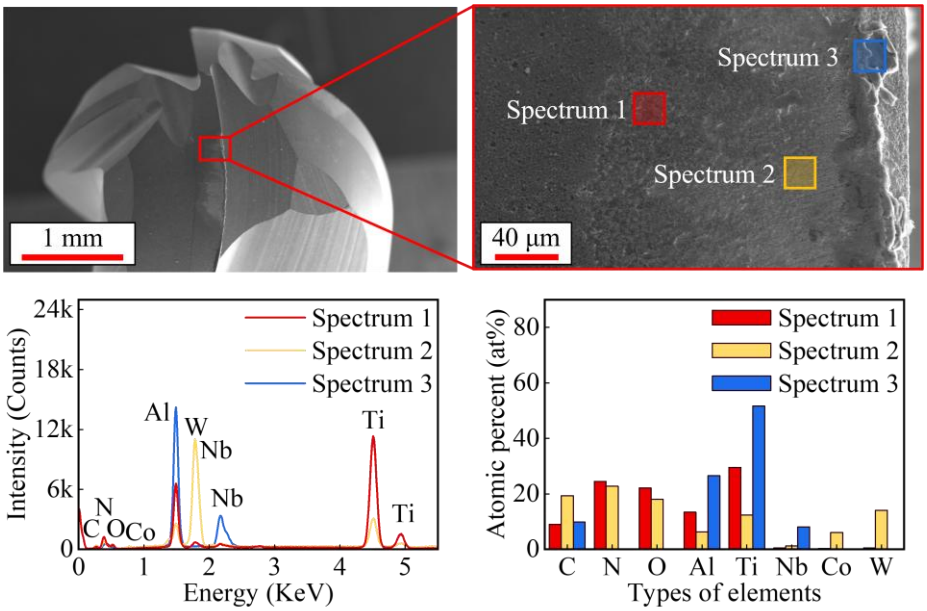


Figure 5.45 EDS analysis of the worn tool surface produced in ultrasonic-assisted milling TNB under dry cut conditions.

The wear mechanism in dry cutting with TiAlN coated tool can be described as the coating material slowly disappearing after continuous abrasive wear. At the same time, the close contact between the workpiece and the tool under high temperature conditions causes more material to adhere to the tool, forming continuous tribo-layers, which forms a protective effect on the cutting edge, thereby significantly improving tool life [307]. Control experiments were conducted using uncoated tools to exclude the influence of coating, and consistent results were obtained. Figure 5.46 illustrates that a large amount of uniform Al and Ti from γ-TiAl is more likely to be adhered under dry cutting conditions.

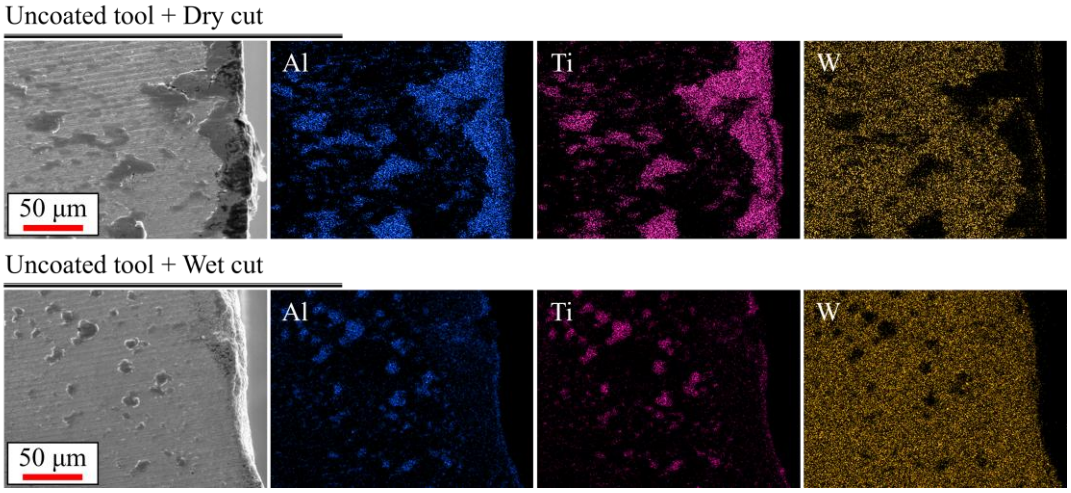


Figure 5.46 Chemical element distributions imaged by EDS mapping mode.

A comparative experiment was arranged to investigate the influence of workpiece material on tool wear mechanism and the result is shown in Figure 5.47. Significant and severe abrasive wear was discovered while milling low-alloy steel in dry cut conditions, as depicted in Figure 5.47(f). Flood lubrication was beneficial to milling this material with lower abrasive wear at the same distance machined (see Figure 5.47(c)). The high aluminium content is a characteristic of γ-TiAl, which also leads to the protection of the cutting edge due to the adhesion of the material under dry cut conditions, regardless of whether the tool was coated. Comparable conclusions were reported widely in cutting γ-TiAl [76], [88], [292]. EDS analysis results of the uncoated tool in milling low-alloy steel validated this viewpoint, as displayed in Figure B.2 and Figure B.3.

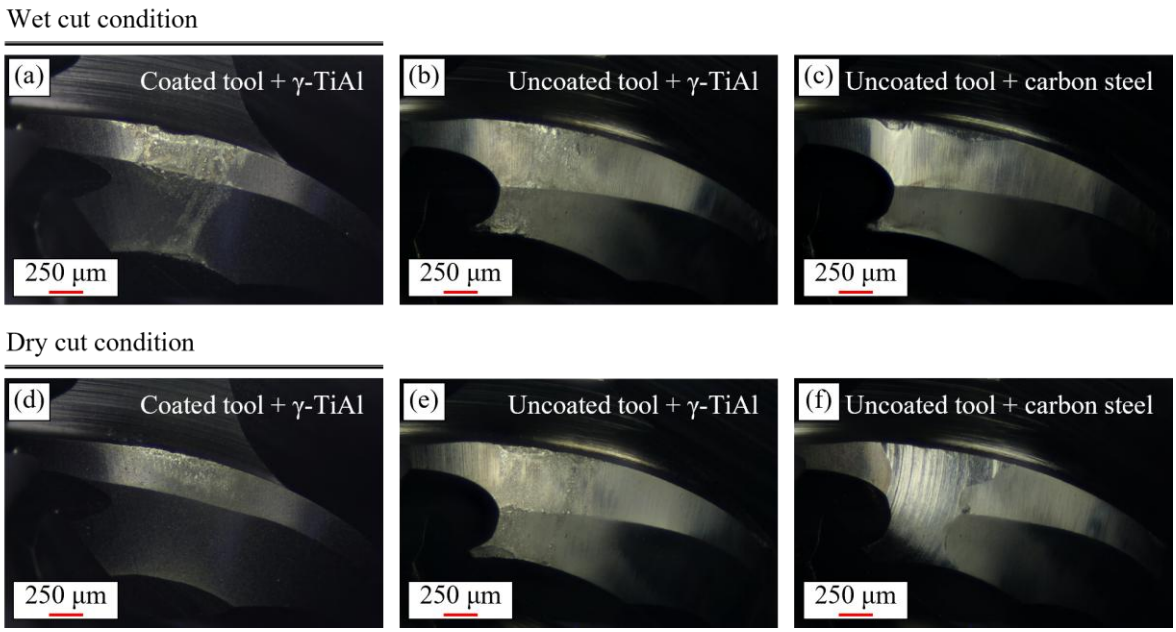


Figure 5.47 Too wear formations in cutting different materials after 55 m distance machined: (a), (b) and (c) Wet cut and (d), (e) and (f) dry cut.

5.3.3 Oxidation and diffusion wear

Both workpiece material γ-TiAl and TiAlN coating material contain high Al and Ti elements concentrations. TiO_2 and Al_2O_3 will be produced during the cutting process and the reactions can be presumed as follows: $TiAlN + O_2 \rightarrow TiO_2 + Al_2O_3$ (amorphous) + NO_x (or N_2) [306], [312]. In accordance with the investigation of Dosbaeva et al. [313], the aluminium rich PVD TiAlCrSiYN coatings with 60 at% of Al could improve the oxidation resistance of titanium aluminide alloy at the temperature 900°C. However, such reactions require a high temperature

to be induced. Barshilia and Rajam [314] investigated the impact of temperature on the oxidation behaviour of various coatings, including CrN, TiN/CrN, TiAlN, and TiAlN/CrN. Their findings revealed that a temperature of 800°C was necessary for forming Al_2O_3. Additionally, other researchers have documented that the temperature required for Al_2O_3 formation on TiAlCrYN coatings exceeded 950°C [315]. This reaction temperature is obviously difficult to exist during flood lubrication, even under dry cut conditions. However, local flash temperatures of the magnitude required for oxides may be generated under the modest cutting parameters [316].

Oxidised workpiece material such as Ti and Al oxide adhering onto the tool surface and oxidised coating were two possible sources of oxygen. Figure 5.48 and Figure 5.49 can verify these two formations respectively. In Figure 5.48 spectrum 2, no N element was detected, and the presence of Nb signals indicated that the coating material on the cutting edge had been worn away and replaced by adhesion transferred from the workpiece material. Meanwhile, the high concentration of O element was discovered in spectrum 2, representing the generation of oxides combining high Ti and Al elements, which may be Al_2O_3 or TiO_2. From the distributions of N element in spectrum 1 and spectrum 2, NO_x may exist. Therefore, when dry cutting γ-TiAl with TiAlN coated tools, the oxidation in the area close to the cutting edge mainly came from the adhered workpiece material, while the oxidation in the area far away from the cutting edge derived from the coating itself.

Figure 5.49 presents the EDS analysis of the worn tool without coating produced in milling γ-TiAl under dry cut conditions. The most noticeable thing was that the cutting edge was covered with a continuous wider layer of adhesion material from the workpiece. The proportions of the three elements Ti, Al, and Nb were consistent with the workpiece material. Uncoated tools were more prone to adhesive wear, resulting in workpiece materials constantly adhering to the cutting edge and insufficient oxygen to participate in the reaction. At the same time, disparate adhered materials were distributed far away, as exhibited in Figure 5.49 spectrum 3. The O element content was detected with high concentration, indicating that the film of Al_2O_3 or TiO_2 was produced and covered the tool surface. At this time, the main source of oxides was the workpiece materials. Figure 5.50 exhibits the element distributions of the worn tool's flank face under the dry cut, validating the widespread existence of oxygen.

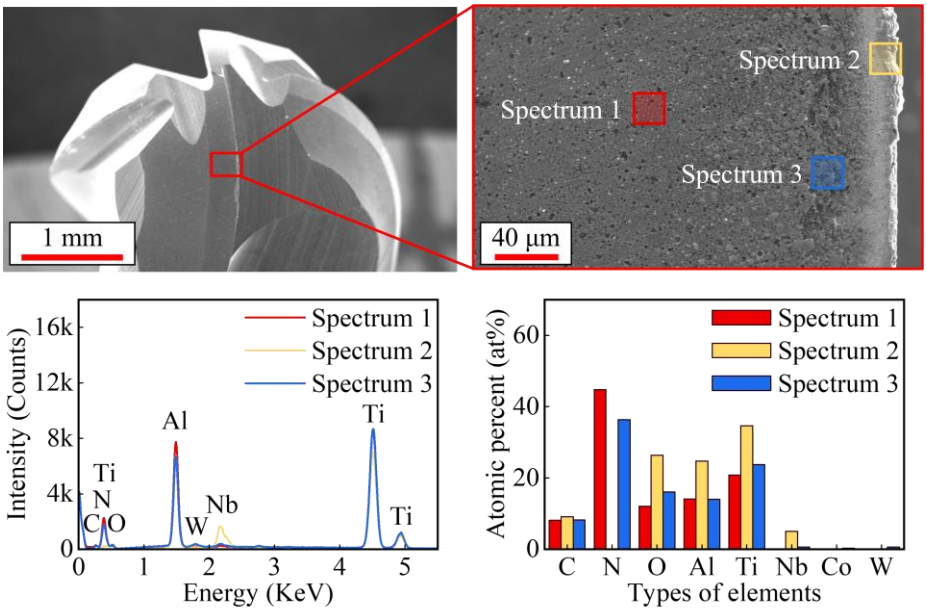


Figure 5.48 EDS analysis of the worn tool (TiAlN coating) surface produced in milling TNB under dry cut conditions with 205.6 m distance machined.

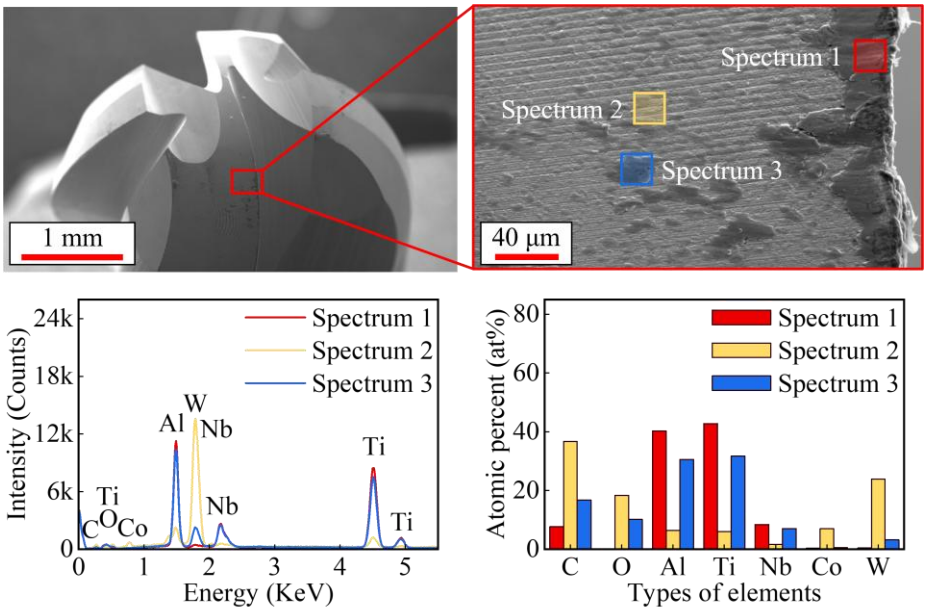


Figure 5.49 EDS analysis of the worn tool (uncoated) surface produced in milling TNB under dry cut conditions with 100.5 m distance machined.

Figure 5.51 shows the EDS analysis results of cutting different materials. No O element was detected, indicating that compared with iron-based low-alloy steel, γ-TiAl with high Al content was easier to oxidation during the cutting process. Due to the low thermal conductivity of γ-TiAl, the cutting zone was more likely to generate heat accumulation and increase the

temperature, which benefitted the oxidation process. Adhered chips were observed in both dry cut and wet cut conditions, as depicted in Figure 5.51(b) and (c).

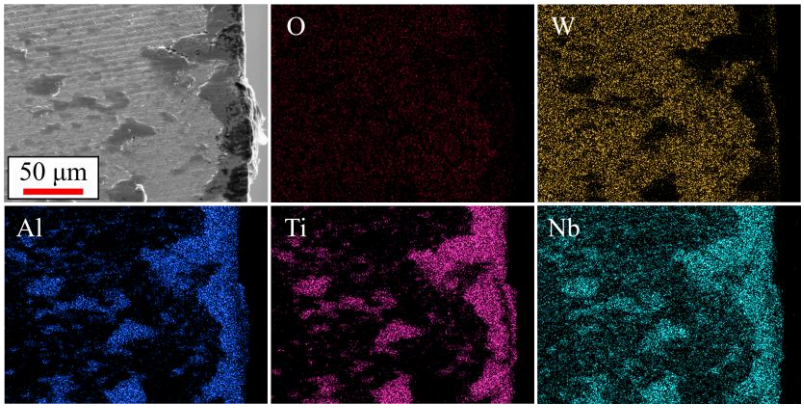


Figure 5.50 Flank face element distributions of worn cutting tool under dry cut conditions.

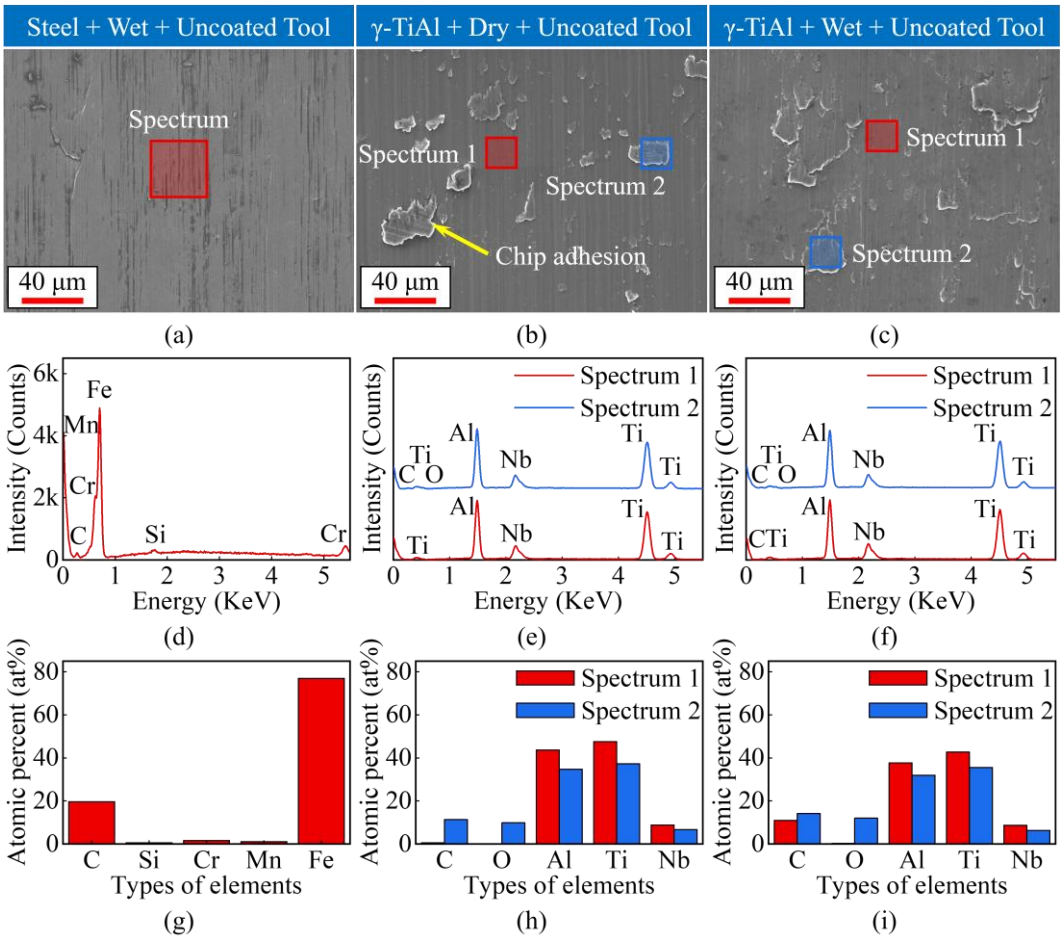


Figure 5.51 EDS analysis of milling surfaces of different materials and cutting conditions; (a), (d) and (g) Low-alloy steel + wet cut, (b), (e) and (h) γ-TiAl + dry cut and (c), (f) and (i) γ-TiAl + wet cut.

These chips may have come from materials adhering to the tool or chips remaining on the machined surface being secondary squeezed onto the machined surface. More O content was discovered in these regions, emanating from thinner chips in greater contact with oxygen in the air. Figure 5.52 presents the element distributions of the adhered chip, and denser O elements were detected at the boundary in particular. All of these oxide films play the role of anti-friction and improve the cutting ability of the tool [317].

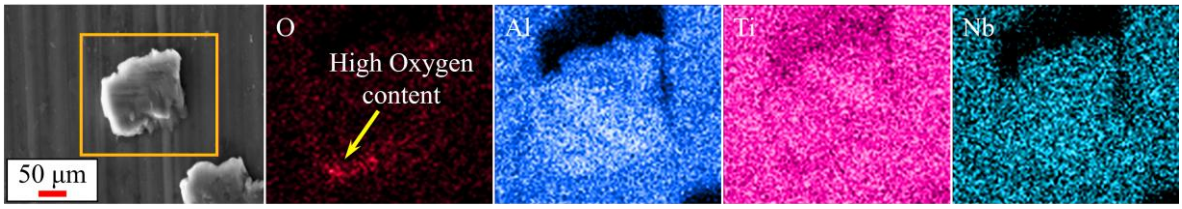


Figure 5.52 EDS element distributions of the adhered chip on workpiece machined surface.

On the other hand, during long distance cutting, the loss of friction heat was slow. Hence, the heat accumulation resulted in an increase in wear temperature. The chemical activity of elements in both the coating and workpiece surface materials increased, triggering mutual diffusion. From Figure 5.51 C element was found at a high level that may come from tungsten carbide (WC) in the tool. Figure 5.53 displays the changing relationship between the proportions of the main elements Al, Ti, and Nb of the tool surface and the workpiece machined surface after milling relative to the initial elements of the TNB. The uncoated tool was adopted in the test to eliminate the influence of coating material containing high Al and Ti.

Under dry cutting conditions, compared with the base material (marked in red), the Al and Nb content on the workpiece surface decreased, while the Ti content increased. At the same time, the content of Al in the adhesion on the tool surface was higher. This indicated that there was diffusion of Al elements from the workpiece surface to the tool surface during the cutting process. When arranged wet cut, in addition to the Al element, the higher Nb element on the tool surface also represented the diffusion of this element. Changes in element content along the depth of the cross-section validated the existence of diffusion, as illustrated in Figure 5.54.

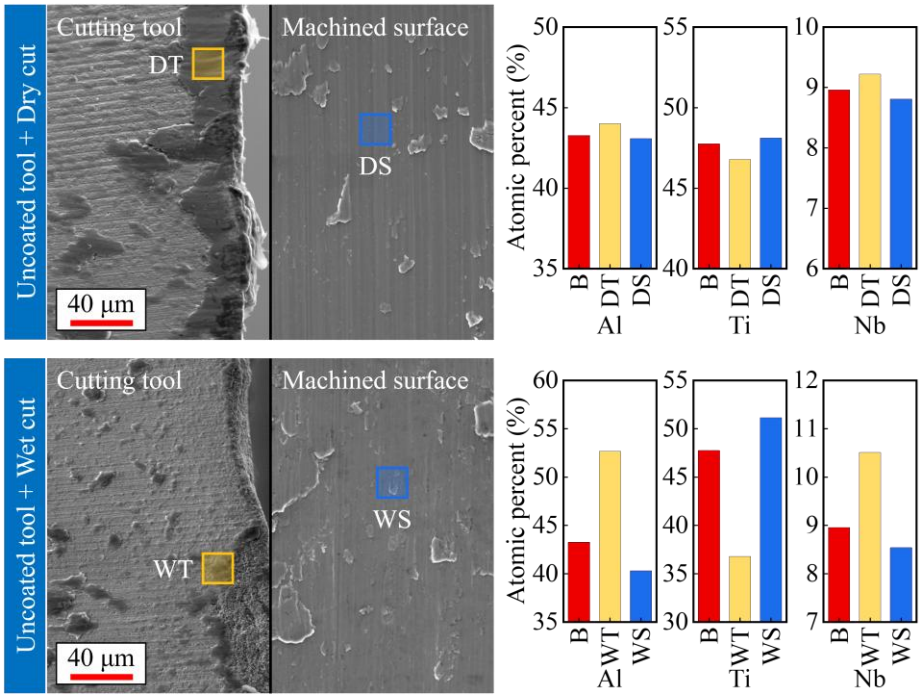


Figure 5.53 Changes in tool surface and machined surface elements distribution.

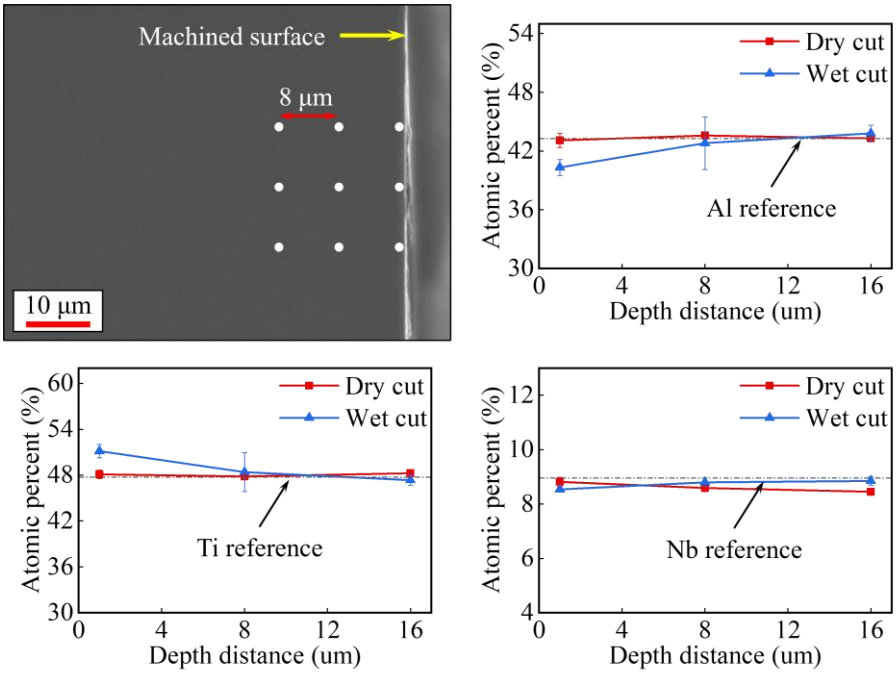


Figure 5.54 Variations in element content along cross-section depth.

5.3.4 Gross fracture and edge chipping

Tool edge chipping, a common indicator of tool failure, was frequently observed during the final stages of wet cutting, as illustrated in Figure 5.55. The primary cause of this tool failure in γ-TiAl was attributed to its low thermal conductivity. This property led to heat accumulation and insufficient heat dissipation at the cutting edge, especially for the rake face, creating a steep temperature gradient that could precipitate tool damage. Researchers have explained that edge chipping intensified as tool wear increased, leading to a rise in cutting forces. The cutting edge, subjected to cyclic impact loads during the intermittent milling process, was ultimately prone to chipping [63], [65], [81].

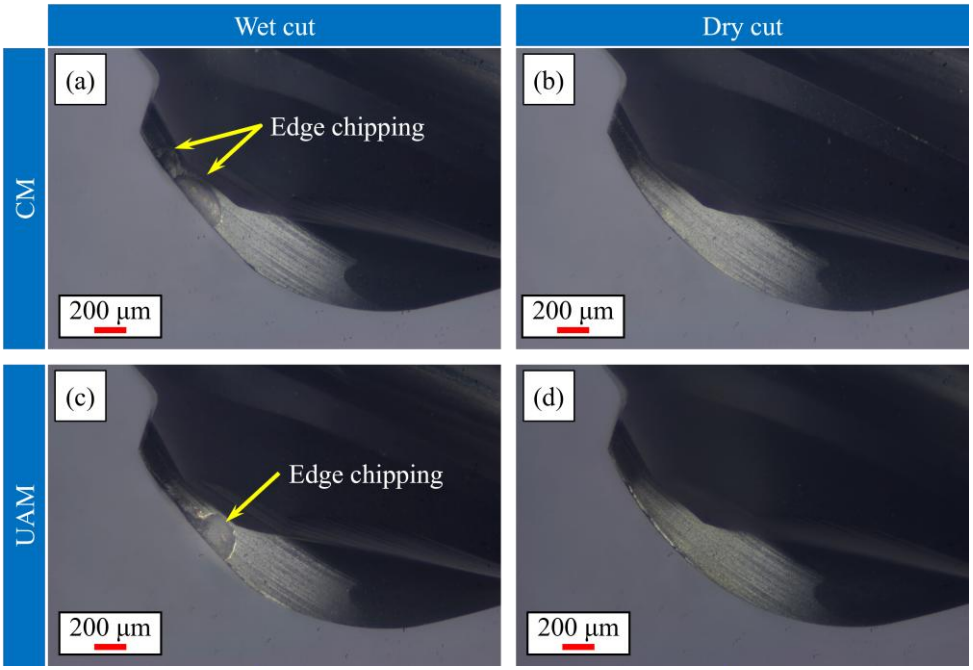


Figure 5.55 Edge chipping on the rake face for Phase 2A experiments: (a) CM + wet cut, (b) CM + dry cut, (c) UAM + wet cut and (d) UAM + dry cut.

Combined with the conclusion that dry cut conditions showed more benefits in cutting γ-TiAl and the lower cutting force was beneficial for diminishing the possibility of tool edge chipping. A significant chipping region was detected in ultrasonic-assisted milling (see Figure 5.55(a)). As cutting operations commence from a state of separation, the inherently sharp yet fragile tool edge was susceptible to microfractures and microcracks, exacerbated by ultrasonic-frequency dynamic impacts. Moreover, the cutting tool was subjected to pulsed cutting forces at ultrasonic frequencies and alternating friction forces at double-ultrasonic frequencies. These forces elicited pulsating compressive and tensile stresses, making the tool vulnerable to impact-

induced microcracks and abrasive wear. Over time, dynamic cutting forces, alternating friction, and high impact energy exacerbated existing fractures and microcracks. This progression ultimately led to flaking and crack failures at the cutting edge [217].

5.4 Phase 2B: Comparative evaluation between the effects of CM and B-UAM on machinability of γ-TiAl

5.4.1 Influence of cutting parameters on tool wear

Figure 5.56 shows the changes in cutting parameters on maximum flank wear. Generally, the tool wear under the wet cut indicated a rapid increase of the tool, while the dry cut conditions altered more gradually. In terms of the conclusion from Section 5.1.1, wet cut had a significant impact on tool wear, which meant that the cutting force increased faster than in dry cut conditions. The tool wear mechanism during wet cutting was mainly abrasive wear, and the coating did not play a role in accordance with the explanations in Section 5.3.1. Edge chipping was prone to occur in the ultrasonic-assisted milling process, as exhibited in Figure 5.55.

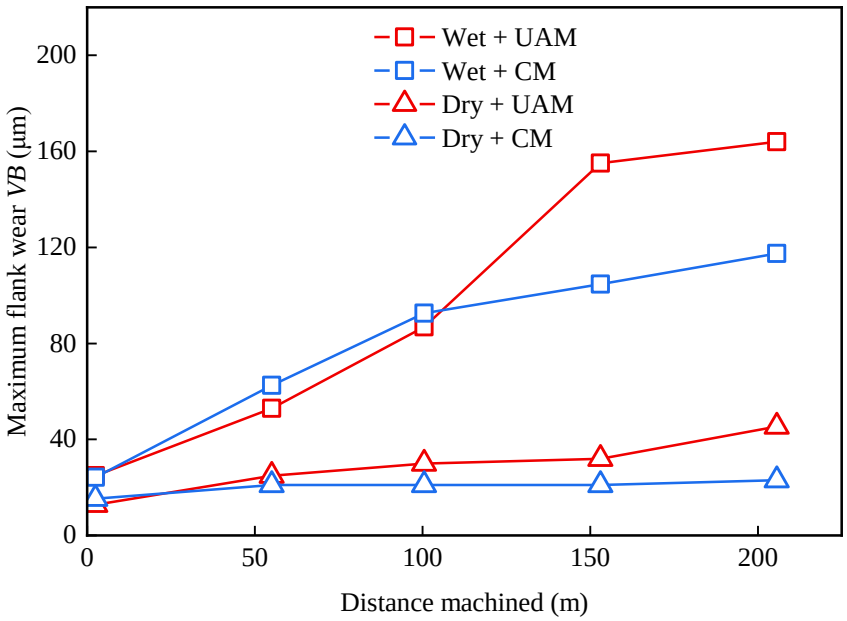


Figure 5.56 Maximum flank wear against distance machined for Phase 2B trilas.

In the first 100.5 m distance machined, UAM had a maximum flank tool wear reduction of 15.9% and quickly surpassed conventional milling. When machined to 205.6 m, the tool wear under UAM reached 164 μm, while that of CM was only 117 μm. Tool wear led to the increase in cutting force [271], [272], [273], and the boost of cutting force was the root cause for

aggravating abrasive wear [270]. The intermittent cutting characteristics of the milling process and the high-frequency cyclic load impact on the tool edge caused by ultrasonic vibration generated pulsating compressive and tensile stresses, rendering the tool susceptible to microcracks, abrasive wear and edge chipping [217]. In addition, due to the low thermal conductivity of the γ-TiAl, the steep temperature gradient caused by heat accumulation at the cutting point aggravated tool damage, especially the rake face in contact with the chip, as shown in Figure 5.55.

However, adhesive and oxidation wear dominated when adopting TiAlN coated tools under dry cutting conditions, as illustrated in Section 5.3.2 and Section 5.3.3. Ultrasonic vibration could suppress temperature rise and thereby reduce the generation of oxidation and adhesion. Meanwhile, the high-frequency separation movement of the cutting edge made it more difficult for the workpiece material to adhere to the tool surface. The maximum flank wear at the late stage of UAM reached 45.3 μm, nearly twice that of CM.

5.4.2 Effects of cutting parameters on cutting force

Figure 5.57 illustrates the variation of the average cutting force F_z over the machined distance. Before the first 25 m, the cutting force in UAM was slightly higher than CM. After that, as the cutting force F_z further increased until milling to 122 m, the force in UAM was significantly lower than that in CM. When milling to 55 m, compared with CM, the average cutting force F_z dropped from 34.03 N to 14.82 N, a decrease of up to 56.45%. However, the average cutting force was greater than that of CM at the end of the milling process.

In accordance with the analysis in Section 5.1.2, the possible reason for the disappearance of the cutting force reduction characteristic was that the current excessive cutting force changed the resonant frequency of the ultrasonic system, resulting in a significant attenuation of the ultrasonic amplitude [222], [274]. This also explained why when milling to 100 m, under almost the same flank wear conditions (UAM: VB_{max} = 86.8 μm, CM: VB_{max} = 92.5 μm), the average cutting force F_z in UAM was still decreased by 36.18% compared to CM. However, the effect of ultrasonic vibration weakened or even failed, the cutting force in UAM exceeded that of CM, and the flank wear also increased rapidly, as depicted in Figure 5.56. However, the minimal difference in cutting force between the UAM and CM was discovered under the dry cut conditions. Although compared with CM, the cutting force reached the maximum difference at

the 100 m distance machined, with 64%, the value of cutting force was still maintained at a very low level, less than 10 N. It was worth noting that under the same processing level, the maximum cutting force of the wet cut was more than 80 N. As analysed previously, the introduction of ultrasonic vibration aggravated tool wear to a certain extent compared to CM under low load conditions. This was why the ultrasonic cutting force increased when the tool was in the initial wear stage.

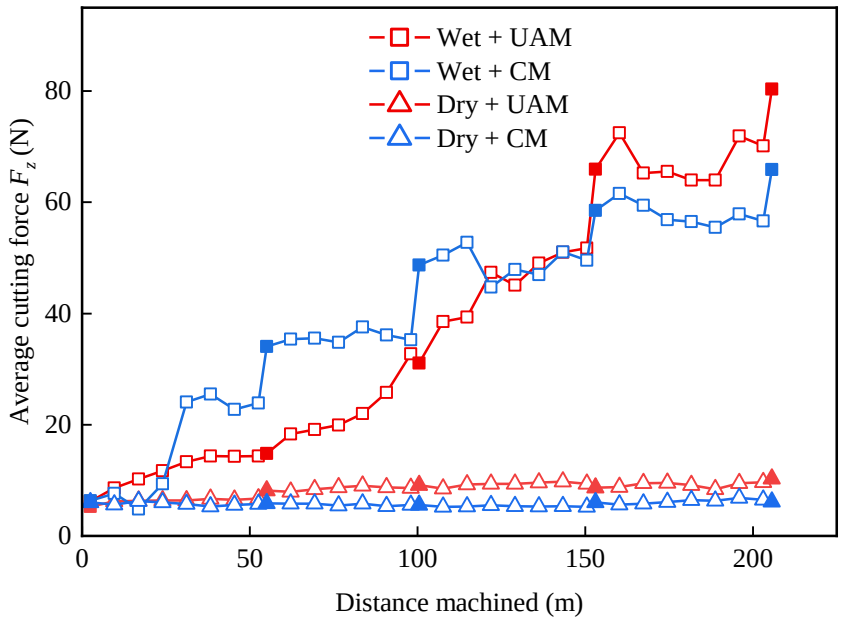


Figure 5.57 Average cutting force against distance machined for Phase 2B trials.

Figure 5.58 shows the comparison of initial three-dimensional cutting forces under different cutting conditions. Regardless of dry or wet cut, the cutting force under UAM was lower than that under CM. Among them, the cutting force in the feed direction (F_x) during UAM dropped by 47.2% under the wet cut. In addition, for a new tool, the cutting environment had little effect on the initial cutting state, and the difference in cutting force between dry and wet cuts was insignificant. Ultrasonic vibration could decrease the friction between the tool and the workpiece and change the material removal process from continuous cutting to intermittent and pulse cutting, resulting in the reduction of cutting [208], [209].

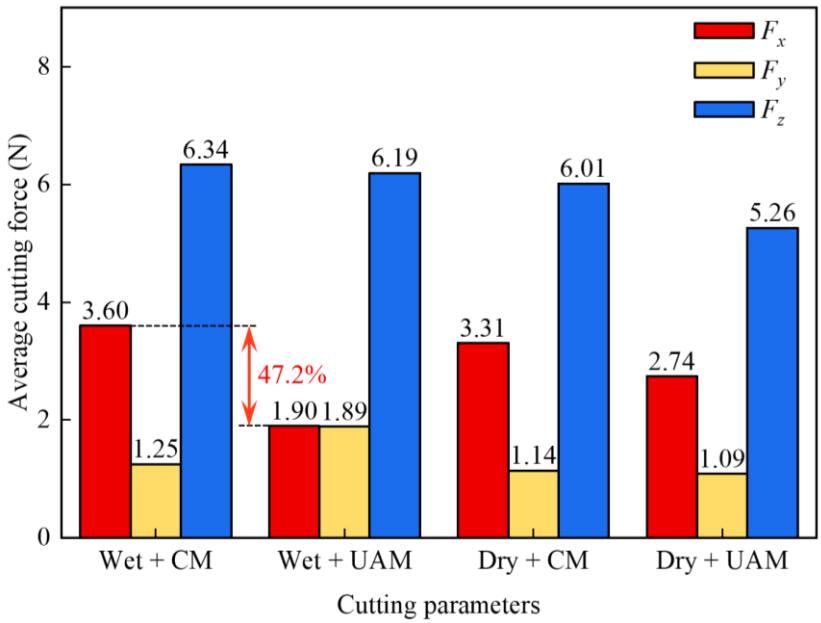


Figure 5.58 The influence of cutting conditions on the cutting force for Phase 2B trials.

5.4.3 Assessment of cutting parameters on workpiece surface integrity

5.4.3.1 Surface morphology and edge quality

Figure 5.59 presents the machined surface morphology at the initial and late stages under the wet cutting conditions. Compared with smooth texture in CM, the clear scale texture feature was observed in UAM due to the impact of ultrasonic vibration. With the deterioration of tool wear, the more significant cutting force and tool nose radius led to reduced surface smoothness. Whether it was UAM or CM, the surface texture became messy. In addition, the increased cutting force generated significant tool bending deflection, resulting in severe rubbing action between the secondary flank surface and the machined surface [289]. The machined surface material pullout phenomenon was detected in both methods because the γ-TiAl exhibited high brittleness at room temperature and was more susceptible to fracture under significantly increased cutting forces. However, the pullout feature was easier to observe in CM. In UAM, due to the hammering effect of ultrasonic vibration, the damage was suppressed or covered by surrounding materials. Figure 5.60 demonstrates the surface morphology under the dry cut. There was little change in the texture of the machined surface before and after wear, resulting from insignificant tool wear and cutting force variations, as illustrated in Figure 5.56 and Figure 5.57 in Section 5.4.2. Besides, the stepover feed marks were clearly visible under dry cutting conditions. The phenomenon of material pullout was replaced by chip adhesion since the defect position in the colour map was not at the lowest position on the machined surface, whereas

pullout presented the lowest colour. Chip adhesions were hard to observe in UAM due to the impact of ultrasonic vibration inherently generating greater height differences on the surface.

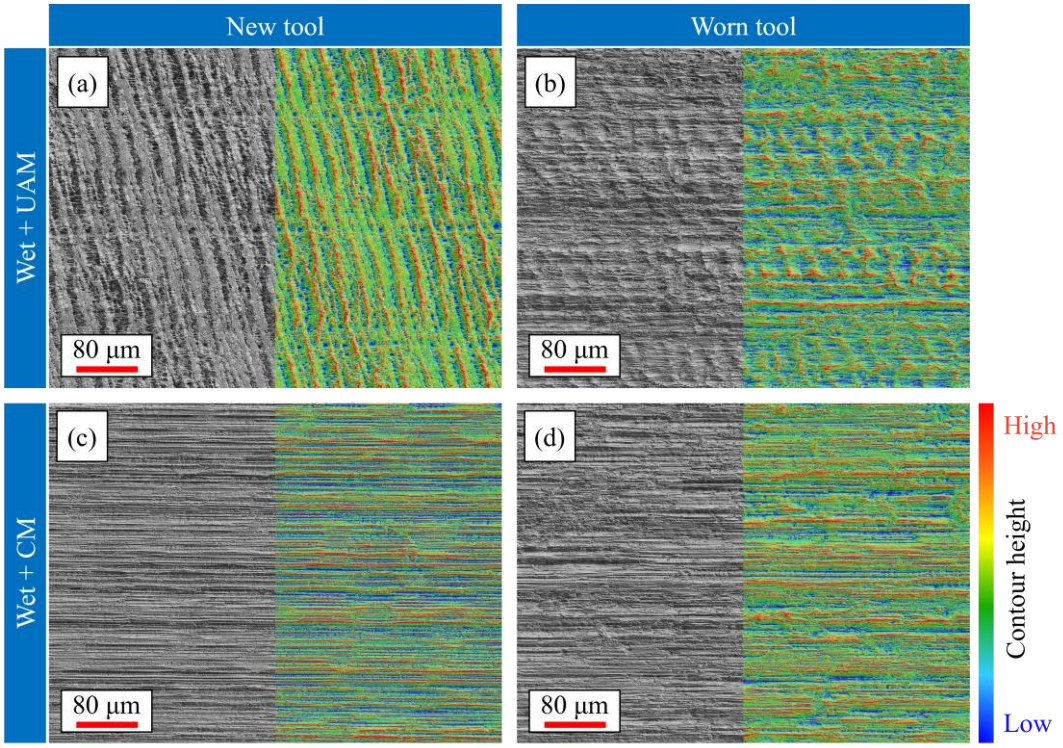


Figure 5.59 Surface morphology under wet cut imaged by Keyence VHX-7000 Opt-SEM.

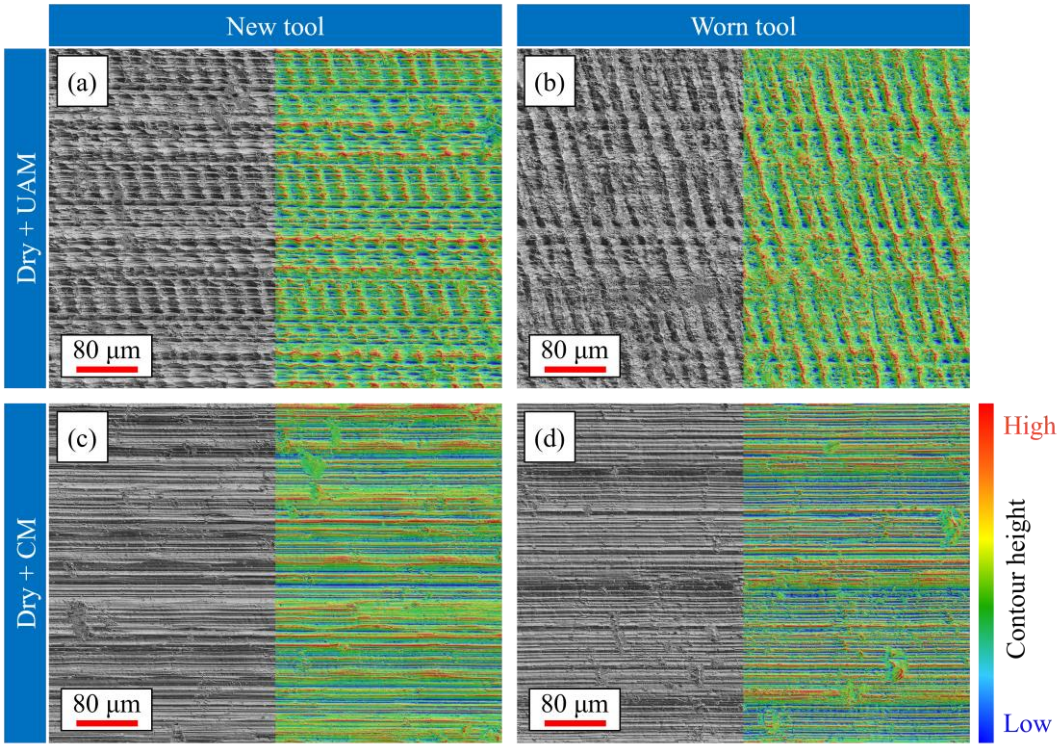


Figure 5.60 Surface morphology under dry cut imaged by Keyence VHX-7000 Opt-SEM.

Figure 5.61 depicts the exit edge contour under different cutting conditions. With the increase of distance machined, improved cutting force generated by severe tool wear resulted in more shearing-induced cracks, leading to negative burr formation [294]. Under UAM processing, the maximum depth of negative burrs gradually increased in the initial stage as the machined distance enlarged (see Figure 5.61(a)), and at the same time, the depth of CM decreased rapidly, as shown in Figure 5.61(b). In the middle of the cutting process, the cutting force and tool wear of UAM were significantly lower than those of CM, as illustrated in Figure 5.56 and Figure 5.57. However, the depth of negative burrs under UAM dropped sharply at the late stage. It even exceeded that of CM, corresponding to the changes in cutting force and wear mentioned above. Besides, the width of burr in UAM could reach ~930 μm, while CM had a similar level of ~910 μm.

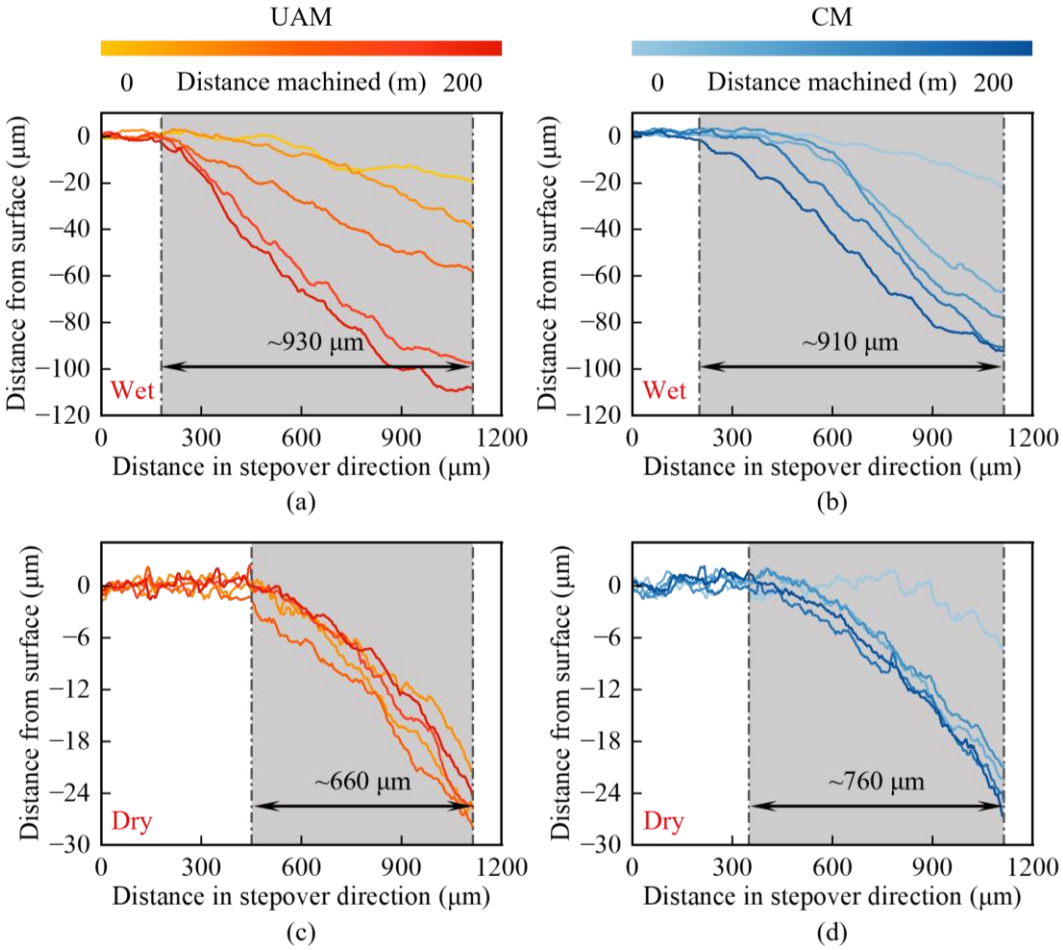


Figure 5.61 Changes in exit edge profile in stepover direction under different conditions: (a) UAM + wet cut, (b) CM + wet cut, (c) UAM + dry cut and (d) CM + dry cut.

Negative burrs or edge collapse was observed in dry cutting conditions as well. The maximum depth of burr did not change significantly with the distance machined. Because the cutting force and tool wear under dry cutting conditions changed very little under both UAM and CM processing, the burr depth measured by UAM and CM was at the same level, approximately 26 μm. However, the burr width at the end of UAM was still decreased from 760 μm to 660 μm, a 13.2% reduction. The test results showed that the deduction of cutting force caused by ultrasonic vibration can effectively reduce the depth and width of exit burrs.

5.4.3.2 Surface roughness and dimensional accuracy

To evaluate the surface quality, areal surface roughness Sa was detected, as shown in Figure 5.62. Generally, the average areal surface roughness increased as the tool wear level increased, except for UAM in wet cutting conditions. In accordance with the previous results, maximum cutting force occurred in UAM when cut to 205.6 m, which led to greater tool bending deflection and intensified the rubbing action between the secondary flank face and machined surface, resulting in secondary smearing. A comparable phenomenon was reported by Pérez [56] when conducted face milling γ-TiAl. In the other cases, the area roughness generated by worn tools was greater than that of new tools due to the increased tool nose radius [63]. Meanwhile, the introduction of ultrasonic vibration determined the change of the tool trajectory from a fixed cutting depth to a dynamic cutting depth, which also resulted in the increase in surface height difference and the rise of area roughness.

Figure 5.63 exhibits the influence of cutting conditions on root mean square gradient Sdq, which was utilised to evaluate the fineness. The degree of fineness became finer as the parameter Sdq became larger. The larger Sdq was measured in the initial stage in UAM under wet cutting conditions, representing the finer surface obtained by UAM. Combined with the surface morphology produced by CM, material pullout was the main reason for poor fineness. Although γ-TiAl had low brittleness at room temperature (wet cutting), the impact of ultrasonic vibration suppressed material fracture. However, the fineness measured at the worn tool stage showed low value in both conditions due to the obvious increment of cutting force and tool wear. When the tool was in the low-wear stage of dry cutting, UAM could maintain the fineness constant after cutting for 206.5 m, while the fineness of CM dropped from 0.17 to 0.12, a reduction of up to 29.4%.

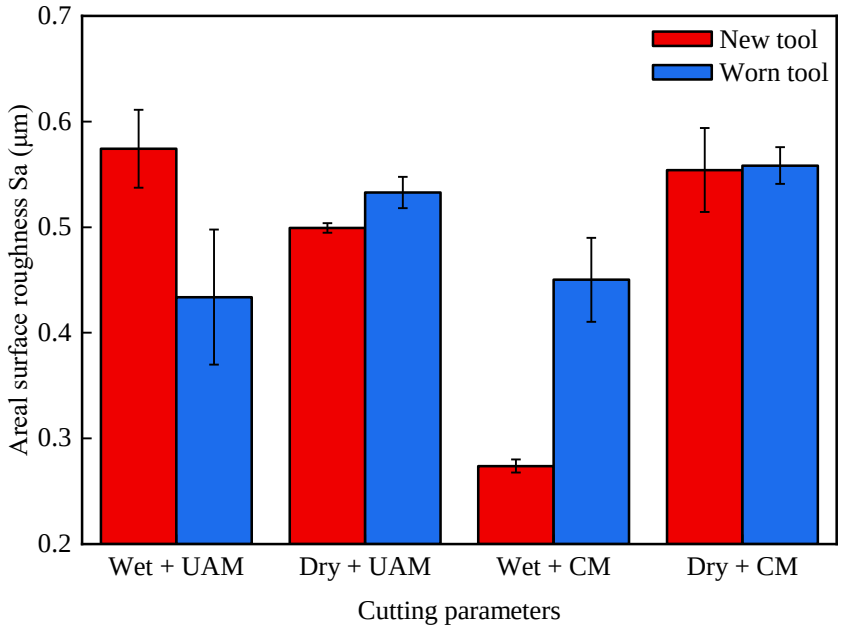


Figure 5.62 Influence of cutting conditions on the average areal surface roughness Sa for Phase 2B experiments.

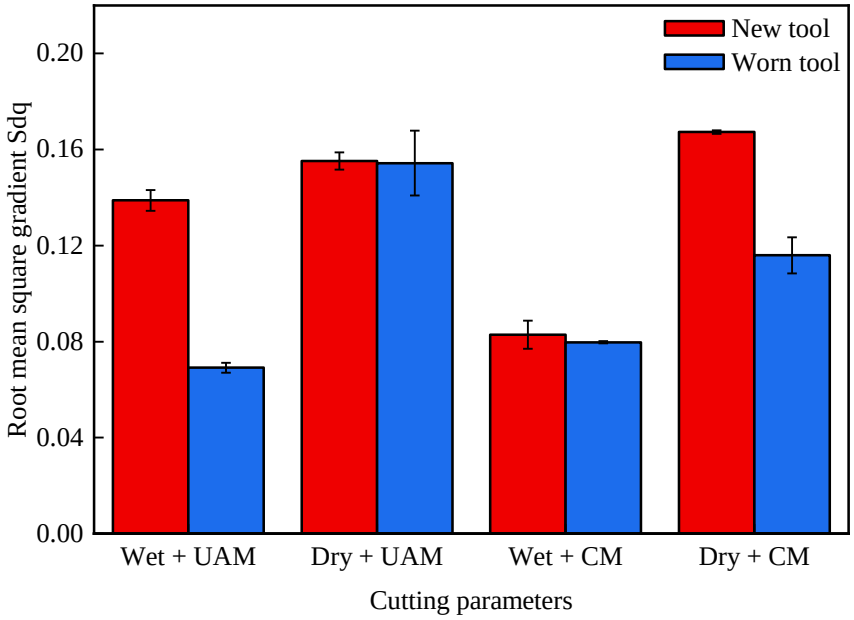


Figure 5.63 Influence of cutting conditions on the root mean square gradient Sdq for Phase 2B experiments.

The depth of cut achievement rate as a function of distance machined under different cutting conditions was illustrated in Figure 5.64. The maximum actual depth of cut could only arrive at about 80% of the theoretical setting value. Tool deflection and the increased tool nose radius

were the dominant reasons. The degree of tool wear determined the variations in cutting force and cutter nose radius. In dry cutting, the cutting forces of UAM and CM were at a low level, as summarised in Figure 5.57. Therefore, weak changes in cutting force did not aggravate the bending deflection. In addition, even slightly higher cutting force and tool wear were observed in UAM, R_{Cd} in UAM was measured higher than that in CM because the ultrasonic vibration changed the motion trajectory of the tool and increased the maximum uncut chip thickness [318]. Although the tool nose radius increased due to wear, the uncut chip thickness was larger under UAM, as illustrated in Figure 5.65, making the cutting easier. On the contrary, due to the increase of the tool nose radius in CM, the difference with the uncut chip thickness decreased, which easily intensified the ploughing effect and inhibited chip formation [301], [302].

Similar to the cutting force distribution, although cutting force and tool wear increased rapidly in wet cutting, UAM could maintain a higher R_{Cd} at the same cutting distance before 122 m, with a maximum lead of up to 72.5%. However, in the later cutting stage, the advantage of ultrasonic vibration in reducing cutting force disappeared, ultrasonic amplitude decreased, wear intensified, bending deflection became larger, and the actual cutting depth dropped to the conventional milling level.

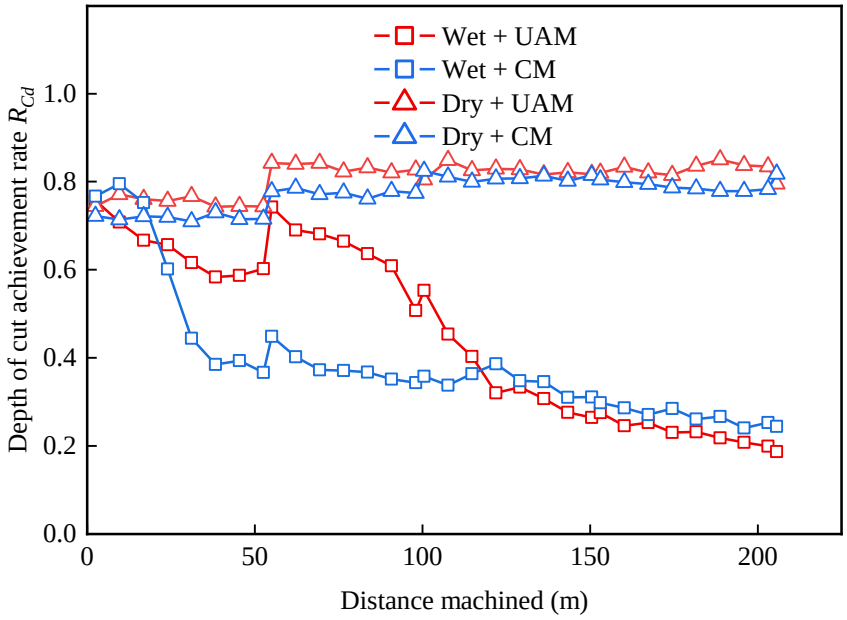


Figure 5.64 Depth of cut achievement rate against distance machined for Phase 2B experiments.

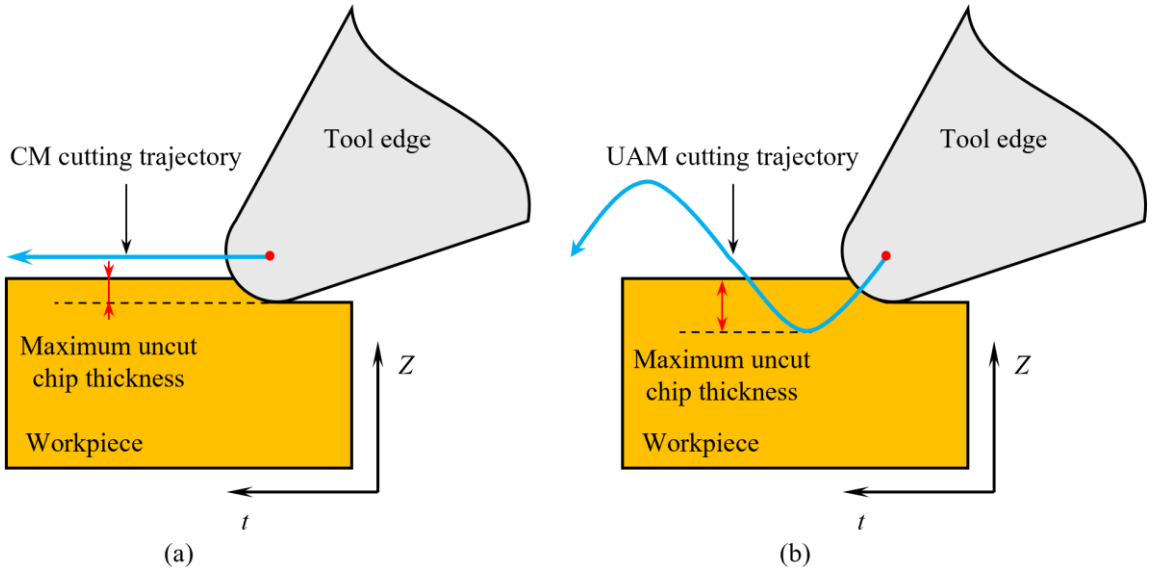


Figure 5.65 The cutting-edge motion trajectory in (a) CM and (b) UAM.

5.4.3.3 Microhardness and residual stress

The microhardness for different cutting conditions is depicted in Figure 5.66. For the new tool, the cutting force was at a similar level and ultrasonic vibration was the primary factor resulting in the microhardness change. The position close to the machined surface had the maximum microhardness, among which the maximum microhardness of UAM with wet cutting was 548 $HV_{0.025}$. UAM, under dry cutting, also showed a high surface microhardness of 497 $HV_{0.025}$. The introduction of ultrasonic vibration was the primary cause of higher microhardness in UAM than in CM. Ultrasonic vibration enhanced strain and strain rate hardening, resulting in larger microhardness even when the average cutting force was close to CM [216]. In addition to mechanical load, thermal load played an important role in microhardness variation. Much more heat was generated in dry cutting processing, which softened materials and triggered a slight reduction of microhardness.

For the worn tools, because of the low tool wear in dry cutting, the maximum microhardness increased from 497 $HV_{0.025}$ to 634 $HV_{0.025}$ and an increment from 440 $HV_{0.025}$ to 511 $HV_{0.025}$ in CM. The main reasons were that the increase in cutting forces and the intensification of tool wear brought enhancing plastic deformation. However, severe tool wear and significantly increased cutting forces under wet cutting were responsible for the intensification of plugging, severe plastic deformation, and greatly aggravated maximum microhardness, as presented in Figure 5.66(b). Zhang et al. [319], [320] investigated the microstructural evolution of magnetic

alloy and defined three regions: the refined grain region, the high-density dislocation region, and the inner matrix. Initially, the microhardness increased in the nearest refined grain region, then peaked within the second-nearest region characterised by numerous dislocations, and finally decreased to the level of the inner matrix. They also proved that the increase in cutting temperature would directly lead to recrystallisation and form the refined grain region.

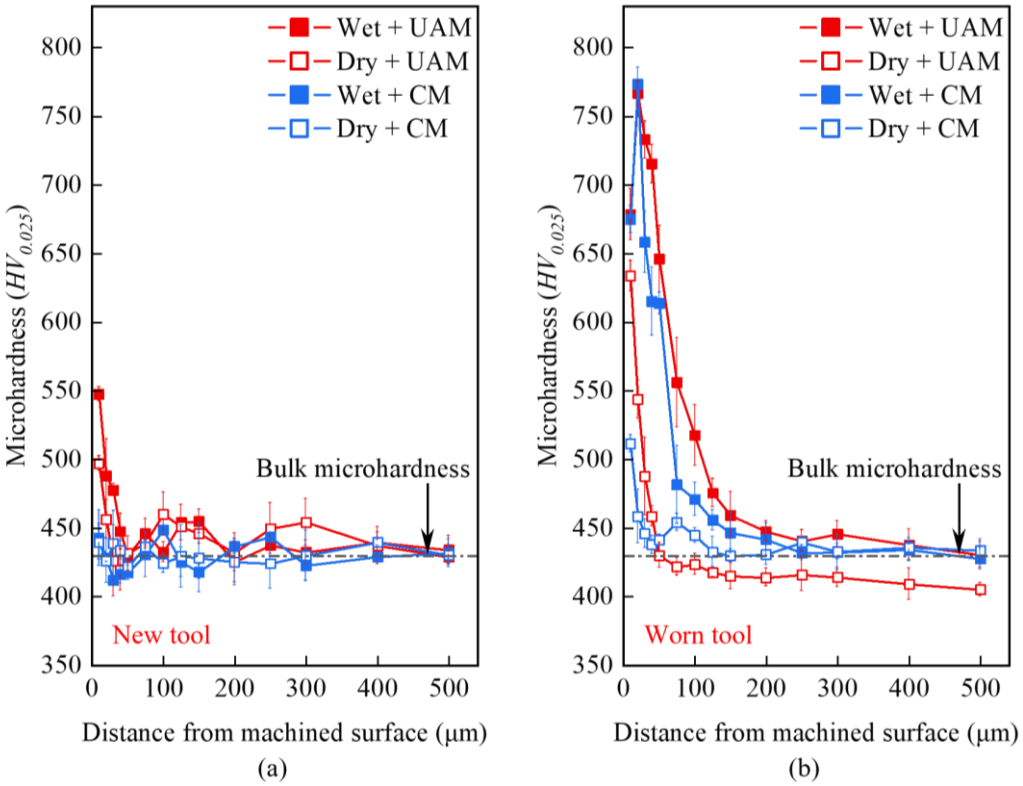


Figure 5.66 Microhardness profiles under different cutting conditions for Phase 2B experiments: (a) new tool and (b) worn tool.

The results of work hardening degree (see Figure 5.67) also showed that as cutting was conducted, both UAM and CM under wet cutting first rapidly grew under the action of increasing cutting force, and then the thermal impact intensified, hardening and softening reached a balance, and the degree of work hardening became gradually stabilise. In particular, although the cutting force and tool wear in UAM and CM were similar under dry cutting conditions, UAM had a higher degree of work hardening due to the increase in strain and strain rate caused by ultrasonic vibration. The effect of the thermomechanical load was employed in the residual stress. Figure 5.68 illustrates the residual stress variation below the machined surface with increasing depth along the feed direction. The compressive residual stress was detected in all cutting tests. For the new tool, the residual stress affected layer thickness was

about 60 μm under the CM, while UAM could reach approximately 150 μm. Enhanced strain and strain rate induced by higher instantaneous cutting speeds were the root cause of increasing residual compressive stress. The maximum compressive residual stress that occurred in UAM was –613 MPa, which was more than twice the residual stress of –300 MPa obtained by wet cutting. The higher compressive residual stress has been validated to reduce fatigue crack initiation and crack propagation and improve the fatigue property [321].

However, when the cutting tool was worn, a significant rise in residual stresses was measured in each condition. The minimal variation occurred in dry cutting due to the slight increase of tool wear and cutting force, resulting in a lower impact of mechanical load. Although the maximum compressive residual stress changed from –584 MPa to –1106 MPa in UAM under the dry cutting conditions, almost constant affected layer thickness represented that the change of tool status only impacted the surface layer. Tool wear changed the tool nose geometry, which intensified grain deformation under the action of ultrasonic vibration and produced greater compressive residual stress [223].

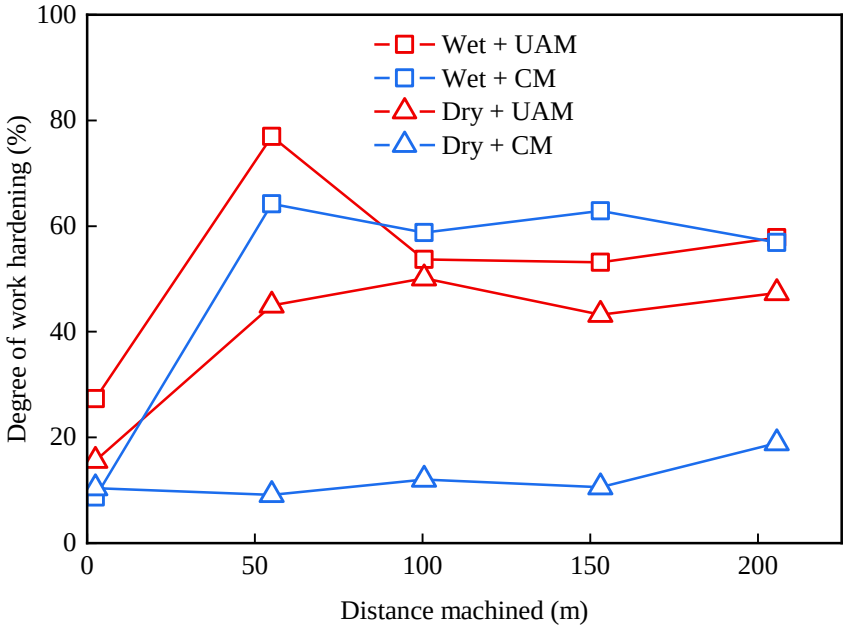


Figure 5.67 Degree of work hardening against distance machined for Phase 2B experiments.

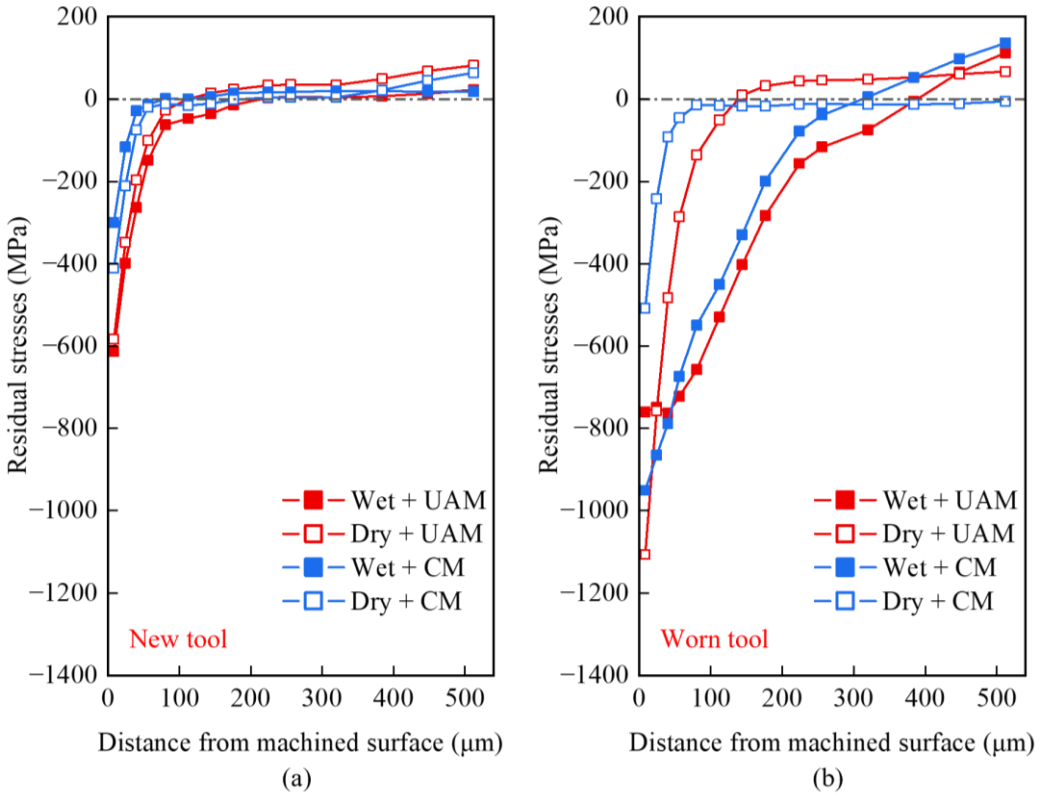


Figure 5.68 Effects of cutting conditions on residual stress in the feed direction for Phase 2B experiments: (a) new tool and (b) worn tool.

As for the wet cutting conditions, the compressive residual stress of the worn tool increased from –300 MPa to –951 MPa in CM and from –613 MPa to –760 MPa in UAM. The rapidly increasing cutting force was dominant. Severe plastic deformation introduced from large cutting force and rubbing action generated from obvious tool deflection led to higher surface residual stress. At the same time, it was found that the surface residual stress under ultrasonic conditions was smaller than that in CM. According to the previous analysis, the excessive cutting force suppressed the ultrasonic vibration, leading to the failure of ultrasonic strengthening. But overall, the compressive residual stress in each depth direction was higher than that of CM due to the higher cutting force of ultrasonic wet cutting of worn tools in terms of cutting force data. In addition, the apparent rising cutting force generated increased residual stress influence depth from ~100 μm to ~300 μm.

Comparable trends were also measured in the stepover direction. Figure 5.69 demonstrates the residual stress distribution in the stepover direction. The variation in residual stress measurements between the feed and stepover directions was primarily due to the complex

cutting process of ball end milling. Differences in the size of uncut chips in these directions resulted in varying cutting forces, leading to different residual stress values.

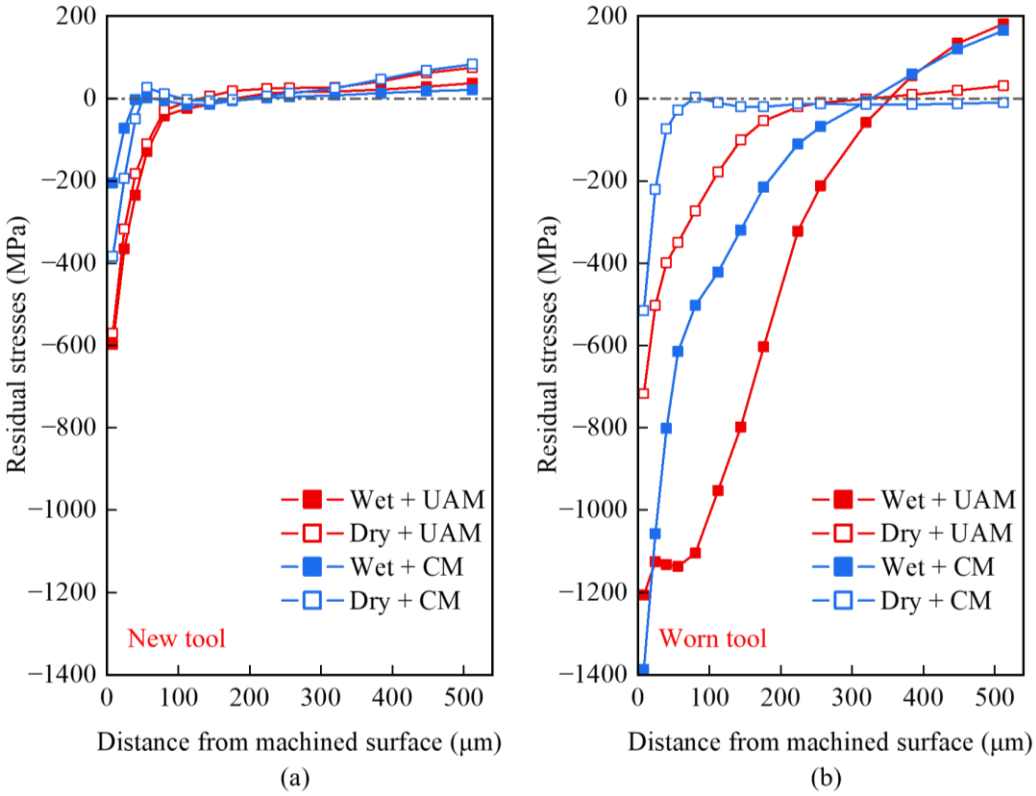


Figure 5.69 Effects of cutting conditions on residual stress in the stepover direction for Phase 2B experiments: (a) new tool and (b) worn tool.

5.4.3.4 Metallographic/microstructural alteration

Micrographs of typical metallurgical alteration produced under wet cutting conditions are detailed in Figure 5.70. Minor deformed layers were observed with ~3.73 μm in UAM and ~3.99 μm in CM for the first cut surface at different cutting methods. However, significant bending lamellar microstructures were obtained with an average depth of ~35.50 μm in UAM and 32.43 μm in CM at the final cutting stage, respectively. The increased subsurface damage while milling under fluid cooling conditions might be due to rapid growth in cutting forces caused by severe tool wear. Besides, a larger tool nose radius led to a rise of minimum uncut chip thickness, which intensified the serious ploughing action with more plastic deformation [301], [302]. In the initial cutting stage, UAM had minor subsurface damage. However, in the final stage, due to the failure of ultrasonic action, the cutting force in UAM exceeded that in CM, and the deformed layer in UAM was greater than that in CM.

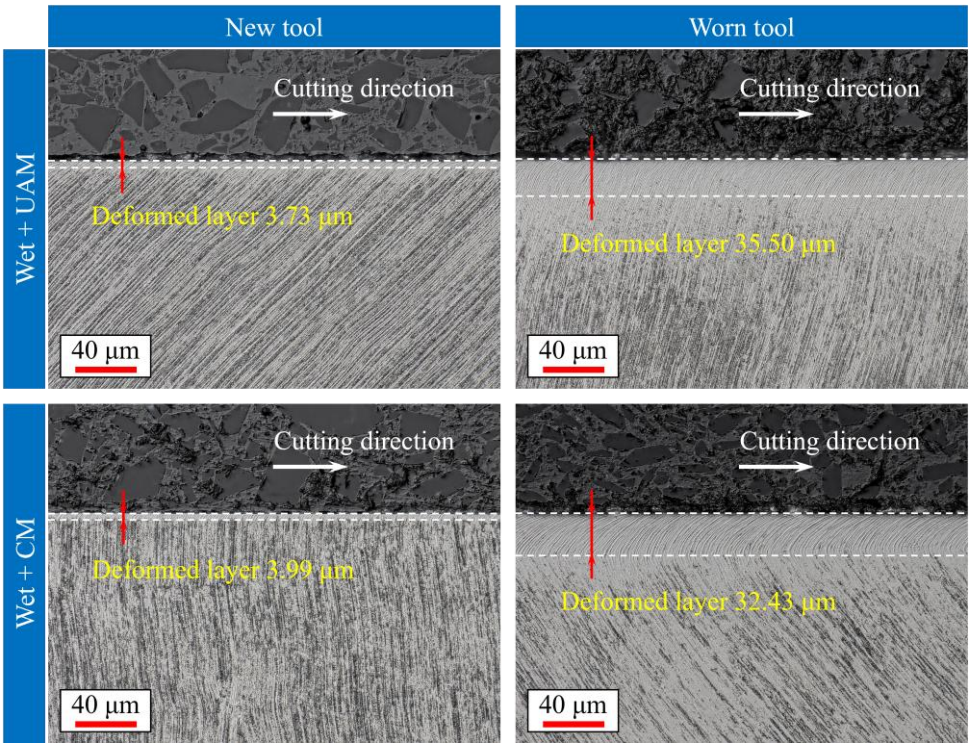


Figure 5.70 Subsurface microstructures along the feed direction in wet cut for Phase 2B trials.

The result of the subsurface microstructure under dry cutting is exhibited in Figure 5.71. Compared with wet cutting, the initial deformed layer thickness in the dry cut was more obvious, with ~6.96 μm in UAM and ~6.24 μm in CM, respectively. More heat was generated in dry cutting, which led to the material soften and easy to cut [91]. Therefore, the lamellar microstructure was more susceptible to deformation under the action of cutting force. The main reason for the differences in microstructure under various cooling conditions was cutting heat. At the final stage of cutting, the deformed microstructures in dry cutting improved to ~11.71 μm in UAM and ~7.31 μm in CM. The slow growth of tool wear and cutting forces also produced a lower increment of subsurface damage. There was little difference in microstructure changes under the optical microscope between UAM and CM. The results of optical microscopy could only reflect the variations in the scale of the lamellar structure and could not show the changes inside different phases. Therefore, it was necessary to combine microhardness and residual stress to explain the deep impact of ultrasonic actuation on metallographic alteration.

The variation trend of deformation layer thickness with machined distance under different cutting conditions is shown in Figure 5.72. As the machined distance increased, the deformed layer thickness under different cutting conditions demonstrated an upward trend. For the wet cutting, the change rate of deformed layer thickness matched the variation of cutting forces and

tool wear, as depicted in Figure 5.56 and Figure 5.57. The large cutting force was the dominant reason for increasing microstructures' deformed layer thickness in wet cutting. Meanwhile, slightly varied cutting force and tool wear in dry cutting led to a slow increment of subsurface damage, where the thermal effect was the root cause for a greater deformed layer.

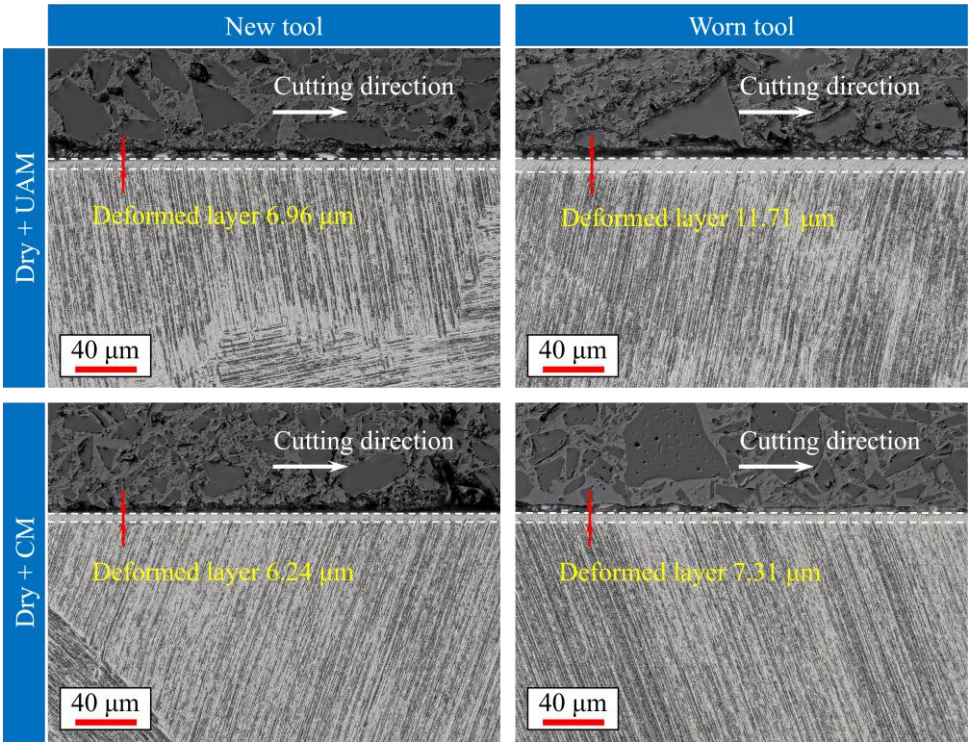


Figure 5.71 Subsurface microstructures along the feed direction in dry cut for Phase 2B trials.

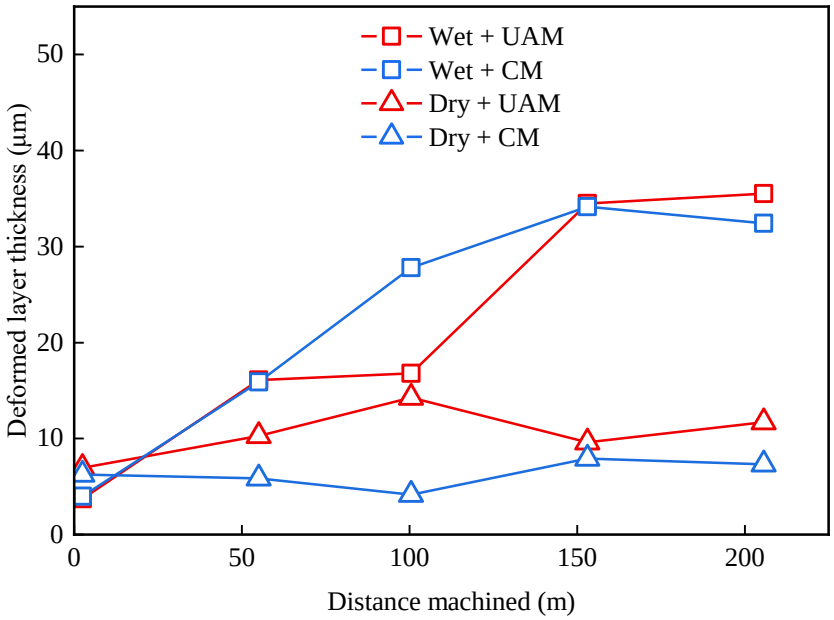


Figure 5.72 Deformed layer thickness under different cutting conditions for Phase 2B trials.

5.5 Phase 3A: Experimental validation of analytical model for predicting machined surface morphology in B-UAM

5.5.1 Influence of axial runout on surface morphology

Axial runout was an inherent error in the machine tool manufacturing process and could not be completely avoided. The experimental and theoretical analysis found that axial runout was the root cause of the phenomenon: the feed mark spacing was twice the feed per tooth on the surface machined by the ball-end mill. Figure 5.73 illustrates the generation of feed marks under ideal and actual conditions. For a 2-fluted ball-end mill, the ridge was the intersection line of two enveloping surfaces generated by two cutting edges in sequence, as depicted in Figure 5.73(a).

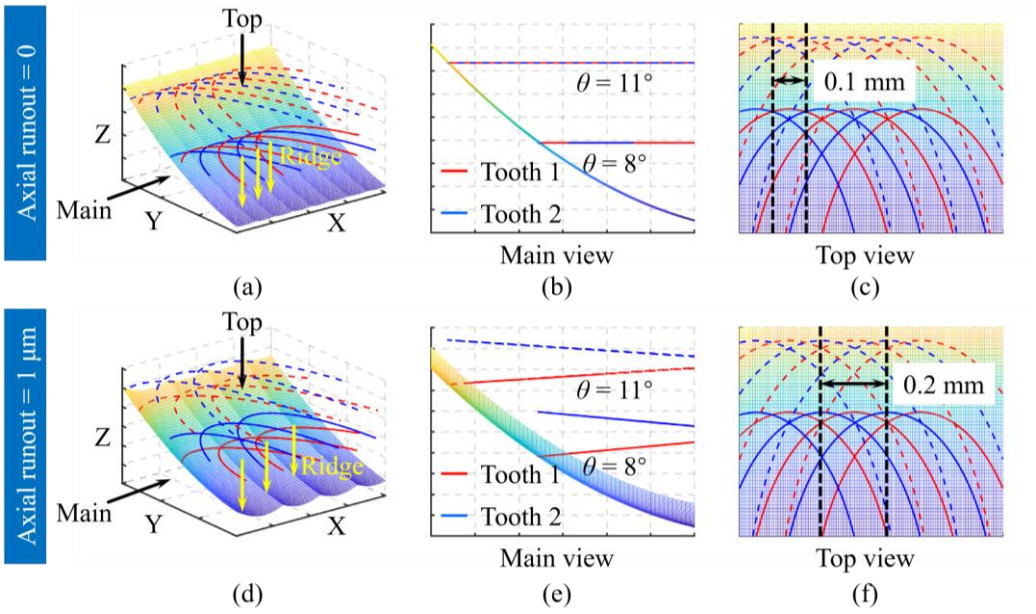


Figure 5.73 Schematic diagram of influence of axial runout on surface morphology; (a), (b) and (c) Axial runout = 0 and (d), (e) and (f) axial runout = 1 μm.

The convex ridge could also be illustrated as consisting of a series of intersection points of the motion trajectories of cutting points on different cutting teeth with the same axial position angle. The 1st tooth indicated by the red line in Figure 5.73 first contacted the workpiece, the blue line represented 2nd tooth, then cut in. Two cutting points with different axial position angles were selected in the model, and the motion trajectories were represented by solid lines and dashed lines, respectively. It could be seen from the main view that the height direction of the two cutting points with the same axial position angle remained the exact longitude in the height direction during the movement, as demonstrated in Figure 5.73(b). Therefore, the distance between the ridges was the feed per tooth in the cutting parameters (see Figure 5.73(c)).

However, even if there were only an extremely minor axial runout, such as 1 μm, would directly change the ridge formation process, as illustrated in Figure 5.73(d). Similar to axial runout-free cutting, the red 1st tooth cut into the workpiece first, followed by the blue 2nd tooth. Consider the presence of axial runout, whose frequency was the same as the spindle rotation frequency. Two adjacent cutting points with the same axial position angle had a phase difference during the movement. That was, their longitudes in the height direction were different, as shown in Figure 5.73(e). In this case, the ridge was formed by the intersection of the enveloping surfaces produced by two adjacent milling processes of 1st tooth. Figure 5.73(f) shows the distance of the feed mark was 0.2 mm in the presence of axial runout, which was twice the feed per tooth. It should be noted that the cutting tooth that entered later also participated in the cutting. Still, there was a position difference between the machined surface it generated and the machined surface of the 1st tooth, and it would be covered when the 1st tooth cut into the workpiece again. In other words, the teeth that cut in later only participated in the cutting process but not in forming ridges. This meant that the fluctuation frequency of the cutting force signal was still consistent with the rotation speed, but the measured value of the feed mark on the machined surface would have multiple relationships with the feed per tooth, which can be expressed by Equation 5-1:

$$d_{fm} = N_t \times f_Z \tag{5-1}$$

where d_{fm} was the distance of the feed mark, N_t was the total number of teeth and f_Z was the feed per tooth.

Figure 5.74 displays the experimental results for validating the influence of axial runout on feed mark distance in ball-end milling. During slotting with ball nose end mills, since the height of the cutting point at the bottom of the tool changed very little with the axial position angle, and the phase difference between different cutting points with the same axial position angle was very small, the influence of axial runout was not significant. Meanwhile, near the axis position, because the nominal radius of the tool approached zero, the cutting velocity of the cutting point was also close to zero, so the surface would have a more obvious ploughing phenomenon, and the feed mark was hard to describe. When the feed per tooth was set to 0.05 mm/tooth, the feed mark at the bottom of the slot was about 0.051 mm, and the area away from the bottom increased

to 0.10 mm. Consistent results were also proven in tilt milling, as exhibited in Figure 5.74(b) and (c), the distance of the feed mark was always twice the feed per tooth.

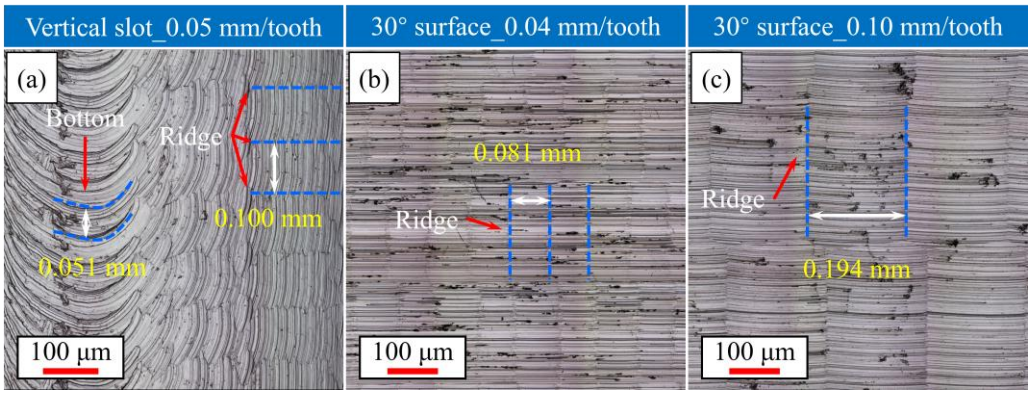


Figure 5.74 Experimental results of influence of axial runout on surface morphology.

5.5.2 Geometrical simulation and analysis of B-UAM surface morphology

- **Comparison of experimental results of vertical milling process**

Figure 5.75 shows the surface morphology and cross-sectional contour predicted by the model and measured experimentally. The protrusion characteristics existing near the tool axis in vertical milling had consistent results in simulation and experiment. However, the material removal process was difficult due to the low cutting velocity near the axis during the experiment, and there was an obvious ploughing phenomenon. As a result, the material removal process of vertical milling could not perfectly fit the theoretical motion trajectory of the tool. This also resulted in the fact that, as shown in Figure 5.75(e) and (f), the wave peak shape had high consistency in the feed or stepover direction, but the theoretical wave trough could not be reached in actual vertical cutting. This was the reason why ball-end mills in practical applications would plan tool paths to avoid the bottom area of the tool from participating in cutting. In addition, the distance between wave peaks was nearly twice the feed per tooth, which once again proved the view mentioned in Section 5.5.1 that axial runout was the cause of the inconsistency between the feed mark measurement and the setting feed per tooth. Besides, regarding computational efficiency, the optimised Z-map algorithm only took about 35 s in simulations of the same level, significantly ahead of the computational time of more than 110 s using a similar method reported by Li et al. [242]. The computational efficiency was greatly improved.

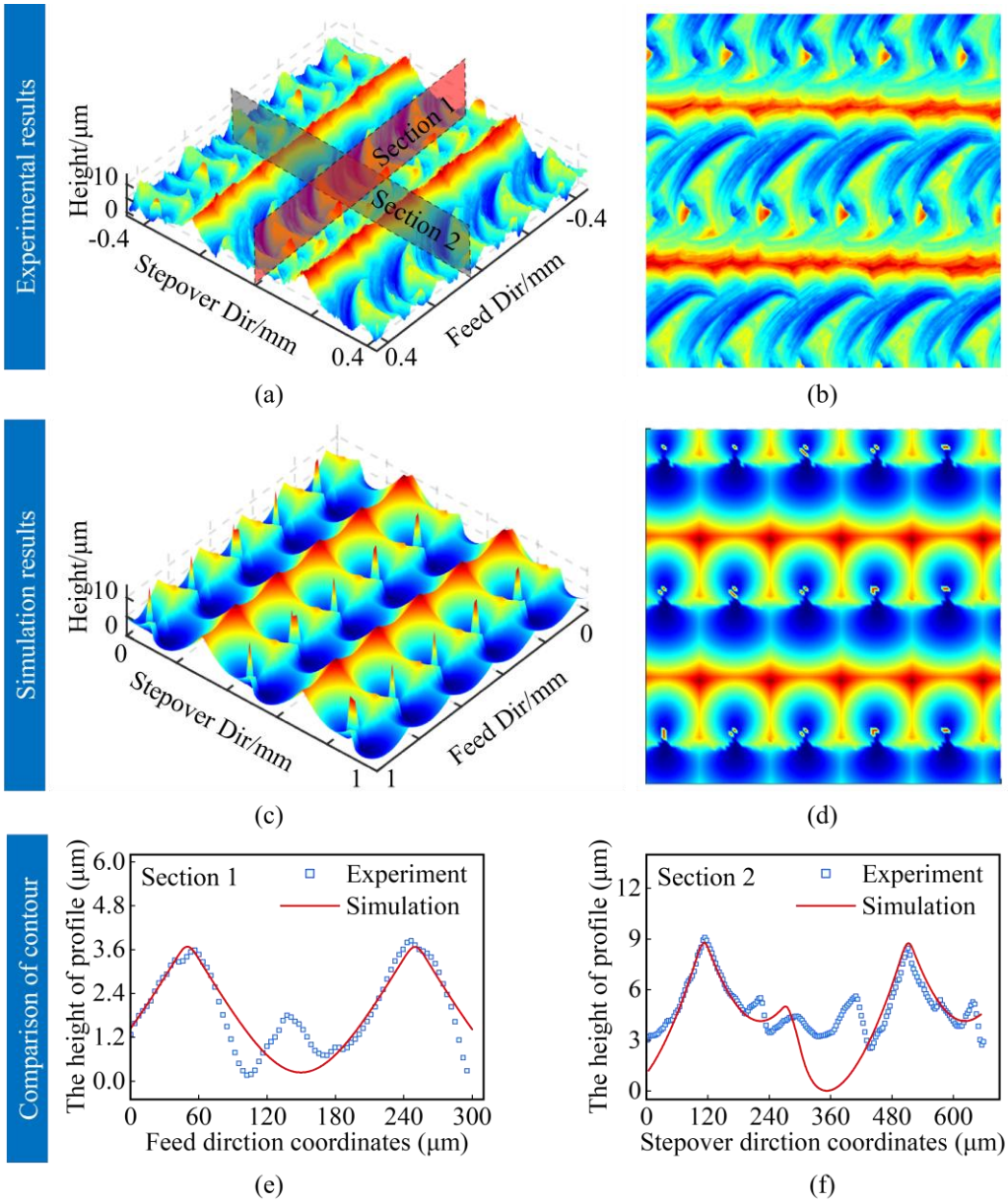


Figure 5.75 Schematic diagram of comparison between modelling prediction and experimental results of machined surface morphology (N = 3000 rpm, f_z = 0.10 mm/tooth, a_p = 0.4 mm, a_e = 0.4 mm, α = 0°, A_U = 0 μm).

➢ **Comparison of experimental results of tilt milling process**

A more regular surface would be obtained when the tilt cutting was adopted in ball-end milling, as presented in Figure 5.76. The colour map of the predicted morphology showed that the morphological characteristics of the inclined milling surface were in good agreement with the actual machining results. At the same time, in the feed cross-section and stepover cross-section profiles, the model predictions of wave peaks and troughs were highly consistent with the

experimental measurements. The fineness of the tilt milled surface was higher than that of the vertical milling due to the cutting process in the high velocity cutting region. More comparison results were listed in Figure B.4 and Figure B.5, which also validated the efficiency of the model.

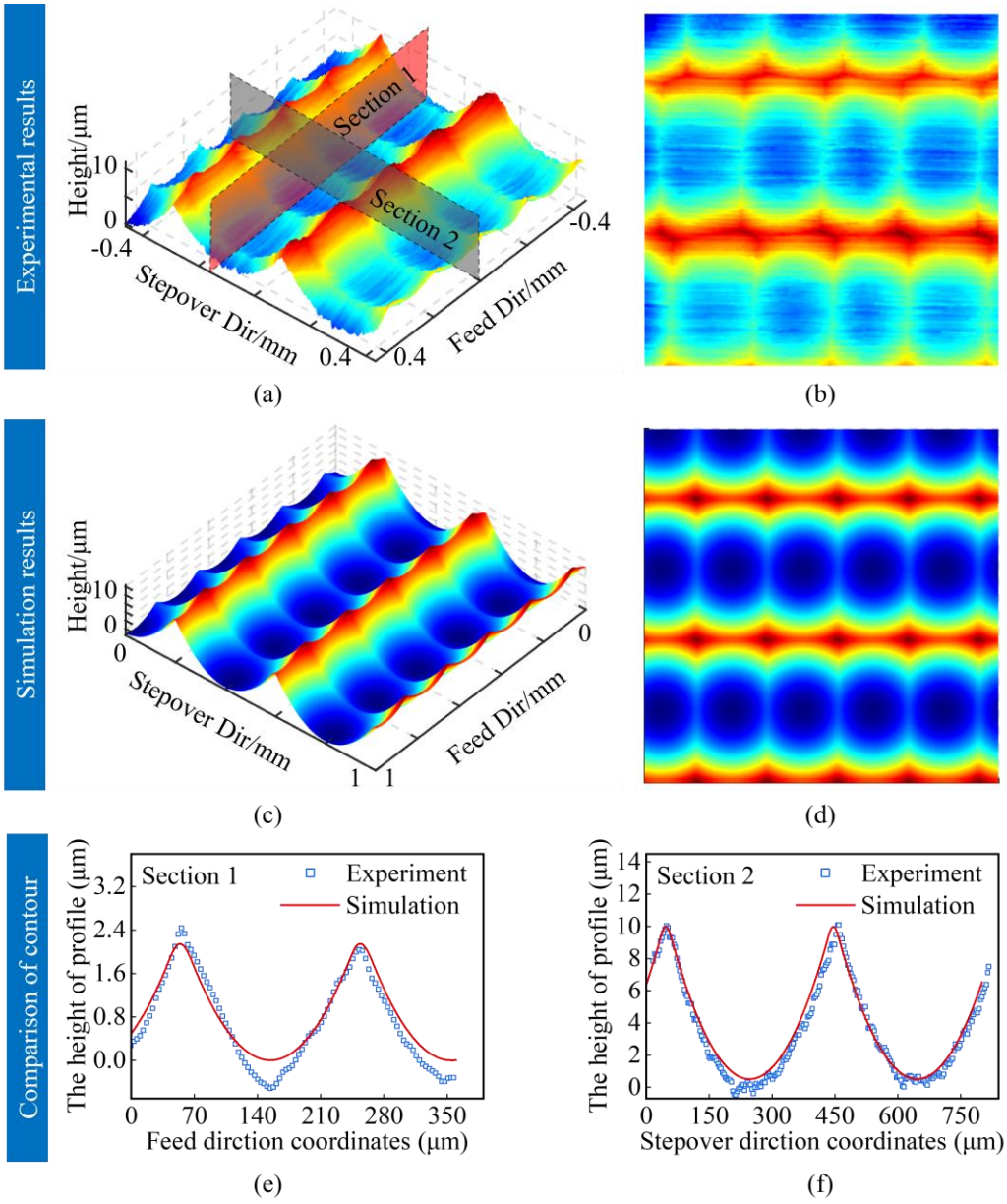


Figure 5.76 Schematic diagram of comparison between modelling prediction and experimental results of machined surface morphology (N = 3000 rpm, f_z = 0.10 mm/tooth, a_p = 0.4 mm, a_e = 0.4 mm, α = 45°, A_U = 0 μm).

➢ **Comparison of experimental results of B-UAM process**

Figure 5.77 demonstrates the comparison results in ball end ultrasonic-assisted milling under the tilt cutting conditions. The texture of the UAN surface in the feed direction was very dense because the ultrasonic vibration frequency was much greater than the spindle frequency, and the high-frequency vibration of the tool trajectory in the feed direction replaced the large-size pit structure simply caused by the feed per tooth.

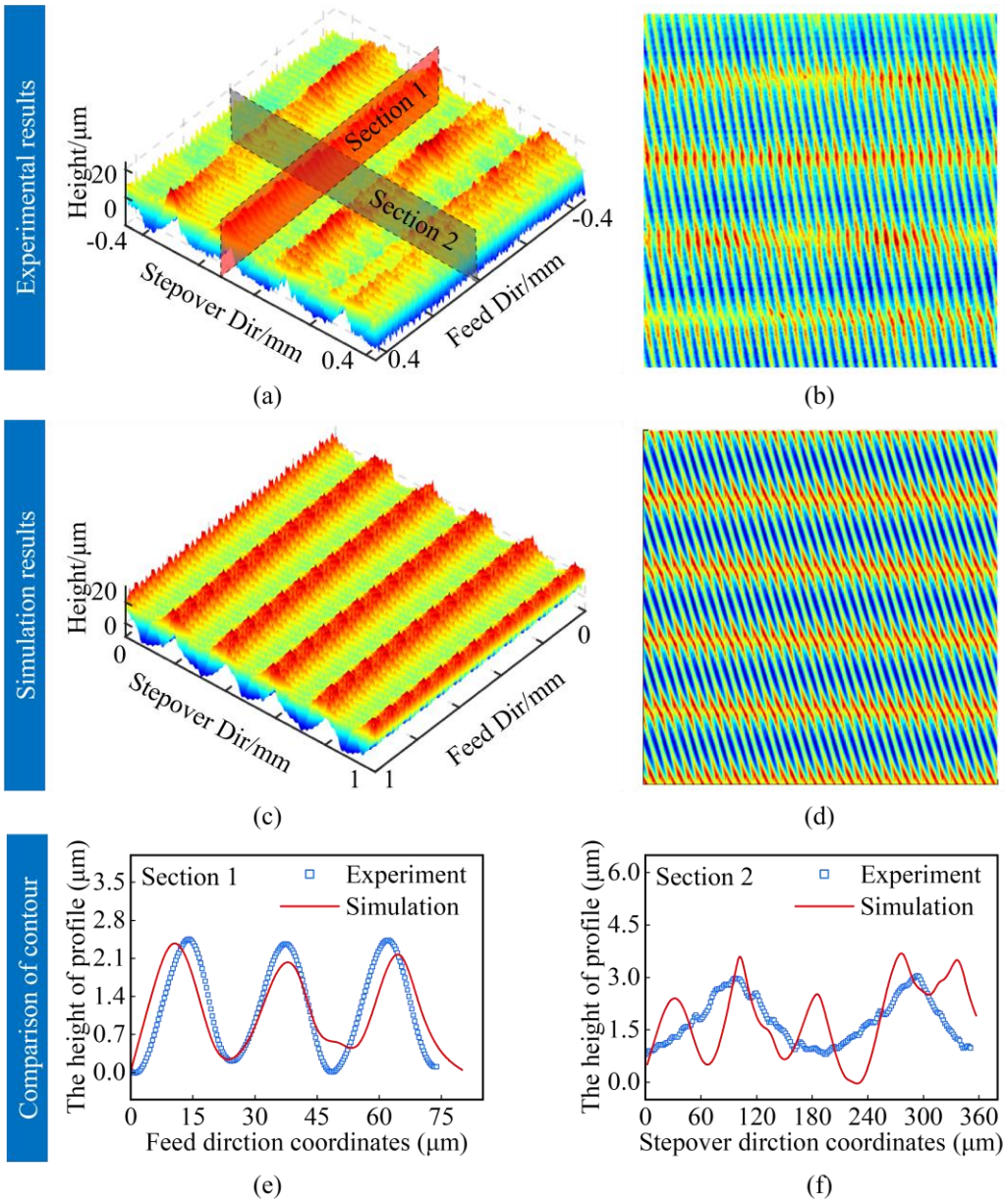


Figure 5.77 Schematic diagram of comparison between modelling prediction and experimental results of machined surface morphology (N = 6000 rpm, f_z = 0.04 mm/tooth, a_p = 0.2 mm, a_e = 0.2 mm, α = 45°, A_U = 6 μm).

The dense pit structure of the morphology prediction model was in good agreement with the actual cutting process, as shown in Figure 5.77(b) and (d). The cross-sectional contour prediction in the feed direction also maintained a high degree of matching with the actual milled contour. The contour consistency in the stepover direction was poor. Although the peak spacing can be distinguished and was numerically consistent with actual milling, the machined surface in the theoretical model only considered the cutting edge sweeping motion trajectory and ignored the influence of the flank and rake faces of the tool. In actual cutting, the flank face might crush the surface processed by the cutting edge, and this phenomenon was more obvious during high-frequency ultrasonic vibration. Therefore, there might be errors in the sidewall height direction of the pit structure. At the same time, the sidewall structure was also a serrated non-smooth curve, and the distribution on the measurement path in the stepover direction was more complex, resulting in larger errors.

Processing parameters had a significant impact on the surface morphology prediction of UAM. Figure 5.78 depicts the comparison of morphology prediction and test results when the cutting parameters were N = 3000 rpm, f_z = 0.10 mm/tooth, a_p = 0.4 mm, a_e = 0.4 mm, α = 45° and A_U = 8 μm. The pit features could still be observed because the depth of cut and feed per tooth had a greater magnitude difference than the ultrasonic amplitude. However, the originally smooth surface inside the pits was filled with more densely packed small pits. In this case, the cross-sectional profile prediction in the stepover direction was more consistent with the experimental results, but the accuracy in the feed direction decreased. The reason for this result was also that the secondary extrusion of the tool face on the machined features was not considered. It was also related to the meshing accuracy in the model. Finer meshing could retain more geometric features but will greatly reduce computational efficiency.

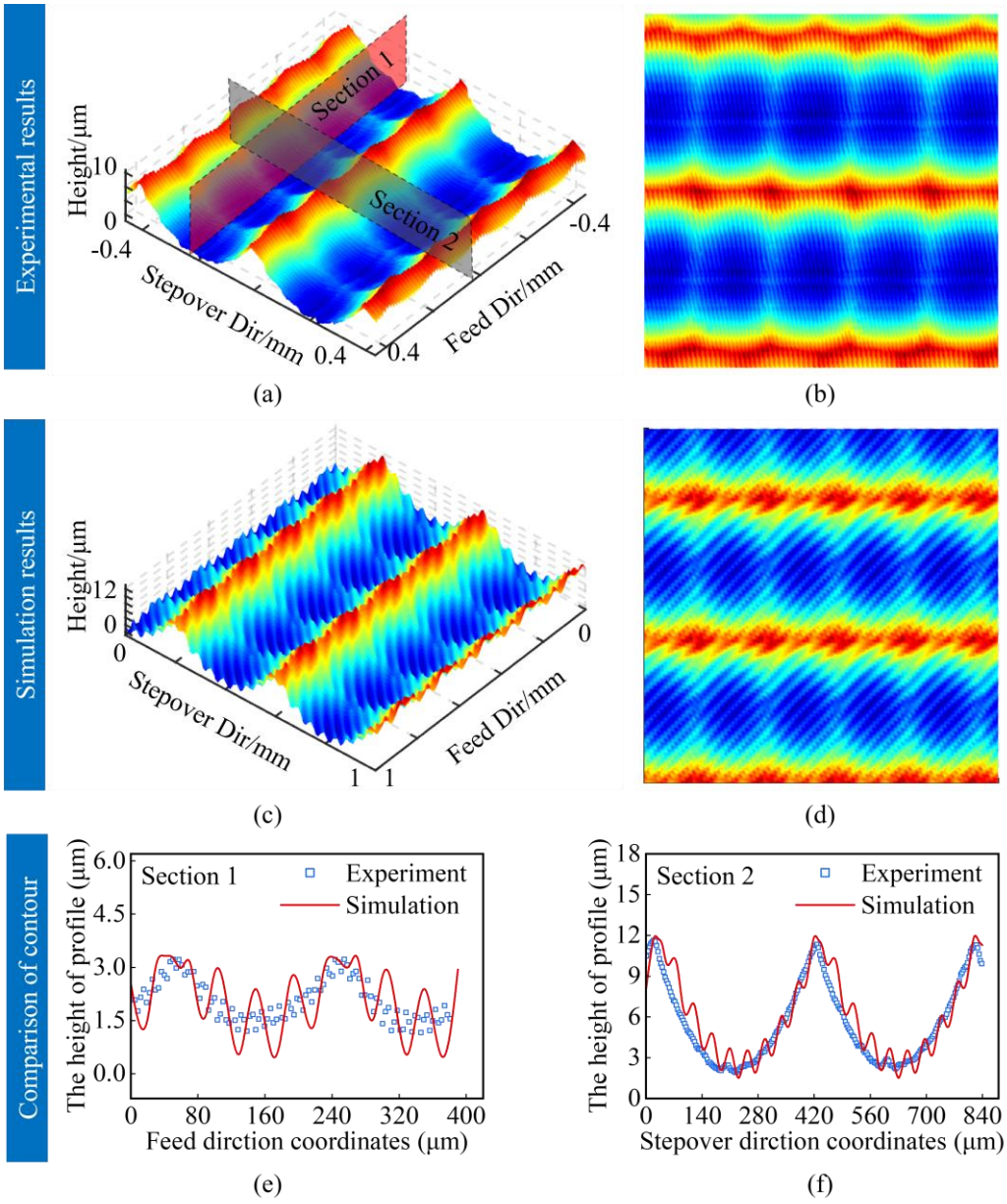


Figure 5.78 Schematic diagram of comparison between modelling prediction and experimental results of machined surface morphology (N = 3000 rpm, f_z = 0.10 mm/tooth, a_p = 0.4 mm, a_e = 0.4 mm, α = 45°, A_U = 6 μm).

5.6 Phase 3B: Experimental validation of analytical model for predicting cutting forces in B-UAM

5.6.1 Prediction of tool bending deflection in B-UAM operation

According to the static deflection model established in Section 4.2.2, the theoretical tool bending deflection could be calculated by the Equation 4-30. Figure 5.79 compares the experimental results and model prediction results. The coefficient of determination R^2 between experimental data and theoretical calculation was 0.9428, demonstrating a strong relationship between the model and the actual data. The experimental results could be predicted with high accuracy by the static bending deflection model. Notably, when the cutting force was low, there was a slightly larger error between the theoretical and experimental values. The cutting force varied dynamically during the actual cutting process. To simplify the calculation in the model, the static load that led to tool bending deflection was set to average cutting force. In this case, when the cutting force was low, bending was significantly affected by force fluctuations, resulting in increased errors.

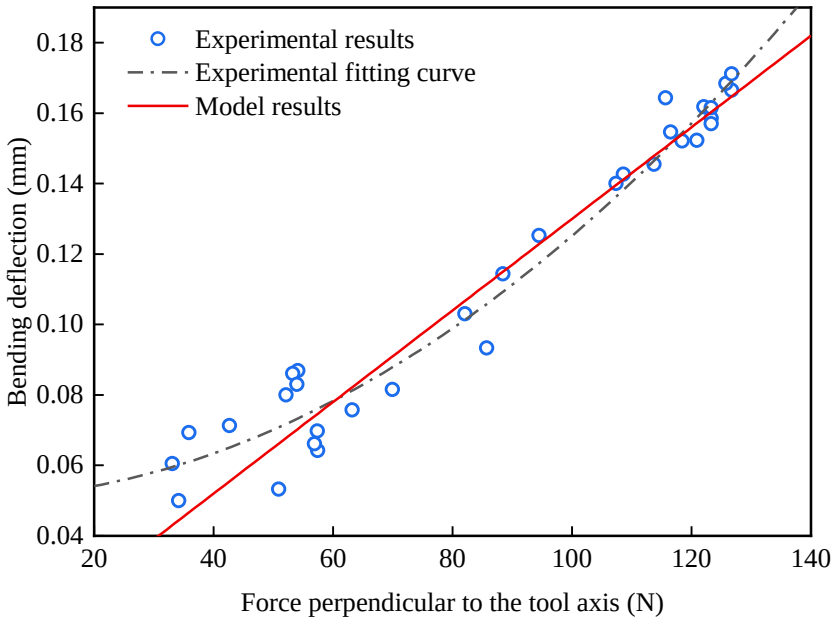


Figure 5.79 The prediction results of tool bending deflection model using Phase 1B data.

5.6.2 Calibration of cutting force coefficients

The cutting force coefficients could be identified by using measured average cutting forces in ball-end ultrasonic-assisted milling slot experiments and the least square methods according to Equations 5-2–5-5:

$$\hat{C} = (X^T X)^{-1} X^T Y \tag{5-2}$$

where $\hat{C}$, X and Y could be expressed as:

$$\hat{C} = [K_{rc0}, K_{rc1}, K_{rc2}, K_{rc3}, K_{tc0}, K_{c1}, K_{tc2}, K_{tc3}, K_{ac0}, K_{ac1}, K_{ac2}, K_{ac3}, K_{re0}, K_{te0}]_{(15\times1)} \tag{5-3}$$

$$X = \begin{bmatrix} \frac{\partial F_x^{P1}}{\partial K_{rc0}} & \frac{\partial F_x^{P1}}{\partial K_{rc1}} & \frac{\partial F_x^{P1}}{\partial K_{rc2}} & \frac{\partial F_x^{P1}}{\partial K_{rc3}} & \frac{\partial F_x^{P1}}{\partial K_{tc0}} & \cdots & \frac{\partial F_x^{P1}}{\partial K_{te0}} \\ \frac{\partial F_y^{P1}}{\partial K_{rc0}} & \frac{\partial F_y^{P1}}{\partial K_{rc1}} & \frac{\partial F_y^{P1}}{\partial K_{rc2}} & \frac{\partial F_y^{P1}}{\partial K_{rc3}} & \frac{\partial F_y^{P1}}{\partial K_{tc0}} & \cdots & \frac{\partial F_y^{P1}}{\partial K_{te0}} \\ \frac{\partial F_z^{P1}}{\partial K_{rc0}} & \frac{\partial F_z^{P1}}{\partial K_{rc1}} & \frac{\partial F_z^{P1}}{\partial K_{rc2}} & \frac{\partial F_z^{P1}}{\partial K_{rc3}} & \frac{\partial F_z^{P1}}{\partial K_{tc0}} & \cdots & \frac{\partial F_z^{P1}}{\partial K_{te0}} \\ & & \vdots & & & & \vdots \\ \frac{\partial F_x^{P10}}{\partial K_{rc0}} & \frac{\partial F_x^{P10}}{\partial K_{rc1}} & \frac{\partial F_x^{P10}}{\partial K_{rc2}} & \frac{\partial F_x^{P10}}{\partial K_{rc3}} & \frac{\partial F_x^{P10}}{\partial K_{tc0}} & \cdots & \frac{\partial F_x^{P10}}{\partial K_{te0}} \\ \frac{\partial F_y^{P10}}{\partial K_{rc0}} & \frac{\partial F_y^{P10}}{\partial K_{rc1}} & \frac{\partial F_y^{P10}}{\partial K_{rc2}} & \frac{\partial F_y^{P10}}{\partial K_{rc3}} & \frac{\partial F_y^{P10}}{\partial K_{tc0}} & \cdots & \frac{\partial F_y^{P10}}{\partial K_{te0}} \\ \frac{\partial F_z^{P10}}{\partial K_{rc0}} & \frac{\partial F_z^{P10}}{\partial K_{rc1}} & \frac{\partial F_z^{P10}}{\partial K_{rc2}} & \frac{\partial F_z^{P10}}{\partial K_{rc3}} & \frac{\partial F_z^{P10}}{\partial K_{tc0}} & \cdots & \frac{\partial F_z^{P10}}{\partial K_{te0}} \end{bmatrix}_{(30\times15)} \tag{5-4}$$

$$Y = \left[F_x^{T1}, F_y^{T1}, F_z^{T1}, F_x^{T2}, F_y^{T2}, F_z^{T2}, \cdots, F_x^{T10}, F_y^{T10}, F_z^{T10}\right]_{(30\times1)} \tag{5-5}$$

where F_x^{P1}, F_y^{P1}, and F_z^{P1} were the components of the average cutting force from the prediction model. F_x^{T1}, F_y^{T1}, and F_z^{T1} were the components of the average cutting force measured from experiments. The identified cutting force coefficients could be obtained by Equation 5-6:

$$\begin{cases} K_{rc} = 164.03 - 1057.3\theta + 2418.5\theta^2 - 1799.2\theta^3 \\ K_{tc} = 11.478 - 179.32\theta + 746.52\theta^2 - 660.31\theta^3 \\ K_{ac} = -85.327 + 665.95\theta - 2200.5\theta^2 + 1976.9\theta^3 \\ K_{re} = -0.19452 \\ K_{te} = -0.11711 \\ K_{ae} = -0.49643 \end{cases} \tag{5-6}$$

5.6.3 Improved cutting force prediction model considering true trajectory of cutting edge in B-UAM

Due to system performance limitations, the sampling frequency of the dynamometer was set to 9 kHz. However, the vibration frequency of the tool in UAM reached 35.5 kHz. The cutting force prediction model discretised time intervals according to the ultrasonic vibration frequency

and then adjusted the sampling frequency of the cutting force model to be consistent with the experimental measurement through a down-sampling operation. Figure 5.80 shows the instantaneous cutting force change after the down-sampling operation and the reduced local fluctuations in the cutting force curve. The down-sampling operation only affected the peak value but not the average value.

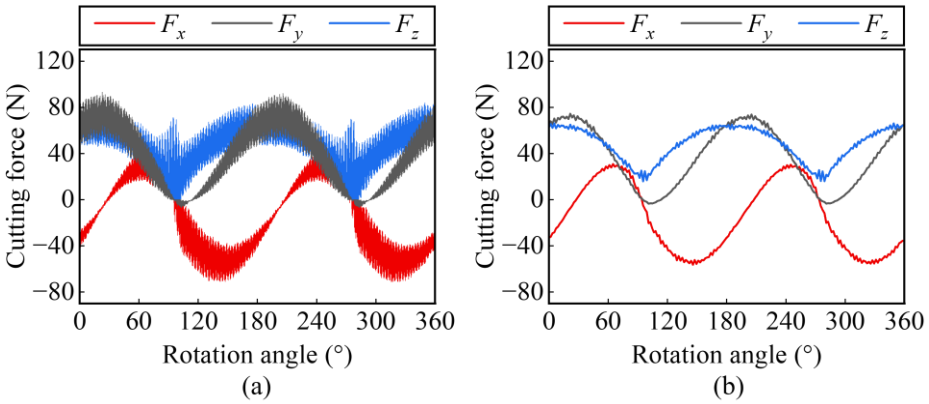


Figure 5.80 Diagram of cutting forces (a) before and after (b) down-sampling operation.

Figure 5.81 shows the comparison results between model prediction and experimental data for the T10 slotting test with B-UAM. In general, the forces modelling method in B-UAM based on the improved Z-map and semi-analytical methods could produce simulation results that were close to actual machining. The average measured cutting forces for F_x, F_y and F_z were 14.43 N, 36.44 N and 46.68 N, separately, while the predicted cutting forces were 14.78 N, 37.32 N and 48.24 N, respectively. The maximum error was only 3.34%, and the modified cutting force model could achieve ideal prediction results.

The results of the validation test are demonstrated in Figure 5.82 to Figure 5.85. In the summary chart, the measured values F_x, F_y and F_z are represented by red, grey, and blue dotted lines, respectively, while solid lines represent the predicted values. Although the work conditions of the B-UAM were very complex, overall, the model prediction results agreed with the actual machining. There were some fluctuations in the actual measured cutting force signal. The possible reasons for these fluctuations mainly include: (a) Charge drift in the dynamometer system. In a separate calibration experiment, the dynamometer used in the experiment showed obvious low-frequency fluctuations in the x-component and y-component in the area that should be zero. This also directly led to the F_x and F_y from ~120° to ~180° being more likely to have obvious abnormal fluctuations in the formal experiment, as shown in Figure 5.84(a). However,

this fluctuation was evenly distributed around 0 N and had little impact on calculating the average cutting force. (b) System vibration during cutting. Although a rigid workpiece and the clamp vice were used, the use of the slender tool, the rigidity of the collet, and the rigidity of the joint between the tool holder and the machine tool spindle taper hole would affect the dynamic characteristics of the cutting system. Therefore, in addition to the static force signal, the cutting force signal was superimposed with a certain amount of dynamic force signal caused by system vibration. (c) The indentation between the bottom of the tool and the workpiece. The linear velocity of the ball end milling cutter head was very small. In actual cutting, it exerted an indentation effect on local parts of the workpiece [322]. The impact of indentation could cause local deformation and plastic lateral flow in the workpiece material. Moreover, this phenomenon was more severe due to the existence of axial ultrasonic vibration. This was the main reason for the large fluctuations in the bottom regions.

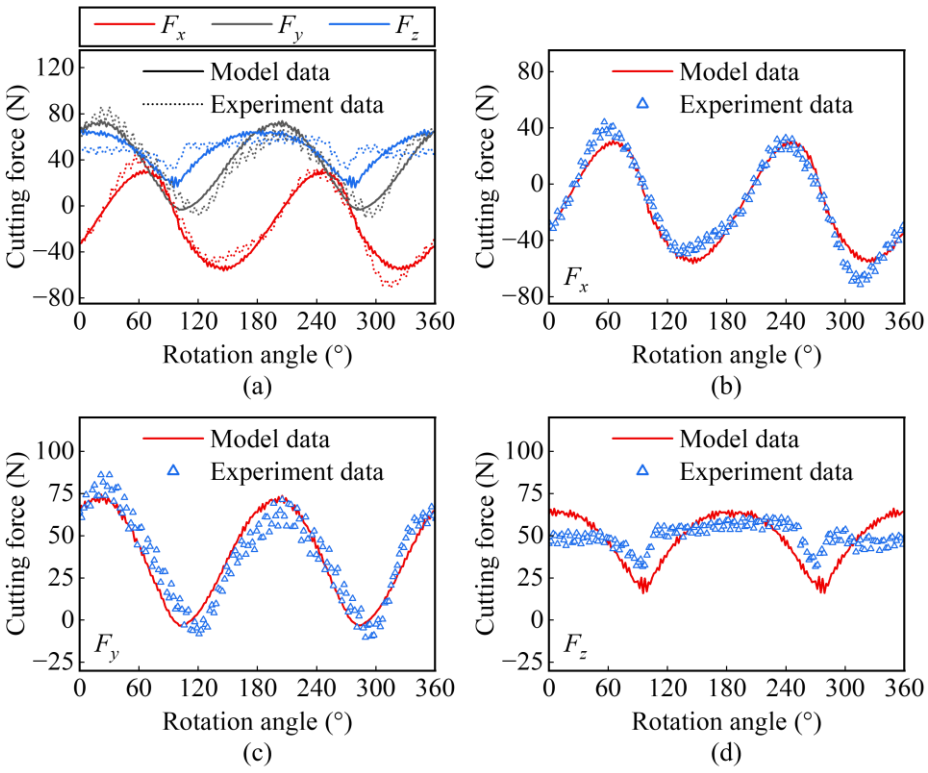


Figure 5.81 Comparison of the predicted cutting forces with experimental data in T10; (a) Total cutting forces, (b) F_x component, (c) F_y component and (d) F_z component.

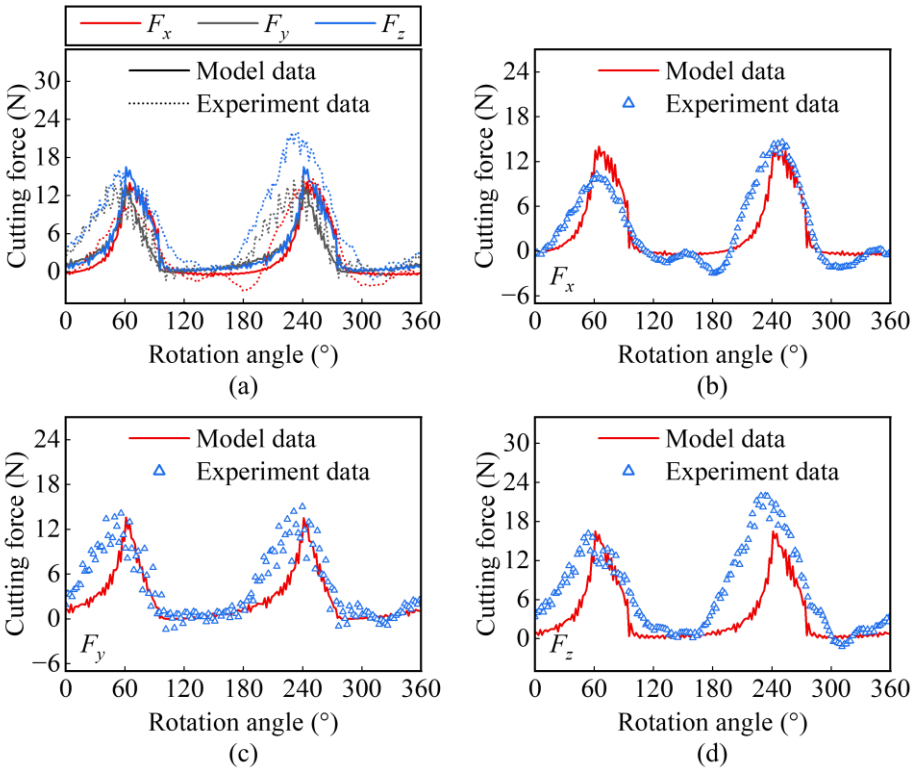


Figure 5.82 Comparison of the predicted cutting forces with experimental data in T11; (a) Total cutting forces, (b) F_x component, (c) F_y component and (d) F_z component.

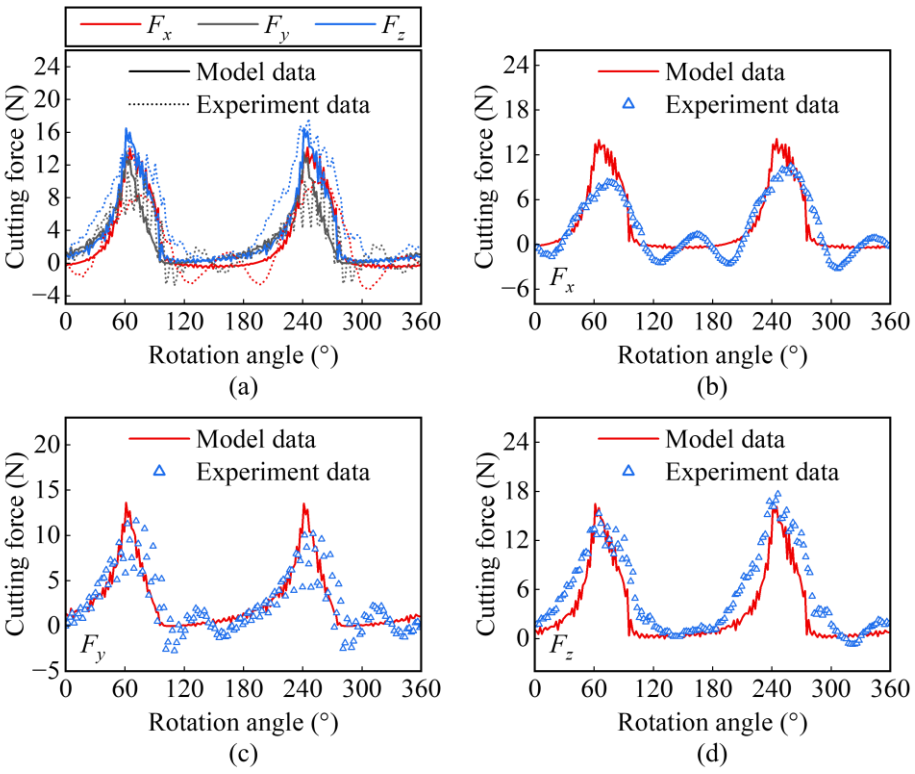


Figure 5.83 Comparison of the predicted cutting forces with experimental data in T12; (a) Total cutting forces, (b) F_x component, (c) F_y component and (d) F_z component.

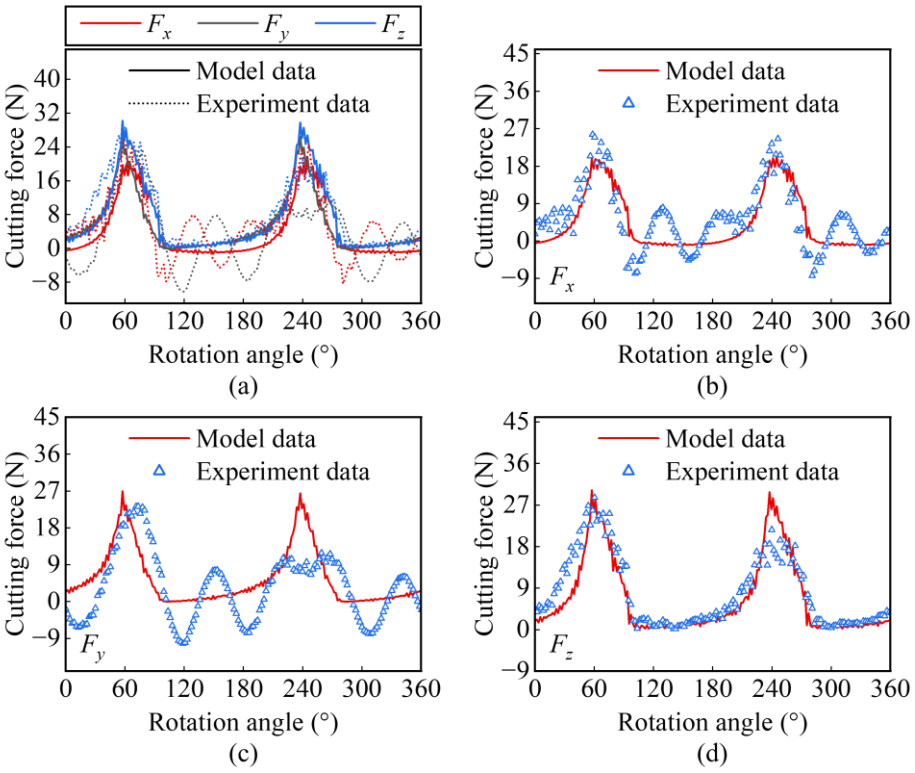


Figure 5.84 Comparison of the predicted cutting forces with experimental data in T13; (a) Total cutting forces, (b) F_x component, (c) F_y component and (d) F_z component.

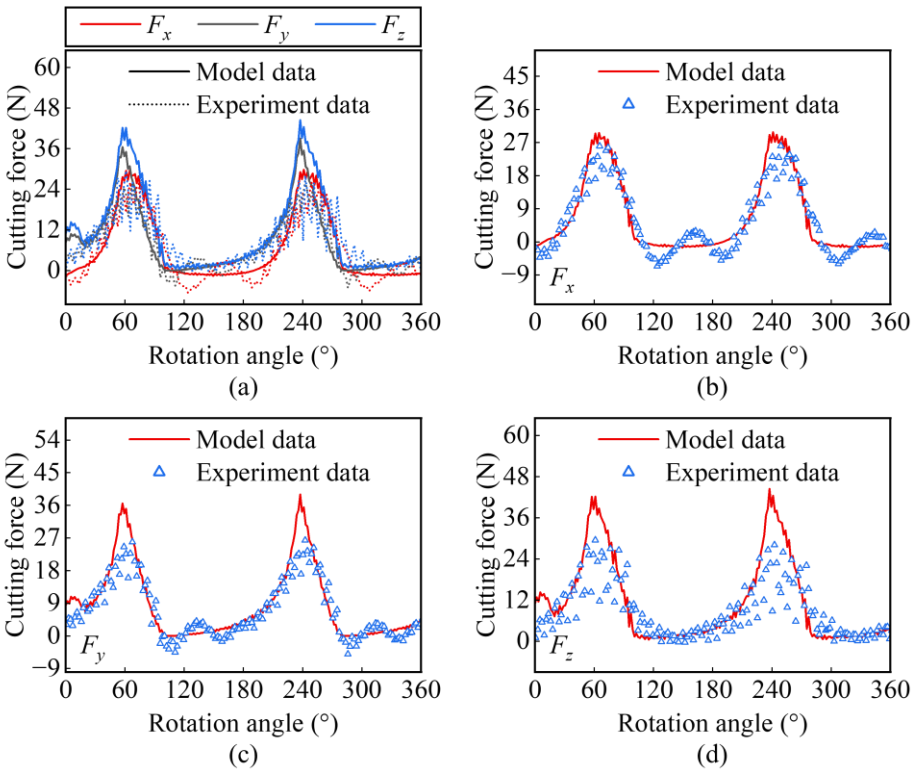


Figure 5.85 Comparison of the predicted cutting forces with experimental data in T14; (a) Total cutting forces, (b) F_x component, (c) F_y component and (d) F_z component.

Taking the cutting force F_x in the feed direction as an example, the verification test results are listed in Table 5.8. It could be seen that the cutting force predicted by the developed model agreed well with the measured results, and the maximum relative error of the average cutting force was less than 20%. Smaller cutting forces were more susceptible to fluctuations and indentation impact. The errors were within the acceptable range for engineering application, considering the extremely complex cutting conditions in ball-end ultrasonic-assisted milling.

Table 5.8 Comparison of average cutting force F_x between the experiment and prediction.

No.	Experimental data (N)	Predicted data (N)	Relative error (%)
T11	2.99	3.19	6.69
T12	2.28	2.70	18.42
T13	3.71	4.13	11.32
T14	5.51	6.45	17.06

Figure 5.86 presents the influence of ultrasonic amplitude on the cutting force components. In terms of the previous analysis, ultrasonic vibration could decrease the friction between the tool and the workpiece and change the material removal process from continuous cutting to intermittent and pulse cutting, resulting in the reduction of cutting [208], [209].

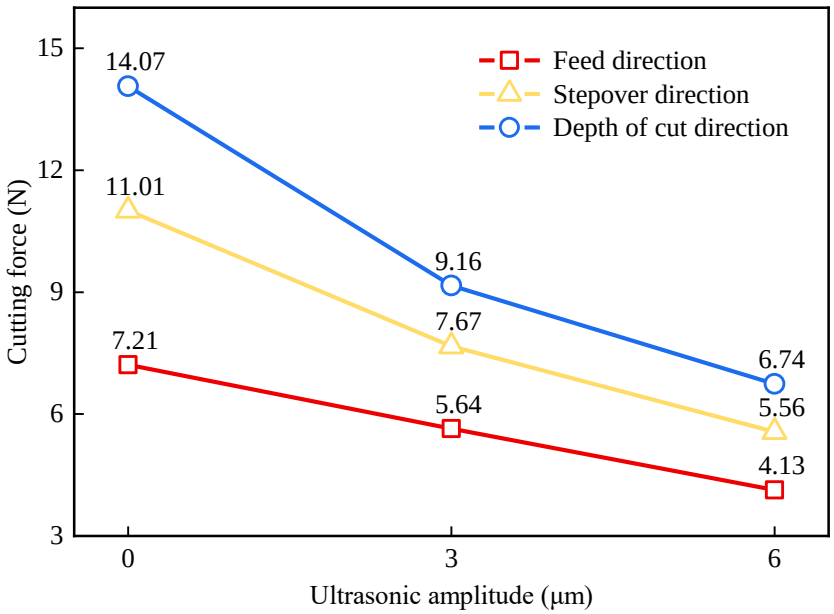


Figure 5.86 The influence of ultrasonic amplitude on the cutting forces for Phase 3B.

Theoretical predictions show that as the amplitude increased from 0 μm to 6 μm, the cutting force components in all directions decreased significantly. The depth of cut direction had the

largest decrease of 52.1%, while even the smallest feed direction had a reduction of 42.7%. A comparable conclusion was reported by Jamshidi and Nategh [210] in UAT that as the amplitude increased from 4 μm to 10 μm, the normal cutting force in UAT was reduced by approximately 19%–82%.

5.7 Phase 3C: Experimental validation of analytical model for predicting tool flank wear in B-UAM

5.7.1 Calibration of coefficients in tool flank wear model

The constant K_w and the coefficients for determining the normal force F_n of the flank tool wear model in Section 4.3 should be calibrated before applying. The identified abrasive wear constant was confirmed according to the experiment designed in Section 3.5.7, where K_w = 2.038×10^{-5}. In addition, varied normal force correction coefficients k_1, k_2, k_3, k_4 and k_5 were confirmed according to the experiment designed in Section 3.5.7 and the normal force F_n could be expressed according to the Equation 5-7:

$$F_n = F_{n0} + 3.08 \times 10^{-18} {V_c}^{-0.401} {f_z}^{21.183} {a_p}^{1.161} t^{21.479} \quad (5\text{-}7)$$

The coefficient of determination R^2 for the normal force F_n was 0.8871, which meant the increase of the actual formal force could be expressed by the formula accurately. In addition, sliding velocity played an important role in tool wear. Xu et al. [323] reported that the constant abrasive wear showed a decreasing trend with elevated sliding velocity, which was attributed to the thermal softening effects in the drilling process. Thus, to avoid the calibration error introduced by cutting speed, a constant spindle speed of 3000 rpm was employed in the test.

5.7.2 Validation of tool flank wear model in B-UAM

Figure 5.87 exhibits the experimental results and predicted results for the tool wear validation tests. The coefficient of determination R^2 between experimental data and theoretical calculation for the four tests were 0.9682, 0.7773, 0.9366 and 0.90162, respectively, demonstrating a strong relationship between the tool wear model and the actual data. The flank wear model could predict the experimental results with high accuracy based on the ball-end ultrasonic-assisted milling.

The prediction results could perfectly display the three stages of tool flank wear: rapid wear zone, steady wear zone, and accelerated wear zone [97]. Due to the special structure of the ball

end mill, the cutting parameters would affect the distribution of force on the cutting edge, which meant that the maximum flank wear occurred at different locations under different parameters. Figure B.6 to Figure B.9 demonstrate the images of tool flank wear for verification tests at the early, middle, and last stages of the tool life trial. To reduce the impact of cutting system stability on the tool wear, the flank wear measured in the test data was the average of the flank wear of all cutting edges.

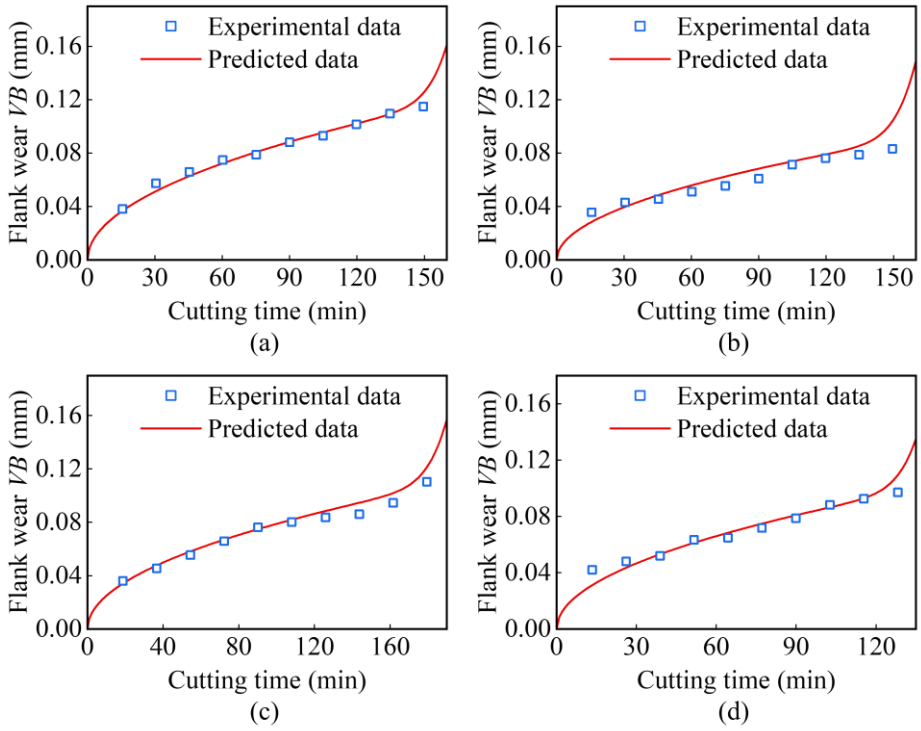


Figure 5.87 Comparison of the predicted flank wear with experimental data: (a) T7 with axial position angle $\theta = 28.268°$, (b) T8 with axial position angle $\theta = 23.645°$, (c) T9 with axial position angle $\theta = 23.958°$ and (d) T10 with axial position angle $\theta = 24.958°$.

5.8 Discussion

The work of this thesis conducted a systematic investigation around ball-end ultrasonic-assisted milling γ-TiAl by using theoretical and experimental research methods. The overall discussion for each part was summarised as follows. This section provides a cohesive synthesis of the results obtained from the theoretical and experimental investigations conducted in this thesis. By discussing the findings across different research phases, emphasise the interconnectedness of the methodologies and demonstrate how each phase contributes to an integrated understanding of ball-end ultrasonic-assisted milling of γ-TiAl. This holistic perspective reveals the strengths of combining various approaches to achieve a robust understanding of the machining process and its implications.

- **Stability assessment of integrated ultrasonic system (Phase 1A) as the foundation**

The stability assessment was crucial for ensuring reliable operation across all experimental stages. Refer to research ideas proposed by Wang et al. [274] on similar types of equipment to conduct an in-depth exploration of the DMG Mori Ultrasonic 20 linear 5-axis CNC machining centre. Ultrasonic amplitude was the most important parameter to evaluate the work status of the ultrasonic system. Under the no-load conditions, the influence of tools' parameters on the ultrasonic amplitude was confirmed based on the current machine tool and the mass of the tool had a significant impact on amplitude. Meanwhile, the optimal overhang length for obtaining better amplitude was reported, which had been less mentioned in previous studies.

The load condition had a direct effect on the resonant frequency of the ultrasonic system and the root cause of the weakening of the ultrasonic effect during the processing [222], [274]. In this case, the operating limits of the ultrasonic system determined the selection of the cutting parameters. A small-depth-cut method was presented to calibrate the actual amplitude, which could be closer to the actual cutting process. Then, the operating limits of the DMG Mori Ultrasonic 20 linear were confirmed by comparing the varying trends of cutting forces in experiments and validated the presence of performance limitation.

The established method could well help understand the performance of machine tools, achieve research objectives, and provide a basis for determining subsequent experimental parameters. However, due to the limitations of experimental conditions, there were insufficient studies on the stability of the ultrasonic system. In terms of the existing research, the thermomechanical

load had a great influence on the ultrasonic amplitude and interacted with each other to change the resonant frequency [222]. The research in this thesis did not conduct quantitative research on thermal effects, which were crucial factors that could not be ignored in the following experiments. In addition, accurately measuring the ultrasonic amplitude during the practical cutting process was always challenging.

The insights into stability were foundational to calibrate the ultrasonic system's parameters for the entire research, impacting both the effectiveness and reliability of the machinability tests and modelling works conducted later.

- **Machinability of γ-TiAl and optimisation of operating parameters (Phase 1B)**

The machinability of γ-TiAl was evaluated from tool wear, cutting force and surface integrity. Cutting parameters were considered, including cutting speed, depth of cut, width of cut, feed rate, cutting orientation, ultrasonic actuation, and cutting environment. When using the PVD TiAlN coated tool, severe tool wear was observed under the wet cutting conditions. The same phenomenon was reported by the previous investigation when cutting γ-TiAl [63], [65], [81]. The preliminary reason was attributed to the high brittleness and hardness of the γ-TiAl at room temperature [22]. Heat accumulation and low heat dissipation in cutting edge regions introduced by steep temperature gradients would lead to rapid tool damage. The increase in tool wear resulted in higher cutting force, which was the main reason for the generation of rake face chipping and secondary relief face wear. On the contrary, lower tool wear was presented in dry cutting conditions and minor tool wear was measured due to the improved machinability of γ-TiAl at higher cutting temperature [91]. Cutting speed was generally considered to have the most sensitive effect on tool life, which increment would result in rising temperature [97], [291]. However, due to the special characteristics of γ-TiAl, the high temperature was conducive to cutting and the feed rate was the factor that had the greatest impact on the tool wear at this experimental design level.

Cutting force and tool wear were a pair of factors that interact with each other, and the depth of cut was identified that had the greatest effect on cutting force by using a statistical method, which was consistent with Richard's investigation on milling γ-TiAl [292]. Meanwhile, the standard of γ-TiAl machined surface integrity was established, including surface morphology, edge quality, surface roughness, dimensional accuracy, microhardness, and metallographic

alteration. Due to the high brittleness of the material, phenomena such as edge chipping, material pull-out and crack appeared in the test, validating the conclusion of similar studies [53], [55], [102]. The influence of cutting parameters on different surface integrity indicators was confirmed at the experimental design level, and ultrasonic-assisted milling showed certain advantages in most indicators.

Orthogonal design experiments could reflect the influence of different cutting parameters on the target under a certain amount of testing. However, due to time constraints, the parameters considered in the experimental design were incomplete, such as tilt angle, tool type, cutting orientation, etc., and only fixed values were selected. In addition, the span range selected for each factor level was limited by the tool size and experimental conditions, and there was a possibility that the differences at each level were not obvious. At the same time, the experimental design was a mixed-level orthogonal experiment. Regarding the number of selected factor levels, the number of experiments in the L_{16} experimental design was too small compared to the full-factor experiment. This further increased the impact of errors on the analysis. In addition, the brittle-ductile transition condition of γ-TiAl was deemed to be 600℃–850℃ [22]. The actual cutting temperature in dry conditions was hard to reach the critical temperature, but the ductility of γ-TiAl was still improved. The deformation mechanism of the brittle-plastic transition stage is yet unclear.

These machinability insights were critical for understanding the wear mechanisms analysed in Phase 2A, as they established a link between operating conditions and tool performance. Moreover, they informed the conditions under ultrasonic vibration could be most beneficial for wear reduction, influencing further exploration in Phase 2B.

- **Tool wear mechanisms and failure of γ-TiAl in B-UAM (Phase 2A)**

Four typical wear formations were identified in milling γ-TiAl, including abrasive, adhesive, oxidation, and diffusion wear. A comparative experiment was designed considering milling methods, cutting experiments and tool coating conditions. The cause of tool coating failure under wet cutting conditions, which was reported widely in cutting γ-TiAl [65], [75], had been attributed to the rapid peeling of the coating during the flood cooling strategy with a steep temperature gradient. However, coated tools could perform as they should under dry cutting conditions due to the generation of oxides, protecting the cutting edge. Meanwhile, in

accordance with the un-coated tool tests, the adhesive materials came from γ-TiAl with high aluminium content, further promoted the formation of oxides and improved the tool life [307]. According to the result of the EDS analysis for the low-alloy steel milling test, the tool self-repair phenomenon was unique to γ-TiAl. Besides, diffusion wear was identified according to EDS analysis. Moreover, a significant chipping region was detected in ultrasonic-assisted milling as a result of exacerbated microfractures and microcracks introduced by ultrasonic-frequency dynamic impacts [217].

The formations of tool wear and failure were analysed in depth and explained the conditions and root causes for the coating to be effective. The self-repair mechanism of cutting tools in γ-TiAl cutting was proposed. However, most studies mainly focused on qualitative analysis. There was a lack of more in-depth quantitative analysis on the specific microstructure of the oxide and the protective mechanism. At the same time, research on diffusion wear only persisted on the surface of the tool, and the depth of element diffusion and its impact on tool strength had not yet been conducted further.

This phase's findings not only corroborate the machinability improvements noted in Phase 1B but also add depth to the understanding of tool durability in ultrasonic-assisted conditions. The wear mechanisms, in turn, reinforced the need for careful parameter selection in ultrasonic systems (Phase 1A) and underscored the modelling considerations explored in Phase 3.

- **Comparative evaluation between the effect of CM and B-UAM on machinability of γ-TiAl (Phase 2B)**

The influence of ultrasonic-assisted milling on γ-TiAl was investigated based on experimental research. Within a certain degree of wear, ultrasonic machining showed lower tool wear and lower cutting forces than conventional cutting under the wet cutting when the TiAlN coated tool was utilised. Reducing the cutting force was the fundamental reason for minimising the tool wear in UAM. Lower friction between the tool and the workpiece and the separated cutting formation was believed to be the root reason for the deduction of the cutting force in UAM [208], [209]. Moreover, the higher tool wear and cutting force were measured from the UAM when the cutting process was in the low wear stage. The severe impact effect caused by the instantaneous speed increase caused by ultrasonic vibration might be why the tool wear in UAM at low cutting force levels was slightly higher than that in CM. There was no doubt that UAM

had obvious advantages in reducing cutting forces when the tool was in a wear-free state. At the same time, UAM achieved better fineness, lower edge burrs, and higher material removal rate. Compared to the CM, the effect of increased tool nose radius on the minimum uncut chip thickness was diminished due to the ultrasonic vibration, resulting in greater actual uncut chip thickness and less ploughing action [318].

Ultrasonic vibration enhanced strain and strain rate hardening, resulting in larger microhardness and surface compressive residual stress [216]. This meant that under the same cutting parameters, UAM could achieve the processing of high compressive residual stress surfaces, which was believed to be an effective method to reduce fatigue crack initiation and crack propagation and improve the fatigue property [321]. For γ-TiAl, which was more brittle at room temperature, reasonable distribution of surface residual stress could reduce the occurrence of defects.

In general, introducing ultrasonic vibration was beneficial in diminishing the cutting force, improving the tool life, and achieving better surface quality. However, the research on the advantages of UAM lacked an in-depth analysis of the changes in the microstructure. In particular, there was a lack of explanation at the level of microstructure evolution for the better machinability of γ-TiAl under dry cutting conditions. Factors that led to changes in microhardness and residual stress might include grain refinement, recrystallisation, high-density dislocations, etc. Existing research on microstructures was limited to optical microscopes with relatively low magnifications, and it was necessary to introduce technologies such as EBSD and TEM to provide theoretical support at a more microscopic level.

The advantages observed in UAM support the theoretical foundation laid out in Phase 3 (modelling) and demonstrate the practical benefits of ultrasonic-assisted milling as initially anticipated in Phase 1A. The comparative findings also highlight how UAM complements the wear mechanisms and stability considerations identified in previous phases.

- **Analytical modelling of B-UAM (Phase 3)**

The theoretical analysis was conducted by a semi-analytic model. The kinematic model was established based on the motion trajectory of the ball-end ultrasonic-assisted milling. A modified model was developed in accordance with the Z-map method and geometrical

simulation was achieved to predict the machined surface morphology with excellent profile consistency in both feed and stepover directions. Meanwhile, it was clear that the axial runout was the fundamental reason the feed mark spacing of the ball-end milling was multiple of the feed per tooth. Besides, the computational efficiency of the optimised algorithm was significantly improved compared to similar studies [242].

An improved Z-map model of ball-end ultrasonic-assisted milling force was proposed on this basis. This improved model considered the tool bending deflection, especially for slender tools with more significant impact. Moreover, a method for calculating the actual uncut chip thickness in ball-end ultrasonic-assisted milling based on the Ray-triangle intersection method was proposed. The coefficients of tangential cutting force, radial cutting force and axial cutting force were identified by the experimental data using the least squares method. In general, the experimental cutting force could be predicted with high accuracy by the semi-analytical model, even though the fluctuation induced by the indentation effect was detected under some cutting parameters [322]. In addition, increasing the ultrasonic amplitude could diminish the cutting force of each component significantly, and this result was consistent with the conclusion of other research [210].

The ball-end ultrasonic-assisted milling tool flank wear model was developed from the pin-on-disc model, in which only abrasive wear was considered [269]. The normal force was equal to the radial cutting force and could be calculated from the cutting force model. The abrasive wear constant was confirmed based on the experiment. Notably, the cutting force increased with the tool wear during the cutting process and affected each other. In order to more accurately predict the change of flank wear, the rate of variation of cutting force was expressed as the change of cutting parameters. The results of the flank wear model showed that the three stages of flank wear, rapid wear zone, steady wear zone, and accelerated wear zone, could be well represented. The predicted results were highly consistent with the experimental data, and the model could effectively predict the flank wear of any cutting point on the cutting edge.

The complete morphology-force-wear integrated model was well realised. Combining the modelling idea of Z-map not only solved the problem of complex structure modelling of a ball-end mill but also simplified the difficult problem of highly complicated motion trajectory caused by ultrasonic high-frequency vibration, making it hard to establish an effective uncut chip calculation model. Besides, factors like axial runout and tool bending deflection were also

considered to achieve higher prediction accuracy. However, the limitation of the semi-analytical model was that the coefficients determined by the calibration test might only apply to changes within a certain range. Recalibration was required for complex working conditions and large-scale parameter changes. Secondly, the normal force in the flank wear model that increased with wear was expressed as a quantity that changes with cutting parameters, which was also obtained through experimental calibration. This meant that the universality of expression was also limited. In addition, the normal force accepted a fixed average cutting force to replace the constantly varying cutting force during the calculation. Especially in ultrasonic-assisted cutting process, the force fluctuation range was more extensive, and the rationality of using the average force needed further evaluation.

The model effectively consolidates the empirical findings by predicting outcomes for cutting force and flank tool wear, offering a theoretical framework that connects back to all phases. This model thus validates the experimental findings and provides a predictive basis for tool life and process optimisation in ultrasonic-assisted milling.

In summary, the integrated findings across all phases reveal a comprehensive understanding of ball-end ultrasonic-assisted milling of γ-TiAl. Each phase contributed unique insights, which starting from the stability foundation in Phase 1A, machinability insights in Phase 1B, detailed wear mechanisms in Phase 2A, comparative benefits of UAM in Phase 2B, and culminating in predictive modelling in Phase 3. By bringing these findings together, this section underscores the complementary nature of each research component and highlights the significance of the combined methodological approach, which collectively advances our understanding of effective machining processes for γ-TiAl.

6 CONCLUSIONS AND RECOMMENDATIONS FOR FUTURE WORK

6.1 Literature review

- Advanced materials are widely used in the aerospace industry and metal materials are the largest. Titanium alloy is one of the most important materials due to its excellent properties, which is an effective lightweight choice. Except for the most common titanium alloys, Ti-6Al-4V, titanium aluminide is critical in replacing nickel-based alloys for manufacturing aerospace engine blades due to its high working temperature. However, only a few published papers investigated the machinability of γ-TiAl in recent years. In terms of the current research, the obvious brittleness at room temperature is the most typical characteristic of γ-TiAl, which limits machining quality.

- The existence of research about machining γ-TiAl focuses on milling and turning operations. The selection of cutting parameters is mainly based on the improvement of material removal rate, that is, rough machining is the leading research object. Therefore, the cutting parameters used in experiments are generally large. There is a lack of research on finish machining γ-TiAl. Meanwhile, there is a lack of systematic evaluation of the research on the surface integrity of machining γ-TiAl.

- Ultrasonic-assisted cutting process has been proven to be an effective operation to reduce the cutting force, improve the tool life and control the cutting heat. It is widely used in grinding brittle materials like crystalline materials. Ultrasonic-assisted cutting can change the critical cutting depth and control the brittle material to be removed in ductile mode. However, there are very few publications on ultrasonic-assisted cutting γ-TiAl, and whether introducing ultrasonic vibration can improve the machinability of γ-TiAl at room temperature is still a blank.

- There are two types of model research on ball-end milling: one is based on pure geometry model building, and the other is based on the Z-map model building idea. Due to the complex calculation caused by the tool structure, the Z-map method has advantages in model building and calculation. However, there is almost no research on the cutting force and tool wear models in ball-end ultrasonic-assisted milling. In order to simplify the

calculation, traditional models usually ignore the effects of axial runout or tool bending deflection, which also leads to many experimental phenomena, such as inconsistent feed mark distance and lower actual cutting depths without theoretical explanation.

6.2 Experimental work

6.2.1 Phase 1A: Stability assessment of integrated ultrasonic system

- The research on ultrasonic system stability on existing DMG Mori Ultrasonic 20 linear 5-axis CNC machining centre was conducted and the effect of tool parameters on the ultrasonic amplitude was investigated. Research indicates that the tool mass is the dominant factor affecting ultrasonic amplitude. The lighter the tool, the greater the amplitude. In this case, for the same size cutting tools, the HSS tool is easier to vibrate than the carbide tool and the small radius tool can reach better amplitude. Meanwhile, the overhang length also impacts the ultrasonic horn, and the experimental results demonstrate that the overhang length is 70% of the total length of the tool to obtain the best ultrasonic amplitude. Besides, a small-depth-cut was designed to determine the amplitude under the loaded conditions, reflecting the amplitude in the actual cutting process.

- The ultrasonic machine tool has a phenomenon of extreme process capability. As the depth of cut increases, when the cutting force exceeds a certain limit cutting force, the ultrasonic amplitude is significantly suppressed, and the ultrasonic machine tool loses the process advantage of significantly reducing cutting force. Increasing the no-load amplitude is an effective way to improve the operating limits of ultrasonic machine tools. When formulating cutting parameters, making the actual cutting force more minor than the extreme cutting force of the ultrasonic system is the primary condition to ensure the effectiveness of the ultrasonic vibration. Besides, typical characteristics are confirmed preliminary, including reduced cutting forces, less chip adhesion, and a scale texture on the machined surface.

6.2.2 Phase 1B: Influence of operating parameters on machinability when milling γ-TiAl

- The machinability and surface integrity of γ-TiAl are studied based on a Taguchi L_{16} orthogonal test, and key indicators of surface integrity are confirmed, including surface morphology, edge quality, surface roughness, dimensional accuracy, microhardness, surface residual stress, and metallographic alteration.

- Within the range of experimental levels, feed rate has the most significant effect on the average tool wear rate. Tool wear and failure formations include abrasion, adhesion and edge chipping. The cutting environment determines abrasion wear formation in milling γ-TiAl when using the TiAlN coated tool under wet cut conditions, whereas adhesion wear is dominant in dry cutting. Rapid tool wear increases cutting force, which also validates that the TiAlN coated tool is unsuitable for wet cutting. The depth of cut is the primary indicator affecting the initial cutting force with the new tool.

- Typical surface defects are observed, such as edge break, material pull-out and burrs, which are attributed to the high brittleness of γ-TiAl under room temperature. As the tool wear aggravates, the cutting force increases and the significant tool bending deflection causes serious machined surface rolling of the secondary relief face. This is the main reason the surface roughness increases first and then decreases during milling.

- Positive burrs and negative burrs are two typical defects of the edge quality. Dutile removal mode generates positive burrs due to the chips being sheared away along the cutting line, whereas shearing-induced cracks form the negative burrs in brittle mode. This means that when the cutting force is larger or under wet cutting conditions, γ-TiAl shows more brittleness regarding the experimental results. In this case, a higher cutting speed is beneficial to reduce the exit burr due to the improvement of ductility of γ-TiAl under higher temperatures.

- The width of cut is the factor that has the greatest effect on initial surface roughness. Selecting a smaller width of cut can achieve better surface roughness. For dimensional accuracy, the depth of cut achievement rate is constantly lower than 1 because as long as the tool is subjected to force, there will be bending deflection. In this case, the depth of cut is the most influential factor, and a lower depth of cut can diminish cutting errors with lower cutting force.

- The cutting environment determines the surface microhardness. The surface microhardness is slightly lower than the bulk material microhardness under dry cutting conditions, while the opposite is true for wet cutting. It has been proven that the machinability of titanium alloy is directly affected by temperature, and high temperature is beneficial. However, as tool wear increases, mechanical loads dominate compared to thermal loads, increasing

surface work hardening. If only considering the initial cutting operations, the width of the cut has the greatest effect on the working hardening degree at experimental levels.

- The depth of cut was the factor that had the greatest effect on initial deformed layer thickness in ultrasonic-assisted milling γ-TiAl and a lower depth of cut will generate less subsurface damage. As the increase of the tool wear, the deformed layer thickness intensifies due to the increment of the cutting force, which is the root cause of influencing the change of microstructures.

6.2.3 Phase 2A: Tool wear mechanisms and failure of γ-TiAl in B-UAM

- Abrasive wear, adhesive wear, oxidation wear and diffusion wear are the four main wear formations in ultrasonic-assisted milling γ-TiAl, and the failure of the tool is identified as the rake face edge chipping.

- Low temperature is the root cause of TiAlN coating tool failure and the coating material peels off quickly during the wet cutting. Abrasive wear is dominant under wet cutting conditions, while adhesive, diffusion, and oxidation wear are characteristics of dry cutting. Oxides such as TiO_2 and Al_2O_3 may be generated in dry cutting and the oxide films play the role of antifriction and improve the cutting ability of the tool.

- Meanwhile, TiAlN coating and workpiece materials γ-TiAl are high Al and Ti content materials and provide ample reflection of the required elements. Besides, the adhered γ-TiAl also protects the cutting edge, combined with the generation of oxides, and is defined as a tool self-repairing mechanism. The control experiment using the uncoated tool validates this conclusion. Moreover, the existence of diffusion wear is confirmed by the variations of element content on the tool and workpiece surface.

- The cutting tool is more likely to form edge chipping under the ultrasonic-assisted milling process. The cutting tool is subjected to pulsed cutting forces at ultrasonic frequencies and alternating friction forces at double-ultrasonic frequencies. The combined effects of dynamic cutting forces, alternating friction, and high impact energy exacerbate existing fractures and microcracks and lead to flaking and crack failures at the cutting edge.

6.2.4 Phase 2B: Comparative evaluation between the effects of CM and B-UAM on machinability of γ-TiAl

- The cutting force gradually increases with the increase of tool wear. Ultrasonic-assisted milling process shows lower wear and smaller cutting force within a certain range under wet cutting conditions. When the cutting force exceeds the extreme capacity of the ultrasonic system, the increased load changes the resonant frequency of the system, causing the amplitude to decay rapidly and resulting in the disappearance of the advantages of ultrasonic-assisted milling.

- Ultrasonic-assisted milling can reduce the adhesion of workpiece material to the tool surface due to the high-frequency separation movement and lower temperature. However, dry cutting γ-TiAl means that tool wear will increase slightly. In the case of dry cutting, the cutting force of both ultrasonic and conventional milling changes slowly and is at a low level. At this time, the advantage of ultrasonic-assisted milling in reducing cutting force cannot be realised. In contrast, if tool wear is not considered, under new tool conditions, ultrasonic-assisted milling can reduce cutting forces by up to 47.2% compared with conventional milling.

- Few materials pull-out phenomenon is observed in ultrasonic-assisted milling process due to the hammering effect of ultrasonic vibration. Besides, ultrasonic-assisted milling can effectively improve the edge quality of the exit. When the tool wear increases, the depth of edge burrs changes more slowly in ultrasonic-assisted milling. The width of the negative burr is also smaller than that of conventional milling.

- Ultrasonic vibration changes the trajectory of the cutting edge, making the constant depth of cut become the dynamic depth of cut, and the area roughness of the machined surface is greater than that of conventional milling. However, ultrasonic-assisted milling can achieve decent fineness due to better tool conditions. In addition, ultrasonic-assisted milling can realise a higher material removal rate owing to the lower cutting forces and higher maximum uncut chip thickness at the same cutting stage.

- The difference in the dominant factors in the thermomechanical loads leads to the difference in microhardness and surface residual stress between dry and wet cutting conditions. Ultrasonic-assisted milling introduces the significantly larger surface microhardness

compressive residual stress caused by enhanced strain and strain rate, which is beneficial to the improvement of fatigue properties. Meanwhile, ultrasonic vibration generates more energy and acts between the workpiece and the cutting tool, which may result in refined grains and high-density dislocations, triggering the increase of microhardness and residual stress.

- There is no apparent difference in the microstructure between ultrasonic-assisted milling and conventional milling under the optical microscope. Still, because the cutting force of ultrasonic-assisted milling is lower, the change in the deformed layer thickness is slower than that in conventional milling.

6.3 Modelling of ball-end ultrasonic-assisted milling

6.3.1 Phase 3A: Experimental validation of analytical model for predicting machined surface morphology in B-UAM

- Based on the kinematics of the ball-end ultrasonic-assisted milling process, a modified surface morphology prediction model is established using the Z-map method. The validation experiment proves that the geometrical simulation is achieved to predict the machined surface morphology with excellent profile consistency in both feed and stepover directions. The model considers factors such as tool orientation adjustment and runout and proves that the axial runout of the system is the fundamental reason why the feed mark spacing has a multiple relationship with the feed per tooth in cutting parameters.

- The improved algorithm has a computational efficiency that is nearly 70% higher than similar studies. Therefore, the simulation method of the geometric morphology of the ball-end ultrasonic-assisted milling surface based on the improved Z-map method proposed in this thesis balances the simulation accuracy and efficiency. The influence of cutting parameters on the machined surface morphology can be analysed through geometric simulation, which provides a basis for selecting actual cutting parameters in the system.

6.3.2 Phase 3B: Experimental validation of analytical model for predicting cutting forces in B-UAM

- The basic idea of static milling force modelling of ball-end ultrasonic-assisted milling is explained and establish the cutting force prediction model according to the improved Z-map method. A method for calculating the actual uncut chip thickness in ball-end ultrasonic-

assisted milling based on the Ray-triangle intersection method is proposed. Tool bending deflection significantly affects the actual depth of cut, which will influence the cutting force directly. Therefore, the tool bending deflection model is established and considered in the improved cutting force model to be close to the actual cutting conditions. Combined with the calibration test, the improved model can predict the cutting force in ball-end ultrasonic-assisted milling with high accuracy.

6.3.3 Phase 3C: Experimental validation of analytical model for predicting tool flank wear in B-UAM

- The ball-end ultrasonic-assisted milling tool flank wear model is developed from the pin-on-disc model and only considers abrasive wear. The normal force acting on the flank face is calculated using the improved cutting force prediction model and the wear coefficient is obtained through calibration tests. In addition, the cutting force increases with the growth of tool wear, and the increased cutting force is expressed as a function expression about the cutting parameters. The verification tests show that the flank wear model can accurately predict the variation of the flank wear of any cutting point over time. The results of the flank wear model also accurately demonstrate three stages of flank wear: rapid wear zone, steady wear zone, and accelerated wear zone.

6.4 Overall conclusions and recommended operating conditions

To address the limitations of ultrasonic-assisted milling of γ-TiAl (research gap I), this study comprehensively examines the effects of cutting parameters on machinability of γ-TiAl. The findings identify critical factors influencing machining quality and demonstrate the potential of ultrasonic actuation to enhance γ-TiAl machinability.

To bridge research gap II, further investigations were conducted based on Phase 1 conclusions, which highlighted coating and cooling conditions as significant influencing factors. Comparative experiments were performed to analyse tool wear mechanisms, revealing that dry cutting conditions are preferable for machining γ-TiAl.

Phases 1 and 2 together form the experimental component of this research. Beyond exploring γ-TiAl machinability in detail, this study also examines the advantages and limitations of ultrasonic-assisted milling. To deepen theoretical understanding, a modelling approach was developed (research gap III). Given the complexities of γ-TiAl wear mechanisms, Ti-6Al-4V

was chosen as a substitute for modelling, as γ-TiAl's wear behaviour was not suited for the pin-on-disc model.

Key conclusions of this study are as follows:

- Tool specimens have a significant impact on the amplitude of the ultrasonic system, and the ultrasonic system also has a critical processing capacity. Reasonable selection of cutting tools and parameters is an important prerequisite to ensure the effectiveness of ultrasonic-assisted cutting process.

- γ-TiAl shows more brittleness at room temperature, which poses a challenge to the selection of cutting parameters. In general, parameters that can increase the processing temperature and reduce the cutting force are more suitable for cutting γ-TiAl. Within the test parameter range of this article, the optimal parameters under various indicators are shown in Table 6.1.

Table 6.1 List of recommended cutting parameters for milling γ-TiAl.

Indicator	Cutting parameters
Tool wear rate	v_c = 80 m/min, a_p = 0.15 mm, a_e =0.15 mm, f_z = 0.02 mm/tooth, HU, Dry, CM
Cutting force	v_c = 100 m/min, a_p = 0.05 mm, a_e =0.15 mm, f_z = 0.04 mm/tooth, Dry
Exit burrs	v_c = 100 m/min, a_p = 0.10 mm, a_e =0.25 mm, f_z = 0.04 mm/tooth, HD, UAM
Surface roughness	v_c = 40 m/min, a_p = 0.05 mm, a_e =0.15 mm, f_z = 0.03 mm/tooth, HU, Wet, CM
Dimension	v_c = 100 m/min, a_p = 0.20 mm, a_e =0.30 mm, f_z = 0.02 mm/tooth, HD, UAM
Working hardening	v_c = 100 m/min, a_p = 0.10 mm, a_e =0.25 mm, f_z = 0.04 mm/tooth, HD, Wet, CM
Deformed layer	v_c = 100 m/min, a_p = 0.10 mm, a_e =0.20 mm, f_z = 0.04 mm/tooth, HD, UAM

- Abrasive wear, adhesive wear, oxidation wear and diffusion wear are tool wear mechanisms in ball-end ultrasonic-assisted milling γ-TiAl. Edge chipping on the rake face is the typical tool failure formation, likely observed in ultrasonic-assisted milling. Regardless of the use of TiAlN coated tools, machining γ-TiAl in dry cutting conditions can generate a protective film, helping to prevent severe tool wear to some extent. However, further investigation should be conducted to identify relevant material structures, such as oxides, adhesion and abrasive particles.

- Ultrasonic-assisted milling can improve tool wear to a certain extent and significantly reduce cutting force at similar wear levels, improve surface quality, diminish burr size, and improve dimensional accuracy. Meanwhile, ultrasonic vibration can introduce greater

compressive residual pressure and microhardness without causing additional damage, achieve surface strengthening, and effectively improve fatigue life.

- The complete morphology-force-wear integrated model is well realised. Based on the Z-map method, several key factors, including axial runout, tool bending deflection, and changes of formal force, are considered to optimise the model and the ideal prediction results are obtained. Built on the idealised assumption that abrasive wear predominated during dry cutting of Ti-6Al-4V with the experimental range in this thesis, the cutting force and tool flank wear models represented a foundational step in ball-end ultrasonic-assisted milling research. Future studies will expand upon this foundation, according for more intricate working conditions to enhance alignment with actual machining process.

6.5 Recommendations for future work

Based on the research results, several areas have been identified as warranting further investigation. These include:

- **Improve the operating limits of the ultrasonic system.** In addition to the influence of mechanical loads, thermal loads can also affect the stability of the ultrasonic actuation system. The amplitude can be better stabilised by reasonably matching the thermomechanical load. At the same time, real-time measurement and monitoring technology of ultrasonic amplitude during processing should be developed. Based on this, the stability of the ultrasonic amplitude can be improved through better frequency tracking or input voltage adjustment, thereby enhancing the critical processing capacity of the ultrasonic system.

- **Multi-objective optimisation of machinability of γ-TiAl.** Evaluating machining quality is a multi-dimensional issue. It is impossible to evaluate the feasibility of a machining plan based on the qualification of a single indicator. The weights of various indicators are different for different workpieces. How to balance the relationship between various indicators, conduct a comprehensive multi-dimensional evaluation of the machining process, and ultimately improve the fatigue life is the focus of subsequent research.

- **Damage formation mechanism and inhibition in ultrasonic-assisted cutting of highly brittle metals.** The formation mechanism of damage, such as edge chipping and subsurface

microcracks that exist in the processing of metal materials with high brittleness at room temperature, such as γ-TiAl, helps to use ultrasonic technology to achieve efficient and low-damage processing of hard and brittle materials. On this basis, a critical model for the brittleness-transition-plasticity of γ-TiAl can be developed to understand the critical ductility region cutting conditions in ultrasonic-assisted cutting γ-TiAl.

- **Developing fully analytical models for ultrasonic-assisted cutting force and tool wear.** In terms of the existing model, establishing an analytical model can improve the scope of application of the model and reduce the amount of calibration experiments. For the tool wear model, in addition to abrasive wear, developing a corresponding wear model for the dominant wear form under different working conditions can be more in line with actual processing.

7 REFERENCES

[1] A. P. Mouritz, *Introduction to aerospace materials*. Elsevier, 2012.

[2] R. M'Saoubi et al., 'High performance cutting of advanced aerospace alloys and composite materials', *CIRP Ann.*, vol. 64, no. 2, pp. 557–580, Jan. 2015, doi: 10.1016/j.cirp.2015.05.002.

[3] T. M. Pollock, 'Alloy design for aircraft engines', *Nat. Mater.*, vol. 15, no. 8, pp. 809–815, Aug. 2016, doi: 10.1038/nmat4709.

[4] O. Genc and R. Unal, 'Development of gamma titanium aluminide (γ-TiAl) alloys: A review', *J. Alloys Compd.*, vol. 929, p. 167262, Dec. 2022, doi: 10.1016/j.jallcom.2022.167262.

[5] M. Perrut, P. Caron, M. Thomas, and A. Couret, 'High temperature materials for aerospace applications: Ni-based superalloys and γ-TiAl alloys', *C. R. Phys.*, vol. 19, no. 8, pp. 657–671, Dec. 2018, doi: 10.1016/j.crhy.2018.10.002.

[6] K. Kothari, R. Radhakrishnan, and N. M. Wereley, 'Advances in gamma titanium aluminides and their manufacturing techniques', *Prog. Aerosp. Sci.*, vol. 55, pp. 1–16, Nov. 2012, doi: 10.1016/j.paerosci.2012.04.001.

[7] Z. Yang, L. Zhu, G. Zhang, C. Ni, and B. Lin, 'Review of ultrasonic vibration-assisted machining in advanced materials', *Int. J. Mach. Tool Manuf.*, vol. 156, p. 103594, Sep. 2020, doi: 10.1016/j.ijmachtools.2020.103594.

[8] B. N. Bhat, Ed., *Aerospace Materials and Applications*. American Institute of Aeronautics and Astronautics, Inc, 2018.

[9] KOBELCO, 'Materials mechanical properties', KOBELCO. Accessed: Apr. 20, 2024. [Online]. Available: https://www.kobelco.co.jp/

[10] S. Lu, H. Tang, M. Qian, Q. Hong, L. Zeng, and D. H. StJohn, 'A yttrium-containing high-temperature titanium alloy additively manufactured by selective electron beam melting', *J. Cent. South Univ.*, vol. 22, no. 8, pp. 2857–2863, Aug. 2015, doi: 10.1007/s11771-015-2818-x.

[11] M. Es-Souni, 'Creep behaviour and creep microstructures of a high-temperature titanium alloy Ti–5.8Al–4.0Sn–3.5Zr–0.7Nb–0.35Si–0.06C (Timetal 834)', *Mater. Charact.*, vol. 46, no. 5, pp. 365–379, May 2001, doi: 10.1016/S1044-5803(01)00136-X.

[12] H. Hu, A. Yu, N. Li, and J. E. Allison, 'Potential Magnesium Alloys for High Temperature Die Cast Automotive Applications: A Review', *Mater. Manuf. Process.*, vol. 18, no. 5, pp. 687–717, Jan. 2003, doi: 10.1081/AMP-120024970.

[13] J. R. Correia, M. M. Gomes, J. M. Pires, and F. A. Branco, 'Mechanical behaviour of pultruded glass fibre reinforced polymer composites at elevated temperature:

Experiments and model assessment', *Compos. Struct.*, vol. 98, pp. 303–313, Apr. 2013, doi: 10.1016/j.compstruct.2012.10.051.

[14] Q. Liu, Z. Zhang, S. Liu, and H. Yang, 'Application and development of titanium alloy in aerospace and military hardware', (in Chinese), *J. Iron Steel Res.*, vol. 27, no. 03, pp. 1–4, Mar. 2015.

[15] C. Leyens and M. Peters, Eds., *Titanium and Titanium Alloys: Fundamentals and Applications*, 1st ed. Wiley-VCH, 2003.

[16] X. Huang, 'Review of the Development of Titanium Alloys for Aviation', (in Chinese), *Dual Use Technol. Prod.*, no. 7, pp. 12–14, Jul. 2012.

[17] Z. Huang, H. Qu, C. Deng, and J. Yang, 'Development and Application of Aerial Titanium and Its Alloys', (in Chinese), *Mater. Rev.*, vol. 25, no. 01, pp. 102–107, Jan. 2011.

[18] Y. Zhang, R. Kang, J. Liu, Y. Zhang, W. Zheng, and Z. Dong, 'Review of Ultrasonic Vibration Assisted Drilling', (in Chinese), *J. Mech. Eng.*, vol. 53, no. 19, pp. 33–44, Oct. 2017.

[19] C. Zhong et al., 'Laser Metal Deposition of Ti6Al4V—A Brief Review', *Appl. Sci.*, vol. 10, no. 3, p. 764, Jan. 2020, doi: 10.3390/app10030764.

[20] M. Yamaguchi, H. Inui, and K. Ito, 'High-temperature structural intermetallics', *Acta Mater.*, vol. 48, no. 1, pp. 307–322, Jan. 2000, doi: 10.1016/S1359-6454(99)00301-8.

[21] L. Lü and M. O. Lai, *Mechanical alloying*. Springer Science & Business Media, 2013.

[22] Z. Xia, C. Shan, M. Zhang, M. Cui, and M. Luo, 'Machinability of γ-TiAl: A review', *Chin. J. Aeronaut*, vol. 36, no. 7, pp. 40–75, Jul. 2023, doi: 10.1016/j.cja.2023.05.029.

[23] F. Appel, J. D. H. Paul, and M. Oehring, *Gamma titanium aluminide alloys: science and technology*. John Wiley & Sons, 2011.

[24] W. E. Voice, M. Henderson, E. F. J. Shelton, and X. Wu, 'Gamma titanium aluminide, TNB', *Intermetallics*, vol. 13, no. 9, pp. 959–964, Sep. 2005, doi: 10.1016/j.intermet.2004.12.021.

[25] L. E. Murr et al., 'Characterization of titanium aluminide alloy components fabricated by additive manufacturing using electron beam melting', *Acta Mater.*, vol. 58, no. 5, pp. 1887–1894, Mar. 2010, doi: 10.1016/j.actamat.2009.11.032.

[26] J. Ding et al., 'Thermal Stability and Lattice Strain Evolution of High-Nb-Containing TiAl Alloy under Low-Cycle-Fatigue Loading', *Adv Eng Mater*, vol. 23, no. 9, p. 2001337, Sep. 2021, doi: 10.1002/adem.202001337.

[27] A. L. Mantle and D. K. Aspinwall, 'Surface integrity and fatigue life of turned gamma titanium aluminide', *J. Mater. Process. Technol.*, vol. 72, no. 3, pp. 413–420, Dec. 1997, doi: 10.1016/S0924-0136(97)00204-5.

[28] H. Clemens, W. Smarsly, V. Güther, and S. Mayer, 'Advanced Intermetallic Titanium Aluminides', in *Proceedings of the 13th World Conference on Titanium*, 1st ed., Hoboken, NJ, USA: John Wiley & Sons, 2016, pp. 1189–1200.

[29] K. Kothari, R. Radhakrishnan, N. M. Wereley, and T. S. Sudarshan, 'Microstructure and mechanical properties of consolidated gamma titanium aluminides', *Powder Metall.*, vol. 50, no. 1, pp. 21–27, Mar. 2007, doi: 10.1179/174329007X186471.

[30] J. Lapin, Klimová, and T. Pelachová, 'Softening of a cast intermetallic Ti-46Al-2W-0.5Si alloy during annealing at 700–800°C', *Scr. Mater.*, vol. 49, no. 7, pp. 681–686, Oct. 2003, doi: 10.1016/S1359-6462(03)00406-8.

[31] B. P. Bewlay, S. Nag, A. Suzuki, and M. J. Weimer, 'TiAl alloys in commercial aircraft engines', *Mater. High Temp.*, vol. 33, no. 4–5, pp. 549–559, Jun. 2016, doi: 10.1080/09603409.2016.1183068.

[32] R. Lumley, Ed., *Fundamentals of Aluminium Metallurgy: recent advances*. Woodhead Publishing, 2018.

[33] E. A. Starke and J. T. Staley, 'Application of modern aluminum alloys to aircraft', *Prog. Aerosp. Sci.*, vol. 32, no. 2–3, pp. 131–172, 1996, doi: 10.1016/0376-0421(95)00004-6.

[34] T. Dursun and C. Soutis, 'Recent developments in advanced aircraft aluminium alloys', *Mater. Des. (1980-2015)*, vol. 56, pp. 862–871, Apr. 2014, doi: 10.1016/j.matdes.2013.12.002.

[35] J. R. Davis, *Aluminum and aluminum alloys*. ASM international, 1993.

[36] A. U. Samuel, A. O. Araoyinbo, R. R. Elewa, and M. B. Biodun, 'Effect of Machining of Aluminium Alloys with Emphasis on Aluminium 6061 Alloy – A Review', *IOP Conf. Ser.: Mater. Sci. Eng.*, vol. 1107, no. 1, p. 012157, Apr. 2021, doi: 10.1088/1757-899X/1107/1/012157.

[37] G. Kiswanto, D. L. Zariatin, and T. J. Ko, 'The effect of spindle speed, feed-rate and machining time to the surface roughness and burr formation of Aluminum Alloy 1100 in micro-milling operation', *ARASET*, vol. 16, no. 4, pp. 435–450, Oct. 2014, doi: 10.1016/j.jmapro.2014.05.003.

[38] H. A. Kishawy, M. Dumitrescu, E.-G. Ng, and M. A. Elbestawi, 'Effect of coolant strategy on tool performance, chip morphology and surface quality during high-speed machining of A356 aluminum alloy', *Int. J. Mach. Tools Manuf.*, vol. 45, no. 2, pp. 219–227, Feb. 2005, doi: 10.1016/j.ijmachtools.2004.07.003.

[39] R. K. Schmidt, *The Design of Aircraft Landing Gear*. SAE International, 2021.

[40] J. R. Davis, *ASM specialty handbook: tool materials*. ASM international, 1995.

[41] TAAC, 'Landing Gear Systems', TAAC. Accessed: Jul. 12, 2024. [Online]. Available: https://taac.com.tr/landing-gear-systems-57

[42] E. O. Ezugwu and Z. M. Wang, 'Titanium alloys and their machinability—a review', *J. Mater. Process. Technol.*, vol. 68, no. 3, pp. 262–274, Aug. 1997, doi: 10.1016/S0924-0136(96)00030-1.

[43] M. Rahman, Y. S. Wong, and A. R. Zareena, 'Machinability of Titanium Alloys', *JSME Int. J. Ser. C.*, vol. 46, no. 1, pp. 107–115, Jan. 2003, doi: 10.1299/jsmec.46.107.

[44] C. Veiga, J. P. Davim, and A. J. R. Loureiro, 'Review on machinability of titanium alloys: the process perspective', *Rev. Adv. Mater. Sci.*, vol. 34, no. 2, pp. 148–164, Jan. 2013.

[45] C. Leyens and M. Peters, *Titanium and titanium alloys: fundamentals and applications*. John Wiley & Sons, 2003.

[46] H. Clemens and W. Smarsly, 'Light-Weight Intermetallic Titanium Aluminides – Status of Research and Development', *AMR*, vol. 278, pp. 551–556, Jul. 2011, doi: 10.4028/www.scientific.net/AMR.278.551.

[47] T. Tetsui, K. Shindo, S. Kaji, S. Kobayashi, and M. Takeyama, 'Fabrication of TiAl components by means of hot forging and machining', *Intermetallics*, vol. 13, no. 9, pp. 971–978, Sep. 2005, doi: 10.1016/j.intermet.2004.12.012.

[48] X. Wu, 'Review of alloy and process development of TiAl alloys', *Intermetallics*, vol. 14, no. 10–11, pp. 1114–1122, Oct. 2006, doi: 10.1016/j.intermet.2005.10.019.

[49] H. Zhang, M. L. H. Wise, and D. K. Aspinwall, 'The Machining of TiA1-Based Intermetallics', in *Proceedings of the Thirtieth International MATADOR Conference*, Manchester: Macmillan Education UK, Mar. 1993, pp. 111–118.

[50] A. L. Mantle and D. K. Aspinwall, 'Surface integrity and fatigue life of turned gamma titanium aluminide', *J. Mater. Process. Technol.*, vol. 72, no. 3, pp. 413–420, Dec. 1997, doi: 10.1016/S0924-0136(97)00204-5.

[51] A. L. Mantle and D. K. Aspinwall, 'Surface integrity of a high speed milled gamma titanium aluminide', *J. Mater. Process. Technol.*, vol. 118, no. 1–3, pp. 143–150, Dec. 2001, doi: 10.1016/S0924-0136(01)00914-1.

[52] A. R. C. Sharman, D. K. Aspinwall, R. C. Dewes, D. Clifton, and P. Bowen, 'The effects of machined workpiece surface integrity on the fatigue life of γ-titanium aluminide', *Int. J. Mach. Tools Manuf.*, vol. 41, no. 11, pp. 1681–1685, Sep. 2001, doi: 10.1016/S0890-6955(01)00034-7.

[53] A. R. C. Sharman, D. K. Aspinwall, R. C. Dewes, and P. Bowen, 'Workpiece surface integrity considerations when finish turning gamma titanium aluminide', *Wear*, vol. 249, no. 5–6, pp. 473–481, Jun. 2001, doi: 10.1016/S0043-1648(01)00575-0.

[54] T. Furusawa, H. Hino, S. Tsuji, S. Koroyasu, and A. Ichikawa, 'Generation of Defects Due to Machining of TiAl Intermetallic Compound and Their Effects on Mechanical Strength', *J. Manuf. Sci. Eng.*, vol. 126, no. 3, pp. 506–514, Aug. 2004, doi: 10.1115/1.1751425.

[55] A. L. Mantle and D. K. Aspinwall, 'The Machining of γ-TiAI Intermetallic Alloys', *CIRP Ann.*, vol. 54, no. 1, pp. 99–104, 2005, doi: 10.1016/S0007-8506(07)60059-6.

[56] R. G. V. Pérez, 'Wear mechanisms of WC inserts in face milling of gamma titanium aluminides', *Wear*, vol. 259, no. 7–12, pp. 1160–1167, Jul. 2005, doi: 10.1016/j.wear.2005.02.062.

[57] E. Uhlmann and S. Herter, 'Studies on conventional cutting of intermetallic nickel and titanium aluminides', *Proc. Inst. Mech. Eng., Part B.*, vol. 220, no. 9, pp. 1391–1398, Sep. 2006, doi: 10.1243/09544054JEM377.

[58] Y. Ge, Y. Fu, and J. Xu, 'Experimental Study on High Speed Milling of γ-TiAl Alloy', *KEM*, vol. 339, pp. 6–10, May 2007, doi: 10.4028/www.scientific.net/KEM.339.6.

[59] K. Weinert, D. Biermann, and S. Bergmann, 'Machining of High Strength Light Weight Alloys for Engine Applications', *CIRP Ann.*, vol. 56, no. 1, pp. 105–108, 2007, doi: 10.1016/j.cirp.2007.05.027.

[60] E. Uhlmann, S. Herter, R. Gerstenberger, and M. Roeder, 'Quasi-static chip formation of intermetallic titanium aluminides', *Prod. Eng. Res. Devel.*, vol. 8, no. 3, pp. 284–291, Sep. 2009, doi: 10.1007/s11740-009-0166-0.

[61] P. C. Priarone, S. Rizzuti, G. Rotella, and L. Settineri, 'Technological and Environmental Aspects in Milling of γ-TiAl', *AMR*, vol. 223, pp. 340–349, 2011, doi: 10.4028/www.scientific.net/AMR.223.340.

[62] A. Beranoagirre and D. Olvera, 'Milling of gamma titanium–aluminum alloys', *Int. J. Adv. Manuf. Technol.*, vol. 62, no. 1–4, pp. 83–88, 2012, doi: 10.1007/s00170-011-3812-6.

[63] P. C. Priarone, S. Rizzuti, and G. Vergnano, 'Effects of cutting angle, edge preparation, and nano-structured coating on milling performance of a gamma titanium aluminide', *J. Mater. Process. Technol.*, p. 10, Dec. 2012, doi: 10.1016/j.jmatprotec.2012.07.021.

[64] D. K. Aspinwall, A. L. Mantle, W. K. Chan, R. Hood, and S. L. Soo, 'Cutting temperatures when ball nose end milling γ-TiAl intermetallic alloys', *CIRP Ann.*, vol. 62, no. 1, pp. 75–78, 2013, doi: 10.1016/j.cirp.2013.03.007.

[65] R. Hood, D. K. Aspinwall, C. Sage, and W. Voice, 'High speed ball nose end milling of γ-TiAl alloys', *Intermetallics*, vol. 32, pp. 284–291, Jan. 2013, doi: 10.1016/j.intermet.2012.09.011.

[66] F. Klocke, D. Lung, M. Arft, P. C. Priarone, and L. Settineri, 'On high-speed turning of a third-generation gamma titanium aluminide', *Int. J. Adv. Manuf. Technol*, vol. 65, no. 1–4, pp. 155–163, Mar. 2013, doi: 10.1007/s00170-012-4157-5.

[67] F. Klocke, L. Settineri, D. Lung, P. Claudio Priarone, and M. Arft, 'High performance cutting of gamma titanium aluminides: Influence of lubricoolant strategy on tool wear and surface integrity', *Wear*, vol. 302, no. 1–2, pp. 1136–1144, Apr. 2013, doi: 10.1016/j.wear.2012.12.035.

[68] T. Tetsui, A. Beranoagirre, and L. N. L. de Lacalle, 'Grinding of Gamma TiAl Intermetallic Alloys', *Procedia Eng.*, vol. 63, pp. 489–498, 2013, doi: 10.1016/j.proeng.2013.08.182.

[69] R. Hood, D. K. Aspinwall, S. L. Soo, A. L. Mantle, and D. Novovic, 'Workpiece surface integrity when slot milling γ-TiAl intermetallic alloy', *CIRP Ann.*, vol. 63, no. 1, pp. 53–56, 2014, doi: 10.1016/j.cirp.2014.03.071.

[70] P. C. Priarone, M. Robiglio, L. Settineri, and V. Tebaldo, 'Milling and Turning of Titanium Aluminides by Using Minimum Quantity Lubrication', *Procedia CIRP*, vol. 24, pp. 62–67, 2014, doi: 10.1016/j.procir.2014.07.147.

[71] L. Settineri, P. C. Priarone, M. Arft, D. Lung, and T. Stoyanov, 'An evaluative approach to correlate machinability, microstructures, and material properties of gamma titanium aluminides', *CIRP Ann.*, vol. 63, no. 1, pp. 57–60, 2014, doi: 10.1016/j.cirp.2014.03.068.

[72] S. Kolahdouz, M. Hadi, B. Arezoo, and S. Zamani, 'Investigation of surface integrity in high speed milling of gamma titanium aluminide under dry and minimum quantity lubricant conditions', *Procedia CIRP*, vol. 26, pp. 367–372, 2015, doi: 10.1016/j.procir.2014.08.016.

[73] P. C. Priarone, F. Klocke, M. G. Faga, D. Lung, and L. Settineri, 'Tool life and surface integrity when turning titanium aluminides with PCD tools under conventional wet cutting and cryogenic cooling', *Procedia Manuf.*, vol. 85, no. 1–4, pp. 807–816, Jul. 2016, doi: 10.1007/s00170-015-7958-5.

[74] A. Beranoagirre, G. Urbikain, A. Calleja, and L. López de Lacalle, 'Drilling Process in γ-TiAl Intermetallic Alloys', *Materials*, vol. 11, no. 12, p. 2379, Nov. 2018, doi: 10.3390/ma11122379.

[75] J. Ren, Z. Zhai, K. Shi, J. Zhou, J. Yang, and J. Cai, 'Tool determination and geometry parameter optimization of carbide tool in high-speed milling of third-generation γ-TiAl alloy', *J Braz. Soc. Mech. Sci. Eng.*, vol. 40, no. 10, p. 491, Oct. 2018, doi: 10.1007/s40430-018-1408-x.

[76] C. Yao, J. Lin, D. Wu, and J. Ren, 'Surface integrity and fatigue behavior when turning γ-TiAl alloy with optimized PVD-coated carbide inserts', *Chin. J. Aeronaut.*, vol. 31, no. 4, pp. 826–836, Apr. 2018, doi: 10.1016/j.cja.2017.06.002.

[77] Y. Cheng, Q. Yuan, B. Zhang, and Z. Wang, 'Study on turning force of γ-TiAl alloy', *Int. J. Adv. Manuf. Technol.*, vol. 105, no. 5, pp. 2393–2402, Dec. 2019, doi: 10.1007/s00170-019-04356-z.

[78] E. Tascioglu, A. Gharibi, and Y. Kaynak, 'High speed machining of near-beta titanium Ti-5553 alloy under various cooling and lubrication conditions', *Int. J. Adv. Manuf. Technol.*, vol. 102, no. 9–12, pp. 4257–4271, Jun. 2019, doi: 10.1007/s00170-019-03291-3.

[79] L. Haiyan, Q. Haiyang, F. Ruicheng, W. Qi, W. Maomao, and L. Jianhua, 'Effect of cutting depth on mechanical properties of single crystal γ-TiAl alloy', *Rare Met. Mater. Eng.*, vol. 49, pp. 1931–1937, 2020.

[80] A. Hussain et al., 'Mechanics of milling 48-2-2 gamma titanium aluminide', *CIRP-JMST*, vol. 30, pp. 131–139, Aug. 2020, doi: 10.1016/j.cirpj.2020.05.001.

[81] Z. Wang and Y. Liu, 'Study of surface integrity of milled gamma titanium aluminide', *J. Manuf. Process.*, vol. 56, pp. 806–819, Aug. 2020, doi: 10.1016/j.jmapro.2020.05.021.

[82] H. Xie, Z. Ma, H. Zhao, and L. Ren, 'Dry machining parameter optimization for γ-TiAl with a rhombic insert', *Procedia Manuf.*, vol. 53, pp. 162–173, 2021, doi: 10.1016/j.promfg.2021.06.020.

[83] J. Jiang, Z. Dong, H. Ma, and L. Sun, 'Computational investigation on the surface cutting of γ-TiAl alloy', *Solid State Commun.*, vol. 342, p. 114618, Feb. 2022, doi: 10.1016/j.ssc.2021.114618.

[84] J. Li, Y. Sun, H. Xie, W. Zhao, C. Xu, and J. Liu, 'Effect of cutting parameters on the depth of subsurface deformed layers of single γ-TiAl alloy during nano-cutting process', *Mater. Today Commun.*, vol. 128, no. 3, p. 189, Mar. 2022, doi: 10.1007/s00339-022-05297-3.

[85] H. Xie, Z. Ma, H. Zhao, and L. Ren, 'Temperature induced nano-scratch responses of γ-TiAl alloys revealed via molecular dynamics simulation', *Mater. Today Commun.*, vol. 30, p. 103072, Mar. 2022, doi: 10.1016/j.mtcomm.2021.103072.

[86] Y. Zhang et al., 'Microstructural modulation of TiAl alloys for controlling ultra-precision machinability', *Int. J. Mach. Tools Manuf.*, vol. 174, p. 103851, Mar. 2022, doi: 10.1016/j.ijmachtools.2022.103851.

[87] E. Benedicto, E. M. Rubio, L. Aubouy, and M. A. Sáenz-Nuño, 'Sustainable Lubrication/Cooling Systems for Efficient Turning Operations of γ-TiAl Parts from the Aeronautic Industry', *Int. J. of Precis. Eng. and Manuf.-Green Tech.*, vol. 10, no. 3, pp. 709–728, May 2023, doi: 10.1007/s40684-022-00435-x.

[88] Y. Liu, L. Liu, H. Li, B. Zhou, H. Cao, and R. Feng, 'Tool Wear and Surface Integrity of γ-TiAl Cryogenic Coolant Machining at Various Cutting Speed Levels', *Lubricants*, vol. 11, no. 6, p. 238, Jun. 2023, doi: 10.3390/lubricants11060238.

[89] X. Wang, Y. Tang, B. Zhao, T. Chen, W. Ding, and J. Xu, 'Grindability of γ-TiAl intermetallic compounds during ultrasonic vibration-assisted high efficiency deep grinding process', *Int. J. Adv. Manuf. Technol.*, vol. 128, no. 3–4, pp. 1127–1138, Sep. 2023, doi: 10.1007/s00170-023-11952-7.

[90] T. Chen, X. Wang, B. Zhao, W. Ding, and J. Xu, 'Surface integrity evolution during creep feed profile grinding of γ-TiAl blade tenon', *Modelling Simul. Mater. Sci. Eng.*, Jan. 2024, doi: 10.1016/j.cja.2024.01.020.

[91] T. Fan, C. Yao, L. Tan, Y. Cao, Y. Sun, and W. Tang, 'The influence of induction-assisted milling on the machining characteristics and surface integrity of γ-TiAl alloys', *J. Manuf. Process.*, vol. 118, pp. 215–227, May 2024, doi: 10.1016/j.jmapro.2024.03.012.

[92] Y. Liu, L. Liu, H. Li, B. Zhou, H. Cao, and R. Feng, 'Effect of repetitive nano-cutting tool parameters on surface quality and subsurface damage of γ-TiAl alloy', *Modelling Simul. Mater. Sci. Eng.*, vol. 32, no. 4, p. 045005, Jun. 2024, doi: 10.1088/1361-651X/ad3665.

[93] Z. Ren, R. Feng, H. Cao, B. Zhou, H. Li, and C. Lei, 'Wear mechanism of diamond-cutting tool in nano-cutting polycrystalline γ-TiAl alloy based on molecular dynamics simulation', *J. Manuf. Process.*, vol. 119, pp. 118–129, Jun. 2024, doi: 10.1016/j.jmapro.2024.03.071.

[94] C. Tao et al., 'Material removal mechanisms in ultrasonic vibration-assisted high-efficiency deep grinding γ-TiAl alloy', *Chin. J. Aeronaut.*, Jan. 2024.

[95] *Tool-life testing with single-point turning tools*, ISO 3685, 1993.

[96] B. Li, 'A review of tool wear estimation using theoretical analysis and numerical simulation technologies', *Int. J. Refract. Hard Met.*, vol. 35, pp. 143–151, Nov. 2012, doi: 10.1016/j.ijrmhm.2012.05.006.

[97] M. C. Shaw, *Metal cutting principles*. New York: Oxford University Press, 2005.

[98] J. T. Burwell and C. D. Strang, 'On the Empirical Law of Adhesive Wear', *J. Appl. Phys.*, vol. 23, no. 1, pp. 18–28, Jan. 1952, doi: 10.1063/1.1701970.

[99] *Tool life testing in milling*, ISO 8688-1, 1989.

[100] D. Ulutan and T. Ozel, 'Machining induced surface integrity in titanium and nickel alloys: A review', *Int. J. Adv. Manuf. Technol.*, vol. 51, no. 3, pp. 250–280, Mar. 2011, doi: 10.1016/j.ijmachtools.2010.11.003.

[101] A. la Monaca et al., 'Surface integrity in metal machining - Part II: Functional performance', *Int. J. Mach. Tools Manuf.*, vol. 164, p. 103718, May 2021, doi: 10.1016/j.ijmachtools.2021.103718.

[102] A. R. C. Sharman, D. K. Aspinwall, R. C. Dewes, D. Clifton, and P. Bowen, 'The effects of machined workpiece surface integrity on the fatigue life of γ-titanium aluminide', *Int. J. Mach. Tools Manuf.*, vol. 41, no. 11, pp. 1681–1685, Sep. 2001, doi: 10.1016/S0890-6955(01)00034-7.

[103] S. V. Joshi, S. P. Vizhian, B. R. Sridhar, and K. Jayaram, 'Parametric Study of Machining Effect on Residual Stress and Surface Roughness of Nickel Base Super Alloy UDIMET 720', *AMR*, vol. 47–50, pp. 13–16, Sep. 2008, doi: 10.4028/www.scientific.net/AMR.47-50.13.

[104] D. Novovic, R. C. Dewes, D. K. Aspinwall, W. Voice, and P. Bowen, 'The effect of machined topography and integrity on fatigue life', *Int. J. Mach. Tools Manuf.*, vol. 44, no. 2–3, pp. 125–134, Feb. 2004, doi: 10.1016/j.ijmachtools.2003.10.018.

[105] *Geometrical product specifications (GPS) — Surface texture: Profile Part 2: Terms, definitions and surface texture parameters*, ISO 21920-2, 2021.

[106] A. I. Nicolas-Silvente, E. Velasco-Ortega, I. Ortiz-Garcia, L. Monsalve-Guil, J. Gil, and A. Jimenez-Guerra, 'Influence of the Titanium Implant Surface Treatment on the Surface Roughness and Chemical Composition', *Materials*, vol. 13, no. 2, p. 314, Jan. 2020, doi: 10.3390/ma13020314.

[107] C. C. Viáfara and A. Sinatora, 'Influence of hardness of the harder body on wear regime transition in a sliding pair of steels', *Wear*, vol. 267, no. 1–4, pp. 425–432, Jul. 2009, doi: 10.1016/j.wear.2008.11.019.

[108] H. Wu, S. Hamada, and H. Noguchi, 'Fatigue strength prediction for inhomogeneous face-centered cubic metal based on Vickers hardness', *Int. J. Fatigue*, vol. 48, pp. 48–54, Mar. 2013, doi: 10.1016/j.ijfatigue.2012.09.021.

[109] P. Fu, K. Zhan, and C. Jiang, 'Micro-structure and surface layer properties of 18CrNiMo7-6 steel after multistep shot peening', *Mater. Des.*, vol. 51, pp. 309–314, Oct. 2013, doi: 10.1016/j.matdes.2013.04.011.

[110] S. A. Bentley, A. L. Mantle, and D. K. Aspinwall, 'The effect of machining on the fatigue strength of a gamma titanium aluminide intertmetallic alloy', *Intermetallics*, vol. 7, no. 8, pp. 967–969, Aug. 1999, doi: 10.1016/S0966-9795(99)00008-4.

[111] Y. Guo, C. Saldana, W. Dale Compton, and S. Chandrasekar, 'Controlling deformation and microstructure on machined surfaces', *Acta Mater.*, vol. 59, no. 11, pp. 4538–4547, Jun. 2011, doi: 10.1016/j.actamat.2011.03.076.

[112] Y. Umakoshi, T. Nakano, and T. Yamane, 'The effect of orientation and lamellar structure on the plastic behavior of TiAl crystals', *Mater. Sci. Eng. A.*, vol. 152, no. 1–2, pp. 81–88, May 1992, doi: 10.1016/0921-5093(92)90050-B.

[113] R. A. Brockman, 'Analysis of elastic-plastic deformation in TiAl polycrystals', *Int. J. Plast.*, vol. 19, no. 10, pp. 1749–1772, Oct. 2003, doi: 10.1016/S0749-6419(02)00102-X.

[114] K. S. Chan and Y.-W. Kim, 'Influence of microstructure on crack-tip micromechanics and fracture behaviors of a two-phase TiAl alloy', *Metall. Trans. A*, vol. 23, no. 6, pp. 1663–1677, Jun. 1992, doi: 10.1007/BF02804362.

[115] *American national standard*, ANSI/ASA S3.20-2015, 2015.

[116] E. Hutli, M. S. Nedeljkovic, A. Bonyár, N. A. Radovic, V. Llic, and A. Debeljkovic, 'The ability of using the cavitation phenomenon as a tool to modify the surface characteristics in micro- and in nano-level', *Tribol. Int.*, vol. 101, pp. 88–97, Sep. 2016, doi: 10.1016/j.triboint.2016.04.006.

[117] R. Oza, N. Shah, and S. Patel, 'Recovery of nickel from spent catalysts using ultrasonication-assisted leaching', *J. Chem. Technol. Biotechnol.*, vol. 86, no. 10, pp. 1276–1281, Oct. 2011, doi: 10.1002/jctb.2649.

[118] J. D. N. Cheeke, *Fundamentals and Applications of Ultrasonic Waves*. Boca Raton: CRC Press, 2002.

[119] T. B. Thoe, D. K. Aspinwall, and M. L. H. Wise, 'Review on ultrasonic machining', *Int. J. Mach. Tools Manuf.*, vol. 38, no. 4, pp. 239–255, Mar. 1998, doi: 10.1016/S0890-6955(97)00036-9.

[120] R. W. Wood and A. L. Loomis, 'XXXVIII.*The physical and biological effects of high-frequency sound-waves of great intensity*', *The London, Edinburgh, and Dublin Philosophical Magazine and Journal of Science*, vol. 4, no. 22, pp. 417–436, Sep. 1927, doi: 10.1080/14786440908564348.

[121] G. Nishimura, Y. Jimbo, and S. Shimakawa, 'Ultrasonic machining-part I', *J. Fac. Eng. Tokyo Univ*, vol. 24, no. 3, pp. 65–100, 1954.

[122] E. A. Neppiras, 'Ultrasonic machining', *Ultrasonics*, vol. 3, no. 2, p. 99, Apr. 1965, doi: 10.1016/0041-624X(65)90007-7.

[123] M. A. Moreland and D. O. Moore, 'Versatile performance of ultrasonic machining', *Am. Ceram. Soc. Bull.*, vol. 67, no. 6, pp. 1045–1047, 1988.

[124] J. Perkins, 'An outline of power ultrasonics', *OEM Design*, 1972.

[125] W.-X. Xu and L.-C. Zhang, 'Ultrasonic vibration-assisted machining: principle, design and application', *Adv. Manuf.*, vol. 3, no. 3, pp. 173–192, Sep. 2015, doi: 10.1007/s40436-015-0115-4.

[126] D. E. Brehl and T. A. Dow, 'Review of vibration-assisted machining', *Precis. Eng.*, vol. 32, no. 3, pp. 153–172, Jul. 2008, doi: 10.1016/j.precisioneng.2007.08.003.

[127] D. Kremer, *New developments on ultrasonic machining*. Society of Manufacturing Engineers, 1991.

[128] D. Clifton, Y. Imai, and J. A. McGeough, 'Some Ultrasonic Effects in Machining Materials Encountered in the Offshore Industries', *Proceedings of the Thirtieth International MATADOR Conference*, pp. 119–123, 1993, doi: 10.1007/978-1-349-13255-3_16.

[129] J. Kumar, 'ULTRASONIC MACHINING-A COMPREHENSIVE REVIEW', *Mach. Sci. Technol.*, vol. 17, no. 3, pp. 325–379, Jul. 2013, doi: 10.1080/10910344.2013.806093.

[130] G. E. Miller, 'Special Theory of Ultrasonic Machining', *J. Appl. Phys.*, vol. 28, no. 2, pp. 149–156, Feb. 1957, doi: 10.1063/1.1722698.

[131] Z. J. Pei, P. M. Ferreira, and M. Haselkorn, 'Plastic flow in rotary ultrasonic machining of ceramics', *J. Mater. Process. Technol.*, vol. 48, no. 1–4, pp. 771–777, 1995, doi: 10.1016/0924-0136(94)01720-L.

[132] J. Wang, 'Ultrasonic Machining: A Total Mechanical Machining Technology Using Loose Abrasive Particles', in *Abrasive Technology-Characteristics and Applications*, IntechOpen, 2018.

[133] M. C. Shaw, 'Ultrasonic grinding', *Microtechnic*, vol. 10, no. 6, pp. 257–265, 1956.

[134] N. H. Cook, *Manufacturing analysis*, vol. 1211. Addison-Wesley Publishing Company, 1966.

[135] G. S. Kainth, A. Nandy, and K. Singh, 'On the mechanics of material removal in ultrasonic machining', *Int. J. Mach. Tool Des. Res.*, vol. 19, no. 1, pp. 33–41, Jan. 1979, doi: 10.1016/0020-7357(79)90019-2.

[136] T. B. Thoe, D. K. Aspinwall, and M. L. H. Wise, 'Review on ultrasonic machining', *Int. J. Mach. Tools Manuf.*, vol. 38, no. 4, pp. 239–255, Mar. 1998, doi: 10.1016/S0890-6955(97)00036-9.

[137] B. R. LAWN, A. G. EVANS, and D. B. MARSHALL, 'Elastic/Plastic Indentation Damage in Ceramics: The Median/Radial Crack System', *J. Am. Ceram. Soc.*, vol. 63, no. 9–10, pp. 574–581, Sep. 1980, doi: 10.1111/j.1151-2916.1980.tb10768.x.

[138] D. B. MARSHALL, B. R. LAWN, and A. G. EVANS, 'Elastic/Plastic Indentation Damage in Ceramics: The Lateral Crack System', *J. Am. Ceram. Soc.*, vol. 65, no. 11, pp. 561–566, Nov. 1982, doi: 10.1111/j.1151-2916.1982.tb10782.x.

[139] H. Zha, P. Feng, J. Zhang, D. Yu, and Z. Wu, 'Material removal mechanism in rotary ultrasonic machining of high-volume fraction SiCp/Al composites', *Int. J. Adv. Manuf. Technol.*, vol. 97, no. 5–8, pp. 2099–2109, Jul. 2018, doi: 10.1007/s00170-018-2075-x.

[140] R. P. Singh and S. Singhal, 'Rotary Ultrasonic Machining: A Review', *Mater. Manuf. Process.*, vol. 31, no. 14, pp. 1795–1824, Oct. 2016, doi: 10.1080/10426914.2016.1140188.

[141] A. P. Nagalingam and S. H. Yeo, 'Effects of ambient pressure and fluid temperature in ultrasonic cavitation machining', *Int. J. Adv. Manuf. Technol.*, vol. 98, no. 9–12, pp. 2883–2894, Oct. 2018, doi: 10.1007/s00170-018-2481-0.

[142] D. G. Shchukin, E. Skorb, V. Belova, and H. Möhwald, 'Ultrasonic Cavitation at Solid Surfaces', *Adv. Mater.*, vol. 23, no. 17, pp. 1922–1934, May 2011, doi: 10.1002/adma.201004494.

[143] W. Pentland and J. A. Ektermanis, 'Improving Ultrasonic Machining Rates—Some Feasibility Studies', *J. Eng. Ind.*, vol. 87, no. 1, pp. 39–46, Feb. 1965, doi: 10.1115/1.3670755.

[144] V. Soundararajan and V. Radhakrishnan, ‘An experimental investigation on the basic mechanisms involved in ultrasonic machining’, *Int. J. Mach. Tool Des. Res.*, vol. 26, no. 3, pp. 307–321, Jan. 1986, doi: 10.1016/0020-7357(86)90008-9.

[145] G. E. Dieter, *Metalurgia Mecânica*, 2nd ed. 1981.

[146] P. L. Guzzo, A. H. Shinohara, and A. A. Raslan, ‘A comparative study on ultrasonic machining of hard and brittle materials’, *J. Braz. Soc. Mech. Sci. & Eng.*, vol. 26, no. 1, pp. 56–61, Mar. 2004, doi: 10.1590/S1678-58782004000100010.

[147] J. P. Choi, B. H. Jeon, and B. H. Kim, ‘Chemical-assisted ultrasonic machining of glass’, *J. Mater. Process. Technol.*, vol. 191, no. 1–3, pp. 153–156, Aug. 2007, doi: 10.1016/j.jmatprotec.2007.03.017.

[148] K. J. Singh, I. S. Ahuja, and J. Kapoor, ‘Ultrasonic, chemical-assisted ultrasonic and rotary ultrasonic machining of glass: a review paper’, *World J. Eng.*, vol. 15, no. 6, pp. 751–770, Dec. 2018, doi: 10.1108/WJE-04-2018-0114.

[149] C. Nath, G. C. Lim, and H. Y. Zheng, ‘Influence of the material removal mechanisms on hole integrity in ultrasonic machining of structural ceramics’, *Ultrasonics*, vol. 52, no. 5, pp. 605–613, Jul. 2012, doi: 10.1016/j.ultras.2011.12.007.

[150] R. Gilmore, *Ultrasonic machining of ceramics*. Society of Manufacturing Engineers, 1990.

[151] J. B. Kohls, ‘Ultrasonic Manufacturing Process: Ultrasonic Machining (USM) and Ultrasonic Impact Grinding (USIG)’, *Carbide Tool J.*, vol. 16, no. 5, pp. 12–15, 1984.

[152] M. A. Moreland, ‘Ultrasonic machining—Book chapter: ceramics and glasses’, *ASM International, Engineering Material Handbook*, vol. 4, pp. 359–362, 1991.

[153] M. Komaraiah and P. Narasimha Reddy, ‘A study on the influence of workpiece properties in ultrasonic machining’, *Int. J. Mach. Tools Manuf.*, vol. 33, no. 3, pp. 495–505, Jun. 1993, doi: 10.1016/0890-6955(93)90055-Y.

[154] P. Legge, ‘Machining without abrasive slurry’, *Ultrasonics*, vol. 4, no. 3, pp. 157–162, Jul. 1966, doi: 10.1016/0041-624X(66)90123-5.

[155] P. Legge, ‘Ultrasonic drilling of ceramics’, *Ind. Dia. Rev.*, vol. 24, p. 20, 1964.

[156] B. Lauwers, F. Klocke, A. Klink, A. E. Tekkaya, R. Neugebauer, and D. Mcintosh, ‘Hybrid processes in manufacturing’, *CIRP Ann.*, vol. 63, no. 2, pp. 561–583, 2014, doi: 10.1016/j.cirp.2014.05.003.

[157] L. O’Toole, C. Kang, and F. Fang, ‘Advances in Rotary Ultrasonic-Assisted Machining’, *Nanomanuf. Metrol.*, vol. 3, no. 1, pp. 1–25, Mar. 2020, doi: 10.1007/s41871-019-00053-3.

[158] W. R. Tyrrell, ‘Rotary ultrasonic machining’, *SME Technical Paper MR*, pp. 70–516, 1970.

[159] Z. J. Pei, P. M. Ferreira, S. G. Kapoor, and M. Haselkorn, 'Rotary ultrasonic machining for face milling of ceramics', *Int. J. Mach. Tools Manuf.*, vol. 35, no. 7, pp. 1033–1046, Jul. 1995, doi: 10.1016/0890-6955(94)00100-X.

[160] A. I. Markov, 'Ultrasonic drilling and milling of hard non-metallic materials with diamond tools', *Mach. Tool.*, vol. 48, no. 9, pp. 45–47, 1977.

[161] J. B. Wachtman, *Materials and Equipment-Whitewares-Refractory Ceramics-Basic Science, Volume 16, Issue 1*. John Wiley & Sons, 2009.

[162] Z. J. Pei and P. M. Ferreira, 'An experimental investigation of rotary ultrasonic face milling', *Int. J. Mach. Tools Manuf.*, vol. 39, no. 8, pp. 1327–1344, Aug. 1999, doi: 10.1016/S0890-6955(98)00093-5.

[163] K. Kuo and C. Tsao, 'Rotary ultrasonic-assisted milling of brittle materials', *Trans. Nonferrous Met. Soc. China*, vol. 22, pp. s793–s800, Dec. 2012, doi: 10.1016/S1003-6326(12)61806-8.

[164] Z. J. Pei, D. Prabhakar, P. M. Ferreira, and M. Haselkorn, 'Rotary ultrasonic drilling and milling of ceramics', *Ceram. Trans.*, vol. 49, pp. 185–185, Apr. 1995.

[165] H. Gong, F. Z. Fang, and X. T. Hu, 'Kinematic view of tool life in rotary ultrasonic side milling of hard and brittle materials', *Int. J. Mach. Tools Manuf.*, vol. 50, no. 3, pp. 303–307, Mar. 2010, doi: 10.1016/j.ijmachtools.2009.12.006.

[166] N. Khanna, Z. J. Pei, and P. M. Ferreira, 'Experimental investigation of rotary ultrasonic grinding of ceramic disks', in *Proceedings of the NAMRC XXIII Conference*, SME, 1995.

[167] F. D. Ning, W. L. Cong, Z. J. Pei, and C. Treadwell, 'Rotary ultrasonic machining of CFRP: A comparison with grinding', *Ultrasonics*, vol. 66, pp. 125–132, Mar. 2016, doi: 10.1016/j.ultras.2015.11.002.

[168] R. C. Skelton, 'Turning with an oscillating tool', *Int. J. Mach. Tool Des. Res.*, vol. 8, no. 4, pp. 239–259, Dec. 1968, doi: 10.1016/0020-7357(68)90014-0.

[169] A. Isaev, 'Ultrasonic vibration of a metal cutting tool', *Vest Mashinos*, vol. 41, 1961.

[170] C. Rahman and S. Andrew, 'A study on ultrasonic vibration cutting of low alloy steel', *J. Mater. Process. Technol.*, vol. 192–193, pp. 159–165, Oct. 2007, doi: 10.1016/j.jmatprotec.2007.04.047.

[171] Y. Zhang, Z. Zhou, J. Wang, and X. Li, 'Diamond Tool Wear in Precision Turning of Titanium Alloy', *Mater. Manuf. Process.*, vol. 28, no. 10, pp. 1061–1064, Oct. 2013, doi: 10.1080/10426914.2013.773018.

[172] V. V. Silberschmidt, S. M. A. Mahdy, M. A. Gouda, A. Naseer, A. Maurotto, and A. Roy, 'Surface-roughness Improvement in Ultrasonically Assisted Turning', *Procedia CIRP*, vol. 13, pp. 49–54, 2014, doi: 10.1016/j.procir.2014.04.009.

[173] L. Yan, Q. Zhang, and J. Yu, 'Analytical models for oil penetration and experimental study on vibration assisted machining with minimum quantity lubrication', *J. Mech. Sci.*, vol. 148, pp. 374–382, Nov. 2018, doi: 10.1016/j.ijmecsci.2018.09.016.

[174] F. Ahmed, T. J. Ko, R. Kurniawan, and Y. Kwack, 'Machinability analysis of difficult-to-cut material during ultrasonic vibration-assisted ball end milling', *Mater. Manuf. Process.*, vol. 36, no. 15, pp. 1734–1745, Nov. 2021, doi: 10.1080/10426914.2021.1944194.

[175] H. Wang, S. Zhang, and G. Li, 'Experimental Study on Ultrasonic-Assisted End Milling Forces in 2195 Aluminum-Lithium Alloy', *Materials*, vol. 15, no. 7, p. 2508, Mar. 2022, doi: 10.3390/ma15072508.

[176] G. Gao, Z. Xia, T. Su, D. Xiang, and B. Zhao, 'Cutting force model of longitudinal-torsional ultrasonic-assisted milling Ti-6Al-4V based on tool flank wear', *J. Mater. Process. Technol.*, vol. 291, p. 117042, May 2021, doi: 10.1016/j.jmatprotec.2021.117042.

[177] J. Gao and Y. Altintas, 'Chatter stability of synchronized elliptical vibration assisted milling', *CIRP J. Manuf. Sci. Technol.*, vol. 28, pp. 76–86, Dec. 2019, doi: 10.1016/j.cirpj.2019.11.006.

[178] M. Lotfi and S. Amini, 'Experimental and numerical study of ultrasonically-assisted drilling', *Ultrasonics*, vol. 75, pp. 185–193, Mar. 2017, doi: 10.1016/j.ultras.2016.11.009.

[179] X. Zhu, W. Wang, R. Jiang, Y. Xiong, and X. Liu, 'Thrust force model for ultrasonic-assisted micro drilling of DD6 superalloy', *Adv. Manuf.*, vol. 10, no. 2, pp. 313–325, Jan. 2022, doi: 10.1007/s40436-021-00381-y.

[180] P. Zai, J. Tong, Z. Liu, Z. Zhang, C. Song, and B. Zhao, 'Analytical model of exit burr height and experimental investigation on ultrasonic-assisted high-speed drilling micro-holes', *J. Manuf. Process.*, vol. 68, pp. 807–817, Jun. 2021, doi: 10.1016/j.jmapro.2021.06.010.

[181] E. Yarar and S. Karabay, 'Investigation of the effects of ultrasonic assisted drilling on tool wear and optimization of drilling parameters', *CIRP J. Manuf. Sci. Technol.*, vol. 31, pp. 265–280, Jun. 2020, doi: 10.1016/j.cirpj.2020.06.002.

[182] X. Li, 'Process Study of Ultrasonic Assisted Vibration Drilling Aluminum and Titanium Alloys', (in Chinese), M.S. thesis, Dept. Mech. Eng., Dalian Unvi. Technol., Dalian, China, 2016.

[183] V. Sharma and P. M. Pandey, 'Recent advances in ultrasonic assisted turning: A step towards sustainability', *Cogent Eng.*, vol. 3, no. 1, p. 1222776, Dec. 2016, doi: 10.1080/23311916.2016.1222776.

[184] G. S. Ghule and S. Sanap, 'Ultrasonic Vibrations Assisted Turning (UAT): A Review', in *Adv. Eng. Des.*, Singapore: Springer, Singapore, Apr. 2021, pp. 275–285. doi: 10.1007/978-981-33-4684-0_28.

[185] J. Liu, X. Jiang, X. Han, and D. Zhang, 'Influence of parameter matching on performance of high-speed rotary ultrasonic elliptical vibration-assisted machining for side milling of titanium alloys', *Int. J. Adv. Manuf. Technol.*, vol. 101, no. 5–8, pp. 1333–1348, Apr. 2019, doi: 10.1007/s00170-018-3006-6.

[186] R. Nosouhi, S. Behbahani, S. Amini, and M. R. Khosrojerdi, 'An Experimental Study on the Cutting Forces, Surface Roughness and the Hardness of Al 6061 in 1D and 2D Ultrasonic Assisted Turning', *AMM*, vol. 680, pp. 224–227, Oct. 2014, doi: 10.4028/www.scientific.net/AMM.680.224.

[187] A. Suárez, F. Veiga, L. N. L. de Lacalle, R. Polvorosa, S. Lutze, and A. Wretland, 'Effects of Ultrasonics-Assisted Face Milling on Surface Integrity and Fatigue Life of Ni-Alloy 718', *J. Mater. Eng. Perform.*, vol. 25, no. 11, pp. 5076–5086, Nov. 2016, doi: 10.1007/s11665-016-2343-6.

[188] R. Kurniawan, S. Ali, K. M. Park, S. T. Jung, and T. J. Ko, 'Experimental Study of Microgroove Surface Using Three-Dimensional Elliptical Vibration Texturing', *J. Micro Nano-Manuf.*, vol. 7, no. 2, Jun. 2019, doi: 10.1115/1.4043957.

[189] F. Ning, W. Cong, H. Wang, Y. Hu, Z. Hu, and Z. Pei, 'Surface grinding of CFRP composites with rotary ultrasonic machining: a mechanistic model on cutting force in the feed direction', *Int. J. Adv. Manuf. Technol.*, vol. 92, no. 1–4, pp. 1217–1229, Sep. 2017, doi: 10.1007/s00170-017-0149-9.

[190] S. S. F. Chang and G. M. Bone, 'Burr height model for vibration assisted drilling of aluminum 6061-T6', *Precis. Eng.*, vol. 34, no. 3, pp. 369–375, Jul. 2010, doi: 10.1016/j.precisioneng.2009.09.002.

[191] M. A. Moghaddas, M. A. Short, N. R. Wiley, A. Y. Yi, and K. F. Graff, 'Improving Productivity in an Ultrasonic-Assisted Drilling Vertical Machining Center', *J. Manuf. Sci. Eng.*, vol. 140, no. 6, Jan. 2018, doi: 10.1115/1.4039109.

[192] R. Teimouri, S. Amini, and N. Mohagheghian, 'Experimental study and empirical analysis on effect of ultrasonic vibration during rotary turning of aluminum 7075 aerospace alloy', *J. Manuf. Process.*, vol. 26, pp. 1–12, Apr. 2017, doi: 10.1016/j.jmapro.2016.11.011.

[193] S. Amini, M. Soleimani, H. Paktinat, and M. Lotfi, 'Effect of longitudinal−torsional vibration in ultrasonic-assisted drilling', *Mater. Manuf. Process.*, vol. 32, no. 6, pp. 616–622, Apr. 2017, doi: 10.1080/10426914.2016.1198027.

[194] M. A. Moghaddas, A. Y. Yi, and K. F. Graff, 'Temperature measurement in the ultrasonic-assisted drilling process', *Int. J. Adv. Manuf. Technol.*, vol. 103, no. 1–4, pp. 187–199, Jul. 2019, doi: 10.1007/s00170-019-03487-7.

[195] L. Wei and D. Wang, 'Comparative study on drilling effect between conventional drilling and ultrasonic-assisted drilling of Ti-6Al-4V/Al2024-T351 laminated material', *Int. J. Adv. Manuf. Technol.*, vol. 103, no. 1–4, pp. 141–152, Jul. 2019, doi: 10.1007/s00170-019-03507-6.

[196] X. Chen, J. Tang, W. Shao, B. Hu, and J. Ye, 'An Analytical and Experimental Study on Cutting Characteristics and Transient Cutting Force Modeling in Feed Directional Ultrasonic Vibration-Assisted Cutting of High Strength Alloys', *Materials*, vol. 15, no. 20, p. 7388, Oct. 2022, doi: 10.3390/ma15207388.

[197] G. Chen, J. Xu, J. Wang, Y. Li, J. Wang, and H. Yu, 'Experimental investigation on cavitation effect and surface quality of ultrasonic-assisted micro-hole drilling', *Int. J. Adv. Manuf. Technol.*, vol. 121, no. 1–2, pp. 919–936, Jul. 2022, doi: 10.1007/s00170-022-09193-1.

[198] Y. Xu, Z. Wan, P. Zou, W. Huang, and G. Zhang, 'Experimental study on cutting force in ultrasonic vibration-assisted turning of 304 austenitic stainless steel', *Proc IMechE Part B: J Engineering Manufacture*, vol. 235, no. 3, pp. 494–513, 2021, doi: 10.1177/0954405420957127.

[199] A. Wadee, H. El-Hofy, and W. Kheir, 'Experimental investigation of ultrasonic assisted helical milling of 2205 duplex stainless steel', *MM. Sci. J.*, pp. 1–9, Oct. 2021.

[200] X. Zhang, Z. Peng, L. Liu, and X. Zhang, 'A Tool Life Prediction Model Based on Taylor's Equation for High-Speed Ultrasonic Vibration Cutting Ti and Ni Alloys', *Coatings*, vol. 12, no. 10, p. 1553, Oct. 2022, doi: 10.3390/coatings12101553.

[201] J. Airao and C. Nirala, 'Machinability of Ti-6Al-4V and Nimonic-90 in ultrasonic-assisted turning under sustainable cutting fluid', *Mater. Today Proc.*, vol. 62, pp. 7396–7400, 2022, doi: 10.1016/j.matpr.2022.02.312.

[202] B. Fang, Z. YuanUAN, D. LI, and L. Gao, 'Effect of ultrasonic vibration on finished quality in ultrasonic vibration assisted micromilling of Inconel718', *Chin. J. Aeronaut.*, vol. 34, no. 6, pp. 209–219, Jun. 2021, doi: 10.1016/j.cja.2020.09.021.

[203] P. Zhang, X. Zhang, X. Yu, and Y. Wang, 'Research on the nanocutting mechanism of Ni-Fe-Cr-based superalloys: Conventional cutting versus UEVC', *Mater. Today Commun.*, vol. 26, p. 101795, Mar. 2021, doi: 10.1016/j.mtcomm.2020.101795.

[204] Z. Zheng, J. Zhang, P. Feng, Z. Li, and J. Wang, 'Fabrication of hierarchical micro/nanostructures on titanium alloy by combining rotary ultrasonic milling and anodizing', *Manuf. Lett.*, vol. 34, pp. 43–48, Oct. 2022, doi: 10.1016/j.mfglet.2022.09.002.

[205] Z. Wang, Y. Pan, Y. Zhang, X. Men, X. Fu, and S. Ren, 'Study on the Material Removal Mechanism of Ultrasonic Elliptical Vibration Cutting of Medical beta Titanium Alloy', *Micromachines*, vol. 13, no. 6, p. 819, Jun. 2022, doi: 10.3390/mi13060819.

[206] X. Wei, C. Yue, D. Hu, X. Liu, Y. Ding, and S. Y. Liang, 'Research on Surface Roughness of Supersonic Vibration Auxiliary Side Milling for Titanium Alloy', *Chin. J. Mech. Eng.*, vol. 35, no. 1, Dec. 2022, doi: 10.1186/s10033-022-00770-9.

[207] S. Wu et al., 'Study on the mechanism of AL2024-T351/Ti-6Al-4V laminated materials by ultrasonic vibration drilling', *Arch. Civ. Mech. Eng.*, vol. 22, no. 4, p. 161, Jul. 2022, doi: 10.1007/s43452-022-00482-w.

[208] A. V. Mitrofanov, V. I. Babitsky, and V. V. Silberschmidt, 'Finite element simulations of ultrasonically assisted turning', *Comput. Mater. Sci.*, vol. 28, no. 3–4, pp. 645–653, Nov. 2003, doi: 10.1016/j.commatsci.2003.08.020.

[209] X. Han, D. Zhang, and G. Song, 'Review on current situation and development trend for ultrasonic vibration cutting technology', *Mater. Today Proc.*, vol. 22, pp. 444–455, 2020, doi: 10.1016/j.matpr.2019.07.715.

[210] H. Jamshidi and M. Nategh, 'Theoretical and experimental investigation of the frictional behavior of the tool-chip interface in ultrasonic-vibration assisted turning', *Int. J. Mach. Tools Manuf.*, vol. 65, pp. 1–7, Feb. 2013, doi: 10.1016/j.ijmachtools.2012.09.004.

[211] W. Xie et al., 'Surface integrity investigation into longitudinal-torsional ultrasonic vibration side milling for a TC18 titanium alloy—part I: the effects of cutting speed on cutting force and surface integrity', *Int. J. Adv. Manuf. Technol.*, vol. 120, no. 3–4, pp. 2701–2713, May 2022, doi: 10.1007/s00170-022-08874-1.

[212] W. Xie et al., 'Research on cutting force and surface integrity of TC18 titanium alloy by longitudinal ultrasonic vibration assisted milling', *Int. J. Adv. Manuf. Technol.*, vol. 119, no. 7–8, pp. 4745–4755, Apr. 2022, doi: 10.1007/s00170-021-08532-y.

[213] W. Ren et al., 'Research on homogenization and surface morphology of Ti-6Al-4V alloy by longitudinal-torsional coupled ultrasonic vibration ball-end milling', *Int. J. Adv. Manuf. Technol.*, vol. 104, no. 1–4, pp. 301–313, Sep. 2019, doi: 10.1007/s00170-019-03668-4.

[214] D. Xiang, B. Wu, Y. Yao, Z. Liu, and H. Feng, 'Ultrasonic longitudinal-torsional vibration-assisted cutting of Nomex® honeycomb-core composites', *Int J Adv Manuf Technol*, vol. 100, no. 5–8, pp. 1521–1530, Feb. 2019, doi: 10.1007/s00170-018-2810-3.

[215] P. Chen, J. Tong, J. Zhao, Z. Zhang, and B. Zhao, 'A study ofthe surface microstructure and tool wear of titanium alloys after ultrasonic longitudinal-torsional milling', *J. Manuf. Process.*, vol. 53, pp. 1–11, May 2020, doi: 10.1016/j.jmapro.2020.01.040.

[216] G. Chen, Y. Zou, X. Qin, J. Liu, Q. Feng, and C. Ren, 'Geometrical texture and surface integrity in helical milling and ultrasonic vibration helical milling of Ti-6Al-4V alloy', *J. Mater. Process. Technol.*, vol. 278, p. 116494, Apr. 2020, doi: 10.1016/j.jmatprotec.2019.116494.

[217] C. Ni, L. Zhu, and Z. Yang, 'Comparative investigation of tool wear mechanism and corresponding machined surface characterization in feed-direction ultrasonic vibration assisted milling of Ti–6Al–4V from dynamic view', *Wear*, vol. 436–437, p. 203006, Oct. 2019, doi: 10.1016/j.wear.2019.203006.

[218] J. Tong, G. Wei, L. Zhao, X. Wang, and J. Ma, 'Surface microstructure of titanium alloy thin-walled parts at ultrasonic vibration-assisted milling', *Int. J. Adv. Manuf. Technol.*, vol. 101, no. 1–4, pp. 1007–1021, Mar. 2019, doi: 10.1007/s00170-018-3005-7.

[219] G. Chen, C. Ren, Y. Zou, X. Qin, L. Lu, and S. Li, 'Mechanism for material removal in ultrasonic vibration helical milling of Ti 6Al 4V alloy', *Int. J. Mach. Tools Manuf.*, vol. 138, pp. 1–13, Nov. 2018, doi: 10.1016/j.ijmachtools.2018.11.001.

[220] C. Ni, L. Zhu, C. Liu, and Z. Yang, 'Analytical modeling of tool-workpiece contact rate and experimental study in ultrasonic vibration-assisted milling of Ti–6Al–4V', *Int. J. Mech. Sci.*, vol. 142–143, pp. 97–111, Jul. 2018, doi: 10.1016/j.ijmecsci.2018.04.037.

[221] M. Zhang, D. Zhang, D. Geng, J. Liu, Z. Shao, and X. Jiang, 'Surface and sub-surface analysis of rotary ultrasonic elliptical end milling of Ti-6Al-4V', *Mater. Des.*, vol. 191, p. 108658, Mar. 2020, doi: 10.1016/j.matdes.2020.108658.

[222] J. Wang, 'Damage Formation Mechanism and Suppression Methods in Rotary Ultrasonic Drilling of Hard Brittle materials & Ceramic Matrix Composites', (in Chinese), Ph.D. dissertation, Dept. Mech. Eng., Tsinghua Unvi., Beijing, China, 2017.

[223] B. Chang, Z. Yi, X. Cao, and J. Duan, 'Defect suppression and grain refinement during ultrasonic vibration-assisted side milling of GH4169 superalloy', *J. Manuf. Process.*, vol. 85, pp. 281–294, Jan. 2023, doi: 10.1016/j.jmapro.2022.11.011.

[224] L. Yang, N. R. Tao, K. Lu, and L. Lu, 'Enhanced fatigue resistance of Cu with a gradient nanograined surface layer', *Scr. Mater.*, vol. 68, no. 10, pp. 801–804, May 2013, doi: 10.1016/j.scriptamat.2013.01.031.

[225] P. F. Wang, Z. Han, and K. Lu, 'Enhanced tribological performance of a gradient nanostructured interstitial-free steel', *Wear*, vol. 402–403, pp. 100–108, May 2018, doi: 10.1016/j.wear.2018.02.010.

[226] H. W. Huang, Z. B. Wang, J. Lu, and K. Lu, 'Fatigue behaviors of AISI 316L stainless steel with a gradient nanostructured surface layer', *Acta Mater.*, vol. 87, pp. 150–160, Apr. 2015, doi: 10.1016/j.actamat.2014.12.057.

[227] Z. Li et al., 'Grinding force model for ultrasonic assisted grinding of γ-TiAl intermetallic compounds and experimental validation', *Rev. Adv. Mater. Sci.*, vol. 63, no. 1, p. 20230167, Feb. 2024, doi: 10.1515/rams-2023-0167.

[228] Z. Han, H. Jin, and H. Fu, 'Cutting force prediction models of metal machining processes: A review', in *2015 International Conference on Estimation, Detection and Information Fusion (ICEDIF)*, IEEE, 2015, pp. 323–328.

[229] S. Wang, T. Zhang, W. Deng, S. Sun, and T. Sandy, 'Analytical modeling and prediction of cutting forces in orthogonal turning: a review', *Int. J. Adv. Manuf. Technol.*, pp. 1–28, Nov. 2021, doi: 10.1007/s00170-021-08114-y.

[230] P. Radu and C. Schnakovszky, ‘A Review of Proposed Models for Cutting Force Prediction in Milling Parts with Low Rigidity’, *Machines*, vol. 12, no. 2, p. 140, 2024, doi: 10.3390/machines12020140.

[231] S. L. Soo, D. K. Aspinwall, and R. C. Dewes, ‘3D FE modelling of the cutting of Inconel 718’, *J. Mater. Process. Technol.*, vol. 150, no. 1–2, pp. 116–123, Jul. 2004, doi: 10.1016/j.jmatprotec.2004.01.046.

[232] C. Constantin, S. M. Croitoru, G. Constantin, and C. F. Bisu, ‘3D FEM analysis of cutting processes’, in *Proceedings of the 3rd WSEAS International Conference on Visualization, Imaging and Simulation*, 2010, pp. 41–46.

[233] J. P. Davim and C. A. Conceição António, ‘Optimisation of cutting conditions in machining of aluminium matrix composites using a numerical and experimental model’, *J. Mater. Process. Technol.*, vol. 112, no. 1, pp. 78–82, May 2001, doi: 10.1016/S0924-0136(01)00551-9.

[234] M. Fontaine, A. Devillez, A. Moufki, and D. Dudzinski, ‘Predictive force model for ball-end milling and experimental validation with a wavelike form machining test’, *Int. J. Mach. Tools Manuf.*, vol. 46, no. 3–4, pp. 367–380, Mar. 2006, doi: 10.1016/j.ijmachtools.2005.05.011.

[235] M. E. Merchant, ‘Mechanics of the Metal Cutting Process. I. Orthogonal Cutting and a Type 2 Chip’, *J. Appl. Phys.*, vol. 16, no. 5, pp. 267–275, May 1945, doi: 10.1063/1.1707586.

[236] G. V. Stabler, ‘The chip flow law and its consequences’, *Adv. Mach. Tool Des. Res.*, vol. 5, pp. 243–251, 1964.

[237] E. J. A. Armarego and R. C. Whitfield, ‘Computer based modelling of popular machining operations for force and power prediction’, *CIRP Ann.*, vol. 34, no. 1, pp. 65–69, 1985.

[238] P. L. B. Oxley, *The mechanics of machining: an analytical approach to assessing machinability*. Ellis Horwood, 1989.

[239] S. Qin et al., ‘CWE identification and cutting force prediction in ball-end milling process’, *Int. J. Mech. Sci.*, vol. 239, p. 107863, Feb. 2023, doi: 10.1016/j.ijmecsci.2022.107863.

[240] R. Wang, S. Zhang, R. Ge, X. Luan, J. Wang, and S. Lu, ‘Modified cutting force prediction model considering the true trajectory of cutting edge and in-process workpiece geometry in ball-end milling operation’, *Int. J. Adv. Manuf. Technol.*, vol. 115, no. 4, pp. 1187–1199, Jul. 2021, doi: 10.1007/s00170-021-07285-y.

[241] Y. Altıntaş and P. Lee, ‘Mechanics and Dynamics of Ball End Milling’, *J. Manuf. Sci. Eng.*, vol. 120, no. 4, pp. 684–692, Nov. 1998, doi: 10.1115/1.2830207.

[242] L. Shujuan, Y. Dong, Y. Li, P. Li, Z. Yang, and R. G. Landers, 'Geometrical simulation and analysis of ball-end milling surface topography', *Int. J. Adv. Manuf. Technol.*, vol. 102, no. 5–8, pp. 1885–1900, Jun. 2019, doi: 10.1007/s00170-018-03217-5.

[243] G. M. Kim, P. J. Cho, and C. N. Chu, 'Cutting force prediction of sculptured surface ball-end milling using Z-map', *Int. J. Mach. Tools Manuf.*, vol. 40, no. 2, pp. 277–291, Jan. 2000, doi: 10.1016/S0890-6955(99)00040-1.

[244] V. Imayev, T. Oleneva, R. Imayev, H.-J. Christ, and H.-J. Fecht, 'Microstructure and mechanical properties of low and heavy alloyed γ-TiAl + α_2-Ti_3Al based alloys subjected to different treatments', *Intermetallics*, vol. 26, pp. 91–97, Jul. 2012, doi: 10.1016/j.intermet.2012.03.010.

[245] X. Yue, J. Shen, Y. Xiong, Q. Li, and S. Zheng, 'Microstructure and mechanical properties of as-cast and directionally solidified large size Ti-45Al-8Nb alloys by electromagnetic confinement', *Mater. Sci. Eng. A*, vol. 825, p. 141938, Sep. 2021, doi: 10.1016/j.msea.2021.141938.

[246] V. Imayev, R. Gaisin, A. Rudskoy, T. Nazarova, R. Shaimardanov, and R. Imayev, 'Extraordinary superplastic properties of hot worked Ti-45Al-8Nb-0.2C alloy', *J. Alloys Compd.*, vol. 663, pp. 217–224, Apr. 2016, doi: 10.1016/j.jallcom.2015.11.228.

[247] WIDIA, 'High-Quality Cutting Tools', WIDIA. Accessed: Jul. 30, 2024. [Online]. Available: https://www.widia.com/gb/en/home

[248] ITC, 'ITC products', ITC Industrial Tooling Corporation. Accessed: Jul. 30, 2024. [Online]. Available: https://www.itc-ltd.co.uk/

[249] DMG MORI, 'ULTRASONIC 20 linear', DMG MORI UK. Accessed: Jul. 27, 2024. [Online]. Available: https://uk.dmgmori.com/products/machines/ultrasonic/ultrasonic-linear/ultrasonic-20-linear

[250] *High-accuracy laser tool setting systems*., Renishaw plc., Gloucestershire, UK, 2019.

[251] DMG MORI, 'Ultrasonic'. DMG Mori Seiki Co., Ltd. [Online]. Available: www.DMGMORI.com

[252] Kistler, 'Measurement systems and sensors', Kistler. Accessed: Jul. 27, 2024. [Online]. Available: https://www.kistler.com/GB/en/

[253] *High-accuracy machine tool probes with RENGAGE™ technology*., Renishaw plc., Gloucestershire, UK, 2019.

[254] *Geometrical product specifications (GPS)Surface texture: ProfilePart 3: Specification operators*, ISO 21920-3, 2021.

[255] *Instruction Manual for Micro Hardness Testing Machine Model: HM-112/114/122/124.*, Mitutoyo Ltd., England & Wales, UK, 2000.

[256] W. A. Baeslack, P. A. McQuay, D. S. Lee, and E. D. Fletcher, 'Metallography of gamma titanium aluminides', *Mater. Charact.*, vol. 31, no. 4, pp. 197–207, Dec. 1993, doi: 10.1016/1044-5803(93)90063-2.

[257] J. Wang, H. Zha, P. Feng, and J. Zhang, 'On the mechanism of edge chipping reduction in rotary ultrasonic drilling: A novel experimental method', *Precis. Eng.*, vol. 44, pp. 231–235, Apr. 2016, doi: 10.1016/j.precisioneng.2015.12.008.

[258] J. Wang, P. Feng, J. Zheng, and J. Zhang, 'Improving hole exit quality in rotary ultrasonic machining of ceramic matrix composites using a compound step-taper drill', *Ceram. Int.*, vol. 42, no. 12, pp. 13387–13394, Sep. 2016, doi: 10.1016/j.ceramint.2016.05.095.

[259] C. K. Toh, 'Surface topography analysis in high speed finish milling inclined hardened steel', *Precis. Eng.*, vol. 28, no. 4, pp. 386–398, Oct. 2004, doi: 10.1016/j.precisioneng.2004.01.001.

[260] Y. Dong, S. Li, X. Hong, P. Li, Y. Li, and Q. Li, 'Modeling on the Milling Force of Ball-end Milling Cutter Based on Z-MAP Method', (in Chinese), *J. Mech. Eng.*, vol. 55, no. 19, p. 201, Oct. 2019, doi: 10.3901/JME.2019.19.201.

[261] G. M. Kim, B. H. Kim, and C. N. Chu, 'Estimation of cutter deflection and form error in ball-end milling processes', *Int. J. Mach. Tools Manuf.*, vol. 43, no. 9, pp. 917–924, Jul. 2003, doi: 10.1016/S0890-6955(03)00056-7.

[262] L. Wang, J. Li, Z. C. Chen, and C. Du, 'An efficient approach to calculating the moment of inertia of solid end-mill flutes', in *Proceedings of the 2014 International Conference on Innovative Design and Manufacturing (ICIDM)*, IEEE, Aug. 2014, pp. 161–166. doi: 10.1109/IDAM.2014.6912688.

[263] T. Möller and B. Trumbore, 'Fast, minimum storage ray/triangle intersection', presented at the ACM SIGGRAPH 2005 Courses, ACM Press, 2005, pp. 7-es. doi: 10.1145/1198555.1198746.

[264] Z. Wei, 'Prediction of the Cutting Force and Tool Deflection Error in Ball End Milling of Sculptured Surfaces', (in Chinese), Ph.D. dissertation, Dept. Mech. Eng., Dalian Unvi. Technol., Dalian, China, 2011.

[265] A. Lamikiz, L. N. Lopez de Lacalle, J. A. Sanchez, and U. Bravo, 'Calculation of the specific cutting coefficients and geometrical aspects in sculptured surface machining', *Mach. Sci. Technol.*, vol. 9, no. 3, pp. 411–436, Sep. 2005, doi: 10.1080/15321790500226614.

[266] E. Budak, Y. Altintas¸, and E. J. A. Armarego, 'Prediction of Milling Force Coefficients From Orthogonal Cutting Data', *J. Manuf. Sci. Eng.*, vol. 118, no. 2, pp. 216–224, May 1996, doi: 10.1115/1.2831014.

[267] A. Khatri and M. P. Jahan, 'Investigating tool wear mechanisms in machining of Ti-6Al-4V in flood coolant, dry and MQL conditions', *Procedia Manuf.*, vol. 26, pp. 434–445, 2018, doi: 10.1016/j.promfg.2018.07.051.

[268] S. Sun, M. Brandt, and J. P. Mo, 'Evolution of tool wear and its effect on cutting forces during dry machining of Ti-6Al-4V alloy', *Proc. Inst. Mech. Eng., Part B.*, vol. 228, no. 2, pp. 191–202, Feb. 2014, doi: 10.1177/0954405413500243.

[269] T. H. Childs, *Metal machining: theory and applications*. Butterworth-Heinemann, 2000.

[270] R. Das, S. S. Joshi, and H. C. Barshilia, 'Analytical Model of Progression of Flank Wear Land Width in Drilling', *J. Tribol.*, vol. 141, no. 1, Jan. 2019, doi: 10.1115/1.4040511.

[271] W. Huang, X. Zhang, C. Wu, S. Cao, and Q. Zhou, 'Tool wear prediction in ultrasonic vibration-assisted drilling of CFRP: A hybrid data-driven physics model-based framework', *Tribol. Int.*, vol. 174, p. 107755, Oct. 2022, doi: 10.1016/j.triboint.2022.107755.

[272] K. Zheng, S. Dong, and W. Liao, 'Investigation on thrust force in rotary ultrasonic drilling of CFRP using Brad drill', *Mach. Sci. Technol.*, vol. 23, no. 6, pp. 971–984, Nov. 2019, doi: 10.1080/10910344.2019.1636277.

[273] B. Luo, K. Zhang, Y. Li, H. Cheng, and S. Liu, 'Modelling of thrust force for worn drill bits characterised by cutting edge radius in drilling carbon fibre–reinforced plastic/Ti-6Al-4V alloy stacks', *Proc. Inst. Mech. Eng., Part B.*, vol. 232, no. 11, pp. 1960–1972, Sep. 2018, doi: 10.1177/0954405416682791.

[274] J. Wang, P. Feng, J. Zhang, W. Cai, and H. Shen, 'Investigations on the critical feed rate guaranteeing the effectiveness of rotary ultrasonic machining', *Ultrasonics*, vol. 74, pp. 81–88, Feb. 2017, doi: 10.1016/j.ultras.2016.10.003.

[275] F. Ma, 'The Development of Ultrasonic Assisted Machining System and Its Application in Machining of Composite', (in Chinese), Ph.D. dissertation, Dept. Mech. Eng., Dalian Unvi. Technol., Dalian, China, 2013.

[276] C. Zhang, P. Feng, and Z. Wu, 'Research on the Properties of Ultrasonic Vibration Amplitude and Actual Cutting Depth in Rotary Ultrasonic Machining', (in Chinese), *Acta Armamentarii*, vol. 34, no. 7, pp. 883–888, Jul. 2013.

[277] J. Wang, P. Feng, J. Zhang, and H. Shen, 'Experimental investigation on the effects of thermomechanical loading on the vibrational stability during rotary ultrasonic machining', *Mach. Sci. Technol.*, vol. 21, no. 2, pp. 239–256, Apr. 2017, doi: 10.1080/10910344.2017.1283962.

[278] S. Chen, P. Zou, Y. Tian, J. Duan, and W. Wang, 'Study on modal analysis and chip breaking mechanism of Inconel 718 by ultrasonic vibration-assisted drilling', *Int. J. Adv. Manuf. Technol.*, vol. 105, no. 1–4, pp. 177–191, Nov. 2019, doi: 10.1007/s00170-019-04155-6.

[279] Z. Deyuan and W. Lijiang, 'Investigation of chip in vibration drilling', *Int. J. Mach. Tools Manuf.*, vol. 38, no. 3, pp. 165–176, Feb. 1998, doi: 10.1016/S0890-6955(97)00047-3.

[280] Z. Yang, P. Zou, L. Zhou, and X. Wang, 'Research on the influence of stress wave on crack and chip formation mechanism in radial ultrasonic vibration assisted grinding', *Ultrasonics*, vol. 133, p. 107054, Aug. 2023, doi: 10.1016/j.ultras.2023.107054.

[281] Y. Feng et al., 'Temperature prediction of ultrasonic vibration-assisted milling', *Ultrasonics*, vol. 108, p. 106212, Dec. 2020, doi: 10.1016/j.ultras.2020.106212.

[282] Q. Liu, J. Xu, and H. Yu, 'Experimental study of tool wear and its effects on cutting process of ultrasonic-assisted milling of Ti6Al4V', *Int. J. Adv. Manuf. Technol.*, vol. 108, no. 9–10, pp. 2917–2928, Jun. 2020, doi: 10.1007/s00170-020-05593-3.

[283] B. Gholamzadeh and H. Soleimanimehr, 'Finite element modeling of ultrasonic-assisted turning: cutting force and heat generation', *Mach. Sci. Technol.*, Nov. 2019, doi: 10.1080/10910344.2019.1636266.

[284] M. Lotfi, S. A. Sajjady, and S. Amini, 'Wettability analysis of titanium alloy in 3D elliptical ultrasonic assisted turning', *Int. J. Lightweight Mater. Manuf.*, vol. 2, no. 3, pp. 235–240, Sep. 2019, doi: 10.1016/j.ijlmm.2019.05.001.

[285] W. Chen, L. Zheng, W. Xie, K. Yang, and D. Huo, 'Modelling and experimental investigation on textured surface generation in vibration-assisted micro-milling', *J. Mater. Process. Technol.*, vol. 266, pp. 339–350, Apr. 2019, doi: 10.1016/j.jmatprotec.2018.11.011.

[286] K. Nakayama, M. Arai, and T. Kanda, 'Machining Characteristics of Hard Materials', *CIRP Ann.*, vol. 37, no. 1, pp. 89–92, Jan. 1988, doi: 10.1016/S0007-8506(07)61592-3.

[287] R. Komanduri and R. H. Brown, 'On the Mechanics of Chip Segmentation In Machining', *J. Eng. Ind.*, vol. 103, no. 1, pp. 33–51, Feb. 1981, doi: 10.1115/1.3184458.

[288] J. Gao and X. Jin, 'Effects of Ultrasonic Vibration Assistance on Chip Formation Mechanism in Cutting of Ti–6Al–4V', *J. Manuf. Sci. Eng.*, vol. 141, no. 12, Dec. 2019, doi: 10.1115/1.4045129.

[289] A. Sharman, R. C. Dewes, and D. K. Aspinwall, 'Tool life when high speed ball nose end milling Inconel 718TM', *J. Manuf. Sci. Eng.*, vol. 118, no. 1, pp. 29–35, Dec. 2001, doi: 10.1016/S0924-0136(01)00855-X.

[290] D. C. Montgomery, *Design and analysis of experiments*. John wiley & sons, 2017.

[291] S. Kalpakjian, *Manufacturing processes for engineering materials*. Pearson Education India, 1984.

[292] R. Hood, 'The machinability of a gamma titanium aluminide intermetallic', Ph.D. dissertation, Dept. Mech. Eng., Unvi. Birmingham, Birmingham, UK, 2010.

[293] S. Y. Jin, A. Pramanik, A. K. Basak, C. Prakash, S. Shankar, and S. Debnath, 'Burr formation and its treatments—a review', *Int. J. Adv. Manuf. Technol.*, vol. 107, no. 5–6, pp. 2189–2210, Mar. 2020, doi: 10.1007/s00170-020-05203-2.

[294] M. Hashimura, J. Hassamontr, and D. A. Dornfeld, 'Effect of In-Plane Exit Angle and Rake Angles on Burr Height and Thickness in Face Milling Operation', *J. Manuf. Sci. Eng.*, vol. 121, no. 1, pp. 13–19, Feb. 1999, doi: 10.1115/1.2830566.

[295] H. Gong, F. Z. Fang, X. F. Zhang, J. Du, and X. T. Hu, 'Study on the Reduction Strategy of Machining-Induced Edge Chipping Based on Finite Element Analysis of In-Process Workpiece Structure', *J. Manuf. Sci. Eng.*, vol. 135, no. 1, p. 011017, Feb. 2013, doi: 10.1115/1.4023458.

[296] J. Wang, P. Feng, J. Zhang, C. Zhang, and Z. Pei, 'Modeling the dependency of edge chipping size on the material properties and cutting force for rotary ultrasonic drilling of brittle materials', *Int. J. Mach. Tools Manuf.*, vol. 101, pp. 18–27, Feb. 2016, doi: 10.1016/j.ijmachtools.2015.10.005.

[297] E. S. Costa, M. B. da Silva, and A. R. Machado, 'Burr produced on the drilling process as a function of tool wear and lubricant-coolant conditions', *J. Braz. Soc. Mech. Sci. & Eng.*, vol. 31, no. 1, pp. 57–63, 2009, doi: 10.1590/S1678-58782009000100009.

[298] J. C. Aurich, H. Sudermann, and H. Bil, 'Characterisation of Burr Formation in Grinding and Prospects for Modelling', *CIRP Ann.*, vol. 54, no. 1, pp. 313–316, 2005, doi: 10.1016/S0007-8506(07)60111-5.

[299] M. Malekian, M. G. Mostofa, S. S. Park, and M. B. G. Jun, 'Modeling of minimum uncut chip thickness in micro machining of aluminum', *J. Mater. Process. Technol.*, vol. 212, no. 3, pp. 553–559, Mar. 2012, doi: 10.1016/j.jmatprotec.2011.05.022.

[300] R. T. Coelho, A. E. Diniz, and T. M. da Silva, 'An Experimental Method to Determine the Minimum Uncut Chip Thickness (h_{min}) in Orthogonal Cutting', *Procedia Manuf.*, vol. 10, pp. 194–207, 2017, doi: 10.1016/j.promfg.2017.07.047.

[301] F. B. de Oliveira, A. R. Rodrigues, R. T. Coelho, and A. F. de Souza, 'Size effect and minimum chip thickness in micromilling', *Int. J. Mach. Tools Manuf.*, vol. 89, pp. 39–54, Feb. 2015, doi: 10.1016/j.ijmachtools.2014.11.001.

[302] C.-J. Kim, M. Bono, and J. Ni, 'Experimental analysis of chip formation in micro-milling', *TECHNICAL PAPERS-SOCIETY OF MANUFACTURING ENGINEERS-ALL SERIES*-, May 2002.

[303] A. Madariaga, J. A. Esnaola, E. Fernandez, P. J. Arrazola, A. Garay, and F. Morel, 'Analysis of residual stress and work-hardened profiles on Inconel 718 when face turning with large-nose radius tools', *Int. J. Adv. Manuf. Technol.*, vol. 71, no. 9–12, pp. 1587–1598, 2014, doi: 10.1007/s00170-013-5585-6.

[304] G. S. Fox-Rabinovich et al., 'Effect of mechanical properties measured at room and elevated temperatures on the wear resistance of cutting tools with TiAlN and AlCrN coatings', *Surf. Coat. Technol.*, vol. 200, no. 20–21, pp. 5738–5742, May 2006, doi: 10.1016/j.surfcoat.2005.08.132.

[305] B. D. Beake, J. F. Smith, A. Gray, G. S. Fox-Rabinovich, S. C. Veldhuis, and J. L. Endrino, 'Investigating the correlation between nano-impact fracture resistance and

hardness/modulus ratio from nanoindentation at 25–500°C and the fracture resistance and lifetime of cutting tools with Ti1−xAlxN (x =0.5 and 0.67) PVD coatings in milling operations', *Surf. Coat. Technol.*, vol. 201, no. 8, pp. 4585–4593, Jan. 2007, doi: 10.1016/j.surfcoat.2006.09.118.

[306] A. Biksa et al., 'Wear behavior of adaptive nano-multilayered AlTiN/MexN PVD coatings during machining of aerospace alloys', *Tribol. Int.*, vol. 43, no. 8, pp. 1491–1499, Aug. 2010, doi: 10.1016/j.triboint.2010.02.008.

[307] K. Bobzin, E. Lugscheider, O. Knotek, M. Maes, P. Immich, and C. Piñero, 'Development of Multilayer TiAlN+ γ–Al_2O_3 Coatings for Difficult Machining Operations', *MRS Online Proc. Libr. (OPL)*, vol. 890, pp. 0890-Y01, 2005.

[308] J. M. Vieira, A. R. Machado, and E. O. Ezugwu, 'Performance of cutting fluids during face milling of steels', *J. Mater. Process. Technol.*, vol. 116, no. 2–3, pp. 244–251, Oct. 2001, doi: 10.1016/S0924-0136(01)01010-X.

[309] M. A. Elbestawi, L. Chen, C. E. Becze, and T. I. El-Wardany, 'High-Speed Milling of Dies and Molds in Their Hardened State', *CIRP Ann.*, vol. 46, no. 1, pp. 57–62, 1997, doi: 10.1016/S0007-8506(07)60775-6.

[310] Y. S. Liao and H. M. Lin, 'Mechanism of minimum quantity lubrication in high-speed milling of hardened steel', *Int. J. Mach. Tools Manuf.*, vol. 47, no. 11, pp. 1660–1666, Sep. 2007, doi: 10.1016/j.ijmachtools.2007.01.007.

[311] Y. S. Liao, H. M. Lin, and Y. C. Chen, 'Feasibility study of the minimum quantity lubrication in high-speed end milling of NAK80 hardened steel by coated carbide tool', *Int. J. Mach. Tools Manuf.*, vol. 47, no. 11, pp. 1667–1676, Sep. 2007, doi: 10.1016/j.ijmachtools.2007.01.005.

[312] R. Niu, J. Li, Y. Wang, J. Chen, and Q. Xue, 'Structure and high temperature tribological behavior of TiAlN/nitride duplex treated coatings on Ti6Al4V', *Surf. Coat. Technol.*, vol. 309, pp. 232–241, Jan. 2017, doi: 10.1016/j.surfcoat.2016.05.016.

[313] G. K. Dosbaeva et al., 'Oxide scales formation in nano-crystalline TiAlCrSiYN PVD coatings at elevated temperature', *Int. J. Refract. Met. Hard Mater.*, vol. 28, no. 1, pp. 133–141, Jan. 2010, doi: 10.1016/j.ijrmhm.2009.09.003.

[314] H. C. Barshilia and K. S. Rajam, 'Raman spectroscopy studies on the thermal stability of TiN, CrN, TiAlN coatings and nanolayered TiN/CrN, TiAlN/CrN multilayer coatings', *J. Mater. Res.*, vol. 19, no. 11, pp. 3196–3205, Nov. 2004, doi: 10.1557/JMR.2004.0444.

[315] C. P. Constable, J. Yarwood, G. Robinson, Q. Luo, D. B. Lewis, and W.-D. Münz, 'Investigation of wear processes on worn tools using Raman microscopy', *Surf. Eng.*, vol. 18, no. 2, pp. 127–132, Apr. 2002, doi: 10.1179/026708402225002703.

[316] W. Y. H. Liew, 'Low-speed milling of stainless steel with TiAlN single-layer and TiAlN/AlCrN nano-multilayer coated carbide tools under different lubrication

conditions', *Wear*, vol. 269, no. 7–8, pp. 617–631, Aug. 2010, doi: 10.1016/j.wear.2010.06.012.

[317] G. Xian et al., 'Study on the growth and wear behavior of the TiAlN-based composite coating deposited on TiCN-based cermets with different binder phase', *Wear*, vol. 460–461, p. 203460, Nov. 2020, doi: 10.1016/j.wear.2020.203460.

[318] Q. Cheng, C. Dai, Q. Miao, Z. Yin, J. Chen, and S. Yang, 'Undeformed chip thickness with composite ultrasonic vibration-assisted face grinding of silicon carbide: Modeling, computation and analysis', *Precis. Eng.*, vol. 86, pp. 48–65, Mar. 2024, doi: 10.1016/j.precisioneng.2023.11.005.

[319] Y. Zhang et al., 'Microstructural evolution of soft magnetic 49Fe-49Co-2V alloy induced by drilling', *Mater. Des.*, vol. 189, p. 108501, Apr. 2020, doi: 10.1016/j.matdes.2020.108501.

[320] Z. Dong et al., 'Mechanism of gradient strengthening layer formation based on microstructure and microhardness of Inconel 718 grinding surface', *Int. J. Adv. Manuf. Technol.*, vol. 120, no. 3–4, pp. 2363–2372, May 2022, doi: 10.1007/s00170-022-08857-2.

[321] H. Soyama, C. R. Chighizola, and M. R. Hill, 'Effect of compressive residual stress introduced by cavitation peening and shot peening on the improvement of fatigue strength of stainless steel', *J. Mater. Process. Technol.*, vol. 288, p. 116877, Feb. 2021, doi: 10.1016/j.jmatprotec.2020.116877.

[322] O. Tuysuz, Y. Altintas, and H.-Y. Feng, 'Prediction of cutting forces in three and five-axis ball-end milling with tool indentation effect', *Int. J. Adv. Manuf. Technol.*, vol. 66, pp. 66–81, Mar. 2013, doi: 10.1016/j.ijmachtools.2012.12.002.

[323] J. Xu, C. Li, J. Dang, M. El Mansori, and F. Ren, 'A Study on Drilling High-Strength CFRP Laminates: Frictional Heat and Cutting Temperature', *Materials*, vol. 11, no. 12, p. 2366, Dec. 2018, doi: 10.3390/ma11122366.

[324] Freeman, 'Advanced Materials Technical Datasheet', Freeman. Accessed: Jul. 20, 2024. [Online]. Available: https://www.freemansupply.com/

[325] Matweb, 'Online Materials Information Resource', Matweb. Accessed: Jul. 31, 2024. [Online]. Available: https://www.matweb.com/index.aspx

APPENDIX A SUPPLEMENTAL INFORMATION

Table A.1 Key information of materials used in Phase 2 and Phase 3 experiments [324], [325].

Name	Type of material	Density	Hardness	Young's modulus
BM 5460	Polyurethane	0.70 g/cm^3	~60–65 Shord D	910–960 MPa
AA6082-T6	Aluminium alloy	2.70 g/cm^3	~100 *HV*	70 GPa
Ti-6Al-4V	Titanium alloy	4.43 g/cm^3	~350 *HV*	114 GPa
AISI 4000 Series	Low-alloy steel	7.85 g/cm^3	~400 *HV*	190–210 GPa

Table A.2 F-table of critical values for significance level = 0.10 [290].

	F-table of Critical Values of α = 0.10 for F(df1, df2)																		
	DF1=1	**2**	**3**	**4**	**5**	**6**	**7**	**8**	**9**	**10**	**12**	**15**	**20**	**24**	**30**	**40**	**60**	**120**	**∞**
DF2=1	39.86	49.50	53.59	55.83	57.24	58.20	58.91	59.44	59.86	60.19	60.71	61.22	61.74	62.00	62.26	62.53	62.79	63.06	63.33
2	8.53	9.00	9.16	9.24	9.29	9.33	9.35	9.37	9.38	9.39	9.41	9.42	9.44	9.45	9.46	9.47	9.47	9.48	9.49
3	5.54	5.46	5.39	5.34	5.31	5.28	5.27	5.25	5.24	5.23	5.22	5.20	5.18	5.18	5.17	5.16	5.15	5.14	5.13
4	4.54	4.32	4.19	4.11	4.05	4.01	3.98	3.95	3.94	3.92	3.90	3.87	3.84	3.83	3.82	3.80	3.79	3.78	3.76
5	4.06	3.78	3.62	3.52	3.45	3.40	3.37	3.34	3.32	3.30	3.27	3.24	3.21	3.19	3.17	3.16	3.14	3.12	3.11
6	3.78	3.46	3.29	3.18	3.11	3.05	3.01	2.98	2.96	2.94	2.90	2.87	2.84	2.82	2.80	2.78	2.76	2.74	2.72
7	3.59	3.26	3.07	2.96	2.88	2.83	2.78	2.75	2.72	2.70	2.67	2.63	2.59	2.58	2.56	2.54	2.51	2.49	2.47
8	3.46	3.11	2.92	2.81	2.73	2.67	2.62	2.59	2.56	2.54	2.50	2.46	2.42	2.40	2.38	2.36	2.34	2.32	2.29
9	3.36	3.01	2.81	2.69	2.61	2.55	2.51	2.47	2.44	2.42	2.38	2.34	2.30	2.28	2.25	2.23	2.21	2.18	2.16
10	3.29	2.92	2.73	2.61	2.52	2.46	2.41	2.38	2.35	2.32	2.28	2.24	2.20	2.18	2.16	2.13	2.11	2.08	2.06
11	3.23	2.86	2.66	2.54	2.45	2.39	2.34	2.30	2.27	2.25	2.21	2.17	2.12	2.10	2.08	2.05	2.03	2.00	1.97
12	3.18	2.81	2.61	2.48	2.39	2.33	2.28	2.24	2.21	2.19	2.15	2.10	2.06	2.04	2.01	1.99	1.96	1.93	1.90
13	3.14	2.76	2.56	2.43	2.35	2.28	2.23	2.20	2.16	2.14	2.10	2.05	2.01	1.98	1.96	1.93	1.90	1.88	1.85
14	3.10	2.73	2.52	2.39	2.31	2.24	2.19	2.15	2.12	2.10	2.05	2.01	1.96	1.94	1.91	1.89	1.86	1.83	1.80
15	3.07	2.70	2.49	2.36	2.27	2.21	2.16	2.12	2.09	2.06	2.02	1.97	1.92	1.90	1.87	1.85	1.82	1.79	1.76
16	3.05	2.67	2.46	2.33	2.24	2.18	2.13	2.09	2.06	2.03	1.99	1.94	1.89	1.87	1.84	1.81	1.78	1.75	1.72
17	3.03	2.64	2.44	2.31	2.22	2.15	2.10	2.06	2.03	2.00	1.96	1.91	1.86	1.84	1.81	1.78	1.75	1.72	1.69
18	3.01	2.62	2.42	2.29	2.20	2.13	2.08	2.04	2.00	1.98	1.93	1.89	1.84	1.81	1.78	1.75	1.72	1.69	1.66
19	2.99	2.61	2.40	2.27	2.18	2.11	2.06	2.02	1.98	1.96	1.91	1.86	1.81	1.79	1.76	1.73	1.70	1.67	1.63
20	2.97	2.59	2.38	2.25	2.16	2.09	2.04	2.00	1.96	1.94	1.89	1.84	1.79	1.77	1.74	1.71	1.68	1.64	1.61
21	2.96	2.57	2.36	2.23	2.14	2.08	2.02	1.98	1.95	1.92	1.87	1.83	1.78	1.75	1.72	1.69	1.66	1.62	1.59
22	2.95	2.56	2.35	2.22	2.13	2.06	2.01	1.97	1.93	1.90	1.86	1.81	1.76	1.73	1.70	1.67	1.64	1.60	1.57
23	2.94	2.55	2.34	2.21	2.11	2.05	1.99	1.95	1.92	1.89	1.84	1.80	1.74	1.72	1.69	1.66	1.62	1.59	1.55
24	2.93	2.54	2.33	2.19	2.10	2.04	1.98	1.94	1.91	1.88	1.83	1.78	1.73	1.70	1.67	1.64	1.61	1.57	1.53
25	2.92	2.53	2.32	2.18	2.09	2.02	1.97	1.93	1.89	1.87	1.82	1.77	1.72	1.69	1.66	1.63	1.59	1.56	1.52
26	2.91	2.52	2.31	2.17	2.08	2.01	1.96	1.92	1.88	1.86	1.81	1.76	1.71	1.68	1.65	1.61	1.58	1.54	1.50
27	2.90	2.51	2.30	2.17	2.07	2.00	1.95	1.91	1.87	1.85	1.80	1.75	1.70	1.67	1.64	1.60	1.57	1.53	1.49
28	2.89	2.50	2.29	2.16	2.06	2.00	1.94	1.90	1.87	1.84	1.79	1.74	1.69	1.66	1.63	1.59	1.56	1.52	1.48
29	2.89	2.50	2.28	2.15	2.06	1.99	1.93	1.89	1.86	1.83	1.78	1.73	1.68	1.65	1.62	1.58	1.55	1.51	1.47
30	2.88	2.49	2.28	2.14	2.05	1.98	1.93	1.88	1.85	1.82	1.77	1.72	1.67	1.64	1.61	1.57	1.54	1.50	1.46
40	2.84	2.44	2.23	2.09	2.00	1.93	1.87	1.83	1.79	1.76	1.71	1.66	1.61	1.57	1.54	1.51	1.47	1.42	1.38
60	2.79	2.39	2.18	2.04	1.95	1.87	1.82	1.77	1.74	1.71	1.66	1.60	1.54	1.51	1.48	1.44	1.40	1.35	1.29
120	2.75	2.35	2.13	1.99	1.90	1.82	1.77	1.72	1.68	1.65	1.60	1.55	1.48	1.45	1.41	1.37	1.32	1.26	1.19
∞	2.71	2.30	2.08	1.94	1.85	1.77	1.72	1.67	1.63	1.60	1.55	1.49	1.42	1.38	1.34	1.30	1.24	1.17	1.00

APPENDIX B ADDITIONAL RESULTS

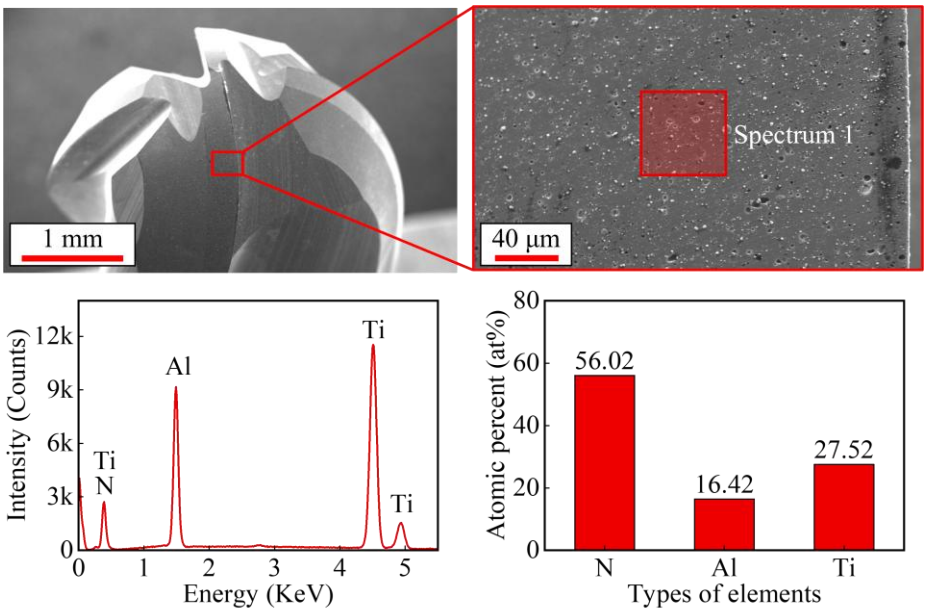


Figure B.1 EDS analysis of the TiAlN coated tool under new condition.

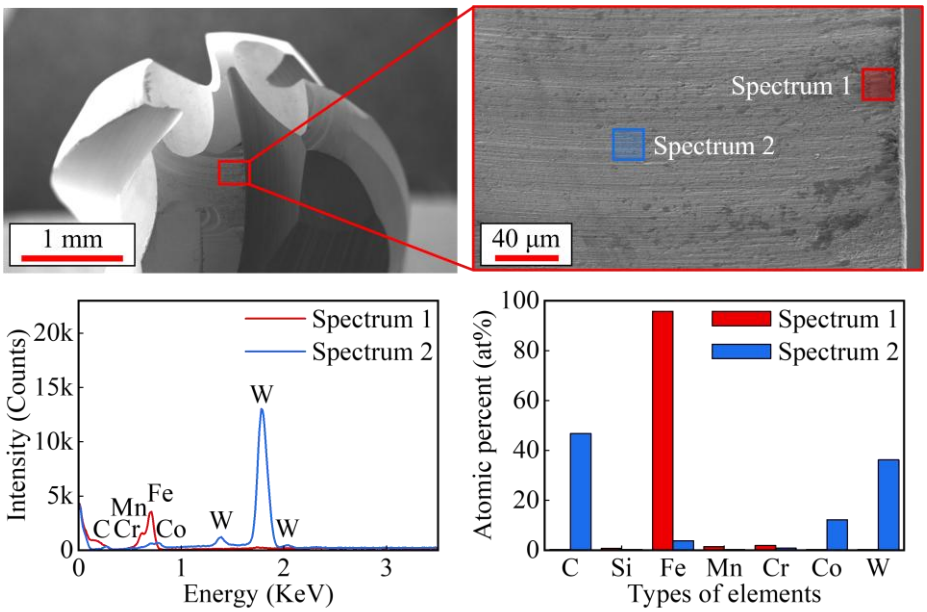


Figure B.2 EDS analysis of the worn tool (no coating) surface produced in milling low-alloy steel in dry cut conditions.

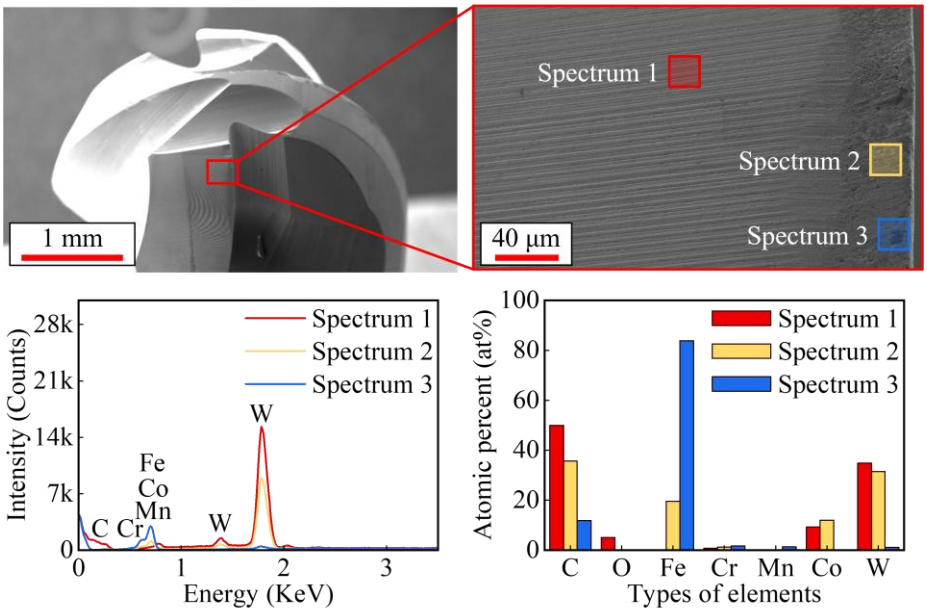


Figure B.3 EDS analysis of the worn tool (no coating) surface produced in milling low-alloy steel in wet cut conditions.

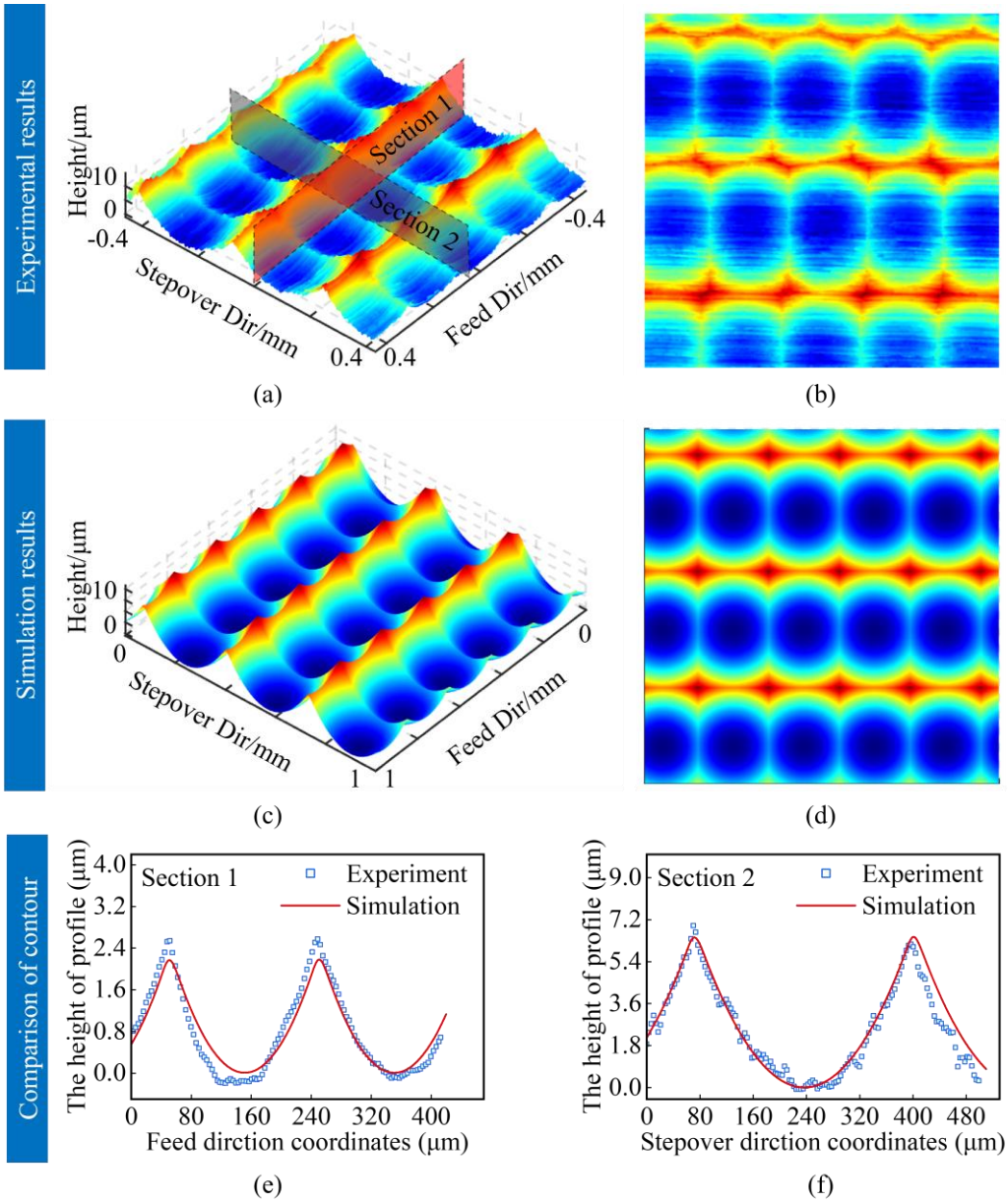


Figure B.4 Schematic diagram of comparison between modelling prediction and experimental results of machined surface morphology (N = 3000 rpm, f_z = 0.10 mm/tooth, a_p = 0.4 mm, a_e = 0.33 mm, α = 30°, A_U = 0 μm).

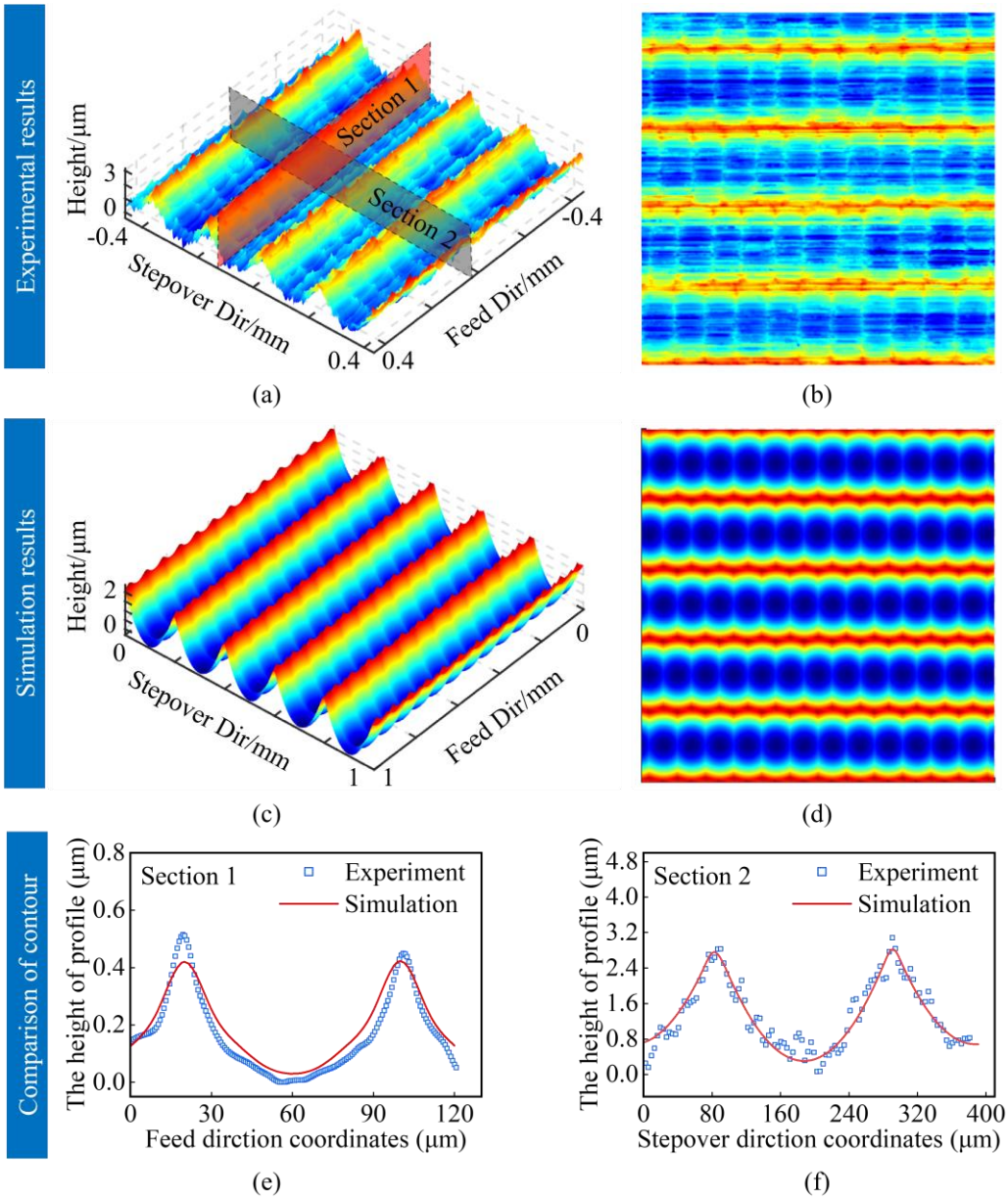


Figure B.5 Schematic diagram of comparison between modelling prediction and experimental results of machined surface morphology (N = 6000 rpm, f_z = 0.04 mm/tooth, a_p = 0.2 mm, a_e = 0.2 mm, α = 30°, A_U = 0 μm).

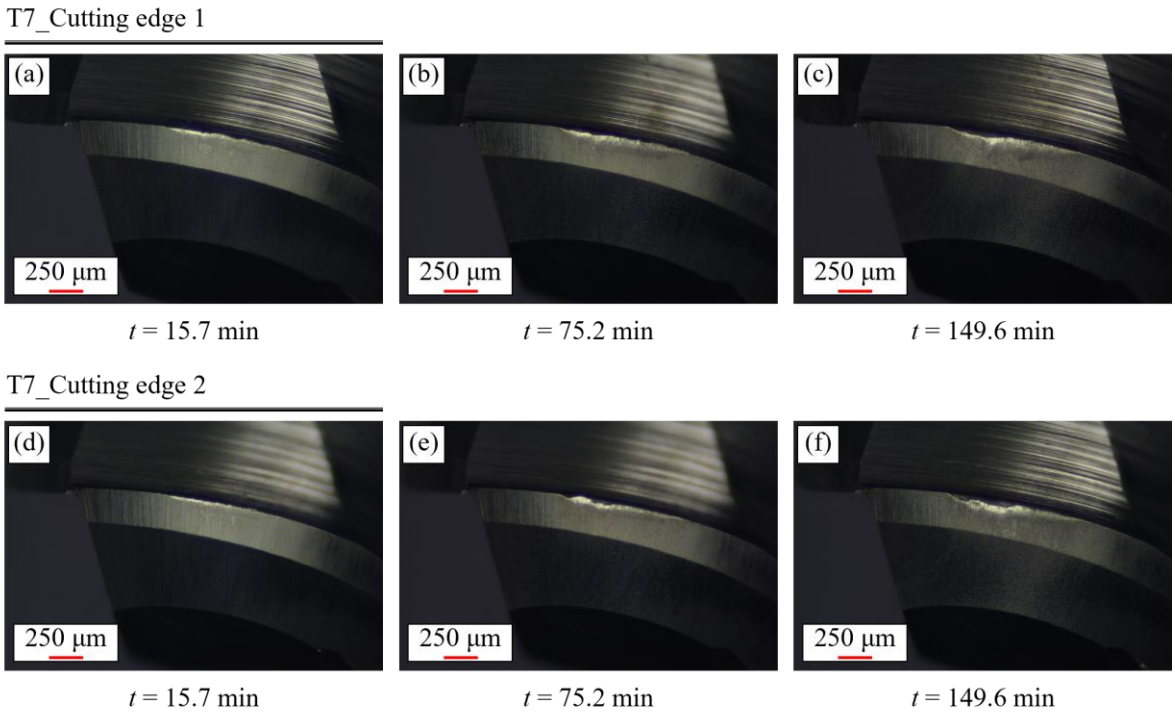


Figure B.6 Tool flank wear evolution for T7 (N = 3000 rpm, f_z = 0.06 mm/tooth, a_p = 0.15 mm, a_e = 0.20 mm, α = 45°, A_U = 6 µm).

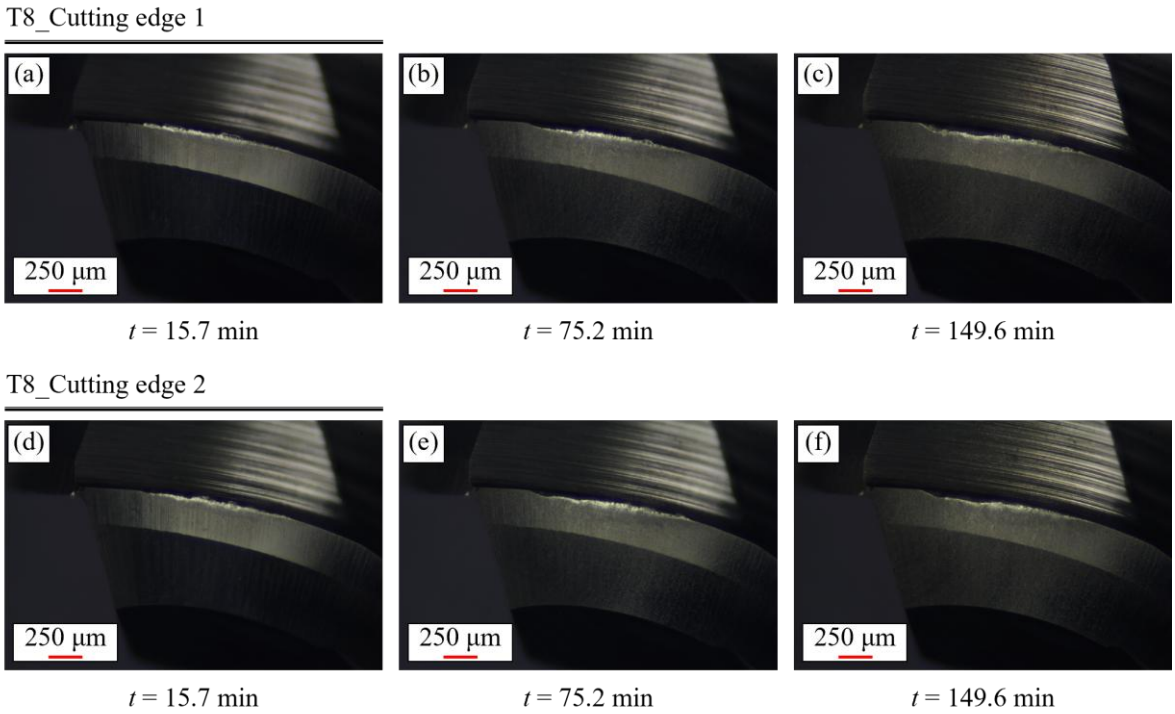


Figure B.7 Tool flank wear evolution for T8 (N = 3000 rpm, f_z = 0.06 mm/tooth, a_p = 0.25 mm, a_e = 0.20 mm, α = 45°, A_U = 6 µm).

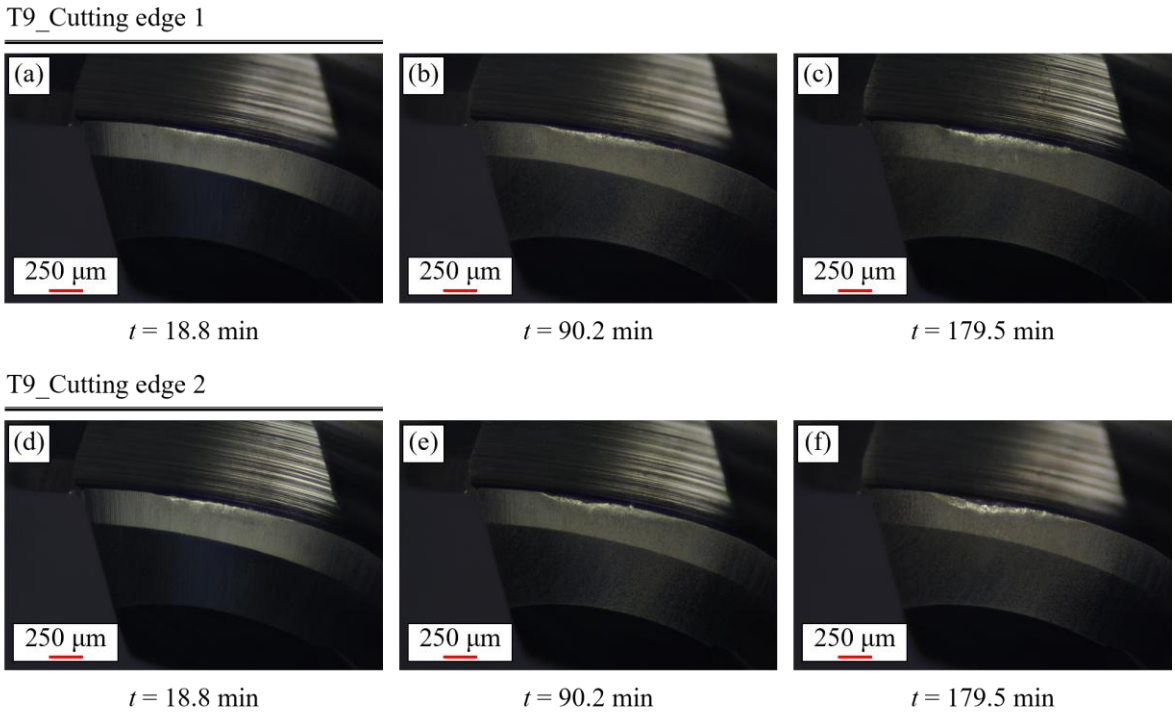


Figure B.8 Tool flank wear evolution for T9 (N = 3000 rpm, f_z = 0.05 mm/tooth, a_p = 0.20 mm, a_e = 0.20 mm, α = 45°, A_U = 6 µm).

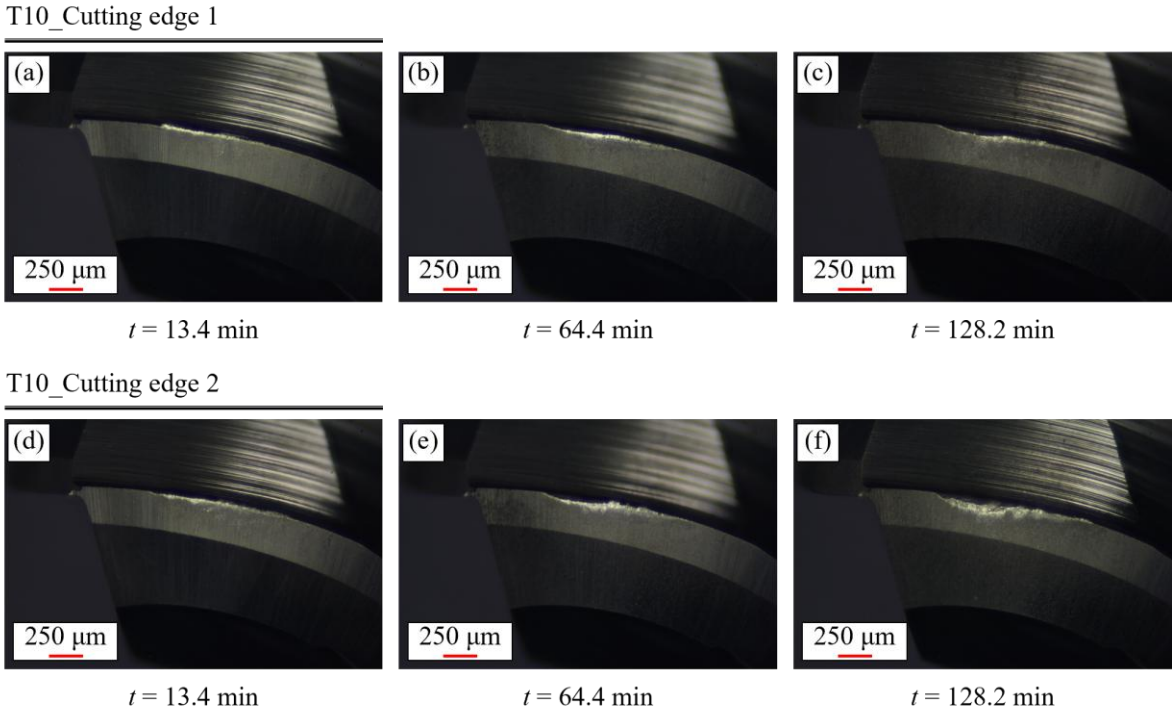


Figure B.9 Tool flank wear evolution for T10 (N = 3000 rpm, f_z = 0.07 mm/tooth, a_p = 0.20 mm, a_e = 0.20 mm, α = 45°, A_U = 6 µm).

APPENDIX C PUBLICATIONS UNDER PREPARATION

- M. Zhang, S. L. Soo, R. Hood, 'The influences of cutting parameters on workpiece surface integrity in milling γ-TiAl', *J. Mater. Process. Technol.*. (Phase 1)
- M. Zhang, S. L. Soo, R. Hood, 'Tool wear mechanisms and failure in ball-end ultrasonic-assisted milling γ-TiAl with TiAlN coated tools', *Wear*. (Phase 2A)
- M. Zhang, S. L. Soo, R. Hood, 'Ultrasonic-assisted milling γ-TiAl: A comparative study of tool wear and workpiece surface integrity', *J. Manuf. Process.*. (Phase 2B)
- M. Zhang, S. L. Soo, R. Hood, 'Predictive modelling of surface geometrical morphology in ball-end ultrasonic-assisted milling', *Int. J. Adv. Manuf. Technol.*. (Phase 3A)
- M. Zhang, S. L. Soo, R. Hood, 'Predictive modelling and experimental validation of ball-end ultrasonic-assisted milling forces with progressive tool flank wear', *Int. J. Mech. Sci.*. (Phase 3B and 3C)